Physics of the Solid State, Vol. 43, No. 2, 2001, pp. 199–206. Translated from Fizika Tverdogo Tela, Vol. 43, No. 2, 2001, pp. 193–199.

METALS AND SUPERCONDUCTORS

Redistribution of Deuterium Atoms in HfV_2D_x Compounds

I. G. Ratishvili* and N. Z. Namoradze**

** Institute of Physics, Academy of Sciences of Georgia, ul. Guramishvili 6, Tbilisi, 380077 Georgia*
e-mail: rati@physics.iberiapac.ge

*** Institute of Cybernetics, Academy of Sciences of Georgia, Tbilisi, 380086 Georgia*
e-mail: namor@cybem.acnet.ge

Received January 27, 2000; in final form, June 16, 2000

Abstract—A solution of hydrogen in the AB_2 intermetallic compound with a *C*-15 structure is considered. The ordering of hydrogen atoms is investigated, which consists in forming their unequal distribution among the sublattices of the A_2B_2 interstices. It is demonstrated on the basis of qualitative analysis and numerical calculations that, in HfV_2D_x compounds, the evolution of the redistribution of the interstitial atoms and their low-temperature order can be different depending on the hydrogen content in the solution and the energy parameter of the system $p \equiv V_2/V_1$. *© 2001 MAIK "Nauka/Interperiodica".*

INTRODUCTION

In AB_2 intermetallic compounds with a *C*-15 structure ($ZrTi_2$, HfV_2, TaV_2, YFe_2, etc.), interstitial hydrogen (deuterium) atoms are distributed among the AB_3 and A_2B_2 interstices [1–4]. The former interstices are called the *e*-type interstices (32 interstices per unit cell), and the latter are referred to as the *g*-type interstices (96 interstices per unit cell). A set of *e* interstices is partitioned into 8 face-centered cubic (FCC) sublattices, and a set of *g* interstices, into 24 FCC sublattices. In $ZrTi_2H_4$ compounds, hydrogen atoms occupy *e* interstices [1], whereas in TaV_2D_x ($1.3 < x < 1.6$), they are concentrated in g interstices [3]. In YFe_2D_x ($1.3 < x < 2.9$), deuterium is located in interstices of both types [4].

The following is known about the HfV_2D_x system under investigation [2]. The metallic matrix HfV_2 with a *C*-15 structure is cubic at $T > 120$ K and undergoes distortions at lower temperatures. At room temperature and H_2 pressure of dozens of atmospheres, the metal lattice absorbs hydrogen up to the composition $HfV_2H_{4.5}$. Hydrogen (deuterium) starts to escape from the sample only when $T > 400$ K. The majority of D atoms are located in the *g*-type interstices, and only a certain part of them occupies *e* interstices [2]. As the temperature decreases, all D atoms are concentrated in *g* interstices [2]. (The H and D interstitial atoms are almost identically distributed in the lattice, and in the following, we will disregard their isotopic difference.) In the HfV_2H_4 compound, hydrogen atoms at low temperatures are nonequiprobably distributed over *g* interstices, i.e., predominantly occupy several *g* sublattices, which results in the corresponding distortion of the matrix [2]. This process is referred to as orientation ordering of hydrogen [5]. Formation of the superstructure in a single sublattice is not observed even down to liquid-helium temperatures [2].

In the following consideration, we will assume that, in the temperature range covered, the composition $HfV_2H(D)_x$ does not vary and that hydrogen is distributed only in the *g*-type interstices.

Reasoning from the model of the static concentration waves for several sublattices [6], Irodova [5] listed all possible nonequiprobable distributions of the interstitial atoms among 24 sublattices and singled out the unique distribution which, in the HfV_2D_4 compound, corresponds to the stoichiometric composition of the solid solution and satisfies the requirements of the interlocking effect in the hydrogen–hydrogen interaction. Note that the interlocking effect limits the minimum distance at which the interstitial H atoms can be located in this compound. It was found that the corresponding distribution function has two long-range order parameters.

The goal of this work was to describe the evolution of the ordering in the $HfV_2H(D)_x$ system by the distribution function of hydrogen in *g* sublattices, which was proposed in [5] for the HfV_2D_4 compound.

2. MATHEMATICAL FORMULATION OF THE PROBLEM

Under conditions of nonequiprobable distribution of the interstitial atoms over the sublattices and the absence of a superstructure in each of them, the forming structure can be specified by a set of the hydrogen concentrations in each of the sublattices $n(z)$ ($z = 1, 2, \ldots, 24$). Irodova [5] introduced a certain numbering of *g* sublattices and proposed the following distribution function for the HfV_2D_4 system:

$$n(z) = [c\mathbf{w}_1 + \eta_1\gamma_1(\mathbf{w}_2 - 2\mathbf{w}_3) + \eta_2\gamma_2\mathbf{w}_4]_z. \qquad (1)$$

Here, $n(z)$ is defined as the ratio N_z/N, where N_z is the number of interstitial atoms in the z sublattice with N sites; $\mathbf{w}_i$ are the vectors in a 24-dimensional space of FCC sublattices [5]

$$\begin{aligned}\mathbf{w}_1 &= \{111111111111111111111111\},\\ \mathbf{w}_2 &= \{1111\bar{1}\bar{1}\bar{1}\bar{1}0000111\bar{1}\bar{1}\bar{1}\bar{1}0000\},\\ \mathbf{w}_3 &= \{11110000\bar{1}\bar{1}\bar{1}\bar{1}11110000\bar{1}\bar{1}\bar{1}\bar{1}\},\\ \mathbf{w}_4 &= \{11\bar{1}\bar{1}\bar{1}\bar{1}1100001\bar{1}\bar{1}\bar{1}\bar{1}110000\};\end{aligned} \tag{2}$$

the symbol $[\ldots]_z$ denotes the z component of the vector; η_1 and η_2 are the order parameters which describe the degree of ordering; γ_1 and γ_2 are normalizing factors; and c is the mean concentration of hydrogen in a single sublattice,

$$c = \Sigma_z n(z)/24. \tag{3}$$

(Compound AB_2H_4 corresponds to the value $c = 1/3$.)

Function (1) does not depend on the coordinates of the sites in the sublattice and is a function of only the temperature (due to the temperature dependence of the order parameters). For different z, this function takes the following three values:

$$n_1 = c + \eta_1\gamma_1 + \eta_2\gamma_2 \quad (z = 1, 2, 7, 8, 13, 14, 19, 20), \tag{4a}$$

$$n_2 = c + \eta_1\gamma_1 - \eta_2\gamma_2 \quad (z = 3, 4, 5, 6, 15, 16, 17, 18), \tag{4b}$$

$$n_3 = c - 2\eta_1\gamma_1 \quad (z = 9, 10, 11, 12, 21, 22, 23, 24). \tag{4c}$$

The values $[\eta_1 = 1, \eta_2 = 1]$ correspond to the total order of the type $[n_1 = 1, n_2 = 0, n_3 = 0]$, which is achieved when

$$c = 1/3, \quad \gamma_1 = 1/6, \quad \gamma_2 = 1/2. \tag{5}$$

Below, it will be seen that at the same values of c, γ_1, and γ_2, the total order can also be described by a set of occupation numbers $[n_1 = 0, n_2 = 0, n_3 = 1]$ which correspond to the order parameters $[\eta_1 = -2, \eta_2 = 0]$. (The total disorder, $n_1 = n_2 = n_3 = c$, corresponds to values $[\eta_1 = 0, \eta_2 = 0]$.)

In the case when $c \neq 1/3$, as the temperature decreases, only the state of the maximum order is achieved if at least one of the occupation numbers n_i is not equal to 0 or 1.

Our purpose was to determine the temperature dependences of the equilibrium order parameters $\eta_1(T)$ and $\eta_2(T)$ and the equilibrium occupation numbers of the sublattices $n_1(T)$, $n_2(T)$, and $n_3(T)$. Usually, $\eta_1(T)$ and $\eta_2(T)$ are determined as the coordinates of the absolute minimum of the free energy $F(\eta_1, \eta_2; c, T)$. Thus, the problem is reduced to the determination of the free energy function of the hydrogen subsystem and the search for its extrema.

3. SOLUTION OF THE PROBLEM

3.1. The free energy function of the ordering subsystem. From the definition of entropy $S = k_B \ln W$, where W is the number of microscopic states which correspond to a given macroscopic state (in our case, to a given number of the interstitial atoms), and taking into account the partitions of g positions into Z_0 sublattices, we obtain the following expression for the entropy of the subsystem of H atoms:

$$S(H) = k_B\Sigma_z \ln\{N!/[N_z!(N - N_z)!]\} \quad (z = 1, 2, \ldots, Z_0), \tag{6}$$

where $N_z = Nn(z)$. Taking into account that $n(z)$ can take only three different values [see Eq. (3)] and that the number of sublattices for which $n(z) = n_1$, n_2, and n_3 is the same and is equal to $\nu = Z_0/3$, we have

$$S(H) = -(NZ_0k_B/3)\Sigma_j[n_j \ln n_j + (1 - n_j)\ln(1 - n_j)] \quad (j = 1, 2, 3). \tag{7}$$

The interaction energy of the interstitial atoms can be represented in the form

$$E(H) = (1/2)\Sigma_{\mathbf{r},\mathbf{r}'}V(\mathbf{r} - \mathbf{r}')n(\mathbf{r})n(\mathbf{r}'), \tag{8}$$

where $V(\mathbf{r} - \mathbf{r}')$ is the potential of the H–H interaction, $n(\mathbf{r})$ designates the probability that the H atom occupies the interstice with the radius vector $\mathbf{r}$; and $\mathbf{r}$ and $\mathbf{r}'$ run through all interstices of the A_2B_2 type.

Taking into account that $\mathbf{r}$ can be represented in the form $\mathbf{r} = \mathbf{R} + \mathbf{h}_p$ (where $\mathbf{R}$ runs through all sites of a single FCC sublattice of A atoms and vector $\mathbf{h}_p$ enumerates all 24 A_2B_2 interstices which surround a given A atom) and that in each of these 24 sublattices no superstructure is formed, we can write $V(\mathbf{r} - \mathbf{r}') = V_{z,z'}(\mathbf{R} - \mathbf{R}')$ and represent the sum in Eq. (8) in the form

$$E(H) = (N/2)\Sigma_{z,z'}V_{z,z'}(0)n(z)n(z'), \tag{9}$$

where

$$V_{z,z'}(0) \equiv (1/N)\Sigma_{\mathbf{R},\mathbf{R}'}V_{z,z'}(\mathbf{R} - \mathbf{R}') \tag{10}$$

and $n(z)$ and $n(z')$ are given by expression (1).

It can be shown by substitution of expression (1) into Eq. (9) that this equation can be reduced to the following form:

$$E(\eta_1, \eta_2) = (Nk_B/2) \times \{V_0c^2 + V_1(\eta_1\gamma_1)^2 + V_2(\eta_2\gamma_2)^2\}, \tag{11}$$

where V_0, V_1, and V_2 are the energy constants (in Kelvins),

$$V_0 \equiv (24/k_B)[v_1 + 2v_2 + 2v_3 + 4v_4],$$
$$V_1 \equiv (24/k_B)[2(v_1 - v_2) + 4(v_3 - v_4)], \quad (12)$$
$$V_2 \equiv (16/k_B)[v_1 - v_2 + 2(v_3 - v_5)].$$

Here, v_1, …, v_5 are the linear combinations of the Fourier components of the H–H interaction potential,

$$v_1 \equiv V_{1.1}(0) + V_{1.3}(0) + V_{1.14}(0) + V_{1.16}(0),$$
$$v_2 \equiv V_{1.5}(0) + V_{1.6}(0) + V_{1.17}(0) + V_{1.18}(0),$$
$$v_3 \equiv V_{1.2}(0) + V_{1.13}(0), \quad v_4 \equiv V_{1.7}(0) + V_{1.19}(0), \quad (13)$$
$$v_5 \equiv V_{1.3}(0) + V_{1.16}(0),$$

where terms $V_{z,z'}(0)$ are determined by formula (10).

Thus, the free energy $F(H) = E(H) - TS(H)$ for all H atoms which are located in the Z_0 interstitial sublattices is represented as

$$F(\eta_1, \eta_2; c, T) = Nk_B\{(1/2) \times [V_0c^2 + V_1(\eta_1\gamma_1)^2 + V_2(\eta_2\gamma_2)^2] + T(Z_0/3)\Sigma_{j=1,2,3}[n_j \ln n_j + (1-n_j)\ln(1-n_j)]\}, \quad (14)$$

where the occupation numbers of the sublattices n_j (j = 1, 2, 3) are determined by formulas (4). The total number of H atoms which are located in all sublattices, $N_H = \Sigma_z N_z$, is assumed to be constant.

3.2. Extrema of the free energy function. It is well known that the coordinates of the extrema of the $F(\eta_1, \eta_2; c, T)$ function in the (η_1, η_2) plane should satisfy the equations

$$\partial F/\partial\eta_1 = 0, \quad \partial F/\partial\eta_2 = 0, \quad (15)$$

which, in the case of function (14), take the following form:

$$\ln\{n_1n_2(1-n_3)^2/[(1-n_1)(1-n_2)n_3^2]\} = -V_1\eta_1\gamma_1/8T, \quad (16a)$$

$$\ln\{n_1(1-n_2)/[(1-n_1)n_2]\} = -V_2\eta_2\gamma_2/8T. \quad (16b)$$

The type of extremum is determined by the determinant $\Delta(\eta_1, \eta_2; c, T)$,

$$\Delta(\eta_1, \eta_2; c, T) = (\partial^2F/\partial\eta_1^2)(\partial^2F/\partial\eta_2^2) - (\partial^2F/\partial\eta_1\partial\eta_2)^2. \quad (17)$$

In the case of function (14), we have

$$(\partial^2F/\partial\eta_1^2) = Nk_B\gamma_1^2\{V_1 + 8T[(n_1(1-n_1))^{-1} + (n_2(1-n_2))^{-1} + 4(n_3(1-n_1))^{-1}]\}, \quad (18a)$$

$$(\partial^2F/\partial\eta_2^2) = Nk_B\gamma_2^2\{V_2 + 8T[(n_1(1-n_1))^{-1} + (n_2(1-n_2))]\}^{-1}, \quad (18b)$$

$$(\partial^2F/\partial\eta_1\partial\eta_2) = 8Nk_BT\gamma_1\gamma_2 \times [(n_1(1-n_1))^{-1} - (n_2(1-n_2))^{-1}]. \quad (18c)$$

The minimum corresponds to $\Delta(\eta_1, \eta_2) > 0$ and $(\partial^2F/\partial\eta_1^2) > 0$; the maximum, to $\Delta(\eta_1, \eta_2) > 0$ and $(\partial^2F/\partial\eta_1^2) < 0$; and the saddle point, to $\Delta(\eta_1, \eta_2) < 0$.

3.3. The domain of the free energy function. Function (14) is defined in the P' domain of the (η_1, η_2) plane in which the occupation numbers of the sites of the sublattices (n_1, n_2, n_3) simultaneously satisfy the conditions

$$0 \le n_j \le 1 \quad (j = 1, 2, 3). \quad (19)$$

The form of the P' domain depends on the concentration c of the solution, but in any event, it is symmetric with respect to the axis η_1, since function (14) is invariant with respect to the replacement of η_2 by $-\eta_2$ (when $n_1 \longrightarrow n_2$, $n_2 \longrightarrow n_1$). This means that if the state $\{\eta_1(T), \eta_2(T)\}$ is an equilibrium state, the state $\{\eta_1(T), -\eta_2(T)\}$ will also be an equilibrium state. Therefore, the domain of the definition P' can be treated as two "half-domains" P which are located in the half-planes $\eta_2 > 0$ and $\eta_2 < 0$ (Fig. 1).

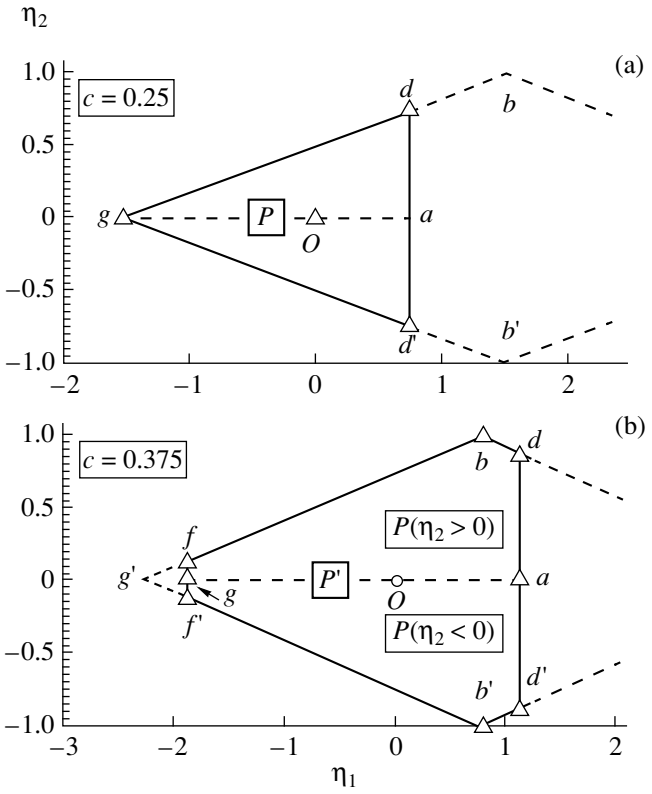

Fig. 1. Domains P' of the free energy function. c = 0.25 and 0.375.

Table 1. Characteristics of the corner points of domain P in which the free energy function (14) is defined for $c < 1/3$ and $c > 1/3$

c	i		$\eta_1(i)$	$\eta_2(i)$	$\varepsilon(i)$
$<1/3$	g	$n_2 = 0$ $\eta_2 = 0$	$-c\gamma_1$	0	V_1c^2
	d	$n_2 = 0$ $n_3 = 0$	$c/2\gamma_1$	$3c/2\gamma_2$	$c^2/4(V_1 + 9V_2)$
$>1/3$	f	$n_3 = 1$ $n_2 = 0$	$-[(1-c)/2\gamma_1]$	$(3c-1)/2\gamma_2$	$[V_1(1-c)^2 + V_2(3c-1)^2]/4$
	b	$n_1 = 1$ $n_2 = 0$	$(0.5-c)/\gamma_1$	1	$V_1(0.5-c)^2 + V_2\gamma_2^2$
	d	$n_1 = 1$ $n_3 = 0$	$c/2\gamma_1$	$(2-3c)/2\gamma_2$	$[V_1c^2 + V_2(2-3c)^2]/4$

Note: The conditions which determine the corner points, the coordinates of corner points, and relative values of the energy at these points are given.

Earlier [7, 8], we showed that in the limits of domain P', the ordering in the temperature range from $T = T_k$ at point O (η_1, $\eta_2 = 0$) to $T = 0$ K at one of the corner points f, b, or d (or at the similar points f', b', and d') is described by a sequence of equilibrium states located within the limits of one half-plane. Therefore, we will restrict our consideration to the analysis of the free energy extrema located within the limits of one of the "half-domains" P when $\eta_2 \geq 0$.

3.4 Analytical treatment of extrema of the *F* function. It is clear that along the η_1 axis, where $n_1 = n_2 = c + \eta_1\gamma_1 \equiv n_0$, Eq. (16b) is satisfied at all points, and each value of η_1 can be related to temperature $T_1(\eta_1)$,

$$T_1(\eta_1) = -(V_1\gamma_1/8)\eta_1/[2\ln\{n_0 \times (1-n_3)/[(1-n_0)n_3]\}], \quad (20)$$

at which Eq. (16a) is also satisfied. The type of this extremum is specified by determinant (17), which in this particular case takes the following form [8]:

$$\Delta(\eta_1, 0; c, T) = (Nk_B)^2\gamma_1^2\gamma_2^2V_1V_2 \times (1-[T_1(\eta_1)/\tau_1(\eta_1)])(1-[T_1(\eta_1)/\tau_2(\eta_1)]). \quad (21)$$

Here, we introduced the temperature parameters $\tau_1(\eta_1)$ and $\tau_2(\eta_1)$,

$$\tau_1(\eta_1) \equiv -(V_1/16)\{[n_0(1-n_0)]^{-1} + 2[n_3(1-n_3)]^{-1}\}^{-1}, \quad (22a)$$

$$\tau_2(\eta_1) \equiv -(V_2/16)[n_0(1-n_0)]. \quad (22b)$$

Note that the stability of the ordered state implies negative values of V_1 and V_2. Then, it is evident from expressions (21) and (22) that the extremum on the η_1 axis is a minimum if $T_1(\eta_1) > \tau_1(\eta_1)$ and $\tau_2(\eta_1)$, a maximum if $T_1(\eta_1) < \tau_1(\eta_1)$ and $\tau_2(\eta_1)$, and a saddle point if $T_1(\eta_1)$ falls in the range between $\tau_1(\eta_1)$ and $\tau_2(\eta_1)$.

Let us consider the straight line $\eta_2 = \eta_1$. Along this line, we have $n_2(\eta_1, \eta_2) = n_3(\eta_1)$. In this case, with the additional constraint $V_2 = V_1 \equiv V$, Eqs. (16a) and (16b) coincide and are satisfied at the corresponding temperature $T_2(\eta_1)$,

$$T_2(\eta_1) = -(V/8)\eta_1/[2\ln\{n_1(1-n_3)/[(1-n_1)n_3]\}]. \quad (23)$$

Similarly, we can be sure that on the straight line $\eta_2 = -\eta_1$, where $n_1(\eta_1, \eta_2) = n_3(\eta_1)$ with the additional constraint $V_2 = V_1 \equiv V$, the set of Eqs. (16a) and (16b) is satisfied at temperatures determined as

$$T_3(\eta_1) = -(V/8)\eta_1/[2\ln\{n_2(1-n_3)/[(1-n_2)n_3]\}]. \quad (24)$$

In all other cases, the numerical solution of the set of Eqs. (16) is required in order to determine the location of the extrema of function (14).

As noted above, the ordered state of the system at $T = 0$ K is described by the coordinates of one of the corner points of domain P. For concentrations $c \leq 1/3$, these are points g and d (Fig. 1a), and in the range $1/3 < c < 2/3$, these are points f, b, and d (Fig. 1b). Table 1 presents the coordinates of the extreme points $\eta_1(i)$ and $\eta_2(i)$ and the corresponding relative values of the internal energy $\varepsilon(i) \equiv [E(i)/2Nk_B - V_0c^2]$, where $E(i)$ is determined by Eq. (11).

Now, we consider the differences $\delta\varepsilon_{i,i'} \equiv \varepsilon(i) - \varepsilon(i')$. It follows from Table 1 that at $c < 1/3$, when the corner points g and d exist, the following equation holds:

$$\delta\varepsilon_{d,a} = [3c^2/4]|V_1|(1-3p), \quad (25a)$$

and at $c > 1/3$ (corner points f, b, and d), we have

$$\delta\varepsilon_{d,f} = [(1-2c)/4]|V_1|[1-3p], \quad (25b)$$

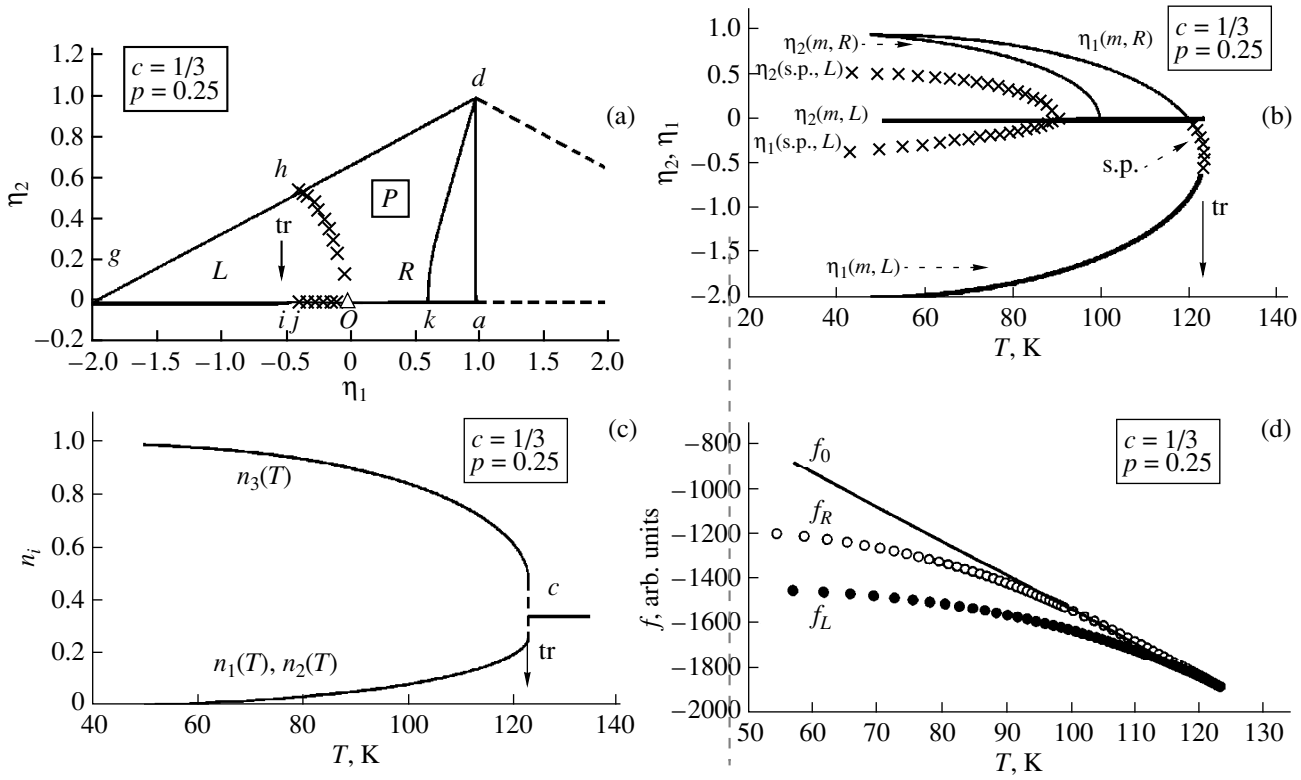

Fig. 2. The process of redistribution of H atoms among the sublattices of the interstices. The case of 24 sublattices. The ordered state of H atoms is described by the distribution function (1) and free energy function (14). $c = 1/3$ and $p = 0.25$. (a) The trajectories of the extrema in the (η_1, η_2) plane. Thick and thin lines are the trajectories of the absolute and local minima, respectively; the sequences of the crosses and triangles are the segments of the trajectories which correspond to the saddle points and the maximum, respectively. (b) Temperature dependences of the coordinates of extrema whose trajectories are shown in Fig. 2a. (c) Temperature variation of the equilibrium occupation numbers of sites in different sublattices n_1, n_2, and n_3. (d) The free energies which correspond to the left (f_L) and right (f_R) local minima and to the disordered state of the system (f_0).

$$\delta\varepsilon_{d,b} = [(1 - 4c + 3c^2)/4]|V_1|[1 - 3p], \qquad (25c)$$

$$\delta\varepsilon_{b,f} = (3c/4)[(2/3) - c]|V_1|[1 - 3p]. \qquad (25d)$$

In formulas (25a)–(25d), we introduced the energy parameter

$$V_2/V_1 \equiv p, \qquad (26)$$

which characterizes the given ordering system.

It follows from Eq. (25) that $p = 1/3 \equiv p_0$ is a critical value: at small concentrations ($c < 0.5$) and low temperatures ($T \approx 0$ K), in the case when $p < p_0$, the absolute minimum of the free energy is located at the corner points g and f, and in the case when $p > p_0$, it will be located either at point d for $c < c_0$ or at point b for $c > c_0$. Here, c_0 is determined from the condition

$$1 - 4c + 3c^2 = 0 \qquad (27)$$

(see Eq. (25c)) and is equal to 1/3.

Hence, in particular, it follows that if the HfV_2D_x system is characterized by the energy parameter $p > 1/3$, then, for $x \le 4$ ($c \le 1/3$), the equilibrium state at $T = 0$ K is the d state [$\eta_1 = \eta_2 = 3c$], which describes the distribution of hydrogen of the type $\{n_1 = 3c, n_2 = n_3 = 0\}$, and in the range $4 < x < 6$ ($1/3 < c < 1/2$), it is the b state [$\eta_1 = 3(1 - 2c)$, $\eta_2 = 1$], which describes a hydrogen distribution of the type $\{n_1 = 1, n_2 = 0, n_3 = 3c - 1\}$. However if $p < 1/3$ in this system, then, at $x \le 4$, the equilibrium state is the g state [$\eta_1 = 3(c - 1)$, $\eta_2 = 0$] with a distribution of the type $\{n_1 = 0, n_2 = 0, n_3 = 3c\}$, and in the range $4 < x < 6$, it is the f state [$\eta_1 = 3(c - 1)$, $\eta_2 = 3c - 1$] with a distribution of the type $\{n_1 = 3c - 1, n_2 = 0, n_3 = 1\}$.

3.5 Numerical solution of the equations for extrema of the free energy function. The set of Eqs. (16a)–(16b) was solved by numerical methods similar to those employed in [9]. The sequence of the values of $\eta_1(T)$ and $\eta_2(T)$ was determined at the fixed parameters c, p, and V_1 of the ordering system. Figures 2–4 display the results of calculations for $c = 1/3$; $V_1 = -25920$ K; and $p = 0.25$, 0.335, and 0.4. (The value of V_1 is determined from the condition of the existence of the order–disorder phase transformation in the HfV_2D_4 compound at $T_{tr} \approx 120$ K [2].) These figures illustrate the behavior of the compounds with identical concentrations which differ by the energy parameter p. Examples

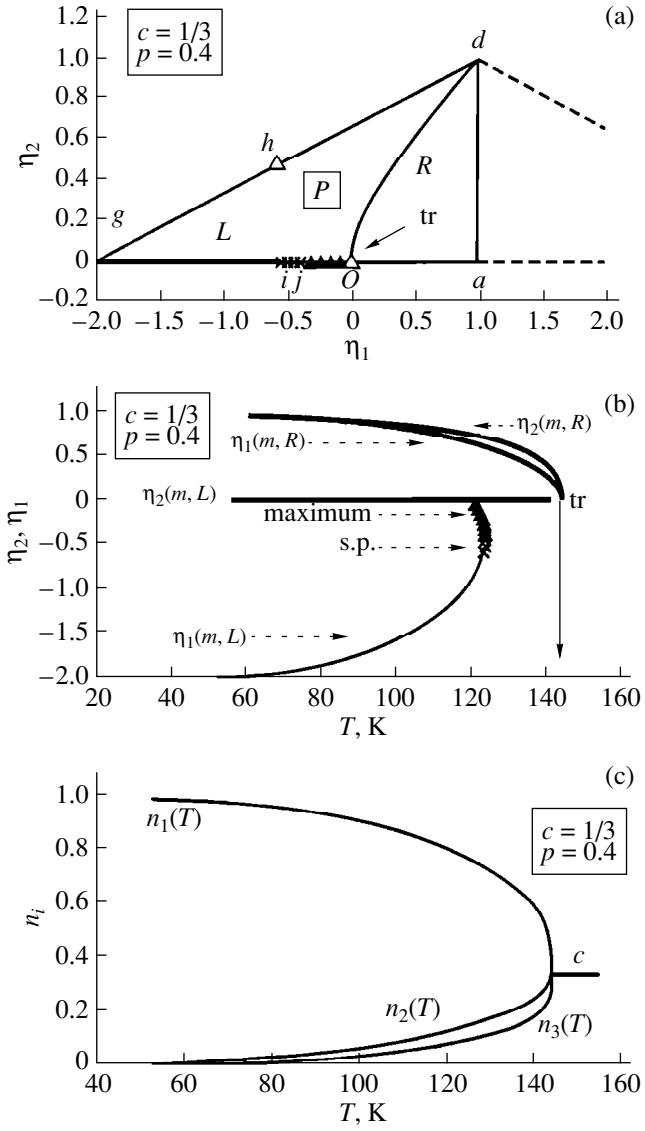

Fig. 3. The same as in Figs. 2a–2c. $c = 1/3$ and $p = 0.4$.

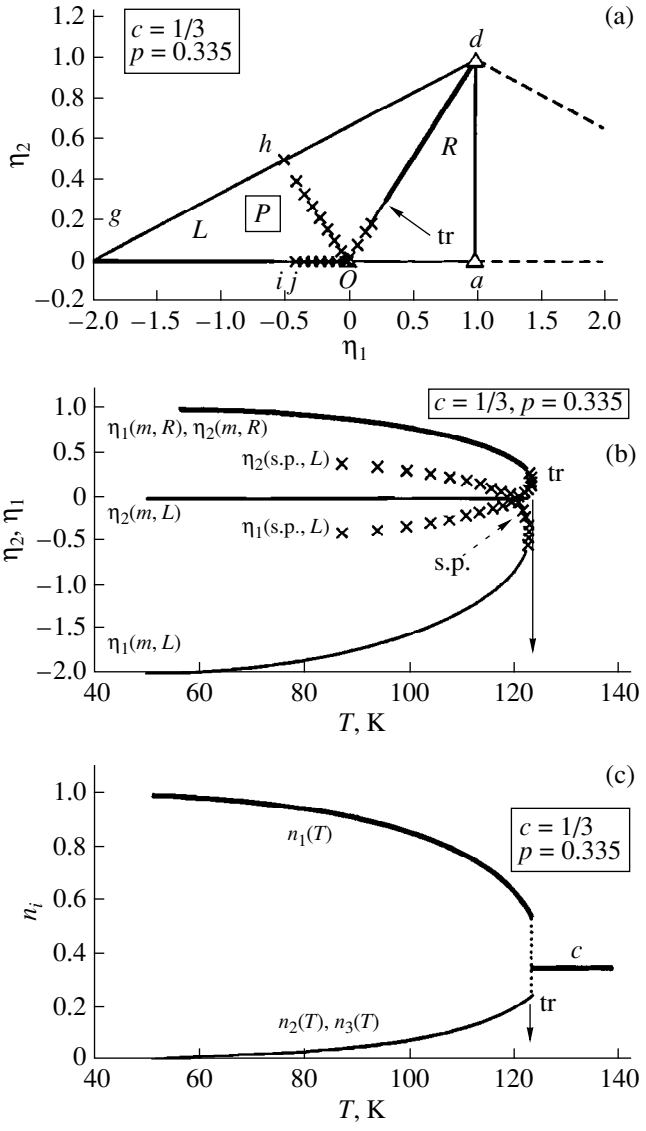

Fig. 4. The same as in Figs. 2a–2c. $c = 1/3$ and $p = 0.335$.

are provided by the systems with $p < 1/3$ (Fig. 2), $p > 1/3$ (Fig. 3), and $p \approx 1/3$ (Fig. 4). In the temperature range $T_{tr} \geq T > 0$, in each case, we determined (i) the sequence of the extreme locations of the F function in the (η_1, η_2) plane (Figs. 2a, 3a, 4a); (ii) temperature dependences of the coordinates of the $\eta_1(T)$ and $\eta_2(T)$ extrema (Figs. 2b, 3b, 4b) and the occupation numbers of sublattices $n_1(T)$, $n_2(T)$, and $n_3(T)$ (Figs. 2c, 3c, 4c); and (iii) the free energies associated with two local minima and with the disordered state (Fig. 2d). Figures 2a–4a show the trajectories of the extrema, and Figs. 2b–4b depict the temperature dependences of the coordinates of the extrema. In these figures, thick and thin lines correspond to the absolute and local minima, respectively, and the sequences of the crosses and triangles, to the saddle point and the maximum, respectively. Figures 2c–4c display the occupation numbers of the sublattices and the values of $n_i(T)$ which correspond to only the absolute minimum of the free energy function. In these figures, thick and thin lines represent the concentrations of the interstitial atoms in the sublattices that are to be occupied by and to be freed from the H atoms, respectively. Figure 2d shows the free energy and the values of $f(\eta_1, \eta_2; c, T) \equiv \{F(\eta_1, \eta_2; c, T)/Nk_B - V_0c^2\}$, which correspond to the disordered state f_0 and are calculated along the trajectories of the left (L) and right (R) local minima. It is evident that among these latter extrema, the absolute minimum is that which corresponds to the lesser value of the free energy. At $p < 1/3$, we have $f_0 \geq f_R \geq f_L$ (Fig. 2d), and at $p > 1/3$ and $p \approx 1/3$, we obtain similar dependences, but in the former case, $f_0 \geq f_L \geq f_R$, and in the latter case, $f_0 \geq f_R \approx f_L$.

4. BRIEF DISCUSSION OF THE RESULTS AND CONCLUSION

In Figs. 2–4, the behavior of a system is described by the distribution function (1) and the free energy function (14). As can be seen, the ordering which is assumed to be equilibrium in the HfV_2D_4 system, i.e., $\{n_1 \approx 1, n_2 \approx 0, n_3 \approx 0\}$ [2, 5], will be such only if the energy parameter of the system is $p > 1/3$. In the case of the system with $p < 1/3$, the evolution of the process will proceed according to another scenario, which corresponds to the determination of the absolute minimum in the left local minimum, and will finish in the formation of an ordering of the type $\{n_3 \approx 1, n_1 \approx 0, n_2 \approx 0\}$.

It is necessary to emphasize that, in a metal matrix with cubic symmetry, both distributions $\{n_1 \approx 1, n_2 \approx 0, n_3 \approx 0\}$ and $\{n_3 \approx 1, n_1 \approx 0, n_2 \approx 0\}$ are identical from the physical point of view. A difference between them will occur only in the case when a preferential direction exists in the crystal due to another subsystem (for example, a subsystem of the magnetic atoms). At the same time, it should be pointed out that the evolution of the ordering in systems with $p < 1/3$ and $p > 1/3$ is somewhat different: in the former case, below the order–disorder transition temperature ($T < T_{tr}$), a distribution of the type $\{n_3 > n_1 = n_2\}$ is formed at any values of $p < 1/3$; and in the latter case when $T < T_{tr}$, the distribution $\{n_1 > n_2 > n_3\}$ is formed, and $(n_2 - n_3)$ is the greater, the smaller the difference $(p - 1/3)$.

As regards the kind of the order–disorder phase transition, it turned out to be the phase transition of the first kind at $p = 0.25$ and 0.335 and the transition of the second kind at $p = 0.4$.

In conclusion, we note that all the above results were obtained under the assumption of the thermodynamic independence of the subsystem of the interstitial atoms, without regard for their influence on other subsystems, for example, on the deformation of the metal matrix or on the exchange interaction in the subsystem of the magnetic atoms.

5. SUPPLEMENT

Clearly, the question arises as to the applicability of the presented results to other hydrides with the AB_2D_x structure. For this purpose, we analyzed (as was suggested by the referee) the structure of the $YMn_2D_{4.3}$ compound investigated in [10].

It turned out that the results of the neutron diffraction investigations of $YMn_2D_{4.3}$ could be conveniently interpreted [10] on the basis of the rhombohedral distorted primitive cell of the FCC lattice which contains 24 interstices of the A_2B_2 type (a single one from each of 24 sublattices). In this cell, hydrogen positions are represented as being located in the planes perpendicular to the crystallographic axis [111] [10], i.e., satisfying the equation $x + y + z = L$. If we put the origin of coordinates on the [111] axis in such a way that adjacent Y atoms take the coordinates (1/8 1/8 1/8) and ($\bar{1}$/8 $\bar{1}$/8 $\bar{1}$/8) (we employ a Cartesian frame of reference unlike the oblique frame used in [10]), the planes occupied by the A_2B_2 interstices correspond to the values L = 3/4, 1, 11/8, 13/8, 2, and 9/4. For each of the L planes, Table 2 presents the numbers of interstitial sites N_L (within a given primitive cell), the indices Q_z of sublattices which contain these sites, and the probabilities n_L of the occupation of the given interstices by D atoms (according to [10]).

Table 2. Parameters N_L, Q_z, and n_L

L	N_L	Q_z	n_L
3/4	3	21, **13**, 17	0
1	3	23, 15, **19**	1
11/8	6	22, 24, **14**, 16, 18, **20**	0.5
13/8	6	10, 12, **1**, 3, 5, 7	0
2	3	**4**, **8**, 9	1
9/4	3	**2**, 6, 11	0

The boldface indices in Table 2 correspond to the sublattices in which, according to the distribution function (1) in the case when $x = 4$, the probability of the occupation of the sites at $[\eta_1 = 1, \eta_2 = 1]$ should be equal to $n_1 = 1$. As can be seen, the hydrogen ordering proposed in [10] does not conform to the distribution function proposed in [5] and considered in the present work. This indicates the different behavior of the hydrogen subsystem in YMn_2D_x and HfV_2D_x compounds.

It is necessary to note that the hydrogen subsystem in other compounds of the RMn_2D_x type (R = Gd, Tb, Dy, and Ho) is ordered in the same manner as the YMn_2D_x compound [11]. In our opinion, this unambiguously indicates the crucial importance of the magnetoelastic interaction in these hydrides, which is caused by the magnetic moments of manganese and rare-earth atoms.

Unfortunately, the free energy function (14) does not allow one to take into account the role of the magnetic subsystem. Therefore, the analysis of the RMn_2D_x hydrides should be the subject of a special investigation based on the function which includes additional terms accounting for the magnetoelastic interaction.

ACKNOWLEDGMENTS

This work was supported by the Scientific Research Program of the Academy of Sciences of Georgia.

REFERENCES

1. N. F. Miron, V. I. Shcherbak, V. N. Bykov, and V. A. Levdik, Kristallografiya **16** (2), 324 (1971) [Sov. Phys. Crystallogr. **16**, 266 (1971)].

2. A. V. Irodova, V. P. Glazkov, V. A. Somenkov, and S. Sh. Shil'shteĭn, Fiz. Tverd. Tela (Leningrad) **22** (1), 79 (1980) [Sov. Phys. Solid State **22**, 45 (1980)].
3. P. Fischer, F. Fauth, A. V. Skripov, *et al.*, J. Alloys Compd. **253–254**, 282 (1997).
4. V. Paul-Boncour, L. Guenee, M. Latroche, *et al.*, J. Alloys Compd. **253–254**, 272 (1997).
5. A. V. Irodova, Fiz. Tverd. Tela (Leningrad) **22** (9), 2559 (1980) [Sov. Phys. Solid State **22**, 1493 (1980)].
6. A. G. Khachaturyan, *The Theory of Phase Transformations and the Structure of Solids Solutions* (Nauka, Moscow, 1974).
7. I. G. Ratishvili, Fiz. Tverd. Tela (Leningrad) **21** (7), 1990 (1979) [Sov. Phys. Solid State **21**, 1141 (1979)].
8. I. G. Ratishvili, Phys. Status Solidi B **87** (2), 461 (1978).
9. I. G. Ratishvili, P. Vajda, A. Boukraa, and N. Z. Namoradze, Phys. Rev. B **49** (22), 15461 (1994).
10. I. N. Goncharenko, I. Mirebeau, A. V. Irodova, and E. Suard, Phys. Rev. B **56** (5), 2580 (1997).
11. I. N. Goncharenko, I. Mirebeau, A. V. Irodova, and E. Suard, Phys. Rev. B **59** (14), 9324 (1999).

Translated by O. Moskalev

Physics of the Solid State, Vol. 43, No. 2, 2001, pp. 207–213. Translated from Fizika Tverdogo Tela, Vol. 43, No. 2, 2001, pp. 200–206.

METALS AND SUPERCONDUCTORS

Physics of the Evolution of Structure and Elastic Stresses in Pd–Mo Alloys Saturated with Hydrogen

A. V. Knyaginichev, Khan Kha Sok, V. M. Avdyukhina, A. A. Katsnel'son, and G. P. Revkevich

Moscow State University, Vorob'evy gory, Moscow, 119899 Russia

e-mail: albert@solst.phys.msu.su

Received June 16, 2000

Abstract—Specific features in the structural evolution of a Pd–Mo alloy after its electrolytic saturation with hydrogen are studied by x-ray diffraction. It is revealed that these features depend on the concentration of absorbed hydrogen, the initial defect structure, and the character of its transformation upon hydrogen saturation. The factors responsible for the structural evolution depend on the concentration of alloy components and the difference between the hydrogen affinities, Debye temperatures, and elastic constants of the components. A model proposed for the evolution of the structure and elastic stresses in palladium–metal–hydrogen systems accounts for the above factors. © *2001 MAIK "Nauka/Interperiodica"*.

1. INTRODUCTION

Several years ago, Piskovets *et al.* [1] found that the strength characteristics of steel-rolled products vary with time in a nonmonotonic manner. Since this effect disappeared after coating a sheet with a special hydrogen-impenetrable film, the authors assumed that nonmonotonic time variations in the mechanical properties are brought about by hydrogen migration over a metal. However, actual rolled products are strongly fouled by numerous impurities. For this reason, the elaboration of approaches to the scientific solution of the problem concerning the elimination of stochastic variations in the physical properties requires investigation of a material which readily dissolves hydrogen but is not prone to severe fouling. Palladium and its alloys are among the most known materials of this type. It was revealed that, after the saturation with hydrogen, these alloys also exhibited a nonmonotonic (oscillating or stochastic) time dependence of the structural and phase transformations. This was especially true for Pd–W [2–4] and Pd–Er [5–9] alloys. A similar stochastic character of time variations in the strength parameters of steels and in the structural characteristics of palladium systems suggests the similarity of the factors responsible for the origin of these phenomena. In this respect, it is very important to answer questions as to how wide the range of materials for which these nontrivial phenomena are observed is and as to which physical factors are responsible for nonmonotonic structural transformations and their features.

In this work, the Pd–Mo alloy was chosen as the object of investigation. This alloy is very interesting from the viewpoint of searching for the physical factors responsible for the structural evolution of hydrogen-containing metal alloys, because it is characterized by a nonlinear dependence of the hydrogen solubility on the concentration of its components [10] and also by a substantial difference between the hydrogen affinities, elastic constants, and Debye characteristic temperatures of the components. At the same time, a small difference in the atomic radii of Pd and Mo [10, 11] allows us to disregard this factor in our consideration. In this case, a strong nonlinear dependence of the hydrogen solubility on the Mo concentration is an additional circumstance that can provide a better insight into the nature of the phenomenon under investigation with the use of the data on the structural evolution of alloys in this system (upon their saturation with hydrogen and subsequent relaxation) as a function of the component concentration in the alloy. In order to ensure the close conditions for hydrogen saturation of the regions with different compositions and strains, the samples to be studied were cut from a Pd–Mo alloy ingot that did not undergo complete homogenization, and hence, each sample involved regions with several compositions.

2. SAMPLES, EXPERIMENTAL TECHNIQUE, AND DATA PROCESSING

The samples were investigated by x-ray diffraction methods [5–9] on a DRON-UM2 diffractometer equipped with a PC 486DX2 computer for control of the experiment and a Pentium Pro computer for the experimental data processing. X-ray experiments were performed with monochromated Cu$K_{\alpha 1}$ radiation. The (111), (200), (220), (311), and (222) diffraction lines were recorded.

We studied two samples cut from the same Pd–Mo (5 at. %) alloy ingot. After the cutting on a machine, the sample surface was ground and polished. As follows

1063-7834/01/4302-0207$21.00

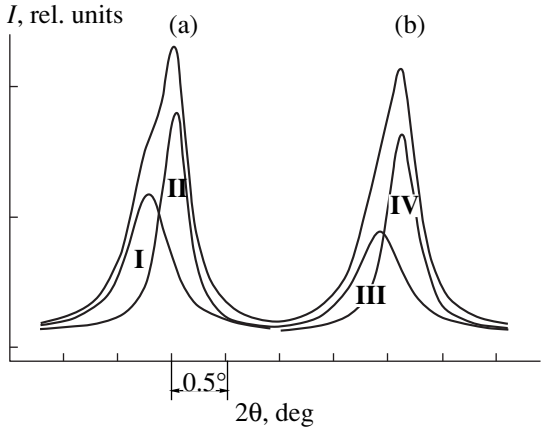

Fig. 1. Diffraction profiles (311) for samples (a) *1* and (b) *2*.

from the diffraction data, the distribution of components over the samples is inhomogeneous and even two-phase in coherent-scattering regions whose crystallographic planes (311) are parallel to the sample surface (Fig. 1). Both phases have a face-centered cubic structure. Note that the solubility of molybdenum in palladium is equal to 30–35 at. %, and only face-centered cubic and body-centered cubic phases can exist in a two-phase equilibrium state [12]. Therefore, the initial structural state of the studied samples is nonequilibrium.

Analysis of all the diffraction profiles was performed according to the Origin software package and other original programs. The (311) diffraction profiles were decomposed into two components. The location, the half-width *w*, and the integrated intensity were determined for each component. For clarity of representation, these components of the (311) line will be designated as follows: for sample *1*, the line located at the smaller 2θ angle (which corresponds to a higher palladium concentration) will be termed component **I** and the second line will be referred to as component **II**; for sample *2*, these lines will be called components **III** and **IV**, respectively. It is seen from Fig. 1 that components **I** and **III** are approximately twice as wide as components **II** and **IV**.

The samples under investigation were electrolytically saturated with hydrogen for 1 h at a current density of 80 mA/cm^2 and then were stored in air under normal conditions.

As was shown in [13, 14], the grinding and polishing of palladium alloy samples give rise to elastic stresses. This results in such an increase (dependent on the Miller indices *hkl*) in the interplanar distances that the values of $a_{hkl} = d_{hkl}(h^2 + k^2 + l^2)^{1/2}$ calculated from the experimental data are different.

The observed dependence of a_{hkl} on the indices *hkl* has the following form:

$$a_{hkl} = a_0 + a_0\sigma K_{hkl}. \quad (1)$$

Here, a_0 is the lattice parameter of a cubic crystal in the absence of the elastic stress σ and

$$K_{hkl} = 1/E_{hkl} = S_{11} - (2S_{11} - 2S_{12} - S_{44})$$
$$\times (h^2k^2 + h^2l^2 + k^2l^2)/(h^2 + k^2 + l^2)^2 = S_{11} - \Delta\Gamma,$$

where E_{hkl} is the Young modulus; S_{11}, S_{12}, and S_{44} are elastic compliance constants; $(2S_{11} - 2S_{12} - S_{44}) = \Delta$ is the anisotropy constant; and $\Gamma = (h^2k^2 + h^2l^2 + k^2l^2)/(h^2 + k^2 + l^2)^2$. If the elastic stress σ is positive (the interplanar distances are increased along the normal to the sample surface), we have $a_{100} > a_{111}$. If $\sigma < 0$, then $a_{100} < a_{111}$.

Since the quantity $a_0\sigma K_{hkl}$ is no more than 1% of the a_0 value, relationship (1) can be rewritten as

$$a_{hkl} = a_0 + \sigma' K_{hkl}, \quad (2)$$

$$\sigma' = \sigma a_0. \quad (3)$$

In this case, the absolute error in the determination of a_0 is no more than $0.0001a_0$, which does not exceed the experimental error in the determination of a_{hkl}. The same is also true for the quantity σ, which is determined from expression (3).

The unknown values of a_0 and σ are calculated by the least-squares method. It is clear that inexact values of the S_{11}, S_{12}, and S_{44} constants will affect the a_0 and σ values determined from the experiment. However, for the given set of a_{exp}, the difference between a_{hkl} and $a_{h'k'l'}$, that is,

$$a_{hkl} - a_{h'k'l'} = \text{const}(\Gamma_{hkl} - \Gamma_{h'k'l'}), \quad (4)$$

is independent of the elastic compliance constants, provided that a_0 and σ are identical for coherent-scattering regions of all the orientations. Therefore, if the discrepancy for any one of the $a_{hkl\,\text{calcd}}$ values is larger than the error of its determination, this can be explained only by the fact that the values of a_0 and σ for coherent-scattering regions of this orientation are different. Hence, in the case when the $a_{hkl\,\text{exp}}$ value was found to be considerably different from $a_{hkl\,\text{calcd}}$, this blunder for a_{hkl} was rejected and the values of a_0 and σ were calculated once again. In this work, we used the mean values of S_{11}, S_{12}, and S_{44} calculated from the corresponding values for pure metals.

3. RESULTS OF THE EXPERIMENT

Figure 2 displays the a_{hkl} values calculated for all the recorded diffraction lines [two a_{hkl} values are given for the (311) line] for both samples. These values turned out to be close for both samples (except for components **II** and **IV**). The least-squares calculations without regard for $a_{311\,\text{exp}}$ gave the following results: $a_0 = (3.884 \pm 0.001)$ Å and $\sigma = (28 \pm 3)$ kg/mm^2 for sample *1* and $a_0 = (3.885 \pm 0.001)$ Å and $\sigma = (24 \pm 3)$ kg/mm^2 for sample *2*. Thus, the values of a_0 and σ are virtually

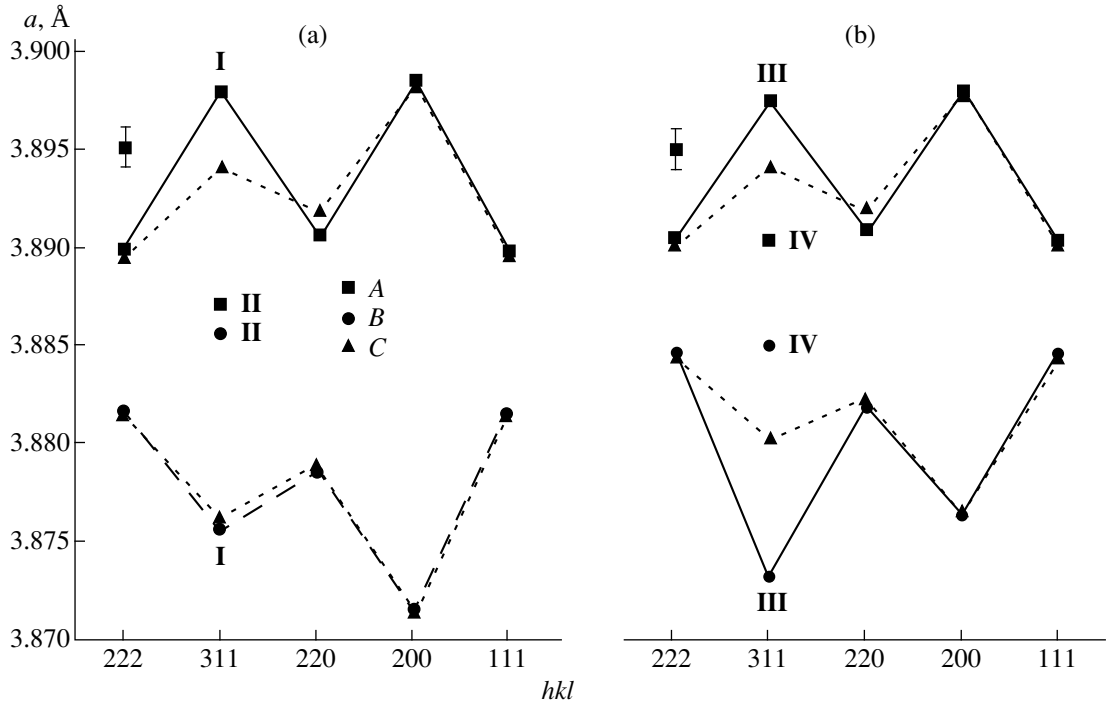

Fig. 2. Lattice parameters a for coherent-scattering regions of different crystallographic orientations (hkl) for samples (a) *1* and (b) *2*: (*A*) the experimental data prior to saturation, (*B*) the experimental data after saturation, and (*C*) the results of calculations by formula (2).

identical for both samples. The found value of a_0 is 0.002–0.003 Å less than that obtained in [10, 11], which can be explained by the sufficiently high concentration of excess vacancies in the studied samples.

The $a_{hkl\,\mathrm{calcd}}$ values calculated from formula (2) with the use of the found values for a_0 and σ are also shown in Fig. 2. It can be seen that, within the limits of experimental error, these values coincide with $a_{hkl\,\mathrm{exp}}$ for all the lines, except for (311). Compared to the calculated data, the experimental values are larger for the wide components (**I** and **III**) of the (311) line and smaller for its narrow components (**II** and **IV**).

According to [10, 11], the lattice parameter a for the Pd–Mo alloy changes only by 0.002 Å with a variation in the C_{Mo} concentration in the range 2.5–10 at. %. This change is substantially less than the difference between $a_{311\,\mathrm{exp}}$ and $a_{311\,\mathrm{calcd}}$. Therefore, the value of σ for the (311) line can be estimated using the a_0 parameter determined above. For components **I**, **II**, **III**, and **IV**, the found σ values are equal to 40, 10, 35, and 15 kg/mm^2, respectively.

The $a_{hkl\,\mathrm{exp}}$ values obtained for the hydrogen-saturated samples after their storage for 50 h under normal conditions are also depicted in Fig. 2. It is seen that the saturation with hydrogen and subsequent relaxation lead to the change in sign of elastic stresses. After rejecting blunders for $a_{311\,\mathrm{exp}}$, the calculations of a_0 and σ gave the following results: $a_0 = (3.8876 \pm 0.0004)$ Å and $\sigma = (-31 \pm 1)$ kg/mm^2 for sample *1* and $a_0 = (3.8893 \pm 0.0005)$ Å and $\sigma = (-24.4 \pm 1.4)$ kg/mm^2 for sample *2*. The a_0 values were found to be somewhat larger than the initial values. This implies that a certain portion of hydrogen is retained in the lattice.

Moreover, we determined the σ values (under the assumption that a_0 is constant) for regions that correspond to components **I**, **II**, **III**, and **IV**. These values are equal to –30, –5, –40, and –10 kg/mm^2, respectively. It should be noted that the found values of σ are not exact, because the actual values of a_0 remain unknown. By assuming that the latter values can differ by 0.002 Å, the calculated σ values can differ by 5–7 kg/mm^2. Even so, it is evident that the experimental values of σ considerably differ for coherent-scattering regions of different orientations, including coherent-scattering regions of different compositions with the (311) orientation.

Of particular interest is the change in $a_{311\,\mathrm{exp}}$ immediately after the hydrogen saturation of the samples and subsequent relaxation (Figs. 3, 4). For component **II** with the minimum value of a_{exp} in the initial state, this parameter remains virtually unchanged upon saturation and relaxation. For component **IV**, a_{exp} decreases upon saturation and remains constant upon relaxation. For components **I** and **III**, the a_{exp} parameters increase upon saturation. Note that this increase for component **I** is twice as large as that for component **III**. In the

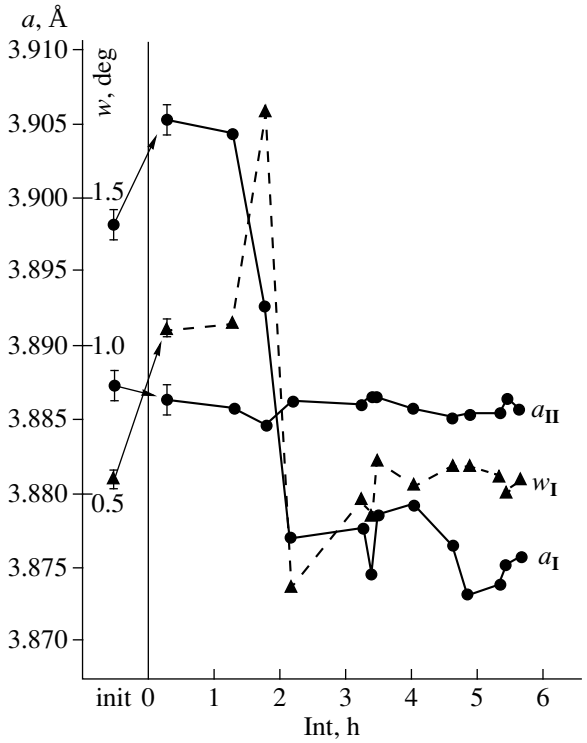

Fig. 3. Time dependences of the lattice parameters $a_{\mathbf{I}}$ and $a_{\mathbf{II}}$ and the half-width $w_{\mathbf{I}}$ for components of the (311) diffraction profile of sample *1*.

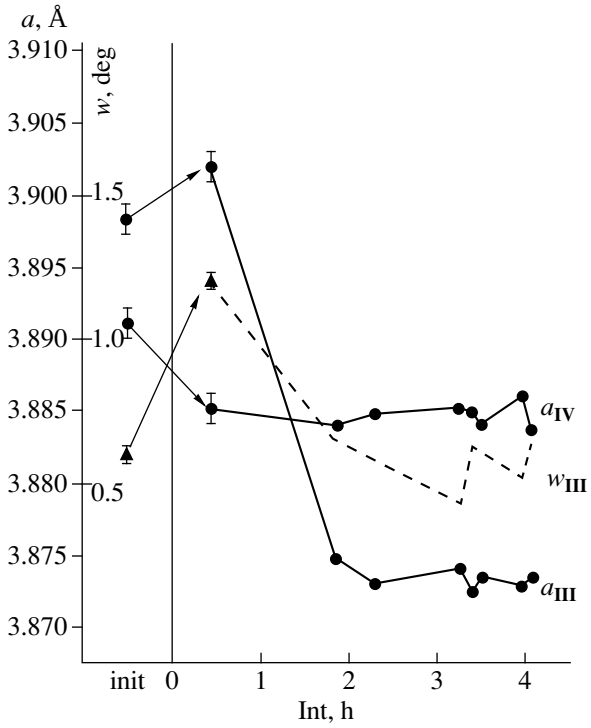

Fig. 4. Time dependences of the lattice parameters $a_{\mathbf{III}}$ and $a_{\mathbf{IV}}$ and the half-width $w_{\mathbf{III}}$ for components of the (311) diffraction profile of sample *2*.

course of relaxation, the behavior of the a_{exp} parameters differs substantially.

For component **I**, the $a_{\mathbf{I}}$ value in the course of relaxation remains virtually unaltered for the first 3.5 h and then sharply decreases (this decrease is observed up to the tenth hour after the onset of relaxation). Thereafter, the $a_{\mathbf{I}}$ parameter oscillates with an amplitude close to 0.002 Å. The mean value of $a_{\mathbf{I}}$ is equal to 3.870 Å. Note that $a_{\mathbf{I}}$ decreases with an increase in the relaxation time. For component **III**, $a_{\mathbf{III}}$ in the course of relaxation decreases for the first 10 h and then remains constant. The reached value of $a_{\mathbf{III}}$ is 0.0025–0.003 Å less than the value of $a_{\mathbf{I}}$.

Now, we dwell on the change in the width *w* for all components of the (311) line in the course of saturation (Figs. 3, 4). The widths of components **II** and **IV** prior to the saturation are approximately equal to 0.3° and do not change upon saturation and relaxation (for this reason, they are not shown in these figures). For components **I** and **III**, the saturation brings about almost a twofold increase in the width *w*.

Upon relaxation, the width of component **I** remains unchanged for the first 3.5 h and then increases by a factor of 1.5 for 2.5 h. As can be seen from Fig. 4, by that time (6 h after the onset of relaxation), the $a_{\mathbf{I}}$ parameter decreases considerably. Thereafter, the width $w_{\mathbf{I}}$, 3 h later, decreases by almost one order of magnitude and then again increases by a factor of 2.5 for 20–30 h. Thus, the change in $w_{\mathbf{I}}$ is nonmonotonic. The width of component **III** also first decreases and then somewhat increases.

4. DISCUSSION

Prior to discussing the results, we determine the Mo (Pd) concentration in regions **I**–**IV** and the dependence of σ on the Mo concentration.

As was shown in [10], the solubility of hydrogen in the Pd–Mo alloys drastically decreases (by a factor of 20–100 depending on the pressure) as the molybdenum concentration C_{Mo} increases from 2.5 to 7.5 at. %. A further increase in C_{Mo} from 7.5 to 10 at. % is accompanied by a slower decrease in the solubility. Such a change in the solubility allows us to estimate the molybdenum concentration in regions **I**–**IV**. Specifically, the Mo concentration in region **II** is higher than 7.5 at. %, because the component that corresponds to this region remains virtually unchanged upon the hydrogen saturation. This can be explained by the fact that hydrogen is not absorbed in this region. The C_{Mo} concentration in region **IV** is somewhat decreased, since this region absorbs a certain amount of hydrogen, which manifests itself in a small variation in the $a_{\mathbf{IV}}$ parameter upon the hydrogen saturation. According to the estimates, region **IV** contains 5–6 at. % Mo. The

molybdenum content is minimum in region **I** for which an increase in the *a* parameter is maximum upon the saturation. From the ratio between the changes in the *a* value for regions **I** and **III**, we obtain that the Mo concentration in these regions is close to 2.5 and 3.5–4.0 at. %, respectively. Therefore, the molybdenum content in the regions under investigation increases in the following order: **I** < **III** < **IV** < **II**. As follows from the data obtained in the preceding section, the σ values in these regions are as follows: 40, 35, 15, and 10 kg/mm^2. This indicates that, under the same deformation conditions, the smaller the molybdenum concentration, the larger the elastic stresses in these regions.

Let us consider factors that determine the dependence of σ on the Mo concentration and the change in σ after hydrogen saturation. The fact that elastic stresses arise in the studied alloys directly follows from the data on the shift in locations of diffraction maxima (prior to the hydrogen saturation) with respect to their locations in the case of a cubic structure. Earlier, the elastic stresses in strained alloys were found in pure metals (Cu and Pd [13, 14]), and the change in the sign of stresses upon the hydrogen saturation was observed in pure Pd and Pd alloys with Cu, Hf, Sm [14], and Er [15]. In strained metals, the elastic stresses responsible for an increase (dependent on the indices *hkl*) in the a_0 parameter along the normal to the sample surface should be provided by defect complexes which are enriched with interstitial atoms and, hence, have a specific volume larger than the specific volume of the matrix. In [15], they were termed the *D–M* complexes, where *M* is the type of interstitial atoms. The observed change in sign of these stresses [14, 15] was explained by the fact that the specific volume of complexes becomes less than the specific volume of the matrix due to a high binding energy of hydrogen with defects in Pd [16]. The latter complexes were referred to as the *H–D–M* complexes [15]. It was shown that the magnitude and the sign of σ for hydrogen-saturated systems depend on the alloy composition, the type of initial *D–M* complexes, the amount of hydrogen absorbed by the *H–D–M* complexes, and the binding energy of hydrogen with alloy components and defects.

It is evident that the elastic stress σ in the initial state should depend on the composition of the *D–M* complexes, their number, and strength. Moreover, the change in σ upon the hydrogen saturation should also be affected by the degree of variation in these quantities after saturation. According to the model proposed in [15], these complexes in the Pd–Mo system are the Pd–Mo complexes. However, in the Pd–Er system considered in [15], the cores of the *H–D–M* complexes are formed by impurity atoms (Er) with a higher hydrogen affinity and a substantially larger atomic radius as compared to those of the Pd atoms. At the same time, the Mo atoms, which, according to this model, are the cores of the *H–D–M* complexes in the Pd–Mo system, have radii identical to those of the Pd atoms, and their hydrogen affinity is less than that of the Pd atoms. Therefore, in order to describe the behavior of systems of the Pd–Mo alloy type, it is insufficient to introduce only the Pd–Mo–H complexes into consideration. In this case, it is necessary to include complexes of one more type. These are the Pd–Pd–H complexes whose cores are formed by the Pd–Pd interstitial complexes.

Now, we demonstrate that the inclusion of these complexes in consideration for the studied system provides a plausible explanation for an increase in σ with an increase in the Pd concentration and a stronger change in this quantity upon the hydrogen saturation. Indeed, the magnitude of σ should be determined by the number of the *D–M* complexes and their strength. In turn, these quantities should be governed by the number of atoms incorporated into the complexes, and this number should depend on the ability of atoms to occupy interstices. It is easily seen that the latter factor should be associated with elastic characteristics of the studied system, specifically with the shear modulus and root-mean-square displacements of atoms. Let us now compare the shear moduli for the most typical slip systems in the body-centered cubic lattice of molybdenum and the face-centered cubic lattice of palladium. These moduli are defined by the same relationship $G = [(4/3)(S_{11} - S_{12}) + (1/3)S_{44}]^{-1}$ [17]. Substitution of the elastic compliance constants for Mo and Pd [18] into this expression gives the ratio $G_{Mo}/G_{Pd} = 4.05$. A considerably lesser value of the shear modulus for Pd correlates with its lower Debye characteristic temperature: $\Theta_{Pd} = 275$ K and $\Theta_{Mo} = 425$ K [19]. It is also interesting that the anisotropy constants Δ for Pd and Mo have different signs and differ by more than one order of magnitude. These data indicate that the Pd–Pd complexes are formed much more readily than complexes of the Pd–Mo type. Therefore, the Pd–Pd complexes actually should be formed in the system under consideration, and their concentration should be substantially higher than the concentration of the Pd–Mo complexes and increase nonlinearly with an increase in the Pd concentration. This explains an increase in the elastic stress σ in the initial state with an increase in the Pd concentration. From this result, it immediately follows that the change in σ upon the hydrogen saturation should be maximum in coherent-scattering regions in which the palladium content is higher, because it is in these coherent-scattering regions that the amount of dissolved hydrogen is maximum.

Thus, the behavior of the Pd–Mo system can be explained by the formation of the Pd–Mo and Pd–Pd complexes. The concentration of the latter complexes should be sufficiently high, because they are responsible for the appearance of elastic stresses and the change in their sign upon hydrogen saturation. Consequently, these complexes can be termed active, unlike the Pd–Mo complexes, which are referred to as passive.

Let us discuss the change in σ upon relaxation. For component **II**, the parameter a_{II} and, correspondingly,

σ in the course of relaxation remain virtually unchanged, which can easily be explained by a low hydrogen solubility at the Mo concentration corresponding to this component. The noticeable decrease in $a_{\mathbf{IV}}$ and σ for coherent-scattering region **IV** upon saturation can be due to the fact that all hydrogen dissolved upon saturation is instantaneously (and almost completely) absorbed by the Pd–Pd complexes, thus transforming them into the Pd–Pd–H complexes already at the saturation stage. Therefore, the $a_{\mathbf{IV}}$ parameter decreases even upon saturation, and the observed constancy of $a_{\mathbf{IV}}$ upon further relaxation indicates a high stability of the resulting complexes.

Compared to coherent-scattering regions **II** and **IV**, regions **I** and **III** are characterized by a lower Mo concentration and, hence, contain a larger amount of dissolved hydrogen. As a result, the $a_{hkl\,\mathrm{exp}}$ parameter increases immediately after saturation. In this case, the number and the strength of the Pd–Pd complexes in coherent-scattering region **I** are likely larger than those in region **III**.

Since the hydrogen solubility in the Pd–Mo alloys nonlinearly depends on the Mo concentration, this concentration can be treated as a controlling parameter [20] which is responsible for the specific features in the evolution of the Pd–Mo–H system. The obtained data demonstrate that the Pd content (as well as the H content after saturation) in coherent-scattering region **I** is somewhat higher than that in coherent-scattering region **III**. Consequently, the amount of absorbed hydrogen in region **I** is so large that hydrogen has no time to be captured in traps at the saturation stage, and this process predominantly occurs at the degassing stage. According to this model, the change in σ takes place at the initial stage of relaxation (rather than upon saturation) in coherent-scattering region **III** and even after a certain latent period in coherent-scattering region **I**.

It is interesting that the dependences of the $a_{\mathbf{III}}$ parameter for coherent-scattering regions **I** and **III** are different in character. This difference can be associated with a larger amount of hydrogen absorbed by coherent-scattering region **I** and also with the fact that a certain portion of hydrogen is unbound by the Pd–Pd–H complexes. In this case, the observed oscillations in $a_{\mathbf{I}}$ for coherent-scattering region **I** at relatively late stages of relaxation can be due to the behavior of hydrogen-saturated regions in the "neighborhoods" of the Pd–Pd–H complexes.

Now, we dwell on the behavior of the widths *w* of components in the processes under investigation. For components **II** and **IV**, the *w* values upon relaxation remain constant. This implies that the changes in *w* are unrelated to the Pd–Pd–H complexes. The widths $w_{\mathbf{I}}$ and $w_{\mathbf{III}}$ increase upon saturation, and this increase can be attributed to an increase in the dispersion of the parameters *a* and σ at the expense of an additional inhomogeneity in the distribution of absorbed hydrogen over the corresponding regions due to the dependence of the hydrogen solubility on the molybdenum concentration. Upon relaxation, this inhomogeneity decreases gradually.

Since coherent-scattering region **I** contains a larger amount of absorbed hydrogen, no changes in macrocharacteristics such as $a_{\mathbf{I}}$ and $w_{\mathbf{I}}$ are observed at the initial stage of relaxation: it takes additional time to initiate the relaxation of the excited hydrogen-supersaturated system. Then, there occurs a very rapid process of trap formation, which involves the absorption of hydrogen atoms by the Pd–Pd complexes, i.e., the formation of the Pd–Pd–H complexes. Owing to the supersaturation of the system with hydrogen, the capture of hydrogen atoms in traps at the initial stage leads to an increase in the inhomogeneity in the system, which results in an increase in *w*. It seems likely that the capture of hydrogen in traps begins with regions in which the hydrogen content is not very high, whereas the hydrogen atoms in the regions supersaturated with hydrogen compete with each other for sites in their quasi-equilibrium arrangement. However, at the later stages when all traps are filled with hydrogen atoms, the spread in the a_{hkl} values decreases considerably. A more ordered distribution of traps also becomes possible, which eventually results in a narrowing of diffraction maxima.

A further change in $a_{\mathbf{I}}$ and $w_{\mathbf{I}}$ has a relaxation character with indications of self-organization processes, which are more pronounced for the $a_{\mathbf{I}}$ parameter. These processes resemble phenomena revealed in our earlier work [2] for Pd–W alloys with similar characteristics. In particular, the width of diffraction maxima for the Pd–W (7 at. %) alloy upon the hydrogen saturation first increased, then decreased, after which again increased, and thereafter remained constant [2]. The dependence $w(t)$ was represented by a relaxation curve whose character reflected the features of variation in the degree of inhomogeneity of the system after the hydrogen saturation. The oscillating behavior observed in the present work for the $a_{\mathbf{I}}$ parameter upon relaxation can be associated with the cooperative migration of hydrogen atoms between traps and the matrix (recall that the system remains nonequilibrium throughout the observation). Moreover, since the changes in a_{hkl} can be caused by variations in the values of *a* (owing to the hydrogen migration) and σ, the oscillating behavior of a_{hkl} can be brought about by the change in each of these quantities. This process is stimulated by the following factors: although the traps become more stable in the course of saturation with hydrogen, the resulting deficit of hydrogen in the matrix leads to the inverse process—the migration of hydrogen into the matrix. It is more probable that the processes under consideration are associated with the redistribution of hydrogen atoms between the matrix and the neighborhoods of traps, because hydrogen atoms are unlike to leave traps in the course of rather short-term relaxation due to their high stabil-

ity. This type of hydrogen migration can be accompanied by a considerably weaker change in the degree of inhomogeneity, and as a result, the relaxation curve $w(t)$ decays more rapidly than the $a_I(t)$ curve.

In a more detailed analysis of the relaxation curves, it should be remembered that actually we deal with both variations in the hydrogen concentration in the matrix and variations in the stress σ due to variations in the hydrogen concentration in traps, as well as with variations in the dispersion of these quantities. The minimum of the total dispersion can be determined by the coincidence of minima of all these dispersions.

5. CONCLUSION

The structural evolution of the Pd–Mo alloys after their saturation with hydrogen is determined by the following factors: the Mo concentration which nonlinearly affects the amount of dissolved hydrogen in the system, the difference between the hydrogen affinities of Mo and Pd, and the differences between their Debye temperatures and elastic characteristics which are responsible for the different initial defect structures. Since the Debye characteristic temperature and the shear modulus of Pd are less than those of Mo, the strain of the Pd–Mo alloys brings about the formation of interstitial, predominantly Pd–Pd complexes (possibly, the interstitial dislocation loops), which give rise to elastic stresses. These stresses increase with an increase in the Pd concentration. Furthermore, the concentration of dissolved hydrogen also increases, and, as a result, the higher the palladium concentration, the larger the change in σ upon the saturation of the alloy with hydrogen.

As a consequence, no structural transformations occur in the alloy with a high Mo concentration (more than 7.5 at. % Mo) upon the hydrogen saturation. In the alloy with a Mo concentration close to 5–6 at. %, the hydrogen atoms have already been completely absorbed by the Pd–Pd complexes upon saturation, which leads to the immediately change in σ. In the palladium alloys with a lower Mo concentration (2.5–3.5 at. %), not all hydrogen atoms absorbed by the system are captured by the traps. In this case, the evolution of the system is governed by the hydrogen atoms captured in traps and the hydrogen atoms remained in the quasi-ideal part of the system.

ACKNOWLEDGMENTS

This work was supported by the Russian Foundation for Basic Research (project no. 99-02-16135) and the "Russian Universities—Basic Research" Program (project no. 990156).

REFERENCES

1. V. M. Piskovets, T. K. Sergeeva, Yu. A. Bashnin, and O. V. Nosochenko, Stal' **7**, 58 (1994).
2. A. A. Katsnel'son, G. P. Revkevich, and I. V. Sukhorukova, Vestn. Mosk. Univ., Ser. 3: Fiz., Astron. **35** (2), 64 (1994).
3. A. A. Katsnel'son, A. I. Olemskoĭ, I. V. Sukhorukova, and G. P. Revkevich, Vestn. Mosk. Univ., Ser. 3: Fiz., Astron. **35** (3), 94 (1994).
4. A. A. Katsnel'son, A. I. Olemskoĭ, G. P. Revkevich, and I. V. Sukhorukova, Usp. Fiz. Nauk **165** (3), 331 (1995) [Phys. Usp. **38**, 317 (1995)].
5. V. M. Avdyukhina, A. A. Katsnel'son, and G. P. Revkevich, Poverkhnost', No. 2, 30 (1999).
6. V. M. Avdyukhina, A. A. Katsnel'son, and G. P. Revkevich, Kristallografiya **44** (1), 49 (1999) [Crystallogr. Rep. **44**, 44 (1999)].
7. V. M. Avdyukhina, A. A. Katsnel'son, and G. P. Revkevich, Vestn. Mosk. Univ., Ser. 3: Fiz., Astron. **40** (4), 45 (1999).
8. V. M. Avdyukhina, L. Dombrovskiĭ, A. A. Katsnel'son, *et al.*, Fiz. Tverd. Tela (St. Petersburg) **41** (9), 1532 (1999) [Phys. Solid State **41**, 1402 (1999)].
9. V. M. Avdyukhina, A. A. Katsnel'son, D. A. Olemskoĭ, *et al.*, Fiz. Met. Metallogr. **88** (6), 63 (1999).
10. M. Ura, Y. Haraguchi, F. L. Chen, and Y. Sakamoto, J. Alloys Compd. **231**, 436 (1995).
11. E. Kudielka-Artner and B. B. Argent, Proc. Phys. Soc. London **80**, 1143 (1962).
12. M. Hansen and K. Anderko, *Constitution of Binary Alloys* (McGraw-Hill, New York, 1958; Metallurgizdat, Moscow, 1962), Vol. 2, p. 1488.
13. Ya. D. Vishnyakov, A. N. Dubrovina, Ya. S. Umanskiĭ, and V. S. Khaĭmovich, Zavod. Lab. **33** (3), 297 (1967).
14. G. P. Revkevich, M. K. Mitkova, A. A. Katsnel'son, *et al.*, Vestn. Mosk. Univ., Ser. 3: Fiz., Astron. **34** (6), 70 (1993).
15. V. M. Avdyukhina, A. A. Katsnel'son, N. A. Prokof'ev, and G. P. Revkevich, Vestn. Mosk. Univ., Ser. 3: Fiz., Astron. **39** (2), 70 (1998).
16. S. M. Myers, M. I. Baskes, H. K. Birnbaum, *et al.*, Rev. Mod. Phys. **64** (2), 559 (1992).
17. Yu. I. Sirotin and M. P. Shaskol'skaya, *Fundamentals of Crystal Physics* (Nauka, Moscow, 1975; Mir, Moscow, 1982).
18. G. Leibfried and N. Brauer, *Point Defects in Metals* (Springer-Verlag, Heidelberg, 1978; Mir, Moscow, 1981).
19. F. J. Blatt, *Physics of Electronic Conduction in Solids* (McGraw-Hill, New York, 1968; Mir, Moscow, 1971).
20. H. Haken, *Synergetics: An Introduction* (Springer-Verlag, Berlin, 1977; Mir, Moscow, 1980), p. 404.

Translated by O. Borovik-Romanova

Physics of the Solid State, Vol. 43, No. 2, 2001, pp. 214–217. Translated from Fizika Tverdogo Tela, Vol. 43, No. 2, 2001, pp. 207–209.

METALS AND SUPERCONDUCTORS

Giant Quantum Oscillations of the Magnetothermoelectric Coefficient in Semimetallic Sb–Bi and Sb–As Alloys

F. M. Muntyanu*, K. M. Pyrtsak*, and A. Gilevski**

**Institute of Applied Physics, Academy of Sciences of Moldova, Chisinau, MD-2028 Moldova*

***International Laboratory of High Magnetic Fields and Low Temperatures, Wroclaw, 53–421 Poland*

Received February 28, 2000; in final form, June 27, 2000

Abstract—Quantum oscillations of the magnetothermoelectric coefficient $\alpha_{ii}(B)$ are investigated in semimetallic Sb–Bi and Sb–As alloys in stationary magnetic fields up to 15 T and at temperatures from 1.9 to 30 K. Quantum oscillations of $\alpha_{ii}(B)$ of a giant amplitude are observed when the longitudinal or transverse magnetic field is oriented along a binary C_2 axis or a bisectory C_1 axis and also when rotating the transverse magnetic field in angle ranges up to [+55°, –55°] around them. © *2001 MAIK "Nauka/Interperiodica".*

Quantum oscillations of the resistance $\rho_{ii}(B)$ and the thermoelectric coefficient $\alpha_{ii}(B)$ in a normal metal (semimetal) are known to be affected in a different way by changes in the scattering processes and by the dependence of the relaxation time of charge carriers on energy $\tau(\varepsilon)$ in a magnetic field. For example, the $\tau(\varepsilon)$ dependence in a magnetic field is not of great importance [1] for the Shubnikov–de Haas effect as the oscillation amplitudes are not very large (~10% of the monotonic part of the resistance) and, in principle, can reach the value of the monotonic part only in sufficiently high fields. The opposite situation occurs for the diffusive part of the magnetothermoelectric coefficient at low temperatures (the net thermoelectric coefficient consists of two components: the diffusive component and that one associated with the phonon-drag effect); its monotonic part is proportional to $\sim(kT/\varepsilon_F)$ and is very small, and the dependence of the relaxation time of charge carriers on energy in a magnetic field can result in [1] anomalously large oscillation amplitudes of $\alpha_{ii}(B)$.

In the present work, the quantum oscillations of $\rho_{ii}(B)$ and $\alpha_{ii}(B)$ are investigated in high-quality samples of Sb (the Fermi surface of Sb consists of three electron pockets centered at the L points and six hole pockets localized at the H points of the Brillouin zone [2]) and the alloys As_xSb_{1-x} ($x \le 0.5$) and $Bi_{1-x}Sb_x$ ($x \ge 0.25$) in stationary magnetic fields up to 15 T and at temperatures from 1.9 to 30 K. The measurements are performed in the International Laboratory of High Magnetic Fields and Low Temperatures (Wroclaw, Poland). The samples for the measurements are produced by a zone-melting method, and their composition was controlled by laser spectroscopy techniques and by x-ray microprobe analyzers. The main results obtained are presented below.

In Sb, the quantum oscillation amplitudes of $\alpha_{ii}(B)$ are not large and amount to as much as several percent of the monotonic component. In contrast, in the alloys As_xSb_{1-x} ($x \le 0.3$) and $Bi_{1-x}Sb_x$ ($x \ge 0.5$), whose Fermi surface is similar to that of Sb [3, 4], the quantum oscillations of the $\alpha_{ii}(B)$ exhibited giant amplitudes (in some samples, $\alpha_{ii}(B)_{osc}/\alpha_{ii}(B)_{mon} \sim 16$) at the orientation of the longitudinal or the transverse magnetic field along a binary C_2 axis or a bisectory C_1 axis and at the rotation of the transverse field in an angle range $\Delta\theta$ around them (Figs. 1, 2). When the As concentration in the As–Sb alloys is increased, $\Delta\theta$ decreases from about [+35°, –35°] at $x = 0.05$ to [+20°, –20°] at $x = 0.3$, and when the Bi concentration in the Bi–Sb alloys is increased, $\Delta\theta$ increases from [+35°, –35°] at $x = 0.95$ to [+55°, –55°] at $x = 0.5$. It should be noted that the giant quantum oscillations (GQO) of the magnetothermoelectric coefficient exhibited the same period as the oscillations of $\rho_{ii}(B)$. The Fourier analysis of these oscillations clearly separated out the frequencies inherent in the energy spectrum of Sb [2] and its alloys with As and Bi. Their identification and their dependence on the alloy composition are presented in [3, 4]; the oscillating part of the magnetoresistance was no more than 10% of the monotonic part of the $\rho_{ii}(B)$.

The quantum oscillations of the magnetothermoelectric coefficient in the case when the magnetic field is oriented outside the $\Delta\theta$ range (with an accuracy of 3–5 %) are described by the existing theories [5, 6]

$$\frac{\alpha_{ii}(B)_{osc}}{\alpha_{ii}(B)_{mon}} \approx \frac{2\pi\varepsilon_F}{\hbar\omega}\frac{\rho_{ii}(B)_{osc}}{\rho_{ii}(B)_{mon}},$$

and their amplitude is not anomalously large.

The temperature dependences of the GQO amplitude of the magnetothermoelectric coefficient $\tilde{\alpha}_{ii}(T)$ in the Sb-based alloys with Bi and As (Fig. 3), as well as the temperature dependences of the longitudinal magnetoresistance in Bi, exhibited a nonmonotonic character with a maximum at $T = T_m$ ($T_m \le 11$ K), whose posi-

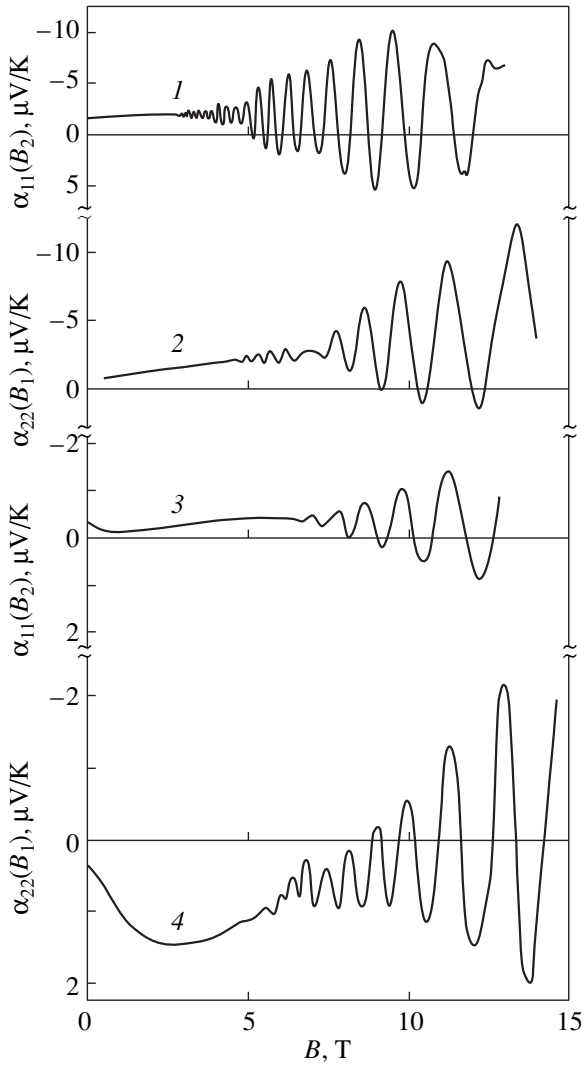

Fig. 1. Quantum oscillations of the magnetothermoelectric coefficient in Sb-based alloys with Bi and As: (*1*) $Bi_{0.1}Sb_{0.9}$, $T = 5.2$ K, $\nabla T \parallel \mathbf{B}^- \parallel \mathbf{C}_2$; (*2*) $Bi_{0.15}Sb_{0.85}$, $T = 6.3$ K, $\nabla T \parallel \mathbf{C}_1$, $\mathbf{B}^- \parallel \mathbf{C}_2$; (*3*) $As_{0.1}Sb_{0.9}$, $T = 9.4$ K, $\nabla T \parallel \mathbf{C}_2$, $\mathbf{B}^- \parallel \mathbf{C}_1$; and (*4*) $As_{0.05}Sb_{0.95}$, $T = 6.4$ K, $\nabla T \parallel \mathbf{C}_1$, $\mathbf{B}^- \parallel \mathbf{C}_2$.

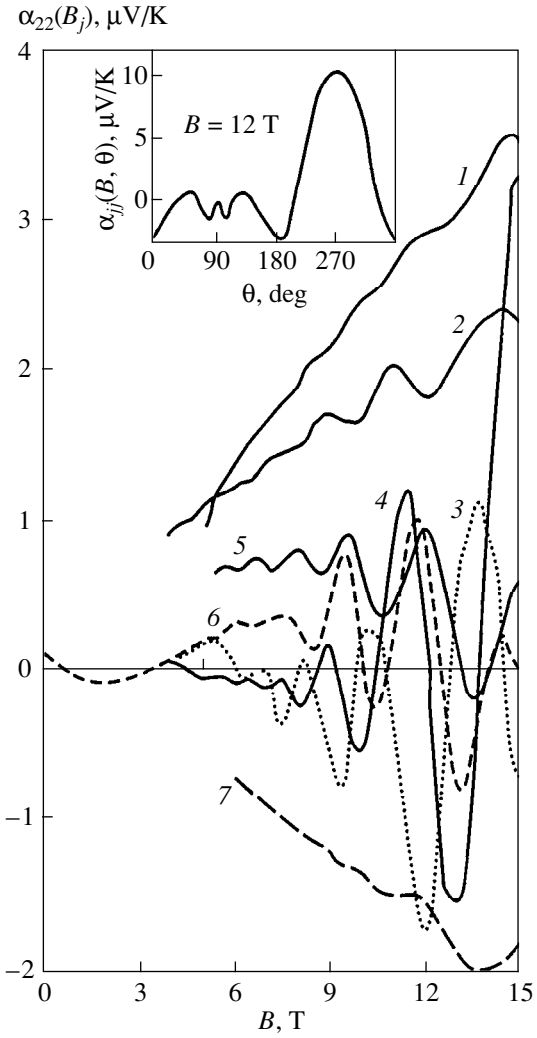

Fig. 2. Magnetic-field dependences of the thermoelectric coefficient in the $Bi_{0.3}Sb_{0.7}$ alloy at 5.2 K, the field is rotated in the trigonal–bisectory plane: (*1*) θ = 0° ($\mathbf{B} \parallel \mathbf{C}_3$), (*2*) θ = 10°, (*3*) θ = 55°, (*4*) θ = 76°, (5) θ = 23°, (*6*) θ = 90°, ($\mathbf{B}^- \parallel \mathbf{C}_1$), and (*7*) θ = 270°, ($\mathbf{B}^+ \parallel \mathbf{C}_1$). The ordinate-axis scale is 1 : 4 for (*7*). The angle dependence of the magnetothermoelectric coefficient in $Bi_{0.3}Sb_{0.7}$ at 5.2 K is shown in the inset.

tion was dependent on the alloy composition and the sample quality. It should be noted that the nonmonotonic change in the oscillation amplitudes of the longitudinal magnetoresistance with temperature was explained in [7] on the basis of the two-band model of the energy spectrum accounting for the electron–phonon and electron–impurity interactions and the dependence of the relaxation time of the charge carriers on the magnetic field.

In addition, it has been found that the GQO amplitude of the magnetic-field–dependent thermoelectric coefficient $\tilde{\alpha}_{ii}(B)$ changes (Fig. 4) according to a power law $\tilde{\alpha}_{ii}(B) \sim B^k$, with the power k being dependent on B ($k \approx 4$–5.5 at $B \leq 7$–9 T and $k \approx 1.2$–2.4 at $B > 9$ T) and being of a considerably larger value than in the case of a purely diffusive contribution to the net thermoelectric coefficient [8].

A remarkable feature in the behavior of the magnetothermoelectric coefficient is observed when reversing the magnetic field direction [9]. For example, when the magnetic field is oriented along the positive direction with respect to the C_2 axis ($\mathbf{B}^+ \parallel \mathbf{C}_2$), we have $\alpha_{22}(B_1)_{osc} < \alpha_{22}(B_1)_{mon}$, whereas for the opposite direction of the magnetic field ($\mathbf{B}^- \parallel \mathbf{C}_2$), we have $\alpha_{22}(B_1)_{osc} \gg \alpha_{22}(B_1)_{mon}$.

The amplitude of quantum oscillations of $\alpha_{22}(B_1)$ changes insignificantly (~15%) as the magnetic field is reversed. Thus, the above-mentioned feature is mainly associated with $\alpha_{22}(B_1)_{mon}$, which, as a result of the tilting of the electron and hole constant-energy surfaces with respect to the basal plane [9], contains even (quadratic) terms in the magnetic field and odd (linear in B) terms changing their sign as the field orientation is reversed from $\mathbf{B}^+$ to $\mathbf{B}^-$. Therefore, $\alpha_{22}(B)_{mon}$ varies in wide limits with the rotating magnetic field, which undoubtedly results in variations in the ratio between the monotonic and oscillating parts of the magnetothermoelectric coefficient.

However, the manifestation of quantum oscillations of the magnetothermoelectric coefficient with an anomalously large amplitude is not associated with the mixed-parity terms, because in the case of $\mathbf{B} \parallel \mathbf{C}_1$, where the odd terms are absent, the GQO of $\alpha_{11}(B_2)$ are observed at both $\mathbf{B}^+$ and $\mathbf{B}^-$.

The phonon drag of charge carriers must be of importance [10, 11] in the temperature range 1.9–30 K, where the magnetothermoelectric coefficients in Sb and its alloys with As and Bi are measured. The phonon-drag effect is strong in Sb (referred to as "total" in [10]) and predominantly contributes to the thermoelectric coefficient when compared to the diffusive component. The anomalies of the quantum oscillations of the magnetothermoelectric coefficient are not detected in Sb, which supports the conclusion made in [12] that only the strong phonon drag of charge carriers (without additional scattering mechanisms except the phonon one) does not result in the GQO of $\alpha_{ii}(B)$.

The phonon-drag effect is considerably weaker in the As_xSb_{1-x} ($x \le 0.3$) and $Bi_{1-x}Sb_x$ ($x \ge 0.5$) alloys, because the phonons are scattered not only by electrons and holes, but also by structural defects and neutral impurities. Many experimental facts are evidence for the strengthening of these scattering mechanisms: small values of the thermoelectric coefficient [13, 14] and of the monotonic part of the magnetothermoelectric coefficient, insignificant changes [14] in the components of the resistivity tensor in the temperature range 4.2–77 K, the small ratio of the residual resistances of samples $2 \le \rho_{300\,K}/\rho_{4.2\,K} \le 10$, and rather high values of the Dingle temperature of charge carriers ($T_D^{e,h} \le 12$ K) [3, 4], as well as the relatively low mobilities of the electrons and holes in the alloys (the mobil-

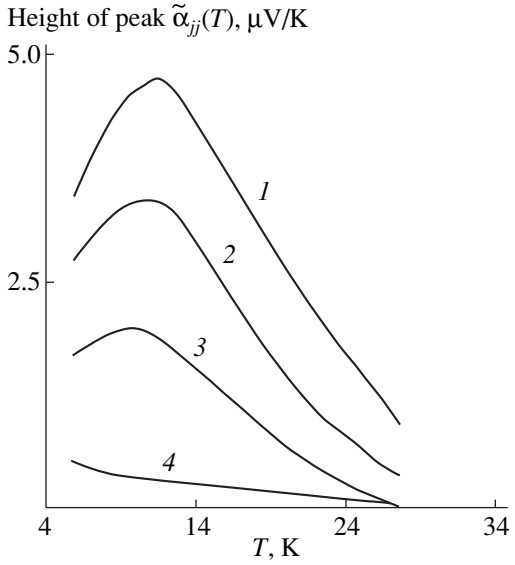

Fig. 3. Temperature dependences of the amplitudes of the quantum oscillations of the magnetothermoelectric coefficient in the $Bi_{0.15}Sb_{0.85}$ alloy at $\mathbf{B}^- \parallel \mathbf{C}_2$, $\nabla T \parallel \mathbf{C}_1$, and different magnetic fields: (*1*) 11.234, (*2*) 9.765, (*3*) 8.64, and (*4*) 6.2 T.

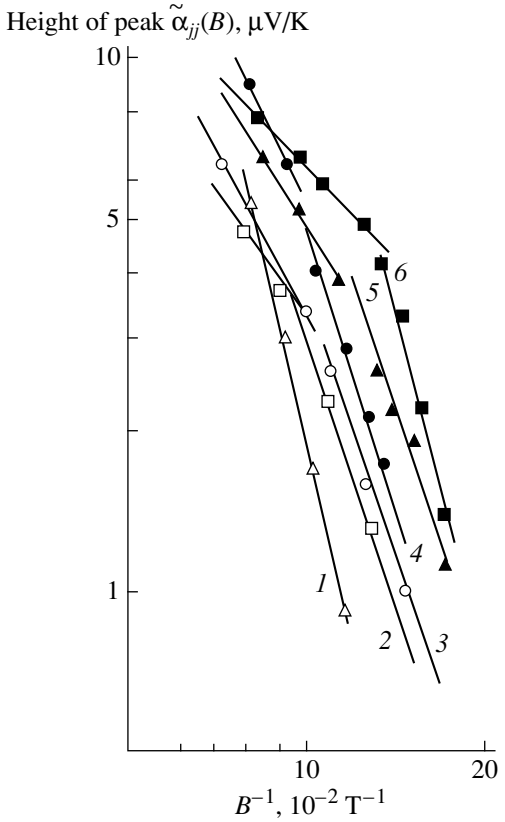

Fig. 4. Magnetic-field dependences of the amplitudes of the quantum oscillations of the magnetothermoelectric coefficient in the Sb-based alloys with As and Bi: (*1*) $As_{0.1}Sb_{0.9}$, $\mathbf{B}^- \parallel \mathbf{C}_1$, $\nabla T \parallel \mathbf{C}_2$, T = 6.53 K; (*2*) $BiO_{0.35}Sb_{0.65}$, the angle between $\mathbf{C}_1$ and $\mathbf{B}^-$ is 30°, $\nabla T \parallel \mathbf{C}_2$, T = 4.6 K; (*3*) $Bi_{0.15}Sb_{0.85}$, $\mathbf{B}^- \parallel \mathbf{C}_2$, $\nabla T \parallel \mathbf{C}_1$, T = 5.2 K; (*4*) $As_{0.05}Sb_{0.95}$, $\mathbf{B}^- \parallel \mathbf{C}_2$, $\nabla T \parallel \mathbf{C}_1$, T = 6.4 K; (*5*) $Bi_{0.1}Sb_{0.9}$, $\mathbf{B}^- \parallel \mathbf{C}_2$, $\nabla T \parallel \mathbf{C}_1$, T = 5.8 K; and (*6*) $Bi_{0.05}Sb_{0.95}$, $\mathbf{B}^- \parallel \mathbf{C}_1$, $\nabla T \parallel \mathbf{C}_2$, T = 5.6 K. The ordinate-axis scales are 4 : 1 for (*1*, *3*, *4*), and 2 : 1 for (*2*).

ities of charge carriers in the alloys are more than two orders of magnitude lower than those in Sb).

In conclusion, the phonon-drag effect is weakened in the As_xSb_{1-x} ($x \le 0.2$) and $Bi_{1-x}Sb_x$ ($x \ge 0.5$) alloys because of the phonon scattering not only at electrons and holes, but also at structural defects and neutral impurities in the case of the magnetic-field orientation within the angle range $\Delta\theta$ (when the cross sections of the electron and hole Fermi surfaces, as well as the cyclotron masses of charge carriers, are close in values [3, 4]). In this case, the relaxation times of charge carriers in the alloys contain additional terms that depend differently on energy in the magnetic field (as supported by the magnetic-field and temperature dependences of GQO of $\alpha_{ii}(B)$) and are responsible for the anomalous contributions to the quantum oscillations of the magentothermoelectric coefficient.

ACKNOWLEDGMENTS

The authors are grateful to Prof. Ya. Klyamut, V. Nizhankovskiĭ, and T. Palevskiĭ for assistance in these investigations in the International Laboratory.

REFERENCES

1. A. V. Pantsulaya and A. A. Varlamov, Phys. Lett. A **136** (6), 317 (1989).
2. J. Ketterson and Y. Eckstein, Phys. Rev. **132** (5), 1885 (1963).
3. F. M. Muntyanu, Phys. Status Solidi B **136**, 749 (1986).
4. F. M. Muntyanu, V. G. Kistol, and I. A. Popov, Phys. Status Solidi B **148**, K37 (1988).
5. Y. Ono, J. Phys. Soc. Jpn. **35**, 1280 (1973).
6. P. Streda and L. Smrcka, Czech. J. Phys., Sect. B **31**, 1114 (1981).
7. P. Streda, Czech. J. Phys., Sect. B **33**, 49 (1983).
8. P. S. Zyryanov and G. I. Guseva, Usp. Fiz. Nauk **95**, 565 (1968) [Sov. Phys. Usp. **11**, 538 (1968)].
9. D. V. Gitsu and F. M. Muntyanu, Phys. Status Solidi B **120**, K45 (1983).
10. R. S. Blewer, N. H. Zebouni, and C. G. Grenier, Phys. Rev. **174** (3), 174 (1968).
11. M. S. Bresler and N. A. Red'ko, Zh. Éksp. Teor. Fiz. **62**, 1867 (1972) [Sov. Phys. JETP **35**, 973 (1972)].
12. E. E. Narimanov and K. A. Sakharov, Fiz. Tverd. Tela (St. Petersburg) **36** (12), 3489 (1994) [Phys. Solid State **36**, 1853 (1994)].
13. D. V. Gitsu, I. M. Golban, A. I. Makeichik, *et al.*, Phys. Status Solidi B **100**, 401 (1980).
14. A. I. Makeĭchik, F. M. Muntyanu, and M. I. Onu, *Semimetals and Narrow-Gap Semiconductors under External Influences* (Shtiintsa, Kishinev, 1983), p. 48.

Translated by N. Kovaleva

Physics of the Solid State, Vol. 43, No. 2, 2001, pp. 218–223. Translated from Fizika Tverdogo Tela, Vol. 43, No. 2, 2001, pp. 210–214.

METALS AND SUPERCONDUCTORS

Heat Conductivity of the Heavy-Fermion Compound $YbAgCu_4$

A. V. Golubkov*, L. S. Parfen'eva*, I. A. Smirnov*, H. Misiorek, J. Mucha**, and A. Jezowski****

**Ioffe Physicotechnical Institute, Russian Academy of Sciences, Politekhnicheskaya ul. 26, St. Petersburg, 194021 Russia*
e-mail: Igor.Smirnov@shuvpop.ioffe.rssi.ru

***Institute of Low-Temperature and Structural Research, Polish Academy of Sciences, Wroclaw, 53-529 Poland*

Received June 28, 2000

Abstract—The heat conductivity and electrical resistivity of a polycrystalline $YbAgCu_4$ sample were measured in the 4.2–300-K temperature range. It is shown that at low temperatures (in the region corresponding to the coherent Kondo lattice) the Lorenz number behaves in accordance with a theoretical model developed for heavy-fermion materials. © *2001 MAIK "Nauka/Interperiodica".*

In recent years, studies of intermetallic compounds of the type $LnMCu_4$ (where Ln stands for a rare-earth element and M stands for In, Ag, Au, Cd, Mg, Tl, Zn, or Pb [1, 2]), which crystallize in an $AuBe_5$-type fcc lattice [C15*b* structure, space symmetry group $F\bar{4}3m(T_d^2)$], have attracted the interest of scientists in the world's leading laboratories. These compounds possess fairly unusual physical properties. Of particular interest in this respect are $YbInCu_4$ and $YbAgCu_4$.

At $T_v \sim 40$–80 K and atmospheric pressure, $YbInCu_4$ exhibits a first-order isostructural phase transition from a Curie–Weiss paramagnet (state with localized magnetic moments) at $T > T_v$ to a Pauli paramagnet, a compound with a rare-earth ion of mixed valence (nonmagnetic Fermi-liquid state), for $T < T_v$.[1]

$YbAgCu_4$ is a typical heavy-fermion compound. However, in contrast to the classical heavy-fermion materials, it is categorized into "moderately" heavy fermion systems [6], because its γ, the coefficient of a term linear in temperature in the electronic specific heat, is only ~200–250 mJ/mol K^2 [1, 2, 4, 7–11], while in classical heavy-fermion systems, $\gamma > 400$ mJ/mol K^2.

$YbAgCu_4$ possesses properties typical of a Kondo lattice [2, 7, 12–14]. It undergoes a transition from a single-impurity Kondo regime at high temperatures, $T > T_K$ (T_K is the Kondo temperature), to a coherent Kondo lattice heavy-fermion regime in the low-temperature domain, $T < T_K$. The T_K temperature derived from measurements of various physical effects ranges from 40 to 130 K [14–20]. Calculations yield 86 K [5]. Experimental values cluster most frequently around ~60–65 K.

The calculated and experimental values of the carrier effective mass in $YbAgCu_4$ for $T < T_K$ are ~$86m_0$ [5] and ~$60m_0$ [2, 17], respectively (m_0 is the electronic mass). No magnetic ordering is observed in $YbAgCu_4$ down to ~0.45 K [2]. The Yb valence is +3 in this compound. This follows from magnetic susceptibility data, by which the experimental value of the Yb ion effective magnetic moment μ_{eff} is ~$(4.25–4.6)\mu_B$, which is close to that for the free Yb^{+3} ion ($J = 7/2$), $\mu_{eff} = 4.54\ \mu_B$, as well as from L_{III} x-ray measurements [1, 18] and XPS and BIS spectra [17].

The Debye temperature Θ of $YbAgCu_4$ is 245–279 K [1, 16]. The above data on $YbAgCu_4$ will be necessary in analyzing our experimental data on the heat conductivity of this compound. To make the picture complete, we present a list of the physical parameters of $YbAgCu_4$ which have been studied in various laboratories around the world in recent years.

The magnetic susceptibility χ [1, 2, 6, 9, 12, 21–24]; magnetization [16, 21, 24]; magnetostriction [21]; heat capacity [1, 2, 8, 9, 16, 21–24]; electrical resistivity ρ [1, 2, 7, 9, 16, 22]; $\Delta\rho/\rho(H)$ [16]; thermopower [25, 26]; Hall constant [1, 8]; variation in ρ, χ, and thermopower under hydrostatic pressure [13, 27–31]; and linear expansion coefficient [6] were measured over a broad temperature range in $YbAgCu_4$. Neutron scattering experiments were carried out [15, 19, 32], photoelectron spectra [14] and NMR [20] were studied, and band structure investigations were performed both experimentally [17] and theoretically [33, 34].

[1] The system existing at $T < T_v$ is called the "light" heavy-fermion system [3]. The main references to experimental and theoretical publications dealing with $YbInCu_4$ can be found in [1, 4, 5].

The study of the heat conductivity κ of $YbAgCu_4$ is dealt with in two publications [35, 36] which presented the same experimental data on κ of this material.[2] We note immediately that our analysis of the results on κ for $YbAgCu_4$ will be based on an approach radically different from the one employed in [35, 36]. We measured the heat conductivity and electrical resistivity of $YbAgCu_4$ within the 4.2- to 300-K range on a cast polycrystalline sample. The sample was prepared by the technique described in [38]. $YbAgCu_4$ was synthesized from doubly distilled Yb remelted in a tantalum crucible (to remove the oxide), Ag of 99.99% purity, and OSCh-V3-grade Cu. The alloy components taken in stoichiometric ratios were remelted in a thin-walled (wall thickness ~0.1 mm), sealed tantalum container evacuated to $\sim 10^{-4}$ mm Hg. The samples were melted in an induction furnace. The sample to be studied was characterized by x-ray diffraction on a DRON-2 setup (CuK_α radiation). The lattice constant a was measured as 7.076 Å. According to literature data, the a constant of $YbAgCu_4$ varies from 7.054 to 7.087 Å [1, 2, 6, 9, 12, 20, 22, 25, 32, 34]. The quantities κ and ρ were measured on a setup similar to the one used in [39].

Figure 1 presents the results obtained for the $\rho(T)$ of the $YbAgCu_4$ sample studied by us. Also shown for comparison are the literature data for this material [1, 7, 9, 13]. The $\rho(T)$ relation is seen to follow the behavior typical of heavy-fermion compounds. In the low-temperature region ($T < T_K$, coherent Kondo lattice), $\rho(T)$ can be presented in the form [9, 13]

$$\rho = \rho_0 + AT^2. \quad (1)$$

Here, ρ_0 is the residual resistivity. The A coefficient is a measure of the electronic density of states at the Fermi level, $A \sim N(E_F)$; in addition, $A \sim 1/T_K^2$ [9, 13].

Figure 2 plots ρ as a function of T^2 for the $YbAgCu_4$ obtained in this work and in [9].

Figures 3 and 4 display our experimental data on the total heat conductivity κ_{tot} of $YbAgCu_4$. Also shown in Fig. 3 for comparison are the data for κ_{tot} of $YbAgCu_4$ quoted in [35, 36].[3] The behavior of the $\kappa_{tot}(T)$ of our sample is similar to that reported in [35, 36]. For a metal, κ_{tot} can be written in the form

$$\kappa_{tot} = \kappa_{ph} + \kappa_e, \quad (2)$$

[2] Our publications [4, 37] on the study of the heat conductivity of $YbInCu_4$, $LuInCu_4$, and $LuAgCu_4$ mentioned that we did not succeed in finding references to measurements of κ for these materials. Indeed, among the copious literature devoted to the investigation of $LnMCu_4$ compounds (Ln = Yb, Lu; M = In, Ag), we could not find any reference to [35, 36]. We have stumbled on them only recently. We hope the authors of [35, 36] will excuse us for overlooking this.

[3] Unfortunately, the original data for $\rho(T)$ on the sample studied are not presented in [35, 36].

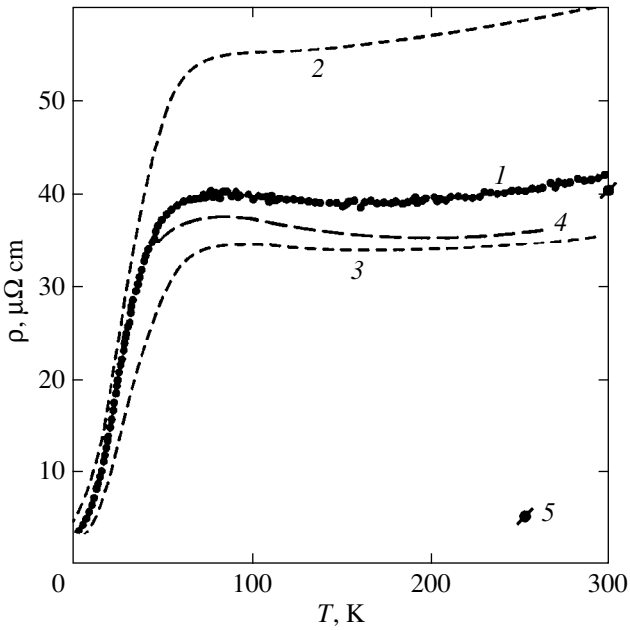

Fig. 1. Temperature dependence of the electrical resistivity of $YbAgCu_4$. (*1*) Our data, (*2*) data from [9], (*3*) [13], (*4*) [1], and (*5*) [7].

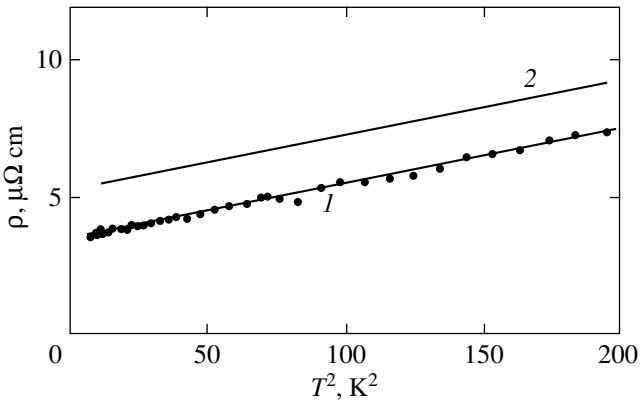

Fig. 2. ρ vs. T^2 relation. (*1*) Our data and (*2*) data of [9].

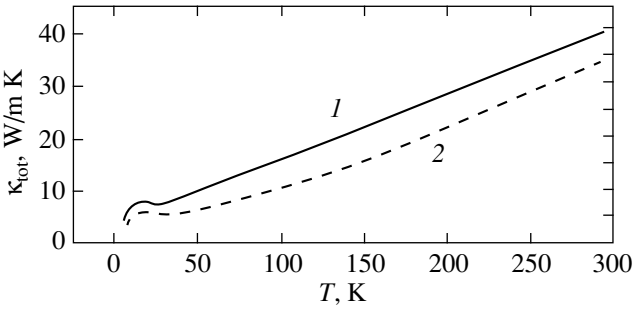

Fig. 3. Temperature dependence of κ_{tot} of $YbAgCu_4$. (*1*) Our data and (*2*) data of [35, 36].

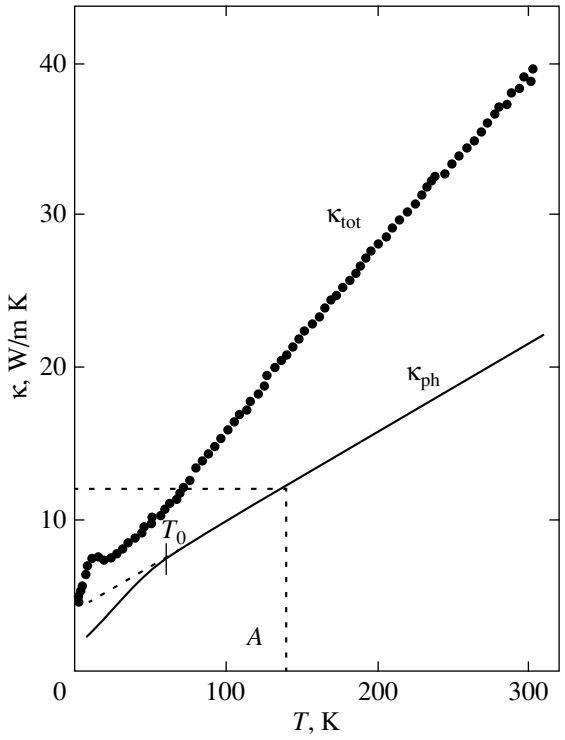

Fig. 4. Temperature dependence of κ_{tot} and κ_{ph} of $YbAgCu_4$.

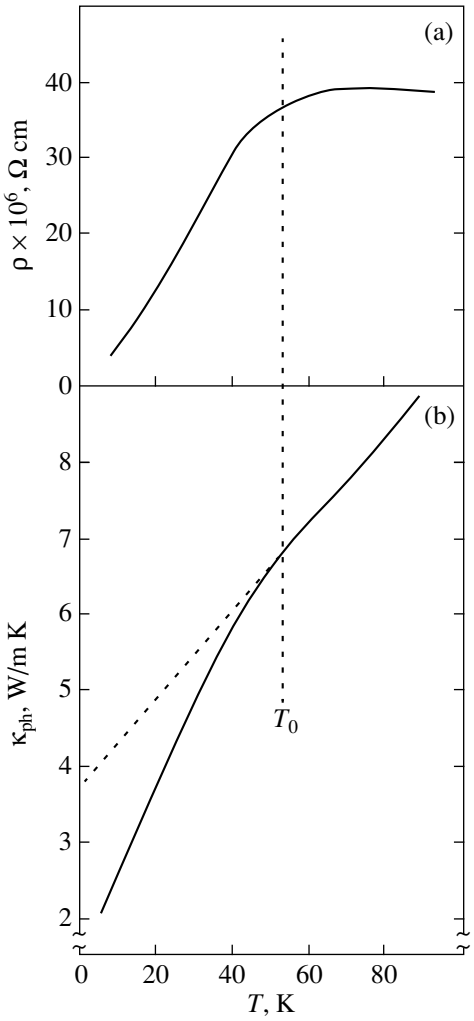

Fig. 5. Comparison of (a) $\rho(T)$ and (b) $\kappa_{ph}(T)$ relations of $YbAgCu_4$ in the low-temperature region (square *A* in Fig. 4).

where κ_{ph} and κ_e are the lattice and electronic components of heat conductivity, respectively. κ_e obeys the Wiedemann–Franz law

$$\kappa_e = LT/\rho, \tag{3}$$

where L is the Lorenz number. For $T \gtrsim \Theta$ and very low temperatures for "clean" samples, and for low and high temperatures for "dirty" samples of metals, we have $L = L_0$[40], where L_0 is the Sommerfeld value of the Lorenz number ($L_0 = 2.45 \times 10^{-8}$ WΩ/K^2). The sample studied by us may not be considered a clean metal, and, therefore, one may assume, as a first approximation, that $L = L_0$ throughout the temperature range studied.

It is also known [41] that the behavior of $L(T)$ in heavy-fermion systems differs substantially from that in both clean and dirty metals. According to [41], L/L_0 first grows with increasing temperature from $T = 0$ K as $L/L_0 \sim T^2$ passes through a maximum, falls off to 0.648, and then increases again and reaches unity around $T \sim T_K$ to remain equal to unity afterwards up to high temperatures.

Figure 4 presents a calculation of κ_{ph} from Eqs. (2) and (3) made under the assumption that $L = L_0$. One readily sees that, from 300 K down to $T_0 = 60$ K, $\kappa_{ph}(T)$ follows a nearly linear dependence ($\kappa_{ph} \sim T^{0.8}$). For $T <$ 60 K, a deviation from this relation is observed (see Fig. 4 and, on an enlarged scale, Figs. 5b and 6a). Putting aside, for the time being, the discussion of the nature of this dependence of κ_{ph} on T for $T > 60$ K, which is not typical of crystalline materials, we shall instead consider the reason for the deviation of κ_{ph} from the $T^{0.8}$ scaling observed for $T < 60$ K. It was found (Fig. 5) that the temperature T_0 in the $\kappa_{ph}(T)$ dependence corresponds to the temperature at which the regime in the $\rho(T)$ dependence changes from incoherent for $T > T_0$ to coherent for $T < T_0$. One may conjecture that the deviation $\kappa_{ph}(T)$ from the $\kappa_{ph} \sim T^{0.8}$ relation for $T < T_0$ results from a wrong choice of the Lorenz number in Eq. (3). In order to remove this deviation, L should be less than L_0. Figure 6b presents an L/L_0 calculation made under the assumption that κ_{ph} for $T < T_0$ is equal to the values corresponding to the dashed line *I*. As can be seen from Figs. 6b and 6c, our $L/L_0(T)$ relation obtained for $YbAgCu_4$ agrees well with the tem-

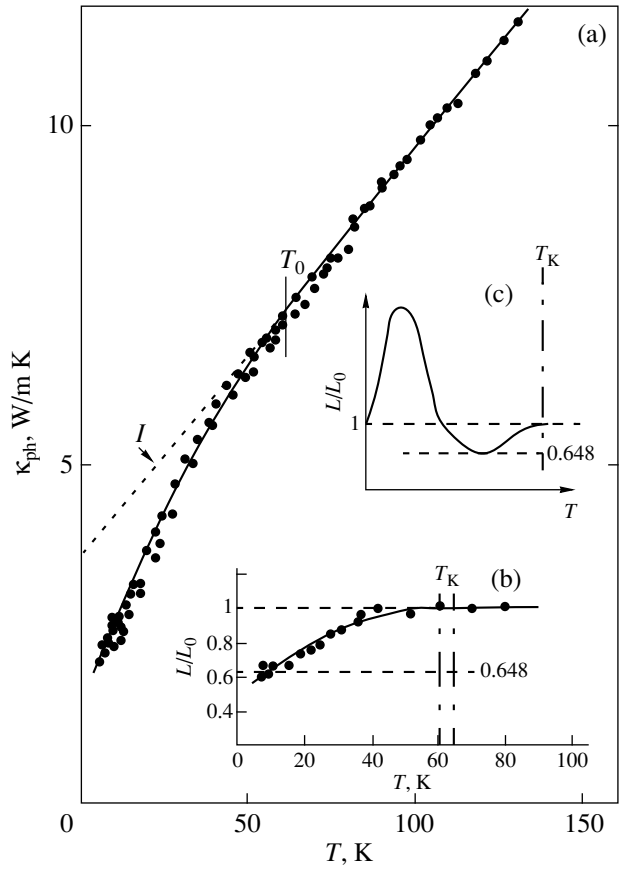

Fig. 6. Experimental dependences (a) $\kappa_{ph}(T)$ (square *A* in Fig. 4) and (b) $L/L_0(T)$ obtained for $YbAgCu_4$. (c) Overall behavior of the theoretical relation $L/L_0(T)$ for heavy-fermion systems [41]. T_K is the Kondo temperature.

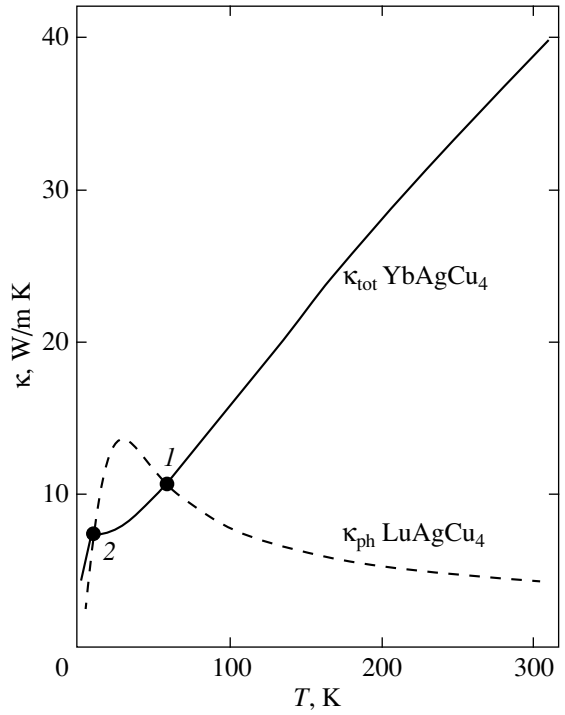

Fig. 7. Temperature dependence of κ_{tot} for $YbAgCu_4$ and of κ_{ph} for $LuAgCu_4$ [37].

perature dependence of the Lorenz number proposed in [41] for heavy-fermion systems. Our attempt to isolate the electronic component of heat conductivity from κ_{tot} of $YbAgCu_4$ [which would permit one to subsequently estimate $L/L_0(T)$] by a standard technique involving the use of $LuAgCu_4$ as a reference material [37] failed. Following this technique, one could suggest that the values of κ_{ph} for $YbAgCu_4$ and $LuAgCu_4$ should be approximately equal in magnitude, so that κ_e of $YbAgCu_4$ would be found from the relation

$$\kappa_e(YbAgCu_4) = \kappa_{tot}(YbAgCu_4) - \kappa_{ph}(LuAgCu_4). \quad (4)$$

However, as can be seen from Fig. 7, at two points, *1* and *2*, we have $\kappa_{ph}(LuAgCu_4) = \kappa_{tot}(YbAgCu_4)$ in the low-temperature domain and, hence, $\kappa_e(YbAgCu_4)$ calculated from Eq. (4) (as well as L) will be zero, while within the 10- to 60-K region they should even be negative, which appears absurd.

The behavior of κ_{ph} at temperatures $T > 60$ K remains a mystery. What could be the reason for the unusual temperature scaling $\kappa_{ph} \sim T^{0.8}$ of crystalline

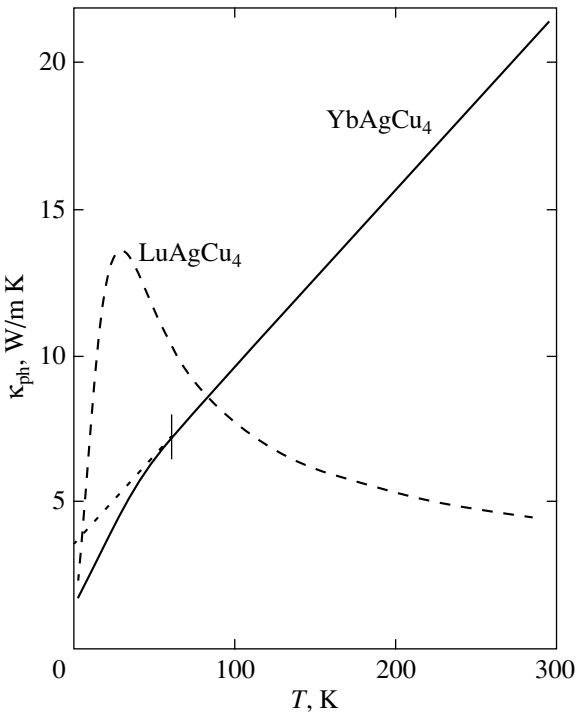

Fig. 8. Temperature dependences of κ_{ph} for $YbAgCu_4$ and $LuAgCu_4$ [37].

materials? Interestingly, a similar temperature dependence of κ_{ph} is also observed in $YbInCu_4$ [4]. This behavior of $\kappa_{ph}(T)$ is characteristic of strongly defected, close to amorphous materials, as well as of semicrystalline materials (i.e., amorphous substances containing crystallized regions) [42]. The heat conductivity of $LuInCu_4$ and $LuAgCu_4$ behaves differently [37] (these materials are related to $YbInCu_4$ and $YbAgCu_4$). The $\kappa_{ph}(T)$ relation in them exhibits features characteristic of conventional, heavily defected crystalline objects; namely, κ_{ph} increases with temperature from $T = 0$ K and passes through a maximum, to subsequently fall off according to the law $\kappa_{ph} \sim T^{-0.5}$. One could try to assign the unusual behavior of $\kappa_{ph}(T)$ of $YbAgCu_4$ (compared to $LuAgCu_4$) to phonon scattering from the crystal-field-split paramagnetic levels of the Yb ions in $YbAgCu_4$ [13, 28], as this has been observed in a large number of rare-earth materials [43, 44]. But then, according to [44], κ_{ph} of $YbAgCu_4$ should be smaller than that of $LuAgCu_4$ throughout the temperature range covered. However, as is evident from Fig. 8, this holds true only for $T \gtrsim 80$ K, whereas in the 4- to 80-K interval, on the contrary, κ_{ph} of $LuAgCu_4$ exceeds that of $YbAgCu_4$. Thus, we can conclude that in the case of $YbAgCu_4$, we have not succeeded in observing an effect of the crystal field on κ_{ph}. Unfortunately, we still cannot offer an unambiguous answer as to why $YbAgCu_4$ (as well as $YbInCu_4$) exhibits a nonstandard temperature dependence of κ_{ph}.

ACKNOWLEDGMENT

The authors are grateful to N.F. Kartenko and N.V. Sharenkova for x-ray structural measurements.

The work was carried out in the framework of a bilateral agreement between the Russian and Polish Academies of Sciences and was supported by the Russian Foundation for Basic Research (grant no. 99-02-18078).

REFERENCES

1. J. L. Sarrao, C. D. Immer, Z. Fisk, *et al.*, Phys. Rev. B **59** (10), 6855 (1999).
2. C. Rossel, K. N. Yang, M. B. Maple, *et al.*, Phys. Rev. B **35** (4), 1914 (1987).
3. I. Felner, I. Nowik, D. Vaknin, *et al.*, Phys. Rev. B **35** (13), 6956 (1987).
4. I. A. Smirnov, L. S. Parfen'eva, A. Jezowski, *et al.*, Fiz. Tverd. Tela (St. Petersburg) **41** (9), 1548 (1999) [Phys. Solid State **41**, 1418 (1999)].
5. A. V. Goltsev and G. Bruls, submitted to Phys. Rev. B.
6. J. L. Sarrao, C. L. Benton, Z. Fisk, *et al.*, Physica B (Amsterdam) **223/224**, 366 (1996).
7. N. Pillmayer, E. Bauer, and K. Yoshimura, J. Magn. Magn. Mater. **104–107**, 639 (1992).
8. A. L. Cornelius, J. M. Lawrence, J. L. Sarrao, *et al.*, Phys. Rev. B **56** (13), 7993 (1997).
9. N. Tsujii, J. He, K. Yoshimura, *et al.*, Phys. Rev. B **55** (2), 1032 (1997).
10. A. Lacerda, T. Graf, M. F. Hundley, *et al.*, Physica B (Amsterdam) **206/207**, 358 (1995).
11. Z. Fisk and M. B. Maple, J. Alloys Compd. **183**, 303 (1992).
12. D. T. Adroja, S. K. Malik, B. D. Padalia, and R. Vijayaraghavan, J. Phys. C **20**, L307 (1987).
13. E. Bauer, R. Hauser, E. Gratz, and K. Payer, Phys. Rev. B **48** (21), 15873 (1993).
14. P. Waibel, M. Grioni, D. Malterre, *et al.*, Z. Phys. B **91**, 337 (1993).
15. P. Schlottman, J. Appl. Phys. **73**, 5412 (1993).
16. T. Graf, J. M. Lawrence, M. F. Hundley, *et al.*, Phys. Rev. B **51** (21), 15053 (1995).
17. J. S. Kang, J. W. Allen, C. Rossel, *et al.*, Phys. Rev. B **41** (7), 4078 (1990).
18. J. M. Lawrence, G. H. Kwei, P. C. Canfield, *et al.*, Phys. Rev. B **49** (3), 1627 (1994).
19. G. Polatsek and P. Bonville, Z. Phys. B **88**, 189 (1992).
20. H. Nakamura, K. Nakajima, Y. K. Kitaoka, *et al.*, Physica B (Amsterdam) **171**, 238 (1991).
21. K. Yoshimura, T. Nitta, M. Mekata, *et al.*, Phys. Rev. Lett. **60** (9), 851 (1988).
22. J. L. Sarrao, C. D. Immer, C. L. Benton, *et al.*, Phys. Rev. B **54** (17), 12207 (1996).
23. K. Yoshimura, T. Nitta, T. Shimizu, *et al.*, J. Magn. Magn. Mater. **90/91**, 466 (1990).
24. M. J. Besnus, P. Haen, N. Hamdaoui, *et al.*, Physica B (Amsterdam) **163**, 571 (1990).
25. R. Casanova, D. Jaccard, C. Marcenat, *et al.*, J. Magn. Magn. Mater. **90/91**, 587 (1990).
26. E. Bauer, Adv. Phys. **40** (4), 417 (1991).
27. J. D. Thompson, H. A. Borges, Z. Fisk, S. Horn, R. D. Parks, and G. L. Wells, in *Theoretical and Experimental Aspect of Valence Fluctuations and Heavy Fermions*, Ed. by L. C. Gupta and S. K. Malik (Plenum, New York, 1987), p. 151.
28. T. Graf, R. Movshovich, J. D. Thompson, *et al.*, Phys. Rev. B **52** (5), 3099 (1995).
29. J. M. Mignot and J. Witting, in *Physics and Solids under Higer Pressure*, Ed. by J. S. Schilling and R. N. Shelton (North-Holland, Amsterdam, 1981), p. 311.
30. E. Bauer, R. Hauser, E. Gratz, *et al.*, Physica B **199/200**, 527 (1994).
31. R. Ruzitschka, R. Hauser, E. Bauer, *et al.*, Physica B (Amsterdam) **230/232**, 279 (1997).
32. A. Severing, A. P. Murani, J. D. Thompson, *et al.*, Phys. Rev. B **41** (4), 1739 (1990).
33. P. Monochesi and A. Continenza, Phys. Rev. B **54** (19), 13558 (1996).
34. A. Continenza and P. Monachesi, J. Appl. Phys. **79** (8), 6423 (1996).
35. E. Bauer, E. Gratz, G. Hutflesz, *et al.*, Physica B (Amsterdam) **186/188**, 494 (1993).

36. E. Bauer, in *Transport and Thermal Properties of f-Electron Systems*, Ed. by G. Oomi, H. Fujii, and T. Fujita (Plenum, New York, 1993), p. 133.
37. A. V. Golubkov, L. S. Parfen'eva, I. A. Smirnov, *et al.*, Fiz. Tverd. Tela (St. Petersburg) **42** (11), 1938 (2000) [Phys. Solid State **42**, 1990 (2000)].
38. A. V. Golubkov, T. B. Zhukova, and V. M. Sergeeva, Izv. Akad. Nauk SSSR, Neorg. Mater. **2** (11), 77 (1966).
39. A. Jezowski, J. Mucha, and G. Pompe, J. Phys. D **20**, 1500 (1987).
40. I. A. Smirnov and V. I. Tamarchenko, *Electron Heat Conductivity in Metals and Semiconductors* (Nauka, Leningrad, 1977).
41. V. I. Belitsky and A. V. Goltsev, Physica B (Amsterdam) **172**, 459 (1991).
42. C. L. Choy and D. Greig, J. Phys. C **8**, 3131 (1975).
43. R. G. Mitarov, L. S. Parfen'eva, V. V. Popov, and I. A. Smirnov, Fiz. Tverd. Tela (St. Petersburg) **42** (12), 2147 (2000) [Phys. Solid State **42**, 2211 (2000)].
44. I. A. Smirnov and V. S. Oskotskii, *Handbook on the Physics and Chemistry of Rare Earths*, Ed. by K. A. Gschneidner, Jr. and L. Eyring (North-Holland, Amsterdam, 1993), Vol. 16, p. 107.

Translated by G. Skrebtsov

Physics of the Solid State, Vol. 43, No. 2, 2001, pp. 224–230. Translated from Fizika Tverdogo Tela, Vol. 43, No. 2, 2001, pp. 215–221.

METALS AND SUPERCONDUCTORS

The Spontaneous Formation of a Vortex Structure in a Type II Superconductor–Ferromagnet Bilayer

Yu. I. Bespyatykh* and W. Wasilevski**

**Institute of Radio Engineering and Electronics (Fryazino Branch), Russian Academy of Sciences, pl. Vvedenskogo 1, Fryazino, Moscow oblast, 141120 Russia*
e-mail: Svg318@ire216.Msk.ru

***Technical University, Radom, Poland*

Received June 6, 2000

Abstract—The conditions for the formation of a vortex structure in a thin superconducting film under the action of a stray field of stripe domain structure of a uniaxial ferromagnet are determined. The critical magnetization of the magnetic material is calculated, above which the mixed state of the superconductor becomes energetically favored over the Meissner phase. It is shown that the critical magnetization decreases monotonically with decreasing thickness of the superconducting film and is of the order of ten gauss in typical actual situations. The critical-current anisotropy in a superconducting film with an induced vortex structure is discussed qualitatively. © *2001 MAIK "Nauka/Interperiodica".*

INTRODUCTION

It is known that the exchange interaction between the spin subsystem of a ferromagnet and the conduction electrons of a type II superconductor can give rise to spatially inhomogeneous states [1–3] similar to the cryptoferromagnetic state of ferromagnetic superconductors [4, 5]. In layered structures with electromagnetic interaction between localized spins of the magnet and paired electrons of the superconductor, the formation of magnetic domains can be suppressed when the thickness of the ferromagnetic layers is less than a critical value [6–11]. The occurrence of weak couplings [12] and artificial pinning [13] and depinning of Abrikosov vortices [14, 15] in ferromagnet–superconductor systems is of particular interest for practical applications.

Experimental studies of transport phenomena in type II superconductors revealed that the critical current increases with the concentration of ferromagnetic impurities [16]. It was established that vortices are attracted to impurities, and this attraction is due to electromagnetic interaction of the magnetic moments of impurity atoms with paired electrons of the superconductor [16, 17]. The influence of ferromagnetic coatings and applications on the distribution and motion of vortices in a superconducting film can be different, depending on the geometry of the system and the preparation method, which determines, in particular, the mechanisms of interaction between the electrons of the superconductor and the spin magnetic moments of the bound electrons of the ferromagnet. For example, the application of an array of small ferromagnetic particles to the superconductor surface leads to an increase in the critical current and to size effects [13] similar to those observed in superconductors with artificial periodic structural defects [18, 19]. Based on calculations of the pinning forces for the case of a cylindrical cavity in an infinite superconducting sample [20], the authors of [13] also attributed the strengthened fluxon pinning to the electromagnetic interaction between vortices and the magnetization. Depinning of vortices can occur in systems with other geometries. An example is a ferromagnet–superconductor layered system placed in a tangential external magnetic field, the strength of which is close to the value at which the second-order phase transition occurs from the single-domain to a multidomain state [14, 15]. In the vicinity of this phase transition, the magnetic susceptibility is large and the interaction between the vortex subsystem and the magnetization compensates for the effect of the stray field of vortices. This leads to a decrease in the energy associated with the displacements of vortices from their equilibrium positions and to a decrease in the critical current, because the stray-field energy is positive.

The critical current has much to do with the existence of vortices and their pinning. Because the superconducting layer is contiguous with a ferromagnetic layer, superconductivity is partially destroyed and the superconductor passes to a mixed state even in a zero external magnetic field. For this reason, the critical points of the ferromagnet–superconductor system can be lower than those of the single superconducting film, especially if the superconductor is in the Meissner phase in the absence of the ferromagnet.

In Section 1 of this paper, we analyze the conditions for the occurrence of the mixed state in superconducting films under the influence of the stray field of the stripe domain structure of a uniaxial ferromagnetic

1063-7834/01/4302-0224$21.00 © 2001 MAIK "Nauka/Interperiodica"

film. An analogous problem was considered in [12] (see also [9]). However, as will be shown below, the estimates made in [12] are of very limited usefulness, because the vortex energy depends heavily on the thickness of the superconducting film, the period of the domain structure, and the material parameters of the system. In Section 2, we discuss the critical-current anisotropy in a superconducting film with a vortex lattice induced by a field of magnetic domains.

1. THE FORMATION OF VORTICES

We consider the influence of the domain structure of a ferromagnetic film on the state of a superconducting film contiguous with it. Only the electromagnetic interaction between the spin subsystem of the magnet and the conduction electrons of the superconductor is taken into account; that is, we assume that the superconducting and ferromagnetic layers are separated by an insulating spacer of thickness δ such that $\xi \ll \delta \ll \lambda$, where ξ is the correlation length of the order parameter and λ is the London penetration depth of the magnetic field into the superconductor. The ferromagnet possesses magnetic anisotropy of the "easy axis" type with an anisotropy constant $\beta = 4\pi Q > 0$ (Q is the quality factor of the magnet) and with the easy axis $\mathbf{n}_a$ perpendicular to the plane of the films. Since most high-temperature superconductors are typical type II superconductors, we restrict our consideration to the case of superconductors characterized by a large Ginzburg–Landau parameter $\kappa = \lambda/\xi \gg 1$. Furthermore, we ignore vortex pinning due to defects of the superconductor. The geometry of the structure is shown in Fig. 1.

The formation of the mixed state caused by the stray field of a domain structure was analyzed in [12], where the case of a semiconducting half-space contiguous with a film of a uniaxial ferromagnet was considered. The vortices were assumed to arise when the tangential component of the domain stray field in a superconductor boundary layer of a thickness of the order of the London penetration depth λ exceeds the lower critical field $H_{c1} \cong (\Phi_0/4\pi\lambda^2)\ln\kappa$ [17], where $\Phi_0 = 2 \times 10^{-7}$ G cm^2 is the flux quantum. Obviously, this criterion is valid if the thickness of the superconducting film l is much larger than the period D of the domain structure ($l \gg D$).

In actual ferromagnet–superconductor systems, as a rule, the thickness of the superconducting film l is small, $l \ll D$. Furthermore, for high-quality films of high-temperature superconductors, we typically have $l < \lambda$. Under these conditions, the simple criterion used in [12] for the transition to the mixed state is inapplicable. In infinitely thin superconducting films, the lower critical field is large in the case of tangential external fields and is zero for normal external fields. Therefore, when analyzing the conditions for the existence of vortices in thin films, one should take into account not only all the components of the stray field of magnetic domains, but also its gradient. If one ignores hysteretic

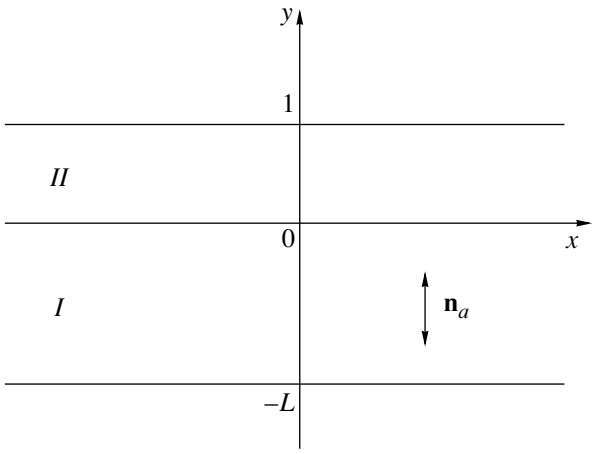

Fig. 1. Geometry of the system consisting of a uniaxial ferromagnet (*I*) and a type II superconductor (*II*). The insulating spacer is not shown.

effects, the natural criterion for the formation of a vortex structure will be the equality of the Gibbs energies of the system in the Meissner and mixed states.

The energy G of the ferromagnet–superconductor system in an external field $\mathbf{H}_0$ has the form

$$G = \frac{1}{8\pi}\int_V dv(\mathbf{H}-\mathbf{H}_0)^2 - \int_{V_f} dv\left(\mathbf{H}_0\mathbf{M} + \frac{\alpha}{2}\frac{\partial\mathbf{M}}{\partial x_i}\frac{\partial\mathbf{M}}{\partial x_i} + \frac{\beta}{2}M_y^2\right) + \frac{\lambda^2}{8\pi}\int_{V_s} dv(\nabla\times\mathbf{H})^2, \quad (1)$$

where V is the total volume of the system; V_f and V_s are the volumes of the ferromagnetic and superconducting layers, respectively; and α is the exchange stiffness parameter of the ferromagnet. In Eq. (1), the first integral term is the magnetic-field energy; the second is the sum of the Zeeman, exchange, and uniaxial-anisotropy energies, respectively; and the third term is the kinetic energy of the superconduction current.

The spatial distribution of magnetization $\mathbf{M}$ and of magnetic field $\mathbf{H}$ in the ferromagnet and vacuum is described by the magnetostatics equations

$$\mathrm{curl}\mathbf{H} = 0, \quad \mathrm{div}\mathbf{B} = 0 \quad (2)$$

and the equation of state

$$\mathbf{M}\times\mathbf{H}_{\mathrm{eff}} = 0, \quad (3)$$

while the distribution of the magnetic field $\mathbf{H}$ in the superconductor is described by the London equation

$$\mathbf{H} + \lambda^2(\nabla\times(\nabla\times\mathbf{H})) = \Phi_0\sum_\nu\int d\mathbf{r}_\nu\delta(\mathbf{r}-\mathbf{r}_\nu), \quad (4)$$

where $\mathbf{B} = \mathbf{H} + 4\pi\mathbf{M}$ is the magnetization induction, $\mathbf{H}_{\text{eff}}$ is the effective magnetic field

$$\mathbf{H}_{\text{eff}} = \mathbf{H} + \beta\mathbf{M}_y\mathbf{n}_y - \alpha\nabla^2\mathbf{M}, \quad (5)$$

and $\mathbf{r}_\nu$ is the position vector of the infinitely small element $d\mathbf{r}_\nu$ of the νth vortex; the summation in Eq. (4) is performed over all vortices and the integration is carried out over the entire length of each vortex. The boundary conditions should be satisfied for the tangential components of magnetic field $\mathbf{H}$ and the normal component of magnetic induction $\mathbf{B}$ such that they are continuous through the interface of the two media. In addition, the normal component of the superconduction current density $\mathbf{j}_s$ should vanish at the surface of the superconductor.

If the thickness of the ferromagnetic layer is fairly large and there is no external magnetic field, the magnet is divided into domains, with their size depending only slightly on the superconductor state [21]. In uniaxial ferromagnets, at temperatures far away from the orientational phase transition point, only the invariants quadratic in the magnetization are of importance in the anisotropy energy. Therefore, the direction of magnetization at any point in the single ferromagnetic film is independent of the magnitude of the saturation magnetization M_0 and the stray field $\mathbf{H}_e$ of the domains is proportional to the saturation magnetization. Assuming that the distribution of the spin magnetic moments over the ferromagnet is the same as that in the absence of the superconductor, let us find the critical magnetization at which the Meissner phase becomes energetically unfavorable in comparison with a mixed state. In this case, a calculation of the critical magnetization reduces to an analysis of the conditions for the transition from the Meissner to a mixed state of a single superconducting film placed in an external nonuniform magnetic field identical to the stray field of the domain structure $\mathbf{H}_e$.

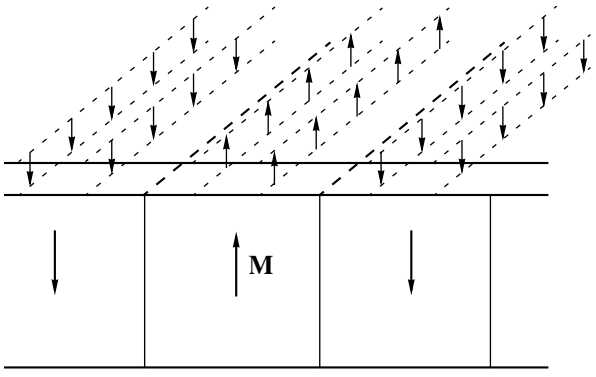

Fig. 2. Abrikosov vortex lattice created in a thin superconducting film by the stray magnetic field of the stripe domain structure of a ferromagnet with its saturation magnetization exceeding its critical value.

We calculate the magnetic field and the Gibbs energy of the single superconducting layer $0 < y < l$ with an arbitrary vortex structure under the assumption that the external magnetic field $\mathbf{H}_e$ is periodic and its sources are not situated in the region $y > 0$. Then, the field $\mathbf{H}_e$ is potential in the half-space $y > 0$ and the y dependence of its Fourier transform $\tilde{\mathbf{H}}_e(y) = \int dxdz\mathbf{H}_e(\mathbf{r})\exp(-i\mathbf{qr})$ in this region has the form

$$\tilde{\mathbf{H}}_e(y) = \tilde{\mathbf{H}}_e(0)\exp(-qy), \quad (6)$$

where $\mathbf{q}$ is a two-dimensional vector $\mathbf{q} = \{q_x, 0, q_z\}$.

Following Brandt [22], we represent the total magnetic field as the sum of the field of sources $\mathbf{H}_{\text{source}}$, the field of vortices $\mathbf{H}_\nu$, and the stray field $\mathbf{H}_{\text{stray}}$:

$$\mathbf{H} = \mathbf{H}_{\text{source}} + \mathbf{H}_\nu + \mathbf{H}_{\text{stray}}, \quad (7)$$

where $\mathbf{H}_\nu$ is the sum of the field of real vortices $\mathbf{H}_{\nu r}$ and the field of the vortex images $\mathbf{H}_{\nu i}$:

$$\mathbf{H}_\nu = \mathbf{H}_{\nu r} + \mathbf{H}_{\nu i}. \quad (8)$$

The source field $\mathbf{H}_{\text{source}}$ consists of the external field $\mathbf{H}_e$ and the field of the Meissner currents $\mathbf{H}_{\text{Meis}}$: $\mathbf{H}_{\text{source}} = \mathbf{H}_e + \mathbf{H}_{\text{Meis}}$. Expressions for the fields $\mathbf{H}_\nu$, $\mathbf{H}_{\text{source}}$, and $\mathbf{H}_{\text{stray}}$ are presented in the Appendix.

Accordingly, the Gibbs potential of the vortex subsystem G can be written as

$$G = G_{\text{source}} + G_\nu + G_{\text{stray}}, \quad (9)$$

where G_{source} is the interaction energy between the vortices and the external field,

$$G_{\text{source}} = (1/4\pi)\int d\nu[\mathbf{H}_{\text{Meis}}(\mathbf{H}_\nu + \mathbf{H}_{\text{stray}}) + \lambda^2(\nabla\times\mathbf{H}_{\text{Meis}})[\nabla\times(\mathbf{H}_\nu + \mathbf{H}_{\text{stray}})]]; \quad (10)$$

G_ν is the energy of the real vortices and their images,

$$G_\nu = (1/8\pi)\int d\nu[(\mathbf{H}_\nu)^2 + \lambda^2(\nabla\times\mathbf{H}_\nu)^2]; \quad (11)$$

and G_{stray} is the stray-field energy of the vortices,

$$G_{\text{stray}} = (1/8\pi)\int d\nu[(\mathbf{H}_{\text{stray}})^2 + \lambda^2(\nabla\times\mathbf{H}_{\text{stray}})^2]. \quad (12)$$

If the thickness of the superconductor is small ($l \ll D$), the tilt of the vortex lines can be ignored and it is sufficient to simply consider the superconducting film with a system of vortex lines perpendicular to the film surface (Fig. 2). If we extend the vortex lines in the layer to infinity, so that they become infinite straight vortex lines in an infinite superconductor, then we will have

$$\mathbf{H}_{\nu i} \equiv 0, \quad P^+ = P^- = P, \quad \Phi^+ = -\Phi^- = -TP/[q(T + q\coth Tl/2)], \quad (13)$$

where the notation of the Appendix is used. We assume that the external field is independent of the coordinate z and that the field component H_{ez} is zero. Substituting formulas (A1)–(A6) of the Appendix into Eqs. (9)–(12) and taking Eq. (13) into account, we arrive at the following expressions for the components of the Gibbs potential:

$$G_\nu \cong [\Phi_0^2 l/(4\pi^2\lambda^2)]\sum_{\mu,\nu}(-1)^{s_{\mu\nu}}K_0 \times (\sqrt{(x_\mu - x_\nu)^2 + (z_\mu - z_\nu)^2 + \xi^2/\lambda}), \quad (14)$$

$$G_{\text{stray}} = \frac{1}{4\pi}\int\frac{dq}{4\pi^2}\Phi_q^- P_{-q}, \quad (15)$$

$$G_{\text{source}} = -\frac{1}{4\pi^2}\int_{-\infty}^{+\infty} dk\Phi_q^-(q = kn_x)H_{ey-k}(0). \quad (16)$$

Here, $\mathbf{H}_{ek}$ is the amplitude of the one-dimensional Fourier transform in the coordinate x and $K_0(x)$ is the zero-order MacDonald function; $s_{\mu\nu} = 0$ if the μth and νth vortices have the same sense and $s_{\mu\nu} = 1$ if they are oppositely sensed. In the radicand in Eq. (14), the term ξ^2 is introduced to prevent the divergence of the self-energy of each of the vortices. As can be seen from Eqs. (14)–(16), only the energy G_{source} depends on the saturation magnetization and, therefore, the critical magnetization is determined immediately from the equation $G = 0$ in a fairly general way.

To determine the conditions for the existence of vortices specifically, let us consider the transition of the superconducting film from the Meissner to a mixed state under a stray field of the stripe domain structure. We assume that the magnetization in the domains is directed perpendicular to the surface of the ferromagnetic layer and the thickness of domain walls is small (equal to zero). The distribution of the normal component of the stray field of the domains in the interface of the magnetic and the superconducting media $H_{ey}(0)$ is described by the expression

$$H_{ey}(0) = -4M_0\sum_{n=-\infty}^{+\infty}(1/n)\sin^2(\pi n/2) \times [1 - \exp(-|k_n|L)]\sin(\pi k_n x), \quad k_n = 2\pi n/D, \quad (17)$$

and, therefore,

$$\tilde{H}_{ey}(0) = 8\pi i M_0\sum_{n=-\infty}^{+\infty}(1/n)\sin^2(\pi n/2) \times [1 - \exp(-|k_n|L)]\delta(k - k_n). \quad (18)$$

The equilibrium number of vortices in the superconducting film increases monotonically with increasing saturation magnetization of the ferromagnetic layer.

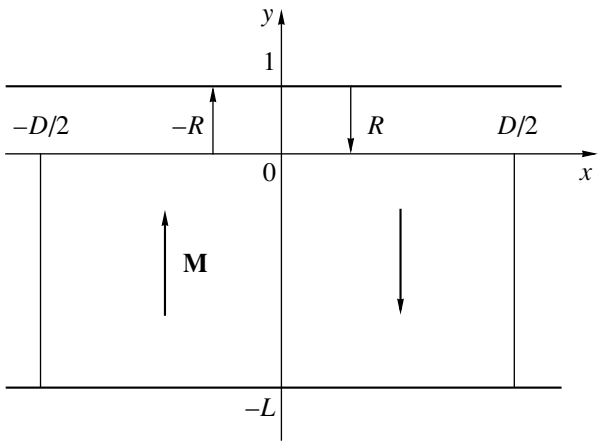

Fig. 3. Ferromagnet–superconductor system with a stripe domain structure in the magnet and a pair of oppositely sensed vortices in the superconductor (schematic). The arrows indicate the directions of magnetization and the vortex lines.

Therefore, the critical saturation magnetization corresponds to the case where, within one spatial period of the domain structure, there appear at most two oppositely sensed vortices (vortex–antivortex pair) in the thin superconducting film, $l \ll D$ (Fig. 3).

Substituting Eq. (18) into Eq. (16) for G_{source}, we find

$$G_{\text{source}} = -(8\Phi_0 M_0 N/\pi\lambda^2) \times \sum_{n=1}^{\infty}\frac{\sin^2(\pi n/2)\sin(k_n R)}{n\tau_n k_n[\tau_n + k_n\coth(\tau_n l/2)]}[1 - \exp(-k_n L)], \quad (19)$$

where N is the number of vortex–antivortex pairs in the superconducting film and $\tau_n^2 = k_n^2 + \lambda^{-2}$. At $L/D \geq 1$, the terms in the sum in Eq. (19) fall off rapidly with increasing n and it will suffice to keep only the first term in order to estimate G_{source}. The energy G_ν is given by Eq. (14) as before.

If there is only one vortex–antivortex pair in the film (Fig. 3), then

$$P_{\mathbf{q}} = (2i\Phi_0/\lambda^2 T^2)\sin(q_x R). \quad (20)$$

In this case, for fairly thick superconducting films $l \gg \lambda$, we find

$$G_\nu \cong (\Phi_0^2 l/4\pi^2\lambda^2)[K_0(\kappa^{-1}) - K_0((2R + \xi)/\lambda)], \quad (21)$$

$$G_{\text{stray}} = (\Phi_0^2/4\pi^2\lambda)\{(\pi - 2)/2 - \pi[\mathbf{J}_\nu(2R/\lambda) - J_\nu(2R/\lambda)]/\sin\pi\nu|_{\nu\to 0} + \exp(-2R/\lambda)\}, \quad (22)$$

$$G_{\text{source}} \cong -(2\Phi_0 M_0 D/\pi^2)[Cl_2(2\pi R/D) + Cl_2(\pi - 2\pi R/D)], \quad (23)$$

where $\mathbf{J}_\nu(x)$ and $J_\nu(x)$ are the Anger and the Bessel functions of order ν, respectively, and $Cl_2(x)$ is the Clausen function of the second order. From Eqs. (21) and (22), it follows that the effect of the stray field is small for fairly thick superconducting films ($G_{\text{stray}}/G_\nu \propto \lambda/l \ll 1$). At $R/\lambda \gg 1$, we have an asymptotic formula

$$[\mathbf{J}_\nu(2R/\lambda) - J_\nu(2R/\lambda)]\big|_{\nu \ll 1} \cong (\lambda/2\pi R)\sin\pi\nu,$$

such that the $G_{\text{stray}}(R)$ dependence is weak and can be neglected in comparison with the $G_{\text{source}}(R)$ dependence. The energy G_ν virtually does not depend on the vortex–antivortex distance $2R$ for $R/\lambda \gg 1$, while the magnitude of G_{source} reaches its maximum at $R = D/4$. Putting $R = D/4$ and equating G to zero, we find the critical magnetization M_c to be

$$M_c \cong (\Phi_0 l/16\lambda^2 D)\ln\kappa. \quad (24)$$

In contrast to the estimate of the critical field made in [12], Eq. (24) involves the factor D/l; therefore, the critical magnetization and the corresponding critical field can be very small. For instance, for a superconducting film of $YBa_2Cu_3O_7$ with a Curie temperature of $T_c \cong 90$ K, $\lambda = 3 \times 10^{-5}$ cm, $l = 10^{-4}$ cm, $\ln\kappa \propto 1$, and a domain structure period equal to $D = 5 \times 10^{-4}$ cm, we have $4\pi M_c \propto 20$ G; that is, the equilibrium state of such a film with a ferrite coating is usually mixed. The Meissner phase can be energetically favorable in a system of a superconducting film with a small London penetration depth λ and a diluted magnet or a magnet near the magnetization compensation point.

If there is a vortex–antivortex pair within each spatial period of the domain structure, then

$$P_{\mathbf{q}} = (4\pi i\Phi_0/\lambda^2 T^2 D)\sum_{n=-\infty}^{+\infty}\sin(k_n R)\delta(q_x - k_n) \quad (25)$$

and the critical magnetization (in the approximation made) is identical to that given by Eq. (24). This is because, in effect, we neglected the interaction between the vortices. When this interaction is taken into account, the critical magnetization for the periodic distribution of the vortices is found to be only slightly smaller than that for a single vortex–antivortex pair.

If the spacing between the vortices is much larger than λ, the dominant contribution to the energy G_{stray} is due to large wave numbers and, therefore, G_{stray} is approximately equal to the sum of the stray-field energies of noninteracting vortices:

$$G_{\text{stray}} \cong (\Phi_0^2 N/8\pi^2)\int_0^\infty \frac{dq}{\lambda^4 T^3[T + q\coth(Tl/2)]}. \quad (26)$$

Estimating the integral in Eq. (26) gives

$$G_{\text{stray}} \propto (\Phi_0^2 N/8\pi\lambda)\coth^{-1}(l/2\lambda) \times \ln[1 + \coth(l/2\lambda)]. \quad (27)$$

It is seen that, within an order of magnitude, G_{stray} does not exceed G_ν for any thickness of the superconducting film and, therefore, we can neglect the influence of the vortex stray field.

Keeping only the first term of the sum in Eq. (19), we obtain the following order-of-magnitude estimate of the critical magnetization in the thickness range of the superconducting film $\xi \ll l \ll D$:

$$\dot{M}_c \propto (\Phi_0 l/16\lambda^2 D)[1 + (2\pi\lambda/D)\coth(l/2\lambda)] \times [1 - \exp(-2\pi L/D)]^{-1}\ln\kappa. \quad (28)$$

According to Eq. (28), M_c decreases monotonically with decreasing film thickness l. At $\lambda^2/lD \gg 1$, the critical magnetization is almost entirely independent of l, because the screening of the magnetic flux by the superconducting film is weak.

2. ANISOTROPY OF THE CRITICAL CURRENT

If the magnetization of the magnetic material exceeds its critical value, the superconducting layer will be in the mixed state and, even when the excess of the magnetization above the critical value is small, the number of vortices created by the field of the domain structure with period $D \gg \lambda$ will be large.

Let us consider the case where a conduction current of density $\mathbf{j}_0$ flows along the superconducting layer and the current density is uniform over the yz cross section. Each element of a vortex line is subjected to the Lorentz force $\mathbf{f}_L$ caused by the current, and the result depends on the thickness of the superconducting layer and the direction of motion of the charge carriers with respect to the domain walls.

Figure 4 shows a system of vortices in a fairly thick superconductor ($l \gg \lambda, D$). The superconducting layer completely screens the stray field of domains, and the vortices do not reach the upper surface of the superconductor. When the current flows perpendicular to the domain walls, the resultant Lorentz forces acting on both halves of a vortex are equal in magnitude but opposite in direction, so that the vortex remains immobile. As the conduction current increases, the situation remains qualitatively the same until the rearrangement of the vortices, the motion of the vortex structure, and the magnetic loss associated with this motion become possible. However, when the current flows along the domain walls (Fig. 4), some vortices are expelled and some are drawn in the bulk of the superconductor. At a certain value of the conduction current, the vortices most deeply penetrating into the superconductor can combine to form a single infinite vortex line. This vortex penetrates further into the bulk of the superconduc-

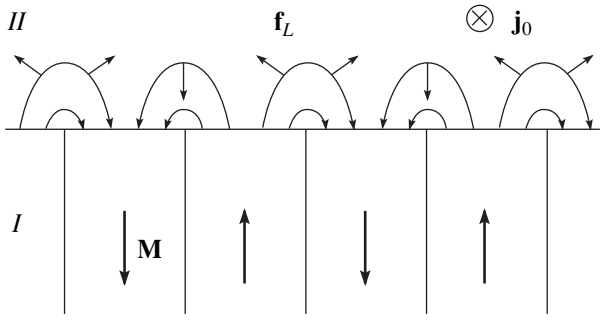

Fig. 4. Schematic distribution of the linear density of the Lorentz forces $\mathbf{f}_L$ exerted on the vortices by the conduction current with a density $\mathbf{j}_0(y)$ flowing through a thick superconducting film.

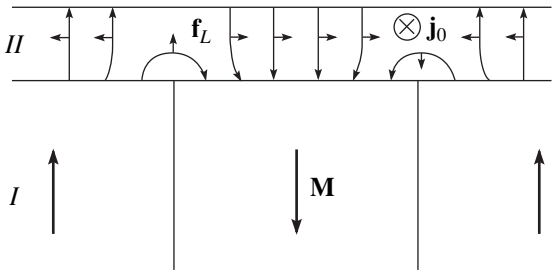

Fig. 5. Schematic distribution of the linear density of the Lorentz forces $\mathbf{f}_L$ exerted on the vortices by the conduction current with a density $\mathbf{j}_0(y)$ flowing through a thin superconducting film.

tor, thereby causing a rearrangement of the vortex structure and a transition of the superconductor into a resistive state.

If the superconducting layer is thin ($l \ll \lambda$), the vortex lines will be virtually perpendicular to its surface (Fig. 5) and the effect of the conduction current will be different in character. When the current is perpendicular to the domain walls, the vortices become mobile, because the shear rigidity of the vortex lattice is low. Therefore, one might expect the critical current to be small if there is no vortex pinning in the superconducting film. In the case where the current is parallel to the domain walls (Fig. 5), the vortex structure becomes unstable when the current is sufficiently large so that the nearest neighbor vortex–antivortex pairs annihilate and new pairs are created.

Thus, the critical current in the ferromagnet–superconductor system can be highly anisotropic. However, for anisotropy of the critical current to be observed, the superconducting material must be very pure.

APPENDIX

Solving the equations of state (3) and (4) in combination with the magnetostatics equations (2) and the boundary conditions at the surface of the superconductor, we arrive at the following expressions for the Fourier transforms of the magnetic field:

The field $\mathbf{H}_{\text{source}}$ produced by external sources and the Meissner currents in the superconducting layer is

$$\begin{aligned}\tilde{H}_{\text{source}x,z} &= iq_{x,z}(a\cosh Ty + b\sinh Ty),\\ \tilde{H}_{\text{source}y} &= (q^2/T)(a\sinh Ty + b\cosh Ty)\end{aligned} \tag{A1}$$

inside the superconducting layer ($0 < y < l$) and

$$\begin{aligned}\mathbf{H}_{\text{source}} &= \mathbf{H}_e + \nabla\Psi,\\ \tilde{\Psi} &= \int dxdz\Psi\exp(-i\mathbf{qr})\\ &= \begin{cases}\Psi^-\exp(qy), & y<0\\ \Psi^+\exp[-q(y-l)], & y>l\end{cases}\end{aligned} \tag{A2}$$

outside this layer, where

$$\Psi^- = -(T^2-q^2)\sinh Tl$$
$$\times\{q[2qT\cosh Tl + (T^2+q^2)\sinh Tl]\}^{-1}\tilde{H}_{ey}(0),$$
$$\Psi^+ = \{-2T[2qT\cosh Tl + (T^2+q^2)\sinh Tl]^{-1}$$
$$+ q^{-1}\exp(-ql)\}\tilde{H}_{ey}(0),$$
$$a = \psi^- - q^{-1}\tilde{H}_{ey}(0), \quad b = (T/q)[\psi^- + q^{-1}\tilde{H}_{ey}(0)].$$

For convenience, we have dropped the index $\mathbf{q}$ from the Fourier transforms of the field and from the coefficients a, b, Ψ^-, and Ψ^+.

The field of real vortices $\mathbf{H}_{vr}$ is described by the expression

$$\tilde{H}_{vr} = (4\pi/\Phi_0)\sum_\mu\int d\mathbf{r}_\mu\tilde{V}(|y-y_\mu|)\exp(-i\mathbf{qr}_\mu), \tag{A3}$$

and the field of the vortex images $\mathbf{H}_{vi}$ is given by

$$\begin{aligned}\tilde{H}_{vix} &= A_1\cosh Ty + B_1\sinh Ty,\\ \tilde{H}_{viy} &= A_2\sinh Ty + B_2\cosh Ty,\\ \tilde{H}_{viz} &= A_3\cosh Ty + B_3\sinh Ty,\end{aligned} \tag{A4}$$

where

$$A_{1,3} = -(4\pi/\Phi_0)\sum_\mu\int dr_{\mu,z}\tilde{V}(|y-y_\mu|)\exp(-i\mathbf{qr}_\mu),$$

$$B_{1,3} = (4\pi/\Phi_0\sinh Tl)\sum_\mu\int dr_{\mu x,z}[\tilde{V}(|y_\mu|)\cosh Tl$$
$$-\tilde{V}(l-y_\mu)]\exp(-i\mathbf{qr}_\mu),$$

$$A_2 = -(i/T)(q_x A_1 + q_z A_3),$$
$$B_2 = -(i/T)(q_x B_1 + q_z B_3),$$

$$V = [\Phi_0^2/(16\pi^2\lambda^2 r)]\exp(-r/\lambda),$$

$$\tilde{V} = \int dxdz V \exp(-i\mathbf{qr}) = [\Phi_0^2/(8\pi\lambda^2 T)]\exp(-T|y|),$$

$$T^2 = q^2 + \lambda^{-2}.$$

Expressions for the stray field $\mathbf{H}_{\text{stray}}$ are similar to Eqs. (A1) and (A2). Inside the superconducting layer ($0 < y < l$), we have

$$\begin{aligned} \tilde{H}_{\text{stray}\,x,z} &= iq_{x,z}(c\cosh Ty + d\sinh Ty), \\ \tilde{H}_{\text{stray}\,y} &= (q^2/T)(c\sinh Ty + d\cosh Ty), \end{aligned} \tag{A5}$$

and outside this layer, we have

$$\begin{aligned} \mathbf{H}_{\text{stray}} &= \nabla\Phi, \quad \tilde{\Phi} = \int dxdz\Phi\exp(-i\mathbf{qr}) \\ &= \begin{cases} \Phi^-\exp(qy), & y < 0 \\ \Phi^+\exp[-q(y-l)], & y > l, \end{cases} \end{aligned} \tag{A6}$$

where

$$c = \Phi^-, \quad d = (\Phi^+ - \Phi^-\cosh Tl)/\sinh Tl,$$

$$\Phi^- = (T/q)[(T\sinh Tl + q\cosh Tl)P^- - qP^+] \times [2qT\cosh Tl + (T^2 + q^2)\sinh Tl]^{-1},$$

$$\Phi^+ = -(T/q)[(T\sinh Tl + q\cosh Tl)P^+ - qP^-] \times [2qT\cosh Tl + (T^2 + q^2)\sinh Tl]^{-1},$$

$$P^- = 4\pi(\Phi_0\sinh Tl)^{-1}\sum_\mu \int dy_\mu [\tilde{V}(y_\mu)\exp(Tl) + \tilde{V}(l - y_\mu)]\exp(-i\mathbf{qr}_\mu).$$

$$P^+ = 4\pi(\Phi_0\sinh Tl)^{-1}\sum_\mu \int dy_\mu [\tilde{V}(l - y_\mu)\exp(Tl) + \tilde{V}(y_\mu)]\exp(-i\mathbf{qr}_\mu).$$

The position vectors $\mathbf{r}_\mu$ of the vortex lines outside the superconductor can be conveniently varied when computing the field.

ACKNOWLEDGMENTS

This work was supported by the Polish Committee for Scientific Research.

REFERENCES

1. A. I. Buzdin, L. N. Bulaevskiĭ, M. L. Kulich, and S. V. Panyukov, Usp. Fiz. Nauk **144**, 597 (1984) [Sov. Phys. Usp. **27**, 927 (1984)].
2. A. I. Buzdin and L. N. Bulaevskiĭ, Zh. Éksp. Teor. Fiz. **94** (3), 256 (1988) [Sov. Phys. JETP **67**, 576 (1988)].
3. M. G. Khusainov, Zh. Éksp. Teor. Fiz. **100** (2), 524 (1996) [JETP **83**, 533 (1996)].
4. P. W. Anderson and H. Suhl, Phys. Rev. **116**, 898 (1959).
5. *Superconductivity in Ternary Compounds*, Vol. 2: *Superconductivity and Magnetism*, Ed. by F. Fisher and M. Maple (Springer-Verlag, Heidelberg, 1982).
6. A. F. Sadreev, Fiz. Tverd. Tela (St. Petersburg) **35** (8), 2099 (1993) [Phys. Solid State **35**, 1044 (1993)].
7. Yu. I. Bespyatykh, W. Wasilewski, M. Gajdek, *et al.*, Fiz. Tverd. Tela (St. Petersburg) **36** (3), 586 (1994) [Phys. Solid State **36**, 323 (1994)].
8. A. Stankiewicz, S. Robinson, G. F. Gering, and V. V. Tarasenko, J. Phys.: Condens. Matter **9**, 1019 (1997).
9. Yu. I. Bespyatykh, W. Wasilewski, É. G. Lokk, and V. D. Kharitonov, Fiz. Tverd. Tela (St. Petersburg) **40** (6), 1068 (1998) [Phys. Solid State **40**, 975 (1998)].
10. Yu. I. Bespyatykh and W. Wasilewski, Radiotekh. Élektron. (Moscow) **44** (9), 1 (1999).
11. Yu. I. Bespyatykh, E. H. Lokk, S. A. Nikitov, and W. Wasilewski, J. Magn. Magn. Mater. **195**, 555 (1999).
12. É. B. Sonin, Pis'ma Zh. Tekh. Fiz. **14** (18), 1640 (1988) [Sov. Tech. Phys. Lett. **14**, 714 (1988)].
13. J. I. Martin, M. Vélez, J. Nogues, *et al.*, J. Magn. Magn. Mater. **177–181**, 915 (1998).
14. Yu. I. Bespyatykh, W. Wasilewski, and V. D. Kharitonov, Fiz. Tverd. Tela (St. Petersburg) **39** (2), 231 (1997) [Phys. Solid State **39**, 200 (1997)].
15. Yu. I. Bespyatykh, W. Wasilewski, and V. D. Kharitonov, Zh. Tekh. Fiz. **67** (7), 27 (1997) [Tech. Phys. **42**, 741 (1997)].
16. T. H. Alden and J. D. Livingston, J. Appl. Phys. **37** (9), 3551 (1966).
17. V. V. Shmidt and G. S. Mkrtchyan, Usp. Fiz. Nauk **112** (3), 459 (1974) [Sov. Phys. Usp. **17**, 170 (1974)].
18. W. Schindler, B. Roas, G. Saemann-Ischenko, *et al.*, Physica C (Amsterdam) **169**, 117 (1990).
19. F. M. Sauerzopf, H. P. Wiesinger, W. Kritscha, *et al.*, Phys. Rev. B **43**, 3091 (1991).
20. I. B. Khalfin and Ya. Shapiro, Physica C (Amsterdam) **207**, 259 (1993).
21. S. Tikazumi, *The Physics of Ferromagnetism: Magnetic Properties and Applications* (in Japanese) (Mir, Moscow, 1987).
22. E. H. Brandt, J. Low Temp. Phys. **44** (1), 59 (1981).

Translated by Yu. Epifanov

Physics of the Solid State, Vol. 43, No. 2, 2001, pp. 231–234. Translated from Fizika Tverdogo Tela, Vol. 43, No. 2, 2001, pp. 222–225.

SEMICONDUCTORS AND DIELECTRICS

Heat Conductivity of Polycrystalline ZnS under Uniform Compression

N. V. Lugueva, N. L. Kramynina, and S. M. Luguev

Institute of Physics, Dagestan Scientific Center, Russian Academy of Sciences, ul. 26 Bakinskikh Komissarov 94, Makhachkala, 367003 Dagestan, Russia

Received April 21, 2000

Abstract—The heat conductivity of polycrystalline zinc sulfide is investigated under hydrostatic pressure up to 0.35 GPa in the temperature range 273–420 K. It is found that an increase in the uniform pressure leads to an increase in the heat conductivity coefficient of ZnS. The Bridgman parameter characterizing the volume dependence of the heat conductivity is determined experimentally. A correlation between the heat conductivity coefficient under uniform compression and the evolution of the phonon spectrum is established. *© 2001 MAIK "Nauka/Interperiodica".*

Investigations into the heat conduction in solids subjected to uniform compression are of great importance for understanding the heat transfer processes associated with crystal lattice dynamics. However, these investigations involve significant technical difficulties, and, as a consequence, mechanisms of heat conduction in solids under pressure are still not clearly understood. The experimental data often poorly agree with their theoretical interpretation.

The heat conduction in nonmetallic crystals subjected to uniform compression changes as a result of the decrease in the crystal volume. The volume dependence of the heat conductivity is expressed in terms of the Bridgman parameter $g = -(\partial \ln\kappa/\partial \ln V)_T$, where κ is the heat conductivity coefficient and V is the volume of the sample. This expression can be transformed into the dependence of κ on the pressure P, which can be determined experimentally; that is,

$$g = -\left(\frac{\partial \ln\kappa}{\partial \ln V}\right)_T = B_T\left(\frac{\partial \ln\kappa}{\partial P}\right)_T, \qquad (1)$$

where B_T is the isothermal bulk modulus. As a consequence of an increase in the pressure and the ensuing decrease in the volume, the lattice vibration frequencies and the bond anharmonicity change and the interatomic forces increase. This manifests itself as an increase in the Debye temperature (Θ) and a decrease in the Grüneisen constant (γ).

The lattice heat conductivity of substances containing more than one atom per unit cell can be determined in the temperature range near and above Θ according to the generalized Leibfried–Schlemann formula [1]

$$\kappa = Bn^{1/3}\delta\overline{M}\overline{\Theta}^3\bar{\gamma}^{-2}T^{-1}, \qquad (2)$$

where B is the coefficient depending on the lattice structure and the type of chemical bonding in the material; n is the number of atoms per unit cell; δ^3 is the mean volume occupied by one atom in the crystal; $\overline{M}$ is the mean atomic mass; and $\overline{\Theta}$ and $\bar{\gamma}$ are the mean values of the Debye temperature and the Grüneisen constant, respectively, for all phonon branches contributing to the heat transfer. It is seen from Eq. (2) that an increase in Θ and a decrease in γ with a rise in pressure increase the heat conductivity coefficient. Therefore, the Bridgman parameter for solids is positive. However, this parameter was found to be negative for a series of substances (ice, NH_4F, and CuCl) [2–5]. The anomalous g values in these substances were explained by negative values of the Grüneisen constant for transverse acoustic phonons and the predominant contribution of transverse phonons to the heat transfer as compared to other phonon branches [2–5].

Zinc sulfide exhibits a negative γ value for transverse acoustic phonon branches [6–9]. Therefore, one can expect a negative or a small positive value of the Bridgman parameter for ZnS. The aim of the present work was to determine experimentally the Bridgman parameter and to elucidate the role of various phonon branches in heat transfer in ZnS.

Zinc sulfide is a compound with a simple crystal structure and well-known elastic constants and phonon spectrum [6–9]. The elastic constants and the sound velocity, which were experimentally found for ZnS polycrystals, differ insignificantly from these parameters for single crystals [9]. Since the heat conductivity of ZnS is high for nonmetallic crystals [10, 11], the absolute values noticeably change under the action of temperature and pressure, which is essential in analysis of the experimental data.

We investigated polycrystalline zinc sulfide samples with a grain size of 1–2 μm, which were prepared by the recrystallization compacting of a ZnS powder under

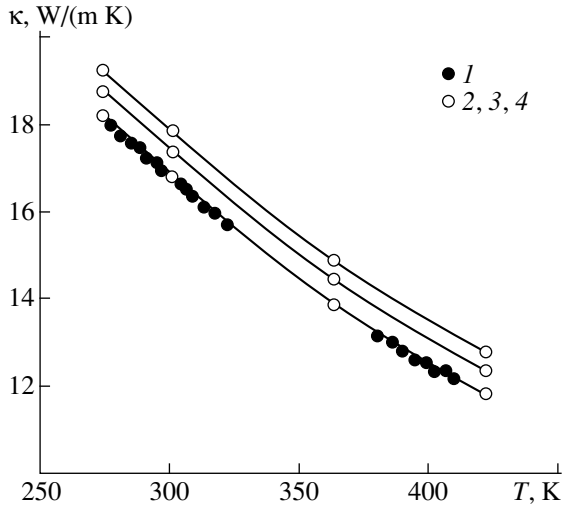

Fig. 1. Temperature dependences of the heat conductivity coefficient for polycrystalline zinc sulfide in various isobaric regimes: (*1*) under vacuum and at (*2*) atmospheric pressure, (*3*) 0.1 GPa, and (*4*) 0.35 GPa.

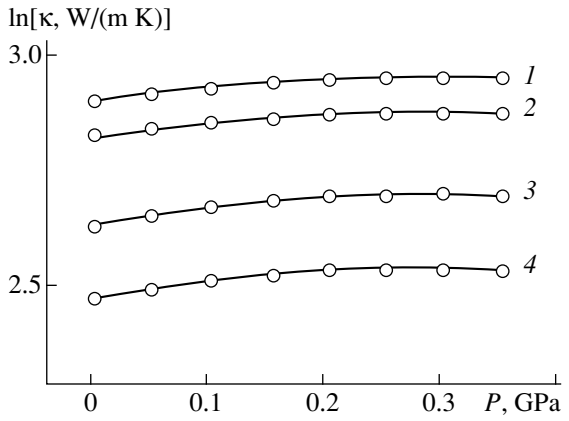

Fig. 2. Pressure dependences of the heat conductivity coefficient for polycrystalline zinc sulfide at different temperatures *T* (K): (*1*) 273, (*2*) 300, (*3*) 360, and (*4*) 420.

vacuum. The sample density was almost equal to that of the single crystal. According to the x-ray diffraction analysis, the samples had a cubic structure (β-ZnS sphalerite).

The heat conductivity coefficient of ZnS was investigated as a function of pressure by the absolute compensation method in the stationary thermal regime according to the procedure described in [12]. The measurements were performed under isobaric conditions in the temperature range 273–420 K and isothermal conditions at a pressure ranging up to 0.35 GPa with a step of 0.05 GPa.

The values of κ were measured under increasing and decreasing pressures in the experimental setup. No hysteresis and residual phenomena were found upon the pressure relief. In addition, the temperature dependence of κ was measured with the same samples under vacuum by the absolute stationary method on a setup similar to the A-type installation described in [13].

The experimental data obtained are displayed in Figs. 1 and 2. The results of the κ measurements under vacuum (installation [13]) and at atmospheric pressure (installation [12]) coincide within the limits of experimental error.

Analysis of the absolute values and temperature dependences of the heat conductivity coefficient of ZnS samples shows that the main mechanism of heat transfer in these samples in the temperature range covered is determined by crystal lattice vibrations. Since the electrical resistivity of ZnS is high, the electron-assisted heat transfer can be ignored. Owing to the optical transparency of the samples studied, we could expect that the heat transfer in these samples is realized through electromagnetic radiation (κ_{phot}). The estimate of κ_{phot} was obtained according to the Hensel formula

$$\kappa_{phot} = \frac{16}{3}\frac{n^2\sigma_0 T^3}{k}, \qquad (3)$$

where σ_0 is the Stefan–Boltzmann constant, n is the refractive index, and k is the absorption coefficient. Using the k values reported in [14] and n taken from [15], we found that $\kappa_{phot} < 10^{-3}$ W/(m K) for the polycrystal with a grain size of 1–2 μm. This value comprises 0.006% of the heat conductivity coefficient for polycrystalline ZnS. Therefore, the photon-assisted heat transfer in ZnS can be ignored in the temperature range covered. The correctness of this approximation is also confirmed by the linear temperature dependence of the thermal resistance in this temperature range. Thus, the κ quantity obtained in the experiment is determined only by heat transfer through crystal lattice vibrations in samples.

The temperature dependence $\kappa \sim T^{-1}$ which was obtained experimentally in the absence of pressure, indicates that the heat in zinc sulfide is transferred by phonons and the phonon scattering mechanisms are determined by the phonon–phonon processes and phonon scattering by defects. The latter processes make a constant contribution to the thermal resistance of samples in the temperature range covered. The smaller absolute values of κ for our samples in comparison with the available data for a ZnS single crystal [10] (by about 35% at 300 K) are due to strong phonon scattering by defects near grain boundaries in the fine-grained polycrystalline ZnS sample.

Figure 2 shows the pressure dependences of the heat conductivity coefficient for ZnS at four fixed temperatures: 273, 300, 360, and 420 K. The heat conductivity increases with an increase in pressure, which indicates

a positive Bridgman parameter for the ZnS samples. By using the pressure dependence of the heat conductivity coefficient (Fig. 2), we calculated the Bridgman parameter g for different temperatures according to formula (1). The bulk moduli B_T were taken from [9] in which the B_T values were obtained for ZnS polycrystals similar to our samples. The calculation by formula (1) for 273 K yields the parameter $g = 13$. As the temperature increases, the Bridgman parameter increases and reaches $g = 16$ at 420 K. A similar increase in g with temperature was found for alkali metal halides [16]. This was explained by the fact that the role of longitudinal phonons in heat transfer increases with a rise in temperature [16]. Since the Grüneisen constant for longitudinal phonons is considerably larger than that for transverse phonons, the value of g also increases as the contribution of longitudinal phonons to heat transfer becomes more significant.

The following relationship for the Bridgman parameter was obtained with the use of expression (2) [1]:

$$g = -\left(\frac{\partial \ln \kappa}{\partial \ln V}\right)_T = -3\left(\frac{\partial \ln \Theta}{\partial \ln V}\right)_T + 2\left(\frac{\partial \ln \gamma}{\partial \ln V}\right)_T - \frac{1}{3}. \quad (4)$$

Since $\gamma = -(\partial \ln \Theta/\partial \ln V)_T$ by definition and the volume dependence of the Grüneisen constant is defined as $q = -(\partial \ln \gamma/\partial \ln V)_T$, we have

$$g = 3\gamma + 2q - \frac{1}{3}. \quad (5)$$

With this formula and the known values of γ and q, we can estimate the value of g.

As a rule, the Grüneisen constant is calculated from the data on thermal expansion or from the experimental dependences of the elastic constants on pressure. In the former case, at $T \geq \Theta$ when all acoustic phonon branches are excited, γ is the arithmetic mean of γ_i for all the acoustic phonon branches. The value $\gamma = 0.75$ for ZnS at 300 K was found from the data on thermal expansion [8]. The γ value for zinc sulfide, which was determined from the pressure dependences of the elastic constants, differs insignificantly from the above value: $\gamma = 0.83$ [7]. Since the unit cell of the ZnS crystal lattice contains two atoms, zinc sulfide is characterized by three optical phonon branches in addition to the acoustic branches. The mass ratio of zinc and sulfur atoms is $M_{Zn}/M_S = 2.05$. According to [17, 18], both an extra heat transfer by optical phonons and scattering of acoustic phonons by optical phonons become possible at this ratio of atomic masses in the unit cell. The Grüneisen constant γ averaged over its values for both acoustic and optical branches should be used in the case when the optical phonons contribute to the heat transfer. According to the technique applied in [5], the $\bar{\gamma}$ value was determined by the formula

$$\bar{\gamma} = \frac{2\gamma_{TA}\Theta_{TA} + \gamma_{LA}\Theta_{LA} + 2\gamma_{TO}E_{TO} + \gamma_{LO}E_{LO}}{2\Theta_{TA} + \Theta_{LA} + 2E_{TO} + E_{LO}}, \quad (6)$$

where Θ_{TA} and Θ_{LA} are the Debye temperatures for transverse and longitudinal acoustic branches, respectively; E_{TO} and E_{LO} are the Einstein temperatures for transverse and longitudinal optical phonons, respectively; and γ_{TA}, γ_{LA}, γ_{TO}, and γ_{LO} are the Grüneisen constants for the transverse and longitudinal acoustic and optical branches, respectively. Using the data of γ_i, Θ_i, and E_i taken from [6], we obtained the Grüneisen constant averaged over all phonon branches: $\bar{\gamma} = 1.6$.

In the temperature range $T \geq \Theta$, q is determined by the expression [19]

$$q = \gamma[1 + 3\alpha(B_S' - 1)T], \quad (7)$$

where α is the linear expansion coefficient and B_S' is the pressure derivative of the adiabatic compressibility. Relationships $3\alpha(B_S' - 1)T \ll 1$ ($\alpha = 6.8 \times 10^{-6}$ K^{-1} [8] and $B_S' = 4.45$ [6]) and $q \simeq \gamma$ are valid for zinc sulfide in the temperature range covered. Then, formula (5) takes the form

$$g = 5\gamma - \frac{1}{3}. \quad (8)$$

By neglecting the contribution of optical phonons to heat transfer and taking $\gamma = 0.83$ in Eq. (8), we have $g = 3.82$, which is 3.5 times less than the g value obtained from the experimental data. If the optical phonons also participate in the heat transfer (this becomes possible at the above ratio of atomic masses in the unit cell of ZnS), we must take $\bar{\gamma} = 1.6$ in calculations of g with the use of formula (8). In this case, we have $g = 7.7$, which is closer to the g value found experimentally. This suggests the participation of optical phonons in the heat transfer in ZnS.

The considerable difference between the values of g that were found directly from the dependence $\ln\kappa = f(P)$ and those that were calculated with the use of relationship (8) is not surprising even with due regard for the contribution of optical phonons to the heat transfer. Indeed, the atomic mass ratio in the unit cell, the configuration of the unit cell, the anisotropy, and the type of interatomic bonding were disregarded when g was determined according to formula (4). All this could lead to a change in g with respect to the value calculated by formula (4). As was shown in [16], if the atomic mass ratio in the unit cell is not equal to unity, g is larger in comparison with the value found from expression (4), because formula (2) takes no account of the differences between the masses of ions forming the unit cell.

Zinc sulfide is a material that possesses an elastic anisotropy. The elastic anisotropy is described by the parameter $\xi = C_{11}/C_{44}$ and characterizes the predominance of the axial polarization of vibrations over the longitudinal–transverse polarization. A correlation between κ and the elastic anisotropy was noted in [17]: as ξ increases, the heat conductivity increases, too.

Since, for ZnS, the pressure derivative for C_{11} is nine times greater than that for C_{44} [6], the elastic anisotropy also increases with a rise in pressure, which leads to an increase in the g value obtained experimentally.

The value of g can also increase due to pressure-induced shifts of peaks of the density of phonon states. The high-frequency peaks shift toward higher frequencies, and the low-frequency peaks are displaced to the low-frequency range [6]. As a result of the increase in the energy gap between the transverse and longitudinal acoustic phonons, as well as between optical phonons, the probability of the scattering of these phonons by one another decreases. In this case, the lattice heat conductivity increases with pressure, resulting in an increase in g.

Thus, the investigation into the pressure dependence of the heat conductivity coefficient of polycrystalline ZnS allowed us to determine the Bridgman parameter g from the experimental data. The increase observed in g with an increase in temperature indicates an enhancement of the role played by optical and transverse acoustic phonons in the heat transfer. The g value obtained from the experimental dependence $\ln\kappa = f(P)$ was larger than that determined from the data on the Grüneisen constant. This can be explained by the approximations in the choice of the γ and q values, the deviation of the atomic mass ratio in the unit cell from unity, the decrease in the phonon–phonon scattering due to the shift of the peaks of the density of phonon states under uniform compression, and the elastic anisotropy in ZnS.

ACKNOWLEDGMENTS

The authors are grateful to G.N. Dronova for supplying samples for the investigations.

REFERENCES

1. G. A. Slack, *Solid State Physics* (Academic, New York, 1979), Vol. 34, p. 1.
2. R. G. Ross, P. Andersson, and G. Backstrom, J. Chem. Phys. **68** (9), 3967 (1978).
3. R. G. Ross, High Temp.–High Pressures **9** (1), 87 (1977).
4. R. G. Ross and O. Sandberg, J. Phys. C **11** (4), 667 (1978).
5. G. A. Slack and P. Andersson, Phys. Rev. B **26** (4), 1873 (1982).
6. D. N. Talwar, M. Vandevyver, K. Kunc, and M. Zigone, Phys. Rev. B **24** (2), 741 (1981).
7. T. Soma, Solid State Commun. **34** (12), 927 (1980).
8. T. F. Smith and G. K. White, J. Phys. C **8** (13), 2031 (1975).
9. D. H. Chung and W. R. Buessem, J. Appl. Phys. **38** (6), 2535 (1967).
10. G. A. Slack, Phys. Rev. B **6** (10), 3791 (1972).
11. N. V. Lugueva, G. N. Dronova, and S. M. Luguev, Opt.–Mekh. Prom-st. **10**, 30 (1983).
12. Sh. M. Ismailov, Ya. B. Magomedov, and N. L. Kramynina, High Temp.–High Pressures **26** (6), 657 (1994).
13. E. D. Devyatkova, A. V. Petrov, I. A. Smirnov, and B. Ya. Moĭzhes, Fiz. Tverd. Tela (Leningrad) **2** (4), 738 (1960) [Sov. Phys. Solid State **2**, 681 (1960)].
14. W. Piper, D. D. Jonson, and D. T. E. Marple, J. Phys. Chem. Solids **8** (3), 475 (1959).
15. J. Czyzek, W. M. Baher, R. C. Crance, and J. B. Howe, J. Opt. Soc. Am. **47** (2), 240 (1957).
16. G. A. Slack and R. G. Ross, J. Phys. C **18** (20), 3957 (1985).
17. Yu. A. Logachev, B. Ya. Moĭzhes, A. V. Petrov, and N. S. Tsypkina, Fiz. Tverd. Tela (Leningrad) **16** (9), 2489 (1974) [Sov. Phys. Solid State **16**, 1623 (1974)].
18. E. D. Devyatkova and I. A. Smirnov, Fiz. Tverd. Tela (Leningrad) **4** (9), 2507 (1962) [Sov. Phys. Solid State **4**, 1836 (1962)].
19. R. Rao, J. Phys. Soc. Jpn. **38** (4), 1080 (1975).

Translated by M. Lebedkin

Physics of the Solid State, Vol. 43, No. 2, 2001, pp. 235–241. Translated from Fizika Tverdogo Tela, Vol. 43, No. 2, 2001, pp. 226–232.

SEMICONDUCTORS AND DIELECTRICS

Effect of an Intermediate Layer with Space-Dependent Permittivity on the Ground State Energy of an Electron in a Spherical Complex Nanoheterosystem

V. I. Boĭchuk and R. Yu. Kubaĭ

Drogobych State Pedagogical University, Drogobych, L'vov oblast, 82100 Ukraine

e-mail: fizmat@drohobych.net

Received January 10, 2000; in final form, May 18, 2000

Abstract—The effect of the interfaces of a multilayer spherical microcrystal on a charged particle is investigated. The case is considered where an intermediate layer with space-dependent permittivity exists near the interfaces. The dependence of the potential energy of the charged particle on distance is established by the method of the classical Green's functions. For the example of an HgS/CdS spherical structure, the energy of the ground and excited states of an electron is calculated both in the presence of an intermediate layer with space-dependent permittivity and in its absence. © *2001 MAIK "Nauka/Interperiodica".*

INTRODUCTION

Advances in the physics of quantum quasi-zero-dimensional nanostructures are associated not only with the constantly increasing possibilities associated with the technology of the production of perfect and complex heterosystems, but also with the development of more adequate theoretical models of these structures.

The first theoretical works [1–8] wherein analysis was carried out on the experimental excitonic absorption spectra of CuCl and CdS nanocrystals dispersed in glass matrices [9–11] were based on a simple model of a spherical, infinitely deep potential well for electrons and holes. On the basis of this model, important theoretical results were obtained which qualitatively agree with the experiment. In particular, it was shown that the short-wave shift of the maximum of the absorption coefficient is inversely proportional to the quantity $m_e a^2$ (m_e is the electron mass and a is the radius of a quantum dot) if $a_h \ll a \ll a_e$ and $a \ll a_h$, a_e (a_h and a_e are the Bohr radii of an electron and a hole) and to the quantity $(m_e + m_h)a^2$ when the radius of the nanocrystal satisfies the condition $a \gg a_h$, a_e.

In [12–17], for heterosystems of a different nature, the existence of bound surface charges was taken into account through the potential of the electrostatic image forces. The conditions for the occurrence of the bound states of electrons near interfaces were investigated. The effect of the surface polarization charges of the heterostructure on the exciton energy and on the oscillator strength of the transition to the exciton state was studied. The calculations demonstrated that, in the case of closeness of the dielectric constants of the layers of the heterosystem, a model of a square infinite potential well can be taken as a basis and the influence of the surface charges can be taken into account by the perturbation theory.

Further experimental investigations made it possible to produce heterostructures in which various semiconductor compounds are used for the nanocrystal and the matrix [18–21].

In recent years, multilayer nanosystems wherein a quantum dot contains a nucleus and several semiconducting layers [20] have been intensely investigated. Interesting results were obtained for heterosystems with closely located quantum wells [20–25].

The theoretical works in which the heterosystems mentioned above have been investigated are based on the models of quantum points where an electron and a hole are located in finite potential wells. This approach allows one to provide a possible explanation for the genesis of the energy spectrum in the case of two particles, the tunneling between the layers of complex nanoheterosystems, and the splitting of the energy levels for closely located quantum dots [20, 24, 25].

Modern technology of the production of complex nanoheterostructures of semiconductors and dielectrics makes it possible to produce them with sufficiently high quality. However, in actual practice, it is very difficult to produce an inhomogeneous system with a jumplike variation of all physical parameters at the interface [26, 27]. Among these parameters are the work function, the effective masses of the electrons (holes), and the dielectric constants of the materials.

It is evident that, in a heterostructure, there always exists an intermediate layer where some physical parameter varies from its value corresponding to one semiconductor (dielectric) to the value corresponding to another crystal [27].

1063-7834/01/4302-0235$21.00

In this work, we consider an intermediate layer in order to take into account the smooth variation of the dielectric constant of the materials near the interfaces of a heterosystem. A model of such a layer is proposed, and in this model, an expression is obtained for the potential energy of a charged particle in a multilayer spherical heterostructure with intermediate regions near the interfaces. For a spherical HgS/CdS structure, the energy of the ground and excited states of the electron is calculated both in the presence of an intermediate layer with space-dependent permittivity and in its absence.

1. FORMULATION OF THE PROBLEM

A multilayer semiconductor nanoheterosystem is considered (Fig. 1); it is composed of crystals with dielectric constants $\varepsilon_1, \varepsilon_2, \ldots, \varepsilon_n$. The interfaces of the heterosystem are concentric spheres with radii $R_1, R_2, \ldots, R_{n-1}$. The dielectric constant of the materials near the interfaces in regions of thicknesses $L_1, L_2, \ldots, L_{n-1}$ depends upon the coordinate r (r is the distance from the center to a given point) and is defined by the formula

$$\varepsilon(r) = \frac{1}{2}\{1 - S(r)\}\sum_{i=1}^{n}\varepsilon_i,$$

where

$$S(r) = \gamma_1 f\left(\frac{r-R_1}{L_1}\right) + \sum_{i=1}^{n-2}\gamma_{i+1} f\left(\frac{r-R_i}{L_i}\right) \times f\left(\frac{r-R_{i+1}}{L_{i+1}}\right) - \gamma_n f\left(\frac{r-R_{n-1}}{L_{n-1}}\right),$$

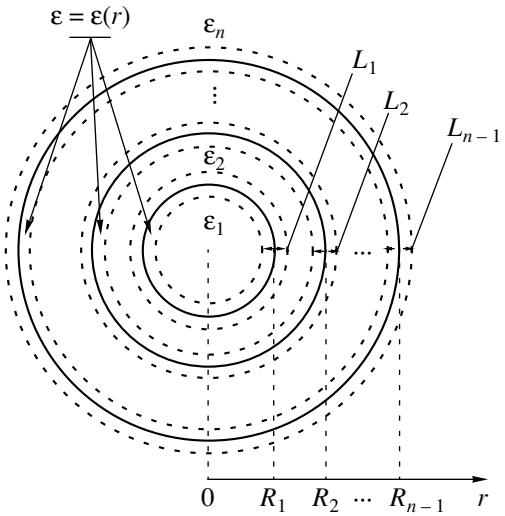

Fig. 1. Model of a spherical multilayer nanoheterosystem.

$$\gamma_j = \frac{\varepsilon_j}{\sum_{i=1}^{n}\varepsilon_i} \quad (j = 1, 2, \ldots, n);$$

$f\left(\frac{r-R_i}{L_i}\right)$ is a monotonic function such that

$$f\left(|x| \geq \frac{1}{2}\right) = \pm 1, \quad f'\left(|x| \geq \frac{1}{2}\right) = 0$$

for any value of i ($i = 1, 2, \ldots, n-1$).

A point charge q located at $\mathbf{r}_0$ generates a potential $\phi(\mathbf{r}, \mathbf{r}_0)$ at point $\mathbf{r}$. This potential is a solution to the Poisson equation

$$\nabla^2\phi(\mathbf{r}, \mathbf{r}_0) + \frac{d}{dr}[\ln\varepsilon(r)]\frac{\partial}{\partial r}[\phi(\mathbf{r}, \mathbf{r}_0)] = -\frac{4\pi q}{\varepsilon(r)}\delta(\mathbf{r} - \mathbf{r}_0),$$

where $\delta(\mathbf{r} - \mathbf{r}_0)$ is the Dirac delta-function. The potential energy of the charge in the polarization field induced by this charge is determined by the formula

$$U(\mathbf{r}) = \frac{q\phi(\mathbf{r})}{2}, \tag{1}$$

where

$$\phi(\mathbf{r}) = \lim_{\mathbf{r}\to\mathbf{r}_0}\left\{\phi(\mathbf{r}, \mathbf{r}_0) - \frac{q}{\varepsilon(r)}\frac{1}{|\mathbf{r} - \mathbf{r}_0|}\right\}. \tag{2}$$

By means of the substitution

$$\phi(\mathbf{r}, \mathbf{r}_0) = -4\pi q[\varepsilon(r)\varepsilon(r_0)]^{-1/2}G(\mathbf{r}, \mathbf{r}_0), \tag{3}$$

the Poisson equation is simplified:

$$\nabla^2 G - V(r)G = \delta(\mathbf{r} - \mathbf{r}_0), \tag{4}$$

where

$$V(r) = \frac{1}{2r^2}\frac{1}{\sqrt{\varepsilon(r)}}\frac{d}{dr}\left[\frac{r^2}{\sqrt{\varepsilon(r)}}\frac{d}{dr}[\varepsilon(r)]\right]$$

and $G(\mathbf{r}, \mathbf{r}_0)$ is the Green's function.

The solution of Eq. (4) is carried out by the method of successive approximations. This method assumes a small value of "potential" $V(r)$. This is the case when

$$\left|\frac{\varepsilon_i - \varepsilon_{i+1}}{\varepsilon_i + \varepsilon_{i+1}}\right| \ll 1,$$

which is satisfied in most experiments [18–20], since heterosystems consist of semiconductors with closely related features. Green's function can be represented in the form of a rapidly convergent series:

$$G = G^{(0)} + G^{(1)} + G^{(2)} + \ldots \equiv G^{(0)} + \Delta G. \tag{5}$$

In zero approximation, Eq. (4) has the form

$$\nabla^2 G^{(0)}(\mathbf{r}, \mathbf{r}_0) = \delta(\mathbf{r} - \mathbf{r}_0).$$

To within a constant multiplier, $G^{(0)}$ is the potential of a point charge; therefore,

$$G^{(0)}(\mathbf{r}, \mathbf{r}_0) = -\frac{1}{4\pi|\mathbf{r}-\mathbf{r}_0|}. \quad (6)$$

When the corrections of higher orders of smallness are consecutively considered, the equation for $G^{(n)}$ can be worked out to

$$\nabla^2 G^{(n)} - V(r)G^{(n-1)} = 0, \quad n = 1, 2, 3, \ldots,$$

where

$$\begin{aligned} G^{(1)}(\mathbf{r}, \mathbf{r}_0) &= \int d\mathbf{r}_1 G^{(0)}(\mathbf{r}, \mathbf{r}_1) V(r_1) G^{(0)}(\mathbf{r}_1, \mathbf{r}_0), \\ G^{(2)}(\mathbf{r}, \mathbf{r}_0) &= \int d\mathbf{r}_1 \mathbf{r}_2 G^{(0)}(\mathbf{r}, \mathbf{r}_1) V(r_1) G^{(0)}(\mathbf{r}_1 \mathbf{r}_2) \\ &\quad \times V(r_2) G^{(0)}(\mathbf{r}_2, \mathbf{r}_0), \\ G^{(n)}(\mathbf{r}, \mathbf{r}_0) &= \int d\mathbf{r}_1 \ldots d\mathbf{r}_n G^{(0)}(\mathbf{r}, \mathbf{r}_1) \\ &\quad \times V(r_1) \ldots V(r_n) G^{(0)}(\mathbf{r}_n, \mathbf{r}_0). \end{aligned} \quad (7)$$

It follows from Eqs. (2), (3), (5), and (6) that $\phi(r)$ in Eq. (1) is determined by the corrections of higher orders:

$$\phi(r) = -\frac{4\pi q}{\varepsilon(r)} \Delta G(\mathbf{r}, \mathbf{r}), \quad (8)$$

where

$$\Delta G(\mathbf{r}, \mathbf{r}) = G^{(1)}(\mathbf{r}, \mathbf{r}) + G^{(2)}(\mathbf{r}, \mathbf{r}) + \ldots.$$

If we expand the functions in a Fourier series,

$$\begin{aligned} G^{(0)}(\mathbf{r}, \mathbf{r}_0) &\equiv G^{(0)}(\mathbf{r} - \mathbf{r}_0) \\ &= -(2\pi)^{-3} \int d\mathbf{q} \frac{1}{q^2} \exp\{i\mathbf{q}(\mathbf{r} - \mathbf{r}_0)\}, \\ V(r) &= (2\pi)^{-3} \int d\mathbf{q} V(\mathbf{q}) \exp\{i\mathbf{q}\mathbf{r}\} \end{aligned}$$

and substitute the result in Eq. (7), we arrive at

$$\begin{aligned} G^{(1)}(\mathbf{r}, \mathbf{r}) &= (2\pi)^{-6} \int d\mathbf{q}_1 d\mathbf{q}_2 d\mathbf{r}_1 \frac{V(r_1)}{q_1^2 q_2^2} \\ &\quad \times \exp[i(\mathbf{q}_1 - \mathbf{q}_2)(\mathbf{r} - \mathbf{r}_1)]. \end{aligned}$$

After passing to a spherical frame of reference and integrating with respect to $\mathbf{q}_1$ and $\mathbf{q}_2$, the formula for $G^{(1)}$ becomes

$$G^{(1)}(\mathbf{r}, \mathbf{r}) = \frac{1}{8\pi r} \int_0^\infty dr_1 r_1 V(r_1) \ln\left|\frac{r_1 + r}{r_1 - r}\right|.$$

The correction $G^{(2)}(\mathbf{r}, \mathbf{r})$ is obtained in a similar manner:

$$\begin{aligned} G^{(2)}(\mathbf{r}, \mathbf{r}) &= -\frac{1}{8\pi r} \int_0^r dr_1 r_1 V(r_1) \int_0^{r_1} dr_2 r_2 V(r_2) Q\left(\frac{r_2}{r}\right) \\ &\quad - \frac{1}{8\pi r} \int_0^r dr_1 r_1 V(r_1) Q\left(\frac{r_1}{r}\right) \int_{r_1}^r dr_2 r_2 V(r_2) \\ &\quad - \frac{1}{8\pi r} \int_0^r dr_1 r_1 V(r_1) \int_r^\infty dr_2 r_2 V(r_2) Q\left(\frac{r_1}{r_2}\right) \\ &\quad - \frac{1}{8\pi r} \int_r^\infty dr_1 r_1 V(r_1) \int_0^r dr_2 r_2 V(r_2) Q\left(\frac{r_2}{r_1}\right) \\ &\quad - \frac{1}{8\pi r} \int_r^\infty dr_{r_1} r_1 V(r_1) Q\left(\frac{r}{r_1}\right) \int_r^{r_1} dr_2 r_2 V(r_2) \\ &\quad - \frac{1}{8\pi r} \int_r^\infty dr_1 r_1 V(r_1) \int_{r_1}^\infty dr_2 r_2 V(r_2) Q\left(\frac{r}{r_2}\right), \end{aligned}$$

where

$$Q(x) = \int_0^x dy \frac{1}{y} \ln\frac{1+y}{1-y}, \quad |x| \le 1.$$

These results are reasonably general. To make them more specific, it is necessary to take into account an explicit form of the function $V(r)$ and to express it via small parameters γ_i. If we expand $V(r)$ in a power series in γ_i and keep only the terms which are proportional to γ_i and γ_i^2, $V(r)$ is represented by the formula

$$\begin{aligned} V(r) \approx &-\frac{1}{2r}\frac{d^2}{dr^2}[rS(r)] - \frac{1}{4r}\frac{d^2}{dr^2}[r[S(r)]^2] \\ &+ \frac{1}{4}\left[\frac{d}{dr}[S(r)]\right]^2. \end{aligned}$$

Now, ΔG can be written in the form

$$\begin{aligned} \Delta G(\mathbf{r}, \mathbf{r}) &= G^{(1)}(\mathbf{r}, \mathbf{r}) + G^{(2)}(\mathbf{r}, \mathbf{r}) \\ &= -\frac{1}{8\pi} \int_0^\infty d[r_1 S(r_1)] \frac{1}{r_1^2 - r^2} - \frac{1}{16\pi} \int_0^\infty d[r_1 [S(r_1)]^2] \frac{1}{r_1^2 - r^2} \\ &\quad - \frac{1}{32\pi r} \int_0^\infty d[r_1 [S(r_1)]^2] \ln\left|\frac{r_1 + r}{r_1 - r}\right| \frac{1}{r_1} \\ &\quad - \frac{1}{8\pi r} \int_0^r d[r_1 S(r_1)] \int_r^\infty d[r_2 S(r_2)] \frac{1}{r_1^2 - r_2^2}. \end{aligned} \quad (9)$$

As indicated by Eqs. (1) and (8), the general expression for the potential energy of the charge is represented via

the corrections to Green's function in Eq. (9):

$$U(r) = -\frac{2\pi q^2}{\varepsilon(r)}\Delta G.$$

The heterosystems which consist of two, three, and even four layers have been investigated experimentally [20]. It is an easy matter to obtain an analytical expression for $U(r)$ in each case, in particular, for a two-layer (nanocrystal–matrix) system when

$$\varepsilon(r) = \frac{\varepsilon_1+\varepsilon_2}{2}\left\{1-\gamma_1 f\left(\frac{r-R_1}{L_1}\right)+\gamma_2 f\left(\frac{r-R_1}{L_1}\right)\right\}$$

$$= \frac{\varepsilon_1+\varepsilon_2}{2}\left\{1-(\gamma_1-\gamma_2) f\left(\frac{r-R_1}{L_1}\right)\right\}$$

$$= \frac{\varepsilon_1+\varepsilon_2}{2}\left\{1-\gamma f\left(\frac{r-R}{L}\right)\right\},$$

$$\gamma = \gamma_1-\gamma_2 = \frac{\varepsilon_1}{\varepsilon_1+\varepsilon_2}-\frac{\varepsilon_2}{\varepsilon_1+\varepsilon_2} = \frac{\varepsilon_1-\varepsilon_2}{\varepsilon_1+\varepsilon_2}$$

and the potential energy of the charge can be represented in the form

$$\begin{aligned}U(r) &= \frac{q^2\gamma}{4\varepsilon(r)}\int_0^\infty d\left[r_1 f\left(\frac{r_1-R}{L}\right)\right]\frac{1}{r_1^2-r^2}+\frac{q^2\gamma^2}{8\varepsilon(r)}\\ &\times\int_0^\infty d\left[r_1\left[f\left(\frac{r_1-R}{L}\right)\right]^2\right]\frac{1}{r_1^2-r^2}+\frac{q^2\gamma^2}{16\varepsilon(r)r}\\ &\times\int_0^\infty d\left[r_1\left[f\left(\frac{r_1-R}{L}\right)\right]^2\right]\ln\left|\frac{r_1+r}{r_1-r}\right|\frac{1}{r_1}+\frac{q^2\gamma^2}{4\varepsilon(r)r}\\ &\times\int_0^r d\left[r_1 f\left(\frac{r_1-R}{L}\right)\right]\int_r^\infty d\left[r_2 f\left(\frac{r_2-R}{L}\right)\right]\frac{1}{r_1^2-r_2^2}.\end{aligned} \tag{10}$$

Detailed determination of $U(r)$ is possible after specification of the function $f = f\left(\frac{r-R}{L}\right)$ is carried out. In the case of the considered heterostructures, this function is not known. Analysis reveals that the final results virtually do not depend on the specific form of $f = f\left(\frac{r-R}{L}\right)$ if it is a smooth function. In this paper, it is assumed that

$$f\left(\frac{r-R}{L}\right) = \tanh\left(\frac{r-R}{L}\right).$$

It is appropriate to represent the potential energy in the form

$$U(r) = U_1(r) + U_2(r), \tag{11}$$

where $U_1(r)$ includes the terms proportional to γ_i and $U_2(r)$ includes those proportional to γ_i^2:

$$\begin{aligned}U_1(r) &= \frac{q^2\gamma}{4\varepsilon(r)}\int_0^\infty dr_1\frac{1}{r_1^2-r^2}\\ &\times\left[\frac{r_1}{L}\operatorname{sech}^2\left(\frac{r_1-R}{L}\right)+\tanh\left(\frac{r_1-R}{L}\right)\right],\end{aligned}$$

$$\begin{aligned}U_2(r) &= \frac{q^2\gamma^2}{8\varepsilon(r)}\int_0^\infty dr_1\frac{1}{r_1^2-r^2}\left[\frac{2r_1}{L}\operatorname{sech}^2\left(\frac{r_1-R}{L}\right)\right.\\ &\left.\times\tanh\left(\frac{r_1-R}{L}\right)+\tanh^2\left(\frac{r_1-R}{L}\right)\right]+\frac{q^2\gamma^2}{16\varepsilon(r)r}\\ &\times\int_0^\infty dr_1\ln\left|\frac{r_1+r}{r_1-r}\right|\frac{1}{r_1}\left[\frac{2r_1}{L}\operatorname{sech}^2\left(\frac{r_1-R}{L}\right)\right.\\ &\left.\times\tanh\left(\frac{r_1-R}{L}\right)+\tanh^2\left(\frac{r_1-R}{L}\right)\right]+\frac{q^2\gamma^2}{4\varepsilon(r)r}\\ &\times\int_0^r dr_1\left[\frac{r_1}{L}\operatorname{sech}^2\left(\frac{r_1-R}{L}\right)+\tanh\left(\frac{r_1-R}{L}\right)\right]\\ &\times\int_r^\infty dr_2\frac{1}{r_1^2-r_2^2}\left[\frac{r_2}{L}\operatorname{sech}^2\left(\frac{r_2-R}{L}\right)+\tanh\left(\frac{r_2-R}{L}\right)\right].\end{aligned}$$

Figure 2 represents the dependences $U = U(r)$ (curve *b*) and $U_1 = U_1(r)$ (curve *c*) for the nanocrystal HgS/CdS for $R = 50$ Å and $L = 5$ Å (physical parameters are represented in Table 1). If we include the polarization charges on the interface in the case of a jump-like change in the dielectric constant, the potential energy of the charged particle will have a Coulomb character [12–17] and the function $U(r)$ will suffer a discontinuity at $r = R$ (curve *a* in Fig. 2):

$$U(r) = \frac{q^2\gamma}{2\varepsilon(r)R}\left\{\frac{R^2}{R^2-r^2}+W\right\}, \tag{12}$$

Table 1. Parameters of the materials

Crystal	$m_e(m_0)$	V_e, meV	ε
HgS	0.036	–5000	11.36
CdS	0.2	–3800	5.5

where

$$\varepsilon(r) = \varepsilon_1\Theta(R-r) + \varepsilon_2\Theta(r-R),$$

$$\Theta(x) = \begin{cases} 1, & x > 0 \\ 0, & x < 0, \end{cases}$$

$$W = \begin{cases} \dfrac{\varepsilon_1}{\varepsilon_2} F\left(1, \gamma_2, \gamma_2 + 1, \left(\dfrac{r}{R}\right)^2\right), & r < R \\ \left(\dfrac{R}{r}\right)^2 F\left(1, \gamma_2, \gamma_2 + 1, \left(\dfrac{R}{r}\right)^2\right), & R < r, \end{cases}$$

and $F(x, y, z, u)$ is the hypergeometric function. However, if $\varepsilon = \varepsilon(r)$ has the form of Eq. (10), then, as can be seen from Fig. 2, the function $U(r)$ becomes continuous (curve *b*) and varies nonmonotonically in the intermediate layer and in its vicinity. In this case, the major contribution to $U(r)$ is made by the term $U_1(r)$ (curve *c*). It is significant that a decrease in the width of the intermediate layer L is accompanied by a sharper $U(r)$ dependence, and in the case $L \longrightarrow 0$, we obtain the known result for the potential of the image forces (curve *b* coincides with curve *a*).

2. THE ENERGY OF THE ELECTRON IN *s* STATES IN THE HgS/CdS SYSTEM

A two-layer spherical nanoheterosystem which consists of a HgS nucleus embedded in a CdS matrix is considered.

The Hamiltonian of the electron has the form

$$H = T + V(r) \equiv H^0 + U(r),$$

where

$$V(r) = V_0(r) + U(r),$$

$$H^0 = T + V_0(r).$$

The main part of the Hamiltonian (H^0) is chosen such that the Schrödinger equation describing this system can be solved exactly when perturbation $U(r)$ is discarded:

$$(E_n^0 - H^0)\Psi_n = 0.$$

According to the choice of the model of the heterosystem, potential energy $V_0(r)$ has the form of a spherically symmetrical finite (Fig. 3) or infinite square potential well. Perturbation $U(r)$ is taken to be a potential which has the form of Eq. (11) or Eq. (12).

When employing either model for the majority of the actual systems, we can limit ourselves to corrections of the first and second orders in perturbation theory:

$$E_n' = V_{nn}, \quad E_n'' = \sum_{n' = 0}^{\infty} \frac{|V_{nn'}|^2}{E_n^0 - E_{n'}^0}, \qquad (13)$$

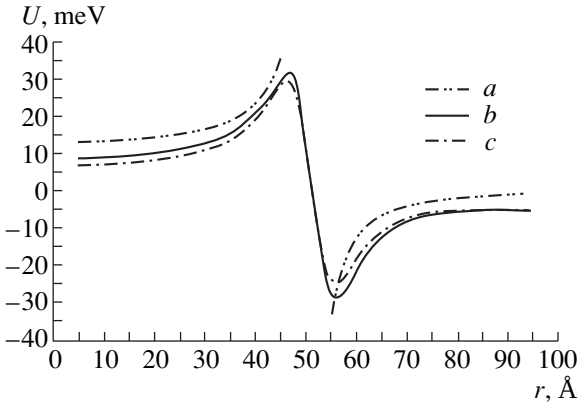

Fig. 2. Dependence of the potential energy of the charged particle upon its distance from the center of the nanocrystal. (*a*) $U(r)$ with the interface polarization charges included and (*b*) $U(r)$ and (*c*) $U_1(r)$ with no interface polarization charges.

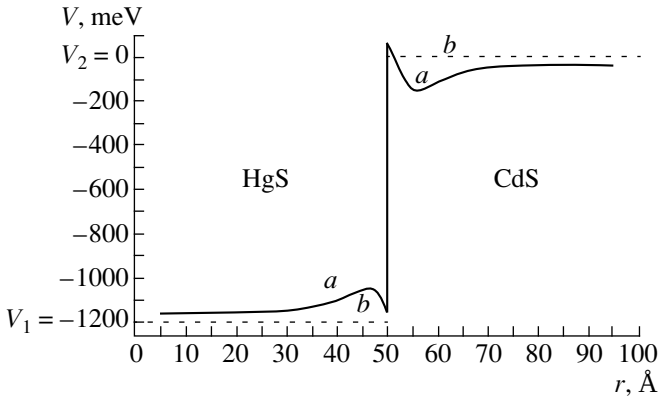

Fig. 3. Model of a finite potential barrier in the presence of an intermediate layer (curve *a*) and in the absence of this layer (curve *b*).

where

$$V_{nn'} = \int R_{n0} U(r) R_{n'0} r^2 dr.$$

Therefore, in order to find E_n' and E_n'', it is necessary to determine the wave functions for the basic Hamiltonian.

First, we consider the model in which, in the zeroth approximation, the electron moves in a radial-symmetric potential of the form

$$V_0(r) = \begin{cases} V_1, & 0 < r < R \\ V_2, & R < r < \infty. \end{cases}$$

The electron has different effective masses in the different media:

$$m = \begin{cases} m_1, & 0 < r < R \\ m_2, & R < r < \infty. \end{cases}$$

Table 2. Energies of the ground and excited states (E_0^0, E_1^0) and corrections to these energies (ΔE_0, ΔE_1) as functions of the radius R for a finite potential well when the width of the intermediate layer is L = 5 Å and for an infinite potential at the interface

R, Å	The potential well							
	finite				infinite			
	E_0^0, meV	E_1^0, meV	ΔE_0, meV	ΔE_1, meV	E_0^0, meV	E_1^0, meV	ΔE_0, meV	ΔE_1, meV
20	–636	–	30.78	–	1411	9246	42.03	46.56
25	–757	–	28.18	–	471	5485	33.62	37.24
30	–841	–	25.62	–	–40	3442	27.96	30.95
35	–902	–	23.31	–	–348	2211	23.89	26.48
40	–948	–	21.11	–	–548	1411	20.76	23.26
45	–984	–73	19.27	10.53	–685	863	18.33	20.67
50	–1012	–244	17.92	13.19	–783	471	16.34	18.59

In order to determine the energy spectrum, it is necessary to solve the time-independent Schrödinger equation

$$\left\{-\frac{\hbar^2}{2}\nabla\frac{1}{m}\nabla + V_0(\mathbf{r})\right\}\Psi(\mathbf{r}) = E_n^0\Psi(\mathbf{r}).$$

Taking into account the spherical symmetry, a solution to this equation can be represented in the form

$$\Psi_{nlm}(r, \Theta, \varphi) = R_{nl}(r)Y_{lm}(\Theta, \varphi).$$

If we consider the s states of the particle (l = 0) and the energy range $V_1 \le E_n^0 \le V_2$, the radial part of the wave function can be expressed in terms of the Bessel spherical functions

$$R_{n0}(r) = \begin{cases} Aj_0(rk_n), & 0 < r < R \\ Bh_0^-(ir\chi_n), & R < r < \infty, \end{cases}$$

where

$$k_n^2 = \frac{2m_1}{\hbar^2}(E_n^0 - V_1), \quad \chi_n^2 = \frac{2m_2}{\hbar^2}(V_2 - E_n^0).$$

In order to determine the unknown coefficients, the conditions of continuity of the wave functions and of the density of the probability flux across the interface and the normalization condition are employed,

$$\begin{aligned} Aj_0(rk_n)\big|_{r=R} &= Bh_0^+(ir\chi_n)\big|_{r=R}, \\ \frac{A}{m_1}\frac{d}{dr}[j_0(rk_n)]\big|_{r=R} &= \frac{B}{m_2}\frac{d}{dr}[h_0^+(ir\chi_n)]\big|_{r=R}, \\ \int_0^\infty |R_{n0}(r)|^2 r^2 dr &= 1. \end{aligned} \tag{14}$$

Substituting the wave functions

$$R_{n0}(r) = \begin{cases} A\dfrac{\sin(rk_n)}{rk_n} \\ -B\dfrac{\exp(-r\chi_n)}{r\chi_n} \end{cases} \tag{15}$$

and their derivatives into Eq. (14) and using the condition for a nonzero solution, we arrive at the following dispersion equation, from which the energies E_n^0 (n = 0, 1, 2, …) of s states can be determined:

$$-\frac{m_1}{k_n}\sin(Rk_n)\exp(-R\chi_n)\left(1 + \frac{1}{R\chi_n}\right)$$
$$+\frac{m_2}{\chi_n}\exp(-R\chi_n)\left(\frac{\sin(Rk_n)}{Rk_n} - \cos(Rk_n)\right) = 0.$$

For comparison, we also consider the model of an infinite potential barrier at the interface, for which the dispersion equation is simplified:

$$\sin(Rk_n) = 0.$$

The first and second corrections to the energy of the nth state are given by Eq. (13).

Table 3. Corrections to the energies (ΔE) as functions of the width of intermediate layer (L) for R = 50 Å

L, Å	1	2	3	4
ΔE_0, meV	16.42	17.71	17.85	17.89
ΔE_1, meV	8.92	11.24	12.42	12.91

3. ANALYSIS OF THE RESULTS

Using the formulas obtained in the preceding sections, we computed the energies of *s* states (E_n^0 and $\Delta E_n = E_n' + E_n''$) in the HgS/CdS nanoheterosystem (Table 2).

The energy levels of the ground and excited states exist in the model of an infinite square potential well for any values of the radii of the nanocrystal. An increase in R leads to lowering of the energy levels, including the electrostatic image forces resulting in increased energies.

For the model of a finite potential well, a discrete energy level emerges in the system when $R \geq 7$ Å. An increase in the radius of the nanocrystal also leads to lowering of the level. When the radius of the nanocrystal becomes greater than 42 Å, a second discrete level comes into existence in the quantum well. As regards the correction ΔE to the energy caused by the existence of the intermediate layer with variable permittivity, an increase in radius R causes this correction to decrease. Physically, this is because an increase in R leads to a decreased effect of the interface on the energy levels of the system.

The calculations demonstrate that the correction to the energy depends on the energy level. For a state with a greater energy (Table 3), the correction decreases. Furthermore, ΔE depends on the thickness of the intermediate layer: a decrease in L is accompanied by a decrease in ΔE. The $\Delta E(L)$ dependence is heavier for the states with greater energies.

4. CONCLUSION

Thus, in this paper, an expression is obtained for the potential energy of a charged particle in a spherical multilayer heterosystem with intermediate regions near the interfaces where the permittivity is a smooth function of the distance. It is shown that, in contrast to the classical potential of the image forces, the potential energy is a continuous function in this case. Different models of the spherical HgS/CdS nanostructure are considered. In these models, the energies of the ground and excited states of the electron are calculated both when the intermediate layer exists and when it is absent. Analysis of the obtained results is carried out.

REFERENCES

1. Al. L. Éfros and A. L. Éfros, Fiz. Tekh. Poluprovodn. (Leningrad) **16** (7), 1209 (1982) [Sov. Phys. Semicond. **16**, 772 (1982)].
2. Y. Kayanuma, Solid State Commun. **59** (6), 405 (1986).
3. Y. Kayanuma, Phys. Rev. B **38** (14), 9797 (1988).
4. S. V. Nair, S. Sinha, and K. C. Rustagi, Phys. Rev. B **35** (8), 4098 (1987).
5. H. M. Schmidt and H. Weller, Chem. Phys. Lett. **129** (6), 615 (1986).
6. G. B. Grigoryan, É. M. Kazaryan, Al. L. Éfros, and T. V. Yazeva, Fiz. Tverd. Tela (Leningrad) **32** (6), 1772 (1990) [Sov. Phys. Solid State **32**, 1031 (1990)].
7. V. A. Golovats'kiĭ and N. V. Tkach, Preprint ITF AN USSR (Kiev, 1990), p. 16.
8. Jian Bai Xia, Phys. Rev. B **40** (12), 8500 (1989).
9. A. I. Ekimov and A. A. Onushchenko, Pis'ma Zh. Éksp. Teor. Fiz. **34** (6), 363 (1981) [JETP Lett. **34**, 345 (1981)].
10. A. I. Ekimov and A. A. Onushchenko, Fiz. Tekh. Poluprovodn. (Leningrad) **16** (7), 1215 (1982) [Sov. Phys. Semicond. **16**, 775 (1982)].
11. A. I. Ekimov and A. A. Onushchenko, Pis'ma Zh. Éksp. Teor. Fiz. **40** (8), 337 (1984) [JETP Lett. **40**, 1136 (1984)].
12. N. A. Efremov and S. I. Pokutniĭ, Fiz. Tverd. Tela (Leningrad) **27** (1), 48 (1985) [Sov. Phys. Solid State **27**, 27 (1985)].
13. N. A. Efremov and S. I. Pokutniĭ, Fiz. Tverd. Tela (Leningrad) **32** (10), 2921 (1990) [Sov. Phys. Solid State **32**, 1697 (1990)].
14. N. A. Efremov and S. I. Pokutniĭ, Fiz. Tverd. Tela (Leningrad) **32** (6), 1637 (1990) [Sov. Phys. Solid State **32**, 955 (1990)].
15. V. I. Boichuk and I. V. Bilynskii, Phys. Status Solidi **174** (1), 463 (1992).
16. V. I. Boĭchuk, V. M. Nitsovich, and N. V. Tkach, Fiz. Tverd. Tela (Leningrad) **22** (3), 669 (1980) [Sov. Phys. Solid State **22**, 410 (1980)].
17. V. I. Boĭchuk, O. N. Voĭtsekhivskaya, V. A. Golovatskiĭ, and N. V. Tkach, Fiz. Tverd. Tela (St. Petersburg) **37** (3), 861 (1995) [Phys. Solid State **37**, 468 (1995)].
18. J. C. Marini, B. Stebe, and E. Kartheuser, Phys. Rev. B **50** (19), 14302 (1994).
19. M. C. Klein, F. Hache, D. Ricord, and C. Flytzanis, Phys. Rev. B **42** (17), 11123 (1990).
20. D. Schooss, A. Mews, A. Eychmuler, and H. Weller, Phys. Rev. B **49** (24), 17072 (1994).
21. R. Romestain and G. Fishman, Phys. Rev. B **49** (3), 1774 (1994).
22. N. E. Kaputkina and Yu. E. Lozovik, Fiz. Tverd. Tela (St. Petersburg) **40** (12), 2226 (1998) [Phys. Solid State **40**, 2021 (1998)].
23. N. E. Kaputkina and Yu. E. Lozovik, Fiz. Tverd. Tela (St. Petersburg) **40** (11), 2127 (1998) [Phys. Solid State **40**, 1929 (1998)].
24. V. V. Krivolapchuk, D. A. Mazurenko, E. S. Moskalenko, *et al.*, Fiz. Tverd. Tela (St. Petersburg) **40** (5), 803 (1998) [Phys. Solid State **40**, 737 (1998)].
25. L. E. Vorob'ev, I. E. Titkov, A. A. Toropov, *et al.*, Fiz. Tekh. Poluprovodn. (St. Petersburg) **32** (7), 852 (1998) [Semiconductors **32**, 757 (1998)].
26. Zh. I. Alferov, Fiz. Tekh. Poluprovodn. (St. Petersburg) **32** (1), 3 (1998) [Semiconductors **32**, 1 (1998)].
27. T. Nakamura, J. Phys. Soc. Jpn. **52** (3), 973 (1983).

Translated by O. Moskalev

Physics of the Solid State, Vol. 43, No. 2, 2001, pp. 242–245. Translated from Fizika Tverdogo Tela, Vol. 43, No. 2, 2001, pp. 233–236.

SEMICONDUCTORS AND DIELECTRICS

The Nature of a Selective Peak in the B*K*-Absorption Edge Spectrum and the Electronic Energy Band Structure of the Crystal 3*C* $BN_{0.99}$

V. V. Ilyasov and I. Ya. Nikiforov

Don State Technical University, Rostov-on-Don, 344010 Russia

e-mail: victor.ilyasov@rost.ru

Received March 23, 2000; in final form, June 28, 2000

Abstract—A new interpretation of the nature of the resonance in the quantum-yield *K* spectra of boron in the crystal 3*C* BN is proposed. This interpretation is based on calculation of the electronic energy band structure of the nonstoichiometric boron nitride 3*C* $BN_{0.99}$, which is carried out by the local coherent potential method in the multiple-scattering approximation. The tops of the valence band and of the XANES range of nonstoichiometric and perfect crystals of boron nitride are compared with the x-ray photoelectron spectrum of 3*C* BN and the B*K*-absorption edge spectrum. The electronic states near the B*K*-absorption edge are modeled and discussed for the relaxed and metastable states caused by the formation of vacancies in the nitrogen sublattice.

INTRODUCTION

Selective peaks (resonances) in the *K*-absorption (quantum-yield) spectra of boron have been recognized for more than a quarter of a century [1–3] and still remain a subject of current investigations [4]. This is because high-temperature wide-band-gap semiconductors have found extensive application in micro- and optoelectronics [5]. In the spectrum of boron nitride with both hexagonal [3] and zinc-blende (cubic) structures [4], there is an energy gap between the top of the valence band and the resonance in the *K*-absorption spectrum of boron, which can be as large as 6 eV [3]. The selective peaks in the B*K* XANES of hexagonal boron nitride are associated with an excited state which arises when a 1*s* electron of boron is knocked out and an x-ray exciton is formed [1]. The excited state is spatially localized near the B-atom core and, according to [3], possesses *p* symmetry, because the selective peak is associated with the transition of a 1*s* electron to an excited level corresponding to a boron 2*p* orbital that is not involved in the formation of bonds in planar hexagonal nets. In the cubic *c*-BN, the presence of a selective peak in the B*K* XANES is associated in [4] with the creation of an excited state of the Wannier-exciton type (so-called core exciton) in the shell of a boron atom.

In this paper, we calculate the electronic band structure of the nonstoichiometric boron nitride *c*-$BN_{0.99}$ in the framework of the multiple-scattering theory and offer a new interpretation of the resonances in the B*K*-XANES spectra of boron nitride.

1. CALCULATION TECHNIQUE

The electronic band structure of the nonstoichiometric boron nitride *c*-$BN_{0.99}$ is calculated by the local coherent potential method in the framework of multiple-scattering theory [6]. The crystal potential is calculated in the virtual-crystal model [7]. This method is notable for the reason that it allows one to investigate systems with crystal symmetry imperfections and, specifically, to calculate the electronic structure of nonstoichiometric *c*-$BN_{0.75}$ [6]. When calculating the potential, we take into account the contributions to the electronic density from neighboring atoms and the Coulomb potential of 30 coordination shells. The exchange potential is calculated in the Slater $X\alpha$ approximation with an exchange correction of $\alpha = 2/3$. The effective crystal potential is found as the sum of the Coulomb, exchange, and Madelung potentials. A deficit in atoms in the nitrogen sublattice can lead to lattice softening due to dangling bonds and to lattice relaxation causing the lattice parameter to decrease [8]. The crystal muffin-tin potential is calculated for the equilibrium state with a lattice parameter of 6.78608 a.u. and for a nonequilibrium state with $a = 6.83136$ a.u. The first seventeen shells of neighbors were taken into account when considering the electron multiple scattering for each of the three clusters used for the calculations. The clusters consisted of 265 atoms each.

The local partial electronic densities of states for a vacancy and B and N atoms can be calculated from

the formula [9]

$$n_l^A(E) = -\frac{\sqrt{E}}{\pi}\int_0^{r_{ws}} (rR_l^A(E,r))^2 dr \frac{\mathrm{Im}\,\mathrm{Tr}\,T^{00,A}_{lm,l'm'}(E)}{\mathrm{Im}\,t_l^A(E)}, \quad (1)$$

where index A specifies the type of atom in the cluster, l is the orbital quantum number, $R(E, r)$ is a radial wave function, and T is the matrix element of the scattering operator. The total electronic density of states (TDOS) of the atoms in 3*C* BN is calculated under the assumption that there are two types (B_1 and B) of scattering boron atoms:

$$\begin{aligned} N(E) &= x\sum_{l=0}^{2} n_l^{\mathrm{vac}}(E) + 4x\sum_{l=0}^{2} n_l^{\mathrm{B_1}}(E) \\ &+ (1-4x)\sum_{l=0}^{2} n_l^{\mathrm{B}} + (1-x)\sum_{l=0}^{2} n_l^{\mathrm{N}}, \end{aligned} \quad (2)$$

where x is the concentration of nitrogen vacancies in the crystal. Boron atoms of type 1 (B_1) are those nearest to a nitrogen vacancy; the other boron atoms are assumed to be situated in a perfect *c*-BN crystal. This separation is possible because the vacancy concentration is low (less than 10%).

2. RESULTS AND DISCUSSION

Figure 1 shows an experimental x-ray photoelectron spectrum (XPS) of a real crystal of c-BN_{1-x}, the TDOS of the nonstoichiometric boron nitride c-$BN_{0.99}$ (in the unrelaxed state), and the B*K*-XANES (quantum-yield) spectrum of *c*-BN. Analysis of the electronic spectra of the nonstoichiometric c-$BN_{0.99}$ and their comparison with those of the stoichiometric *c*-BN allow one to make some suggestions. For example, in the vicinity of the XANES, the electronic structure of the nonstoichiometric c-$BN_{0.99}$ exhibits a fine structure which is not typical of the stoichiometric *c*-BN. This structure is associated with localization of the unoccupied *s* and *p* states of boron atoms of type 1 (peaks a_3 and b_3) and of the vacancy states (peak a_2). It is significant that the unoccupied energy level 1.34 Ry involved in the electron scattering by vacancies coincides with the position of the *CE* resonance peak in the B*K*-XANES spectrum of *c*-BN. Therefore, an excited 1*s* electron passes to the unoccupied vacancy *p* states, rather than to the boron 2*p* states as indicated in [3]. The unoccupied boron *p* states (peaks a_4 and b_4) are localized in a high-energy range and cannot be responsible for the *CE* resonance. As indicated in [4], the *CE* resonance and the spectral features in its vicinity are associated with the 1*s* and 2*s* Wannier core excitons. It should be noted that these excitonic levels cannot be described in terms of the one-electron boron 2*s* states localized at energies of 1.22 and 1.46 Ry, which are responsible for the *K*-absorption edge structure just below the threshold. The absence of the *CE* resonance (1.34 Ry) in the calculated energy bands in [4], in our opinion, can be due to the one-electron approximation used. This approximation is known to give one-electron states which can differ from the excitonic states belonging to the whole crystal [10]. Since the selection rules for quantum transitions can be violated in real crystals (with lattice imperfections) [10], one can assume the occurrence of the process of excitonic excitation mentioned above, namely, the transition of a boron 1*s* electron to the excitonic level, as proposed in [1, 4]. However, if in the boron nitride crystals studied the nitrogen sublattice exhibited nonstoichiometry, as was the case with the crystals studied in [11, 12], then one can assume that the *CE* resonance (1.34 Ry) is associated with vacancies. The presence of vacancies in *c*-BN crystals can be due both to the conditions under which the x-ray absorption spectra were recorded and to the conditions of crystal synthesis. Since the data on the lattice parameter of the crystal studied are not presented in [4], we consider both possibilities.

It is known that, e.g., in a CdS crystal under irradiation, sulphur atoms are observed to be emitted [13] and, therefore, among other structural imperfections, vacancies are created. Since recombination is not an instantaneous process, one can assume, as in [13], that two states can arise in a *c*-BN crystal; one state is equilibrium (with the lattice parameter a = 6.78608 a.u.) and the other is unrelaxed (a = 6.83136 a.u.). The former state can be in an as-grown crystal, as in [12], or it can arise when quantum-yield spectra are recorded. In the approximation employed in this paper, we also calculated the electronic density of states for the equilibrium state in c-$BN_{0.99}$, in which there is no shift of the top of the valence band to lower energies, in contrast to the case of boron B_1 (Fig. 1c). It is significant that, in the equilibrium state, there is an energy gap of 2 eV between peak a_2 due to vacancies and an unoccupied one-particle electronic energy level, 1.5 eV, of a boron atom. In the unrelaxed state, the calculated density of unoccupied electronic states of a boron atom with an energy of 1.34 Ry is very low. Thus, in a c-$BN_{0.99}$ crystal in the unrelaxed state, there is some probability that a 1*s* electron of a boron atom will pass to the unoccupied states associated with both a vacancy and a boron atom (peak a_3).

The reason for the formation of vacancies in a *c*-BN crystal during absorption spectrum recording [4], in our opinion, has to do with the conditions under which the quantum-yield spectrum was measured. For example, the surface of a sample under irradiation can heat up, which leads to thermal activation of the diffusion of boron (nitrogen) atoms in the bulk of the sample, as was the case with the hexagonal *h*-BN and cubic *c*-BN after heat treatment [14]; on the other hand, charge accumulation will occur on the surface, resulting in a decrease of the potential and, perhaps, in the singularity of the state with an energy of 1.34 Ry. The formation of struc-

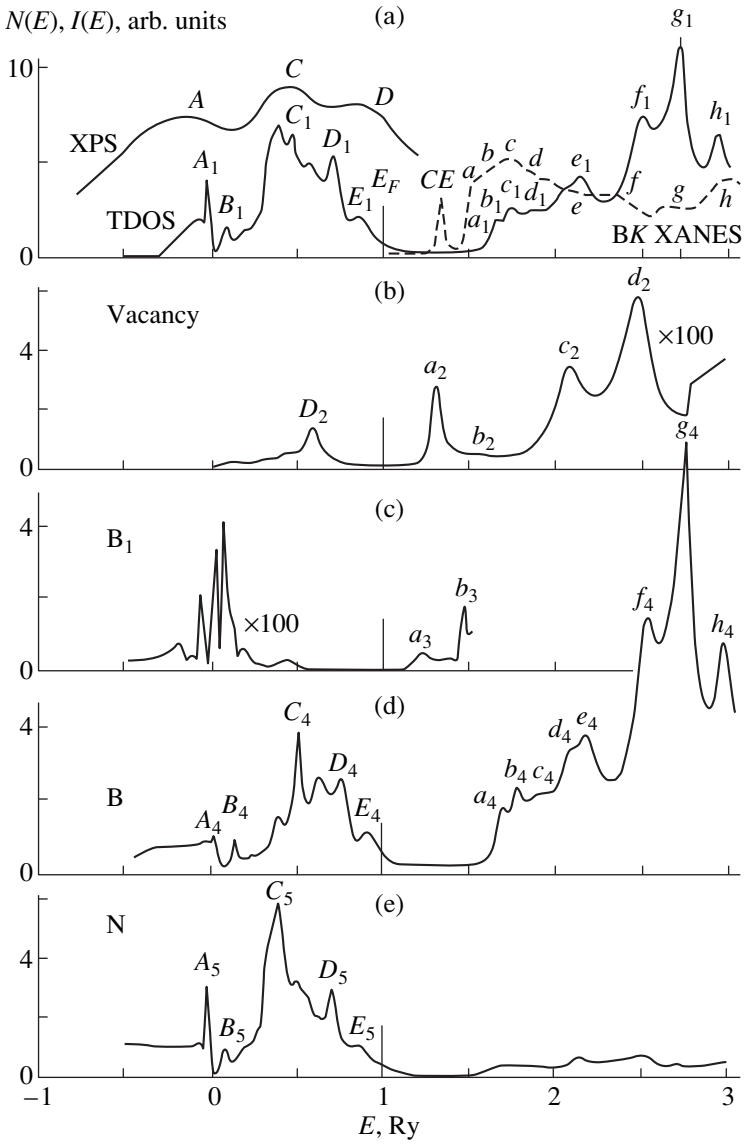

Fig. 1. (a) Total and (b–e) local electronic densities of states of (b) a vacancy and (c, d) boron and (e) nitrogen atoms in boron nitride c-$BN_{0.99}$. The x-ray photoelectron spectrum of the valence band [14] and the K-absorption spectrum of boron [4] in c-BN are also presented in (a).

tural defects (vacancies for the most part) in diamond-like semiconductors under laser radiation was experimentally established in [13]. It was shown that, when irradiated at 300 K by nanosecond pulses (20 ns) of a ruby laser ($\lambda = 0.69$ μm, and the energy of a quantum being less than the energy gap width), single crystals of CdS accumulate structural defects in their surface region. Hall effect measurements also showed [13] that the concentration of donor centers in a surface layer approximately 0.6 μm thick became two orders of magnitude higher after a sevenfold increase in the irradiation dose (relative to the initial value 10^{14} cm^{-3}). The facts presented above are evidence in favor of our statement that the *CE* resonance in the B*K* XANES of boron nitride is associated with vacancies.

Of interest is the energy gap between the *CE* resonance and the Fermi level in c-$BN_{0.99}$. This energy gap equals 4.6 eV and is 1.4 eV smaller than the energy separation between the short-wave limit of the emission band and the selective peak (in the quantum yield) for the hexagonal boron nitride h-BN [2]. This difference can be explained in terms of the energy band structure of h-BN, in which the band gap is larger [15, 16].

The Fermi level E_F is found from the formula

$$N_{ve} = 2\int_0^{E_F} N(E)dE,$$

where the factor of 2 is due to the spin degeneracy and N_{ve} is the number of valence electrons (per unit cell) in the compound. The number N_{ve} does not allow for the 2*s* electrons of nitrogen, whose energy lies below the zero of the muffin-tin potential.

In the nonstoichiometric *c*-$BN_{0.99}$, the electronic spectrum is rearranged near the top of the valence band, so that the state with an energy of 0.4 Ry becomes localized. This state can be considered the ground state for valence electrons of nitrogen atoms. The *p* states of a vacancy on the nitrogen sublattice, which are localized with an energy of about 0.60 Ry (peak D_2), make a contribution (proportional to their concentration) to peak D_1 in the TDOS curve for *c*-$BN_{0.99}$. The largest contribution to this feature is made by the occupied *s* and *p* states of boron and nitrogen atoms.

Thus, the *CE* resonance in the range just below the *K*-absorption (quantum-yield) edge of boron in *c*-BN, in our opinion, can be associated not only with an excited state of the crystal of the Wannier core-exciton type, but also with the transition of a 1*s* electron to unoccupied vacancy states. The model of the resonance in the absorption spectrum of boron in *c*-BN proposed in this paper is consistent with the published experimental data on the structure of the electronic spectra of real crystals of 3*C* BN. This model enhances the understanding of the nature of the selective peak in the B*K* XANES of cubic boron nitride. If our interpretation of the *CE* peak in the *K*-absorption spectrum of boron is true, the intensity of this peak has to be proportional to the vacancy concentration, which can be high in a real crystal.

ACKNOWLEDGMENTS

The authors are grateful to A.P. Popov for useful discussions of the results.

REFERENCES

1. V. A. Fomichev, Fiz. Tverd. Tela (Leningrad) **9**, 3167 (1967) [Sov. Phys. Solid State **9**, 2496 (1967)].
2. V. A. Fomichev, T. M. Zimkina, and I. I. Lyakhovskaya, Fiz. Tverd. Tela (Leningrad) **12** (1), 156 (1970) [Sov. Phys. Solid State **12**, 123 (1970)].
3. I. I. Lyakhovskaya, T. M. Zimkina, and V. A. Fomichev, Fiz. Tverd. Tela (Leningrad) **12** (1), 174 (1970) [Sov. Phys. Solid State **12**, 138 (1970)].
4. A. Agui, S. Shin, M. Fujisawa, *et al.*, Phys. Rev. B **55** (4), 2073 (1997).
5. Yu. A. Vodakov and E. N. Mokhov, Fiz. Tverd. Tela (St. Petersburg) **41** (5), 822 (1999) [Phys. Solid State **41**, 742 (1999)].
6. I. Ya. Nikiforov, V. V. Ilyasov, and N. Yu. Safontseva, J. Phys.: Condens. Matter **7**, 6035 (1995).
7. A. A. Lavrent'ev, B. V. Gabrel'yan, and I. Ya. Nikiforov, Zh. Strukt. Khim. **39** (6), 1076 (1998).
8. V. V. Ilyasov and I. Ya. Nikiforov, Fiz. Tverd. Tela (St. Petersburg) **39** (6), 1064 (1997) [Phys. Solid State **39**, 955 (1997)].
9. V. V. Ilyasov, N. Yu. Safontseva, and I. Ya. Nikiforov, Fiz. Tverd. Tela (St. Petersburg) **36** (2), 451 (1994) [Phys. Solid State **36**, 247 (1994)].
10. A. S. Davydov, *Quantum Mechanics* (Nauka, Moscow, 1973; Pergamon, Oxford, 1976).
11. A. P. Garshin and V. E. Shvaĭko-Shvaĭkovskiĭ, Poroshk. Metall., No. 8, 22 (1992).
12. E. M. Shishinok, V. B. Shipilo, A. I. Lukomskiĭ, and A. E. Rud', Zh. Prikl. Spektrosk. **57** (1–2), 128 (1992).
13. N. A. Davydova and I. Yu. Shabliĭ, Fiz. Tverd. Tela (Leningrad) **24** (5), 1547 (1982) [Sov. Phys. Solid State **24**, 887 (1982)].
14. V. G. Aleshin, A. N. Sokolov, and A. A. Shul'zhenko, Sverkhtverd. Mater., No. 5, 12 (1985).
15. V. A. Fomichev and M. A. Rumsh, J. Phys. Chem. Solids **29**, 1015 (1968).
16. Yong-Nian Xu and W. Y. Ching, Phys. Rev. B **44** (15), 7787 (1991).

Translated by Yu. Epifanov

Physics of the Solid State, Vol. 43, No. 2, 2001, pp. 246–250. Translated from Fizika Tverdogo Tela, Vol. 43, No. 2, 2001, pp. 237–241.

SEMICONDUCTORS AND DIELECTRICS

Quasi-Dynamic Structural Disorder Induced by Fast Neutrons in $Be_3Al_2Si_6O_{18}$ Crystals

I. A. Weinstein, A. F. Zatsepin, and V. S. Kortov

Ural State Technical University, ul. Mira 19, Yekaterinburg, 620002 Russia

e-mail: wia@dpt.ustu.ru

Received May 30, 2000

Abstract—The UV absorption spectra of beryl crystals exposed to fast neutrons with a fluence of 10^{14}–10^{19} cm^{-2} are investigated. It is found that as the fluence of particles increases, a characteristic fan-shaped broadening of the long-wavelength edge is observed for the impurity adsorption band with a charge transfer. The experimental results are interpreted on the basis of the generalized Urbach rule in the approximation of an induced quasi-dynamic disorder. The effective cross section of radiation-induced lattice disordering in the crystals under investigation is estimated at a value ($\sigma = 2.58 \times 10^{-18}$ cm^2) close to the neutron amorphization cross sections for other crystalline silicates. © *2001 MAIK "Nauka/Interperiodica".*

1. INTRODUCTION

Intensive studies of radiation resistance of solids and practical application of fast neutron flows from nuclear reactors for modifying the physical properties of materials require an analysis of the regularities of induced defect formation. The structural disorder created by neutron irradiation and the nature of the resulting crystal lattice distortions are similar in many respects to atomic disordering associated with thermal and deformation effects [1–3]. Radiation-induced effects have been studied in detail for semiconductors, alkali halide crystals, and simple wide-gap oxides [1, 4]. At the same time, the behavior of complex oxide-based insulators in radiation fields has been studied insufficiently. The presence of several types of anionic and cationic sublattices in such objects and the related possibility of forming a variety of complex defects give rise to a complex energy excitation spectrum in the electronic and vibrational subsystems of the crystal. In this case, an analysis of the response to irradiation for particular types of distortions is complicated and requires the application of special approaches using generalized microscopic parameters characterizing the structural disorder of the system as a whole.

By way of an approach to an analysis of the radiation-induced disorder in multicomponent oxide crystals, we can interpret the temperature behavior of the optical spectra of disordered materials on the basis of the equivalence principle of the static and dynamic components of the overall atomic disorder [5, 6]. This approximation makes it possible to clarify the role of atomic disordering effects in the spectral and temperature characteristics of the object on a qualitative as well as a quantitative level [7].

In this work, we studied the radiation-induced disordering in a beryl single crystal. This crystal is a beryllium–aluminum–silicon triple oxide and is of practical interest as a promising matrix for creating quantum amplifiers in the microwave range. The beryl crystal $Be_3Al_2Si_6O_{18}$ belongs to the group of ring silicates. Its crystal structure is formed by hollow channels built up of the rings of six SiO_4 tetrahedra which are arranged one above another and rotated relative to one another through a certain angle. The channels are connected into a three-dimensional lattice via Al^{3+} and Be^{2+} cations in the sixfold- and fourfold-coordinated oxygen environments, respectively. The main microscopic impurity is formed by chromium and iron atoms in various charge states and atomic positions, which can serve at the same time as a peculiar probe for studying the radiation-induced modification of the properties of the oxide. The aim of this work was to analyze the optical spectra of beryl single crystals irradiated by fast neutrons in the UV range.

2. SAMPLES AND EXPERIMENTAL TECHNIQUE

The samples under investigation were cut in the direction parallel to $\mathbf{z}([11\bar{2}0])$ from a nominally pure beryl single crystal grown by using the solution–melt technique. In the final form, the samples were transparent plane-parallel 5×5-mm plates of thickness 0.7 mm with polished surfaces of optical quality.

The crystals were irradiated in air by fast neutrons in an IBR-30 reactor. The sample temperature during irradiation did not exceed 50°C. The exposure time was chosen so that the fluence Φ of particles varied from 10^{14} to 10^{19} cm^{-2}. The irradiation by fast neutrons ruled out transmutation effects, and a smooth variation in the fluence allowed us to dose the radiation-induced damage in the crystal lattice.

1063-7834/01/4302-0246$21.00

The UV absorption spectra of the crystals were measured on a Specord M40 spectrophotometer at room temperature.

3. RESULTS

Figure 1 shows the measured dependences of the absorption coefficient α on the photon energy $h\nu$ for the initial beryl single crystal and irradiated samples. The corresponding fluences Φ are indicated in this figure. It can be seen that, for all the samples, the curves can be successfully approximated by linear characteristics (solid straight lines) in semilogarithmic coordinates. With increasing fluences in the range $\Phi < 10^{17}$ cm^{-2}, the straight lines describing the spectral dependences exhibit a parallel displacement to the low-energy range. As the fluence increases to $\Phi > 10^{17}$ cm^{-2}, the straight lines continue their displacement toward lower energies, but their slope decreases. It should be noted that extrapolation to the high-energy range of the spectrum leads to the intersection of the straight lines at a single point. The region of convergence of the curves in Fig. 1 is marked by the circle.

Figure 2 displays the induced absorption spectra, which were obtained by subtracting the spectrum of the initial crystal from the spectrum of the sample exposed to neutrons with the corresponding fluence. It is clearly seen that the observed dependences can also be approximated by straight lines in semilogarithmic coordinates. For $\Phi = 10^{14}$–10^{18} cm^{-2}, the straight lines have the same slope, which noticeably decreases in the range of $\Phi \approx 10^{18}$ cm^{-2} and remains unchanged upon a further increase in the fluence.

Figure 3 shows the dependence of the reciprocal logarithmic slope $E_0 = \partial h/\partial\alpha$ on the neutron fluence Φ. The experimental point on the ordinate axis corresponds to the slope in the initial unirradiated sample. It can be seen that for $\Phi < 10^{18}$ cm^{-2}, the parameter E_0 remains constant within an error of 3% (closed circles) for the main absorption spectra (Fig. 1). However, upon a further increase in the neutron flux, the slope increases from 0.102 ± 0.003 to 0.158 ± 0.005 eV. Curve *1* in Fig. 3, which is drawn through experimental points, visually illustrates the behavior described above. The inset to Fig. 3 shows the values of E_0 for induced absorption (open circles). We can clearly see two regions of constant values of the slope: $E_0 = 0.120 \pm 0.004$ eV for $\Phi = 10^{14}$–10^{18} cm^{-2} and $E_0 = 180 \pm 0.005$ eV for $\Phi > 10^{18}$ cm^{-2}.

In the general case, the parameter E_0 characterizes the width of the corresponding optical band and simultaneously reflects the degree of overall structural disorder which is present in the system and affects the optoelectronic transitions [5]. We will analyze the obtained results from the viewpoint of increasing atomic disorder in a crystal exposed to fast neutrons.

4. DISCUSSION

Irradiation by fast neutrons creates a variety of defects in the bulk of silicate matrices with various degrees of ordering of the silicon–oxygen sublattice. Among these defects, distortions of the oxygen-deficiency type, which are detected as paramagnetic *E*'-centers, are most abundant and have been studied most thoroughly [2, 8, 9]. In the optical absorption spectra of phenacite Be_2SiO_4 and quartz α-SiO_2 crystals, which

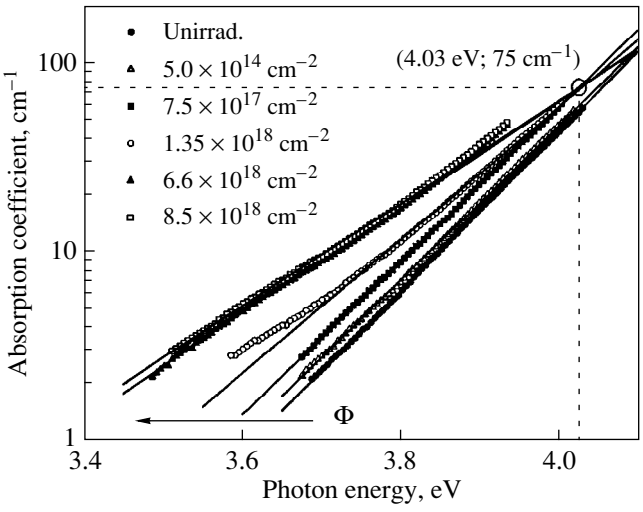

Fig. 1. Optical absorption spectra of beryl crystals irradiated by fast neutrons. The fluences Φ are indicated for each symbol.

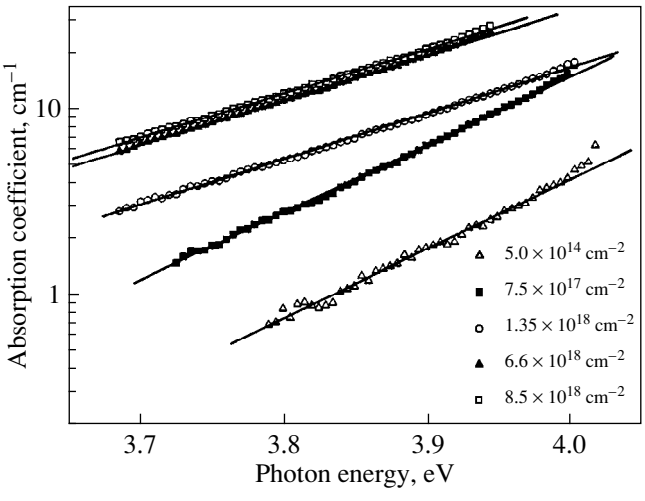

Fig. 2. Induced optical absorption spectra. The fluences Φ are indicated for each symbol.

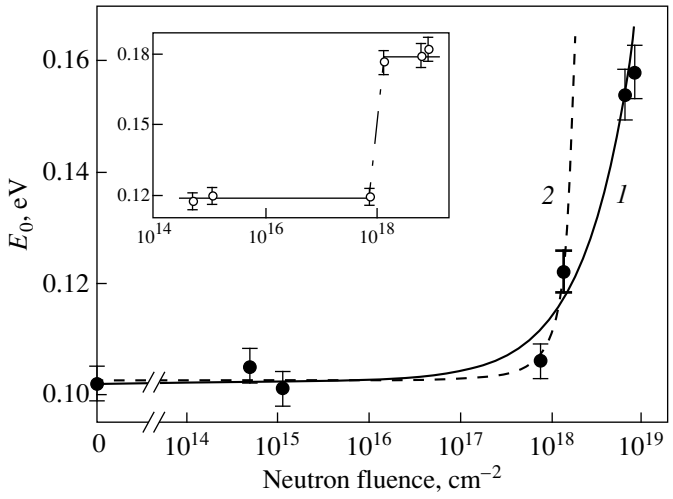

Fig. 3. Dependence of the disorder parameter E_0 on the neutron fluence. Curve *1* and dark circles correspond to experimental data, and curve *2* is the result of an approximation by formula (3). The inset shows the dependence of Φ on the parameter E_0 for induced absorption; the axes are the same as in the main figure.

are akin to beryl, these centers correspond to bands at 5.6 and 5.9 eV, respectively [2, 8, 9]. Along with *E*'-centers, complementary hole-type O_1^0-centers, as well as mono- and divacancies of oxygen, are also detected. The latter are associated with twofold-coordinated silicon atoms Si_2^0 in crystalline silicates (the so-called B_2 band in optical absorption spectra) [8, 10, 11]. It was proved earlier [2] that the absorption induced in irradiated beryl crystals falls in the region of strong absorption characteristic of the original matrix. The formation of paramagnetic *E*'-centers in beryl exposed to fast neutrons is recorded by the corresponding EPR signals and by measurements of the thermally stimulated electron emission [2].

The spectra observed for all the samples under investigation correspond to the long-wavelength edge of the wide absorption band associated with an optical transition with a charge transfer $O^{2-} \longrightarrow Fe_4^{3+}$ (iron impurity at the beryllium site) [12]. In our experiment, the characteristic bands associated with the generation of *E*'-centers are completely masked by a more intense charge transfer band. Thus, we can assume that, in this case, the transformation of the impurity absorption band edge reflects the overall disordering processes occurring in the bulk of the crystal.

The obtained exponential dependences (see Fig. 1) can be described using the Urbach rule [13, 14]. It was shown earlier [5, 15] that the spectral–temperature dependence of the absorption edge can be represented by an exponential dependence of the general form

$$\alpha(h\nu, T, X) = \alpha_0 \exp\left(\frac{h\nu - E_g(T)}{E_0(T, X)}\right), \qquad (1)$$

where α_0 is a constant; $h\nu$ is the photon energy; $E_g(T)$ is the temperature function of the optical gap width (the most probable energy of the optoelectronic transition in the present case); and $E_0(T, X)$ is the function of the overall disorder in the system, which can be represented as the sum of the parameters of static and dynamic disordering of lattice atoms [16, 17]:

$$E_0(T, X) = K(\langle u^2\rangle_X + \langle u^2\rangle_T). \qquad (2)$$

Here, $\langle u^2\rangle_T$ and $\langle u^2\rangle_X$ are the mean square displacements of lattice atoms from their equilibrium positions, which are associated with dynamic (thermal phonons) and static ("frozen" phonons) disorders, respectively. The coefficient *K* has the meaning of the second-order deformation potential constant. The value of E_0 of the logarithmic slope of a spectral curve characterizes the averaged smearing of band tails or selective bands in the electron density of states due to breaking of the atomic ordering [5, 18, 19].

The parameter *X* is used here for denoting static disorder. By analogy with the conventional temperature *T* used to characterize the dynamic component of disorder, the parameter *X* can have the meaning of an effective temperature at which the phonon disorder is "frozen" and which, therefore, can characterize the static disorder in the crystal structure. The universal dependence (1) makes it possible to obtain the "crystalline" (with a fan-shaped shift in temperature) and "vitreous" (with a parallel shift in temperature) versions of the Urbach rule, disregarding either the static or the dynamic term, respectively, in the function $E_0(T, X)$ of the overall disorder [5, 6].

However, an analysis of Eqs. (1) and (2) leads to another important conclusion. The parameters *T* and *X* are absolutely equivalent. Hence, the absorption edge at a fixed parameter *T* should exhibit, apart from the traditional Urbach fan in temperature, a fanlike behavior in the parameter *X*, which is related to the "freezing" temperature. In our case, it is just the parameter *X* which is varied upon a change in the neutron fluence.

Indeed, Fig. 1 shows a typical Urbach fan in Φ at room temperature. For small fluences, the spectral characteristics exhibit a parallel displacement, but their slope decreases upon a further increase in the fluence. In this case, the coordinates of the focal point E_f(4.03 ± 0.05 eV, 75 ± 5 cm^{-1}) are in good agreement with the parameters of the maximum of the optical absorption band under investigation ($E_m \approx 4.05$ eV) [20]. Qualitatively similar patterns for various crystals with Urbach fans in temperature can be found in the well-known review by Kurik [13].

The electron transition energy E_g can be written as a function of different types of disorder through the second-order deformation potential constant D, that is,

$$E_g(X, T) = E_g(0, 0) - D(\langle u^2\rangle_X + \langle u^2\rangle_T), \qquad (3)$$

where $E_g(0, 0)$ is the transition energy in the absence of disorder, which takes into account zero-point thermal and "frozen" vibrations. Using Eq. (2), we can write [17, 21, 22]

$$E_g(X, T) = E_g(0, 0) - \frac{D}{K}E_0(X, T). \qquad (4)$$

Substituting this expression into Eq. (1), we can determine the ratio D/K for each straight line in Fig. 1. The obtained values fall in the range (0.20–0.50) ± 0.05 (see table).

In the above approach, $E_g(0, 0)$ coincides with the energy of the focal point. The experimental dependence (4) was plotted by Cody *et al.* [17] for amorphous hydrogenized silicon. In our case, the values of E_g for different samples are unknown. It can be assumed only for the original crystal that this quantity corresponds to the band maximum, i.e., $E_g(0, 293\ \mathrm{K}) = 4.05$ eV. However, since we consider the band edge and assume that E_g is a linear function of $h\nu$ in semilogarithmic coordinates, we can plot the dependence $h\nu(E_0)$ for different values of the absorption coefficient. Figure 4 shows such functions for $\alpha = 10$–$25\ \mathrm{cm}^{-1}$. Moreover, assuming that the averaged value of $D/K = 0.35$, we can calculate the function $E_g(E_0)$ (Fig. 4). It can be seen from this figure that the calculated straight line and the straight lines approximating the obtained experimental dependences converge at the point (0 eV, 4.08 ± 0.05 eV). The energies that correspond to focal points in Figs. 1 and 4 coincide to within the experimental error. Thus, the obtained dependences $\alpha(h\nu)$ and $h\nu(E_0)$ are fan-shaped, which can be interpreted as a manifestation of the quasi-dynamic nature of the neutron-induced structural disorder.

In turn, the dose dependence $E_0(\Phi)$ (see Fig. 3) has a functional form similar to the typical temperature dependence of the optical band half-width for crystals (see, for example, [23]). For small fluences, i.e., low temperatures of phonon freezing, the slope varies insignificantly. For $\Phi > 10^{18}\ \mathrm{cm}^{-2}$ (high freezing temperature), the parameter under investigation increases considerably. As a first approximation, the observed relation between the parameter E_0 and the degree of structural disorder makes it possible to describe the

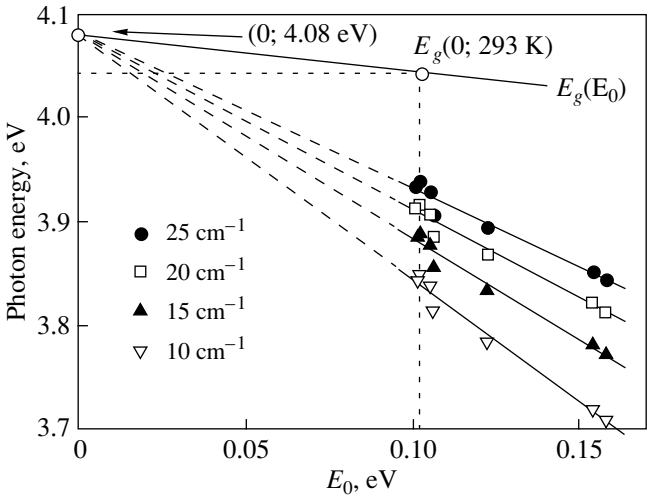

Fig. 4. Linear dependences of the optical transition energy on the disorder parameter E_0 for discrete absorption coefficients. Symbols mark the experimental results corresponding to the indicated values of α. The dependence $E_g(E_0)$ is calculated using formula (4).

dynamics of the disordering process in the form

$$E_0(\Phi) = E_0(0) + C\exp(\sigma\Phi). \qquad (5)$$

Here, $E_0(0)$ is the slope of the spectral curve for the initial unirradiated sample, σ is the effective cross section of structure disordering, and C is a constant numerically characterizing the increment of E_0 in the range of fluences $\Phi\sigma \ll 1$.

The approximation of experimental data by formula (5) is shown in Fig. 3 (curve *2*). In this case, $\sigma = 2.58 \times 10^{-18}\ \mathrm{cm}^2$ and $C = 6 \times 10^{-4}$ eV. The disordering cross section is close to the values of similar quantities characterizing the amorphization of the crystal structure of the orthosilicate Be_2SiO_4 ($\sigma = 1 \times 10^{-19}\ \mathrm{cm}^2$) and the simple oxide α-SiO_2 ($\sigma = 3 \times 10^{-19}\ \mathrm{cm}^2$), in which neutron irradiation also intensively generates anion–vacancy defects [24]. At the same time, Fig. 3 shows that for large fluences ($\approx 10^{19}\ \mathrm{cm}^{-2}$), the calculated dependence (curve *2*) noticeably deviates from the experimental dependence (curve *1*). In this range of Φ, the cross section of the process itself is apparently a function of the neutron fluence, which decreases upon an increase in Φ. Although the exact form of the $\sigma(\Phi)$ dependence is unknown, the variation in the cross section for large Φ indicates substantial transformations of the structure and properties of the crystal, which, in

Table

Dependence of D/K on the neutron fluence							
Φ (cm^{-1})	0	5×10^{14}	1.15×10^{15}	7.5×10^{17}	1.35×10^{18}	6.6×10^{18}	8.8×10^{18}
D/K:	0.25	0.31	0.33	0.52	0.43	0.35	0.35

turn, affects the efficiency of radiation-induced processes.

The nontrivial dependence of the cross section σ on fluence Φ is in excellent agreement with the dose dependence of the parameter E_0 for induced absorption. The inset to Fig. 3 clearly illustrates the two-stage disordering in the range of fluences under investigation. The region $\Phi < 10^{18}$ cm^{-2} apparently corresponds to processes of primary defect formation under neutron irradiation. In particular, the radiation-induced generation of E'-centers dominates in this region [2]. At $\Phi > 10^{18}$ cm^{-2}, the formation of other defects (e.g., oxygen divacancies, oxygen hole-type centers, and defect complexes) and radiation-induced annealing are intensified considerably. This is accompanied by an increase in the overall disordering of the atomic lattice, which manifests itself in a sharp increase in the disorder parameter E_0 for induced absorption (see the inset to Fig. 3). Moreover, for these values of neutron fluence, the slope parameters of the main spectral dependences (see Fig. 3) increase, curves *1* and *2* in Fig. 3 noticeably diverge, and the effective disordering cannot be described in the constant cross section approximation any longer.

Thus, assuming that the parameter E_0 reflects the overall disorder in the lattice of a complex oxide, we conclude that the magnitude of the neutron fluence corresponds to a quite definite equilibrium temperature of structural disordering. In other words, the modification of optical spectra of the studied objects under neutron irradiation can be successfully analyzed on the basis of the generalized Urbach rule taking into account the equivalence principle of static and dynamic disorders. With this approach, the observed effects of radiation-induced damage of the structure and modification of the properties of beryl crystals should be treated as a result of the formation of an induced quasi-dynamic disorder. At the same time, the closeness of the effective cross sections of beryl disordering and the cross sections of amorphization in quartz and phenacite indicates the important role of the silicon–oxygen sublattice of the crystals in radiation-induced processes and, hence, the similarity of the mechanisms of defect formation in the structure of simple and complex oxides belonging to the class of silicates.

REFERENCES

1. K. K. Shvarts and Yu. A. Ékmanis, *Dielectric Materials: Radiation Processes and Radiation Resistance* (Zinatne, Riga, 1989).
2. A. F. Zatsepin, V. I. Ushkova, and V. A. Kalent'ev, Poverkhnost', No. 6, 100 (1990).
3. S. F. Dubinin, V. D. Parkhomenko, S. G. Teploukhov, and B. N. Goshchitskiĭ, Fiz. Tverd. Tela (St. Petersburg) **40** (9), 1584 (1998) [Phys. Solid State **40**, 1436 (1998)].
4. V. S. Vavilov, N. P. Kekelidze, and L. S. Smirnov, *Radiation Effect on Semiconductors* (Nauka, Moscow, 1988).
5. I. A. Vaĭnshteĭn, A. F. Zatsepin, and V. S. Kortov, Fiz. Khim. Stekla **25** (1), 70 (1999).
6. I. A. Vaĭnshteĭn, A. F. Zatsepin, V. S. Kortov, and Yu. V. Shchapova, Fiz. Tverd. Tela (St. Petersburg) **42** (2), 224 (2000) [Phys. Solid State **42**, 230 (2000)].
7. I. A. Weinstein, A. F. Zatsepin, and Yu. V. Schapova, Physica B (Amsterdam) **263–264** (1–4), 167 (1999).
8. J. A. Weil, Phys. Chem. Miner. **10**, 149 (1984).
9. S. M. Brekhovskikh and V. A. Tyul'nin, *Radiation Centers in Inorganic Glasses* (Énergoatomizdat, Moscow, 1988).
10. L. Skuja, J. Non-Cryst. Solids **239**, 16 (1998).
11. A. F. Zatsepin, V. S. Kortov, V. A. Kalent'ev, and V. I. Ushkova, Fiz. Tverd. Tela (Leningrad) **30** (5), 1305 (1988) [Sov. Phys. Solid State **30**, 757 (1988)].
12. A. N. Platonov, M. N. Taran, and V. S. Balitskiĭ, *The Nature of Semiprecious Stone Coloration* (Nedra, Moscow, 1984).
13. M. V. Kurik, Phys. Status Solidi A **8**, 9 (1971).
14. B. L. Gel'mont, V. I. Perel', and I. N. Yassievich, Fiz. Tverd. Tela (Leningrad) **25** (3), 727 (1983) [Sov. Phys. Solid State **25**, 415 (1983)].
15. G. D. Cody, J. Non-Cryst. Solids **141**, 3 (1992).
16. J. Tauc, Mater. Res. Bull. **5**, 721 (1970).
17. G. D. Cody, T. Tiedje, B. Abeles, *et al.*, Phys. Rev. Lett. **47** (20), 1480 (1981).
18. N. F. Mott and E. A. Davis, *Electronic Processes in Non-Crystalline Materials* (Clarendon, Oxford, 1979; Mir, Moscow, 1982).
19. Sh. Abe and Y. Toyozawa, in *Amorphous Semiconductor Technologies and Devices*, Ed. by Y. Hamakawa (Ohmsha, Tokyo, 1981; Metallurgiya, Moscow, 1986).
20. A. N. Platonov, M. N. Taran, É. V. Pol'shin, and O. E. Min'ko, Izv. Akad. Nauk SSSR, Ser. Geol., No. 10, 54 (1979).
21. G. D. Cody, in *Hydrogenated Amorphous Silicon*, Ed. by J. Pankove (Academic, New York, 1984), Part B, p. 11.
22. L. Ley, in *The Physics of Hydrogenated Amorphous Silicon*, Vol. 2: *Electronic and Vibrational Properties*, Ed. by J. D. Joannopoulos and G. Lucovsky, with contributions by D. E. Carlson *et al.* (Springer-Verlag, New York, 1984; Mir, Moscow, 1988).
23. I. A. Vaĭnshteĭn and V. S. Kortov, Fiz. Tverd. Tela (St. Petersburg) **42** (7), 1223 (2000) [Phys. Solid State **42**, 1259 (2000)].
24. A. F. Zatsepin, V. S. Kortov, V. I. Ushkova, and V. A. Kalent'ev, Poverkhnost', No. 4, 43 (1992).

Translated by N. Wadhwa

Physics of the Solid State, Vol. 43, No. 2, 2001, pp. 251–254. Translated from Fizika Tverdogo Tela, Vol. 43, No. 2, 2001, pp. 242–245.

SEMICONDUCTORS AND DIELECTRICS

Dynamics of Photorefractive Response in Sillenite Crystals with Double-Ionized Donor Centers and Shallow Traps

A. M. Plesovskikh, S. M. Shandarov, and E. Yu. Ageev

Tomsk State University of Control Systems and Radio Electronics, Tomsk, 634050 Russia

e-mail: shand@stack.ru

Received June 8, 2000

Abstract—The dynamics of the photorefractive response in the $Bi_{12}TiO_{20}$ crystal with double-ionized donor centers and shallow traps is analyzed. Consideration is given to the time dependences of the recording of a photorefractive grating in the absence of an external electric field, its storage in the dark, and its development upon the application of an external field and turning on of a reading light beam. © *2001 MAIK "Nauka/Interperiodica".*

INTRODUCTION

When recording holographic gratings in photorefractive sillenite crystals, the effects of a nonmonotonic diffraction efficiency [1–3], the development of a latent image [4], and photostimulated light absorption [5] are observed that cannot be described in terms of the single-level monopolar model of band transport [6]. In order to consider the processes of photostimulated absorption of light, an additional shallow trap is introduced into the model [7] and the nonmonotonic time dependence of the photorefractive response in nominally undoped crystals of $B_{12}SiO_{20}$ and $Bi_{12}TiO_{20}$ is usually explained by the effect of minority charge carriers (holes) on it [1–3]. However, it follows from Grachev's work [8, 9] that, in the region of impurity absorption, the contribution of holes to the photoconductivity of these materials is negligible in comparison with that of electrons.

In this paper, we show that the specific features of holographic recording effects observed in sillenite crystals can be explained based on the model [10] that includes deep donor centers (that allow double ionization) and shallow traps.

RESULTS AND DISCUSSION

The set of material equations that describes the processes of a redistribution of charges in such a crystal is as follows:

$$\frac{\partial N_D^{1+}}{\partial t} = S_D I(N_D - N_D^{1+} - N_D^{2+}) - \gamma_1 n N_D^{1+} + \gamma_2 n N_D^{2+} - S_1 I N_D^{1+}, \quad (1)$$

$$\frac{\partial N_D^{2+}}{\partial t} = S_1 I N_D^{1+} - \gamma_2 n N_D^{2+}, \quad (2)$$

$$\frac{\partial M}{\partial t} = -(S_T I + \beta)M + \gamma_T n(M_T - M), \quad (3)$$

$$\frac{\partial}{\partial t}(N_D^{1+} + 2N_D^{2+} - M - n) + \frac{1}{e}\nabla(e\mu n E + \mu k_B T \nabla n) = 0, \quad (4)$$

$$\nabla E = -\frac{e}{\varepsilon}(n - N_D^{1+} - 2N_D^{2+} + N_A + M), \quad (5)$$

where N_D, M_T, and N_A are the total concentrations of donors, shallow traps, and acceptors, respectively; N_D^{1+}, N_D^{2+}, M, and n are the concentrations of single- and double-ionized donors, filled shallow traps, and electrons, respectively; S_D, S_1, and S_T are the photoionization cross sections and γ_1, γ_2, and γ_T are the recombination constants for neutral donors (D), single-ionized (index 1) and double-ionized (index 2) donors and shallow traps (T), respectively; β is the coefficient of thermal excitation of shallow traps; μ is the electron mobility; k_B is the Boltzmann constant; T is the temperature; e is the electron charge; and ε is the static permittivity of the crystal.

We consider a photorefractive grating that was formed in the crystal upon the interaction of a reference and signal light beams with intensities I_R and I_S, respectively. For the interference pattern, we have

$$I = I_0[1 + m\cos(Kz)], \quad (6)$$

where $I_0 = I_R + I_S$ is the average intensity, $m = 2\sqrt{I_R I_S}/I_0$ is its contrast, and the grating vectors $K = Kz_0$ and the external applied field $E_0 = E_0 z_0$ are assumed to be directed along the z axis of the coordinate system. In the approximation of small contrast ($m \ll 1$), Eqs. (1)–(5) can be linearized by representing the solutions for

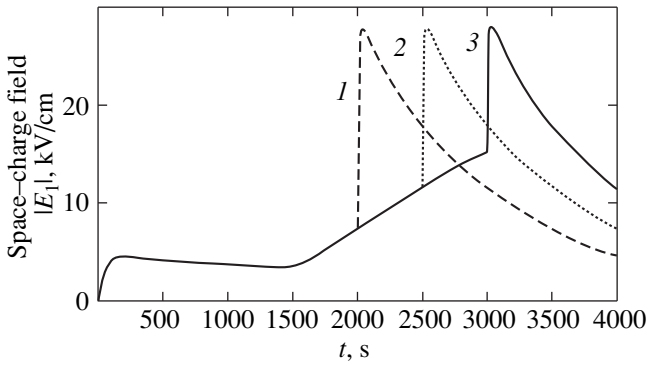

Fig. 1. Dynamics of the variation of the amplitude of the space-charge field of a photorefractive grating with a period $\Lambda = 5$ μm depending on the conditions of its formation. The reference and signal beam are switched off at time $t = 1000$ s; the dc electric field with an amplitude $E_0 = 17.5$ kV/cm is switched on at $t = 1400$ s; the reading beam is switched on at time moments $t^s = (1)$ 2000, (2) 2500, and (3) 3000 s.

the functions $N_D^{1+}(z, t)$, $N_D^{2+}(z, t)$, $M(z, t)$, $n(z, t)$, and $E(z, t)$ in the form

$$F(z, t) = F_0(t) + 0.5[F_1(t)\exp(iKz) + F_2^*(t)\exp(-iKz)]. \quad (7)$$

The use of the approximations of quasi-continuous illumination ($\partial n/\partial t = 0$) and low intensity ($I_0$), when the average concentration of electrons is small as compared to the average values for other charge gratings, yields two sets of equations for the amplitudes of the zero (N_0^{1+}, N_0^{2+}, M_0, and n_0) and first (N_1^{1+}, N_1^{2+}, M_1, and n_1) spatial harmonics. The first of them included equations that contained no amplitudes of the first harmonics and the external field; this system was integrated numerically for the case where the illumination is switched on at moment of time $t = 0$ for the initial conditions $N_0^{1+}(0) = N_A$, $N_0^{2+}(0) = 0$, and $M_0(0) = 0$. The resultant dependences of the average concentrations of charges $N_0^{1+}(t)$, $N_0^{2+}(t)$, $M_0(t)$, and $n_0(t)$ were then used for the numerical integration of the set of equations for the first spatial harmonics. The technique of the analysis of the dynamics of the photorefractive response permitted us to simulate the switching on and off of the reference and signal beams and the dc external field applied to the crystal at arbitrary time moments. The amplitude of the first harmonic of the space charge was determined in accordance with Eqs. (5) and (7) from the equation

$$E_1(t) = -i\frac{e}{\varepsilon K}[N_1^{1+}(t) + 2N_1^{2+}(t) - M_1(t) - n_1(t)]. \quad (8)$$

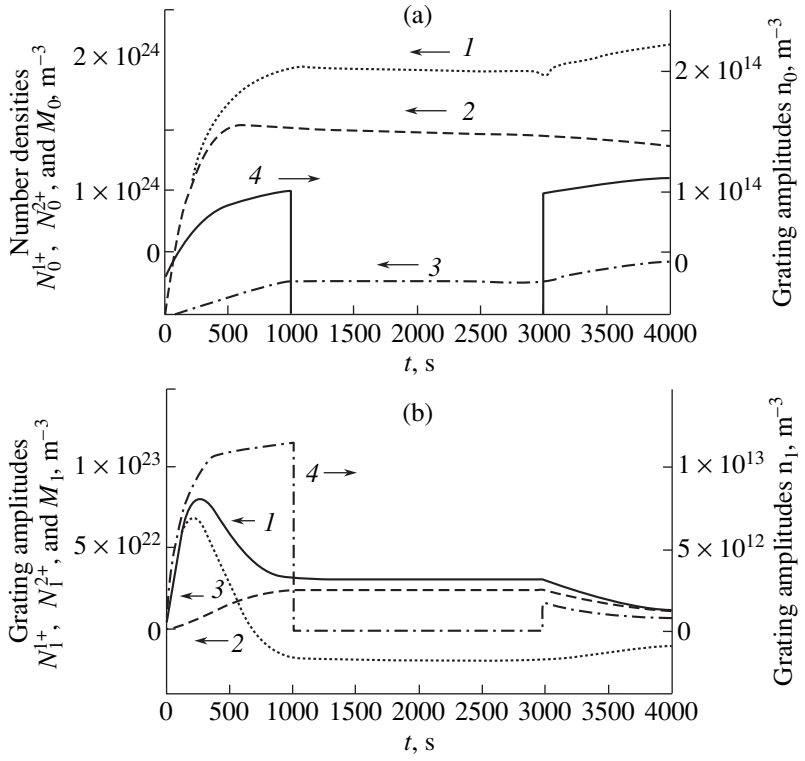

Fig. 2. Dynamics of the variation of (a) the average values and (b) amplitudes of spatial harmonics for various centers: (1) shallow traps; (2) single-ionized and (3) double-ionized traps; and (4) electrons. The conditions of the grating formation are the same as in Fig. 1.

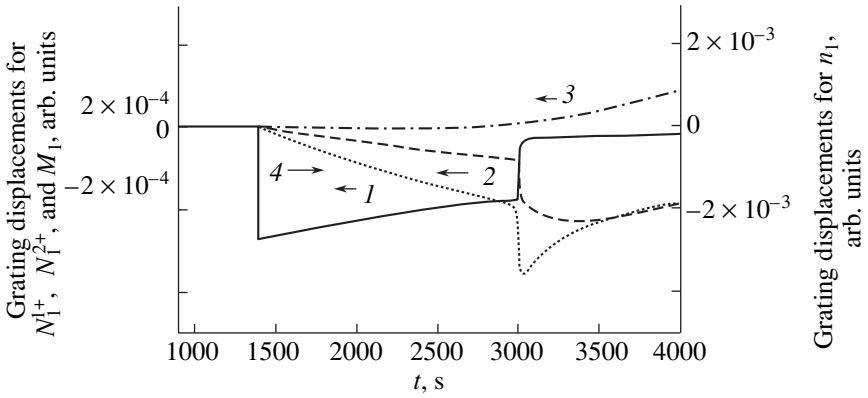

Fig. 3. Time dependences of the shift (normalized to the spatial period) of charge gratings along the coordinate z relative to their initial positions for various centers: (*1*) shallow traps; (*2*) single-ionized and (*3*) double-ionized donors; and (*4*) electrons. The conditions of the grating formation are the same as in Fig. 1.

Typical curves that characterize the dynamics of the variation of the field of the space charge of the photorefractive grating with period $\Lambda = 2\pi/K = 5$ μm depending on the conditions of recording and development of the grating are shown in Fig. 1 for the $Bi_{12}TiO_{20}$ crystal with parameters $M_T = N_D = 10^{25}$ m^{-3}, $N_A = 10^{22}$ m^{-3}, $S_D = 6.5 \times 10^{-6}$ m^2/J, $S_T = 10^{-4}$ m^2/J, $S_1 = 2.5 \times 10^{-6}$ m^2/J, $\gamma_1 = 3.5 \times 10^{-17}$ m^3/s, $\gamma_T = 2.6 \times 10^{-17}$ m^2/s, $\gamma_2 = 4.9 \times 10^{-18}$ m^3/s, $\beta = 5.5 \times 10^{-5}$ s^{-1} [10], and $\mu = 2 \times 10^{-6}$ m^2/(V s). After the illumination of the crystal at the moment of time $t_0 = 0$ with an interference pattern with a contrast $m = 0.1$ and average intensity $I_0 = 100$ W/m^2, the amplitude of the first harmonic of the space-charge field begins growing owing to the diffusion mechanism of grating formation. Note that this growth occurs against the background of the simultaneous changes in the average values of the concentrations N_0^{1+}, N_0^{2+}, and M_0 of the single-ionized and double-ionized donors and shallow traps (Fig. 2a). The average concentration of electrons in the conduction band monotonically increases (curve *4* in Fig. 2a); i.e., the process of the formation of the grating occurs under conditions of non-steady-state photoconductivity. As a result, the space-charge field grows nonmonotonically; after it reaches a maximum at $t \approx 200$ s, the field begins slowly decreasing (Fig. 1). Note that the nonsteady photoconductivity was indicated as the possible cause of the nonmonotonic character of the dynamics of the space-charge field in [9].

We assume that both light beams that form the photorefractive grating are switched off simultaneously at $t_1 = 1000$ s ($I_R = I_S = 0$, $m = 0$). Because of the sharp drop in the concentration of electrons in the conduction band, which can only be thermally excited into it from shallow traps, the processes of redistribution of charges over the existing levels at $t > t_1$ become strongly decelerated. However, if for the average concentrations (Fig. 2a) their decrease is virtually unnoticeable, the fall-off of the space-charge field E_1 in the dark can easily be seen in Fig. 1.

After a dc external field with an amplitude $E_0 = 17.5$ kV/cm is applied to the crystal at the moment of time $t_2 = 1400$ s, a monotonic growth of the amplitude of the first spatial harmonic begins even in the absence of both light beams (Fig. 1). The process continues until only the reading beam (with intensity $I_R = 100$ W/m^2) is switched on at a certain moment of time $t = t^s$. In all three cases presented in Fig. 1, the switching-on of the reading beam leads to a fast growth of the amplitude of the grating until a value $|E_1| \approx 280$ V/cm is reached, which is followed by a relatively slow decrease. Thus, the model suggested describes the effects of the enhancement of the latent image in the crystal in the dark upon the application of an external field and its development upon the switching-on of the reading beam, which were earlier observed experimentally in [4].

The physical cause of the effects of the enhancement and development is a spatial shift of charge gratings corresponding to single- and double-ionized donors and shallow traps relative to one another without changing their amplitudes. This can clearly be seen in Figs. 2b and 3, which display the dynamics of the first spatial harmonics of the concentrations $N_1^{1+}(t)$, $N_1^{2+}(t)$, $M_1(t)$, and $n_1(t)$ and of their shifts along the coordinate z relative to the initial position. In the dark, this shift begins after an external field is switched on at time $t_2 = 1400$ s and is slow because of the low conductivity of the crystal. Note that the spatial shift of the charge gratings in an external field can be treated as the excitation of trap-charge-exchange waves (TCEWs) [11]. Immediately after the switching-on of the reading beam at time $t = t^s$, the electron concentration in the conduction band increases sharply, and the velocity of the TCEWs increases as well. However, in the absence of a signal beam at $t > t^s$, there occurs a noticeable increase in the rate of the decrease in the amplitude of

the charge gratings (Fig. 2b), which leads to a slow decrease in the amplitude of the space-charge field (Fig. 1), i.e., to the erasure of the photorefractive grating by the reading beam.

ACKNOWLEDGMENTS

We are grateful to O.V. Kobozev for fruitful discussions.

REFERENCES

1. A. A. Kamshilin and M. P. Petrov, Fiz. Tverd. Tela (Leningrad) **23**, 3110 (1981) [Sov. Phys. Solid State **23**, 1811 (1981)].
2. S. G. Odoulov, K. V. Shcherbin, and A. N. Shumelyuk, J. Opt. Soc. Am. B **11**, 1780 (1994).
3. M. Miteva and L. Nicolova, Opt. Commun. **67**, 192 (1988).
4. M. P. Petrov, M. G. Shmelin, N. O. Shalaevskiĭ, *et al.*, Zh. Tekh. Fiz. **55**, 2247 (1985) [Sov. Phys. Tech. Phys. **30**, 1331 (1985)].
5. S. Shandarov, A. Reshet'ko, A. Emelyanov, *et al.*, Proc. SPIE **2969**, 202 (1996).
6. N. V. Kukhtarev, V. B. Markov, S. G. Odulov, *et al.*, Ferroelectrics **22**, 949 (1979).
7. P. Tayebati and D. Mahgerefteh, J. Opt. Soc. Am. B **8**, 1053 (1991).
8. A. I. Grachev, Fiz. Tverd. Tela (St. Petersburg) **40**, 2178 (1998) [Phys. Solid State **40**, 1975 (1998)].
9. A. I. Grachev, Fiz. Tverd. Tela (St. Petersburg) **41**, 1012 (1999) [Phys. Solid State **41**, 922 (1999)].
10. O. V. Kobozev, S. M. Shandarov, A. A. Kamshilin, and V. V. Prokofiev, J. Opt. A **1**, 442 (1999).
11. A. C. Furman, Fiz. Tverd. Tela (Leningrad) **29** (4), 1076 (1987) [Sov. Phys. Solid State **29**, 617 (1987)].

Translated by S. Gorin

Physics of the Solid State, Vol. 43, No. 2, 2001, pp. 255–256. Translated from Fizika Tverdogo Tela, Vol. 43, No. 2, 2001, pp. 246–247.

SEMICONDUCTORS AND DIELECTRICS

Radiation-Stimulated Pulse Conductivity of Alkali Halide Crystals with a NaCl Lattice

B. P. Aduev, É. D. Aluker, V. N. Shvayko, and V. M. Fomchenko

Kemerovo State University, ul. Krasnaya 6, Kemerovo, 650043 Russia

e-mail: lira@kemsu.ru

Received June 15, 2000

Abstract—The temperature dependence of the pulse conductivity σ for crystals of alkali halides with the NaCl-type lattice is measured at different densities *j* of excitation with an electron beam of picosecond duration. It is demonstrated that an increase in *j* leads to a weakening of the σ(*T*) dependence. This effect is due to the overlap of the wave functions of recombination centers and a decrease in the activation energy of separation of genetic electron–hole pairs. © *2001 MAIK "Nauka/Interperiodica".*

Earlier [1–3], we reported the data on the lifetime τ of conduction band electrons generated by an electron beam of picosecond duration in alkali halide crystals with a NaCl lattice. It was shown that, in the ranges of excitation densities and temperatures under investigation, τ was shorter than 100 ps. The simplest situation was observed for KCl: τ was limited by the bimolecular recombination of electrons with autolocalized holes (V_k centers) at excitation densities $j \le 10^3$ A/cm^2 [2].

The temperature dependence of conductivity σ(*T*), which was measured at a relatively low excitation density, allowed us to propose a model according to which the major portion of the electrons and holes undergo a thermalization in genetic (or correlated) pairs; i.e., the thermalized electrons occur in the Coulomb field of the V_k center and rapidly recombine. The conductivity observed is associated with electrons leaving their genetic partners due to temperature fluctuations (this process requires the activation energy *E*) and also with a small portion of electrons which are already capable of leaving their genetic partners at the thermalization stage [3].

This paper is devoted to the investigation into the pulse conductivity of KCl, KBr, and NaCl crystals upon excitation with an electron beam. The parameters of the excitation pulse were as follows: 0.2 MeV, 50 ps, and 10^2–10^4 A/cm^2. The time resolution of the measurement procedure was ~150 ps, and the temperature range was 12–300 K. The σ(*T*) dependence was studied for various excitation densities. The experimental results for two excitation densities are shown in the figure. It follows from the figure that an increase in *j* leads to weakening the σ(*T*) dependence (see insets in the figure).

Let us consider this result for KCl in the framework of the model similar to that proposed in [3]. Since the quasi-stationary approximation is valid for experimental conditions, the concentration of band electrons in the case of the bimolecular recombination is determined from the expression

$$n = \sqrt{\frac{G(T)}{VS}}, \quad (1)$$

where *V* is the thermal velocity of electrons, *S* is the effective cross section of the e–V_k recombination, and *G*(*T*) is the generation rate for electrons contributing to conduction. As in [3], the Coulomb interaction cross section *S* is approximated with the exponential law

$$S = CT^{-\alpha}. \quad (2)$$

The generation rate *G* is represented as

$$G(T) = G_0 - G_\Gamma, \quad (3)$$

where G_0 is the rate of generation of the electron–hole pairs by the electron beam and G_Γ is the e–V_k recombination rate of the correlated electron–hole pairs. The G_0 quantity is calculated using the expression [4]

$$G_0 = \frac{jE}{2E_q d}, \quad (4)$$

Parameters of relationship (7) for the KCl crystal

Parameter	j = 300 A/cm^2	j = 700 A/cm^2
	$G_0 = 1.71 \times 10^{27}$ cm^{-3} s^{-1}	$G_0 = 3.99 \times 10^{27}$ cm^{-3} s^{-1}
G_k, cm^{-3} s^{-1}	1.7×10^{27}	3.93×10^{27}
C, cm^2 K$^{3.5}$	2.65×10^{-4}	3.21×10^{-4}
E, eV	0.06	0.04
α	3.5	3.5

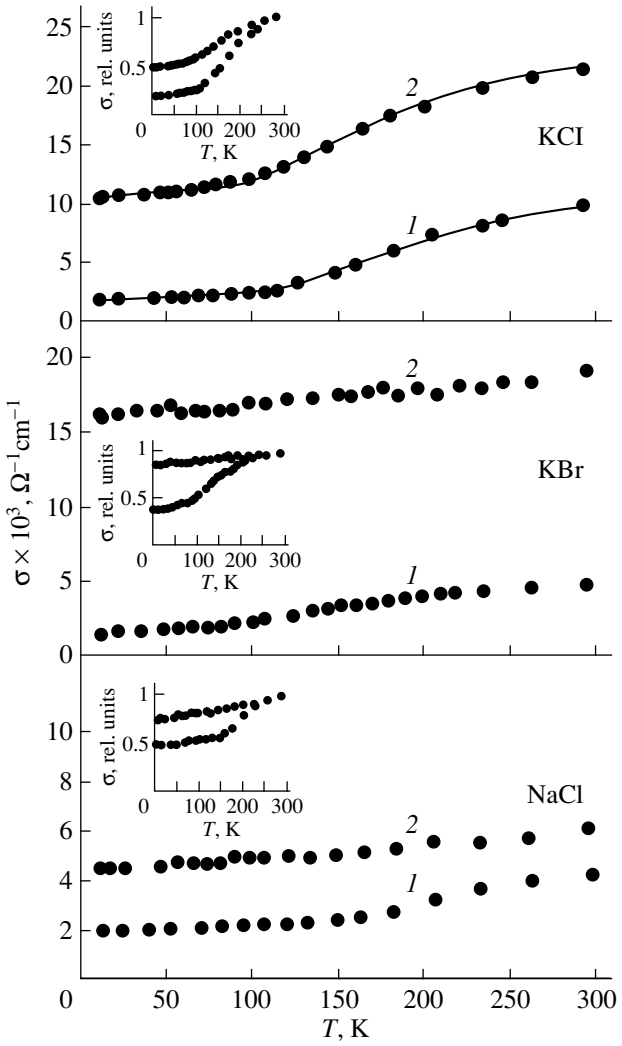

Temperature dependences of the conductivity for KCl, KBr, and NaCl crystals at different excitation densities j, A/cm^2: (*1*) 300 and (*2*) 700. The σ conductivities normalized to the largest values are shown in the insets.

where $E = 0.15$ MeV is the effective energy of the beam electrons, E_q is the band gap, and d is the crystal thickness. The expression for G_Γ can be written in the form

$$G_\Gamma = G_k(1 - e^{-E/kT}), \qquad (5)$$

where G_k is the generation rate of the correlated electron–hole pairs and the parenthetic quantity is the probability that the electron will leave its genetic partner due to thermal fluctuations. The thermal velocity of electrons is described by the following expression:

$$V = \sqrt{\frac{3kT}{m^*}}, \qquad (6)$$

where $m^* = 0.5m_0$ is the effective electron mass.

In terms of expressions (1)–(6), the formula for the experimental data processing takes the form

$$\sigma = ne\mu = e\mu\left[\frac{G_0 - G_k(1 - e^{-E/kT})}{(3kT/m^*)^{1/2}CT^{-\alpha}}\right]^{1/2}. \qquad (7)$$

The mobility $\mu(T)$ was taken from [5, 6].

The solid curves in the figure were constructed using formula (7) for the parameters given in the table. Two conclusions follow from the data presented. First, the overwhelming majority of the electrons and holes undergo a thermalization in genetic pairs ($G_k \approx G_0$). Second, an increase in j leads to a decrease in E.

The latter conclusion allows us to suppose that the recombination centers (V_k centers) at high excitation densities are not isolated centers. A similar effect was observed for medium- and highly doped semiconductors in which the ionization energy gradually decreases and tends to zero as the impurity concentration increases (see, for example, [7]). In our case, the electron undergoing thermalization in the genetic pair can be considered as being trapped in the upper excited state of the V_k center. As n increases with an increase in the excitation density j under experimental conditions, the onset of overlapping of the wave functions of the centers and the lowering of the activation barrier E bring about the weakening of the $\sigma(T)$ dependence.

ACKNOWLEDGMENTS

This study was supported by the Ministry of Education and Vocational Training of the Russian Federation.

REFERENCES

1. B. P. Aduev, G. M. Belokurov, and V. N. Shvayko, Fiz. Tverd. Tela (St. Petersburg) **37** (8), 2537 (1995) [Phys. Solid State **37**, 1392 (1995)].
2. B. P. Aduev and V. N. Shvayko, Fiz. Tverd. Tela (St. Petersburg) **41** (7), 1200 (1999) [Phys. Solid State **41**, 1093 (1999)].
3. B. P. Aduev, V. M. Fomchenko, and V. N. Shvayko, Fiz. Tverd. Tela (St. Petersburg) **41** (3), 429 (1999) [Phys. Solid State **41**, 384 (1999)].
4. É. D. Aluker, D. Yu. Lusis, and S. A. Chernov, *Electronic Excitations and Radioluminescence in Alkali Halide Crystals* (Zinatne, Riga, 1979).
5. R. K. Ahrenkiel and F. C. Brown, Phys. Rev. A **36** (1), 223 (1964).
6. C. H. Seager and D. Emin, Phys. Rev. B **2** (8), 3421 (1970).
7. R. A. Smith, *Semiconductors* (Cambridge Univ. Press, Cambridge, 1978; Mir, Moscow, 1982).

Translated by N. Korovin

Physics of the Solid State, Vol. 43, No. 2, 2001, pp. 257–262. Translated from Fizika Tverdogo Tela, Vol. 43, No. 2, 2001, pp. 248–253.

DEFECTS, DISLOCATIONS, AND PHYSICS OF STRENGTH

Mechanism of the Formation of Deformation Steps of Nanometric Sizes at the Surface of Plastically Deformed Crystals

G. A. Malygin

Ioffe Physicotechnical Institute, Russian Academy of Sciences, Politekhnicheskaya ul. 26, St. Petersburg, 194021 Russia
e-mail: malygin.ga@pop.ioffe.rssi.ru

Received June 9, 2000

Abstract—The mechanism of the formation of nanometric-size deformation steps at the surface of plastically deformed crystals is discussed theoretically. Such steps are detected by means of a scanning tunneling microscope or by high-resolution speed filming. The analysis shows that the exponential step distribution by height is due to the double cross slip (DCS) of screw dislocations and that the growth kinetics of separate steps is determined by the kinetics of the Frank–Read dislocation sources appearing as a result of the DCS. © *2001 MAIK "Nauka/Interperiodica".*

INTRODUCTION

Step formation at slip line exits at the crystalline surface is a well-known phenomenon observed in the process of plastic deformation of crystals. The steps form the characteristic linear deformation relief at the surface when a single slip system operates [1–5]. As the other slip systems (planes) start to operate and the deformation increases, the relief becomes more complex, the steps roughen, and the slip lines become wavy.

Direct optical observations of the deformation relief allow one to determine the step height and the distance between the slip lines when these parameters are greater than 0.3 μm. The use of an optical interferometer or the method of making surface replicas with their further analysis by an electron microscope allows one to increase the resolution up to 10–100 nm [2, 3, 6, 7].

Due to the studies made, it has been discovered that the slip line formation process has a hierarchic character and takes place at different scale levels from 10 nm up to 100 μm [1–7]. At the same time, the dislocation structures in deformed crystals have largely been investigated by means of microscopic methods (selective etching [8], transmission electron microscopy [5, 9]). As a result, a connection between the process of step formation at the crystalline surface and the formation and motion of dislocations was established.

A new method for investigation of the relief at the surface of plastically deformed crystals was developed recently. This is scanning tunneling microscopy (STM) [10–14]. This method has a high resolution (up to 1 nm). Its other advantage is the possibility of the time observation of the deformation relief and its separate details. However, due to an insufficient scanning rate, the kinetics of the formation of deformation steps and slip lines can be studied only at time intervals exceeding 10 s. Before the advent of STM, the dynamics (kinetics) of the formation of slip lines and of the corresponding deformation steps in the nanometric range was studied by means of high-resolution speed filming (HSF) [4, 6, 15]. This method was used over a broad time interval of 10^{-6}–10^{3} s but with lower (up to 10 nm) resolution than STM. Thus, the above-mentioned methods complement one another as to the duration range of examining nanometric objects. A high potential resolution of the STM method supposes a high quality of the specimen surface, in particular, the total absence of or minimal thickness of surface oxide films. The experiments made with gold [13, 14] have shown that the data obtained by this method for other metals do not considerably differ in a qualitative or quantitative way from those obtained for gold.

In this work, we conducted a theoretical analysis of some results obtained by STM and HSF methods. These results concern the histograms of the deformation step height distribution and the kinetics of their formation. Analysis shows that the steps observed by the techniques mentioned above do indeed have a deformation origin and are due to the characteristic dislocation processes developing in the crystal with the applied mechanical stress.

1. THE HEIGHT DISTRIBUTION OF THE DEFORMATION STEPS

Figure 1 shows, in semilogarithmic coordinates, the data obtained from histograms of the height distribution of the steps (the number of steps with a given height H per unit area) for polycrystalline copper [11] and molybdenum [12] samples. It is clear that the data

1063-7834/01/4302-0257$21.00 © 2001 MAIK "Nauka/Interperiodica"

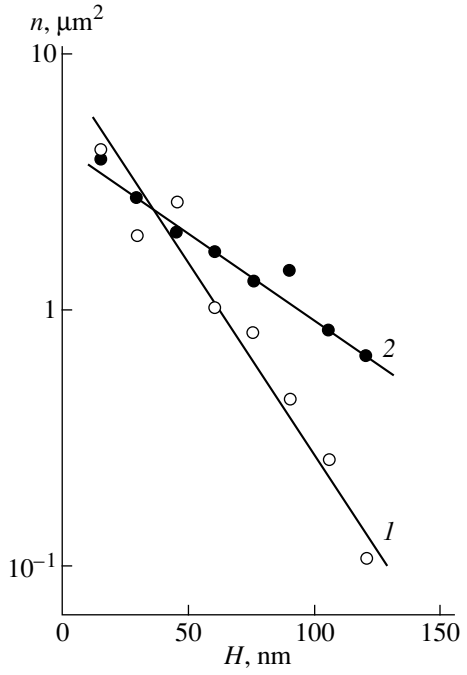

Fig. 1. The height distribution densities of the deformation steps (*1*) in Cu [11] and (*2*) in Mo [12].

exhibit an exponential Poisson distribution

$$n(H) = n_0 \exp\left(-\frac{H}{H_c}\right), \quad (1)$$

where n_0 is a constant and H_c = 28 (Cu) and 66 nm (Mo).

Deformation steps at the crystalline surface can be formed as a result of the action of the dislocation sources placed at the surface, near the surface, or in the bulk of the crystal. The latter sources can be formed, for example, as a result of the double cross slip (DCS) of screw dislocations [16]. Since the amount of dislocations generated by one source usually equals 10–200 [4], the step height should be of the order of 3–60 nm. This corresponds to the step size observed by HSF and STM methods. As an example, the table lists the characteristic (elementary, see Section 2) step sizes H_m for a number of metals and the corresponding amounts of dislocations $m_{\max} = H_m/b$, where b is the Burgers vector of a dislocation.

One of the possible assumptions concerning the exponential height distribution of deformation steps given by Eq. (1) is that this distribution is due to the exponential distribution of the dislocation sources with respect to the number of dislocations generated by them. However, there are no experimental data and theoretical calculations based on this mechanism.

The other mechanism for the Poisson step height distribution could be connected with the DCS mechanism for screw dislocations. The DCS, as has been shown experimentally, is the basic mechanism of the dislocation multiplication and of the formation of slip lines in crystals [8, 16–18]. According to this mechanism, the probability density of the transition (ejection) of the screw segment of a dislocation to the neighboring parallel slip plane, placed at a distance h, is determined by the equation [16, 17, 19, 20]

$$P(h) = h_c^{-1} \exp\left(-\frac{h}{h_c}\right), \quad (2)$$

where h_c is the characteristic ejection distance. If the ejection distance $h > h_0$, where

$$h_0 = \frac{\mu b}{8\pi(1-\nu)(\tau-\tau_f)}, \quad (3)$$

then the Frank–Read dislocation source is formed at the parallel plane, which produces a novel slip line. If the ejection distance of the screw segment of a dislocation is smaller than h_0, then a static edge dipole is formed instead of a slip line. In Eq. (3), μ is the shear modulus, τ is the mechanical stress applied to the crystal, τ_f is the friction stress for a dislocation, and ν is the Poisson ratio.

The ejection distance distribution of screw dislocation segments and the height distribution of edge dipoles according to the probability in Eq. (2) are well-proven facts [16–21]. The straight line *1* in Fig. 2 demonstrates the integral distribution, namely, the number of dipoles N for which the ejection distance exceeds h, in copper (obtained in [16] by processing the data of [9])

$$\frac{N(h)}{N_\Sigma} = \exp\left(-\frac{h}{h_c}\right), \quad (4)$$

where N_Σ is the total number of dipoles and h_c = 20 nm.

It was shown that the distance between the slip lines Λ in the nanometric range also exhibits an exponential distribution (obtained in [18] by processing the data of [6] for the Cu10Al alloy, curve *3* in Fig. 2)

$$\frac{N(\Lambda)}{N_\Sigma} = \exp\left(-\frac{\Lambda}{\Lambda_c}\right). \quad (5)$$

From the slope of the exponential portion of this curve, we find that Λ_c = 65 nm.

The straight line *2* in Fig. 2 shows the result of integration of the distribution in Eq. (1) for the deformation steps in copper (straight line *1* in Fig. 1)

$$\frac{N(H)}{N_\Sigma} = \exp\left(-\frac{H}{H_c}\right), \quad (6)$$

where $N_\Sigma = n_0 S$ and S is the area of the crystal surface studied. It is obvious that there is a statistical connection between the distributions in Eqs. (4)–(6). To determine this connection, let us consider the mechanism of

the formation of slip lines in the nanometric range of the interline distances [20].

Figure 3 illustrates the consecutive formation of four of such slip lines with a DCS of screw dislocations. These lines form a slip band *ab*. The motion of screw segments of dislocations between parallel slip planes is shown by solid arrows. The dislocation sources that appear as a result of the DCS are shown by filled circles. For simplicity, the mean ejection distance of a screw segment to the parallel slip plane h is considered to be everywhere the same. The relation between the plastic deformation (the shear γ) in the band, the step height H, the mean distance between the slip lines at the crystal surface Λ, and the distance between the active slip bands h is given by the relations

$$\tan\gamma = \frac{H}{\Lambda + H/\tan\varphi}, \quad \Lambda = \frac{h}{\sin\varphi}, \tag{7}$$

where φ is the tilt angle of the slip plane to the crystal surface. In particular, for $\varphi = 45°$ and $\gamma \ll 1$, we get $H \approx \sqrt{2}\,\gamma h$ and $\Lambda = \sqrt{2}\,h$. These relations explain the statistical connection between the ejection distance of the screw segment into a parallel slip plane h, the distance between the slip lines at the crystal surface Λ, and the size of the corresponding surface deformation steps H, that is, the stochastic character of the elementary slip in the nanometric range of these parameters and the exponential character of their distribution.

According to Eq. (3), the slip lines are not formed if the ejection distances of the screw segments of dislocation loops satisfy the inequality $h < h_0$. This fact explains the deviation of the distribution of the distances between the slip lines from the exponential law (5) for small values of Λ (curve *3* in Fig. 2). Similar deviations from the exponential law are sometimes observed for distributions of deformation steps [11]. As for the distribution of edge dipoles, a deviation from the exponential law was not observed in this case, at least for the well-studied LiF crystals [16, 21].

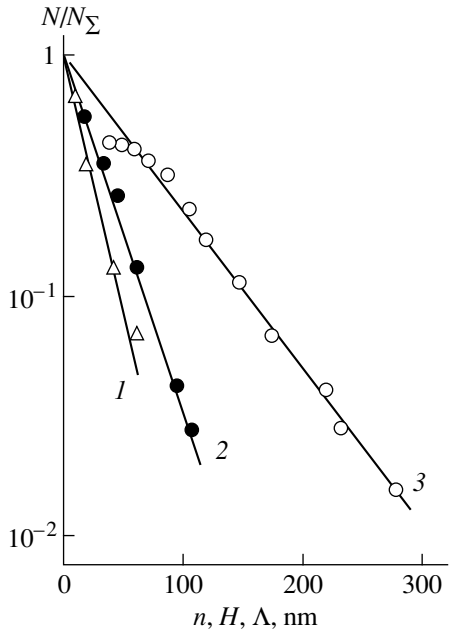

Fig. 2. Distribution (*1*) of the number of dipoles with respect to the distance exceeding h [16, 20], (*2*) of the deformation steps with the height exceeding H [11] in copper, and (*3*) of the distance between the slip lines exceeding Λ in a Cu10Al alloy [6].

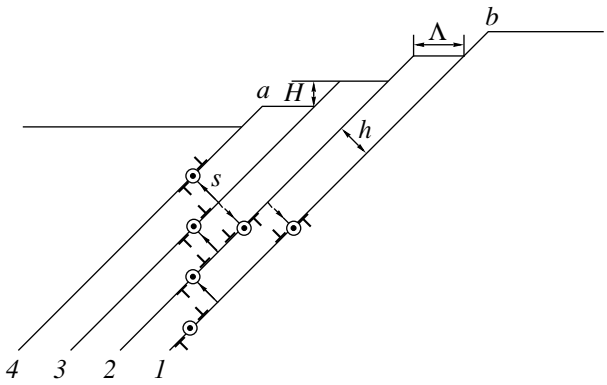

Fig. 3. Formation of the deformation steps in the slip band under the action of dislocation sources (shown with circles).

2. THE KINETICS OF FORMATION OF DEFORMATION STEPS

The use of the HSF and STM methods made it possible to study the kinetics of formation of separate deformation steps and slip lines. In Fig. 4a, the experimental points demonstrate the time dependence of the step height at the first stage of deformation of the Cu12Al alloy [4]. The step height changes from zero up to a maximal value H_m. It is also seen that the step growth rate gradually tends to zero. This means that the dislocation source that generates the corresponding slip line stops operating.

The generation rate of the dislocation loops by a source is determined by the following simple equation:

$$\frac{dm}{dt} = \frac{u}{l_F} - \frac{u}{\lambda_s}m, \tag{8}$$

where m is the number of loops, u is the dislocation velocity, l_F is the critical length of the Frank–Read source, and λ_s is the free path of the screw segments of a loop between the DCS acts. Since the step height equals $H(t) = bm(t)$ and changes each time a dislocation appears at the crystalline surface, we obtain the following time dependence of the step height by integrating Eq. (8):

$$H(t) = H_m\left(1 - \exp\left(-\frac{t}{t_m}\right)\right), \tag{9}$$

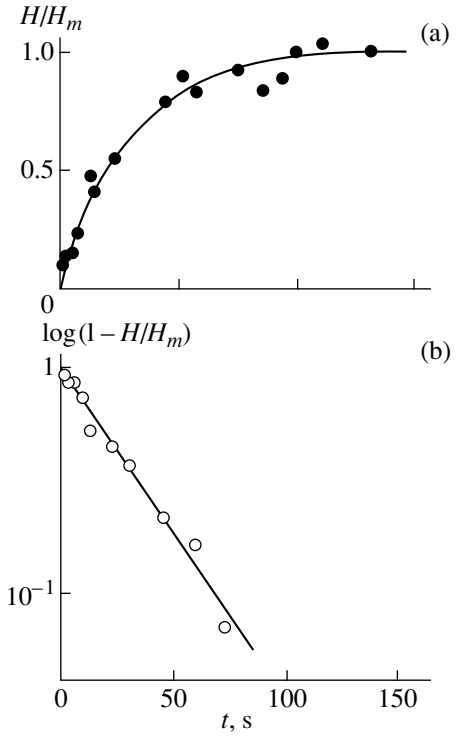

Fig. 4. Kinetics of the formation of a separate deformation step in a Cu12Al alloy [4] in (a) normal and (b) semilogarithmic coordinates.

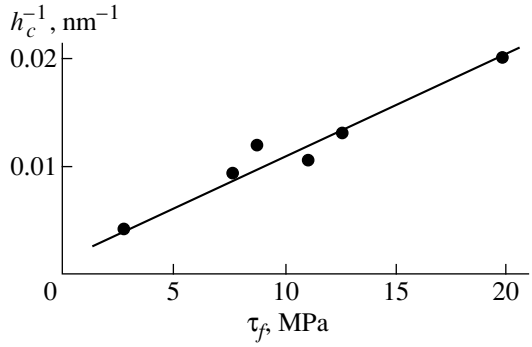

Fig. 5. Dependence of the inverse value of the characteristic DCS distance h_c upon the friction stress τ_f in LiF crystals [16].

where $H_m = bm_{\max}$, $m_{\max} = \lambda_s/l_F$ is the number of dislocations generated by a source till it stops (see table), and $t_m = \lambda_s/u$ is the characteristic operating time of the dislocation source.

Characteristic values of the deformation steps H_m and the numbers of dislocations generated by dislocation sources $m_{\max}$ in some metals [10–14]

Metal	H_m, nm	$m_{\max}$, nm
Cu	15	59
Au	22	76
Mo	18	66
Pd	5	18

Figure 4a shows the time dependence of the relative step height $H(t)/H_m$ calculated by Eq. (9). The exponential dependence $H(t)$ is plotted in Fig. 4b in semilogarithmic coordinates $\log(1 - H/H_m)$ versus t. From the slope of this straight line, we find the characteristic operating time of the dislocation source in the alloy studied: $t_m = 29.6$ s.

One also finds from Eqs. (8) and (9) that the growth rate of a step at the initial instant

$$H(0) = H_m/t_m = b\frac{u}{l_F} \qquad (10)$$

is determined by the initial rate of dislocation generation by the source $\dot{m}(0) = u/l_F$ and depends linearly on the maximal height of the step H_m. Such a proportionality, with the characteristic time $t_m = 8 \times 10^{-7}$ s, was indeed observed by the HSF method in the Cu30Zn alloy [15].

The characteristic operating time of a dislocation source $t_m = \lambda_s/u$ depends upon the distance λ_s between the obstacles that initiate the DCS acts and upon the dislocation velocity $u = \dot{\varepsilon}/b\rho$, where $\dot{\varepsilon}$ and ρ are the mean plastic strain rate and the dislocation density in the crystal, respectively. It is evident that this operating time can be varied largely depending on the crystalline structure and the deformation conditions. For example, under the conditions of loading in [12–14], this time can be as long as several minutes and even several hours. Indeed, for $\dot{\varepsilon} = 10^{-6}$–$10^{-5}$ s^{-1}, $\rho = 10^{12}$ m^{-2}, $b = 0.256$ nm (Cu), and $\lambda_s = 10^{-4}$–10^{-3} m, the operating time is 10^2–10^4 s. For the critical length of a source $l_F = 3$ μm, the number of dislocations generated by the source is $m_{\max} = \lambda_s/l_F = 30$–$300$ and the step size is $H_m = 10$–100 nm.

Let us also evaluate the mean value of the crystallographic shear related to a single deformation step (an elementary slip line). It follows from Eq. (7) that the mean shift

$$\tan\gamma \approx \frac{H_m}{\sqrt{2}h_c} = \frac{b\lambda_s}{\sqrt{2}h_c l_F} \qquad (11)$$

is determined by the parameters of the elementary dislocation processes. For $h_c = 20$ nm and the other parameters indicated above, the shift is about 0.3–1.2. Since all the parameters considered are sensitive to structural variations and depend on the concentration of obstacles to the dislocation motion in the crystal, the shift is also a structure-sensitive parameter. According to [16, 20], we have $\lambda_s \sim l_F \sim h_c \sim \tau_f^{-1}$ and, therefore, $\gamma \sim \tau_f$; that is, the shift varies in proportion to the friction stress of dislocations. Such a dependence, indeed, takes place [16]. In Fig. 5, the results of treatment of the data from [16]

on the DCS studies in LiF crystals are shown as an illustration of the relation between the cross slip parameter h_c and the friction stress τ_f. The critical slip stress is taken for the friction stress in crystals with different concentrations of calcium ions.

Another very important fact revealed by the STM and HSF methods is the time sequences of the formation of the deformation steps and the slip lines. For example, it was found in [12] that large deformation steps are formed as a result of the successive addition of elementary steps described by Eq. (9). Figure 6 demonstrates a sequence of three such elementary steps (curve *1*) plotted in accordance with Eq. (9). These steps are synchronized in time and shifted relative to each other by a time lag of $\Delta t = 10t_m$. The superposition of elementary steps means that either the dislocation sources operate at slip planes very close together according to the scheme of Fig. 3 or the source operation has a cyclic character due to the analogous character of its activation. If the scheme of Fig. 3 is valid (solid arrows and filled circles), then the time that passes between the end of the operation of one source and the beginning of the operation of the next source is determined by the development time of the DCS act. It was also observed in experiments [12] that, in many cases, the already formed or just growing big steps abruptly start to diminish their height. Figure 6 illustrates the disappearance of such a big step (curve *2*). Curves *3–6* in the lower part of this figure demonstrate the frequently observed case when separate elementary steps, after reaching the height limit, start to decrease in their heights and disappear. A new step appears in their place after some time (after $\Delta t = 7t_m$ in Fig. 6).

What is the reason for such an inverse step motion? This can be related to the following: (1) a dislocation source of the opposite sign starts to operate near the step, (2) the operating source is reversed for some reasons and starts to generate dislocations of the opposite sign, and (3) the conjugate slip systems (planes) become active. Figure 3 shows, by the dashed arrows and circles, the case when at the point marked by the letter *s* the DCS initiates the transitions of the screw segments into the initial slip planes. This leads to the creation of dislocation sources in these planes. These sources are opposite in sign to the previously operating sources and cause the steps to disappear. Crystal blocks of nanometric sizes displacing in opposite directions were observed in [14]. As a result of these displacements, the surface of a plastically deformed crystal "breathes."

Thus, due to the elementary DCS acts and the operation of dislocation sources, the plastic deformation of crystals has a stochastic character on the nanometric distance scale. It was shown in [18] how the next scale level arises from this "nanometric" chaos and how mesoscopic dislocation and deformation structures of the micrometric scale are formed.

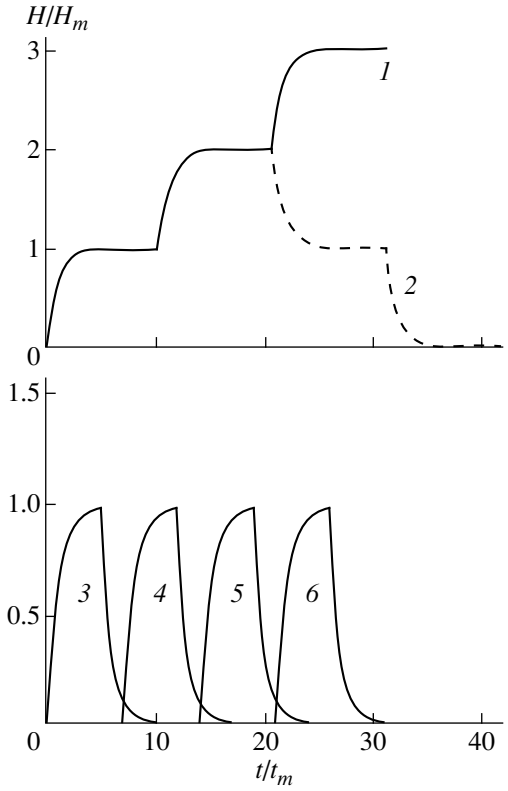

Fig. 6. Time evolution of the formation of the combined deformation steps for the successive (curve *1*) and reverse (curves *2–6*) operation of dislocation sources.

ACKNOWLEDGMENTS

The author is grateful to V.I. Vettegren' for stimulating discussions on the results of the use of the STM for investigation of the surface deformation relief in crystals.

REFERENCES

1. L. M. Clarebrough and M. E. Hargreaves, Prog. Met. Phys. **8**, 1 (1959).
2. M. V. Yakutovich, E. S. Yakovleva, R. M. Lerner, and N. N. Buĭnov, Izv. Akad. Nauk SSSR, Ser. Fiz. **15** (3), 383 (1951).
3. J. Diehl, S. Mader, and A. Seeger, Z. Metallkd. **46** (9), 650 (1955).
4. H. Neuhäuser, *Dislocation in Solids*, Ed. by F. R. N. Nabarro (North-Holland, Amsterdam, 1983), Vol. 6, p. 319.
5. Z. S. Basinski and S. J. Basinski, Philos. Mag. **9** (97), 51 (1964).
6. G. Welzel, J. Plessing, and H. Neuhäuser, Phys. Status Solidi A **166** (2), 91 (1998).
7. L. A. Teplyakova, E. S. Kunitsyna, and É. V. Kozlov, Izv. Vyssh. Uchebn. Zaved., Fiz., No. 4, 51 (1998).

8. J. J. Gilman and W. G. Johnston, Phys. Status Solidi **13** (1), 147 (1962).
9. V. Essmann, Phys. Status Solidi **12** (2), 70 (1965).
10. V. I. Vettegren', S. Sh. Rakhimov, and V. N. Svetlov, Fiz. Tverd. Tela (St. Petersburg) **37** (4), 913 (1995) [Phys. Solid State **37**, 495 (1995)].
11. V. I. Vettegren', S. Sh. Rakhimov, and V. N. Svetlov, Fiz. Tverd. Tela (St. Petersburg) **37** (12), 3635 (1995) [Phys. Solid State **37**, 2001 (1995)].
12. V. I. Vettegren', S. Sh. Rakhimov, and V. N. Svetlov, Fiz. Tverd. Tela (St. Petersburg) **38** (4), 1142 (1996) [Phys. Solid State **38**, 632 (1996)].
13. V. I. Vettegren', V. N. Svetlov, and S. Sh. Rakhimov, Fiz. Tverd. Tela (St. Petersburg) **38** (2), 590 (1996) [Phys. Solid State **38**, 323 (1996)].
14. V. I. Vettegren', S. Sh. Rakhimov, and V. N. Svetlov, Fiz. Tverd. Tela (St. Petersburg) **40** (12), 2180 (1998) [Phys. Solid State **40**, 1977 (1998)].
15. A. Hampel and H. Neuhäuser, Phys. Status Solidi A **104** (1), 171 (1987).
16. B. I. Smirnov, *Dislocation Structure and Hardening of Crystals* (Nauka, Leningrad, 1981).
17. M. Wiedersich, J. Appl. Phys. **33**, 3 (1962).
18. G. A. Malygin, Usp. Fiz. Nauk **169** (9), 979 (1999).
19. F. Appel, U. Messerschmidt, V. Schmidt, *et al.*, Mater. Sci. Eng. **56** (3), 211 (1982).
20. G. A. Malygin, Fiz. Tverd. Tela (St. Petersburg) **37** (1), 3 (1995) [Phys. Solid State **37**, 1 (1995)].
21. I. N. Zimkin, G. A. Malygin, T. V. Samoĭlova, and B. I. Smirnov, Fiz. Tverd. Tela (Leningrad) **22** (3), 852 (1980) [Sov. Phys. Solid State **22**, 496 (1980)].

Translated by A. Sonin

Physics of the Solid State, Vol. 43, No. 2, 2001, pp. 263–269. Translated from Fizika Tverdogo Tela, Vol. 43, No. 2, 2001, pp. 254–260.

DEFECTS, DISLOCATIONS, AND PHYSICS OF STRENGTH

Plastic-Strain-Softening Waves in Crystals

G. F. Sarafanov

Nizhni Novgorod State Pedagogical University, Nizhni Novgorod, 603600 Russia

Received June 20, 2000

Abstract—A system of equations describing the process of plastic deformation in a crystal is used to investigate self-sustained traveling structures theoretically. The equations for the velocity and density of dislocations are shown to describe two types of instability which are associated with anomalous damping of dislocations and structural disordering, respectively. Specific models are proposed for these two cases and investigated theoretically. Wavelike solutions, such as traveling fronts, solitons, and periodic waves, are found to exist. © *2001 MAIK "Nauka/Interperiodica".*

INTRODUCTION

One of the most important problems of physical metallurgy is explanation of the intricate lawlike regularities of the occurrence and evolution of inhomogeneous dislocation structures observed in experiments on the plastic deformation of a material. In spite of advances having been made in experimental studies of deformed solids [1, 2], many phenomena that accompany the process of plastic deformation remain unexplained theoretically. In particular, it is unclear why plastic flow is unstable and deformation of a crystal proceeds discontinuously and is frequently accompanied by localization of the plastic flow [3–5].

Physically, this phenomenon has much to do with the softening of the material. One of the typical causes of loss of strength was first established by Cottrell [6] to be the anomalous damping of dislocations (negative friction). This effect is most pronounced in alloys, where the dependence of the damping force $F(V)$ acting on dislocations on their velocity V is depicted by an N-shaped curve at elevated temperatures. It was assumed that, at the critical point corresponding to the peak of the $F'(V)$ curve, dislocations break away from the impurity-atom atmosphere locking them, which leads to the plastic flow becoming unstable on the negative-friction portion of the curve. At lower temperatures, this instability [$F(V) < 0$] can have a dynamic nature and be due, for example, to the dispersion of the elastic moduli at high dislocation velocities [7] or to thermoplastic instability [8, 9]. In addition to this mechanism of instability of plastic deformation, there can be instability associated with a "dry"-friction type loss of strength of the material (structural softening). In this case, moving dislocations destroy obstacles that impede them (e.g., precipitates [3]) and the barrier damping of dislocations is decreased.

The unstable modes of plastic deformation directly or indirectly associated with the instability mechanisms indicated above were considered in many papers [3–5, 8–11], but their consistent unified analysis has not been conducted in the literature. In this paper, we propose models based on general equations of the dynamics of dislocations [4, 7] and employ them to investigate wavelike modes of plastic deformation associated with the mechanisms of crystal softening mentioned above.

1. BASIC EQUATIONS

Mathematically, the problem of unstable modes of plastic deformation can be formulated using a set of nonlinear equations describing the time variation of the density of continuously distributed dislocations. These evolution equations follow from the law of conservation of the Burgers vector of a system of dislocations. This vector is conserved during various reactions and multiplication of dislocations [4, 7]. The Burgers vector conservation law can be written in the form of a differential consistency equation

$$\partial\alpha_{ik}/\partial t + e_{ilm}\partial j_{mk}/\partial x_l = 0,$$

which relates the tensors of the density α_{ik} and of the flux j_{ik} of dislocations [7]. These tensors are expressed in terms of the scalar dislocation density $\rho_a(\mathbf{r}, t)$ as

$$\alpha_{ik} = \sum_a l_i b_k^a \rho_a, \quad j_{ik} = e_{ijm}\sum_a l_j b_k^a \rho_a v_m^a,$$

where $\mathbf{v}_a(\mathbf{r}, t)$ is the average velocity dislocation glide and the index a enumerates the possible directions of the Burgers vector $\mathbf{b}$ of a dislocation relative to the unit vector $\mathbf{l}$ tangential to the dislocation line. The set of evolution equations for the dislocation density $\rho_a(\mathbf{r}, t)$ follows from the consistency equation and has the form

$$\frac{\partial\rho_a}{\partial t} + \mathrm{div}\rho_a\mathbf{v}_a = G_a(\rho_a), \tag{1}$$

which reduces to the continuity equation if the local interaction of dislocations is neglected ($G_a = 0$). This can be done if the plastic deformation is localized in a narrow slip band and is dynamic in character. In this case (further considered here) the equation of motion

for dislocations, from which the velocity $\mathbf{v}_a(\mathbf{r}, t)$ can be found, has the form [7]

$$m^*_{ik}\frac{dv^a_k}{dt} = e_{ijm}l_j b^a_k\{\sigma^{\text{ext}}_{mk} + \sigma^{\text{int}}_{mk}(\rho_a) - \sigma^{\text{f}}_{mk}(C_j, \alpha_j)\} - F_i(\mathbf{v}^a). \quad (2)$$

In the right-hand side of Eq. (2), the first term is the Peach–Köhler force per unit dislocation length, with σ^{ext}_{mk} being the component of the external stress tensor in the slip plane of dislocations; σ^{int}_{mk} is the component of the long-range internal stress tensor which is produced by a system of distributed dislocation charges and is a functional of ρ_a; $\sigma^{\text{f}}_{mk}(C_j, \alpha_j)$ is the "dry"-friction stress caused by various local obstacles, which are distributed in space with density C_j and have stopping-force characteristics α_j; m^*_{ik} is the effective dislocation mass tensor; and $F_i(\mathbf{v}^a)$ is the dissipative friction force.

Equations (1) and (2) are derived under the assumption that the radius of curvature R_c of the dislocation lines is much larger than the average spacing $\bar{r}$ between dislocations. In this approximation, dislocations as a whole can be treated as straight lines, and, when studying the evolution of the entire ensemble of dislocations, one can divide this ensemble into smaller ensembles, each of which is a system of parallel dislocation lines. In this paper, we will investigate the dynamics of one of these ensembles.

Let us consider an ensemble of dislocations in a slip band of a width $L > \bar{r}$. The x axis is taken to be along the slip direction of the given slip system of dislocations. Let the plastic flow involve a subsystem of positive edge dislocations ($\mathbf{b} \perp \mathbf{l}$) characterized by a density $\rho_+(\mathbf{r}, t) = \rho(\mathbf{r}, t)$, with its equilibrium value being equal to $\rho^0_+(\mathbf{r}, t) = \rho_0$. Then the plastic flow in the slip band chosen is described by the set of equations

$$m^*\left(\frac{\partial v}{\partial t} + v\frac{\partial v}{\partial x}\right) = b\{\sigma_{\text{ext}} + \sigma_{\text{int}}(\rho) - \sigma_{\text{f}}(C_j, \alpha_j)\} - F(v), \quad (3)$$

$$\frac{\partial \rho}{\partial t} + \frac{\partial}{\partial x}(\rho v) = 0, \quad (4)$$

where the stress field σ_{int} acting on dislocations in their slip plane is given by [12, 13]

$$\sigma_{\text{int}}(\mathbf{r}, t) = -\frac{\partial}{\partial x}\int_{-\infty}^{\infty}\int_{-L/2}^{L/2}\rho(\mathbf{r}')\frac{\partial \psi_{\text{eff}}(\mathbf{r}-\mathbf{r}')}{\partial y}d\mathbf{r}'. \quad (5)$$

Here, $\psi_{\text{eff}}(\mathbf{r}) = D_e r_D \sinh(y/r_D)K_0(r/r_D)$ is the effective stress (Airy function) of edge dislocations, $\mathbf{r} = (x, y)$ is the position vector ($\mathbf{r} \perp \mathbf{l}$), r_D is the screening radius of the elastic field of dislocations, $K_0(r/r_D)$ is the MacDonald function, and $D_e = Gb/2(1 - \nu)$ [13].

Dry-friction stress σ_{f} is usually considered a fitting parameter. However, in the case of structural crystal softening, the quantities C_j and α_j can be a function of dislocation density ρ; therefore, one should generally assume that $\sigma_{\text{f}} = \sigma_{\text{f}}(\rho)$.

The set of Eqs. (3) and (4) has a time-independent uniform solution:

$$\rho = \rho_0, \quad v = v_0, \quad (6)$$

where v_0 is determined from the requirement of the right-hand side of Eq. (3) being equal to zero,

$$F(v_0) = b\sigma_{\text{ext}} - b\sigma_{\text{f}}(\rho_0) = b\sigma_{\text{t}}, \quad (7)$$

while the density ρ_0 is determined from the boundary conditions. The effective stress (Airy function) $\psi_{\text{eff}}(\mathbf{r})$ in Eq. (5) reduces to the classical expression $\psi(r) = -D_e y\ln(r/r_0)$ [11] at small distances ($r \ll r_D$) and exponentially decreases in the dislocation glide direction [$K_0(r/r_D) \simeq \sqrt{\pi r_D/2r}e^{(-r/r_D)}$] at large distances $r \gg r_D$. We will assume that the time-independent density of mobile dislocations ρ_0 is a small fraction of the total dislocation density ρ_{tot} ($\rho_0 \ll \rho_{\text{tot}}$). Because $r_D^{-2} = \mu\rho_{\text{tot}}$, where μ is a dislocation parameter of order unity [12], we have $r_D \simeq \rho_{\text{tot}}^{-1/2} \ll \bar{r} = \rho_0^{-1/2}$. Therefore, the elastic field of each mobile dislocation is screened and only the effective interaction of dislocations is important; for these conditions, integral formula (5) can be simplified.

Introducing the relative coordinates $\xi = x' - x$ and $\eta = y' - y$ and expanding the function $\rho(\mathbf{r}') = \rho(\mathbf{r} + \mathbf{x})$ in a power series in $\mathbf{x} = (\xi, \eta)$, we obtain the following approximate expression in the case of $r_D \ll r$:

$$\sigma_{\text{int}}(\mathbf{r}, t) = -\frac{\partial}{\partial x}\int_{-\infty}^{\infty}d\xi\int_{-L/2-y}^{L/2-y}\rho(\mathbf{r}+\mathbf{x}) \times \frac{\partial \psi_{\text{eff}}(\mathbf{x})}{\partial \eta}d\eta \simeq -A_e\frac{\partial \rho(\mathbf{r})}{\partial x}, \quad (8)$$

where A_e is given by

$$A_e = \int_{-\infty}^{\infty}d\xi\int_{-L/2-y}^{L/2-y}\frac{\partial \psi^{\text{eff}}(\xi, \eta)}{\partial \eta}d\eta = \pi D_e r_D^2\left[1 - \cosh\frac{2y}{r_D}\exp\left(\frac{-L}{r_D}\right)\right] \simeq \pi D_e r_D^2. \quad (9)$$

Since the set of Eqs. (3), (4), and (8) involves only one spatial coordinate, we will assume that $\rho = \rho(x, t)$ and $v = v(x, t)$.

2. INSTABILITY OF PLASTIC DEFORMATION

Let us analyze the stability of the time-independent uniform solution (6) of the set of Eqs. (3) and (4) taking into account the assumptions made about $\sigma_{int}(\rho)$ and $\sigma_f(\rho)$. Linearizing the original equations and introducing dimensionless quantities

$$n(x, t) = \frac{\rho(x, t)}{\rho_0} - 1, \quad u(x, t) = \frac{v(x, t)}{v_0} - 1, \quad (10)$$

we arrive at the equations

$$\frac{\partial u}{\partial t'} + \frac{\partial u}{\partial x'} = -\beta\frac{\partial n}{\partial x'} + an - \gamma u, \quad (11)$$

$$\frac{\partial n}{dt'} + \frac{\partial n}{\partial x'} + \frac{\partial u}{\partial x'} = 0. \quad (12)$$

Here, we have also introduced the dimensionless variables $x' = x/\tau v_0$ and $t' = t/\tau$ and the parameters $\beta = bA_e\rho_0/m^*v_0^2$, $\tau = m^*v_0/b\sigma_t$, $a = -\sigma_f'(\rho_0)\rho_0/\sigma_t$, and $\gamma = F'(v_0)v_0/b\sigma_t$. For wavelike solutions n, $u \sim \exp(\lambda t' - ikx')$, we obtain the dispersion relation

$$\lambda^2 + \lambda(\gamma - 2ik) - ik(\gamma + \alpha) + k^2(\beta - 1) = 0,$$

from which it follows that the unstable-mode branch is characterized by $\lambda_+ = \mu + i\omega$ given by

$$\mu = -\frac{\gamma}{2} + \frac{1}{2\sqrt{2}} \times\left[\gamma^2 - 4k^2\beta + \sqrt{[\gamma^2 - 4k^2\beta]^2 + 16k^2a^2}\right]^{1/2}, \quad (13)$$

$$\omega = k + \frac{ak}{\gamma + 2\mu}. \quad (14)$$

Therefore, the solution becomes unstable ($\mathrm{Re}\lambda_+ = \mu > 0$) in two cases,

$$\gamma < 0 \quad (15)$$

and

$$a > \gamma\sqrt{\beta}, \quad \gamma > 0. \quad (16)$$

In the case of inequality (15), we have an instability that is associated with negative friction [$F'(v) < 0$] in the dislocation dynamics (we will refer to this instability as that of the first type), while in the case of inequality (16), an instability (of the second type) occurs because the barrier damping of the dislocations in the slip band becomes weaker as the dislocation density increases [$\sigma_f'(\rho_0) < -\gamma\sqrt{\beta}\,\sigma_f/\rho_0$]. It should be noted that there is an instability threshold in the latter case.

As follows from Eq. (13), the instabilities corresponding to inequalities (15) and (16) occur in the wave number range $0 < k^2 < \infty$. The fact that the spectrum of unstable modes contains zero-wavelength harmonics signifies that the set of Eqs. (3) and (4) has no stationary nonhomogeneous solutions in the class of continuous functions. This will not be the case if the viscosity of the dislocation "gas" is taken into account. Physically, viscosity arises because moving dislocations pass into adjacent slip planes, thereby transferring their momentum into those planes. In gases, this is known to be the reason for internal friction between layers [14].

It can easily be shown that if the right-hand side of Eq. (3) contains the term ηv_{xx} responsible for viscosity (η is the coefficient of dynamic viscosity), the spectrum of the unstable modes will be limited and, therefore, the problem will become regular. In this case, expressions (13) and (14) for the branch of unstable modes are redefined by the change in parameter γ ($\gamma \longrightarrow \gamma + \nu k^2$, where $\nu = \eta/m^*v_0^2\tau$ is the dimensionless coefficient of kinematic viscosity).

We will consider the set of nonlinear Eqs. (3) and (4) further and separately for each type of instability with regard to the specific features of plastic deformation and the assumption made above.

3. DEFORMATION WAVES IN THE CASE OF ANOMALOUS DISLOCATION DAMPING

Let us consider a model in which the first-type instability occurs [$F_v'(v) < 0$]. The possible dependence of the dry-friction stress on dislocation density will be ignored ($\sigma_f = \mathrm{const}$). In this case, with allowance made for viscosity, the original set of Eqs. (3) and (4) takes the form

$$m^*\left(\frac{\partial v}{\partial t} + v\frac{\partial v}{dx}\right) = -bA_e\frac{\partial \rho}{\partial x} + \eta\frac{\partial^2 v}{\partial x^2} + b\sigma - F(v), \quad (17)$$

$$\frac{\partial \rho}{\partial t} + \frac{\partial}{\partial x}(\rho v) = 0, \quad (18)$$

where $\sigma = \sigma_t = \mathrm{const}$ and the nonlinear function $F(v)$ is depicted by an N-shaped curve like that shown in Fig. 1a.

The straight line $b\sigma = b\sigma_t$ can be positioned differently with respect to the $F(v)$ curve. We consider the case where these two lines intersect at three points, corresponding, e.g., to velocities v_0, v_1, and v_2 ($v_0 < v_1 < v_2$). Therefore, the system described by Eqs. (17) and (18) has three equilibrium states, two of which are stable (at $v = v_0$ and $v = v_2$), while the third is unstable (at $v = v_1$).

In order to find stationary solutions of the traveling-wave type to Eqs. (17) and (18), we introduce the variable $\xi = x - ct$, which is characteristic of self-similar waves, and assume that $v = v(\xi)$ and $\rho = \rho(\xi)$. Substi-

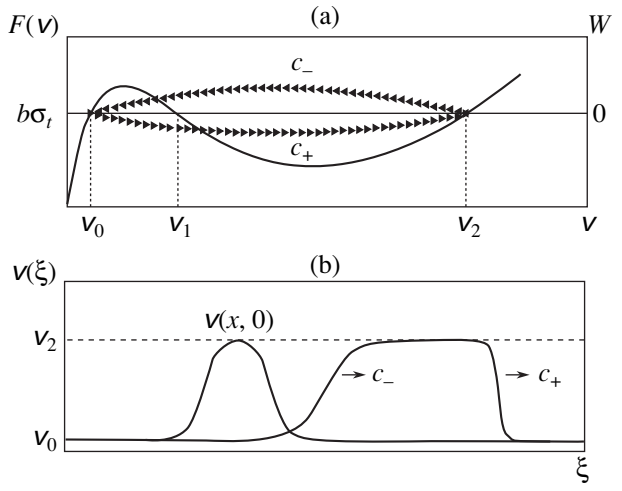

Fig. 1. (a) Phase portrait for the set of Eqs. (21) and (22) in the (v, W) phase plane and (b) the process of formation of a strengthening ($c = c_-$) and a softening wave ($c = c_+$) caused by a local perturbation $v(x, 0)$ (schematic).

tuting these functions into the original equations and integrating Eq. (18), we obtain

$$m^*(v-c)\frac{dv}{d\xi} = -bA_e\frac{d\rho}{d\xi} + \eta\frac{d^2v}{d\xi^2} + b\sigma_t - F(v), \quad (19)$$

$$\rho = \rho_0\frac{c-v_0}{c-v}, \quad (v<c). \quad (20)$$

It is convenient to introduce the variable $W = dv/d\xi$ and investigate Eqs. (19) and (20) in the (v, W) phase plane. Eliminating the variable ρ between these equations, we arrive at the set of equations

$$\eta\frac{dW}{d\xi} = -m^*\left[c - v - \frac{v_0^2\beta(c-v_0)}{(c-v)^2}\right]W - F(v), \quad (21)$$

$$\frac{dv}{d\xi} = W. \quad (22)$$

This set has three fixed singular points in the phase plane, namely, (v_0, 0), (v_1, 0), and (v_2, 0). At the (v_1, 0) point, we have a focus, while the (v_0, 0) and (v_2, 0) singular points, through each of which two trajectories pass, are saddle points. Only those stationary solutions are stable which are represented by the separatrixes going from one saddle point to the other; these solutions correspond to certain values $c_\pm$ of the wave velocity (Fig. 1a).

Equations (21) and (22) can be reduced to the boundary-value problem

$$\eta W\frac{dW}{dv} + m^*\left[c - v - \frac{v_0^2\beta(c-v_0)}{(c-v)^2}\right]W + F(v) = 0 \quad (23)$$

with boundary conditions $W(v_0) = W(v_2) = 0$.

We will treat this problem analytically under the assumption that $v \ll c$ (the validity of this assumption will be substantiated below). Approximating $F(v)$ by a cubic polynomial $F(v) = \kappa(v-v_0)(v-v_1)(v-v_2)$ and assuming that $W = \delta(v-v_0)(v-v_2)$, we find

$$c = c_\pm = V_\delta/2 + \sqrt{V_\delta^2/4 + \beta v_0^2}, \quad (24)$$

$$\delta = \delta_\pm = \frac{m^*}{4\eta}(1 \pm \sqrt{1 + 8\eta\kappa/m^{*2}}), \quad (25)$$

where $V_\delta = v_1 + (\delta\eta/m^*)(v_0 + v_2 - 2v_1)$.

The wavelike solutions differ in character depending on parameter δ. It follows from Eqs. (24) and (25) that there are two types of solitary waves; they correspond to two different values of the parameter δ ($\delta_+ > 0$, $\delta_- < 0$) and have different propagation velocities, c_+ and c_-. Integrating the equation $W = dv/d\xi = \delta(v-v_0)(v-v_2)$, we find the profile of these waves:

$$v(x,t) = v_0 + (v_2 - v_0)\left[1 + C_0\exp\left(z_\delta\frac{x-ct}{\Lambda_\delta}\right)\right]^{-1}, \quad (26)$$

where $\Lambda_\delta = |\delta(v_2 - v_0)|^{-1}$ is the characteristic width of the wave front, $z_\delta = |\delta|/\delta$, and C_0 is a constant of integration.

From Eq. (26), it follows that at positive $\delta = \delta_+$, we have a switching wave from the v_0 state to the v_2 state (softening wave), while at negative $\delta = \delta_-$, we have a switching wave from v_2 to v_0 (strengthening wave). As $\eta \longrightarrow 0$, the width of the softening wave front tends to zero, because $\Lambda_+ \simeq 2\eta/m^*(v_2 - v_0)$ in this case, whereas the width of the strengthening wave front tends to $\Lambda_- \simeq m^*/\kappa(v_2 - v_0)$. Therefore, $\Lambda_- \gg \Lambda_+$ in this limit.

Now, we analyze the possible situations occurring with the solutions given by Eq. (26). Let a perturbed dislocation density $\rho(x, 0)$ ($x \in \Omega$) be produced in a region Ω of a slip band at an initial instant of time. Internal stresses $\sigma_{int} \sim \partial\rho/\partial x$ that arise in this case give rise to a changed dislocation velocity $v(x, 0) \approx v_2$. Because of this, the right-hand boundary of the perturbation will propagate as a softening wave with a velocity of $c = c_+$, while its left-hand boundary will propagate as a strengthening wave with a velocity of $c = c_-$ (Fig. 1b).

Let us estimate the propagation velocity of the strengthening wave front. Assuming that the motion of dislocations is "nonrelativistic," i.e., that the dislocation velocity ν is much less than the sound velocity c_t, the parameter β is calculated to be

$$\beta = \frac{bA_e\rho_0}{m^*v_0} \simeq (c_t/v_0)^2(\rho_0/\rho_{tot}),$$

from which it follows that parameter β can be fairly large. Accordingly, the velocity of the solitary wave is

seen from Eq. (24) to tend to the value $c \sim c_t\sqrt{\rho_0/\rho_{tot}} \gg v$, and, therefore, it increases as $\sqrt{\rho_0}$ with increasing dislocation density in the slip band. Physically, this result is clear. Dislocations in the softening wave front generate a high internal stress field $\sigma_{int} > 0$, which causes dislocations to move rapidly and thereby ensures a high switching-wave phase velocity close to the sound velocity when dislocation density ρ_0 is fairly high. Similar arguments can be used and estimates made in the case of the strengthening wave (where $\sigma_{int} < 0$).

The velocity of the softening wave c_+ is higher than the strengthening wave velocity c_- under the condition that $v_0 + v_2 - 2v_1 > 0$. In this case, the wave fronts of these waves move father apart with relative velocity:

$$\Delta c = c_+ - c_- \simeq \frac{\sqrt{1 + 8\eta\kappa/m^{*2}}}{4} \times (v_0 + v_2 - 2v_1)(1 + 2v_1/v_0\sqrt{\beta}). \quad (27)$$

In the opposite case of $v_0 + v_2 - 2v_1 < 0$, the softening wave does not arise, because it is suppressed by the strengthening wave. Therefore, there is a critical value of flow stress $\sigma = \sigma_c$ (corresponding to the condition $\Delta c = 0$) below which ($\sigma < \sigma_c$) the perturbation of the dislocation density decays and the material is deformed macroscopically smoothly, without generation of inhomogeneous wavelike structures. At a certain critical load ($\sigma = \sigma_c$), the propagation of a soliton of a peculiar dissipative kind becomes possible; the leading and trailing edges of the pulse move with the same velocity $c_+ = c_- = v_1/2 + \sqrt{v_1^2/4 + \beta v_0^2}$. The width of a soliton of this kind depends on the conditions under which it arises.

In solving the initial-value problem, we took the boundary conditions in the form $v(\pm\infty, t) = v_0$. However, in the case of active loading of the crystal, where the plastic strain rate is kept fixed, the boundary conditions should be taken to be $v(-\infty, t) = v_2$ and $v(\infty, t) = v_0$ in the problem in question. Under these conditions, only the softening wave arises. When passing through the entire crystal, this wave produces a zone of localized plastic deformation in which dislocations move with an increased velocity equal to v_2.

4. STATIONARY STRUCTURAL SOFTENING WAVES

Now, we consider a model that exhibits the second-type instability associated with structural softening ($a > \gamma\sqrt{\beta}$). For the sake of definiteness, we assume that the dissipative damping of the dislocations is purely viscous; i.e., $F(v) = Bv$, where B is the viscous damping constant. In this case, the parameter γ involved in the condition for the instability of plastic deformation is equal to unity. We also assume that the dependence of the dry-friction stress on the dislocation density has the form $\sigma_f \sim (K + \rho)^{-1}$, where K is a constant (the Michaelis–Menten law [15]). In our problem, this law can be shown to be valid by using the following line of reasoning.

Let dislocations cut obstacles (e.g., precipitates) when moving through them, so that these obstacles exhibit less resistance to each subsequent dislocation moving in the same slip plane and their stopping-force characteristics α_j decrease. On the other hand, the deformation (cutting) of an obstacle by dislocations leads to an increase in the obstacle's surface energy; therefore, the obstacles tend to relax to their initial state with initial stopping-force characteristic α_{0j}. Taking these processes into account, one can write the kinetic equation for the variable α_j

$$\frac{\partial\alpha_j}{\partial t} = \frac{\alpha_{0j} - \alpha_j}{\tau_\alpha} - \kappa\alpha_j\rho, \quad (28)$$

which, combined with Eqs. (3) and (4), forms a complete set. Here, τ_α is the relaxation time to equilibrium value α_{0j} and $\kappa(C_{0j})$ is a constant characterizing the interaction between the dislocations and stoppers. We assume that recovery of the configuration of the obstacles occurs rather quickly ($\tau_\alpha \ll \tau$). Therefore, α_j varies adiabatically and one can put $\partial\alpha_j/\partial t = 0$ in Eq. (28); from which it follows that $\alpha_j(\rho) = \alpha_{0j}/(1 + \kappa\tau_\alpha\rho)$. Further, putting $\sigma_f \sim \alpha_j$, we finally obtain $\sigma_f(\rho) = \sigma_{0f}/(1 + \kappa\tau_\alpha\rho)$, where σ_{0f} is the friction stress in the absence of softening. It should be noted that the work-softening mechanism considered above is not the only possible one for which the density of structural defects C_j is constant.

With the assumptions formulated above, the original equations take the form

$$m^*\left(\frac{\partial v}{\partial t} + v\frac{\partial v}{\partial x}\right) = -bA_e\frac{\partial\rho}{\partial x} + \eta\frac{\partial^2 v}{\partial x^2} + b\sigma_{ext}\left(-\frac{b\sigma_{0f}}{1 + \kappa\tau_\alpha\rho}\right) - Bv, \quad (29)$$

$$\frac{\partial\rho}{\partial t} + \frac{\partial}{\partial x}(\rho v) = 0. \quad (30)$$

From Eq. (29), the steady-state velocity can easily be determined to be $v_0 = b[\sigma_{ext} - \sigma_{0f}/(1 + \kappa\tau_\alpha\rho_0)]/B$. This value can differ significantly from the velocity $V = b(\sigma_{ext} - \sigma_{0f})/B$ in the absence of the softening effect. For example, if the crystal softening is limited by friction stress, we have $\sigma_{eff} = \sigma_{ext} - \sigma_{0f} \ll \sigma_{ext}$. In this case, $V \ll v_0 \simeq b\sigma_{ext}/B(1 + p)$, where the parameter $p = (\kappa\tau_\alpha\rho_0)^{-1}$ is less than or of order unity.

We will seek inhomogeneous wavelike solutions of Eqs. (29) and (30) in the class of self-similar solutions

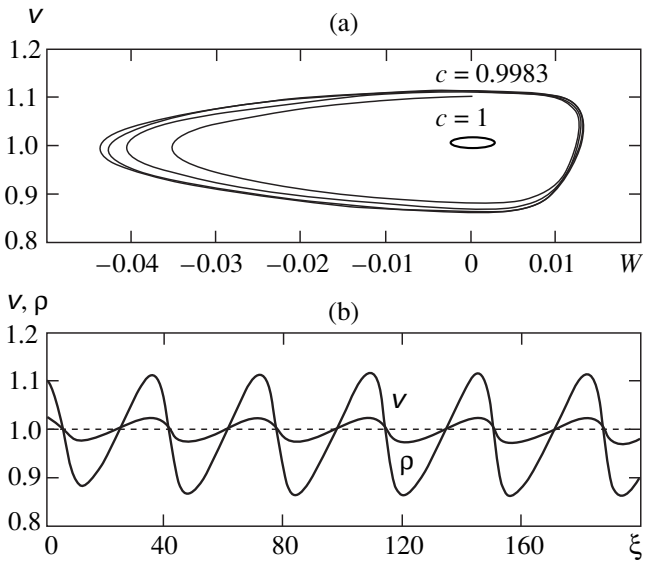

Fig. 2. Stationary periodic solutions of the set of Eqs. (29) and (30) found by solving Eqs. (31) and (32): (a) phase trajectories beyond the limit cycle in the (v, W) phase plane for small-amplitude (c = 1) and cnoidal oscillations (c = 0.9983) and (b) the shape of cnoidal waves of density $\rho(x, t)$ and velocity $v(x, t)$ of dislocations which propagate with a phase velocity of $c = 0.9983c_0$. Calculations were performed for the parameters a = 5.2, β = 25, and ν = 0.1. The variables v, ρ, W, and ξ are normalized to v_0, ρ_0, τ^{-1}, and v_0, τ, respectively, and the phase velocity c is normalized to $c_0 = v_0(1 + \sqrt{\beta})$.

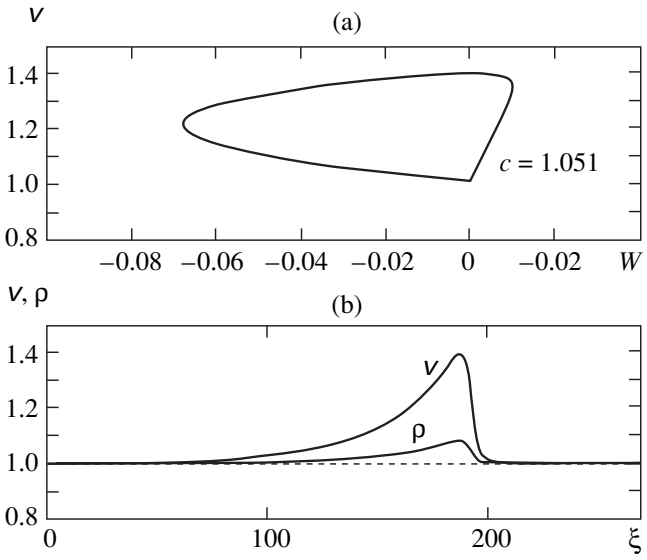

Fig. 3. Stationary solitary-wave solutions of the set of equations (29) and (30) found by solving Eqs. (31) and (32): (a) the phase trajectory that is the separatrix passing through the (0, 1) saddle point in the (W, v) phase plane and (b) the shape of solitary waves in the form of solitons for density $\rho(x, t)$ and velocity $v(x, t)$ of dislocations which propagate with a phase velocity of $c = 1.051c_0$. Calculations are performed for the same values of parameters as those in Fig. 2.

by putting $v = v(\xi)$ and $\rho = \rho(\xi)$, where $\xi = x - ct$. Substituting these into the original equations, we obtain

$$\eta\frac{\partial^2 v}{\partial\xi^2} + R(v)\frac{dv}{d\xi} = -Q(v) = -\frac{\partial U}{\partial v}, \qquad (31)$$

$$\rho = \rho_0\frac{c - v_0}{c - v}, \quad (v < c), \qquad (32)$$

where

$$R(v) = -m^*\left[v - c + \frac{\beta(c - v_0)v_0}{(c - v)^2}\right],$$

$$Q(v) = B(v - v_0)\left[\frac{a(1 + p)v_0}{p(c - v) + c - v_0} - 1\right].$$

Equation (31) describes a nonlinear oscillator with a damping force $R(v)v'_\xi$. Therefore, the problem is reduced to investigating the motion of a particle in an effective potential well $U(v)$, which has the form of an integral of $Q(v)$. The function $Q(v)$ vanishes at singular points $v = v_0$ and $v = v_0[1 + (c/v_0 - 1 - a(1 + p))/p] = v_c$, at which the potential $U(v)$ has extremal values. The maximum of U is reached at $v = \min\{v_0, v_c\}$, while the minimum is at $v = \max\{v_0, v_c\}$. The equilibrium state at $v = v_c$, which arises in the system because of the change of variables, is always absolutely unstable, in contrast to the physically reasonable state at $v = v_0$. This means that the solutions of Eq. (31) that describe finite motion can exist only in the vicinity of the minimum of the potential $U = U(v_0)$ for $c < v_0(1 + a)$. [It is easy to verify that $v_c < v_0$ if $c < v_0(1 + a)$.] Possible solutions that describe infinite motion must satisfy the condition $v(\pm\infty) = v_0$, which can be the case only if $c > v(1 + a)$, i.e., when the motion is represented in the (v, v'_ξ) phase plane by a separatrix going out and then entering the saddle point (v_0, 0).

First, we consider possible solutions of Eq. (31) that describe finite motion, which is a self-oscillation of the variable v. This oscillation will be undamped if the work of the damping force is equal to zero in the average, which will be the case if

$$c \le c_0 = v_0(1 + \sqrt{\beta}).$$

The maximum wave velocity ($c = c_0$) corresponds to small-amplitude oscillations, $|v - v_0| \ll v_0$. In this case, Eq. (31) can be approximated by

$$\eta\frac{\partial^2 v}{\partial\xi^2} - 3m^*(v - v_0)\frac{dv}{d\xi} + B(v - v_0)(a/\sqrt{\beta} - 1) = 0, \qquad (33)$$

which is easily integrated by putting $dv/d\xi = W$. The result is

$$\left(\frac{v}{v_0} - 1\right)^2 - \left(\frac{v_w}{v_0} - 1\right)^2 = \frac{2\nu}{3}$$
$$\times \left[W\tau + \frac{a - \sqrt{\beta}}{3\sqrt{\beta}} \ln\left(1 - \frac{3W\tau\sqrt{\beta}}{a - \sqrt{\beta}}\right)\right],$$

where $\nu = \eta/m^* v_0^2 \tau$ and v_w is the value of v for $W = 0$.

In the (v, W) phase plane, this equation describes a family of closed trajectories which represents small-amplitude waves in the continuous system described by Eqs. (29) and (30). Stationary waves of a relatively large amplitude propagate with a velocity c, which is only slightly less than c_0. In this case, the stationary wavelike solutions of Eqs. (29) and (30) correspond to the limit cycle of Eq. (31) in the (v, W) phase plane (Fig. 2a). The wave velocity c is uniquely determined by the wave amplitude, which, in turn, depends on the given initial conditions. The corresponding wavelike solutions for the density and average velocity of dislocations are shown in Fig. 2b.

Now, we consider solitary waves in the system described by Eqs. (31) and (32). As indicated above, Eq. (31) describes the motion of a particle of mass η in potential $U(v)$ in the presence of damping force $R(v)v'_\xi$, which depends on the velocity of propagation of the solitary wave c. The possible values of c lie in the interval $c_{\min} < c < c_{\max}$. The lower limit $c_{\min} = v_0(1 + a)$ is determined by the boundary conditions $v(\pm\infty) = v_0$, while the upper limit $c_{\max} = v_0[1 + a(1 + p)]$ follows from the condition $v_c < c$ in Eq. (32), i.e., from the condition for the positiveness of density ρ.

For a given potential $U(v)$, there is only one value of velocity c at which the energy loss due to damping in infinite motion of the particle (corresponding to the motion along the separatrix in the phase plane) is strictly equal to zero. A numerical solution of Eq. (31) reveals that, in this case, the motion along a closed trajectory in the phase plane corresponds to a solitonlike solution (Fig. 3). The soliton velocity c is close to the minimum value $c_{\min} = v_0(1 + a)$.

The invariant solutions found by using Eq. (31) are the basic elements for a solution to the Cauchy problem for the continuous system described by Eqs. (29) and (30). Numerical calculations for this system show that these solutions describe the asymptotic behavior of the solution to the Cauchy problem for a wide class of initial values. After the process is developed, the wave consists of two parts, a head and a tail. The head is a solitary wave in the form of a soliton, while the tail is a periodic wave, which gradually lags behind the head with a relative velocity equal to $\Delta c \simeq v_0(a - \sqrt{\beta})$.

ACKNOWLEDGMENTS

This work was supported by the Russian Foundation for Basic Research, grant no. 98-02-16976.

REFERENCES

1. B. I. Smirnov, *Dislocation Structure and Hardening of Crystals* (Nauka, Leningrad, 1981).
2. V. I. Trefilov, V. F. Moiseev, É. P. Pechkovskiĭ, *et al.*, *Strain Hardening and Destruction of Polycrystalline Materials* (Naukova Dumka, Kiev, 1987).
3. B. I. Smirnov and V. I. Nikolaev, Fiz. Tverd. Tela (St. Petersburg) **35** (7), 1840 (1993) [Phys. Solid State **35**, 919 (1993)].
4. G. A. Malygin, Fiz. Tverd. Tela (St. Petersburg) **37** (1), 3 (1995) [Phys. Solid State **37**, 1 (1995)].
5. Sh. Kh. Khannanov, Fiz. Met. Metalloved. **57** (4), 14 (1992).
6. A. H. Cottrell, *Dislocations and Plastic Flow in Crystals* (Clarendon Press, Oxford, 1953; Metallurgizdat, Moscow, 1958).
7. A. M. Kosevich, *Dislocation in the Theory of Elasticity* (Naukova Dumka, Kiev, 1978).
8. N. N. Davidenkov, Fiz. Tverd. Tela (Leningrad) **3** (8), 2458 (1961) [Sov. Phys. Solid State **3**, 1785 (1962)].
9. G. A. Malygin, Fiz. Met. Metalloved. **40** (1), 21 (1975).
10. I. L. Maksimov and G. F. Sarafanov, Pis'ma Zh. Éksp. Teor. Fiz. **61** (5), 405 (1995) [JETP Lett. **61**, 411 (1995)].
11. J. P. Hirth and J. Lothe, *Theory of Dislocations* (McGraw-Hill, New York, 1967; Atomizdat, Moscow, 1972).
12. G. F. Sarafanov, Fiz. Tverd. Tela (St. Petersburg) **39** (9), 1575 (1997) [Phys. Solid State **39**, 1403 (1997)].
13. G. F. Sarafanov, *Bulletin of Nizhni Novgorod State University. Mathematical Modeling and Optimal Control* (Nizhegorodsk. Univ., Nizhni Novgorod, 1999), Vol. 1 (20), p. 101.
14. E. M. Lifshitz and L. P. Pitaevskiĭ, *Physical Kinetics* (Nauka, Moscow, 1979; Pergamon, Oxford, 1981).
15. J. Murray, *Lectures on Nonlinear-Differential Equations Models in Biology* (Clarendon Press, Oxford, 1981; Mir, Moscow, 1982).

Translated by Yu. Epifanov

Physics of the Solid State, Vol. 43, No. 2, 2001, pp. 270–273. Translated from Fizika Tverdogo Tela, Vol. 43, No. 2, 2001, pp. 261–264.

DEFECTS, DISLOCATIONS, AND PHYSICS OF STRENGTH

Kinetics of Pore Formation upon Plastic Deformation of Crystals with a Cesium Chloride Structure

A. A. Vakulenko, S. A. Kukushkin, and A. V. Shapurko

Institute of Problems in Machine Science, Russian Academy of Sciences, Vasil'evskiĭ ostrov, Bol'shoĭ pr. 61, St. Petersburg, 199178 Russia

e-mail: ksa@math.ipme.ru

Received May 11, 2000; in final form, July 10, 2000

Abstract—The kinetics of pore formation upon plastic deformation of crystals with a cesium chloride structure was studied as the first stage of a first-order phase transition in a deformable media. The shape and the critical dimensions of microvoids depending on the critical shear stress were found. The number of critical microvoids per unit volume arising per unit time on the surface of a slip plane was determined based on the kinetics of formation of pairs of charged vacancies. The volume fraction of pores at the initial stage of plastic deformation in CsBr and CsI crystals was estimated. © *2001 MAIK "Nauka/Interperiodica".*

INTRODUCTION

Nonuniform plastic deformation in crystals is associated with the local appearance of microvoids, such as vacancies, divacancies, and their clusters. Experimental and theoretical investigations of the interrelation between the nonconservative slip (climb) of dislocations and the "density defect" in ionic crystals have been known for a long time [1–3]. The results of experimental investigations [2, 3] mainly concern the determination of the concentration of vacancies that arise upon nonconservative motion of dislocations in crystals with a sodium chloride structure, at normal temperature. Among the investigations of this kind, direct observations of microvoids that show the initial kinetics of fracture upon deformation of crystals are of great importance [4, 5]. However, for ionic crystals, the direct observations with the help of optical microscopy imply the use of annealing of the crystals after a certain degree of plastic deformation is attained; therefore, the coalescence of vacancies that had been generated during deformation is primarily ensured by the thermal effect on the crystal.

In this work, we theoretically estimate the contribution of slip to the process of pore formation in an ionic crystal. The investigation is based on the work [6] devoted to the formation of a new phase in the volume of a material. It was shown in [6] that, under certain conditions, microvoids begin nucleating in a solid not through the diffusion of vacancies but rather by the mechanism of vacancy generation near the surface or directly at the surface of a pore and through their direct passage from the solid to the pore. In this work, we consider the state of a metastable equilibrium that arises near a slip surface. The process of shear on the slip surface generates microvoids of a type that is more favorable energetically than spherical microvoids; namely, these are spherical segments that are bounded by a slip plane. This feature of the failure process carries no significant changes into the analysis of the phase transition providing that the newly formed porous phase does not affect the slip process. On this assumption, the subsequent analysis will be considered as the first approximation for two principal parameters of pore formation: the critical radius of a void and the number of voids that arise per unit time per unit volume after the onset of plastic deformation in the crystal. In this work, this model is applied to the estimation of pore formation in cesium halides with a cesium chloride structure at the initial stage of plastic deformation.

1. MODEL OF VOID NUCLEATION AT A SLIP SURFACE

It is well known that the driving force of any first-order phase transition is the difference of the thermodynamic potentials of the new and old phases. In the case of solutions, such a potential difference is the consequence of the difference in the concentrations and, correspondingly, in the energy states of atoms in the new and old phases. Upon growth of voids under a load, the driving force for their formation is the difference in the thermodynamic potentials of the continuous medium (old phase) and pore (new phase). This difference of potentials is a consequence of the difference in the states of a vacancy in a solid and in a pore when the solid is under a load.

In the case of a "weak metastability," the main characteristics of the process of pore formation will be determined as before [6] on the basis of the classical theory of nucleation. We only emphasize that in this case the new phase is formed on a slip surface. When a nucleus of a new phase is formed on a substrate, the minimum work, as is known [7], is proportional to the

1063-7834/01/4302-0270$21.00

wetting angle. The angle Θ between the tangent to the surface of the void and the slip surface at the point of their contact will be considered to be analogous to the wetting angle in the theory of nucleation of disperse particles on a substrate upon deposition from a solution. In addition, we assume that the newly formed nucleus of a void does not interact with the substrate (slip plane). In this case, the minimum work of the formation of a nucleus of the new phase is written as [7]

$$A_{\min} = Z(\Theta)A^0_{\min}, \quad (1)$$

where $A^0_{\min}$, in turn, is the minimum work of formation of a nucleus in the volume of a loaded material and is given by the relation [6] $A^0_{\min} = 4\pi r^3(\mu(\sigma_v) - \mu'(\sigma_v))/3Q_v + 4\pi\gamma r^2$ [6], where μ and μ' are the chemical potentials of structural elements that comprise the nucleus of the void, Ω_v is the volume of such a structural element, and σ_v is the tensor of stresses corresponding to the metastable state of a localized region.

The surface tension of the substrate required in the new model of formation of the phase represents the work of formation of a unit area of the slip surface (γ_2). The angle Θ is determined by the equality [7] $\Theta = \arccos(\gamma_2/\gamma)$, where γ is the surface tension of the free surface of the void. The quantity Z is the ratio of the volume of a spherical segment to a spherical nucleus of radius r. It is determined by the equality $Z = (1/4)(2 - 3\cos(\Theta) + \cos^3(\Theta))$ [7] and can be written as

$$Z = (1/4)(2 - 3\gamma_2/\gamma + (\gamma_2/\gamma)^3). \quad (2)$$

Let us assume for simplicity that a slip begins in a single system. Let Ω_τ be the volume of the structural element at the upper face of which a shear stress acts and S_b be the area of the slip surface. Then, the work of formation of the slip surface per unit area of this surface is written in the first approximation as $\gamma_2 = \varepsilon_{\max}\tau_{\max}\Omega_\tau/S_b$, where $\varepsilon_{\max}$ is the deformation caused by $\tau_{\max}$ in a volume Ω_τ. Since for a cubic crystal we have $\Omega_\tau = S_b h$, where h is the distance between the slip planes, the specific work of formation of the slip surface has the form

$$\gamma_2 = \varepsilon_{\max}\tau_{\max}h. \quad (3)$$

Simulation of the formation of a substrate in the form of a slip plane in a crystal defines the argument in Eq. (2) as a tensor with one nonzero component $\tau_{\max}$. The chemical potentials $\mu(\sigma_v)$ and $\mu'(\sigma_v)$ in the case where the substrate is represented by a slip plane can be linked, in the first approximation, without allowance for the hydrostatic compression, as follows:

$$\mu(\tau_{\max}) = \mu'(\tau_{\max}) + \varepsilon_{\max}\tau_{\max}\Omega_v,$$

where $\varepsilon_{\max}\tau_{\max}\Omega_v$ is the work done by shear stresses upon the formation of a structural element. The role of a structural element in this model, which considers the nonuniform slip in ionic crystals, is played, in view of the requirement of the electrical neutrality of the crystal, by a pair of charged vacancies. The volume Ω_v of the structural element is the sum of the volumes of a positive and a negative ion $\Omega_v^+ + \Omega_v^-$. The zero value of the derivative of the minimum work of formation $A^0_{\min}$ of a spherical nucleus in the bulk of the material without a substrate yields the critical radius of the nucleus

$$r_c = \frac{2\gamma}{\varepsilon_{\max}\tau_{\max}}. \quad (4)$$

The kinetics of formation of microvoids near a slip plane in terms of a steady-state flux of nuclei I is treated as in [6]. The flux I in a unit volume per unit time can be written on the basis of known formulas [6, 7] as

$$I = \frac{2D_c}{a^4}\sqrt{\frac{\gamma Z}{T}}\exp\left(-\frac{A_{\min}}{T}\right), \quad (5)$$

where D_c is the diffusion coefficient in the space of dimensions and a is the parameter of the cubic lattice. In the general case [6], D_c is determined by the critical size, the radius of the structural element, its volume, and the kinetic parameter (measure of the flux of structural elements that pass from the medium into the nucleus). It follows from Eq. (4) that, in the model with nonuniform slip, the diffusion coefficient in the space of dimensions has the form

$$D_{r_c} = \frac{\beta T\Omega_v\varepsilon^2_{\max}\tau^2_{\max}}{16\pi a_v\gamma^2}, \quad (6)$$

where β is the kinetic parameter, T is the temperature, Ω_v is the volume of a vacancy pair, and $a_v = 3\Omega_v^{1/3}/4\pi$ is the effective size of the structural element.

In expression (6), we should determine the parameter β [Å eV^{-1} s^{-1}], which is related to the rate of incorporating a vacancy pair into the nucleus of a pore per unit area per unit time β_0 [Å^{-2} s^{-1}] as follows: $\beta = \beta_0\Omega_v a_v/T$ (β_0 is defined by an activation formula given in [1, 7]). The generation of vacancies as distortions of a slip plane can be ascribed, in the first approximation, to the effect of the maximum shear stress, whose magnitude is calculated through the effective shear modulus related to the nonuniformity of the slip. Thereby, the energy of formation of a vacancy pair E_i is estimated as $\Omega_v\varepsilon_{\max}\tau_{\max}$ without allowance for the energy of elastic relaxation. If the number of like dislocations per unit area of the slip surface is N, then

$$\beta_0 = \frac{N}{q}\nu\exp(-E_i/T), \quad (7)$$

where ν is the frequency and q is the number of slip directions in the slip plane. The minimum work of formation of a nucleus for $r = r_c$, which substantially affects the magnitude of the flux I of critical nuclei in a

Some characteristics of CsBr and CsI single crystals with a structure of the cesium chloride type

	τ_{max}, GPa	r_c, Å	Z	Ω_v, Å^3	V_c, Å^3	β, Å^2/eV s	D_c, Å^2/s	IV_c
CsBr	0.86	19	0.01	50	290	10^2–10^6	10^{-1}–0.5×10^3	10^{-5}–10^{-1}
CsI	0.68	24	0.10	60	5200	10^{-1}–10^3	10^{-4}–0.5	10^{-13}–10^{-10}

unit volume per unit time, decreases by a factor of $1/Z$ in comparison with the volume model of pore formation [6] and is expressed as

$$A_{min}(r_c) = \frac{16\pi Z\gamma^3}{3\varepsilon_{max}^2\tau_{max}^2}. \quad (8)$$

With allowance for Eqs. (2), (4), (5), (6), and (8), the expression (5) for the flux takes on the form

$$I = \frac{N\nu\sqrt{TZ}\Omega_v\varepsilon_{max}^2\tau_{max}^2}{8q\pi a^4 a_v\gamma\sqrt{\gamma}} \times \exp\left(-\left(\frac{\varepsilon_{max}\tau_{max}}{T}\Omega_v + \frac{4\pi Z\gamma^3}{T\varepsilon_{max}^2\tau_{max}^2}\right)\right). \quad (9)$$

In this expression, the geometric factor is determined by dependences (2) and (3). If the specific work of slip-surface formation γ_2 is small relative to the surface tension at a given temperature, the flux of pores has a maximum at $\varepsilon_{max}\tau_{max} = 4^{1/3}Z_1$, where $Z_1 = h\gamma/a_v^2$. If the specific work of the slip-surface formation is close to the surface tension at a given temperature, then the maximum flux of pores can arise at $\varepsilon_{max}\tau_{max} = 3^{1/2}Z_1/(1 + 3Z_1^3)^{1/3}$. The proportionality between $\varepsilon_{max}\tau_{max}$ and γ, which is characteristic of the classical model of brittle fracture by cleavage [8], leads in this case to a localized pore formation in the crystal.

It follows from Eq. (9) that the maximum flux in a unit volume depends on the crystal structure, slip system, and surface tension. If we assume that temperature variations from crystal to crystal in a series of experiments on plastic deformation do not affect the slip system, then the maximum flux I increases with increasing temperature. In the general case, i.e., upon the deformation of an arbitrary crystal, the temperature dependence of the flux is nonlinear, since quantities entering into Eq. (9), such as the number of slip lines per unit area of the surface, the maximum shear stress, and the surface tension, all depend on temperature.

2. DISCUSSION

Measurements of the density defect upon plastic deformation of sodium chloride are known [2] to give values on the order of 10^{-2} to 10^{-4}, which is characteristic of plastic deformation of ionic crystals at normal temperature. This model for the crystals with a sodium chloride structure yields values of the critical size so small that the introduction of the concept of surface tension cannot be justified. As the model crystals, we chose the halides CsBr and CsI, which have low and, consequently, close to realistic, values of the maximum shear stress τ_{max} in the {110} plane in the direction ⟨001⟩. According to the Frenkel model [1], we have $\tau_{max} = Gb/(2\pi h)$ for shear in a volume Ω_τ, where G is the shear modulus, b is the Burgers vector, and $\varepsilon_{max} = 0.25$. The allowance for the nonuniformity of slip in a chosen slip system (MacKenzie hypothesis [8]) means the choice of the shear modulus being equal to the modulus of rigidity ($G = C_{44}$), whose magnitudes for the CsBr and CsI crystals are 7.6 and 6.2 GPa, respectively [9]. The distance between the slip planes and the absolute magnitude of the Burgers vector are expressed through the lattice parameter a ($h = \sqrt{2}a$ and $b = a$) for the chosen slip system, in which, according to [10], $a = 4.29$ Å for CsBr and 4.57 Å for CsI. The critical radius in Eq. (4) and, especially, flux in Eq. (9) substantially depend on the surface tension, which for ionic crystals is of order $\gamma \approx 0.01$ eV/Å^2 [11]. The volume of a charged vacancy pair Ω_v was calculated according to [10] as the sum of the volumes of a positive and a negative ion. In the {110} plane, there are two slip directions [9]; consequently, $q = 2$ and, according to [1], $N = 10^8$–10^{12} m^{-2}. The order of the magnitudes of the kinetic parameter β, dispersion D_c, and volume fraction of microvoids (IV_c) ($V_c = Z4\pi r_c^3/3$) found by formulas (7)–(9) are given in the table.

The estimates of the critical radius by formula (4) given in the table show that the critical radii for the halides with structures of the cesium chloride type are on the order of a few tens of angstroms. The magnitudes of the geometrical factor found by formulas (3) and (2) differ for crystals differing in even only the lattice parameter, which is essential for the estimation of the main characteristic of the process I in view of relationship (1). The table illustrates two results characteristic of real physical processes in ionic crystals. One is related to the different intensity of formation of critical nuclei after the onset of plastic deformation; the other consists in a slip along the plane in which the maximum shear stress is operative. The effects of this or other ionic process on the crystal state are estimated with the help of the parameter β. The same parameter is important for determining the order of dispersion D_c in Eq. (6); a significant variation of this quantity is a sign of brittle behavior of the material (scatter in the sizes of microvoids).

In this model, the specific work of the shear stress ($\tau_{max}\varepsilon_{max}h$) for the first time is related to surface tension. This relationship looks as the well-known direct proportionality between the cleavage energy and the surface tension in the crystal [8], but, in contrast to the latter, it has the sense of the maximum localization of fracture on a microscopic level in the beginning of plastic deformation of the crystal.

ACKNOWLEDGMENTS

This work was supported in part by the Russian Foundation for Basic Research, project no. 99-03-32768, and the Russian Federal Center "Integratsiya," project no. A 0151.

REFERENCES

1. H. G. van Bueren, *Imperfections in Crystals* (North-Holland, Amsterdam, 1961; Inostrannaya Literatura, Moscow, 1962).
2. B. I. Smirnov, Fiz. Tverd. Tela (Leningrad) **33** (9), 2513 (1991) [Sov. Phys. Solid State **33**, 1419 (1991)].
3. G. A. Andreev, Phys. Status Solidi A **67** (1), K127 (1981).
4. A. V. Shapurko, L. A. Gromov, S. A. Kukushkin, and V. I. Shtan'ko, Fiz. Tverd. Tela (St. Petersburg) **42** (1), 163 (2000).
5. A. V. Gektin, I. M. Krasnovitskiĭ, V. Ya. Serebryanyĭ, and N. V. Shiran, Fiz. Tverd. Tela (Leningrad) **30** (4), 1011 (1988) [Sov. Phys. Solid State **30**, 560 (1988)].
6. A. A. Vakulenko and S. A. Kukushkin, Fiz. Tverd. Tela (St. Petersburg) **42** (1), 163 (2000) [Phys. Solid State **42**, 179 (2000)].
7. S. A. Kukushkin and V. V. Slezov, *Dispersion Systems on Solid Surfaces (Evolutional Approach)* (Nauka, St. Petersburg, 1996).
8. A. Kelly, *Strong Solids* (Oxford Univ. Press, London, 1971; Mir, Moscow, 1976).
9. C. Kittel, *Introduction to Solid State Physics* (Wiley, New York, 1976; Nauka, Moscow, 1978).
10. N. W. Ashcroft and N. D. Mermin, *Solid State Physics* (Holt, Rinehart and Winston, New York, 1976; Mir, Moscow, 1979), Vol. 2.
11. J. J. Gilman, J. Appl. Phys. **31** (12), 2208 (1960).

Translated by S. Gorin

Physics of the Solid State, Vol. 43, No. 2, 2001, pp. 274–278. Translated from Fizika Tverdogo Tela, Vol. 43, No. 2, 2001, pp. 265–269.

MAGNETISM AND FERROELECTRICITY

Structure and Stationary Dynamics of the Interphase Boundary in an La_2CuO_4 Antiferromagnet

M. A. Shamsutdinov* and V. N. Nazarov**

**Bashkortostan State University, ul. Frunze 32, Ufa, 450074 Bashkortostan, Russia*
e-mail: ShamsutdinovMA@bsu.bashedu.ru

***Institute of Molecular and Crystal Physics, Russian Academy of Sciences, Ufa, 450075 Bashkortostan, Russia*

Received May 5, 2000

Abstract—The structure of an interphase boundary is studied theoretically. The external magnetic field normal to the Cu–O layers at which an interphase boundary is formed in the La_2CuO_4-type four-sublattice antiferromagnet is determined. The effect of interplanar interactions on the structure of the interphase boundary is analyzed. The dependence of the stationary dynamics of this boundary on the external magnetic field is investigated. © *2001 MAIK "Nauka/Interperiodica".*

1. INTRODUCTION

The La_2CuO_4 compound is an antiferromagnet with a weakly noncollinear structure whose unit cell contains four magnetic copper ions. If a strong magnetic field is directed normal to the Cu–O planes, spin angularity from the Cu–O planes toward the magnetic field vector is observed and transition to a weak ferromagnetic state occurs [1]. A similar transition was revealed experimentally in [2], and the phase transition field was determined. It is known that stoichiometric La_2CuO_4 exhibits no ferromagnetic moment in zero or weak magnetic fields [3]. However, a weak ferromagnetism was found in weakly oxygen-doped crystals in external magnetic fields $H < 50$ Oe [4]. In the case when the impurity oxygen is ordered over certain positions in the unit cell of La_2CuO_4, a weak ferromagnetic moment **m** normal to the Cu–O plane can appear in zero fields. This phenomenon was revealed experimentally in [5].

It is known that an intermediate state can exist upon the formation of thermodynamically stable interphase boundaries in magnetically ordered crystals in the vicinity of a first-order phase transition. If the external magnetic field changes, the phase equilibration is disturbed and the interphase boundary begins to move. The dynamics of similar boundaries was investigated within the model of two-sublattice antiferromagnets, including orthoferrites, and the vibrations and drift of the boundary were revealed in an alternating field [6]. No consideration was given to the structure and dynamic properties of the interphase boundaries in four-sublattice La_2CuO_4.

This paper is devoted to theoretical investigation of the structure and stationary dynamics of an interphase boundary which is formed in a four-sublattice antiferromagnet of the La_2CuO_4 type in an external magnetic field normal to the Cu–O layers. The specific feature of the interphase boundary under consideration is that it is formed by rotating magnetizations for only two of four magnetic sublattices. The magnetizations of the two other sublattices of the domain wall exhibit small deviations from the antiferromagnetic axes, which coincide for the antiferromagnetic and weak ferromagnetic states.

2. ENERGY DENSITY AND THE STRUCTURE OF THE INTERPHASE BOUNDARY

We will start from the following form of a free energy density written in terms of the ferromagnetic $\mathbf{m}_j$ and antiferromagnetic $\mathbf{l}_j$ ($j = 1, 2$) vectors [7, 8]:

$$W = 2M_0\Bigg\{\sum_{j=1}^{2}\Big[\frac{1}{2}H_e\mathbf{m}_j^2 + H_D[\mathbf{m}_j\mathbf{l}_j]_x + \frac{1}{2}(H_{AZ}l_{jz}^2 - H_{AY}l_{jy}^2) - \mathbf{H}\mathbf{m}_j - \frac{1}{2}\mathbf{H}_m\mathbf{m}_j + \frac{1}{4}\alpha M_0(\partial\mathbf{l}_j/\partial x_i)^2\Big] + h_e\mathbf{l}_1\mathbf{l}_2 - h_a(l_{1x}l_{2x} - l_{1y}l_{2y})\Bigg\}, \quad (1)$$

$$\mathbf{m}_{1,2} = \frac{\mathbf{M}_{1,3} + \mathbf{M}_{2,4}}{2}, \quad \mathbf{l}_{1,2} = \frac{\mathbf{M}_{1,3} - \mathbf{M}_{2,4}}{2}.$$

Here, the Cartesian z axis is normal to the Cu–O layers; M_0 is the saturation magnetization of sublattices; H_e and h_e describe the intra- and interlayer exchange interaction, respectively; α is the parameter of the nonuniform exchange interaction; H_D is the Dzyaloshinski field; H_{AZ} and H_{AY} are the fields of tetragonal and rhombic anisotropies, respectively; h_a is the field of an interplanar anisotropy; **H** is the external magnetic field (in what follows, it will be considered to be directed along

the z axis); and $\mathbf{H}_m$ is the magnetostatic field determined by the equations of magnetostatics.

The character of the ground state is determined by minimization (1), which gives two possible phases:

$$\text{(I)}\ H_e(H_{AY} + h_e + h_a) + H_D(H_D - H) > 0,$$
$$\mathbf{l}_2 \uparrow\downarrow \mathbf{l}_1 \uparrow\uparrow y,$$

$$\text{(II)}\ H_e(H_{AY} - h_e - h_a) + H_D(H_D + H) > 0,$$
$$\mathbf{l}_2 \uparrow\uparrow \mathbf{l}_1 \uparrow\uparrow y.$$

Antiferromagnetic ordering corresponds to the first phase (in the single-domain state, the antiferromagnetic vectors $\mathbf{l}_1$ and $\mathbf{l}_2$ are antiparallel). For the second phase, vectors $\mathbf{l}_1$ and $\mathbf{l}_2$ are parallel and a nonzero weak ferromagnetic moment $\mathbf{m} = \mathbf{m}_1 + \mathbf{m}_2$ exists. The stability regions of the weak ferromagnetic and antiferromagnetic phases overlap (Fig. 1a). The transition between the phases occurs through a jump (the first-order phase transition) in the field $H = H_e(h_e + h_a)/H_D$, which is determined by the equality of the energies for both phases. The magnitudes of the fields

$$H_1 = H_D + H_e(H_{AY} + h_e + h_a)/H_D,$$
$$H_2 = -H_D - H_e(H_{AY} - h_e - h_a)/H_D$$

determine the boundaries of the existence regions of the metastable phases. According to [1, 9], an antiferromagnetic phase with $m = 0$ is formed in La_2CuO_4 at $h_e + h_a > 0$ in zero or weak fields. A weak ferromagnetic phase with $m_z = 2(H_D + H)/H_e$ is formed in the field $H > 30$ kOe. The symmetry analysis carried out by E.A. Turov demonstrated that the transition from the state with $m = 0$ to the state with $m \neq 0$ in the field $\mathbf{H} \uparrow\uparrow z$ is the magnetic structural phase transition from an antiferromagnetic structure ($I^+2_x^+2_y^-\tau^-$) to another antiferromagnetic structure ($I^+2_x^+2_y^-\tau^+$) [9]. This transition is reduced to a repositioning of the signs of the sublattice magnetizations M_3 and M_4, i.e., to the change of the $\mathbf{l}_2$ direction to the opposite direction. In the field $\mathbf{H} \uparrow\downarrow z$, this effect is reduced to the change of sign for $\mathbf{I}_1$. Below, we will consider the structure and stationary dynamics of the interphase boundary in the field $\mathbf{H} \uparrow\uparrow z$. In this case, the interphase boundary can be formed only through the rotation of the $\mathbf{I}_2$ vector.

According to [8], La_2CuO_4 can contain domain walls with a rotation of $\mathbf{I}_1$ and $\mathbf{I}_2$ in the Cu–O plane (xy) and the plane normal to the Cu–O layers (yz). Earlier [10, 11], we showed that the existence of domain boundaries with rotation of the $\mathbf{I}_1$ and $\mathbf{I}_2$ vectors in the yz plane becomes possible in sufficiently strong external magnetic fields parallel to the Cu–O layers. Here, we consider the fields $\mathbf{H}$ normal to the Cu–O layers, and hence, we will restrict our consideration to the case of interphase boundaries with rotation of the sublattice magnetizations in the Cu–O layer (xy planes). It is

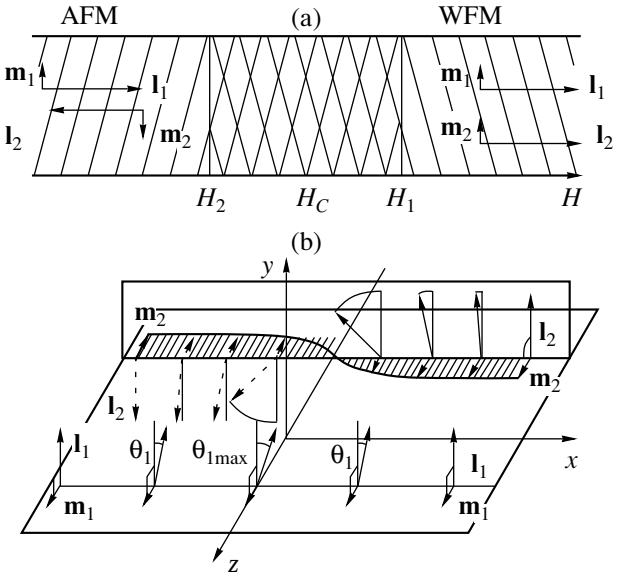

Fig. 1. (a) Magnetic phases and (b) the structure of the interphase boundary.

assumed that the plane of a one-dimensional interphase boundary is located normally to the x axis. In this structure, the magnetization vector of the sample $\mathbf{m} = \mathbf{m}_1 + \mathbf{m}_2$ has only one component parallel to the z axis. In this case, the magnetostatic field is $\mathbf{H}_m = -16\pi M_0(m_{1x} + m_{2x})\mathbf{e}_x = 0$. For a flat one-dimensional wall which executes a stationary motion, we have $\mathbf{M}_n = \mathbf{M}_n(x - Vt)$ ($n = 1, 2, 3$, and 4), where V is the velocity of the domain wall motion. For $\mathbf{m}_j$ and $\mathbf{I}_j$ with allowance made for $|\mathbf{m}_j| \ll |\mathbf{I}_j|$ and changing over to angular variables $\mathbf{I}_j = (-1)^{j+1}(\sin\theta_j, \cos\theta_j, 0)$, the Landau–Lifshitz equations of motion can be written as

$$\frac{d^2\theta_+}{d\xi^2} - \sin\theta_+\cos\theta_- - \frac{\delta_y - \delta_x}{\beta_2}\sin\theta_-$$
$$- 2\frac{h}{\beta_2}\sin\frac{\theta_-}{2}\cos\frac{\theta_-}{2} = \frac{\lambda V}{gM_0\beta_2\Delta(V)}\frac{d\theta_+}{d\xi},$$
$$\frac{d^2\theta_-}{d\xi^2} - \sin\theta_-\cos\theta_- - \frac{\delta_y + \delta_x}{\beta_2}\sin\theta_- \qquad (2)$$
$$- 2\frac{h}{\beta_2}\sin\frac{\theta_+}{2}\cos\frac{\theta_-}{2} = \frac{\lambda V}{gM_0\beta_2\Delta(V)}\frac{d\theta_-}{d\xi},$$

where $\theta_+ = \theta_1 + \theta_2$ and $\theta_- = \theta_1 - \theta_2$.

$$\xi = \frac{x - Vt}{\Delta(V)}, \quad \Delta(V) = \sqrt{\frac{\alpha}{\beta_2}\left(1 - \frac{V^2}{c^2}\right)}. \qquad (3)$$

In Eqs. (2), the parameters are $\beta_2 = 2(H_{AY} + H_D^2/H_e)/M_0$, $\delta_x = 2(h_e - h_a)/M_0$, $\delta_y = 2(h_e + h_a)/M_0$, $\chi_\perp =$

$2M_0/H_e$, $c = g\sqrt{\alpha M_0 H_e/2}$ is the minimum phase velocity of spin waves, g is the gyromagnetic ratio, λ is the dimensionless Hilbert damping parameter, and $h = \chi_\perp H_D H/M_0^2$.

Now, we determine the structure of an interphase domain wall with the boundary conditions

$$\theta_\pm(\xi \longrightarrow -\infty) = 0, \quad \theta_\pm(\xi \longrightarrow \infty) = \pm\pi, \quad \left.\frac{d\theta_\pm}{d\xi}\right|_{\xi \to \pm\infty} = 0. \tag{4}$$

In Eqs. (2), we expand θ_+ and θ_- into the series

$$\theta_+ = \theta_0 + \vartheta_1 + \vartheta_2 + \ldots, \quad \theta_- = -\theta_0 + \psi_1 + \psi_2 + \ldots, \tag{5}$$

where ϑ_i and ψ_i are small deviations from θ_0. The zero member θ_0 of the expansion into series (5) corresponds to the rotation of the $\mathbf{I}_2$ vector in the Cu–O plane when the position of the $\mathbf{I}_1$ vector is invariant. The remaining members of the expansion are due to the interplanar interactions. The first-order members, as will be shown below, correspond to the deviation of $\mathbf{I}_1$ in the domain boundary from the equilibrium direction $\mathbf{I}_1 \uparrow\uparrow y$. The second-order members correspond to the deviation of $\mathbf{I}_2$ from the distribution $\theta_0 = \theta_0(\xi)$.

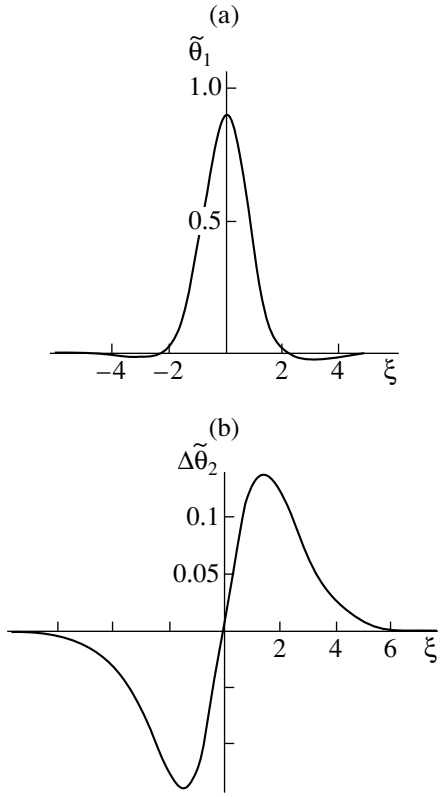

Fig. 2. Angle distribution (a) $\tilde{\theta}_1 = \theta_1(\xi)/(\delta_x/\beta_2)$ for deviation of $\mathbf{I}_1$ from the antiferromagnetic axis and (b) $\Delta\tilde{\theta}_2 = (\theta_2(\xi) - \theta_0(\xi))/(\delta_x^2/\beta_2^2)$ in the domain boundary.

Substituting expansion (5) in Eqs. (2), we derive the following equation for θ_0 in a zero approximation with respect to small parameters δ_x, δ_y, h, and λ:

$$\frac{d^2\theta_0}{d\xi^2} - \sin\theta_0\cos\theta_0 = 0.$$

The solution of this equation that satisfies the boundary conditions (4) is

$$\sin\theta_0 = 1/\cosh\xi, \quad \cos\theta_0 = -\tanh\xi. \tag{6}$$

For an immobile wall ($V = \lambda = 0$), in a first approximation with respect to small parameters δ_x, δ_y, and h, we derive the following equations:

$$\hat{L}(\vartheta_1 - \psi_1) = -\frac{2(\delta_y - h)}{\beta_2\cosh\xi}, \tag{7}$$

$$\hat{N}(\vartheta_1 + \psi_1) = -\frac{2\delta_x}{\beta_2\cosh\xi}, \tag{8}$$

where the differential operators $\hat{L}$ and $\hat{N}$ take the form

$$\hat{L} = -\frac{d^2}{d\xi^2} + 1 - \frac{2}{\cosh^2\xi}, \quad \hat{N} = \frac{d^2}{d\xi^2} - 1. \tag{9}$$

The solution of the homogeneous equation (7) takes the form $\vartheta_1 - \psi_1 = \text{const}/\cosh\xi$. From the solvability condition for Eq. (7), we determine the field at which the interphase boundary is formed; that is,

$$H_C = \frac{H_e(h_e + h_a)}{H_D}. \tag{10}$$

This field coincides with the field of the first-order phase transition between antiferromagnetic and weak ferromagnetic states. According to the estimates for La_2CuO_4, the external magnetic field of the transition antiferromagnet $\longleftrightarrow$ weak ferromagnet corresponds to the field of the phase transition $H_C \approx 30$ kOe [9]. For La_2CuO_{4+x} enriched with oxygen, the field $H_C \longrightarrow 0$.

Upon rotation of the $\mathbf{I}_2$ vector, the $\mathbf{I}_1$ vector deviates from the equilibrium state by a small angle θ_1 due to interactions between the layers. From Eq. (8), using the boundary conditions (4), we obtain

$$\theta_1 \approx \frac{\vartheta_1 + \psi_1}{2} = \frac{\delta_x}{\beta_2}(\cosh\xi\ln(2\cosh\xi) - \xi\sinh\xi). \tag{11}$$

This function is plotted in Fig. 2a. The largest deviation θ_1 is reached in the center of the interphase boundary $\max(\theta_1) \sim \delta_x/\beta_2$, and θ_1 becomes zero at $\xi \longrightarrow \pm\infty$. For La_2CuO_4 [12], we obtain the estimate $\delta_x/\beta_2 \approx 0.1$. Hence, it follows that $\max(\theta_1) \approx 0.06 \ll \theta_0 \approx \pi/2$. The rotation of the ferromagnetic and antiferromagnetic vectors in such an interphase boundary is shown in Fig. 1b. The terms of expansion (5), which correspond

to the second order of smallness, describe the distortion of the interphase domain wall structure $\theta_0 = \theta_0(\xi)$ with the rotation of the $\mathbf{I}_2$ vector. The form of this distortion is described by the expression

$$\Delta\theta_2 = \theta_2 - \theta_0 \approx \frac{1}{2}(\vartheta_2 - \psi_2) = \frac{1}{2}\left(\frac{\delta_x}{\beta_2}\right)^2$$

$$\times \int_{-\infty}^{\infty} G(\xi, \xi')\tanh\xi'(\cosh\xi'\ln 2\cosh\xi' - \xi'\sinh\xi')$$

$$\times\left(1 - \frac{1}{2}\ln 2\cosh\xi' + \frac{1}{2}\xi'\tanh\xi'\right)d\xi',$$

where $G(\xi, \xi')$ is the Green function for the equation $\hat{L}G(\xi, \xi') = \delta(\xi - \xi')$. The form of this distortion is shown in Fig. 2b. The largest distortion of the structure is reached at the interphase boundary edges in the vicinity of points $\xi \approx \pm 1.6$. In this case, $\max(\Delta\theta_2) \approx 0.13(\delta_x/\beta_2)^2 \ll \theta_0(|\xi| = 1.6) \approx 0.4$.

The additions of ΔE to the interphase boundary energy due to the interplanar interactions δ_x represent a small quantity. Actually,

$$E = E_0 + \Delta E_1 + \Delta E_2,$$

$$\Delta E_1 = -M_0^2\sqrt{\alpha\beta_2}\frac{\delta_x^2}{\beta_2^2}$$

$$\times\int_0^{\infty}(\ln(2\cosh\xi) - \xi\tanh\xi)d\xi \approx -0.4E_0\frac{\delta_x^2}{\beta_2^2}, \quad (12)$$

$$\Delta E_2 = M_0^2\sqrt{\alpha\beta_2}\int_0^{\infty}\frac{(\Delta\theta_2)^2}{\cosh^2\xi}d\xi \approx 0.004E_0\frac{\delta_x^4}{\beta_2^4},$$

where $E_0 = 2M_0^2\sqrt{\alpha\beta_2}$. It is seen that the first correction ΔE_1, which is determined by the deviation of $\mathbf{I}_1$ due to interplanar interactions, decreases the interphase boundary energy. Each sequential correction for energy decreases as $(\delta_x/\beta_2)^2$. The estimates demonstrate that $\Delta E_1 \approx -0.0035E_0$ and $\Delta E_2 \approx 3 \times 10^{-7}E_0$; i.e., $\Delta E_2 \ll |\Delta E_1| \ll E_0$. Thus, the energy additions due to the interplanar interactions are very small quantities, specifically ΔE_2, which is determined by the deviation of θ_2 from θ_0. For this reason, the $\Delta\theta_2$ distortions can be ignored when investigating the stationary dynamics of the interphase boundary.

3. STATIONARY DYNAMICS OF THE INTERPHASE BOUNDARY

Upon deviation of the external magnetic field from the value that corresponds to the interphase boundary formation, the interphase boundary moves toward increasing volume of the energetically favorable phase. At fields $H > H_C$, the energetically favorable phase is the weak ferromagnetic phase. The weak ferromagnetism vector as a function of the coordinate ξ and velocity V in the external field takes the form

$$m_z = m_{1z} + m_{2z}$$

$$= \frac{1}{H_e}\left(H_D(1 - \cos\theta_0) + 2H + \frac{V}{\Delta(V)g}\frac{d\theta_0}{d\xi}\right).$$

For an antiferromagnetic phase, $m_z = 2H/H_e$, whereas for a weak ferromagnetic phase, $m_z = 2(H_D + H)/H_e$. The magnitude of a weak ferromagnetic moment at the center of the interphase boundary strongly depends on the velocity of the interphase boundary motion (Fig. 3a). In a first approximation with respect to the small parameters of the problem (λ is taken as one more small parameter), Eq. (2) for the velocity in terms of Eq. (4) has the following form:

$$\hat{L}(\vartheta_1 - \psi_1) = 2F(\theta_0, V), \quad (13)$$

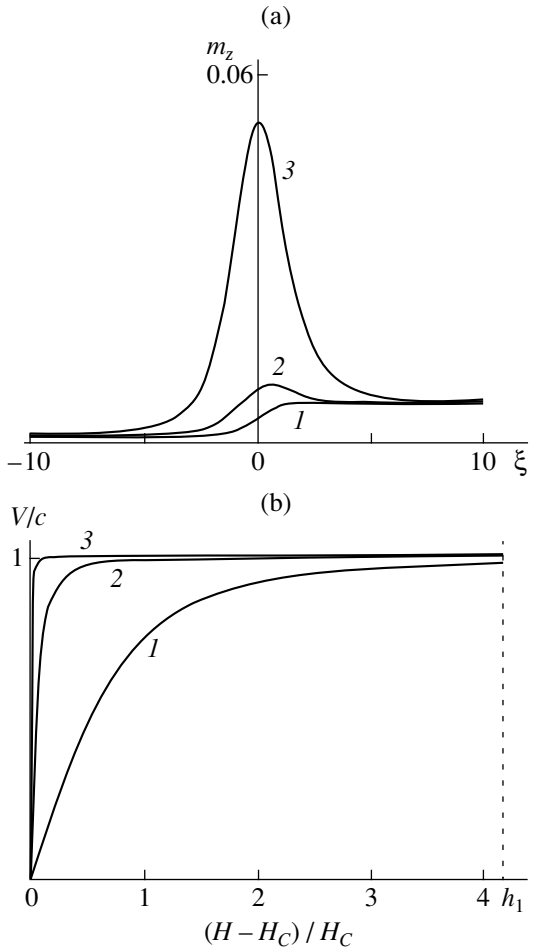

Fig. 3. External magnetic field dependences of (a) the ferromagnetic vector **m** at velocities (*1*) $V/c = 0.1$, (*2*) $V/c = 0.6$, and (*3*) $V/c = 0.99$ and (b) the velocity of the interphase boundary at (*1*) $\lambda \sim 10^{-3}$, (*2*) $\lambda \sim 10^{-4}$, and (*3*) $\lambda \sim 10^{-5}$. $h_1 = (H_1 - H_C)/H_C$ is the metastability boundary of an antiferromagnetic phase.

where

$$F(\theta_0, V) = \frac{\lambda V}{gM_0\beta_2\Delta(V)}\frac{d\theta_0}{d\xi} - \frac{\delta_y - h}{\beta_2\cosh\xi}.$$

From the solvability condition for Eq. (13), we obtain

$$V = \frac{|\rho|}{\sqrt{1 + (\rho/c)^2}},$$
$$\rho = H_D(H_C - H)\frac{g}{\lambda}\sqrt{\frac{2\alpha M_0}{H_e(H_eH_{AY} + H_D^2)}}. \quad (14)$$

It is seen from Eqs. (14) that the interphase moves in fields differing from the field of the interphase boundary formation H_C. In this case, the velocity of its motion increases as the field approaches the value H_1, which corresponds to the metastability boundary of the antiferromagnetic phase. The velocity of the interphase boundary motion strongly depends on λ. Taking into account that $H_D^2 \gg H_eH_{AY}$ [12], it can easily be shown that, at $\lambda \ll \lambda_C$, where

$$\lambda_C \approx (h_e + h_a)/H_D \sim 10^{-4},$$

the V velocity approaches the minimum phase velocity of spin waves $c \sim 10^4$ m/s already in the fields close to H_C and far from the metastability boundary field H_1. For $\lambda \gg \lambda_C$, the velocity does not necessarily reach the limiting value even at $H = H_1$. The dependence of the interphase boundary velocity on the external magnetic field for different λ is shown in Fig. 3b. The energy of the moving interphase boundary is $E(V) = E/\sqrt{1 - V^2/c^2}$.

Note that at velocities $V < c$, the deviation of the $\mathbf{l}_1$ vector from the antiferromagnetic axis is also determined from Eq. (8) and has form (11). This deviation can be considered a solitary wave (Fig. 2a) which moves with velocity V. It should be noted that we neglected the deviation of $\mathbf{l}_j$ from the xy plane when we considered the structure and velocity of the interphase domain wall motion. According to the estimates, this assumption is justified at velocities $V < c$. This constraint is met for the region of the existence of the interphase boundary. In this case, the main approximations $|\mathbf{m}_j| \ll |\mathbf{l}_j| \approx 1$ and $\Delta(V) \gg a_0$ (a_0 is the lattice constant), which were used to solve the Landau–Lifshitz equations, are also fulfilled.

4. CONCLUSION

The theoretical investigations demonstrated that the interface between the antiferromagnetic and weak ferromagnetic phases is formed in an external magnetic field which is normal to the Cu–O layers and equal to the field of the first-order phase transition. Unlike the known models of interphase boundaries in two-sublattice antiferromagnets, the interphase boundary in the four-sublattice antiferromagnet is formed by rotating only one of the two antiferromagnetic vectors in the Cu–O layer through 180°. The other antiferromagnetic vector executes a small deviation from the antiferromagnetic axis due to interplanar interactions. This deviation is nonuniform over the thickness of the interphase boundary. In magnetic fields exceeding the field of the first-order phase transition, the interphase boundary moves with a maximum velocity in the field that corresponds to the metastability boundary of the antiferromagnetic phase. Approaching of the velocity of the interphase boundary to the minimum phase velocity of spin waves, i.e., to a nonlinear motion mode, turned out to be strongly dependent on the ratio of the damping parameter to its characteristic value, which is determined by the ratio of the interplanar interaction fields to the Dzyaloshinski field.

ACKNOWLEDGMENTS

This work was supported by the Foundation for Basic Natural Sciences of the Ministry of Education of the Russian Federation, project no. 97-0-7.3-1.

REFERENCES

1. A. S. Borovik-Romanov, A. I. Buzdin, N. M. Kreĭnes, and S. S. Krotov, Pis'ma Zh. Éksp. Teor. Fiz. **47** (11), 600 (1988) [JETP Lett. **47**, 697 (1988)].
2. T. Thio, T. R. Thurston, and N. W. Preyer, Phys. Rev. B **38** (1), 905 (1988).
3. A. A. Nikonov, O. E. Parfenov, and A. A. Zakharov, Pis'ma Zh. Éksp. Teor. Fiz. **66** (3), 159 (1997) [JETP Lett. **66**, 165 (1997)].
4. A. A. Zakharov, A. A. Nikonov, and O. E. Parfenov, Pis'ma Zh. Éksp. Teor. Fiz. **64** (3), 152 (1996) [JETP Lett. **64**, 162 (1996)].
5. E. L. Vavilova and N. N. Garif'yanov, Pis'ma Zh. Éksp. Teor. Fiz. **66** (7), 470 (1997) [JETP Lett. **66**, 498 (1997)].
6. V. S. Gerasimchuk and A. L. Sukstanskiĭ, Fiz. Tverd. Tela (St. Petersburg) **41** (2), 274 (1999) [Phys. Solid State **41**, 245 (1999)].
7. V. G. Bar'yakhtar, V. M. Loktev, and D. A. Yablonskiĭ, Preprint ITF-88-81R (Kiev, 1988).
8. V. G. Bar'yakhtar, A. L. Sukstanskiĭ, and D. A. Yablonskiĭ, Fiz. Tverd. Tela (Leningrad) **32** (4), 1231 (1990) [Sov. Phys. Solid State **32**, 723 (1990)].
9. E. A. Turov, *Kinetic, Optical, and Acoustical Properties of Antiferromagnets* (Ural. Otd. Akad. Nauk SSSR, Sverdlovsk, 1990).
10. M. A. Shamsutdinov and V. N. Nazarov, Fiz. Tverd. Tela (St. Petersburg) **40** (8), 1510 (1998) [Phys. Solid State **40**, 1370 (1998)].
11. M. A. Shamsutdinov, V. N. Nazarov, and A. A. Khalfina, J. Magn. Magn. Mater. **214** (1–2), 139 (2000).
12. V. N. Krivoruchko and T. E. Primak, Fiz. Nizk. Temp. **19** (8), 871 (1993) [Low Temp. Phys. **19**, 620 (1993)].

Translated by N. Korovin

Physics of the Solid State, Vol. 43, No. 2, 2001, pp. 279–283. Translated from Fizika Tverdogo Tela, Vol. 43, No. 2, 2001, pp. 270–273.

MAGNETISM AND FERROELECTRICITY

Selective Suppression of the Higher Harmonics of Magnetization in a Superparamagnetic System

Yu. L. Raikher and V. I. Stepanov

Institute of Continuum Mechanics, Ural Division, Russian Academy of Sciences, Perm, 614013 Russia

e-mail: raikher@icmm.ru

Received May 16, 2000

Abstract—The low-frequency dynamic magnetization of a superparamagnetic particle is studied. It is shown that selective suppression of higher harmonics in the spectrum of the system can occur with a variation in both the temperature (noise-induced resonance) and the excitation intensity (force-induced resonance). © *2001 MAIK "Nauka/Interperiodica"*.

INTRODUCTION

Studies on stochastic resonance have revealed many remarkable features of nonlinear stochastic oscillators. In particular, so-called noise-induced resonance (NIR) was discovered, which can occur in both double-well [1] and single-well potentials [2]. The NIR effect is selective suppression of higher harmonics in the system response to a sinusoidal perturbation in the presence of noise of a rather high intensity. At the present time, various applications of NIR are discussed for developing signal-processing techniques in order to optimize standard circuits [3] and to devise new-type detectors [4].

A model of an overdamped nonlinear oscillator placed in a thermal reservoir is commonly used when studying the stochastic resonance and related phenomena theoretically (see, e.g., review [5]). A real and simple object suited for this purpose is a single-domain magnetic particle. Recent precise measurements showed [6, 7] that the magnetic behavior of isolated nanoparticles is adequately described by Brownian magnetodynamics (superparamagnetism). We will consider a statistical ensemble of such particles without regard for their interaction. Stochastic resonance in a superparamagnet was treated in [8–12] in the linear-response approximation. Some features of the superparamagnet response to a finite-amplitude excitation were considered in [13–15], and the magnetodynamics in a strong stationary field was investigated in [16]. However, the occurrence of NIR in such systems has not yet been discussed.

In [1, 2], the existence of NIR was shown using the small-parameter method; the spectrum of the response was expanded in a power series in a parameter ξ (the ratio of the external excitation energy to the thermal energy), and the kth harmonic was calculated dropping all terms with orders higher than ξ^k. Therefore, the theory developed in [1, 2] is true for $\xi < 1$.

In this paper, we briefly analyze the response of a system with an unharmonic potential which is under the action of a stationary (bias) field and an alternating (exciting) field, whose amplitudes are fairly large. Going beyond the perturbation theory reveals that NIR is a typical feature of the nonlinear behavior of a thermalized oscillator and is always accompanied by another effect which we refer to, by analogy, as force-induced resonance (FIR). FIR is also selective suppression of higher harmonics, but the control parameter is the excitation intensity in this case.

1. RESULTS AND DISCUSSION

Let us consider a nanoparticle of a ferromagnet whose size is so small (~10 nm) that it is a single-domain particle. Therefore, its magnetic state is entirely determined by the orientation of its magnetic dipole moment whose value equals $\mu = IV$, where I and V are the magnetization and the volume of the ferromagnetic particle, respectively; far from the Curie point, the value of μ can be assumed to be constant. If the particle is embedded in a solid matrix, the motion of the dipole moment will be due solely to its rotation in the particle and can be described by a unit vector $\mathbf{e}$ or by two spherical coordinates θ and ϕ (with the polar axis taken to be along the easy magnetization axis). When rotating, the vector $\boldsymbol{\mu} = \mu\mathbf{e}$ experiences the bulk magnetic anisotropy field (characterized by a symmetric double-well potential), the bias field $\mathbf{H}_0$ and the time-harmonic field $\mathbf{H}_1(t) = \mathbf{H}_1\cos\omega t$ (the vectors $\mathbf{H}_0$ and $\mathbf{H}_1$ are assumed to be along the anisotropy axis). The excitation frequency ω is assumed to be small in comparison with the Larmor frequency, $\omega \ll \gamma(H_0 + H_1)$, where γ is the gyromagnetic ratio.

The magnetodynamics of a single-domain particle placed in a thermal reservoir of temperature T is described by an equation of the Fokker–Planck type

[17, 18] for the orientation distribution function $W(\mathbf{e}, t)$ of the magnetic moment:

$$2\tau\dot{W} = \hat{\mathbf{J}}W\hat{\mathbf{J}}(U/T + \ln W), \quad (1)$$

where $\hat{\mathbf{J}}$ is the infinitesimal rotation operator with respect to the angles of the vector $\mathbf{e}$ and U is the orientation-dependent component of the particle energy. The characteristic time of the rotational diffusion of the vector $\mathbf{e}$ is

$$\tau = \beta I/2\lambda\gamma, \quad (2)$$

where $\beta = V/T$ and λ is the dimensionless damping constant involved in the Landau–Lifshitz equation. In the case under study, the potential depends only on the polar angle θ and has the form

$$U/T = -\sigma\cos^2\theta - (\xi_0 + \xi_1\cos\omega t)\cos\theta, \quad (3)$$

with the dimensionless parameters

$$\xi_0 = \beta I H_0, \quad \xi = \beta I H_1, \quad \sigma = \beta K, \quad (4)$$

where $K > 0$ is the magnetic anisotropy energy density.

When using the kinetic description based on Eq. (1), the physical quantities are calculated averaging the corresponding "microscopic" variables with respect to the distribution function $W(\theta, t)$. Of prime interest is the magnetization $M(t) = I\Phi\langle\cos\theta\rangle$, where Φ is the volume concentration of particles in the system. Rather than $M(t)$, we will use the dimensionless function $m(t) = M(t)/I\Phi = \langle P_1(\cos\theta)\rangle$, where $P_1(\cos\theta)$ is the Legendre polynomial.

By expressing the kinetic equation in terms of the moments $\langle P_l(\cos\theta)\rangle$ and using Eqs. (3) and (4), we arrive at a set of differential–difference equations [14, 19]

$$2\tau\frac{d}{dt}\langle P_l\rangle + l(l+1)\langle P_l\rangle - 2\sigma\left[\frac{(l-1)l(l+1)}{(2l-1)(2l+1)}\langle P_{l-2}\rangle + \frac{l(l+1)}{(2l-1)(2l+3)}\langle P_l\rangle - \frac{l(l+1)(l+2)}{(2l+1)(2l+3)}\langle P_{l+2}\rangle\right] \quad (5)$$
$$-(\xi_0 + \xi\cos\omega t)\frac{l(l+1)}{2l+1}[\langle P_{l-1}\rangle - \langle P_{l+1}\rangle] = 0.$$

We use these equations to investigate generation of the multiple harmonics of the magnetization. Representing the statistical moments in the form of a frequency Fourier series,

$$\langle P_l\rangle = \sum_{k\geq 0} b_{lk}(\omega)e^{ik\omega t}. \quad (6)$$

Equation (5) is reduced to an infinite-matrix equation, which allows one to find the set of amplitudes $b_{lk}(\omega)$ with any degree of accuracy by the matrix sweep method. The subset $\{b_{1k}(\omega)\}$ of this set, according to Eq. (6), determines the spectrum of oscillations of the magnetization, which can be written as

$$m(t) = \sum_{k\geq 0} m_k(\alpha, \xi_0, \varepsilon, \omega\tau)\exp[i(k\omega - \varphi_k)], \quad (7)$$

where m_0 is the constant component and m_k with $k \geq 1$ are the harmonic amplitudes; these quantities are all real and nonnegative by definition. For the sake of convenience, the set of material parameters in Eq. (7) is taken different from that in Eq. (4); the quantities $\alpha \equiv \xi/\xi_0$ and $\varepsilon = \sigma/\xi_0$ are temperature independent.

We will seek a solution of the set of Eqs. (5) for magnetically isotropic particles ($\varepsilon = 0$). As in the case considered in [1, 2], the influence of noise is most pronounced in the adiabatic regime, i.e., when $\omega\tau \longrightarrow 0$. In this limit, an asymptotic form of solutions to the complete set of Eqs. (5) for the nonequilibrium system can be found using the quasi-Boltzmann distribution function $W(t) \propto \exp(-U/T)$, where the energy is given by Eq. (3). A numerical solution of the complete set of Eqs. (5), checked against the asymptotic formulas for the m_{1-5} harmonic amplitudes of the magnetization, is shown in Fig. 1 in the form of tone diagrams; the shade is lighter for larger values of m_k. When the bias field H_0 is constant, the parameter α is proportional to the amplitude of the exciting field and the parameter ξ_0 has the physical meaning of the inverse temperature. The dark "arms" in Figs. 1c–1e correspond to the regions around the level lines $\alpha_k = \alpha_k(\xi_0)$ along which the corresponding amplitudes (m_3, m_4, m_5) are zero. Since the contrast of the diagrams is poor and these lines are hidden from view in the vicinity of the abscissa axis, these are intensified by light markers. As one moves in the diagram, crossing the zero-level line corresponds to suppression of the corresponding harmonic in the system response. It should be noted that for the system under study, as in the case of the oscillations considered in [1, 2], the zero-level lines for the first two harmonics are trivial and coincide with the coordinate axes in the (α, ξ_0) plane; that is, the first and second harmonics are not selectively suppressed.

In [1, 2], NIR was defined as selective suppression of higher harmonics in the system response to an exciting field of a low intensity when the noise intensity is varied. In Fig. 1, the corresponding range of the system parameters is represented by the narrow band $\alpha \ll 1$ adjacent to the ξ_0 axis. The set of Eqs. (5) is not subject to these limitations and allows one to describe the behavior of the system for any excitation levels. From Fig. 1, it follows that NIR also occurs for $\alpha > 1$, i.e., in the range where nonlinearity is significant. In this case, the slope of the zero-level lines $\alpha_k = \alpha_k(\xi_0)$ with respect to the straight lines $\alpha = \text{const}$ (along which the temperature of the system is varied) decreases with the increasing excitation amplitude.

Now, we will show that, in the adiabatic limit, saturation takes place as $\xi_0 \longrightarrow \infty$ for all zero-level lines. To do this, we note that the asymptotic values

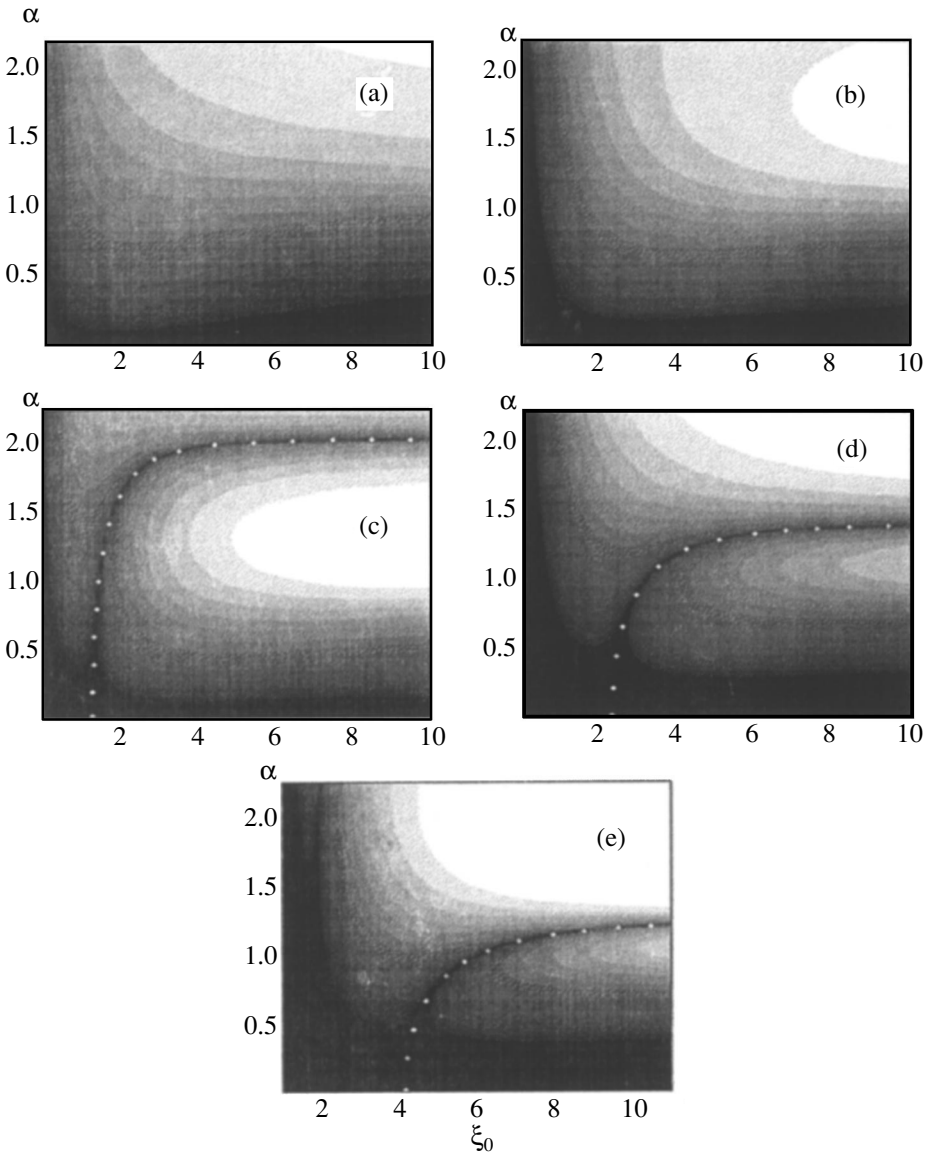

Fig. 1. Magnetization harmonic amplitudes m_k as a function of the parameters $\alpha = H_1/H_0$ and $\xi_0 \propto 1/T$ for different values of k: (a) 1, (b) 2, (c) 3, (d) 4, and (e) 5. A light tone corresponds to a larger amplitude.

$\alpha_k(\xi_0 = \infty)$ can be found from the condition that the kth coefficient of the Fourier series for the Langevin function $L[\xi_0(1 + \alpha\cos x)]$ in $\cos(nx)$ vanishes. Replacing the function L by a step function, we obtain the estimate

$$\alpha_k(\infty) = \sec(\pi/k), \quad (k \geq 3). \tag{8}$$

This quantity is maximal for the third harmonic [$\alpha_3(\infty) = 2$] and decreases to unity as $k \longrightarrow \infty$.

According to Eq. (8), as the excitation level approaches $\alpha_k(\infty)$ from below, "temperature stabilization" of NIR for the kth harmonic occurs; namely, the ξ_0 range in which the magnetization m_k is close to zero increases indefinitely. From Fig. 1, it also follows that, in accordance with Eq. (8), NIR does not occur in the range $\alpha > \alpha_k(\infty)$.

The configuration of the "valleys" (the lines of the minima of the amplitudes m_k in Fig. 1 suggests another mode of higher harmonics suppression different from NIR. If we take the exciting field amplitude α, rather than the temperature (ξ_0), as the control parameter, we should consider the lines parallel to the α axis in Fig. 1 in this case. It is seen that a straight line $\xi_0 = C = \text{const}$ (independent of α) is certain to intersect the zero-level line if the constant C lies in the (ξ_{0k}, ∞) interval.[1] Therefore, the spectrum is controlled by varying the

[1] The value ξ_{0k} corresponds to the point at which the zero-level line of the kth harmonic ceases to coincide with the ξ_0 axis. In the adiabatic limit, ξ_{0k} can be found from the $(k + 1)$th cumulant of the equilibrium ($\xi = 0$) distribution function of the system as a root of the equation $Q_{k+1}(\xi_{0k}) = 0$ [2].

intensity of the regular action (force) rather than the temperature (noise); that is, we have a force-induced resonance.

Each zero-level line in Fig. 1 can be roughly divided into three portions: a rapid increase, a crossover, and saturation described by the asymptotic expression (8). Comparing the points at which the straight lines parallel to the coordinate axes of Fig. 1 intersect these portions, we arrive at the conclusion that NIR is sharp and FIR is broad in the rapid-increase region, both resonances have comparable widths in the crossover region, and FIR is sharp and the NIR has an infinitely increasing width in the saturation region.

2. CONCLUSION

Thus, we have shown that, in forced low-frequency oscillations of the dipole moment of a superparamagnetic particle, the third and higher harmonics can be selectively suppressed. This effect can be revealed in two alternative ways: by varying the noise level (noise-induced resonance [1, 2]) or by varying the excitation intensity (force-induced resonance). The results obtained are directly applicable to specific physical systems such as magnetically isotropic nanoparticles dispersed in a solid matrix and colloidal suspensions of single-domain particles (magnetic fluids). In the latter case, magnetic anisotropy can be arbitrary, because it is effectively "switched off" in the low-frequency range in the case where particles have mechanical rotational degrees of freedom [18]. It is clear that, if the magnetic quantities are replaced by their respective electric counterparts, the results obtained in this paper will also be true for the nonlinear polarization in polar liquids and colloids. Theoretically, the results suggest that the combined noise-induced and force-induced resonances are a universal property of any stochastic nonlinear oscillator.

It is significant that the influence of the polydispersity of real magnetic nanosystems on a possible experimental observation of NIR and FIR is essentially different. Indeed, in the case of NIR, the amplitude of a harmonic becomes minimal as the parameter ξ_0 is varied. According to Eq. (4), this parameter is proportional to the particle volume. Therefore, in a polydisperse system, there is a continuous set of critical values of ξ_0 rather than a single value and NIR either will be very broadened in comparison with that in a monodisperse system or will not occur at all. In the case of FIR, the variable parameter is the ratio $\xi/\xi_0 = H_1/H_0$, which is independent of the particle size, as is seen from Eq. (4). Since the zero-level lines are virtually parallel to the abscissa axis in Fig. 1 in the range $\xi_0 > 2$, the conditions for FIR virtually do not depend on the parameter ξ_0 which is sensitive to polydispersity. Therefore, in a polydisperse superparamagnetic system, the force-induced resonance for any kth harmonic in the magnetization, corresponding to a minimum of the $m_k(\alpha)$ function, will not be noticeably broadened in comparison with that in the monodisperse system considered above.

The characteristic-parameter ranges in which the resonances described above should occur are easily accessible. Indeed, according to Fig. 1, the NIR and FIR effects are pronounced for $\xi_0 > 1$, $\alpha \sim 1$, and frequencies $\omega\tau \ll 1$. Let us make an estimate for a system of particles of gamma iron oxide of a typical size of $a \sim 10$ nm; the magnetization of the material is $I \approx 400$ G. From Eq. (4), it follows that, at room temperature, ξ_0 is of the order of unity in a bias field $H_0 \sim T/\pi I a^3 \sim 200$ Oe. The amplitude H_1 of the exciting alternating field should be of the same order of magnitude, because $\alpha = \xi/\xi_0 = H_1/H_0$. As for the upper limit of the frequency band for the nanoparticles in question, with $\lambda \sim 0.1$ and the gyromagnetic ratio $\gamma \sim 2 \times 10^7$ Oe s^{-1} (electrons), we obtain $\omega \approx 12\lambda\gamma T/\pi I a^3 \sim 10^5$ s^{-1}.

It should be noted that, before [1, 2], the effect which can be called force-induced resonance with respect to the orientational order parameter $\langle P_2 \rangle$ was discovered in [20, 21] when theoretically investigating induced birefringence in dipole colloids.

ACKNOWLEDGMENTS

The authors are grateful to Yu.P. Kalmykov for helpful discussions.

This work was supported in part by the Russian Foundation for Basic Research, grant no. 98-02-16453, and INTAS, grant no. 96-0663.

REFERENCES

1. R. Bartussek, P. Hanggi, and P. Jung, Phys. Rev. E **49** (5), 3930 (1994).
2. P. Jung and P. Talkner, Phys. Rev. E **51** (3), 2640 (1995).
3. M. E. Inchiosa and A. R. Bulsara, Phys. Rev. E **58** (1), 115 (1998).
4. K. Loerincz, Z. Gingl, L. B. Kiss, and A. R. Bulsara, Phys. Lett. A **254** (4), 154 (1999).
5. L. Gammaitoni, P. Hanggi, P. Jung, and F. Marchesoni, Rev. Mod. Phys. **70** (1), 223 (1998).
6. W. Wernsdorfer, E. Bonet Orozco, K. Hasselbach, *et al.*, Phys. Rev. Lett. **78** (9), 1791 (1997).
7. H. Casalta, P. Schleger, C. Bellouard, *et al.*, Phys. Rev. Lett. **82** (6), 1301 (1999).
8. A. N. Grigorenko, V. I. Konov, and P. I. Nikitin, Pis'ma Zh. Éksp. Teor. Fiz. **52** (11), 1182 (1990) [JETP Lett. **52**, 593 (1990)].
9. É. K. Sadykov, Fiz. Tverd. Tela (Leningrad) **33** (11), 3302 (1991) [Sov. Phys. Solid State **33**, 1862 (1991)].
10. E. K. Sadykov, J. Phys.: Condens. Matter **4**, 3295 (1992).
11. A. Pérez-Madrid and J. M. Rubi, Phys. Rev. E **51** (5), 4159 (1995).
12. Yu. L. Raikher and V. I. Stepanov, Phys. Rev. B **52** (5), 3493 (1995).

13. J. M. G. Vilar, A. Pérez-Madrid, and J. M. Rubi, Phys. Rev. E **54** (6), 6929 (1996).
14. Yu. L. Raikher, V. I. Stepanov, A. N. Grigorenko, and P. I. Nikitin, Phys. Rev. E **56** (6), 6400 (1997).
15. Yu. L. Raikher and V. I. Stepanov, Phys. Rev. B **55** (22), 15005 (1997).
16. Yu. P. Kalmykov and S. V. Titov, Fiz. Tverd. Tela (St. Petersburg) **40** (9), 1642 (1998) [Phys. Solid State **40**, 1492 (1998)].
17. W. F. Brown, Jr., Phys. Rev. **130** (5), 1677 (1963).
18. Yu. L. Raikher and M. I. Shliomis, Adv. Chem. Phys. **87**, 595 (1994).
19. É. K. Sadykov and A. G. Isavnin, Fiz. Tverd. Tela (St. Petersburg) **38** (7), 2104 (1996) [Phys. Solid State **38**, 1160 (1996)].
20. Yu. L. Raikher, S. V. Burylov, and V. I. Stepanov, Pis'ma Zh. Éksp. Teor. Fiz. **47** (5), 273 (1988) [JETP Lett. **47**, 330 (1988)].
21. Yu. L. Raikher, V. I. Stepanov, and S. V. Burylov, J. Colloid Interface Sci. **144** (2), 308 (1991).

Translated by Yu. Epifanov

Physics of the Solid State, Vol. 43, No. 2, 2001, pp. 284–289. Translated from Fizika Tverdogo Tela, Vol. 43, No. 2, 2001, pp. 274–278.

MAGNETISM AND FERROELECTRICITY

Determination of Magnetic Anisotropy of Complex Rare-Earth Compounds from Mössbauer and NMR Spectra

Yu. P. Irkhin and V. Yu. Irkhin

Institute of Metal Physics, Ural Division, Russian Academy of Sciences, ul. S. Kovalevskoĭ 18, Yekaterinburg, 620219 Russia

e-mail: Valentin.Irkhin@imp.uran.ru

Received June 9, 2000

Abstract—Experimental data and theoretical papers on the magnetic anisotropy (MA) of rare-earth–transition metal intermetallic compounds are reviewed. Discrepancies between the experimental data obtained by different authors, as well as between these data and the theoretical calculations of the MA constants, are indicated. A technique is proposed for determining the crystal-field parameters and the effective charges Q_i^* of ions in intermetallic compounds. Using experimental Mössbauer and NMR spectroscopic data, possible values of Q_i^* are determined for R_2T_{17-x} and $R_2T_{17-x}Ti_x$ compounds, which allow one to find the MA constants of these systems with different R and T in a unified way. The problem of the sign of the contribution from the rare-earth metal sublattice to the MA is discussed. The heavy x dependence of this contribution in the $R_2T_{17-x}Ti_x$ system is explained to be due to the contribution to the crystal field from Ti ions in the dumbbells. © *2001 MAIK "Nauka/Interperiodica".*

INTRODUCTION

In the 1980s and 1990s, much research was devoted to the magnetism of compounds of rare-earth (RE) metals, which offer considerable promise as magnetic materials [1–3]. Nevertheless, many problems remain to be solved, among them the physical mechanisms that determine important physical characteristics of these materials, such as the magnetization, Curie point T_C, and magnetic anisotropy (MA) constant, which is defined by the equation

$$\mathscr{E}_{MA} = K_1 \sin^2\theta + \ldots . \quad (1)$$

Of even greater interest are the heavy dependences of the magnetic properties on the material composition, in particular, on different substitutional and interstitial impurities.

A typical example is Sm_2Fe_{17}-based systems. The undoped compound has its T_C located near 400 K and a MA of the "easy-plane" type. The introduction of an interstitial impurity of nitrogen ($Sm_2Fe_{17}N_x$) causes the sign of the MA to change, and the constant K_1 becomes as large as 10 MJ/m^3 for $x = 3$. The addition of a small amount of a substitutional impurity of titanium ($Sm_2Fe_{17-x}Ti_x$, $x = 0.75$) also leads to a considerable change in K_1 [2]. This dramatic effect of impurities on the MA is basically due to their influence on the parameters A_{mn} of the crystal field acting on the magnetic RE ions. It is well known (see, e.g., [3]) that nitrogen ions enter interstitial positions of the 9*e* type in Sm_2Fe_{17} (which are situated in the RE-ion planes perpendicular to the c axis, $\theta_\mathbf{R} = \pi/2$) and make a negative contribution to the parameter A_{20} defined by

$$A_{20} = -\sum_\mathbf{R} Q^*(\mathbf{R}) \frac{3\cos^2\theta_\mathbf{R} - 1}{2R^3}, \quad (2)$$

where the summation is carried out over all ions of the lattice, $\theta_\mathbf{R}$ is the polar angle of the vector $\mathbf{R}$, and $Q^*(\mathbf{R})$ is the corresponding effective ion charge. According to Eq. (2), we have a positive (easy-plane-type) contribution to K_1(Sm) for $Q^*(N) < 0$. In the $SmFe_{11}Ti$ compound, on the contrary, nitrogen ions enter 2*b* positions located along the c axis with respect to R ions ($\theta_\mathbf{R} = 0$) and make a negative (easy-plane-type) contribution to K_1(Sm). Therefore, the sign of the nitrogen-ion contribution to MA depends on the geometric factors.

In addition to the geometry, the distribution of the charge density of different ions in compounds is of importance. The screening of ionic charges in a metal (caused, in particular, by conduction electrons) can lead to their strong renormalization and even to the change in their sign [4].

Possible radical distinctions of the crystal-field model in metals were discussed by Coehorn [5], who assumed that the 6*p* and 5*d* electrons of the RE ion itself, which are located within its Wigner–Seitz sphere, make a dominant contribution to the parameter A_{20}. Their anisotropic distribution is dictated by the electron densities of the adjacent cells. This model is associated in [5] with the well-known "microscopic"-

Effective charges in the R_2Fe_{17} compounds calculated by different methods

Compound	$Q_R^*(6c)$	Q_f^*	Q_d^*	Q_h^*	Q_{db}^*	Q_N^*	Ref.
Nd_2Fe_{17}	0.42	0.13	0.24	–0.03	0.24	–0.54	[7]
Sm_2Fe_{17}	0.24	0.11	0.06	–0.06	0.11	–0.45	[7]
Nd_2Fe_{17}	0.97[a]	–1.28	–0.84	–0.24	0.79	–0.15	[8]
Sm_2Fe_{17}	3	0.06	0.06	0.06	0.06		[9]
Tb_2Fe_{17}	2.95	0.62	0.62	0.62	0.97		

Note: The values we calculated from the NMR data [10] are presented in the last row.

[a] The charge is likely to have been calculated without regard for the *f* electrons of Nd.

atom model of Miedema in the alloy cohesion theory. In this case, the sign of A_{20} is opposite to that in the ion model in the point-charge approximation. However, based on the experimental data, Malaman *et al.* [6] drew the conclusion that the usual crystal-field mechanism determined by the adjacent ionic charges is likely to be dominant.

In principle, the effective ionic charges can be found using currently available calculations of the electronic band structures. These calculations were also carried out for the R_2T_{17} compounds, and the number of electrons N_e was found in a sphere of a radius R_0 centered at an ion site [7]. The effective ionic charge can easily be estimated as $Q^* = Q_r(R_0) - N_e$, where $Q_r(R_0)$ is the charge of the ionic core, without the outer shell [for example, $Q_r(f^6s^2) = 8$ for Sm and $Q_r(3d^64s^2) = 8$ for Fe]. The values of Q^* thus obtained for Sm_2Fe_{17} for R_0 equal to the ionic radius are listed in the table. It is seen that the charges Q^* of Sm and Fe ions at different positions are small in magnitude. For nitrogen ions at the 9*e* positions, we have $Q^* = -0.45$ for $x = 3$; that is, nitrogen atoms are acceptors. Using the charge distribution found, the authors of [7] calculated the MA and reported that the result was in good agreement with experiment, but no details were presented in [7]. Furthermore, the charges Q^* calculated in [8] for Nd_2Fe_{17} differ drastically from those found in [7], which means that the results are unstable with respect to the calculational technique and to the approximations made in calculating the electronic band structure.

In actuality, however, the charges Q^* calculated in the way indicated above cannot be used immediately in crystal-field theory. First, the expressions for the effective charge that determines the value of K_1 including the screening effect of conduction electrons were found in [4] to have a more complicated structure and involve both the total screening charge and its derivatives. For the spherical charge density distribution, we have

$$Q^*(\mathbf{R}) = Q_0 + Q_{\text{el}}(R) - \frac{4}{3}\pi R^3[Z(R) - RZ'(R)], \quad (3)$$

where $Q_{\text{el}}(R)$ is the conduction electron charge within a sphere of a radius of R centered at the point-charge position,

$$Q_{\text{el}}(R) = 4\pi\int_0^R \rho^2 d\rho Z(\rho) \quad (4)$$

and $Z(R)$ is the charge density; therefore, $Q'_{\text{el}}(R) = 4\pi r^2 Z(R)$. Second, it is significant that the charge $Q^*(R)$ is taken for the distances R between RE atoms and the ions producing the crystal field; these distances are nearly twice as large as the atomic radii R_0. It was shown in [3] that, in order to explain the experimental value of K_1 in $Sm_2Fe_{17}N_3$, the charge Q^* of the nitrogen ion should be taken to be –0.15, rather than the value of –0.45 in the second row of the table.

Thus, there is a need to develop a crystal-field model for compounds with ions of different species, which will allow the crystal-field parameters to be uniquely determined from the experimental data, in particular, from the data on magnetic properties and from the NMR and Mössbauer spectroscopic data.

The unknown parameters of this model will be the effective ionic charges Q_i^*.

1. A TECHNIQUE FOR CALCULATING THE CRYSTAL-FIELD PARAMETERS AND EFFECTIVE CHARGES

A consistent theoretical and experimental determination of the parameters Q_i^* is of importance to the understanding of the MA of compounds. The MA constant defined in Eq. (1) is given by the expression

$$K_1 = -3e^2A_{20}\langle r_f^2\rangle\alpha_J J(J - 1/2). \quad (5)$$

Here, $\langle r_f^2\rangle$ is the mean square radius of the *f* shell, J is the total angular momentum of the RE ion, α_J is the Stevens factor, and the crystal-field parameter A_{20} is given by Eq. (2). Because the effective ionic charges Q^* depend on the distance, their values are different

even for equivalent positions of the RE-ion neighbors differing in their distance from the RE ion. Therefore, the charges Q^* are characteristics of pairs of ions and they tend to zero at large distances (complete screening). Perhaps this is an added reason for using the nearest neighbor approximation and for not taking into account a large number of neighbors on the lattice when calculating the sum in Eq. (2).

A rough estimate of $Q^*(\mathbf{R})$ based on valence arguments is not valid for metallic magnets, where this quantity varies over a wide range and can even change its sign because of screening effects [4].

In the simplest case of pure RE metals, Eq. (5) leads to reasonable results, but even in this case, Q^* is nearly twice as small as its nominal value for trivalent RE ions ($Q = 3$). For multicomponent compounds, the situation is far more complicated, because we have several parameters Q_i^* and only one observable quantity K_1. The poor accuracy of the relevant experimental data makes it difficult to make use of the higher order anisotropy constants; in addition, the effective charges involved in them are different from those given by Eq. (3).

For these reasons, it is helpful to separate the contributions of ions at different sites by comparing the magnetic anisotropies of compounds differing in one structural element with a given Q_i^*. As an example, we refer to the interstitial impurities B = H, N, and C in the $R_2T_{17}B_x$ systems or the substitutional impurities in the $R_2Fe_{17-x}Ti_x$ compounds. Using the change in the MA constant ΔK_1 due to the introduction of an impurity, we can write additional equations to determine the corresponding Q_i^*. Of course, the charges Q_i^* of the host ions can change in this case, but one might expect this effect to be insignificant.

The individual contributions can also be separated taking into account the difference in structural elements of closely related structures. For example, in the case of rhombohedral (r) and hexagonal (h) structures of R_2Fe_{17}, one can separate the charges Q_i^* of Fe ions in the dumbbells and R ions at the 2b and 2d sites.

In the h structure, in contrast to the r structure, all the 6c dumbbells that lie on the edges of the unit cell in the r structure are displaced to the centers of the hexagons in the RT planes and substituted for the R atoms of the unit cell of the r structure. The most important distinction is that there appear two types of R sites, one of which is the 2b site (having only R atoms as its nearest neighbors along the c axis) and the other is the 2d site (the nearest neighbors along the c axis are dumbbells). Because of the displacement indicated above, the unit cell becomes one-third shorter along the c axis.

For the sake of convenience, we divide Eq. (2) into the terms corresponding to different structural elements of the lattice. Using the standard notation for the atomic sites in the r lattice, Eq. (2) can be written in the nearest neighbor approximation as

$$A_{20} = 12A_{20}(h) + 6A_{20}(f) + A_{20}(c). \tag{6}$$

Here, the lattice is assumed to be perfect and the charges Q_i^* at the h, b, and d sites, to be identical. A calculation gives

$$A_{20}(h) = -\frac{e^2}{2}\frac{(2-y^2)Q_h^*}{(c/6)^3(1+y^2)^{5/2}},$$
$$A_{20}(f) = \frac{27e^2}{2}\frac{Q_f^*}{a^3}, \tag{7}$$

where a and c are the r-lattice parameters and $y = 2a/c$. Expressions (7) are similar to the well-known formulas for the hcp and RCo_5 structures [1, 11]. The contributions given by Eq. (7) are the same for the r and h structures, while the contributions $A_{20}(c)$ from the dumbbells of T ions are different. In the r structure, the nearest neighbors of an $R(6c)$ ion along the c axis are one $T(6c)$ dumbbell and one $R(6c)$ ion. In the h structure, two types of nearest neighbor ion configurations are possible for R ions: (i) two R ions (the 2b site) and (ii) two dumbbells (the 2d site). Accordingly, the terms in Eq. (6) are

$$A_{20}^r(6c) = -\frac{e^2Q_R^*(6c)}{(c/3)^3} - \frac{2e^2Q_T^*}{(c/3-\delta_{db})^3}, \tag{8}$$

$$A_{20}^h(2b) = -\frac{2e^2Q_R^*(2b)}{(c/3)^3},$$
$$A_{20}^h(2d) = -\frac{2e^2Q_T^*}{(c/3-\delta_{db})^3}, \tag{9}$$

where $2\delta_{db}$ is the dumbbell length (about $0.2c$). Equations (6)–(9) can be used both to calculate K_1 from formula (5) and to interpret the values of A_{20} obtained from NMR and Mössbauer spectra for different types of RE-ion lattice sites. The latter provides additional equations for the charges Q_i^*, which makes the set of equations more determinate. Since the compounds R_2T_{17} with various R differ little in their parameters, we may expect that the charges Q_i^* thus found will be universal for all compounds with this structure.

Unfortunately, there is little available experimental data from which A_{20} can be determined for different ionic sites, and their accuracy is not satisfactory. For Tb_2Fe_{17}, three NMR lines were measured [10] to be $H_1 = 1.9 \pm 2.6$ K, $H_2 = -0.6 \pm 2.6$ K, and $R = 0.9 \pm 2.6$ K. A considerable margin of error for H is due, in particular, to the uncertainty in the Sternheimer antishielding factor γ_∞ for the nucleus, which enters the relation

between the crystal-field parameter and the crystal-field gradient V_{zz},

$$A_{20} = -\frac{1}{4}\frac{1-\sigma_2}{1-\gamma_\infty}V_{zz}, \quad (10)$$

where $1 - \sigma_2$ is the shielding factor for *f* electrons. In intermetallic compounds, the ratio A_{20}/V_{zz} ranges generally from –20 to –60. However, within the series of compounds in question, the value of γ_∞ is constant to a reasonable accuracy. For example, according to [12], $A_{20}/V_{zz} = -46 \pm 3$ for R_2T_{17}.

The corresponding average values of A_{20} in units of K/a_0^2 (a_0 is the Bohr radius) are

$$A_{20} = \frac{B_{20}}{\alpha_J\langle r_f^2\rangle} = \begin{cases} -253 & H_1 \\ 80 & H_2 \\ -120 & R. \end{cases}$$

The values H_1 and H_2 correspond to the 2*b* and 2*d* sites of Tb ions in the hexagonal phase, respectively, while *R* corresponds to the Tb(6*c*) ion in the rhombohedral phase (both phases coexist in Tb_2Fe_{17}). Substituting numerical values of the parameters *c* and *a* and putting $\delta_{db} = 0.1$ Å and $e^2/\text{Å}^3 = 2.3 \times 10^5$ erg/cm^2, for the Tb(6*c*) site in the *r* lattice and the 2*b* and 2*c* sites in the *h* lattice, we obtain the equations

$$\begin{aligned} -12.4Q_f^* + 1.4Q_R^*(6c) + 3.9Q_{db}^*(6c) &= 0.26, \\ -12.4Q_f^* + 2.8Q_R^*(2b) &= 0.55, \\ -12.4Q_f^* + 7.8Q_{db}^*(6c) &= -0.17. \end{aligned} \quad (11)$$

Here, Q_{db}^* is the Fe-ion charge in the dumbbell and it has been assumed that $Q_f^* = Q_h^* = Q_b^* = Q_d^*$ that is, only two different Fe-ion charges (in the planes and in the dumbbells) are taken into account. Thus, we have a set of three nonhomogeneous equations in four unknowns. Physically, it is clear that $Q_R^*(2b)$ and $Q_R^*(6c)$ have about the same value. However, when they are identical, the set of Eqs. (11) becomes indeterminate, because the determinant of the corresponding set of homogeneous equations vanishes. A physically reasonable solution is obtained if we assume that $Q_R^*(2b) = 3$, i.e., that this charge is equal to its nominal value for the R^{3+} ion. In this case, from Eqs. (11) we obtain

$$Q_R^*(6c) = 2.95, \quad Q_f^* = 0.62, \quad Q_{db}^* = 0.97.$$

If we assume that $Q_R^*(2b) = 2$, the charges Q_i^* will become about 30% smaller. It should be noted that the correspondence of the *I* and *II* NMR lines to the 2*b* and 2*d* sites is not uniquely established. However, interchanging the corresponding right-hand sides of Eqs. (11) affects the charges Q_i^* only insignificantly, because the contributions to the left-hand sides of these equations nearly compensate each other.

Similar results are also obtained for the compounds Er_2Fe_{17} and Er_2Ni_{17}; the corresponding experimental values of A_{20} were found in [13] and [14], respectively. In this case, in spite of significant differences in A_{20}, the charges Q_i^* also appear to differ only insignificantly.

In the case where A_{20} (and the local values of K_1) for *R* sites of the 2*b* and 2*d* types are opposite in sign, noncollinear structures can form (and these were actually observed in Tb_2Fe_{17} and Er_2Fe_{17} and in the respective nitrides [15]) and spin-reorientational phase transitions occur depending on the temperature.

2. MAGNETIC ANISOTROPY OF THE R_2T_{17} AND $R_2T_{17-x}Ti_x$ SYSTEMS

The crystal-field parameters of Er_2Fe_{17} were calculated in [9] in the point-charge approximation. The shielding parameter was taken to be $\sigma_2 = 0.9$, so that $A_{20}^* = (1 - \sigma_2)A_{20} = 0.1A_{20}$. The charges Q_R^* and Q_{Fe}^* were assumed to be the same for all sites. Using the experimental Mössbauer spectra, these charges were found to be 3 and 0.06, respectively (see table). It should be noted that earlier a value of $Q_{Fe}^* = -0.5$ was found [16] in the same way for the $Nd_2Fe_{14}B$ system for a given $Q_R^* = 3$.

In [9], the following crystal-field parameters were determined for Er ions:

$$\langle r_f^2\rangle A_{20}^*(2b) = 191 \text{ K}, \quad \langle r_f^2\rangle A_{20}^*(2d) = -180 \text{ K}.$$

With these values and $Q_R^* = 3$, Eqs. (11) give $Q_f^* = 0.7$ and $Q_{db}^* = 1.2$. The values of A_{20} for Tm and Nd ions were found in [9], but only the data for nitrides $R_2Fe_{17}N_3$ were presented there. Thus, the results of [9] are partly supported by a more detailed calculation with no phenomenologically introduced screening. In this case, the decrease in A_{20} (as is the case with Tb_2Fe_{17}) is due to the balance of the contributions, opposite in sign, from the Fe ions in the mixed *R*Fe plane and the *R* ions [to $A_{20}(2b)$] or from the Fe ions in the mixed *R*Fe plane and the Fe ions in the dumbbells [to $A_{20}(2d)$]. Thus, in our model, the contributions from different sites are described in detail and the important role of the Fe-ion dumbbells, whose effective charge differs noticeably from that of the Fe ions at other sites, is revealed.

From the experimental Mössbauer spectra for Er_2Ni_{17}, it was found that $A_{20}(2b) = -183$ K/a_0^2 and $A_{20}(2d) = -418$ K/a_0^2. With these values, solving

Eqs. (11) yields the effective charges $Q_R^*(2b) = 3$, $Q_f^* = 0.6$, and $Q_{db}^* = 1$, which are close to the corresponding values for Er_2Fe_{17} presented above.

In order to determine K_1(Sm) for Sm_2Fe_{17}, we use the NMR data for Tb_2Fe_{17} from [11], where, in addition to two *h*-phase lines corresponding to Tb sites of the 2*b* and 2*d* types in the *h* lattice, a line corresponding to the *r* phase was observed. Because the value $A_{20}^r(6c) = -120\ \mathrm{K}/a_0^2$ calculated for terbium is virtually the same as those for other RE ions, we use it to make an estimate in the case of Sm_2Fe_{17} and find $K_1(\mathrm{Sm}) = 0.36\ \mathrm{MJ/m^3}$. Since the margin of experimental error of the NMR measurement (±2.6 K) is large in comparison with the average value 0.9 K, the accuracy of our calculation is poor. Nevertheless, the result is reasonable and agrees with the wide scatter of the experimental data on K_1(Sm) (including the change in sign) available in the literature.

A dramatic effect of the substitutional Ti impurity in $Sm_2Fe_{17-x}Ti_x$ on the value of K_1 was observed in [2]. At relatively small values of $x < 0.75$, the magnitude of K_1 was drastically decreased, so that its extrapolation to $x = 0.8$ gave $K_1 \longrightarrow 0$, whereas the contribution from the Fe sublattice (as determined by comparing with $Y_2Fe_{17-x}Ti_x$) was varied only insignificantly. It should be noted that, among the transition metals investigated, only titanium causes K_1 to increase in $Sm_2Fe_{17-x}M_xN_yC_z$, as was shown in [17] for the systems with $x < 0.4$.

In view of the wide scatter of the experimental values of $K_1(Sm_2Fe_{17})$, it is convenient to introduce the quantity

$$\Delta K_1(\mathrm{Sm}, x) = K_1(Sm_2Fe_{17-x}Ti_x) - K_1(Y_2Fe_{17-x}Ti_x) - K_1(\mathrm{Sm}, x = 0). \quad (12)$$

With the values taken from [2], we find $\Delta K_1(\mathrm{Sm}, x = 0.75) \simeq 3\ \mathrm{MJ/m^3}$. In our effective-charge model, this change is due to the substitution of Ti for Fe ions and can be calculated from the formula

$$Q^*(\mathrm{Fe}) \longrightarrow Q_{db}^*(\mathrm{Fe}) + \frac{x}{2}[Q_{db}^*(\mathrm{Ti}) - Q_{db}^*(\mathrm{Fe})]. \quad (13)$$

This relation has been derived under the important assumption that titanium substitutes for the iron at the 6*c* sites in the dumbbells. If the 17 Fe ions in the formula unit were all replaced with equal probabilities, the effect would be much weaker. Substituting expression (13) into the first equation in Eqs. (11), we can find the change in the crystal-field parameter ΔA_{20}, which is related to $\Delta K_1(\mathrm{Sm}, x)$ by Eq. (5). The value of A_{20} thus obtained is actually an average, because the effective charge given by Eq. (13) is the average ionic charge of the nearest neighbors upon replacement of the Fe ions in the dumbbells. This value will, in general, be different from the local quantity A_{20} obtained from the experimental NMR and Mössbauer spectra. The latter local quantity (in the nearest-neighbor approximation) should have two values corresponding to the SmFe(6*c*) and SmTi(6*c*) configurations. Unfortunately, there are no experimental data of this kind for $Sm_2Fe_{17-x}Ti_x$.

Nevertheless, we can calculate ΔQ^* from Eq. (13) by considering $\Delta K_1(\mathrm{Sm}, x)$ to mean the quantity

$$\Delta K_1(\mathrm{Sm}, x) = K_1(\mathrm{Sm}, \mathrm{Fe}) + (x/2)[K_1(\mathrm{Sm}, \mathrm{Ti}) - K_1(\mathrm{Sm}, \mathrm{Fe})]. \quad (14)$$

The coefficient $x/2$ in Eq. (14) is introduced because only one-half of the overall number of Sm sites contributes to the change in anisotropy caused by Ti-ion doping. The possible substitution of Ti ions for both Fe ions in the dumbbell has not been taken into account in Eq. (14). Using Eq. (14) and putting $K_1(\mathrm{Sm}, \mathrm{Fe}) = 0.36\ \mathrm{MJ/m^3}$, $\Delta K_1(\mathrm{Sm}, \mathrm{Ti}) = 3\ \mathrm{MJ/m^3}$, and $Q_R^*(2b) = 3$, we find $\Delta Q^* = Q_{db}^*(\mathrm{Ti}) - Q_{db}^*(\mathrm{Fe}) = 0.6$ from Eq. (13). Therefore, if $Q_{db}^*(\mathrm{Fe}) = 1$, we have $Q_{db}^*(\mathrm{Ti}) = 1.6$.

Thus, the large increase in K_1(Sm) caused by the introduction of titanium into Sm_2Fe_{17} can be explained by the difference in the effective charge of iron and titanium, due to which the balance of the contributions to the crystal field which was in the undoped compound is disturbed. (In this case, the specific positions of Ti ions are of importance.) The question concerning possible deeper physical reasons for this balance (which is typical for intermetallic compounds and is unlikely to be accidental) is an open question. An alternative explanation of the significant influence of titanium can be based on the assumption that all effective charges in the host lattice are fairly small because their heavy screening by conduction electrons and, therefore, the local disturbance produced by the Ti impurity become significant.

A similar analysis of the magnetic anisotropy of the compounds $RFe_{11}Ti$ (*R* = Y, Sm, Tb), single crystals of which have recently been investigated [18], is of interest.

ACKNOWLEDGMENTS

The authors are grateful to A.S. Ermolenko, N.V. Mushnikov, E.V. Shcherbakova, S.A. Nikitin, G.V. Ivanova, and I.S. Tereshina for discussions.

This work was supported in part by the Russian Foundation for Basic Research, grant no. 99-02-16268.

REFERENCES

1. Yu. P. Irkhin, Usp. Fiz. Nauk **151** (2), 321 (1988) [Sov. Phys. Usp. **31**, 163 (1988)].
2. A. Paoluzi and L. Paretti, J. Magn. Magn. Mater. **189** (1), 89 (1998).

3. R. Skomski, M. D. Kuz'min, and J. M. D. Coey, J. Appl. Phys. **73** (10), 6934 (1993).
4. V. Yu. Irkhin and Yu. P. Irkhin, Phys. Rev. B **57** (5), 2697 (1998); Yu. P. Irkhin and V. Yu. Irkhin, Fiz. Tverd. Tela (St. Petersburg) **42** (6), 1055 (2000) [Phys. Solid State **42**, 1087 (2000)].
5. R. Coehorn, J. Magn. Magn. Mater. **99** (1–3), 55 (1991).
6. B. Malaman, G. Venturini, R. Welter, *et al.*, J. Magn. Magn. Mater. **202** (3), 519 (1999).
7. Z. Zeng, Q. Zheng, W. Lai, and C. Y. Pan, J. Appl. Phys. **73** (10), 6916 (1993).
8. Z. Gu, W. Lai, X.-Fu Zhong, and W. Y. Ching, J. Appl. Phys. **73** (10), 6928 (1993).
9. Y. Xu, T. Ba, and Y. Liu, J. Appl. Phys. **73** (10), 6937 (1993).
10. Yu. P. Irkhin, E. I. Zabolotskiĭ, E. V. Rozenfel'd, and V. P. Karpenko, Fiz. Tverd. Tela (Leningrad) **15** (10), 2963 (1973) [Sov. Phys. Solid State **15**, 1976 (1973)].
11. Y. Li, R. G. Graham, D. St. P. Bunbury, *et al.*, J. Magn. Magn. Mater. **140–144**, 1007 (1995).
12. M. V. Dirken, R. C. Thiel, R. Coehorn, *et al.*, J. Magn. Magn. Mater. **94** (1–2), L15 (1991).
13. T. S. Zhao, T. W. Lee, K. S. Pang, and J. I. Lee, J. Magn. Magn. Mater. **140–144**, 1009 (1995).
14. P. C. M. Gubbens, A. A. Moolenar, G. A. Stewart, *et al.*, J. Magn. Magn. Mater. **140–144**, 1011 (1995).
15. S. A. Nikitin, E. A. Ovchentsov, A. A. Salamova, *et al.*, J. Alloys Compd. **261** (1), 15 (1997).
16. J. M. Cadogan, J. P. Cavigan, D. Givord, and H. S. Li, J. Phys. F **18** (4), 779 (1988).
17. X. Chen, Er. Girt, and Z. Altounian, J. Appl. Phys. **75** (10), 5997 (1994).
18. S. A. Nikitin, T. I. Ivanova, and I. S. Tereshina, Neorg. Mater. **34** (5), 566 (1998).

Translated by Yu. Epifanov

Physics of the Solid State, Vol. 43, No. 2, 2001, pp. 290–299. Translated from Fizika Tverdogo Tela, Vol. 43, No. 2, 2001, pp. 279–288.

MAGNETISM AND FERROELECTRICITY

Effect of Hydrogenation on Spin-Reorientation Phase Transitions and Magnetic Anisotropy Constants of RFe$_{11}$Ti Single Crystals (R = Lu, Ho, and Er)

S. A. Nikitin[1], I. S. Tereshina[1], Yu. V. Skourski[1, 3], N. Yu. Pankratov[1], K. P. Skokov[2], V. V. Zubenko[1], and I. V. Telegina[1]

[1] *Moscow State University, Vorob'evy gory, Moscow, 119899 Russia*
e-mail: nikitin@rem.phys.msu.su

[2] *Tver State University, Sadovyĭ per. 35, Tver, 170000 Russia*

[3] *International Laboratory of Strong Magnetic Fields and Low Temperatures, Wroclaw, 53-421 Poland*

Received March 13, 2000; in final form, June 11, 2000

Abstract—The magnetic anisotropy and spin-reorientation phase transitions in single crystals of the RFe$_{11}$Ti (R = Lu, Ho, and Er) compounds and their hydrides are investigated. Measurements are carried out on capacitance and torque magnetometers. The magnetic anisotropy constants K_1 and K_2 are determined by the mathematical processing of experimental magnetization curves in terms of the phenomenological theory of the anisotropic ferromagnet magnetization. It is demonstrated that the hydrogenation strongly affects the magnitude and the sign of magnetic anisotropy constants, as well as the spin-reorientation phase transitions. The hydrogenation of the HoFe$_{11}$Ti compound leads to the change in sign of the magnetic anisotropy constant K_1. The inference is made that a change in the atomic volume and the axial ratio c/a cannot result in the observed effects. A change in the magnetic anisotropy constants upon hydrogenation is primarily due to the change in the interaction of the quadrupole moment of a 4f electron subshell of rare-earth ions with surrounding ions of the crystal lattice and also with valence and conduction electrons. © *2001 MAIK "Nauka/Interperiodica".*

1. INTRODUCTION

In recent years, compounds RFe$_{11}$Ti with a crystal structure of the ThMn$_{12}$ type have been extensively studied in a number of laboratories [1–3]. Owing to the features of crystal and magnetic structures, these alloys are convenient model objects for investigating the fundamental problems in the physics of magnetic phenomena.

The RFe$_{11}$Ti compound can be treated as a two-sublattice magnet [2]. The rare-earth metal and iron sublattices contribute to the net magnetization and anisotropy. The magnetic moments in both sublattices are ordered ferromagnetically for light rare-earth metals and ferrimagnetically for heavy rare-earth metals. The net anisotropy is predominantly contributed by the rare-earth metal sublattice at low temperatures and by the iron sublattice at high temperatures. The compensation for contributions to the anisotropy from two sublattices in some compounds, for example, TbFe$_{11}$Ti and DyFe$_{11}$Ti, leads to spin-reorientation transitions with a change in temperature [4, 5].

The aim of this work was to investigate in detail the effect of hydrogenation on the magnetocrystalline anisotropy constants of the RFe$_{11}$Ti (R = Lu, Ho, and Er) compounds. In order to solve the posed problem, we measured the magnetization curves for single crystals of LuFe$_{11}$TiH, HoFe$_{11}$TiH, and ErFe$_{11}$TiH hydride compounds for the first time. The measured curves were compared with similar curves for the initial samples of LuFe$_{11}$Ti, HoFe$_{11}$Ti, and ErFe$_{11}$Ti single crystals.

2. SAMPLE PREPARATION AND EXPERIMENTAL TECHNIQUE

The procedures of preparing the RFe$_{11}$Ti samples and checking their quality were similar to those described earlier in [6]. The samples in the form of single-crystal blocks with a misorientation of 1°–2° were used for magnetic measurements. The crystals were checked according to the Laue x-ray diffraction patterns. The samples were prepared in the form of disks (for measurements on a torque magnetometer) ~0.3–0.4 mm thick and ~4 mm in diameter. The planes of disks coincided with the crystallographic planes (110) or (001). The magnetization curves were measured with samples in the form of balls ~2 mm in diameter.

Single crystals were hydrogenated according to the technique described in detail in our earlier work [7]. The hydrogen content in hydrides for all the studied compositions was equal to approximately one hydrogen atom per formula unit. The error δ in the determination of the amount of absorbed hydrogen was $\delta = \pm 0.05$ hydrogen atom per formula unit (H atoms/f.u.).

X-ray powder diffraction analysis of hydrides was performed on a "DRON-2" diffractometer (CuK_α) by using powder samples. According to analysis, the studied samples were single-phase and crystallized in the $ThMn_{12}$ structural type. The lattice parameters are in good agreement with the data available in the literature [8]. The x-ray diffraction patterns contain the reflections that correspond only to this structure. The α-Fe impurities, which sometimes occur in iron-rich cast alloys, are not observed in the x-ray diffraction patterns.

The magnetic measurements were carried out on torque and capacitance magnetometers. The experimental curves of the mechanical torque were recorded on a torque magnetometer in the temperature range 77–700 K in magnetic fields up to 13 kOe. The torque moments were measured in 2° intervals upon rotation of single crystals with respect to the magnetic field. The magnetization curve were obtained with a capacitance magnetometer at the International Laboratory of Strong Magnetic Fields and Low Temperatures (Wroclaw, Poland) in the temperature range from 4.2 to 300 K in fields up to 140 kOe.

The magnetic anisotropy constants were determined by a method consisting in a special mathematical processing of the magnetization curves, which were measured along the easy and hard magnetization directions with the use of the theoretical relationships derived on the basis of the phenomenological theory of the magnetization of anisotropic magnets [9].

3. RESULTS AND DISCUSSION

3.1. Effect of hydrogenation on the magnetic anisotropy of the $LuFe_{11}Ti$ compound. The magnetization curves for the $LuFe_{11}Ti$ and $LuFe_{11}TiH$ single crystals at 4.2 K are displayed in Fig. 1. It is seen that the saturation magnetization upon hydrogenation noticeably increases (by ~10%). The magnetization curve measured along the easy magnetization axis (EMA) (the **c** axis coinciding with the [001] crystallographic direction) is saturated in relatively weak fields, whereas the magnetization curve in the field perpendicular to the **c** axis in the basal plane (the [110] direction]) reaches saturation in fields higher than the magnetic anisotropy field H_A (54 kOe for $LuFe_{11}TiH$ and 40 kOe for $LuFe_{11}Ti$). The magnetic anisotropy constant K_1 was determined by the relationship

$$K_1 = H_A M_S/2,$$

where M_S is the saturation magnetization (magnetic moment per unit volume).

The high magnetocrystalline anisotropy ($K_1 = 1.9 \times 10^7$ erg/cm^3) of $LuFe_{11}Ti$ compounds is explained by a partial "defreezing" of the orbital angular momentum L of iron ions in the anisotropic local crystal field, which strongly differs for different crystallographic positions. In this case, the orbital angular momentum component L is aligned along the easy magnetization axis and, in turn, orients the total spin angular momentum due to the spin–orbit interaction.

The above assumption concerning the nature of the magnetocrystalline anisotropy was confirmed by the neutron diffraction investigation performed by Yang *et al.* [10], who showed that, for example, in the $YFe_{11}Ti$ compound, the magnetic moments localized on iron atoms (which, in the $ThMn_{12}$ structure, occupy three nonequivalent positions 8*i*, 8*j*, and 8*f*) are equal to 1.92, 2.28, and 1.8 μ_B, respectively. These values substantially differ from those observed for bivalent and trivalent iron ions (4 and 5μ_B, respectively). A similar situation most likely occurs for the $LuFe_{11}Ti$ compound. Hence, it follows that the iron sublattice magnetism, to a certain degree, has a band character.

Let us consider the effect of hydrogenation on the magnetic ordering temperature of the $LuFe_{11}Ti$ compound. It is known that the hydrogenation brings about

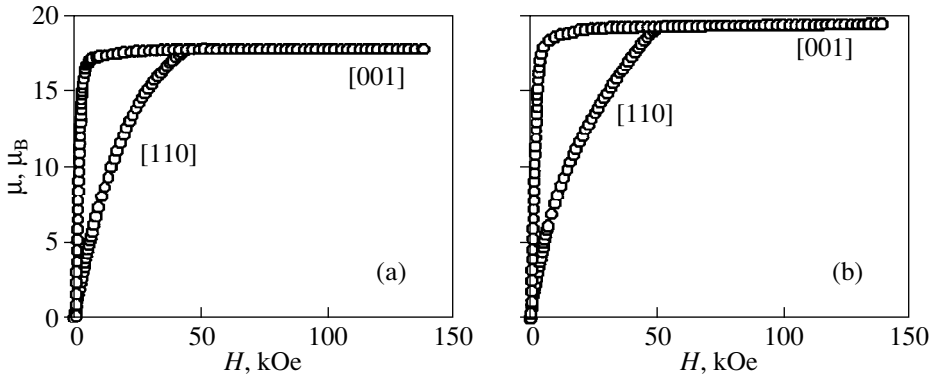

Fig. 1. Magnetization curves for (a) $LuFe_{11}Ti$ and (b) $LuFe_{11}TiH$ single crystals along the [001] and [110] directions at 4.2 K.

Table 1. Crystal lattice parameters a and c, unit cell volume V, magnetic anisotropy constant K_1, and specific saturation magnetization σ_S for the $LuFe_{11}Ti$ compound and its hydride at $T = 4.2$ K

Compound	a, Å	c, Å	c/a	V, Å^3	$\Delta V/V$, %	$K_1 \times 10^7$, erg/cm^3	T_C, K	H_A, kOe	σ_S, emu/g
$LuFe_{11}Ti$	8.42	4.78	0.57	338.9	–	1.9	490	40	130
$LuFe_{11}TiH$	8.48	4.79	0.56	344.5	1.6	2.13	545	54	144

an increase in interatomic distances and the unit cell volume and, for a number of compounds, such as R_2Fe_{17}, a substantial increase in the Curie temperature [11]. For the $LuFe_{11}Ti$ compound, the Curie temperature T_C is determined by the exchange interactions between iron atoms, because a lutecium ion has no localized magnetic moment.

In our work, the Curie temperature T_C was determined as the temperature of the sharpest decrease in the magnetization upon the transition from the ferromagnetic state to the paramagnetic state in a weak magnetic field. The T_C temperature for $LuFe_{11}Ti$ was found to be 490 K, which is substantially less than the T_C temperature for metallic iron. The performed calculations of interatomic distances in the $LuFe_{11}Ti$ compound demonstrated that the shortest distances between Fe atoms are observed in the pairs 8*f*–8*f* (2.358 Å) and 8*i*–8*i* (2.390 Å). At these short Fe–Fe distances, the negative exchange interactions become possible. The hydrogenation of the $LuFe_{11}Ti$ compound leads to a noticeable increase in the lattice constant a and the unit cell volume V (the relative change in the volume $\Delta V/V \approx 1.6\%$) and only a slight change in the lattice constant c (see Table 1). The Curie temperature for $LuFe_{11}TiH$ hydride substantially increases (almost by 55 K). An increase in the T_C temperature can be due to an increase in the exchange energy with an increase in the distances between iron atoms and the atomic volume.

The introduction of hydrogen into the crystal lattice of the $LuFe_{11}Ti$ compound is also accompanied by a considerable increase in the saturation magnetization (Fig. 1) at $T = 4.2$ K ($\sigma_S = 130$ emu/g for $LuFe_{11}Ti$ and 144 emu/g for $LuFe_{11}TiH$). Our investigations revealed that the dependence $\sigma_S(T)$ for the $LuFe_{11}TiH$ compound, as for the initial compound, exhibits a typical ferromagnetic behavior with a monotonic decrease in the magnetization σ upon heating.

It was also of interest to obtain information on the character of the effects responsible for the change in the magnetic anisotropy upon hydrogenation. As is known, the relationship for the magnetic anisotropy constant K_1 within the single-ion theory of localized moments takes the form [12]

$$K_1 \sim M_S^3[1 - (c/a)^2]. \quad (1)$$

However, the application of this formula for estimating the change in K_1 due to a variation in the magnetization and the axial ratio $\eta = c/a$ upon hydrogenation leads to inadequate results. As follows from the data presented in Table 1 and formula (1), the K_1 constant should vary by ~2.7%, whereas the experimental change in K_1 appears to be larger and is equal to ~10%.

Consequently, the magnetic anisotropy theory in the approximation of the single-ion model in our case is inapplicable. The hydrogenation is attended not only by the change in the crystal fields produced by the charges of surrounding ions, but also by strong effects of different nature.

The $RFe_{11}Ti$ compounds absorb up to two hydrogen atoms per formula unit. In this case, the process of introducing light elements, such as hydrogen, can be treated as the process of forming the $RFe_{11}TiH_x$ (where x is the hydrogen concentration) compound with quite new magnetic properties (Curie temperature, saturation magnetization, and magnetic anisotropy). In the $ThMn_{12}$ structure, hydrogen atoms can occupy interstices of two types: tetrahedral and octahedral depending on the hydrogen concentration. Hydrogen atoms occupy octahedral sites at low hydrogen concentrations ($x \leq 1$) and begin to occupy tetrahedral sites at the hydrogen concentrations $x > 1$. Upon hydrogenation of $LuFe_{11}Ti$, the hydrogen concentration x is equal to ~1, and, hence, hydrogen atoms occupy octahedral interstices [13]. From the experimental data (Table 1), it follows that the hydrogenation leads to an increase in the unit cell volume. This results in a narrowing of the 3*d* band of collective 3*d* electrons. A change in the local environment of Fe atoms due to the incorporation of hydrogen atoms brings about a weakening of valence bonds between iron atoms and the redistribution of the electron density of the valence [14] and conduction [15] electrons. Most likely, it is these effects that can explain the increase in the magnetic anisotropy constant of the $LuFe_{11}TiH$ compound, which was observed in the present work.

Thus, the investigation performed demonstrates that the hydrogenation of $LuFe_{11}Ti$ single crystals leads to an increase in the Curie temperature, the saturation magnetization, and the magnetic anisotropy constant K_1.

3.2. Effect of hydrogenation on the magnetic anisotropy of the $HoFe_{11}Ti$ single crystal. Unlike Lu^{3+} ions, Ho^{3+} ions possess a nonzero localized magnetic moment. The crystal data (the a and c unit cell parameters and the unit cell volume V) for $HoFe_{11}Ti$ and its hydride are listed in Table 2. The relative change

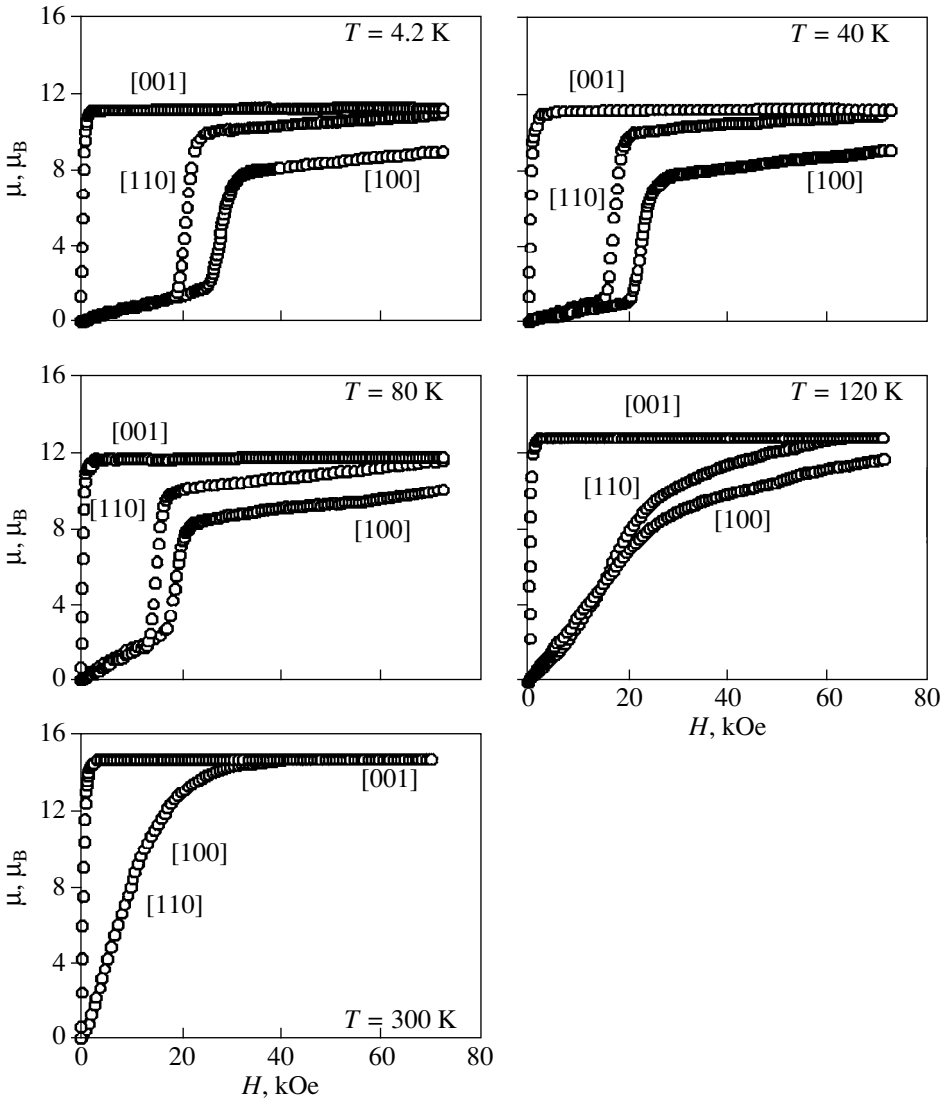

Fig. 2. Magnetization curves for the $HoFe_{11}Ti$ single crystal along the [001], [110], and [100] crystallographic directions at different temperatures.

in the unit cell volume $\Delta V/V$ upon hydrogenation is equal to 1.2%. The axial ratio c/a, as for $LuFe_{11}Ti$, slightly decreases as a result of the incorporation of hydrogen atoms into octahedral sites.

According to the magnetic properties and the magnetic anisotropy measured using the torque and capacitance magnetometers, the $HoFe_{11}Ti$ single crystal exhibits a uniaxial magnetic anisotropy over the entire studied range of temperatures from 4.2 K to the Curie points, which is anomalous for compounds of this class. This is explained by the fact that the crystal field potential acting on Ho rare-earth ions is considerably contributed by the crystal field parameters of orders higher than the second order, namely, by the fourth-order and sixth-order parameters [4].

Figure 2 depicts the experimental field dependences of the magnetization for the $HoFe_{11}Ti$ single crystal along the easy magnetization axis [001] and the axes [110] and [100] in the basal plane at different temperatures in fields up to 70 kOe. As follows from Fig. 2, $HoFe_{11}Ti$ is a high-anisotropy magnet (the magnetic anisotropy field H_A is substantially higher than 70 kOe at T = 4.2 K). Note that the H_A field considerably decreases with an increase in the temperature (for example, H_A = 35 kOe at T = 300 K).

Table 2. Crystal data for the $HoFe_{11}Ti$ single crystal and its hydride

Composition	a, Å	c, Å	c/a	V, Å^3	$\Delta V/V$, %
$HoFe_{11}Ti$	8.46	4.75	0.5615	339.9	–
$HoFe_{11}TiH$	8.50	4.76	0.5600	343.9	1.2

The magnetization curves for the $HoFe_{11}Ti$ single crystal along the [110] and [100] directions in the basal plane (Fig. 2) show a sharp jump of the magnetization in the temperature range 4.2–80 K at the specific threshold fields H_{cr}. This can be explained by the irreversible rotation of the magnetization vector at $H = H_{cr}$. The obtained anomalous dependences of the magnetization on the magnetic field strength are confirmed by the experimental data published earlier for $HoFe_{11}Ti$ single-crystal samples [4]. It should be noted that the transitions attended by a sharp jump in the magnetization at $H = H_{cr}$ are the first-order transformations. These transitions—the first-order magnetization processes (FOMP)—were theoretically studied by a number of researchers [9, 16]. They occur as a result of changing over the magnetization vector between two nonequivalent minima of the free energy of anisotropy in a sufficiently strong magnetic field. The theory of the FOMP-type processes for uniaxial ferromagnets was treated in detail by Asti and Bolzoni [9] with allowance made for the third-order magnetic anisotropy constants. However, the experimental observation of these transitions in rare-earth–Fe intermetallic compounds involves certain experimental problems associated with the necessity of using sufficiently perfect single crystals, strong magnetic fields, and low temperatures. By assuming that the antiparallel orientation of magnetic moments in the rare-earth and iron sublattices is retained in fields up to 100 kOe, we now consider the possibility of describing the experimental magnetization curves on the basis of the theoretical relationships obtained in [9]. Our assumption seems to be sufficiently justified, because the applied magnetic fields are substantially weaker than the exchange fields: the exchange field within the Fe sublattice is equal to 8.1×10^6 Oe, and the exchange field between the sublattices is 2.7×10^6 Oe.

According to the theory [9], upon magnetization of a uniaxial ferromagnet in the direction perpendicular to the tetragonal **c** axis, the expression for the total energy with due regard for the anisotropy constants of the first K_1, second K_2, and third K_3 orders is written as

$$F = K_1\sin^2\theta + K_2\sin^4\theta + K_3\sin^6\theta - HM_S\sin\theta, \quad (2)$$

where θ is the angle between the magnetization vector M_S and the **c** axis. The equilibrium equation $dF/d\theta = 0$ is given by

$$HM_S = 2\sin\theta(K_1 + 2K_2\sin^2\theta + 3K_3\sin^4\theta). \quad (3)$$

With the use of the normalized variables $h = 2H/|H_{A1}|$ and $m = M/M_S = \sin\theta$ ($H_{A1} = 2K_1/M_S$), we obtain

$$h = 2m(1 + 2xm^2 + 3ym^4)K_1/|K_1|, \quad (4)$$

where $x = K_2/K_1$ and $y = K_3/K_1$.

As follows from [9], two types of the first-order transitions induced by the magnetic field can take place: FOMP-1 and FOMP-2, which differ in the final magnetization state. At FOMP-1, the magnetization jumpwise changes to the saturation state. At FOMP-2, the magnetization in the final state does not reach saturation and the condition for the transition is the equality of energies in the initial and final states. Upon magnetization perpendicular to the **c** axis (in the basal plane), the condition for the first-order transition is written in the form

$$\begin{aligned} &K_1m_1^2 + K_2m_1^4 + K_3m_1^6 - HM_Sm_1 \\ &= K_1m_2^2 + K_2m_2^4 + K_3m_2^6 - HM_Sm_2, \end{aligned} \quad (5)$$

where m_1 and m_2 are the relative magnetizations prior to and after the transition. Both quantities obey the stability condition. Then, we have a set of equations

$$\begin{aligned} &(m_1 + m_2) + x(m_1^2 + m_2^2) + y\{(m_1^2 + m_2^2)^2 + m_1^2m_2^2\} \\ &\qquad = hK_1/|K_1|, \\ &h = 2m_1(1 + 2xm_1^2 + 3ym_1^4)K_1/|K_1|, \\ &h = 2m_2(1 + 2xm_2^2 + 3ym_2^4)K_1/|K_1|. \end{aligned} \quad (6)$$

The critical fields and the magnetization in the transition range are defined by the relationships

$$\begin{aligned} h_{cr} &= \frac{2}{5}A\left[2 - \frac{17x^2 + x\sqrt{60y - 11x^2}}{30y}\right], \\ m_1 &= \frac{A - D}{2}, \quad m_2 = \frac{A + D}{2}, \end{aligned} \quad (7)$$

where

$$\begin{aligned} A &= \left[\frac{-3x + \sqrt{60y - 11x^2}}{10y}\right]^{1/2}, \\ D &= \left[\frac{-5x - \sqrt{60y - 11x^2}}{6y}\right]^{1/2}. \end{aligned} \quad (8)$$

For the $RFe_{11}Ti$ compounds with a tetragonal symmetry, the magnetic anisotropy energy at low temperatures is considerably contributed by the anisotropy constants of the second K_2' and third K_3' orders in the basal plane. Taking into account the anisotropy in the basal plane, the energy defined by formula (2) can be rewritten in the following form:

$$\begin{aligned} F &= K_1\sin^2\theta + (K_2 + K_2'\cos 4\varphi)\sin^4\theta \\ &+ (K_3 + K_3'\cos 4\varphi)\sin^6\theta - HM_S\sin\theta. \end{aligned} \quad (9)$$

For the [100] direction, we have $\cos 4\varphi = 1$ and the effective constants $(K_2 + K_2')$ and $(K_3 + K_3')$ can be used in the relationship for the total energy. Similarly,

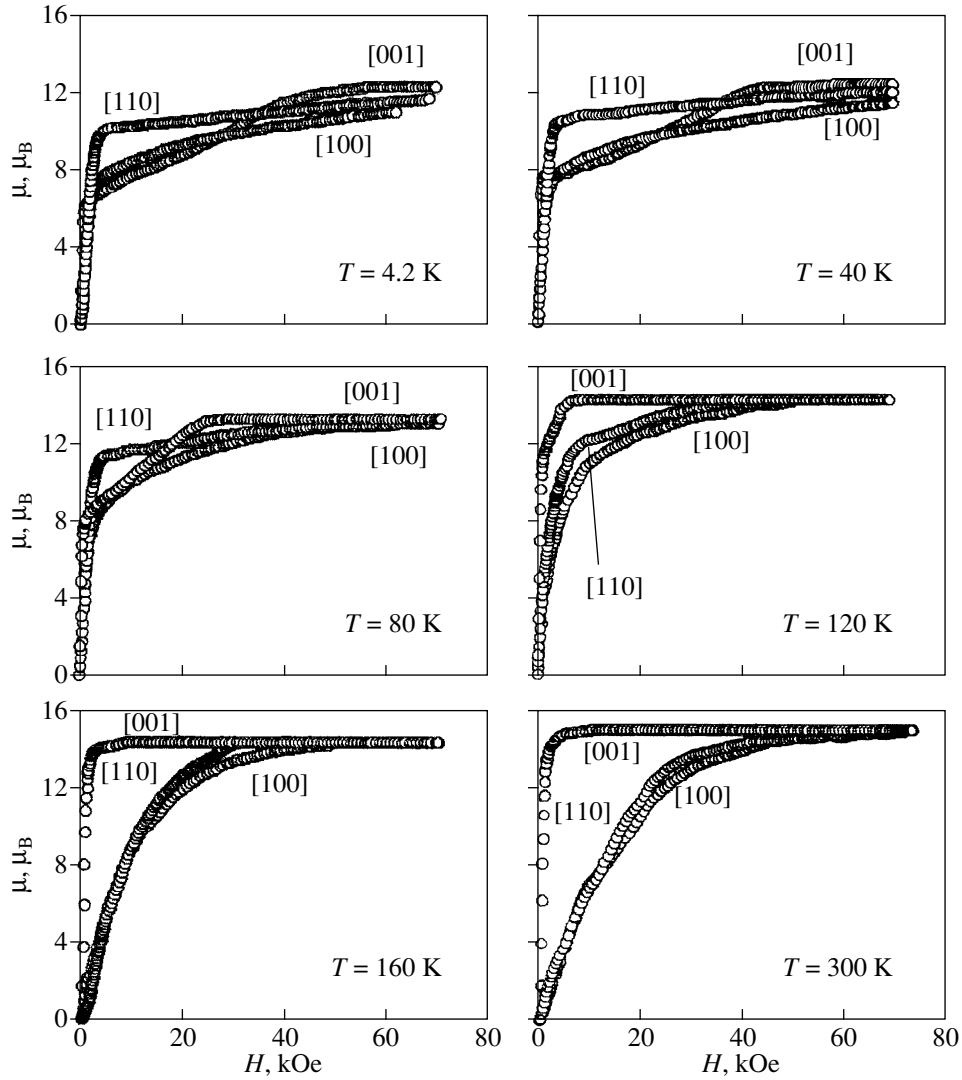

Fig. 3. Magnetization curves for the $HoFe_{11}TiH$ single crystal along the [001], [110], and [100] crystallographic directions at different temperatures.

for the [110] direction, $\cos 4\varphi = -1$ and the effective constants take the form $(K_2 - K_2')$ and $(K_3 - K_3')$.

The mathematical treatment of the h_{cr}, m_1, and m_2 experimental values with the above formulas gives the following magnetocrystalline anisotropy constants for $HoFe_{11}Ti$ at $T = 4.2$ K: $K_1 = 4.7 \times 10^7$, $K_2 = -9.1 \times 10^7$, $K_3 = 6.8 \times 10^7$, $K_2' = 1.0 \times 10^7$, and $K_3' = -2.2 \times 10^7$ erg/cm^3.

As can be seen from Fig. 3, the threshold fields are not observed in the field dependences of the magnetization for $HoFe_{11}TiH$, which indicates the absence of first-order phase transitions in hydride upon magnetization. In this case, the magnetic anisotropy constants can be calculated during the mathematical treatment of the magnetization curve $\sigma(H)$ along the [001] axis with the use of equations following from the theory proposed in [9]. Upon magnetization along the **c** axis, the expression for the total energy has the form

$$F = K_1 \sin^2\theta + K_2 \sin^4\theta + K_3 \sin^6\theta - HM_S \cos\theta \quad (10)$$

and the equilibrium equation $dF/d\theta = 0$ is written as

$$HM_S = -2\cos\theta(K_1 + 2K_2 \sin^2\theta + 3K_3 \sin^4\theta). \quad (11)$$

By using the normalized variables $m = M/M_S = \cos\theta$ and $H_{A1} = 2K_1/M_S$, we obtain

$$H = -H_{A1} m(1 + 2x(1 - m^2) + 3y(1 - m^2)^2). \quad (12)$$

In this case, it is possible to determine reliably only the K_1 constant, because the theory from [9] ignores the anisotropy in the basal plane. The saturation field can be determined from Eq. (12) at $m = 1$,

$$H(m = 1) = H_{A1} = 2K_1/M_S. \quad (13)$$

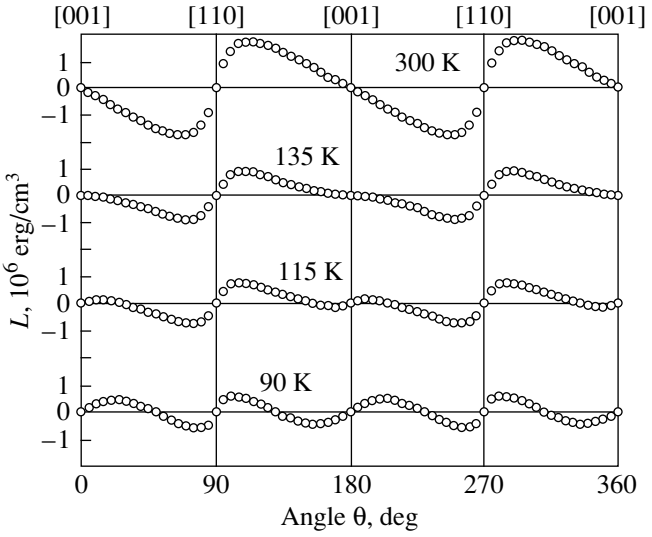

Fig. 4. Experimental curves of the mechanical torque L for the $HoFe_{11}TiH$ single crystal in the magnetic field H = 13 kOe at different temperatures.

According to our experimental data (Figs. 2, 3), the magnetic anisotropy in the basal plane of the $HoFe_{11}Ti$ and $HoFe_{11}TiH$ single crystals at low temperatures (T < 120 K) is rather pronounced. The magnetization curves along the [100] and [110] axes in the basal plane differ from each other at the fields $H > H_{cr}$. Moreover, the critical fields for $HoFe_{11}Ti$ differ for these crystallographic directions. In particular, H_{cr} at T = 4.2 K is equal to 21 kOe for the [110] direction and 28 kOe for the [100] direction. The correct inclusion of the anisotropy in the basal plane calls for further development of the theory. However, in order to estimate a change in the magnetic anisotropy constant K_1 for $HoFe_{11}TiH$ hydride, it is possible to apply the above theoretical relationship (13), because the field dependence of the magnetization along the easy magnetization axis does not depend on the magnetic anisotropy in the basal plane. The mathematical treatment of the curves along the [110] and [001] directions for hydride at the temperature T = 4.2 K with the use of formula (11) leads to the following constants: $K_1 = -1.52 \times 10^7$ erg/cm^3, $(K_2 - K_2') = -1.96 \times 10^7$ erg/cm^3, and $(K_3 - K_3') = 2.05 \times 10^7$ erg/cm^3.

With the above results, we now consider Fig. 3 in more detail. It is seen from Fig. 3 that the magnetization curves for $HoFe_{11}TiH$ hydride substantially differ from those for the initial $HoFe_{11}Ti$ compound. At T = 300 K, the curves have the form typical of a uniaxial state: the tetragonal axis **c** is the easy magnetization axis, and the [110] and [100] axes in the basal plane are the hard magnetization axes. Upon cooling below 140 K, the curves transform due to the spin reorientation. A further decrease in the temperature brings about a change in the direction of the easy and hard magnetization axes (Fig. 3); namely, at T < 80 K, the [110] axis lying in the basal plane becomes the easy magnetization axis. Therefore, the magnetic anisotropy radically changes in character, which can be explained by the formation of a cone structure in the $HoFe_{11}TiH$ hydride in the low-temperature range. As shown above, the hydrogenation leads to the change not only in the magnitude of the first-order magnetic anisotropy constant K_1, but in its sign as well. The absence of saturation in the $\sigma(H)$ curves along the [110] and [100] directions at T = 4.2 K is associated with the rotation of the magnetic moment from the position corresponding to local minima of the magnetic anisotropy energy toward the direction of the magnetic field.

The curves of the mechanical torque moments $L(\theta)$ measured over a wide range of temperatures made it possible to determine the spin reorientation temperature T_{SR} = 140 K for $HoFe_{11}TiH$. The experimental curves $L(\theta)$ measured in the (010) plane at different temperatures in the field H = 13 kOe are depicted in Fig. 4. At T = 300 K, the crystallographic directions [001] (L = 0 and $\partial L/\partial\theta < 0$) and [110] ($L$ = 0 and $\partial L/\partial\theta > 0$) are the easy and hard magnetization axes, respectively. As the temperature decreases below T_{SR} = 140 K, the spin-reorientation transition takes place as evidenced by the appearance of additional maxima and minima near the [001] direction. The character of the $L(\theta)$ curves indicates the presence of the EMA–EMA cone second-order phase transition with a decrease in the temperature.

Therefore, analysis of the magnetization curves $\sigma(H)$ in the temperature range 4.2–300 K also indicates that, as the temperature T decreases below 140 K, the magnetic anisotropy constant K_1 changes sign ($K_1 > 0$ at $T > T_{SR}$ and $K_1 < 0$ at $T < T_{SR}$) and the [110] direction becomes the easy magnetization axis. In $HoFe_{11}TiH$ hydride, the threshold fields are absent and, what is particularly important, the [001] direction at T < 80 K is not the easy magnetization direction. Furthermore, the results obtained demonstrate that the magnetic anisotropy in the basal plane (001) upon cooling very strongly increases, becomes equal, and, likely, even exceeds the anisotropy in the (110) plane.

Thus, the complex investigation performed allows us to argue that the cooling of the $HoFe_{11}TiH$ hydride actually leads to the EMA–EMA cone spin-reorientation transition. The main magnetic characteristics (Curie temperature, saturation magnetization, and the spin-reorientation transition temperature) for $HoFe_{11}Ti$ and its hydride are presented in Table 3.

3.3. Effect of hydrogenation on the magnetic anisotropy of the $ErFe_{11}Ti$ compound. The magnetic properties of $ErFe_{11}Ti$ single crystals in fields up to 12 kOe were previously studied by Andreev *et al.* [17]. The magnetic properties of $ErFe_{11}Ti$ and $ErFe_{11}TiH$ powder samples oriented in magnetic fields as high as 240 kOe were investigated by Isnard and Guillot [18].

Table 3. Magnetic data for the $HoFe_{11}Ti$ single crystal and its hydride

Composition	σ_S, emu/g		T_C, K	T_{SR}, K	Easy magnetization direction	
	4.2 K	300 K			4.2 K	300 K
$HoFe_{11}Ti$	75.2	76.5	518	–	**c** axis	**c** axis
$HoFe_{11}TiH$	83.3	93	561	140	EMA cone	**c** axis

Table 4. Structural and magnetic properties of the $ErFe_{11}Ti$ single crystal and its hydride

Composition	a, Å	c, Å	c/a	V, Å^3	$\Delta V/V$, %	T_C, K	σ_S, emu/g		T_{SR}, K
							295 K	77 K	
$ErFe_{11}Ti$	8.480	4.775	0.563	343.4	–	515	96	81	50
$ErFe_{11}TiH$	8.507	4.781	0.562	346.0	0.8	563	99	86	41

The purpose of our investigation is to study the magnetic properties of the $ErFe_{11}Ti$ and $ErFe_{11}TiH$ single crystals in magnetic fields up to 140 kOe in the low-temperature range 4.2–100 K. The structural and main magnetic characteristics obtained in our work for these samples are given in Table 4.

Figure 5 shows the magnetization isotherms for the $ErFe_{11}Ti$ single crystal at different crystallographic directions. It is seen that the [001] direction is the easy magnetization axis. The magnetization curves $\sigma(H)$ along the [100] and [110] axes are strongly nonlinear in character and have inflection points in the field range $H \sim 10$ kOe. The inflection points can be explained by the presence of magnetic moment projection onto the basal plane in the absence of field, i.e., by the occurrence of a cone of the easy magnetization axis. As the temperature increases, the $\sigma(H)$ curve becomes more linear, which indicates a decrease in the moment projection onto the basal plane upon heating. The data obtained earlier by Andreev *et al.* [17] demonstrate the transformation of the easy magnetization cone into the easy magnetization axis at $T > 60$ K. This statement does not contradict our experimental data. The magnetic anisotropy constants for the $ErFe_{11}Ti$ compound, which were determined according to the technique described in [9], are as follows: $K_1 = -4.6 \times 10^7$ erg/cm^3 and $K_2 = 18.4 \times 10^7$ erg/cm^3.

In order to determine more exactly the spin-reorientation transition temperature, the temperature dependences of the susceptibility were studied for the initial $ErFe_{11}Ti$ compound and its hydride [19]. The results of measurements are listed in Table 4, from which it can be seen that the hydrogenation leads to the shift in the transition temperature toward the low-temperature range.

The hydrogenation of $ErFe_{11}Ti$ results in an increase in the magnetic anisotropy of the single crystal. The hydrogenation produces the strongest effect on the magnetic anisotropy constant K_1 ($K_1 = -3.67 \times 10^7$ erg/cm^3), whereas the change in the constant $K_2 = 18.3 \times 10^7$ erg/cm^3 is insignificant. The cone of the easy magnetization axes is clearly observed in the $\sigma(H)$ curves at $T = 4.2$ K, which manifests itself in the presence of the spontaneous magnetic moment component not only along the [001] axis, but along the [110] and [100] axes as well. These spontaneous moments can be found by the extrapolation of the $\sigma(H)$ curves to $H \longrightarrow 0$. The apex angle of the cone can be defined as $2\theta_0 = 2\arctan(\sigma_{0\|}/\sigma_{0\perp})$, where $\sigma_{0\|}$ and $\sigma_{0\perp}$ are the spontaneous magnetic moments measured along the tetragonal axis and in the basal plane. For the $ErFe_{11}Ti$ compound at $T = 4.2$ K, $\theta_0 = 22°$, the hydrogenation brings about a decrease in the apex angle of the cone and the θ_0 angle becomes equal to 18°. Our magnetic data enable us to conclude that the cone structure in $ErFe_{11}Ti$ hydride is formed at a lower temperature, namely, at $T \approx 40$ K, which is in agreement with the experimental data on the magnetic susceptibility measured for the same single crystals [19].

The results of the measurements performed make it possible to construct the magnetic phase diagrams for the $RFe_{11}Ti$ (R = Lu, Ho, and Er) single crystals (Fig. 6). As can be seen, the $LuFe_{11}Ti$ and $LuFe_{11}TiH$ compounds are the uniaxial magnets. The hydrogenation leads to an enhancement in the uniaxial magnetic anisotropy of the iron sublattice. In the $HoFe_{11}Ti$ compound, the spin-reorientation transition is not observed and the **c** axis is the easy magnetization axis over the entire studied temperature range of magnetic ordering. By contrast, for the $ErFe_{11}Ti$ compound, an increase in the temperature results in the EMA cone–EMA spin-reorientation transition at $T_{SR} = 50$ K. At 4.2 K, the calculated contribution of the rare-earth sublattice to the K_1 constant is positive for holmium ($K_{1Ho} > 0$) and negative for erbium ($K_{1Er} < 0$). According to the single-ion anisotropy model for the $RFe_{11}Ti$ compounds with R = Sm, Tm, Nd, Tb, and Dy, the sign of the K_{1R} constant coincides with the sign of the Stevens factor α_J. For the

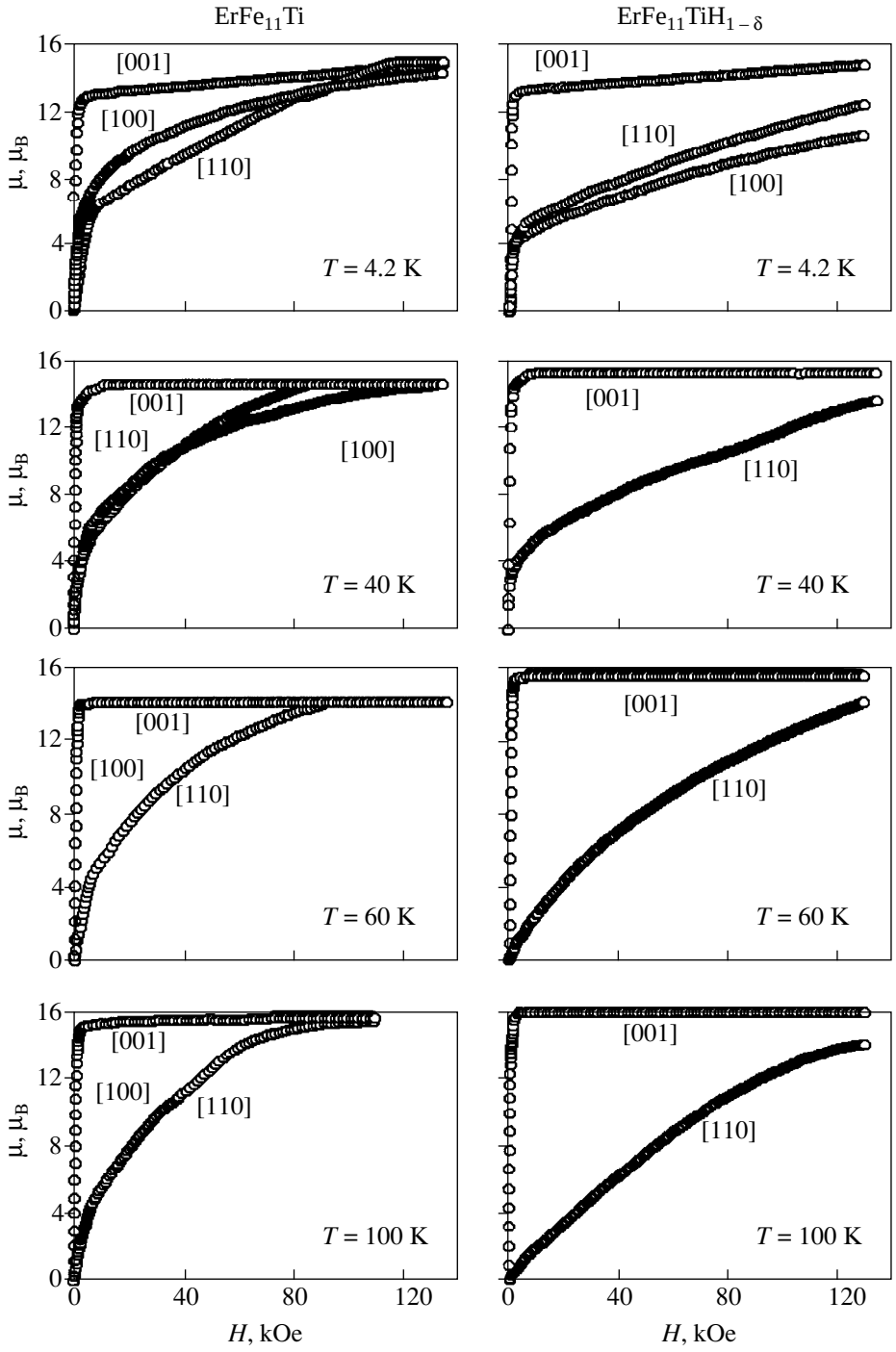

Fig. 5. Magnetization curves for the $ErFe_{11}Ti$ and $ErFe_{11}TiH$ single crystals along the [001], [110], and [100] crystallographic directions at different temperatures.

$HoFe_{11}Ti$ and $ErFe_{11}Ti$ compounds studied in the present work, the contributions from the Ho^{3+} ($\alpha_J < 0$) and Er^{3+} ($\alpha_J > 0$) ions to the K_{1R} constant are opposite in sign to the Stevens factor. This can be explained by the fact that the crystal field potential affecting the Ho and Er rare-earth ions is considerably contributed by the magnetocrystalline interaction parameters of orders higher than the second order. As a consequence, the magnitude of the magnetic anisotropy constant K_2 at low temperatures appears to be larger than that of the K_1 constant and the cone structure is formed at $T < 50$ K in $ErFe_{11}Ti$. The hydrogenation leads to an increase in the magnetic anisotropy of the iron sublattice. However, the hydrogenation exerts even a stronger effect on the magnetic anisotropy of the rare-earth sublattice and brings about a substantial change in the K_1 and K_2 mag-

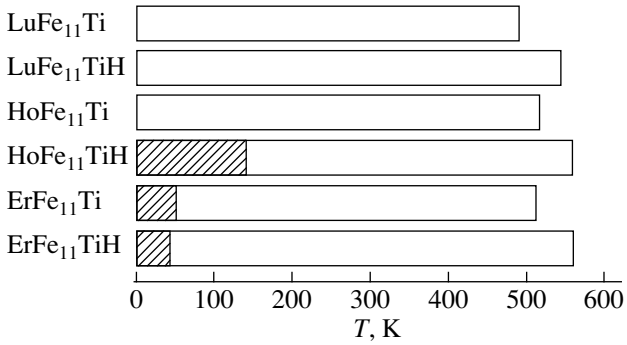

Fig. 6. Magnetic phase diagrams for the RFe$_{11}$Ti (R = Lu, Ho, and Er) compounds and their hydrides. Hatched regions correspond to the EMA cone, and $M \parallel \mathbf{c}$ in nonhatched regions.

netic anisotropy constants (including the change in sign of the K_1 constant for HoFe$_{11}$Ti) and also, likely, the corresponding change in the magnetocrystalline interaction parameters. As a result of hydrogenation, the HoFe$_{11}$TiH compound upon heating undergoes the EMA cone–EMA spin-reorientation transition at T_{SR} = 140 K. Upon hydrogenation of ErFe$_{11}$TiH, the region of the uniaxial states increases and the spin-reorientation transition is shifted toward the low-temperature range (T_{SR} = 41 K).

All these changes occur against the background of an increase in the atomic volume, on average, by ~1.2% (even though the deviations from this value are observed depending on the sort of rare-earth metal). They could be attributed to a change in the distance between iron and rare-earth metal atoms. However, the data on the effect of hydrostatic pressure on the magnetic anisotropy constants for the HoFe$_{11}$Ti compound demonstrate that the quantity $\partial K/\partial p$ is close to zero [20]. Therefore, it can be inferred that changes in the atomic volume and the axial ratio c/a cannot lead to the observed effects, such as the change in sign of the magnetic anisotropy constant upon hydrogenation. This effect is predominantly contributed by the change in the crystal field, specifically in the electric field gradient at the rare-earth ion site, upon introduction of hydrogen into the crystalline lattice. These fields act on the anisotropic 4f subshell with a nonzero orbital angular momentum and a nonzero quadrupole moment in the case of Ho and Er rare-earth ions. As is known, hydrogen atoms in the RFe$_{11}$Ti crystal lattice (a tetragonal structure of the ThMn$_{12}$ type) occupy octahedral holes (at $x \leq 1$) located on the **c** axis, which induces additional electric fields acting on rare-earth ions.

The interstitial atoms modify the contributions to the electric field gradient, which are associated with the change in the interaction of the 4f electron subshell with surrounding ions and also with $5s^2 5p^6$ valence and conduction electrons [14, 15].

ACKNOWLEDGMENTS

We are grateful to V.N. Verbetsky and A.A. Salamova for the hydrogenation of single crystals.

This work was supported by the State Program of Support for Leading Scientific Schools of the Russian Federation (project no. 00-15-96695) and the Russian Foundation for Basic Research (project no. 99-02-17821).

REFERENCES

1. K. Yu. Guslienko, X. C. Kou, and R. Grossinger, J. Magn. Magn. Mater. **150**, 383 (1995).
2. B.-P. Hu, H.-S. Li, and J. M. D. Coey, Phys. Rev. B **41** (4), 2221 (1990).
3. A. V. Andreev, N. V. Kudrevatykh, S. M. Razgonyaev, and E. N. Tarasov, Physica B (Amsterdam) **183**, 379 (1993).
4. C. Abadia, P. A. Algarabel, B. García-Landa, *et al.*, J. Phys.: Condens. Matter **10**, 349 (1998).
5. I. S. Tereshina, I. V. Telegina, and K. P. Skokov, Fiz. Tverd. Tela (St. Petersburg) **40** (4), 699 (1998) [Phys. Solid State **40**, 643 (1998)].
6. I. S. Tereshina, S. A. Nikitin, T. I. Ivanova, and K. P. Skokov, J. Alloys Compd. **275–277**, 625 (1998).
7. S. A. Nikitin, I. S. Tereshina, V. N. Verbetsky, and A. A. Salamova, Fiz. Tverd. Tela (St. Petersburg) **40** (2), 285 (1998) [Phys. Solid State **40**, 258 (1998)].
8. O. Isnard, S. Miraglia, M. Guillot, and D. Fruchart, J. Alloys Compd. **275–277**, 637 (1998).
9. G. Asti and F. Bolzoni, J. Magn. Magn. Mater. **20**, 29 (1980).
10. Y.-C. Yang, H. Sun, and L.-S. Kong, J. Appl. Phys. **64** (10), 5968 (1988).
11. J. M. D. Coey, H. Sun, and D. P. E. Hurley, J. Magn. Magn. Mater. **101**, 301 (1991).
12. F. Bolzoni, J. P. Gavigan, D. Givord, *et al.*, J. Magn. Magn. Mater. **66**, 158 (1987).
13. D. Fruchart and S. Miraglia, J. Appl. Phys. **69** (8), 5578 (1991).
14. R. Coehoorn and K. H. J. Buschow, J. Appl. Phys. **69** (8), 5590 (1991).
15. V. Yu. Irkhin and Yu. P. Irkhin, Phys. Rev. B **57** (11), 2697 (1998).
16. A. I. Mitsek, N. P. Kolmakova, and D. I. Sirota, Fiz. Met. Metalloved. **38** (1), 35 (1974).
17. A. V. Andreev, V. Sechovsky, N. V. Kudrevatykh, *et al.*, J. Less-Common Met. **144**, L21 (1988).
18. O. Isnard and M. J. Guillot, J. Appl. Phys. **83** (11), 6730 (1998).
19. I. S. Tereshina, S. A. Nikitin, V. N. Verbetsky, *et al.*, in *Abstracts of the VI International Conference "Hydrogen Materials Science and Chemistry of Metal Hydrides," Katsively, Yalta, Ukraine, 1999*, p. 144.
20. Z. Arnold, J. Kamarad, O. Mikulina, *et al.*, J. Magn. Magn. Mater. **196–197**, 748 (1999).

Translated by O. Borovik-Romanova

Physics of the Solid State, Vol. 43, No. 2, 2001, pp. 300–304. Translated from Fizika Tverdogo Tela, Vol. 43, No. 2, 2001, pp. 289–292.

MAGNETISM AND FERROELECTRICITY

Components of the Low-Temperature Heat Capacity of Rare-Earth Hexaborides

V. V. Novikov

Bryansk State Pedagogical University, ul. Bezhitskaya 14, Bryansk, 241036 Russia

Received January 24, 2000; in final form, June, 23, 2000

Abstract—The temperature dependence of heat capacity $C_p(T)$ was studied for nine rare-earth hexaborides MB_6 (M = La, Ce, Pr, Nd, Sm, Eu, Gd, Tb, and Dy) at temperatures of 5–300 K. Using the correspondence principle for lattice heat capacities of isostructural compounds, the lattice contribution $C_1(T)$ and the excess contribution $\Delta C(T)$ to the heat capacity of the hexaborides were determined. The lattice heat capacity $C_1(T)$ is represented as the sum of the Debye contributions of the metal and boron sublattices: $C_1(T) = C_M(T) + 6C_B(T)$. The Debye temperatures θ_M and θ_B of the metal and boron sublattices were determined. The anomalies in the excess heat capacity $\Delta C(T) = C_p(T) - C_1(T)$ are related to the magnetic ordering effects, the Schottky contribution, and the Jahn–Teller effect. © *2001 MAIK "Nauka/Interperiodica".*

INTRODUCTION

One of the main problems in studying the heat capacity of magnets is the separation of the various contributions to the total heat capacity. In the general case, the total heat capacity of a magnet is written as the sum of lattice (C_l), electron (C_e), nuclear (C_n), ferro- or antiferromagnetic (C_f or C_{af}), and paramagnetic (C_{pm}) contributions [1], to which a contribution from an anharmonic component (C_α) is added at high temperatures.

The contribution from free electrons $C_e(T)$ linearly changes with temperature in a wide temperature range. The other contributions to heat capacity at high temperatures are complex functions of the temperature. Therefore, in order to separate the total heat capacity into the lattice and excess components, the method of the correspondence of lattice heat capacities of isostructural compounds [2, 3] is frequently used. In the simplified version of this method, the lattice heat capacities are assumed to be proportional to the molar masses. Peysson *et al.* [4] compared the calculated Debye heat capacities of CeB_6 and of nonmagnetic LaB_6 to determine excess (magnetic) heat capacity.

RESULTS AND DISCUSSION

In this paper, we made an attempt to separate the lattice and the excess components of the heat capacities of nine rare-earth hexaborides MB_6 (M = La, Ce, Pr, Nd, Sm, Eu, Gd, Tb, and Dy) at temperatures of 5–300 K, as well as to determine the contributions of the metal and boron sublattices to the excess heat capacity of these hexaborides.

In Fig. 1, our experimental data [5–12] on the heat capacities $C_p(T)$ of the above nine hexaborides are compared with the data of other investigators [4, 13–17]. Note the following characteristic features in the $C_p(T)$ curves: (i) the existence of anomalies in $C_p(T)$ at low temperatures (except for SmB_6 and LaB_6), which have a complex form in some hexaborides; and (ii) the close-to-linear course of the $C_p(T)$ curves at enhanced temperatures.

The separation of the lattice component of the heat capacity was performed on the assumption that at room temperature, all the contributions to the heat capacity of hexaborides, except for the lattice one, are negligibly small and that the heat capacity of LaB_6 contains only a lattice component in the entire temperature range investigated [18]. Following [3], we assume that the lattice heat capacities of isostructural compounds represent identical functions of the thermodynamic and Debye temperatures $f(\theta/T)$. The ratio of the characteristic temperatures of the lanthanum hexaboride and the hexaboride of any other rare-earth metal at room temperature,

$$\theta_{LaB_6}(300\ \mathrm{K})/\theta_{MB_6}(300\ \mathrm{K}) = r,$$

is assumed to be constant for a given hexaboride in the whole temperature range investigated. The Debye temperatures of the hexaborides at 300 K and the corresponding values of r are given in the table. From the relation

$$\theta_{MB_6}(T) = \theta_{LaB_6}(T)/r$$

1063-7834/01/4302-0300$21.00

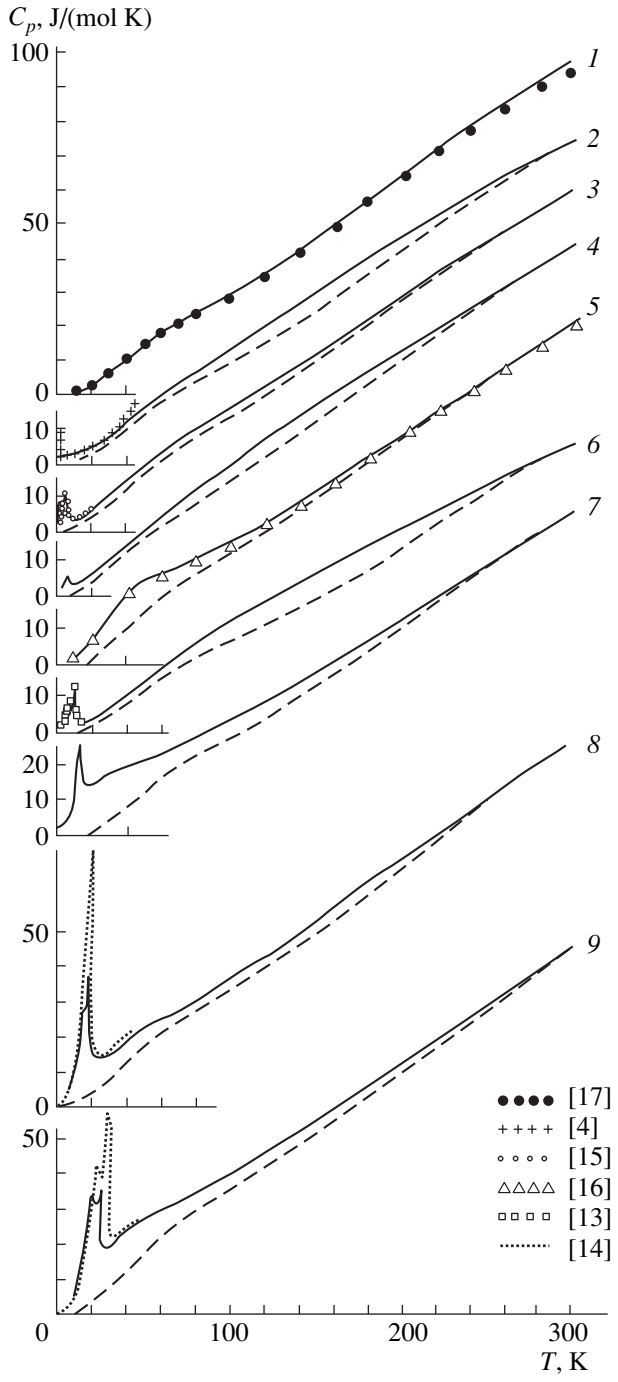

Fig. 1. Molar heat capacity $C_p(T)$ of rare-earth hexaborides: (*1*) lanthanum; (*2*) cerium; (*3*) praseodymium; (*4*) neodymium; (*5*) samarium; (*6*) europium; (*7*) gadolinium; (*8*) terbium; and (*9*) dysprosium. Solid lines, our data [5–12]; dashed lines, the lattice contributions to heat capacities; data points, borrowed from [4, 13–17].

and tabulated Debye functions [19], we determined the temperature variations of the lattice heat capacities $C_l(T)$ of the hexaborides in the range of 5–300 K (Fig. 1).

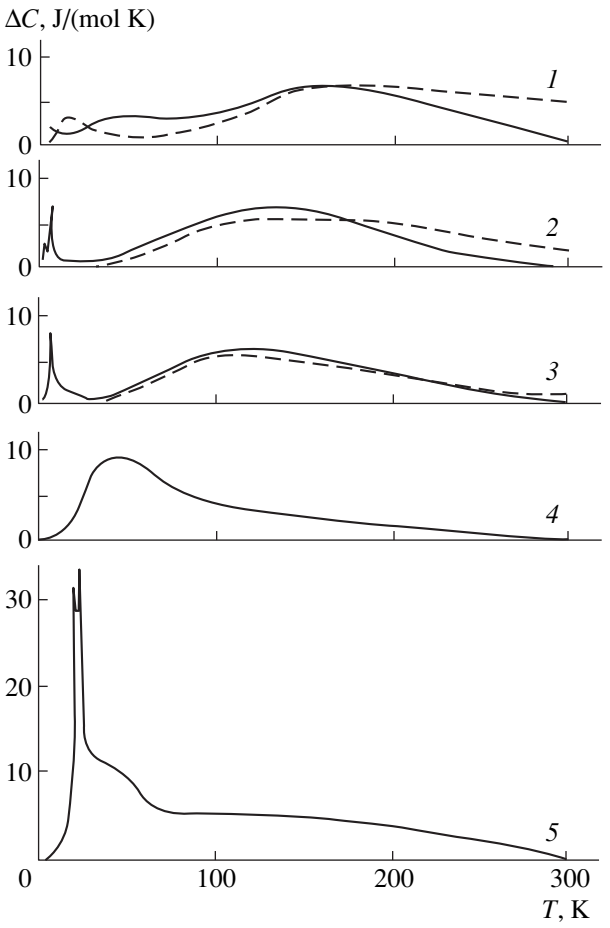

Fig. 2. Excess heat capacities $\Delta C = C - C_l$ of some rare-earth hexaborides: (*1*) cerium; (*2*) praseodymium; (*3*) neodymium; (*4*) samarium; and (*5*) dysprosium. Dashed lines correspond to the calculated Schottky contributions.

By subtracting the lattice components from the total heat capacities, we determined the temperature dependence of the excess heat capacities of the hexaborides:

$$\Delta C(T) = C(T) - C_l(T).$$

Figure 2 displays typical dependences $\Delta C(T)$ for some hexaborides.

The sharp anomalies in the $\Delta C(T)$ curves at low temperatures are due to processes of magnetic ordering.

The diffuse maxima in the region of moderate temperatures (100–200 K, see Fig. 2) represent the Schottky contributions. The dashed lines in the figure correspond to the calculated Schottky heat capacities of CeB_6, NdB_6, and PrB_6 according to the data of [20, 21] on the splitting of energy levels by the crystal electric field [11].

The anomalies near 30–40 K in the $\Delta C(T)$ curves of DyB_6 (Fig. 2) and GdB_6 and TbB_6 (not given in the figure) appear to be due to the Jahn–Teller effect [22].

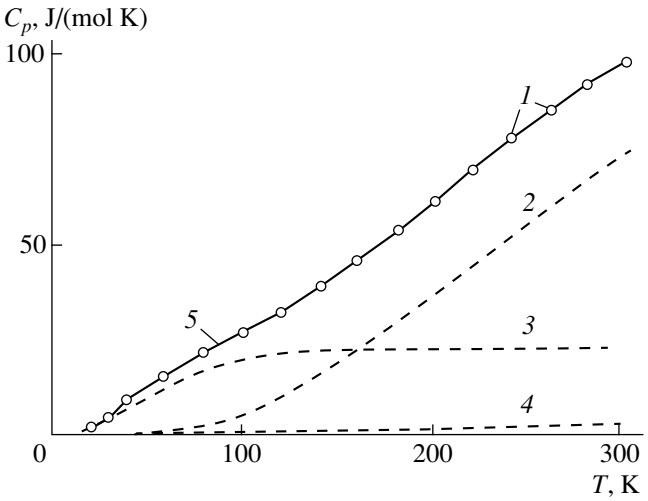

Fig. 3. Heat capacity of the lanthanum hexaboride: (*1*) experimental values of $C_p(T)$; (*2–4*) calculated temperature dependences of the heat capacities of the boron sublattice $6C_B$, lanthanum sublattice C_{La}, and electron gas C_e, respectively; and (*5*) the total calculated heat capacity $C_{La} + 6C_B + C_e$.

The anomalies of the temperature dependences of the excess heat capacity $\Delta C(T)$ of the hexaborides will be considered in our future publications.

The molar lattice heat capacity of a hexaboride is written as the sum of Debye heat capacities of the metal and boron sublattices:

$$C_{MB_6}(T) = C_M(T) + 6C_B(T).$$

The characteristic temperature of the boron sublattice θ_B was determined from the value of the gram-atomic heat capacity at $T = 300$ K:

$$C_B(300\ \text{K}) = \frac{1}{6}[C_l(300\ \text{K}) - 0.98 \cdot 3R].$$

Here, $C_l(300\ \text{K})$ is the total lattice heat capacity of a hexaboride at $T = 300$ K. From it, the heat capacity of the metal sublattice is subtracted, whose magnitude at $T = 300$ K is assumed to be close to the DuLong's one.

The characteristic temperature $\theta_M(T)$ of the metal sublattice is determined by the extrapolation (to absolute zero) of the $\theta_M(T)$ dependence in the region of 5–100 K obtained from the temperature dependence of the heat capacity of the metal sublattice:

$$C_M(T) = C_l(T) - 6C_B(T).$$

The thus-obtained magnitudes of the characteristic Debye temperatures of the metal (θ_M) and boron (θ_B) sublattices are listed in the table. It can be seen that, for all the hexaborides studied, the values of θ_M are close to one another.

As an example, Fig. 3 shows the temperature dependences of the heat capacities of the lanthanum and boron sublattices in LaB_6 calculated from the obtained values of θ_{La} and θ_B, as well as the total calculated heat capacity of lanthanum hexaboride with allowance for the contribution of free electrons. As is seen from the figure, the calculated magnitudes satisfactorily agree with the experimental ones. Figure 4 shows experimental $C_p(T)$ curves for the lanthanum, neodymium, samarium, and gadolinium hexaborides for the temperature range of 5–1000 K according to [23, 24] and the calculated dependences

$$C_{MB_6}(T) = C_M(T) + 6C_B(T) + C_e(T) + C_\alpha(T)$$

for these hexaborides. It was assumed that the magnitudes of the electron contributions $C_e(T)$ to the heat capacity of lanthanum hexaboride and to that of rare-earth metals are identical and are equal to $C_e(T) = 2.5 \times 10^{-3}$ T [8]. The contribution to the heat capacity caused by thermal expansion was calculated for all the hexaborides by the relation $C_\alpha(T) = 3\alpha C_p T/a$, where α is the thermal expansion coefficient of LaB_6 equal to 5×10^{-6} K^{-1} [6] and a is a constant equal to 0.74 [25]. As is seen from the figure, the calculated $C_p(T)$ curves satisfactorily agree with the experimental data.

Note that the magnitudes of θ_B in the approach assumed prove to be somewhat underestimated, since they are obtained without allowance for the Schottky contribution to the heat capacity of the hexaborides at $T = 300$ K. The Schottky heat capacity for CeB_6, NdB_6, and PrB_6 (Fig. 2) at $T = 300$ K is 1–4 J/(mol K). Neglect

Characteristic temperatures of rare-earth hexaborides $\theta_{MB_6}(300\ \text{K})$ at $T = 300$ K, Debye temperatures of the metal (θ_M) and boron (θ_B) sublattices, and the Debye temperature ratios $r = \theta_{LaB_6}(300\ \text{K})/\theta_{MB_6}(300\ \text{K})$

Compound	LaB_6	CeB_6	PrB_6	NdB_6	SmB_6	EuB_6	GdB_6	TbB_6	DyB_6
θ_{MB_6}, K	1085	1140	1080	1044	1065	1220	1113	990	970
r	1	0.9518	1.005	1.039	1.019	0.8893	0.9748	1.096	1.119
θ_M, K	205	203	210	200	210	198	212	207	208
θ_B, K	1230	1293	1218	1170	1200	1383	1254	1025	1074

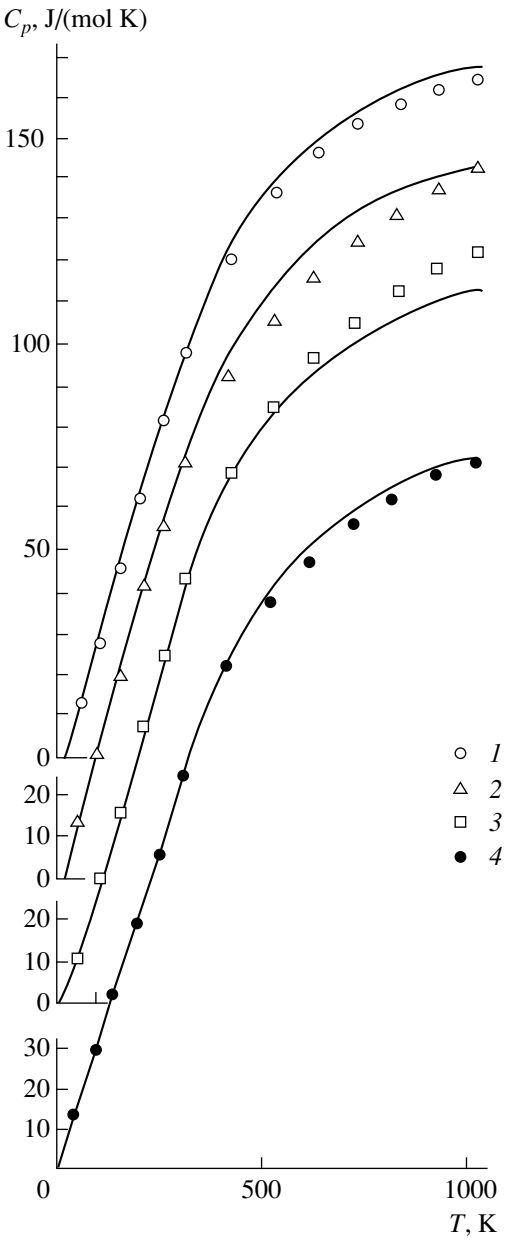

Fig. 4. Heat capacities of some rare-earth hexaborides in a range of 5–1000 K: (*1*) lanthanum; (*2*) neodymium; (*3*) amarium; and (*4*) gadolinium. Solid lines represent calculated curves; (*1–4*) experimental values (below 300 K, they only include the lattice part of heat capacity).

of the Schottky contribution leads to an underestimation of θ_{MB_6}(300 K) by 15–30 K and of θ_B by 20–50 K. Therefore, at T = 1000 K, the calculated values of $6C_B$ and, consequently, C_{MB_6} prove to be overestimated by 0.5–1.5 J/(mol K). This value is less than the error of determining heat capacity near T = 1000 K and can be neglected. The magnitude $\Delta\theta_B = \pm 150$ K should, apparently, be regarded as the absolute error of θ_B magnitudes listed in the table.

CONCLUSION

The main results of this work are as follows: (a) the lattice contribution to the heat capacity of rare-earth hexaborides can be separated from the total heat capacity on the basis of the correspondence principle for the lattice heat capacities of isostructural compounds; (b) at temperatures of 5–1000 K, the heat capacity of the crystal lattice of rare-earth hexaborides can be represented as the sum of contributions of noninteracting Debye sublattices of a metal and boron; and (c) using the characteristic temperatures of the sublattices θ_M and θ_B, one can calculate the lattice heat capacity of rare-earth hexaborides to temperatures of up to 1000 K.

ACKNOWLEDGMENTS

This work was supported in part by the Ministry of General and Special Education of the Russian Federation, project no. 79-5-1.1-25.

REFERENCES

1. K. P. Belov, *Magnetothermal Phenomena in Rare-Earth Magnets* (Nauka, Moscow, 1990).
2. R. Carlin, *Magnetochemistry* (Springer, Heidelberg, 1986; Mir, Moscow, 1989).
3. J. M. Stout and E. Katalano, J. Chem. Phys. **23** (11), 2013 (1995).
4. Y. Peysson, C. Ayache, J. Rossat-Mignod, *et al.*, J. Phys. (Paris) **47**, 113 (1986).
5. N. N. Sirota, V. V. Novikov, and S. V. Antipov, Izv. Ross. Akad. Nauk, Neorg. Mater. **34** (9), 1086 (1998).
6. N. N. Sirota, V. V. Novikov, V. A. Vinokurov, and Yu. B. Paderno, Fiz. Tverd. Tela (St. Petersburg) **40** (11), 91 (1998) [Phys. Solid State **40**, 1856 (1998)].
7. N. N. Sirota, V. V. Novikov, V. A. Vinokurov, and L. V. Batova, Zh. Fiz. Khim. **73** (3), 432 (1999).
8. N. N. Sirota, V. V. Novikov, V. A. Vinokurov, and Yu. B. Paderno, Zh. Fiz. Khim. **72** (11), 1967 (1998).
9. N. N. Sirota and V. V. Novikov, J. Mater. Process. Manuf. Sci. **7** (1), 111 (1998).
10. N. N. Sirota and V. V. Novikov, Zh. Fiz. Khim. **74** (2), 333 (2000).
11. V. V. Novikov, Zh. Fiz. Khim. **74** (10), 1710 (2000).
12. N. N. Sirota, V. V. Novikov, and V. A. Vinokurov, Zh. Fiz. Khim. **74** (10), 1924 (2000).
13. T. Fujita, M. Suzuki, and Y. Isikawa, Solid State Commun. **33** (9), 947 (1980).
14. K. Segawa, A. Tomita, K. Iwashita, *et al.*, J. Magn. Magn. Mater. **104**, 1233 (1992).
15. C. M. McCarthy, C. W. Tompson, R. J. Graves, *et al.*, Solid State Commun. **36**, 861 (1980).
16. E. S. Konovalova, Yu. B. Paderno, V. E. Yachmenev, and E. M. Dudnik, Izv. Akad. Nauk SSSR, Neorg. Mater. **14** (12), 2191 (1978).
17. H. G. Smith, G. Dooling, S. Kunii, *et al.*, Solid State Commun. **53** (1), 15 (1985).

18. Yu. B. Paderno and N. Yu. Shitsevalova, in *Borides*, Preprint No. 1, Akad. Nauk Ukr. SSR, Inst. Problem Materialovedeniya im. I.N. Frantsevicha (Frantsevich Institute of Materials Science Problems, National Academy of Sciences of Ukraine, Kiev, 1990), p. 1.
19. N. N. Sirota, *Thermodynamics and Statistical Physics* (Vyshéĭshaya Shkola, Minsk, 1969).
20. M. Loewenhaupt and M. Prager, Z. Phys. B **62**, 195 (1986).
21. E. Zirngiebl, B. Hillebrands, S. Blumenröder, *et al.*, Phys. Rev. B: Condens. Matter **30** (7), 4052 (1984).
22. S. Nakamura, T. Goto, S. Kunii, *et al.*, J. Phys. Soc. Jpn. **63** (2), 623 (1994).
23. T. Fujita, M. Suzuki, T. Komatsubara, *et al.*, Solid State Commun. **35**, 1589 (1980).
24. A. S. Bolgar and V. B. Muratov, Zh. Fiz. Khim. **62** (7), 1771 (1988).
25. S. P. Gordienko, Poroshk. Metall., No. 1 (217), 83 (1981).

Translated by S. Gorin

Physics of the Solid State, Vol. 43, No. 2, 2001, pp. 305–308. Translated from Fizika Tverdogo Tela, Vol. 43, No. 2, 2001, pp. 293–296.

MAGNETISM AND FERROELECTRICITY

Relaxation Nature of a Current Settling upon the Application of an Electric Voltage in $LaMnO_3$ Crystals

M. K. Gubkin, T. M. Perekalina, A. M. Balbashov*, V. V. Kireev, and S. V. Pushko

Shubnikov Institute of Crystallography, Russian Academy of Sciences, Leninskiĭ pr. 59, Moscow, 117333 Russia

** Moscow Power Institute, Krasnokazarmennaya ul. 14, Moscow, 111250 Russia*

e-mail: gubkin@ns.crys.ras.ru

Received June 26, 2000

Abstract—The electrical conductivity of $LaMnO_3$ crystals was measured at room temperature to determine that the transition to a stable magnitude of electric current corresponding to the applied voltage has a relaxational nature with a characteristic time of about 10 min. The steady-state value of the current depends on the preceding voltage applied to the sample. The effect was observed in both dc and ac measurements. Detailed characterization of the crystals was performed using magnetic and x-ray methods. *© 2001 MAIK "Nauka/Interperiodica".*

INTRODUCTION

Lanthanum manganite-based perovskite-like compounds $La_{1-x}A_xMnO_3$ (where A are usually divalent ions Ca^{2+} or Sr^{2+}) are of great interest because of the effect of giant magnetoresistance [1, 2], which is promising for applied microelectronics. Part of the available works is devoted to relaxation phenomena in manganites. Thus, in [3], the relaxation of magnetization (magnetic viscosity) in thin ferromagnetic films of manganites is reported. Fisher *et al.* [4], in their work performed on single crystals of $La_{1-x}A_xMnO_3$, revealed the relaxation of electrical resistivity ρ related to the relaxation of magnetization and suggested a phenomenological explanation of the effect based on the assumption of the magnetically non-single-phase state of the samples. In both cases, relaxation processes were observed upon varying the external magnetic field H. In this work, we studied the resistivity of $LaMnO_3$ single crystals and found the relaxation of ρ upon the application of electric voltage to the sample in the absence of a magnetic field.

Lanthanum manganite $LaMnO_3$ has a perovskite structure that is distorted by Jahn–Teller interactions in the system of Mn^{3+} ions. The exchange interaction in the (100) planes is ferromagnetic; the interaction between these planes is antiferromagnetic. The Néel temperature of $LaMnO_3$, according to different authors, [5–7] varies between 100 and 141 K. In the presence of an overstoichiometric oxygen, part of the Mn^{3+} ions transforms into the tetravalent state; correspondingly, $LaMnO_{3+\delta}$ ($\delta > 0$) acquires an uncompensated magnetic moment. At $\delta = 0.15$, $LaMnO_3$ becomes ferromagnetic. Most authors believe that it is the Zener double exchange [8] that is responsible for the ferromagnetic interaction. The physical properties of stoichiometric $LaMnO_3$ have been studied insufficiently. In the first works in which its magnetic properties were studied, $LaMnO_3$ was assumed to be antiferromagnetic (see, e.g., [8, 9]). However, later, the majority of authors arrived at a conclusion that it exhibits weak ferromagnetism [2, 6]. The electrical properties of $LaMnO_3$ have also not been studied in detail. Urishibara *et al.* [10] reported that it is a semiconductor and only reveals intrinsic conductivity and that the electrical resistivity ρ of pure stoichiometric $LaMnO_3$ at room temperature is 2×10^2 Ω cm. Note that most investigations of physical properties of $LaMnO_3$ were performed on polycrystalline samples.

EXPERIMENTAL

The $LaMnO_3$ samples that were studied in this work were prepared by zone melting using laser heating [11]. Their structure was studied by powder x-ray diffraction and x-ray diffraction topography; they showed the presence of numerous twin boundaries (of six types) characteristic of the orthorhombic structure of $LaMnO_3$ [11]. The sample that has been studied had the shape of a parallelepiped with dimensions of $5 \times 3 \times 6$ mm.

The magnetization of the $LaMnO_3$ crystals were conducted on a vibration-sample magnetometer in a temperature range of 77–300 K in magnetic fields of up to 13 kOe; the measurements of the hf susceptibility were performed by the induction method at a frequency of 20 MHz.

RESULTS AND DISCUSSION

Figure 1 displays the magnetization curve $\sigma(H)$ at 77 K. It can be satisfactorily described by the dependence $\sigma = \sigma_0 + \chi H$ characteristic of the weak ferromagnets, with a residual magnetization $\sigma_0 = 1.9$ emu/g. We

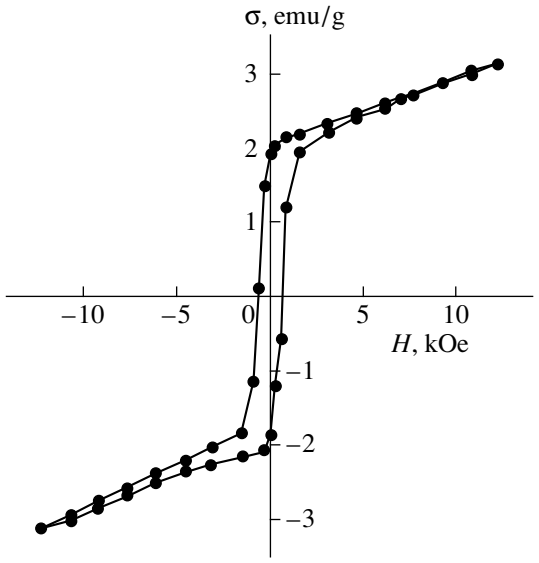

Fig. 1. Magnetization curve $\sigma(H)$ of a $LaMnO_3$ crystal at 77 K.

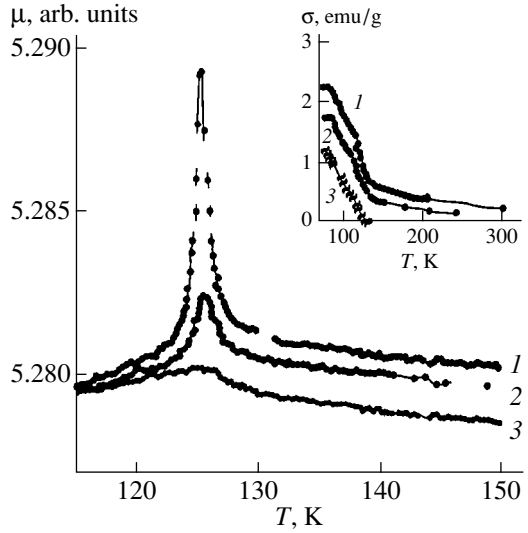

Fig. 2. Temperature dependence of the magnetic permeability μ of an $LaMnO_3$ crystal in different magnetic fields: (*1*) $H = 0$, (*2*) 2, and (*3*) 8 kOe. In the inset, the temperature dependence of the magnetization $\sigma(T)$ is shown in different magnetic fields: (*1*) $H = 6.2$, (*2*) 3, and (*3*) 0 kOe.

observed identical (within the experimental error) magnetization curves for both the plane *ab* and the direction parallel to the *c* axis of the crystal; this is undoubtedly related to the large density of twins (as is seen from [12], where more perfect crystals were used in the investigation, the $LaMnO_3$ crystals possess a significant anisotropy). Figure 2 shows the temperature dependence of the magnetic permeability $\mu(T)$; the inset displays the temperature dependence of the specific magnetization $\sigma(T)$ (all the curves were recorded during heating). Both dependences correspond to three external magnetic fields differing in magnitude. At $T = 126$ K, a sharp peak of the hf susceptibility is observed, which is easily eliminated by a small (in comparison with the characteristic exchange fields) external field. It is precisely at this temperature that the residual magnetization σ_0 vanishes (see curve *3* in the inset). The peak appears to be due to specific features of the process of technical magnetization, i.e., by the motion and rotation (under the effect of the magnetic field) of macroscopic objects ("domains") in a weak ferromagnet. The presence of spontaneous magnetization (which is approximately one-fiftieth of that which would exist upon ferromagnetic ordering of the magnetic moments of the Mn^{3+} ions) is most likely related to the sublattice angularity rather than to the presence of some amount of ferromagnetic inclusions in the antiferromagnetic matrix. The temperature of the disappearance of σ_0 appears to represent the Néel point or is at least close to it.

The electrical resistivity of $LaMnO_3$ crystals was studied by the two-probe technique in both dc and ac (50 Hz) regimes. The contacts located on the opposite faces of a sample were prepared by the evaporation of silver. The estimation of the electrical resistivity, based on the sample dimensions and the configuration of the electrodes, yields values $\rho \sim 10^2\ \Omega$ cm at room temperature. Thus, it would be a sufficiently correct procedure to replace the magnitudes of $R(\Omega)$ by $\rho(\Omega$ cm) in Figs. 3–5. Note that, in the $LaMnO_3$ crystal that was studied in our work, no magnetoresistance was observed in the temperature range of 77–300 K. However, we revealed that, when an electric voltage was applied to the sample, the magnitude of the current corresponding to this voltage was established within a time period of about 10 min rather than immediately. Below, we describe in detail the main features of this process.

Figure 3 displays the variation of the electrical resistance *R* of an $LaMnO_3$ single crystal as a function of the time *t* at a temperature of 290 K upon the application of a constant electric voltage *U*. The voltage *U* was successively increased from 1 to 9 V (curves *1*–*9*, respectively), after which it was successively decreased from 9 to 1 V (curves *8*'–*2*', respectively). The experiment was performed as follows. At time moment $t = 0$, a voltage $U = 1$ V was applied to the sample and the variation of *R* in time was observed for 10 min (the resistance decreased in magnitude and finally reached an approximately constant value at the end of this period). After this, the voltage was increased to 2 V and again the $R(t)$ dependence was measured, etc., until a voltage $U = 9$ V was reached. After application of the voltage $U = 9$ V and measuring the $R(t)$ dependence, the voltage *U* was decreased to 8, 7, …, 1 V and each time measurement of $R(t)$ was performed. In this case, the resistance *R* increased with time (see primed curves in Fig. 3).

In the stable state, i.e., after a 10-min holding of the sample under a constant voltage, the resistances *R* taken from the unprimed curves do not coincide with those taken from the primed curves. The less the differ-

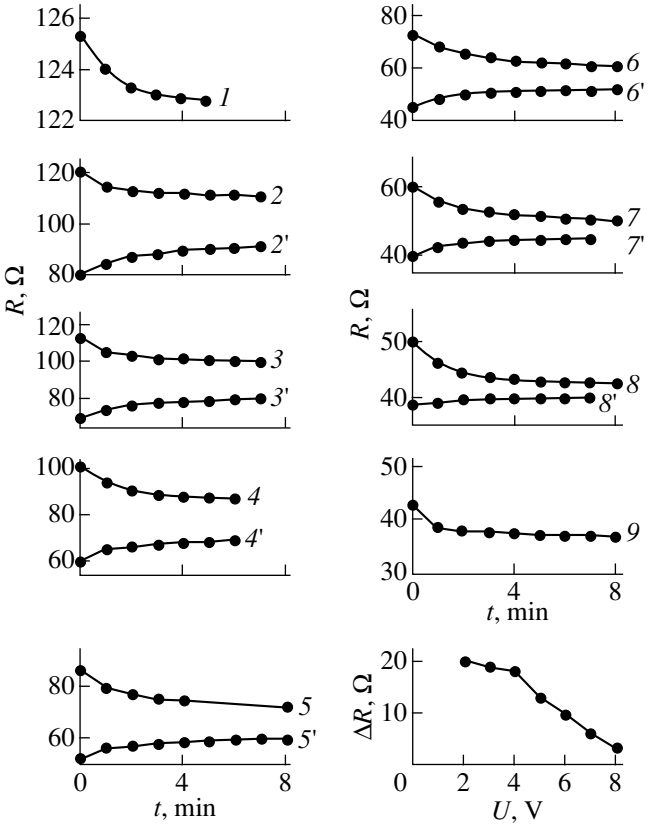

Fig. 3. Time dependences of the electrical resistance R at $T = 290$ K at different values of the applied voltage U. The numerals *1, 2, 3, …, 9* correspond to the voltages 1, 2, 3, …, 9 V, respectively; the unprimed curves were obtained with the voltage being increased; the primed curves correspond to decreasing voltage. ΔR is the difference between the asymptotic (equilibrium) values of R obtained from the primed and unprimed $R(U)$ curves.

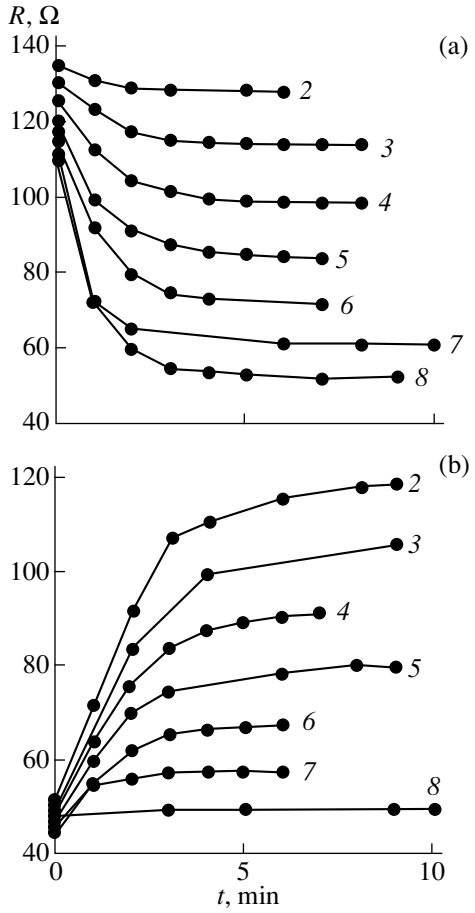

Fig. 4. Time dependences of the electrical resistance R at $T = 290$ K for various sequences of the applied voltage U (see the main text): (a) 1, 8, 1, 7, …, 1, 2 V; and (b) 9, 2, 9, 3, …, 9, 8 V.

ence between the largest applied voltage and the decreased voltage, the less the difference of the resistances ΔR. The $\Delta R(U)$ dependence is shown in the right-hand lower corner of Fig. 3. Even after a much longer holding of the sample under a voltage (30 min), the ΔR difference does not tend to zero.

Figure 4a shows the $R(t)$ dependences for the following experiment. First, a voltage $U = 1$ V is applied to the sample and is kept for the 10 min that are required, as was indicated above, for the sample to acquire a stable value of R. Then, the voltage is increased to 8 V and the resistance variation is measured for ten minutes (curve *8*). After this, the sample is again held at $U = 1$ V until an equilibrium magnitude of R is established and the $R(t)$ dependence is recorded at $U = 7$ V, etc. In other words, the sequence of the voltages applied to the sample was as follows: 1, 8, 1, 7, …, 1, 2 V. A similar experiment was performed using another sequence of voltages applied to the sample, namely, 9, 2, 9, 3, …, 9, 8 V (Fig. 4b). On the basis of these two experiments, we constructed the $R(U)$ dependence for stable values of R, i.e., at $t \sim 10$ min (Fig. 5). It is seen from Fig. 5 that the $R(U)$ dependences for both experiments are similar.

The results of measurements of the $LaMnO_3$ resistance at lower temperatures, in the temperature range of 200–290 K, do not differ qualitatively from the above results. Below 200 K, no time dependence of $R(t)$ was observed.

The "diffuse" times of the "settling" of stable magnitudes of electrical resistance suggest the possible influence of ionic conduction and the formation of a double diffusion layer in the region of the contacts. The ionic conductivity is characteristic of most insulators with a perovskite structure; it is characteristic of the $LaMnO_3$ crystals as well [13]. Therefore, we repeated the above experiments in the ac mode; in this case, the settling time for establishing a stable current is several orders of magnitude greater than the time of the change of the polarity of the applied voltage to the opposite. The $R(t)$ curves that were obtained in this case were quite analogous to those shown in Figs. 2–4. We also used copper electrodes instead of silver; however, the

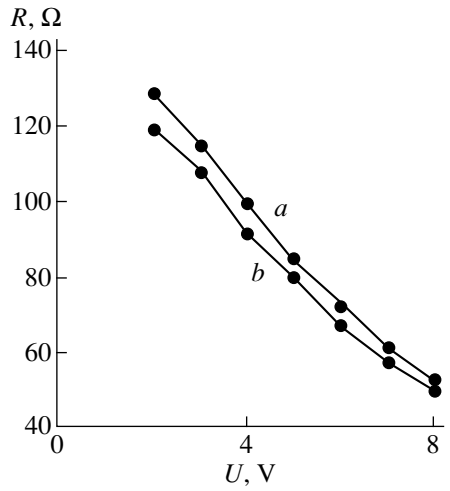

Fig. 5. Stable values of the electrical resistance R at various applied voltages U (T = 290 K) with the voltage (*a*) being successively increased and (*b*) decreased.

change of the electrode material also had no effect on the course of the time dependences of R. Thus, the effect observed cannot be explained by a directional diffusion of ions in an electric field.

Note that all the above curves can be explained merely by the process of settling of the temperature that is varied because of the release of Joule heat in a semiconductor sample upon the passage of an electric current. However, from a comparison of the observed variations of the current with the temperature dependence of the sample resistance (which is activated in nature, with an activation energy of about 0.17 eV), it is seen that the sample temperature should change by 10–15 K in this case. However, the thermocouple fixed directly at the sample exhibited no temperature changes upon current passage.

Finally, there are experimental data [14] that indicate that the passage of a low-frequency alternating electric current through samples of $La_{0.7}Pb_{0.3}MnO_3$ changes their electrical properties (in particular, the microwave conductivity). The nature of this effect is unknown, but Volkov *et al.* [14] suggested a qualitative interpretation based on the concept of the phase separation of magnetic phases in the sample. Therefore, it cannot be ruled out that the relaxation curves that we observed in this work are related to the effect of the flowing electric current on the magnetic homogeneity of $LaMnO_3$.

CONCLUSION

Thus, when studying electrical and magnetic properties of $LaMnO_3$ single crystals, we revealed a relaxational nature of the process of transition to a stable magnitude of current when a constant or alternating voltage was applied to the sample. We failed to find a consistent explanation for the obtained experimental $R(t)$ curves. Additional investigations are required to clarify whether the effect observed is one more manifestation of the complex relation between the charge carriers and magnetic subsystem characteristic of the perovskite-like manganites or if this is a specific consequence of some other factors.

REFERENCES

1. S. Jin, T. H. Tiefel, M. McCormack, *et al.*, Science **264**, 413 (1994).
2. É. L. Nagaev, Usp. Fiz. Nauk **166**, 833 (1996) [Phys.–Usp. **39**, 781 (1996)].
3. O. Iglesias, F. Badida, A. Labarta, and L. Balsells, J. Magn. Magn. Mater. **140–144**, 399 (1995).
4. L. M. Fisher, A. V. Kalinov, S. E. Savel'ev, *et al.*, J. Phys.: Condens. Matter **10**, 9769 (1998).
5. E. O. Wollan and W. C. Koehler, Phys. Rev. **100**, 545 (1955).
6. G. Matsumoto, J. Phys. Soc. Jpn. **29**, 606 (1970).
7. R. Pauthenet and C. Veygret, J. Phys. (Paris) **31**, 65 (1970).
8. C. Zener, Phys. Rev. **82**, 403 (1951).
9. J. B. Goodenough, A. Wold, R. J. Arnott, and N. Menyuk, Phys. Rev. **124**, 373 (1961).
10. A. Urishibara, Y. Moritomo, T. Arima, *et al.*, Phys. Rev. B **51**, 14103 (1995).
11. A. M. Balbashov, M. K. Gubkin, V. V. Kireev, *et al.*, Zh. Éksp. Teor. Fiz. **117** (3), 542 (2000) [JETP **90**, 474 (2000)].
12. V. Yu. Ivanov, V. D. Travkin, A. A. Mukhin, and S. P. Lebedev, J. Appl. Phys. **83**, 7180 (1998).
13. M. S. Islam and M. Cherry, Solid State Ionics **97**, 33 (1997).
14. N. V. Volkov, G. A. Petrakovskiĭ, K. A. Sablina, and S. V. Koval', Fiz. Tverd. Tela (St. Petersburg) **41**, 2007 (1999) [Phys. Solid State **41**, 1842 (1999)].

Translated by S. Gorin

Physics of the Solid State, Vol. 43, No. 2, 2001, pp. 309–310. Translated from Fizika Tverdogo Tela, Vol. 43, No. 2, 2001, pp. 297–298.

MAGNETISM AND FERROELECTRICITY

Optical Absorption of Copper Metaborate CuB_2O_4

L. N. Bezmaternykh, A. M. Potseluĭko, E. A. Erlykova, and I. S. Édel'man

Kirenskiĭ Institute of Physics, Siberian Division, Russian Academy of Sciences, Akademgorodok, Krasnoyarsk, 660036 Russia
e-mail: ise@iph.krasnoyarsk.su

Received June 28, 2000

Abstract—High-quality single crystals of copper metaborate CuB_2O_4 with a volume exceeding 1 cm^3 are grown. The optical absorption spectra of these crystals are recorded for the first time owing to their sufficiently large size. The spectra exhibit a broad transmission window in the visible region and an intense absorption peak around ~2.0 eV, which is already split into two bands at room temperature. A weak anisotropy is revealed in unpolarized light upon light beam propagation along the *a* and *c* axes. The spectra are compared with the absorption spectrum of $CuGeO_3$. © *2001 MAIK "Nauka/Interperiodica".*

Nowadays, copper oxide compounds are of particular interest in connection with a large variety of low-temperature magnetic phases. Until recently, the $CuGeO_3$ crystal received the greatest attention. Although CuB_2O_4 crystals were synthesized as early as 1964 [1], their properties were studied in only a few works. In particular, the lack of information on the optical properties of CuB_2O_4 can be explained by the extremely small sizes of samples that have been prepared successfully to date.

The crystal structure of CuB_2O_4 was first determined in [1] and then refined in [2–4]. The crystal belongs to the tetragonal crystal system with space group $I\bar{4}2d$. The unit cell contains twelve formula units. The unit cell parameters are $a = 11.506$ Å and $c = 5.644$ Å [2]. The copper ions occupy positions of two types. In the first positions, the oxygen ions form a perfect square, and in the second positions, they are arranged in a distorted octahedron. In the latter case, the long axis is inclined at a certain angle to the basal plane and the angles in the base plane are not equal.

The magnetic properties of copper metaborate CuB_2O_4 were first studied in [5]. It was found that this crystal is paramagnetic at temperatures above 21 K, a phase transition to a weakly ferromagnetic state takes place at 21 K, and the Morin transition is observed at 10 K. Since the copper ions occupy nonequivalent, strongly distorted sites in CuB_2O_4, its optical properties can be rather interesting. The present work reports the first results of an investigation into the absorption spectra of copper metaborate in the visible and near ultraviolet spectral regions.

Single crystals of CuB_2O_4 were grown from the ternary Li_2O–CuO–B_2O_3 system by solution–melt crystallization. The choice of the solution–melt composition {43.6 wt % (B_2O_3 + 0.5Li_2O) + 56.4 wt % CuB_2O_4} was based on the diagram given in [4]. The solution–melt mass was 100 g. The initial components were lithium carbonate (analytical grade), copper oxide (analytical grade), and boron oxide (high-purity grade). The solution–melt batch was prepared by successive melting of B_2O_3, Li_2CO_3, and CuO in a platinum crucible at a temperature of 1000°C. The solution–melt saturation temperature was 915°C. The crystals were grown by slow cooling in the temperature range 915–850°C. The maximal size of crystals grown on a single-crystal seed was $2 \times 1.5 \times 1.5$ cm^3.

Samples in the form of disks 0.01–0.06 cm thick and 0.05 cm in diameter were prepared for optical measurements. The disks were cut so that their faces were perpendicular to the *a* or *c* axis. The disk faces perpendicular to the *a* and *c* axes were polished. The absorption spectra were recorded at room temperature on an UVICON 943 spectrophotometer in the spectral range 300–900 nm (which corresponds to the energy range 4.14–1.38 eV).

The figure shows absorption spectra for two samples of different orientations, which were cut from the same single crystal. The spectra for the other samples had a similar shape. The absorption is rather high in the larger part of the range covered and drastically decreases in the energy range 2.65–3.27 eV, which shows up as a transmission window. At energies below 2.5 eV, the spectra contain a broad maximum which consists of two peaks at ~2.3 and ~1.7 eV. The absorption edge corresponds to ~3.5 eV. A spectral anisotropy clearly manifests itself in the unpolarized light. The absorption edge for the section normal to the *a* axis is shifted toward higher energies in comparison with that for the section normal to the *c* axis. The intensities of peaks in the low-energy region of the spectrum studied vary differently. For the plane normal to the *a* axis, the short-wavelength component is more intense and the long-wavelength component is less intense as compared to the spectrum of the section normal to the *c* axis.

Let us compare the spectrum obtained with the spectrum of $CuGeO_3$, the optical properties of which were thoroughly studied in [6, 7]. The spectra under investiga-

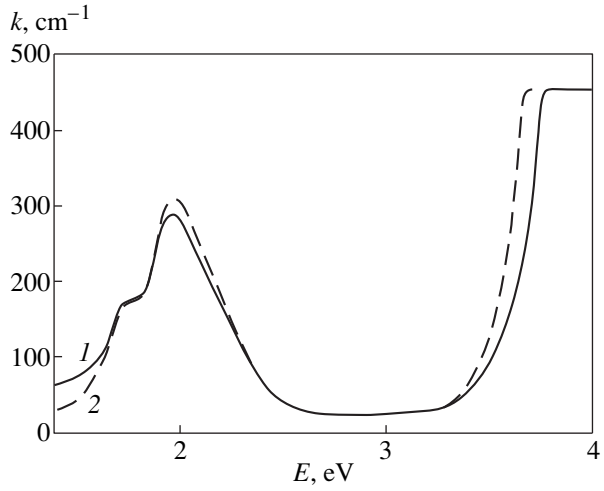

Optical absorption spectra of CuB_2O_4 at room temperature for samples cut perpendicularly to the (*1*) *a* and (*2*) *c* axes.

tion are quite similar to each other. First of all, this concerns the location and shape of the fundamental absorption edge and the presence of a broad band in the low-energy region of the spectrum. However, there are essential differences. A broad structureless absorption band at ~1.75 eV is observed for $CuGeO_3$ at room temperature. It is split into three bands upon cooling. The low-energy component of the maximum observed in the long-wavelength spectral region of CuB_2O_4 coincides in location with the absorption band of $CuGeO_3$, but its amplitude is halved. This band was associated with transitions between the Cu^{2+} *d* levels in distorted CuO_6 octahedra [7]. The second, more intense maximum in the absorption spectrum of CuB_2O_4 has no analogue in the spectrum of $CuGeO_3$. This maximum is most likely caused by electron transitions in Cu^{2+} ions located in oxygen squares.

It is well known that bivalent copper ions have a $3d^9$ electron configuration, which is characterized by only one term, namely, ^2D. In the cubic field, this term is split into two terms $^2T_2$ and ^2E, which represent the lower levels in the tetrahedral and octahedral fields, respectively. The degeneracy of these states can be removed in a lower symmetry field. Thus, the peaks observed in the spectra of CuB_2O_4 can be associated with the transitions $^2E_g \longrightarrow {}^2T_{2g}$ (1.75 eV) and $^2T_2 \longrightarrow {}^2E$ (2.3 eV). Both transitions are allowed. Therefore, their intensity should not, in principle, depend on the distortion of crystallographic sites of the Cu^{2+} ion, as is the case in forbidden transitions. The difference in the intensities of the $^2E_g \longrightarrow {}^2T_{2g}$ bands in $CuGeO_3$ and CuB_2O_4 is most likely due to the difference in their band structures. The spectral anisotropy revealed in unpolarized light cannot be explained without regard for the band structure. The bands associated with pure single-ion transitions should not exhibit such anisotropy. The band structure of CuB_2O_4 was not calculated. We expect that the first data on the optical spectra of copper metaborate, which are presented here, will stimulate calculations of the band structure of this compound.

REFERENCES

1. C. E. Weir and R. A. Schroeder, J. Res. Natl. Bur. Stand., Sect. A **68**, 465 (1964).
2. P. F. Rza-Zade, G. K. Abdulaev, and Kh. S. Mamedov, Zh. Neorg. Khim., No. 7, 2098 (1971).
3. M. Martínez-Pipoll, S. Martínez-Carrera, and S. García-Blanco, Acta Crystallogr., Sect. B: Struct. Crystallogr. Cryst. Chem. **B27**, 677 (1971).
4. G. K. Abdulaev and Kh. S. Mamedov, Zh. Strukt. Khim. **22**, 184 (1981).
5. G. Petrakovskiĭ, D. Velikanov, A. Vorotinov, *et al.*, J. Magn. Magn. Mater. **205**, 105 (1999).
6. M. N. Popova, A. B. Sushkov, S. A. Golubchik, *et al.*, Zh. Éksp. Teor. Fiz. **110**, 2230 (1996) [JETP **83**, 1227 (1996)].
7. S. D. Devic, Z. V. Popovic, A. Breitschwerdt, *et al.*, Phys. Status Solidi B **203**, 579 (1997).

Translated by M. Lebedkin

Physics of the Solid State, Vol. 43, No. 2, 2001, pp. 311–319. Translated from Fizika Tverdogo Tela, Vol. 43, No. 2, 2001, pp. 299–306.

MAGNETISM AND FERROELECTRICITY

Electron Paramagnetic Resonance of Quasi-One-Dimensional Crystal $[Nd_2(Cl_3COO)_6(H_2O)_3]_n \cdot nH_2O$

V. K. Voronkova*, R. T. Galeev*, J. Legenjievich, and G. Ochko****

**Zavoĭskiĭ Physicotechnical Institute, Russian Academy of Sciences, Sibirskiĭ trakt 10/7, Kazan, 420029 Tatarstan, Russia*
e-mail: vio@dionis.kfti.knc.ru

***Wroclaw University, Wroclaw, 50-383 Poland*

Received July 17, 2000

Abstract—A quasi-one-dimensional single crystal of $[Nd_2(Cl_3COO)_6(H_2O)_3]_n \cdot nH_2O$ in which chains are built up of two alternating neodymium-ion dimer fragments is studied by the EPR technique. It is found that anisotropic interactions between neodymium ions in a chain are responsible for the complex shape of the EPR spectrum. Two groups of EPR signals are distinguished in the spectrum. Each group corresponds to one of the chain dimers disturbed by the interaction with neighbors in the chain. The shape of the EPR spectra is interpreted as a superposition of the spectra of chain fragments which have different lengths and are formed by the alternating magnetic triplet and nonmagnetic singlet states in the chain. Consideration is given to two cases when two alternating dimer fragments are either equivalent or nonequivalent to each other. It is shown that the spectral shape is primarily determined by the superposition of the spectra of an isolated triplet state ($S = 1$), two interacting triplet states, and three interacting triplet states whose weighting contributions differ for the above two cases. The tensors of the anisotropic spin–spin interaction are determined, and the contribution from the isotropic component of the interaction is estimated. © *2001 MAIK "Nauka/Interperiodica".*

1. INTRODUCTION

One-dimensional magnetic systems have attracted considerable attention as model objects for the development of theoretical concepts concerning exchange interactions [1, 2]. In the last decade, particular interest has been expressed by researchers in chains with alternating interactions. In the present work, we investigated the properties of the chains with a strong anisotropy of spin–spin interaction. For this purpose, we chose neodymium ions which exhibit both an anisotropy of local properties and anisotropic interactions. It is for these neodymium ions that the splitting of the EPR line due to the dipole–dipole interaction between the nearest neighbors in a concentrated crystal was observed by Bleaney *et al.* [3]. Using the $[Nd_2(Cl_3COO)_6(H_2O)_3]_n \cdot nH_2O$ compound as an example, in this work, we studied the specific features of the EPR spectra of chains built up of nonequivalent fragments. The anisotropy of spin–spin interactions between neodymium ions and the chain structure of a crystal predetermined the main aspects of our investigation: the character of the anisotropic interaction between neodymium ions and its manifestation in the EPR spectra. It should be noted that the observed EPR spectra have a complex shape. It was necessary to propose a model that would describe the observed spectra and could explain the characteristic features of the given system.

2. STRUCTURAL DATA

According to our data, the unit cell parameters of the $[Nd_2(Cl_3COO)_6(H_2O)_3]_n \cdot nH_2O$ crystal are as follows: $a = 11.66$ Å, $b = 12.92$ Å, $c = 15.46$ Å, $\alpha = 71.2°$, $\beta = 78.1°$, and $\gamma = 65.2°$. These parameters coincide (within 0.2 Å) with those for the $[Er_2(Cl_3COO)_6(H_2O)_3]_n \cdot nH_2O$ crystal, which indicates that these crystals are isostructural. Crystals of $[Er_2(Cl_3COO)_6(H_2O)_3]_n \cdot nH_2O$ [4, 5] and neodymium crystals are built up of polymer chains running parallel to the [011] axis. Pairs of rare-earth ions linked through either four carboxyl groups or two carboxyl groups and one oxygen atom of a water molecule alternate in the chain. The environment of the rare-earth ions and bridging ligands is schematically represented in Fig. 3 in [4]. The chains are arranged in layers aligned parallel to the (100) plane.

The complexes of four neodymium ions form a repetitive chain fragment. Hereafter, the pairs of equivalent rare-earth ion fragments linked by four carboxyl groups will be referred to as dimers. In this terminology, the chains are composed of two alternating structurally nonequivalent dimers Nd_1–Nd_1 and Nd_2–Nd_2. All rare-earth ions (specifically, neodymium ions) have an eightfold coordination in the form of a square antiprism [4, 5].

The Nd_1–Nd_1, Nd_1–Nd_2, and Nd_2–Nd_2 distances are equal to 4.430, 4.823, and 4.267 Å, respectively. It is seen that the distance between dimer fragments is larger than the distances between ions inside the dimers.

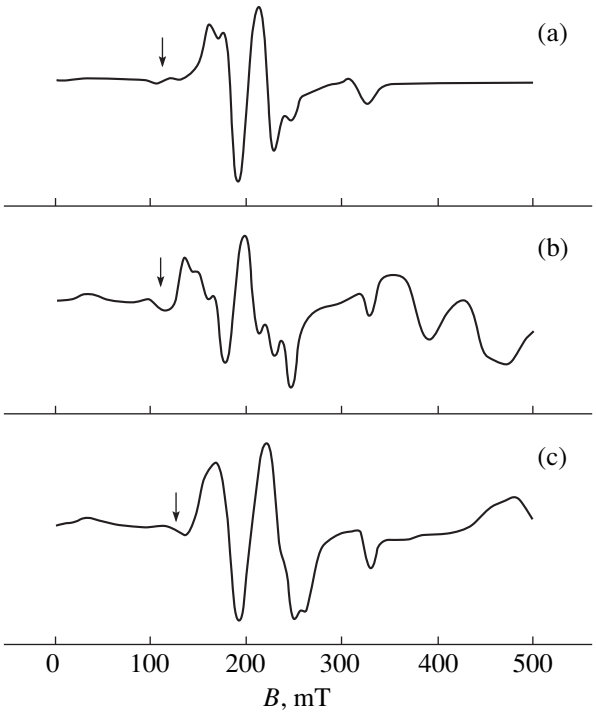

Fig. 1. EPR spectra of the $[Nd_2(Cl_3COO)_6(H_2O)_3]_n \cdot nH_2O$ crystal at $T = 4.2$ K for several orientations of the magnetic field in the *ac* plane. Arrows show the "forbidden" transitions.

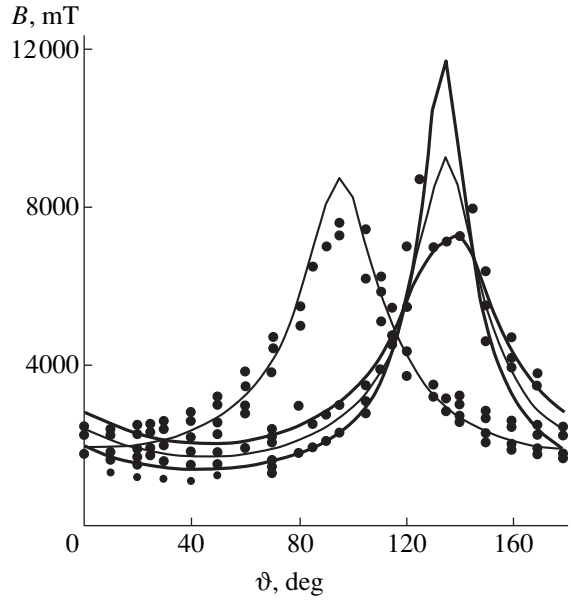

Fig. 2. Angular dependences of the resonant fields of the experimental EPR lines (points) for magnetic field orientations in the *ZX* plane. ϑ is the angle between the directions of the magnetic field and the *Z* axis. Solid lines represent the calculated angular dependences of the resonant fields for two nonequivalent dimers without regard for the anisotropy of intradimeric interaction (thin lines) and for one of the dimers with inclusion of the interaction anisotropy (thick lines).

3. RESULTS

The EPR spectra of the $[Nd_2(Cl_3COO)_6(H_2O)_3]_n \cdot nH_2O$ crystal were studied in the *X* band in the temperature range 4.2–30 K. At $T > 20$ K, the EPR spectra are broadened and the fine structure of the spectra becomes less resolved. The angular dependence of the spectra was investigated in three mutually perpendicular planes. The crystals grew with a well-defined *ac* plane. For this reason, the angular dependence was examined first in this plane and then in the other two orthogonal planes.

The EPR spectra contain a large number of lines whose location depends on the orientation of a single crystal in the magnetic field. The characteristic spectra are displayed in Figs. 1a–1c. Note that the spectra shown in Figs. 1b and 1c correspond to the orientations differing by only 5°. The angular dependences of the resonant fields of the experimental EPR lines in the *ac* plane designated as *ZX* are depicted in Fig. 2.

Analysis of the angular dependences of the resonant fields demonstrates that the tendency of their variation is primarily due to the anisotropy of the *g* values for neodymium ions. Figure 2 shows the angular dependences of the resonant fields for two nonequivalent dimers (thin lines), which are determined only by the angular dependences of two $\{g\}$ tensors whose principal values and orientations are given in Table 1. As can be seen, the calculated angular dependences of the resonant fields satisfactorily reflect the tendency of variation in the center of gyration of two groups of lines in the spectra. The case in point is the tendency of variation in the center of gyration of particular groups of lines. Consequently, the accuracy in the determination of the $\{g\}$ tensors is not very high. However, the revealed separation of the spectrum into two groups of lines made it possible to analyze these spectra in more detail. It should be remarked that the low-field lines shown by smaller-sized circles in Fig. 2 (in the range $B \sim 100$ mT) had a noticeably lower intensity and were ignored at this stage. The high-field EPR lines in the *ab* plane will be discussed below. Now, we only note that each group of lines in this range is split into two subgroups, one of which is considerably shifted toward the high-field range.

It is evident that the observed spectral structure is determined by the interactions between neodymium ions in the chain. The splittings due to the spin–spin interaction are observed virtually for all orientations of the magnetic field with respect to the crystallographic axes of the crystal. The magnitudes of splittings associated with the anisotropic component of the interaction do not exceed the Zeeman interaction energy.

Analysis of the angular dependence demonstrates that the spectra for the majority of orientations can be represented as a superposition of the spectra of two nonequivalent dimers disturbed by the interaction with their neighbors in the chain.

4. DISCUSSION

The ground term $(4f^3)^4I_{9/2}$ of a trivalent neodymium ion in a low-symmetry field is split into five Kramers doublets. At high temperatures, when all the doublets are occupied, fast relaxation times are characteristic of the systems containing neodymium ions. At low temperatures, when only one (the lowest-lying) out of five doublets is occupied, the electron paramagnetic resonance occurs as the result of transitions between the levels of this doublet [6, 7]. Hence, the effective spin $S' = 1/2$ is introduced for the description of the resonance at single neodymium centers. The splitting of the doublet in a magnetic field is described by the effective g tensor whose degree of anisotropy is completely governed by the anisotropy of the ground state. Since there are two nonequivalent centers, two tensors $\{g_1\}$ and $\{g_2\}$ are used for the representation of the interactions between neodymium ions and the magnetic field. In order to describe the Nd_1–Nd_1, Nd_1–Nd_2, and Nd_2–Nd_2 interionic interactions in a chain fragment containing four ions, it is necessary to introduce the three tensors of spin–spin interaction $\{K_{11}\}$, $\{K_{12}\}$, and $\{K_{22}\}$, respectively. The Hamiltonian for describing these interactions in an infinite chain can be written as follows:

$$\begin{aligned} H = \sum (&\{g_i\}\mu_B B(S_i + S_{i+1}) \\ &+ \{g_{i+2}\}\mu_B B(S_{i+2} + S_{i+3}) + S_i\{K_{i,i+1}\}S_{i+1} \\ &+ S_{i+1}\{K_{i+1,i+2}\}S_{i+2} + S_{i+2}\{K_{i+2,i+3}\}S_{i+3}). \end{aligned} \quad (1)$$

Here, the first two terms represent the Zeeman interaction and the next three terms describe the spin–spin interactions. The three tensors of the spin–spin interaction $\{K_{i,i+1}\}$, $\{K_{i+1,i+2}\}$, and $\{K_{i+2,i+3}\}$ sequentially characterize three interactions $\{K_{11}\}$, $\{K_{12}\}$, and $\{K_{22}\}$ along the chain. The components of these tensors are equal to the sums of contributions from the exchange $\{K^{ex}\}$ and dipole–dipole $\{K^{d-d}\}$ interactions (for example, $\{K_{i,i+1}\} = \{K^{ex}_{i,i+1}\} + \{K^{d-d}_{i,i+1}\}$). Moreover, in this form, the interaction tensors include the isotropic $K^{iso} = 1/2(K_{xx} + K_{yy} + K_{zz})$ and anisotropic (the $\{K'\}$ tensors with zero spur) components of interaction. In the strict sense, the two tensors that describe the interactions between equivalent centers (intradimeric interactions) are symmetric and the tensor that represents the interaction between nonequivalent centers (interdimeric interaction) is nonsymmetric. However, since the latter tensor accounts for the weakest interactions, its nonsymmetric form is neglected.

Hamiltonian (1) describes only the interactions between the nearest neighbors. As a rule, the shape of the spectra of concentrated systems, including one-dimensional systems, is analyzed taking into account only the anisotropy of dipole–dipole interaction [6–8]; in this case, the exchange interaction is assumed to be purely isotropic and is accounted for in a separate way. The isotropic exchange interaction in chains can result in the averaging of a hyperfine or fine structure of interacting centers when the interaction energy exceeds the corresponding splittings. In the case of the interaction between nonequivalent centers, the isotropic exchange whose energy is higher than the difference in the Zeeman energies averages the EPR lines of nonequivalent centers. Making allowance for the dipole–dipole interactions leads to a change in the width and the shape of the line of an individual center and, in the general case, to a broadening of the spectrum. The exception is provided by interactions of the Ising type when only the ***z*** components of spins $K^{zz}_{i,i+1}S_{iz}S_{i+1,z}$ participate in the interaction. The exact solution of Hamiltonian (1), in this case, gives a set of frequencies that describe discrete transitions for an infinite chain. For this type of interaction between centers, it can be expected that the spectrum will consist of several signals [9], as is observed in experiments. Since the local properties of neodymium ions are strongly anisotropic, this assumptions is quite reasonable but should be proved. We can exactly calculate (and will calculate below) only the dipolar contribution to the parameters of the spin–spin interaction. Therefore, we considered the possibility of simulating the spectrum with a shape similar to that observed in the experiment for the anisotropy of interaction in the general form. The functions of dimer fragments are chosen as the basis functions. The functions of dimer fragments, in which spins with $S = 1/2$ are cou-

Table 1. Principal values and directions of the $\{g_1\}$, $\{g_2\}$, and $\{K'_{11}\}$ tensors

Principal value		Principal direction		
		X	*Y*	*Z*
g_{x1}	0.55 ± 0.05	0.682	−0.335	0.650
g_{y1}	1.35 ± 0.05	0.259	0.941	0.254
g_{z1}	3.75 ± 0.05	−0.698	−0.035	0.715
g_{x2}	0.70 ± 0.05	0.968	0.231	0.093
g_{y2}	1.40 ± 0.05	−0.235	0.972	−0.032
g_{z2}	3.40 ± 0.05	−0.082	−0.053	0.995
K'_{xx}	(+)0.08 cm^{-1}	−0.620	0.225	0.747
K'_{yy}	(+)0.03 cm^{-1}	−0.342	−0.939	0.03
K'_{zz}	(–)0.11 cm^{-1}	0.706	−0.257	0.660
K'^{d-d}_{xx}	0.042 cm^{-1}	0.654	−0.366	0.661
K'^{d-d}_{yy}	0.048 cm^{-1}	0.237	0.919	0.313
K'^{d-d}_{zz}	−0.090 cm^{-1}	−0.731	−0.078	0.678

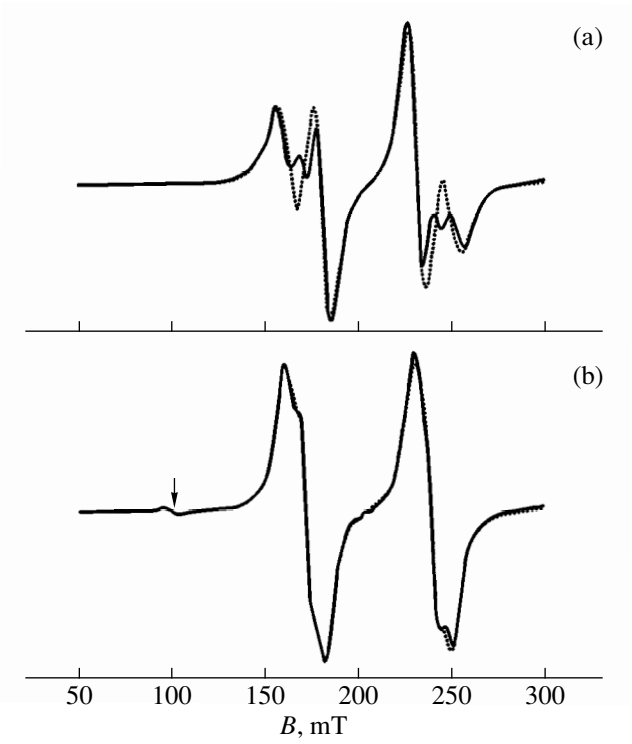

Fig. 3. Model spectra of fragments containing three interacting dimers (solid lines) and a closed fragment consisting of four dimers (dashed lines) for $g_1 = 3.2$ and $g_2 = 1.5$: (a) $K_{11,zz} = K_{22,zz} = 0.120$, $K_{11,xx} = K_{11,yy} = K_{22,xx} = K_{22,yy} = 0.015$, $K_{12,zz} = 0.03$, and $K_{12,xx} = K_{12,yy} = -0.015$ cm^{-1} and (b) $K_{11,zz} = K_{22,zz} = 0.220$, $K_{11,xx} = K_{11,yy} = K_{22,xx} = K_{22,yy} = 0.115$, $K_{12,zz} = 0.03$ and $K_{12,xx} = K_{12,yy} = -0.015$ cm^{-1}.

pled through the exchange interaction, are split into the singlet *S* and the triplet *T*; that is,

$$S = (|1/2, -1/2\rangle - |-1/2, 1/2\rangle)/\sqrt{2},$$
$$T_+ = |1/2, 1/2\rangle, \quad T_- = |-1/2, -1/2\rangle,$$
$$T_0 = (|1/2, -1/2\rangle + |-1/2, 1/2\rangle)/\sqrt{2},$$

where $|m_1, m_2\rangle$ is the product of the projections of the spin states of two interacting ions in the dimer.

The splitting between the singlet and the triplet is determined by the isotropic component of the interaction, and its anisotropic component results in the triplet splitting. The EPR spectra of dimers are associated with the transitions between the triplet states, because the transitions between the singlet and triplet states in the general case are forbidden [7, 10]. Now, we separately consider two cases: a chain composed of nonequivalent dimer fragments and a chain consisting of identical fragments. In the latter case, the system can be described using only one $\{g\}$ tensor and two tensors of spin–spin interaction (inside the dimers and between the dimers). This situation is close to that observed in the studied system in the *ac* plane at the angle $\theta \sim 20°$ (Fig. 2). The spectral shape for this orientation allows us to assume that the $\{g\}$ tensors for two dimers, as well as the interaction in these dimers, are close to each other. We dwell on analysis of this system in order to demonstrate certain regularities in the EPR spectra. The experimental spectrum for this orientation is displayed in Fig. 1a.

4.1. EPR spectra of a chain consisting of nonequivalent dimers. We analyzed the spectra of chain fragments containing *N* spins ($N = 2$, 4, 6, 8, and 10) and the possibility of extrapolating the obtained results to infinite chains. In the case of nonequivalent dimers, we simulate the spectra for orientations at which the difference between the Zeeman energies is larger than the interaction energy. As can be seen from the angular dependence of the EPR spectra, the last situation is realized for the majority of orientations of the studied crystal.

Under this approximation, the simulated spectrum involves two parts. In particular, for a fragment consisting of three dimers in which the central dimer with g_1 interacts with two nearest neighbors with g_2, we have

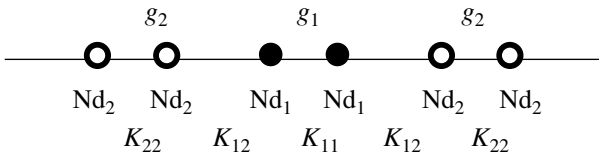

Similarly, the dimer with g_2 interacts with the two nearest dimers with g_1.

First, let us consider a simpler case when the chain is built up of alternating nonequivalent dimers with spin $S = 1/2$ and the energy of interaction between them is less than the difference between the Zeeman energies. It is known that, in this case, the effect of nondiagonal terms of the interaction on the energy spectrum manifests itself in the second order of the perturbation theory and is inversely proportional to the difference between the Zeeman energies of the neighboring centers. Consequently, as a first approximation, it is sufficient to include only the diagonal terms (the flip–flop processes are inefficient). This situation is similar to the interaction in the Ising model: the signal of each nonequivalent center is split into three components due to the interaction with two nearest neighbors [9]. In the studied crystal, the dimer fragments are treated as nonequivalent fragments. As follows from the model spectra depicted in Figs. 3a and 3b, only for the chain in which the energy of interaction between the dimers is considerably less than that of the intradimeric singlet–triplet splitting, an increase in the number of fragments virtually does not affect the spectral shape (otherwise, the chain should be analyzed with due regard for the alternation of equivalent and nonequivalent fragments). The closed chains (the last spin interacts with the first spin) simulate the situation close to that observed for an

infinite chain when each dimer *a* is surrounded by two dimers *b* (where *a* and *b* are nonequivalent dimers). For simplicity, the spectra were calculated under the assumption that the directions of the principal axes of the interaction tensors and the $\{g\}$ tensor coincide and the magnetic field is aligned along the *z* axis. The shape of the model spectra is determined by the ratio between the interaction parameters $\{K_{11}\}$, $\{K_{22}\}$, and $\{K_{12}\}$ and reproduces substantial changes observed in the shape of experimental spectra. As mentioned above, the spectra were calculated for the magnetic field oriented along the *z* axis of the tensors. Hence, the parameters of the interaction tensors were varied in calculations, even though the observed dependences of the splitting were obtained upon change in the orientation of the magnetic field with respect to the principal axes of these tensors.

The spectra calculated within the six-spin approximation enable us to determine the parameters of the interaction between equivalent centers (intradimeric interactions) and to estimate the parameter of the interaction between nonequivalent centers (interdimeric interaction) for each specific orientation with respect to the direction of the magnetic field. Moreover, the interaction between dimers leads to the mixing of singlet–triplet states, and the transitions between the triplet and singlet states (which are forbidden in a dimer fragment) become partly allowed when the interaction between the dimers is taken into account. The energies of these transitions depend on the isotropic contribution of the intradimeric interaction. The experimental spectra contain weak signals that correspond to these transitions, and their location makes it possible to determine the isotropic contribution: $K_{11}^{iso} \cong |0.12 \pm 0.03|$ cm^{-1}. These results will be discussed below.

4.2. EPR spectra of a chain consisting of equivalent dimers. The angular dependence of the spectra demonstrates that the hyperfine structure in the spectra is observed irrespective of the difference between the Zeeman energies of the two dimers. Consequently, the conditions that allow for the hyperfine structure of the EPR spectrum are realized in the studied crystal even in the case of equivalent dimer fragments in the chain. First of all, we note that the discrete spectrum of an infinite chain composed of identical fragments can be observed for the Ising interaction (or interaction close to the Ising type) between the fragments.

The $\{K_{12}\}$ *tensor of interaction.* Let us calculate the dipole–dipole contribution to the $\{K_{12}\}$ tensor. The tensor of the dipole–dipole interaction

$$H = (\mu_0\mu_B^2/4\pi r^3)S_{ip}S_{jq}\{g_{ips}g_{jqs} - 3str^{-2}g_{ips}g_{jqs}\} \quad (2)$$

(where each of the *p*, *q*, *s*, and *t* indices takes the values *X*, *Y*, and *Z* [7]) is nonsymmetric in the case of interaction between nonequivalent ions. The components of the tensor defined by relationship (2) were calculated in the *X'YZ'* coordinate system which was rotated with respect to the *XYZ* coordinate system in such a way that the Z^3 axis was aligned along the radius vector $\mathbf{r}_{12}$ connecting the nonequivalent neodymium fragments. As follows from the parameters listed in Table 2, the interaction along the *Z'* axis is virtually one order of magnitude stronger than the interactions in the perpendicular directions [for simplicity, we neglected the differences between the principal values of the $\{g_1\}$ and $\{g_2\}$ tensors (see Table 1)] and the tensor is substantially nonsymmetric. The antisymmetric component of interaction results in the mixing of singlet–triplet states, the splitting between which is larger than the energy of interaction between the dimer fragments. Therefore, to a first approximation, we can ignore the antisymmetric interaction and retain only the $K_{12,zz}^{d-d}$ component in analyzing the tensor of the dipole–dipole interaction between the dimers.

The EPR spectra of chains under the assumption of the Ising character $S_1\{K_{12}\}S_2$ of the interaction are depicted in Fig. 4. The spectra simulated at $K_{12,zz} = K_{12,zz}^{d-d}$ (see, for example, Fig. 4a) disagree with the experimental spectrum for the given orientation (Fig. 1a). The experimental parameter of interaction is less than the dipole–dipole interaction parameter. This suggests the presence of an exchange contribution $\{K_{12}^{ex}\}$ to the parameters of the spin–spin interaction $\{K_{12}\}$. Figure 4b shows the EPR spectrum of a chain involving dimers coupled by the Ising interaction with the parameters that provide the best agreement with the experimental spectrum. In this case, the $K_{12,zz}$ parameter is less than the $K_{12,zz}^{d-d}$ parameter. The difference between the shapes of the simulated and experimental spectra argues for a non-Ising form of the interaction.

The EPR spectrum of a chain without constraint on the anisotropy of the $\{K_{12}\}$ *tensor.* Recall that the interaction between the neodymium ions in a dimer fragment results in the states with the total spins $S = 0$ and $S = 1$. When the interactions inside the dimers are stronger than the interaction between the dimers, the triplet magnetic states and singlet nonmagnetic states of the dimers can be chosen as the zeroth approximation. Then, to a first approximation, the infinite chain can be treated as a sequence of magnetic and nonmagnetic

Table 2. Components of the $\{K_{12}^{d-d}\}$ tensor (cm^{-1}) for dipole–dipole interaction between dimers in the *Z'X'Y* coordinate system

K_{xx}^{d-d}	K_{xy}^{d-d}	K_{xz}^{d-d}	K_{yx}^{d-d}	K_{yy}^{d-d}	K_{yz}^{d-d}	K_{zx}^{d-d}	K_{zy}^{d-d}	K_{zz}^{d-d}
–0.012	0.0	0.028	0.0	0.008	0.0	–0.028	0.0	–0.079

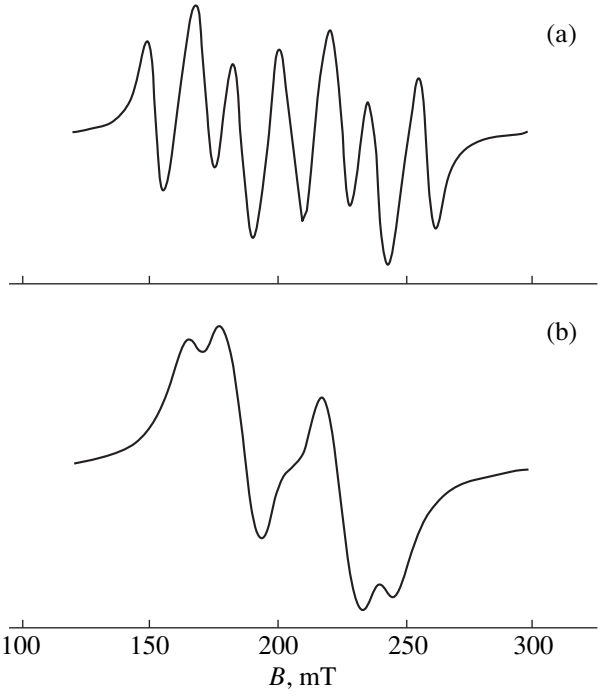

Fig. 4. Model spectra of three equivalent dimer fragments ($g_{1,2}$ = 3.2) whose interaction is described only by the $K_{12,zz}$ component: (a) $K_{12,zz} = K_{22,zz} = 0.08$, $K_{11,zz} = 0.21$, and $K_{11,xx} = K_{11,yy} = K_{22,xx} = K_{22,yy} = 0.12$ cm^{-1} and (b) $K_{12,zz} = 0.052$, $K_{11,zz} = K_{22,zz} = 0.194$, and $K_{11,xx} = K_{11,yy} = K_{22,xx} = K_{22,yy} = 0.128$ cm^{-1}.

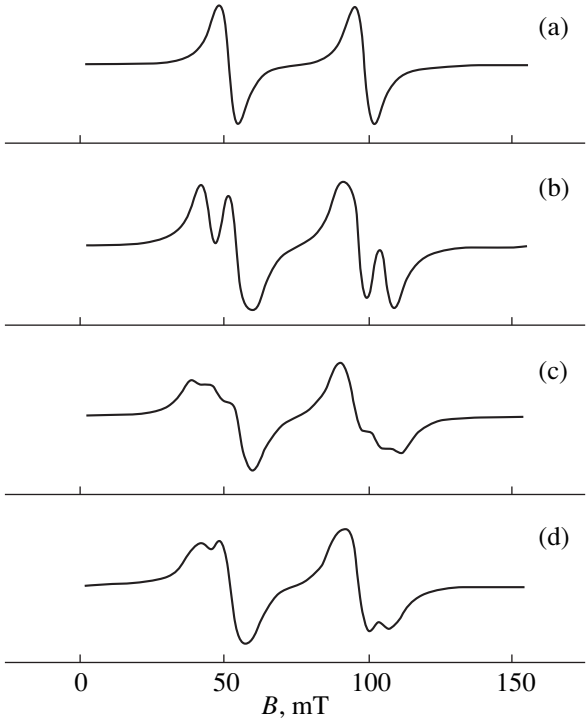

Fig. 5. Calculated spectra of (a) an isolated triplet, (b) two interacting equivalent triplets, and (c) three interacting equivalent triplets. (d) The sum of these spectra with the weighting contributions $P_1 : P_2 : P_3 = 16 : 12 : 9$. Triplet splitting $D = 0.04$ cm^{-1}. The parameters of the interaction between triplets are $K_{12,zz} = 0.008$ cm^{-1} and $K_{12,xx} = K_{12,yy} = -0.004$ cm^{-1}. Line width is $\delta B = 8$ mT.

states alternating with a certain probability, which gives rise to fragments consisting of magnetic centers with different lengths. The probability of population of the triplet state T in the dimer is given by the relationship

$$P = X/(1 + X), \quad (3)$$

where $X = 3\exp(-K_{11}^{iso}/kT)$. When the singlet and triplet states in the chain alternate in a random way, the probability that the cluster is formed by n interacting triplets can be written as [11]

$$P_n = P^n(1 - P)^2, \quad n = 1, 2, 3\ldots .$$

The ratio between the intensities of the spectra of isolated and interacting triplets is determined by the quantity X.

In the studied temperature range, the interaction energies are less than kT and the difference between the level populations due to the Boltzmann distribution can be neglected. Then, the ratio between the probabilities that the fragment is formed from one (P_1), two (P_2), or three (P_3) triplet states is $P_1 : P_2 : P_3 = 3/4 : 9/16 : 27/64$. Now, we demonstrate that the spectra of these three fragments make the main contribution to the spectrum of the chain. The spectra calculated as the sum of the contributions from isolated, two interacting, and three interacting triplets (Fig. 5d), as a whole, reproduce the shape of the spectrum for the orientation when the dimers can be considered equivalent (Fig. 1a).

A further increase in the length of the fragment results in a further decrease in the probability of its formation. Although the intensity shows no sharp decrease when changing over to four and five interacting triplets (Fig. 6a), the shape of the spectra calculated as the sum of contributions does not change considerably upon addition of contributions from four and five interacting triplets (Fig. 6b).

Therefore, the shape of the spectrum of a chain built up of dimers is predominantly determined by a superposition of the spectra of isolated, two interacting, and three interacting triplet states. For the equivalent dimers, the weighting contributions from these spectra correspond to the probabilities of the formation of the appropriate fragments in an infinite chain. In the case when the dimers are strongly nonequivalent, it is sufficient to take into account the interaction with the two nearest dimers, and, correspondingly, the probabilities of the isolated and interacting triplet states will differ from those in an infinite chain.

Note that the spectra calculated within the proposed model reproduce the experimental spectra for the orien-

tation at which the parameters of the anisotropic interaction and the g tensors coincide (Figs. 1a, 5d). The experimental and calculated spectra are in agreement when the spurs of the $\{K_{11}\}$ and $\{K_{22}\}$ tensors are nonzero and the anisotropy of the parameters is comparable in magnitude to the anisotropy of the interdimeric interaction. To a first approximation, the spectra are determined only by the interaction between the triplet states. However, as was noted above, the interaction between dimers leads to the mixing of the singlet–triplet states. This gives rise to partially forbidden signals which are not observed in the model spectra in Fig. 5. For the resonant fields of the "forbidden transitions," the relationships that are obtained with due regard only for the interaction $K_{12,zz}S_{1z}S_{2z}$ between three dimers coincide with the corresponding expressions for the isolated dimer. For example,

$$B = (h\nu - K_{11}^{iso} - 1/2(K_{11,zz} - K_{11,xx}))/\mu_B g_{11}, \quad (4)$$

where $h\nu$ is the energy of the radio-frequency quantum. From relationship (4), we determined the isotropic component of the interaction

$$K_{11}^{iso} \cong |0.12 \pm 0.03| \text{ cm}^{-1}.$$

Anisotropy of the intradimeric interaction. The parameters of the anisotropic intradimeric interaction were calculated from the angular dependence of the resonant fields without regard (at this stage) for the splitting due to the interaction between dimers. Within this assumption, the observed angular dependence of the EPR spectra is interpreted as a superposition of the angular dependences of the spectra for two dimers.

Figure 2 displays the angular dependence of the resonant fields for one of the two dimers, which was calculated with due regard for the anisotropy of interaction. The principal values of the anisotropic interaction tensor with a nonzero spur ($K'_{ii} = K_{ii} - (1/3)\Sigma K_{ii}$) and the direction cosines of this tensor are presented in Table 1. The parameters of the anisotropic interaction were determined to within a sign from analysis of the angular dependence. The parenthetic signs (see Table 1) obtained from analysis of the dipolar and exchange contributions are hypothetical. The calculated angular dependence of the resonant fields for a dimer with intradimeric interaction described by the $\{K_{11}\}$ tensor adequately reproduces the experimentally observed tendency of variation in the resonant fields near $\{g_1\}$. For certain orientations, the lines are split as a result of the interactions between dimers in the chain. It is worth noting that the high-field part of the spectrum in the XZ plane at angles of 130°–150° is clearly separated into two groups of lines (the overall spectrum for this orientation contains three groups of lines), which is characteristic of the fine structure of the dimer fragment. Note that one group of signals is substantially shifted toward the high-field range beyond the fields permissible in our experiment (900 mT). We will restrict our consideration to a quantitative description of the interaction for only one dimer fragment, because both dimer fragments are characterized by close parameters of the anisotropic interaction (the differences between these parameters are of the order of the accuracy in their determination).

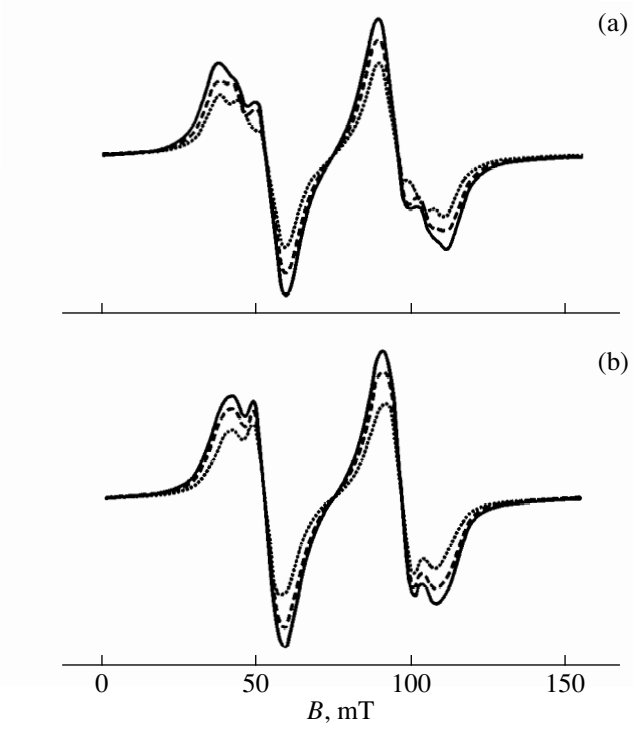

Fig. 6. (a) Model spectra of three (dotted line), four (dashed line), and five (solid line) interacting triplets and (b) the overall spectra calculated taking into account the contributions from three (dotted line), four (dashed line), and five (solid line) interacting triplets. The parameters of the interaction are the same as in Fig. 5.

It is seen from Table 1 that the maximum splitting caused by the $\{K_{11}\}$ interaction is observed near the minimum value of the $\{g\}$ tensor. As already noted, the tensor of the spin–spin interaction is the sum of contributions from the $\{K^{d-d}\}$ dipole–dipole and $\{K^{ex}\}$ exchange interactions. Analysis of the orientations of two $\{g\}$ tensors and the directions of bonds in two structurally nonequivalent polyhedra suggests that the spectral part under consideration can be associated with the dimer fragment in which Nd–Nd distance is equal to 4.439 Å. In this case, the radius vector directions of two dimer fragments (Nd_1–Nd_1 and Nd_2–Nd_2) correlate with the directions of the z axes of two $\{g\}$ tensors. The radius vector of the dimer fragment under investigation (referred to as the first dimer) forms an angle of 11° with the g_z direction and lies virtually in the ZX plane (the radius vector of the other dimer fragment makes an angle of 8° with the corresponding g_z direction). These results are consistent with the data for the crystal field of a distorted square antiprism [12]. In the principal

axes of the $\{g\}$ tensor, the tensor of the dipole–dipole interaction can be represented with an accuracy of 0.001 cm^{-1} in the form

$$\begin{matrix} 0.001 & 0 & 0.004 \\ & 0.008 & 0.008 \\ & & -0.131 \end{matrix}$$

The principal values and directions of the principal axes (with respect to the *XYZ* coordinate system) of the tensor of the dipole–dipole intradimeric interaction are given in Table 1.

By changing over to the tensor with zero spur, we calculated the dipolar contribution to the anisotropic component of the spin–spin interaction $\{K'\}$. The directions of principal axes of the $\{K^{d-d}\}$ tensor are close to those of the $\{g\}$ tensor. The splitting observed near the *z* orientation of the $\{g\}$ tensor coincides in order of magnitude with the splitting expected for the dipole–dipole interaction. However, the splitting in the high-field range exceeds the value expected for this interaction, which suggests the presence of an exchange contribution to the anisotropic interaction. Earlier, Baker *et al.* [13, 14] proposed a simple model for the interrelation between the parameters of the anisotropic exchange interaction on effective spins and the effective *g* values under the assumption that the exchange on actual spins is isotropic; i.e., $JS_1 \cdot S_2$. In this case, the parameters of the anisotropic exchange on the effective spins are proportional to $g_i g_j$ and, after changing over to the tensor with zero spur, the diagonal terms are proportional to $g_i^2 - 1/3\Sigma g_i^2$.

For a dimer formed by equivalent neodymium ions, the proportionality coefficients that characterize the exchange contribution to K'_{xx} and K'_{zz} are as follows: $K'^{ex}_{xx} \sim (g_x^2 - 1/3\Sigma g_i^2) = -5.2$ and $K'^{ex}_{zz} \sim (g_z^2 - 1/3\Sigma g_i^2) = 8.9$, respectively. Since the parameters $K'_{xx} = K'^{ex}_{xx} + K'^{d-d}_{xx}$ and $K'_{zz} = K'^{ex}_{zz} + K'^{d-d}_{zz}$ are virtually equal in magnitude (Table 1), it is reasonable to assume that the contributions from the exchange and dipole–dipole interactions are opposite in sign. This reasoning leads to the signs of the total anisotropic interaction that are given in the table and correspond to the antiferromagnetic isotropic interaction on actual spins. It should be noted that K^{iso} was estimated at ~ 0.12 cm^{-1} by analyzing the spectral shape. The same result follows from the treatment of the exchange interaction on the effective spins with the use of the *g* values: the magnitudes of $(1/3)\Sigma g_{ii}^2$ and $g_{xx}^2 - (1/3)\Sigma g_{ii}^2$ are virtually identical due to the smallness of g_{xx}. However, it should be remarked that the spur of the dipole–dipole interaction tensor is also nonzero in the case of strongly anisotropic *g* values.

5. CONCLUSION

The above investigation demonstrated that the observed spectral features can be explained as follows.

(1) The parameters of interaction ($\{K_{11}\}$, $\{K_{22}\}$, and $\{K_{12}\}$) differ along the chain, and the chain properties, to a first approximation, are governed by the dimer fragments. At each specific instant, the dimer is either in the singlet state *S* or in the triplet state *T*, and the chain can be treated as a sequence of these states arising in a random way. The *T*–*T* triplet–triplet and *S*–*T* singlet–triplet interactions give rise to substantially different features in the EPR spectrum. The former interactions are responsible for additional splittings in the spectrum as compared to the spectrum of an isolated triplet, and the latter interactions lead to the appearance of additional weaker signals. These signals correspond to the forbidden transitions in a noninteracting dimer. The interactions between dimers partially remove this forbiddenness. The degree of forbiddenness depends on the ratio between the parameters of interactions inside and between the dimers. The observation of these additional, partially forbidden signals made it possible to determine the isotropic component $K^{iso} \sim 0.12$ cm^{-1}.

(2) The substantial anisotropy is characteristic not only of the interaction inside the dimer fragments but also of the interaction between the dimers.

Analysis of the shape of the model spectra allowed us to make certain inferences concerning the ratio between the parameters of interactions at which the anisotropic interaction can give rise to splittings in the spectra of chains. It is important that both interdimeric and intradimeric interactions have dipolar and exchange components.

ACKNOWLEDGMENTS

We are grateful to K.M. Salikhov for useful discussions, A.R. Kessel' and M.M. Shakirzyanov for helpful remarks, and G. Drulis for his assistance in performing the experiment.

This work was supported by the Russian Foundation for Basic Research (project no. 00-15-97410) and the "Fullerenes and Atomic Clusters" Program of the Ministry of Science and Technology of the Russian Federation (project no. 98084).

REFERENCES

1. *Extended Linear Chain Compounds*, Ed. by J. S. Miller (Plenum, New York, 1983), Vol. 3.
2. *Magnetic Molecular Materials*, Ed. by D. Gatteschi, O. Kahn, J. Miller, and F. Palacio (Kluwer, Dordrecht, 1991), NATO ASI Ser., Ser. E **198** (1991).
3. B. Bleaney, R. J. Elliott, and H. E. D. Scovil, Proc. Phys. Soc. London, Sect. A **64**, 933 (1951).
4. A. S. Antsyshkina, M. A. Poraĭ-Koshits, and V. N. Ostrikova, Zh. Neorg. Khim. **33** (8), 1950 (1988).

5. T. Imai and A. Ouchi, Bull. Chem. Soc. Jpn. **60**, 408 (1987).
6. S. A. Al'tshuler and B. M. Kozyrev, *Electron Paramagnetic Resonance* (Nauka, Moscow, 1972; Academic, New York, 1964).
7. A. Abragam and B. Bleaney, *Electron Paramagnetic Resonance of Transition Ions* (Clarendon Press, Oxford, 1970; Mir, Moscow, 1973).
8. A. Bencini and D. Gatteschi, *Electron Paramagnetic Resonance of Exchange Coupled Systems* (Springer-Verlag, Berlin, 1990).
9. A. R. Kessel' and G. O. Berim, *Magnetic Resonance of Ising Magnets* (Nauka, Moscow, 1982).
10. Yu. V. Yablokov, V. K. Voronkova, and L. V. Mosina, *Electron Paramagnetic Resonance of Exchange Clusters* (Nauka, Moscow, 1988).
11. D. Snaathors and C. P. Keijzers, Mol. Phys. **51** (2), 509 (1984).
12. B. Z. Malkin, A. V. Vinokurov, J. M. Baker, *et al.*, Proc. R. Soc. London, Ser. A **452**, 2509 (1996).
13. J. M. Baker, Rep. Prog. Phys. **34** (2), 109 (1971).
14. J. M. Baker, C. A. Hatchison, A. A. Jenkins, and A. L. Tronconi, Proc. R. Soc. London, Ser. A **453**, 417 (1997).

Translated by O. Borovik-Romanova

Physics of the Solid State, Vol. 43, No. 2, 2001, pp. 320–324. Translated from Fizika Tverdogo Tela, Vol. 43, No. 2, 2001, pp. 307–311.

MAGNETISM AND FERROELECTRICITY

Anomalous Critical Behavior of NaV_2O_5

S. V. Demishev*, A. A. Pronin*, N. E. Sluchanko*, N. A. Samarin*, A. N. Vasil'ev, M. Isobe***, and Y. Ueda*****

** General Physics Institute, Russian Academy of Sciences, ul. Vavilova 38, Moscow, 117942 Russia*
e-mail: demis@lt.gpi.ru

*** Moscow State University, Vorob'evy gory, Moscow, 119899 Russia*

**** Institute for Solid State Physics, The University of Tokyo, 5-1-5 Kashiwanoha, Kashiwa, Chiba 277-8581, Japan*

Received March 14, 2000; in final form, June 22, 2000

Abstract—The temperature dependences and critical behavior of the dielectric constant were studied in NaV_2O_5 along the *c* axis in a frequency range of 1 MHz–1GHz and a temperature range of 4.2–300 K. An analysis of the data obtained, along with literature data on the heat capacity, magnetic losses, and the ultrasound velocity, indicates that the various physical quantities demonstrate similar temperature dependences in the vicinity of the transition, which corroborates the conclusion on the universality of the critical behavior in NaV_2O_5. Deviations from the predictions of the standard theory of second-order phase transitions were found, such as the asymmetry of the critical behavior above and below the transition and the presence of an anomalous base line. © *2001 MAIK "Nauka/Interperiodica".*

INTRODUCTION

After the discovery of the first inorganic spin-Peierls compound $CuGeO_3$, great attention was attracted to another low-dimensional metal oxide compound, NaV_2O_5. Based on EPR and magnetic susceptibility data, it was first supposed that a spin-Peierls transition occurs in NaV_2O_5 at a temperature $T_c \sim 35$ K [1, 2]. However, later experiments demonstrated substantial deviations from the spin-Peierls behavior (see, e.g., [3]). Moreover, detailed structural studies [4] showed that all the vanadium atoms are equivalent above the transition temperature and have an average charge +4.5. Therefore, the very existence of chains of spins $S = 1/2$ that correspond to V^{4+} ions that are necessarily required for the development of spin-Peierls instability [5], as well as interpretation of the low-temperature magnetic transition [1, 2], was doubted. In [6], a model was suggested according to which NaV_2O_5 should be considered not as a pure spin-Peierls material, but rather as a spin ladder with the filling of 1/4, in which the chains of spins $S = 1/2$ can arise as a result of the localization of electrons at the sites and at the legs of the ladder.

In any case, the magnetic anomaly that is observed in the system such as a spin ladder at $T = T_c$ suggests that, along with spin ordering, a substantial role can be played by processes of charge ordering; therefore, investigation of the dielectric properties of NaV_2O_5 can prove very important for the understanding of the origin of the transition in this compound. Measurements of the temperature dependence of the dielectric constant $\varepsilon(T)$ in a frequency range of 0.1–100 kHz showed the presence of a strong anisotropy and a λ-type anomaly along the *c* axis [7]. Analogous critical behavior was revealed for the heat capacity $c(T)$ [3, 8], ultrasound velocity $V(T)$ [9], thermal expansion coefficient $\alpha(T)$ [8], and magnetic losses $\chi''(T)$ in the microwave range [2]. However, a quantitative analysis of the critical behavior of NaV_2O_5 has not been yet performed and no information on its critical exponents has been published.

This paper has two aims. First, if charge ordering in NaV_2O_5 does occur, the physical picture of the transition can prove to be similar to phase transformations in ferroelectric materials; thus, it is desirable to obtain information on the behavior of the dielectric constant $\varepsilon(T)$ in a maximally wide frequency range. For example, one can expect the appearance of dispersion of the dielectric constant at higher frequencies as compared to those used in [7].

Another task consisted in a quantitative analysis of the available data on the critical behavior of various physical quantities in the vicinity of the critical temperature T_c and in a comparison of the observed λ-type anomalies in NaV_2O_5 with theoretical predictions for second-order phase transitions.

EXPERIMENTAL

In order to investigate the temperature dependence of the dielectric constant $\varepsilon(T)$, we chose high-quality crystals of NaV_2O_5 of a characteristic size of $0.8 \times 7 \times 0.15$ mm; the electric field was oriented along the *c* axis. The measurements were performed in a frequency range $\omega/2\pi = 1$ MHz–1 GHz using a specially designed experimental setup based on an HP4191A Hewlett Packard impedance analyzer [10] that permitted us to

gradually regulate and stabilize the sample temperature in a range of 4.2–300 K. The active part R of the impedance of the NaV_2O_5 sample, $Z = R - iX$, at low temperatures proved to be much greater than the reactive one ($R \gg X$) and substantially higher than the sensitivity of the measuring device (~10^5 Ω) (the dc resistance of the sample was ~10^7 Ω). Thus, we were able to measure the quantity $X = (\omega C)^{-1}$, from which, using the standard formula for a plane capacitor, we calculated the dielectric constant $\varepsilon(T)$. The absolute error of measuring ε was mainly determined by the accuracy of the measurements of the geometrical dimensions of the capacitor; in our case, it did not exceed 20%. At the same time, the relative accuracy of measurements was much better (was about 10^{-4}).

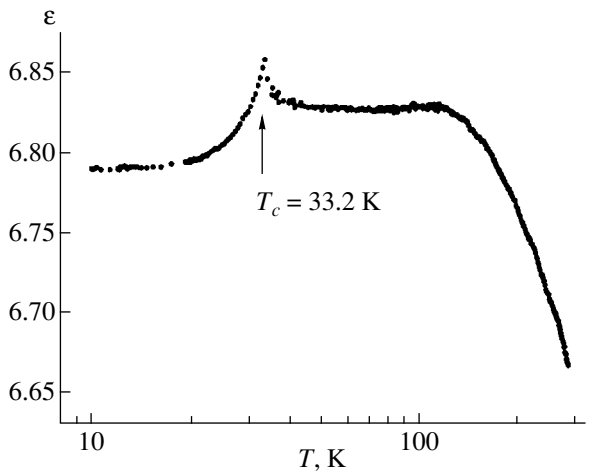

Fig. 1. Temperature dependence of the dielectric constant of NaV_2O_5 along the c axis at a frequency of 150 MHz.

RESULTS AND DISCUSSION

A typical curve of the temperature dependence of the dielectric constant $\varepsilon(T)$ measured along the c axis at a frequency $\omega/2\pi$ = 150 MHz is shown in Fig. 1. A decrease in the temperature from ~300 to 150 K leads to an increase in ε by about 2.4%. At temperatures of $T < 150$ K, the $\varepsilon(T)$ curve first saturates and then, at T_c = 33.2 K, demonstrates a clear anomaly of the λ type with an amplitude of the jump of about 0.5%. The successive cycles of cooling and heating in the vicinity of T_c show no noticeable hysteresis, which agrees with the fact that the magnetic transition in NaV_2O_5 is a second-order phase transition.

The virtually temperature-independent base line on which the λ anomaly is observed (Fig. 1) makes it possible to accurately perform a quantitative analysis of the critical behavior (see the next section). Note that a similar feature in $\varepsilon(T)$ that was recorded in [7] was observed against a strong temperature dependence, which appeared to be due to the incorrect allowance for the parasitic contribution of the connecting cables.

It is of interest that, in the entire frequency range investigated (1 MHz–1 GHz), no noticeable dispersion of the dielectric constant $\varepsilon(\omega, T = \text{const})$ was revealed and the condition $\varepsilon(\omega, T = \text{const}) \approx \text{const}$ was fulfilled at all temperatures studied. This suggests that, in the given frequency range, the condition $\omega\tau \ll 1$ is satisfied for the characteristic time τ of the relaxation processes and, therefore, the magnitude of τ in NaV_2O_5 should be substantially less than 1.6×10^{-11} s.

Before proceeding with the analysis of the critical behavior in NaV_2O_5 in the vicinity of T_c, we briefly summarize the main theoretical predictions for the second-order phase transitions [11–14].

Let us represent the temperature dependence of a physical quantity $y(T)$ in the vicinity of the transition as the sum of two contributions:

$$\begin{aligned} y(T) &= A_1 + B_1 f_1(T - T_c), \text{ for } T > T_c, \\ y(T) &= A_2 + B_2 f_2(T - T_c), \text{ for } T < T_c, \end{aligned} \quad (1)$$

where $f_{1,2}(x \longrightarrow 0) = \infty$ and the indices 1 and 2 refer to the parameters above and below the second-order transition, respectively. In a widely applied approximation, the divergent part $f_{1,2}(T - T_c')$ can be written in the form [13]

$$f_{1,2}(T - T_c) = |T - T_c|^{-p_{1,2}}. \quad (2)$$

In this case, the scaling theory [13] requires that the critical exponents above and below the transition temperature be equal; i.e., $p_1 = p_2 = p$.

Since there is an anomaly of the dielectric constant in NaV_2O_5, it is natural to consider the transitions in ferroelectrics as the starting physical model. This class of phase transitions was studied in detail and is described well by the Landau theory [11]. The dielectric constant (without allowance for fluctuations) follows the Curie law and, for the case where $y \equiv \varepsilon$, the following relations between the parameters in Eqs. (1) and (2) are valid: $A_1 = A_2 = 0$, $|B_1| = 2|B_2|$, and $p_1 = p_2 = 1$ [11]. The heat capacity $c(T)$ in the same approximation experiences a finite jump and the following conditions should be fulfilled: $B_1 = B_2 \equiv 0$ and $A_2 > A_1$ [11, 12]. The allowance for fluctuations leads to the appearance of a divergence in $c(T)$ at the transition point with $p_1 = p_2 = 0.5$ [11].

Figures 2a and 2b display the temperature dependences of the dielectric constant and of the diverging part of the heat capacity $\delta c(T)$ borrowed from [3]. It is seen that both the $\varepsilon(T)$ and $\delta c(T)$ dependences in NaV_2O_5 demonstrate substantial deviations from the above-described "classical" behavior, even if we suppose that the diverging part of $\varepsilon(T)$ is superimposed by a substantial temperature dependence, so that we have $A_{1,2} \neq 0$ in Eq. (1). First of all, it proved to be impossible to approximate the experimental data for $\varepsilon(T)$ and $\delta c(T)$, as well as the critical behavior of $\chi''(T)$ ([2], Fig. 2c) and the anomalous part of the velocity of ultra-

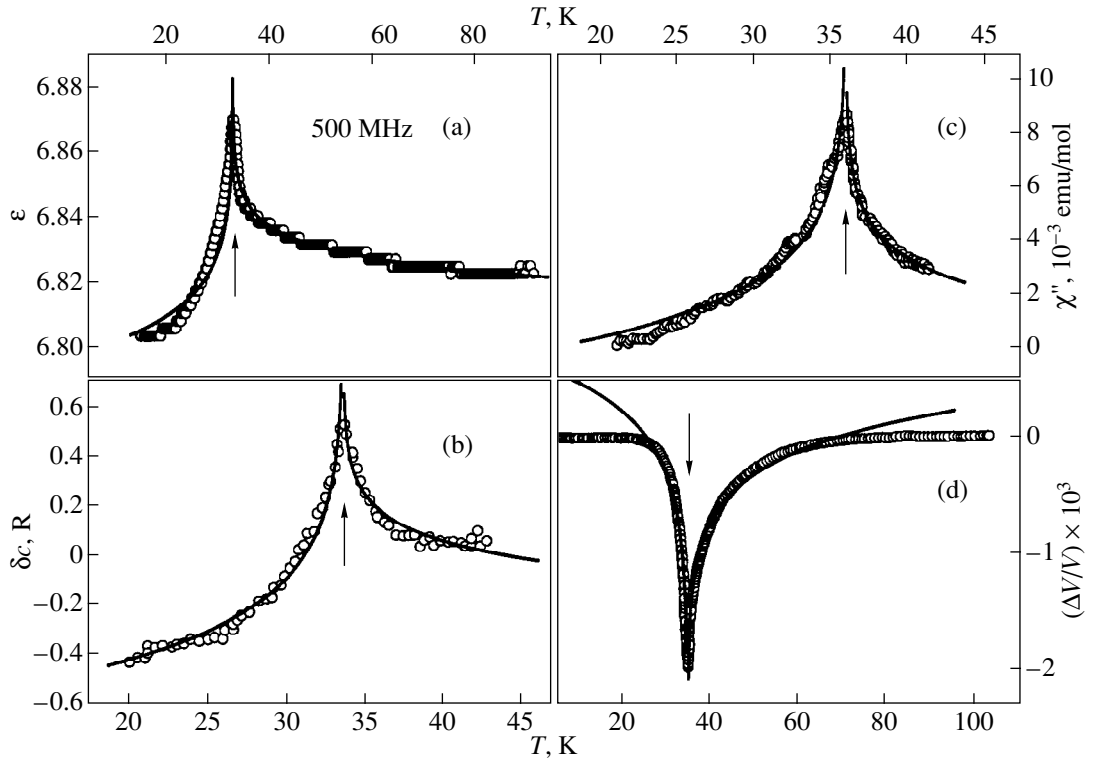

Fig. 2. Critical behavior of (a) the dielectric constant, (b) the anomalous parts of the heat capacity [3], (c) magnetic losses $\chi''(T)$ at a frequency of 36.2 GHz, and (d) the velocity of ultrasound [9]. Data points correspond to experimental data; solid lines, to logarithmic approximations using Eq. (3); and arrows indicate the transition points listed in the table.

sound propagation $\Delta V/V(T)$ ([9], Fig. 2d) using relations (1) and (2). When analyzing the data using the least-squares method according to the Levenberg–Marquardt algorithm, a clear tendency $p_{1,2} \longrightarrow 0$ is observed, which is accompanied by a corresponding growth of the parameters $B_{1,2}$. This indicates that the physical characteristics of NaV_2O_5 should exhibit either a logarithmic divergence or a finite jump at $T = T_c$. Below, we will analyze both these possibilities quantitatively.

In the case of a logarithmic divergency, the functions $f_{1,2}(T - T_c)$ coincide and have the form [14]

$$f_{1,2}(T - T_c) = \ln\left|\frac{T - T_c}{T_c}\right|. \qquad (3)$$

Note that for the ferroelectric materials, the changeover from a power dependence (2) to a logarithmic dependence (3) reflects the lowering of the dimensionality of the fluctuations [11], which seems sufficiently natural for low-dimensional systems such as NaV_2O_5.

Since the critical temperature is known, Eqs. (1)–(3) contain two adjustable parameters above and below the transition and the ranges $T > T_c$ and $T < T_c$ can be analyzed separately. The use of Eqs. (1)–(3) to approximate experimental data does not lead to the appearance of the above-noted problems with the divergence of the numerical procedure. As follows from Fig. 2, in which solid lines correspond to the results of numerical calculations using Eqs. (1)–(3), the use of the logarithmic law (3) leads to a good enough agreement with the experiment for all investigated physical quantities.

Nevertheless, in the case of logarithmic divergence as well, the relations between the parameters in Eq. (1) differ markedly from those expected in the standard theory [11–14]. For a second-order phase transition, the condition $|B_1| = |B_2|$ should be fulfilled [14], whereas the analysis of the experimental data gives $|B_2| \approx 2|B_1|$, $|B_2| \approx 3|B_1|$, and $|B_2| \approx 1.4|B_1|$in the case of the heat capacity, dielectric constant, and magnetic losses, respectively. The "best" coincidence is observed for the velocity of ultrasound, although, even in this case, $|B_2| \approx 1.2|B_1|$. Such an asymmetry of the λ point upon phase transition ($|B_2| > |B_1|$) is accompanied by the fulfillment of the inequality $|A_1| > |A_2|$ for $\varepsilon(T)$, $\delta c(T)$, and $\chi''(T)$ (Figs. 2a–2c). It should be emphasized that, in the Landau theory, the greater value of the heat capacity always corresponds to the phase with a finite value of the order parameter and the condition $|A_1| < |A_2|$ should be fulfilled for NaV_2O_5 [10–13].

Another unexpected aspect of our analysis is that all physical quantities demonstrate universal critical behavior described by logarithmic divergence (3). At the same time, the existent theory of second-order phase transitions predicts different critical behavior for

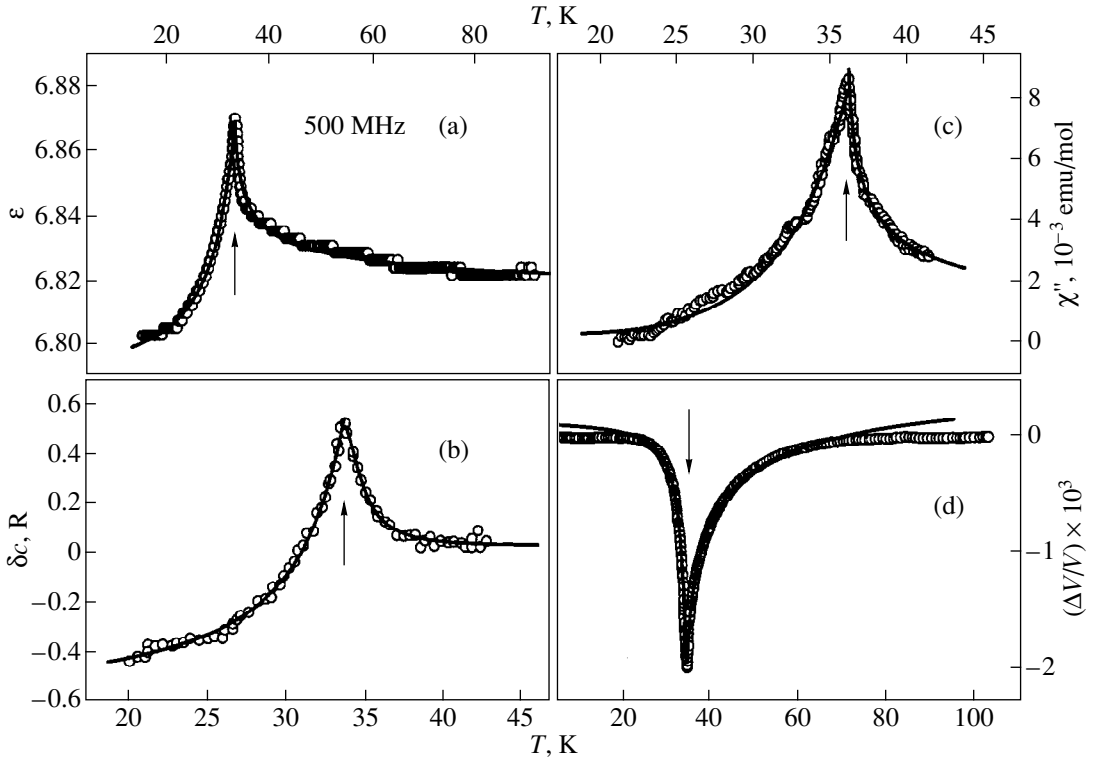

Fig. 3. Analysis of the critical behavior of experimental data shown in Fig. 2 using the phenomenological relationship (4) (see the main text). For designations, see Fig. 2.

various quantities, e.g., for heat capacity and the dielectric constant [11, 13].

In view of the observed deviations from the standard theory of second-order phase transitions, which gives a "rigid" description of the structure of the critical region, the question arises as to what extent this result is stable toward the choice of a mathematical procedure. Remember that the case of $p \longrightarrow 0$ in the power divergence (2) may correspond to not only a logarithmic behavior but also to a finite jump of a physical quantity. In the case of a finite jump, we may choose the functions $f_{1,2}$ in the following model form:

$$f_{1,2}(T - T_c) = (|T - T_c|^{p_{1,2}} + D_{1,2})^{-1}. \qquad (4)$$

A phenomenological description of the experimental data shown in Fig. 2 using formulas (1) and (4) is displayed in Fig. 3. In spite of the fact that the number of free parameters in this case reaches four, the numerical procedure of the approximation of the experimental data was well convergent and the results of the calculations were independent of the initial values of the parameters. The characteristic error of determining the parameters $A_{1,2}$, $B_{1,2}$, and $D_{1,2}$ was ≈15%; the errors of determining the critical exponents $p_{1,2}$ are given in the table.

As follows from Fig. 3, the suggested procedure of the approximation based on Eqs. (1) and (4) permits us to satisfactorily describe the shape of all experimental curves demonstrating critical behavior. Note that the relationships between the parameters A and B that were found above ($|A_1| > |A_2|$ and $|B_1| < |B_2|$) remain valid and the universality of the form of the anomaly at the transition point is confirmed. The table contains the calculated values of the critical exponents occurring in formula (4), along with the corresponding transition temperatures. Although the values of T_c differ within 3 K (this may be related to the susceptibility of the transition to the quality of crystals), below the transition, all exponents prove to be approximately equal ($p_2 \approx 1.1$) and are independent of the type of physical quantity analyzed.

In the temperature range of $T > T_c$, the universality is retained for $\varepsilon(T)$, $\delta c(T)$, and $\Delta V/V(T)$, for which the

Critical exponents for NaV_2O_5

Quantity	Refs.	$p_1(T > T_c)$	$p_2(T < T_c)$	T_c, K
ε	This work	0.59 ± 0.04	1.14 ± 0.04	33.2
χ''	[2]	0.60 ± 0.02	1.09 ± 0.12	36.1
$\Delta V/V$	[9]	0.69 ± 0.03	1.19 ± 0.04	34.8
δc	[3]	1.84 ± 0.06	1.06 ± 0.09	33.6
	[15]	1.59 ± 0.05	1.08 ± 0.06	33.5

critical exponent is $p_1 = 0.6–0.7$ (see table). At the same time, the heat capacity is characterized by twofold–threefold greater values $p_1 = 1.6–1.8$, although even in this case, the exponent p_1 is not coincident with the corresponding value p_2 for $T < T_c$. Thus, the comparison of critical exponents corresponding to the regions above and below the critical temperature upon the description of the critical region using formulas (1) and (4) gives additional grounds to believe that the usually accepted symmetry of fluctuations is broken in NaV_2O_5.

CONCLUSION

Thus, we showed that the critical behavior of various physical quantities, including the dielectric constant measured along the *c* axis, demonstrates noticeable deviations from the predictions of the standard theory. The most significant of them are the asymmetry of the critical region above and below the transition point; the appearance of anomalous base lines, against the background of which the features are observed; and the virtually identical form of critical curves irrespective of the physical quantity considered (this aspect is especially strongly pronounced at $T < T_c$). To date, it is not completely clear whether or not the experimental data for NaV_2O_5 can be interpreted in terms of an appropriately modified Landau theory. We may suppose that the true critical region for NaV_2O_5 is narrower and the features observed are not related to fluctuations. Moreover, we cannot rule out that the smearing of features near T_c may be related to structural defects of the NaV_2O_5 crystals. Nevertheless, one of the results of this paper is the occurrence of a finite jump in the dielectric constant of NaV_2O_5 at $T = T_c$ rather than the infinite divergence ($\varepsilon \longrightarrow \infty$). Therefore, in order to decisively answer the question of the nature of the anomalous critical behavior of NaV_2O_5, additional measurements of the divergences of physical quantities are required using a greater temperature resolution.

ACKNOWLEDGMENTS

This work was supported by the grant of the President of the Russian Federation (grant no. 96-15-96929), the Russian Foundation for Basic Research (grants no. 98-02-17163 and 99-02-17828), INTAS (grant no. 96-0451), and the ERBIC15 CT98 0812 grant.

REFERENCES

1. M. Isobe and Y. Ueda, J. Phys. Soc. Jpn. **65**, 1178 (1996).
2. A. N. Vasil'ev, A. I. Smirnov, M. Isobe, and Y. Ueda, Phys. Rev. B: Condens. Matter **56**, 5065 (1997).
3. J. Hemberger, M. Lohmann, N. Nicklas, *et al.*, Europhys. Lett. **42**, 661 (1998).
4. T. Chatterji, K. D. Liss, G. J. McIntyre, *et al.*, Solid State Commun. **108**, 23 (1998).
5. M. C. Cross, Phys. Rev. B: Condens. Matter **20**, 4606 (1979).
6. S. Nishimoto and Y. Ohta, cond-mat/9805336.
7. Y. Sekine, N. Takeshita, N. Mori, *et al.*, Tech. Rep. ISSP Jpn., Ser. A, No. 3371 (Japan, 1998).
8. M. Koppen, D. Pankert, R. Hauptmann, *et al.*, Phys. Rev. B: Condens. Matter **57**, 8466 (1998).
9. P. Fertey, M. Poirier, M. Castonguay, *et al.*, Phys. Rev. B: Condens. Matter **57**, 13698 (1998).
10. S. V. Demishev, A. A. Pronin, N. E. Sluchanko, *et al.*, Pis'ma Zh. Éksp. Teor. Fiz. **65** (4), 527 (1997) [JETP Lett. **65**, 342 (1997)].
11. B. A. Strukov and A. P. Livanyuk, *Physical Principles of Ferroelectric Phenomena in Crystals* (Nauka, Moscow, 1983).
12. J.-C. Toledano and P. Toledano, *The Landau Theory of Phase Transitions* (World Scientific, Singapore, 1994).
13. S. Ma, *Modern Theory of Critical Phenomena* (Benjamin, Reading, 1976; Mir, Moscow, 1980).
14. R. P. Feynman, *Statistical Mechanics: A Set of Lectures* (Benjamin, Reading, 1972; Mir, Moscow, 1978).
15. D. K. Power, J. W. Brill, Z. Zeng, and M. Greenblatt, Phys. Rev. B: Condens. Matter **58**, R2937 (1998).

Translated by S. Gorin

Physics of the Solid State, Vol. 43, No. 2, 2001, pp. 325–328. Translated from Fizika Tverdogo Tela, Vol. 43, No. 2, 2001, pp. 312–315.

MAGNETISM AND FERROELECTRICITY

Polarization Switching Kinetics in Ferroelectrics in the Region of Strong Metastability

S. A. Kukushkin and A. V. Osipov

Institute for Problems in Mechanical Engineering, Russian Academy of Sciences, Vasil'evskiĭ ostrov, Bol'shoĭ pr. 61, St. Petersburg, 199178 Russia
e-mail: ksa@math.ipme.ru

Received April 5, 2000

Abstract—The thermodynamics and kinetics of polarization switching in ferroelectrics are studied in the framework of the field theory in the vicinity of the critical point of first-order phase transitions. The study is exemplified by the switching of intrinsic ferroelectrics with 180° domains. An expression describing the dependence of the domain critical size on the switching field is derived. The switching process is studied at high switching fields. Relationships for calculating the field dependence of the number of switched domains are obtained. © *2001 MAIK "Nauka/Interperiodica".*

1. INTRODUCTION

Earlier [1, 2], we studied polarization switching in ferroelectrics acted upon by an electric field below the Curie temperature and constructed the binodal and spinodal curves. They are shown in the figure. A theory of polarization switching in ferroelectrics far from the critical point of first-order phase transitions was developed [1, 2]. In order to analyze switching processes in the vicinity of the critical point, it is necessary to use the field theory of nucleation [3]. This paper will deal with this approach.

2. THE FIELD THEORY OF THE NUCLEATION OF SWITCHED REGIONS

According to [3], the Hamiltonian of a ferroelectric near the critical point (see figure) can be written in the form proposed by Ginzburg and Landau[1]:

$$H\{P_z\} = \int\left[\Phi_0 + \frac{\delta}{2}(\nabla P_z)^2 + \frac{a}{2}(T - T_c)P_z^2 + \frac{b}{4}P_z^4 - E_z P_z\right]dr, \quad (1)$$

where Φ_0 denotes the thermodynamic potential terms which do not depend on the degree of polarization, T is the temperature of the medium in which the crystal is immersed, E_z is the z component of the electric field, T_c is the Curie temperature, and a and b are the coefficients of the thermodynamic potential expansion in powers of P_z.

Because we are interested in the relaxation of the order parameter P_z, we have to establish whether the latter is retained in the phase transition or not. Depending on the answer to this question, the kinetic equation describing the order-parameter relaxation will have essentially different forms.

A ferroelectric phase transition brings about atomic displacements, which implies that the polarization vector does not necessarily retain its total magnitude. This sets ferroelectric phase transitions apart from magnetic phase transitions in which the elementary magnetic moment originating from the exchange coupling does not vanish as the temperature passes through the Curie point; i.e., the total magnetic moment in a ferromagnet is retained. Therefore, in this case, we can write, according to [3], the following equation describing the order parameter relaxation:

$$\frac{1}{\Gamma_n}\frac{\partial P_z}{\partial t} = -\frac{\delta H\{P_z\}}{\delta P_z} + f_e, \quad (2)$$

where Γ_n is the kinetic coefficient, $\delta H\{P_z\}/\delta P_z$ is the variational derivative, and f_e is the external force simulating the thermal ensemble.

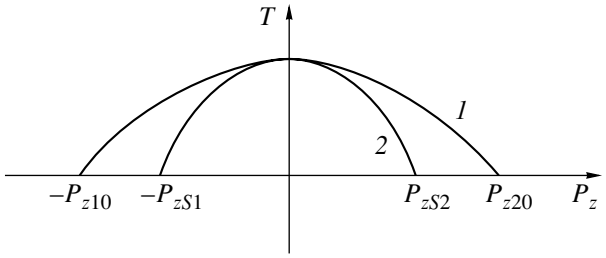

(*1*) Phase equilibrium line for a ferroelectric with states of "polarization-up" P_z and "polarization-down" $-P_z$; $P_{z1,\,20}$ are equilibrium values of the polarization. (*2*) Spinodal curve bounding the regions within which the polarization of a ferroelectric can in no case be uniform; $P_{z1,\,2s}$ are the boundaries of the metastability region.

[1] See paper [1] for the expansion of the thermodynamic potential in powers of the order parameter P_z (Eq. (1) in [1]).

The following designations are used: $a(T_c - T) = \alpha$, $r = \sqrt{2\delta/|a|}\,\xi$, $t'(2/\Gamma_n|\alpha|) = t$, $\tilde{P}_z(\xi, t) = P_z(\xi, \acute{t})/\varphi_S$, $\varphi_S = \sqrt{|\alpha|/b}$, and $z = \tilde{z}\sqrt{2\delta/|\alpha|}$.

In order to solve Eq. (2), it is necessary to know the domain shape. As a first approximation, we assumed [1] that the domains have a cylindrical shape. By calculating the variational derivative for the case of cylindrical symmetry and substituting it in Eq. (2) for $f_e = 0$, we obtain

$$\frac{\partial \tilde{P}_z}{\partial \acute{t}'} = \frac{\partial^2 \tilde{P}_z}{\partial \xi^2} + 2(\tilde{P}_z - \tilde{P}_z^3) + E_z + \frac{1}{\xi}\frac{\partial \tilde{P}_z}{\partial \xi} + \frac{1}{\xi^2}\frac{\partial^2 \tilde{P}_z^2}{\partial \Theta^2} + \frac{\partial^2 \tilde{P}_z}{\partial \tilde{z}^2}, \tag{3}$$

where Θ is the angle in the cylindrical coordinate system.

According to [3], this equation can be solved if the width of the nucleus boundary $\xi_0(t)$ is small compared to the nucleus size. In this case, Eq. (3) can be recast in the form

$$\frac{\partial \tilde{P}_z}{\partial \acute{t}'} = \frac{\partial^2 \tilde{P}_z}{\partial \xi^2} + 2(\tilde{P}_z - \tilde{P}_z^3) + E_z + \frac{1}{\xi_0}\frac{\partial \tilde{P}_z}{\partial \xi} + \frac{1}{\xi_0^2}\frac{\partial^2 P_z^2}{\partial \Theta^2} + \frac{\partial \tilde{P}_z}{\partial \tilde{z}^2}. \tag{4}$$

The solution to this equation is well known and has the form [3–6]

$$\tilde{P}_z = \pm \tanh[\xi - \xi_0(\Theta, t')] + \frac{\tilde{E}_z}{4}, \tag{5}$$

where $\tilde{E}_z = (2\sqrt{b}/\alpha\sqrt{|a|})E_z$.

The velocity of the nucleus boundary motion can be represented in the form

$$\xi_0(\Theta, t') = \sum_{n=0}^{\infty} \xi_0^n(t')\cos(n\Theta + \beta_n), \tag{6}$$

where $\beta_0 = 0$ and $\beta_n = \text{const}$ at $n \gg 1$ are determined by the boundary conditions. Substituting Eqs. (5) and (6) in Eq. (4) yields

$$\frac{d\xi_0}{dt'} = -\frac{1}{\xi_0} + \frac{3}{2}\tilde{E}_z, \qquad \frac{d\xi_0^n}{dt'} = -\frac{n^2 - 1}{\xi_0^2}\xi_0^n. \tag{7}$$

From here, for $\xi_0^n(t')$, we have

$$\xi_0^n(t') = \xi'(0)\exp\left[-\int_0^{t'} \frac{(n^2-1)}{\xi_0(t'')}dt''\right],$$

and for the nucleus growth rate, we obtain

$$\frac{1}{\Gamma|\alpha|}\frac{dr_0}{dt}\frac{2\sqrt{|\alpha|}}{\sqrt{2\delta}} = -\frac{1}{r_0}\sqrt{\frac{2\delta}{|\alpha|}} + \frac{3\sqrt{b}}{|\alpha|\sqrt{|\alpha|}}E_z, \qquad \frac{dr_0}{dt} = \Gamma\left(\frac{3\sqrt{2\delta}\sqrt{b}}{2|\alpha|}E_z - \frac{\delta}{r_0}\right). \tag{8}$$

The quantity $(1/E_z)(\sqrt{2\delta}\,|\alpha|/3\sqrt{b})$ is nothing else but the radius of the critical nucleus; i.e.,

$$R_c = \frac{\sqrt{2\delta}|\alpha|}{3\sqrt{b}E_z}. \tag{9}$$

Introducing the correlation radius as $r_c = \sqrt{2\delta/|\alpha|}$, we obtain

$$R_c = \frac{2}{3}\frac{r_c}{\tilde{E}_z}.$$

On the other hand, it can be shown that the critical radius is related to the interface half-width $l(x)$ as

$$R_c = \frac{4}{3}l(x), \tag{10}$$

where $l_x \sim \sqrt{2\delta/|\alpha|}\,(1/E_z)$.

A comparison of Eq. (9) with the expression describing the field dependence of the critical nucleus (see [1]) reveals their similarity. However, unlike the latter expression, Eq. (9) contains a number of constants which cannot always be determined. In order to take into account the effect of small-scale fluctuations on nucleation, it is necessary to analyze Eq. (2). This can be done by analogy with [3]. In the presence of small-scale fluctuations, Eqs. (7) take the following form:

$$\frac{d\xi_0}{dt'} = -\frac{1}{\xi_0} + \frac{3}{2}\tilde{E}_z + 6V(\xi_0, t'), \qquad \frac{d\xi_0}{dt'} = -\frac{n^2-1}{\xi_0^2}\xi_0^n U + 6V(\xi_0^0(t', t')), \tag{11}$$

where $V(\xi_0, t')$ describes the response of the field $\tilde{P}_z(\xi_0, t')$ to the force $f(\xi_0, t')$ and is the solution to the equation

$$\frac{\partial^2 V}{\partial t'} = \nabla^2 V - 4V + f(\xi, t').$$

By analogy with [3], it can be shown that a random fluctuation of the force $f(\xi, t')$ results in small fluctua-

tions of the amplitude $\tilde{P}_z(\xi_0, t')$; i.e., it makes the nucleus boundary slightly diffuse.

In order to calculate the flux of the nuclei formed in a unit crystal volume per unit time, we can use the Kolmogorov equation for the probability distribution of the critical configurations of the order parameter field, as was done, for instance, in [3]. On the other hand, we can use the expression derived for the nucleus flux in [1] (see Eqs. (34), (35) in [1]). Indeed, the expression for the flux derived there was based on the solution of the Fokker–Planck equation, which was obtained under practically the same limitations as the ones accepted in solving the Kolmogorov equation. Therefore, we can substitute the critical radius (9) into the expression for the nucleus flux (Eq. (35) in [1]), with due regard for the fact that, according to [4], surface tension near the critical point can be represented as $\sigma = \frac{2\sqrt{2\delta}}{3b}\alpha^{3/2}$. Finally, we obtain

$$I = \frac{N_v \beta_0 H^{1/2} \omega^{3/2} \alpha^{1/4} E_z^{1/2}}{2\sqrt{k_B T} b^{1/4}} \exp\left(-\frac{4\pi H \delta \alpha^{5/2}}{9 b^{3/2} k_B T E_z}\right), \quad (12)$$

where β_0 is the kinetic coefficient, ω is the unit cell volume, and N_v is the number of unit cells per unit volume of the crystal. The specific expressions for these quantities are given in [1]. Substituting Eq. (12) into Eq. (38) derived in [2], we can readily obtain an equation determining the switching current in the vicinity of the critical point.

Note that the representation of the Hamiltonian in the form of Eq. (1) and, accordingly, Eq. (12), becomes possible in the vicinity of the critical point in which the Landau mean-field theory is valid. The region of its applicability is specified by the Ginzburg–Levanyuk criterion G_i [4], subject to the condition that

$$G_i = \frac{(k_B T_c)^2 b^2}{\delta^3} \ll |\alpha| \ll 1 \quad (13)$$

and

$$\frac{R_{max}}{k_B T} \gg 1,$$

where R_{max} is the maximum work needed to form the new phase, which was calculated in [1]. Conditions (13) indicate, on the one hand, that the Landau theory is valid and, on the other hand, that the system is in the region of weak metastability. Far from T_c, i.e., at $T \ll T_c$, in the region of weak metastability, we cannot, in the general case, use an expansion of type (1) and should instead invoke the results obtained in [1, 2].

3. NUCLEATION OF SWITCHED REGIONS NEAR THE INSTABILITY REGION

Let us consider the figure and expressions (1) and (4) given in [1]. We expand the thermodynamic potential in the vicinity of the P_{z20} point (see Eq. (1) in [1]), which corresponds to the boundary of the metastable region, in a Taylor series and obtain

$$H\{\tilde{\Phi}_{pz}\} = \tilde{\Phi}_0 + \Phi'(P_s)(P_z - P_s) + \frac{\Phi''(P_s)}{2!}(P_z - P_s)^2 + \frac{\Phi'''(P_s)}{3!}(P_z - P_s)^3 + \dots . \quad (14)$$

Let

$$\Phi'(P_s) = \frac{\mu_s}{2}, \quad q = -\frac{\Phi'''(P_s)}{2}.$$

Note that the derivative $\Phi'(P_s)$ is nothing other than the chemical potential at the point P_s. The second derivative $\Phi''(P_s)$ in the effective Hamiltonian taken at point P_s is zero; i.e., $\Phi''(P_s) = 0$, because the spinodal is found from the condition that the second derivative of the effective Hamiltonian vanishes. With this in mind, Eq. (14) can be recast as

$$\tilde{\Phi}_{pz} = \tilde{\Phi}_0 + \frac{\mu_s}{2}(P - P_s) - \frac{q}{3}(P - P_s)^3. \quad (15)$$

In Eqs. (14) and (15),

$$\frac{\Phi'''(P_s)}{6} = \frac{4\sqrt{T_c a b}}{\sqrt{6}}\sqrt{1 - \frac{T}{T_c}}. \quad (16)$$

Note that $\Phi''(P_s)$ was found with the use of Eqs. (1) and (3) taken from [1].

We introduce a new variable

$$\varphi = \sqrt{\frac{q}{\mu_s}}(P - P_s)$$

and denote

$$\frac{\mu_s}{2}\sqrt{\frac{\mu_s}{q}} = \frac{k_1}{2}, \quad \frac{q}{3}\left(\sqrt{\frac{\mu_s}{q}}\right)^3 = \frac{k_2}{3}, \quad \frac{c}{2} = \delta\left(\frac{\mu_s}{q}\right)^2.$$

Now, we can write the effective Hamiltonian in the form

$$H\{\varphi\} = \int\left[\tilde{\Phi}_0 + \frac{c}{2}(\nabla\varphi)^2 + \frac{k_1}{2}\varphi - \frac{k_2}{3}\varphi^3\right]dz. \quad (17)$$

This Hamiltonian coincides with the one obtained in [3]. For the equations of motion of such a system, we obtain

$$\frac{1}{\Gamma_n}\frac{\partial\varphi}{\partial t} = -\frac{\delta H\{\varphi\}}{\delta\varphi} + f_{st}(\mathbf{x}, t), \quad (18)$$

where Γ_n is the kinetic coefficient and $f_{st}(\mathbf{x}, t)$ is the external force simulating the thermal ensemble.

Let the fluctuating fields in the metastable phase be small, $\varphi \simeq 0$, so that the field fluctuation amplitude in a region with dimensions of the order of the correlation radius R_0 is small compared to $\varphi = \mu/q$.

At the onset of the metastable state, the system occurs near the relative minimum of the effective Hamiltonian at $\varphi = 0$. Random fluctuations can produce a supercritical configuration with $\varphi > \varphi_0$, which is unstable upon further growth of the φ amplitude. As a result, this element of the ferroelectric volume transforms into a stable state with the polarization vector aligned with the field. In the case of small fluctuations, i.e., for

$$\gamma = \frac{(\mu_s c)^{3/2}}{k_B T q^2} \geq 1,$$

this process will predominantly pass through the critical configuration $\varphi(x)$,

$$\left.\frac{\delta H}{\partial \varphi}\right|_{\varphi_0(x)} = 0, \quad (19)$$

which corresponds to the minimum work required to form a nucleus of a supercritical size. Now, we can use the results obtained in an analysis of this system in [3] and described, for example, in [5, 6], to derive an expression for the flux of the polarization switching nuclei that overcome the activation barrier at high fields. As follows from the calculations, this expression has the form

$$I(\xi) = \sqrt{\frac{\lambda_0}{4\pi\gamma}} \exp\{-H\{\varphi_0\} q P_{z10}^2 (\xi_{\max} - \xi)^2\}, \quad (20)$$

where, according to [3, 5], $\lambda_0 \sim 6.59$, $H\{\varphi_0\} = 40$, and the largest attainable superpolarization $\xi_{\max} = |P_{z1s}|/|P_{z10}| - 1$ (see [1]).

Thus, in the case of large polarization switching, the switched regions are small and the fluctuations affect not only their boundary but also the switched region as a whole. As is evident from the last equation, the rate of domain formation at a large polarization switching differs substantially from that in the region of weak metastability (see Eq. (36) in [1]).

4. POLARIZATION SWITCHING KINETICS IN THE REGION OF INSTABILITY (SPINODAL DECOMPOSITION OF THE SWITCHED FERROELECTRIC)

In our opinion, spinodal decomposition cannot be experimentally realized in ferroelectrics under polarization switching conditions. Actually, there are two possible ways for its realization. One of them consists in moving along the horizontal axis (see figure) until crossing the boundary, to enter the region bounded by the line of absolute instability. According to the theory, this should entail polarization switching throughout the crystal volume without nucleation. However, as was shown in [4], the electric fields involved should exceed the experimentally observed coercive fields by more than an order of magnitude. As follows from our previous study, polarization switching nuclei start to form in a ferroelectric before the instability line is reached. However, at high fields, domains can be of the same size and become aligned in rows, a process resembling spinodal decomposition.

The second way to reach the instability region, which can sometimes be realized in solid solutions, consists in a fast cooling (quenching) of the solid solution lying above the spinodal down to the temperature that corresponds to the region within the spinodal. In our opinion, this process cannot occur in ferroelectrics under switching conditions. Indeed, in the case when a ferroelectric occurs at a temperature above the Curie point, the polarizing field lowers the symmetry of the crystal. When this crystal is cooled below the Curie temperature, the phase transition becomes diffuse; i.e., no spinodal decomposition can take place in such a system. If there is no external field, a second-order phase transition is observed as the temperature crosses the critical line. If the field is turned on at the instant of this transformation, the transition becomes diffuse. These processes, however, are beyond the scope of this work.

ACKNOWLEDGMENTS

This work was supported in part by the Russian Foundation for Basic Research (project nos. 98-03-32791 and 99-03-32768), the Russian Federal Center "Integration" (project no. A0151), the NATO "Science for Peace" Program (grant Stp 973252), and the CONACYT Program (grant no. 32208).

REFERENCES

1. S. A. Kukushkin and A. V. Osipov, Fiz. Tverd. Tela (St. Petersburg) **43** (1), 80 (2001) [Phys. Solid State **43**, 82 (2001)].
2. S. A. Kukushkin and A. V. Osipov, Fiz. Tverd. Tela (St. Petersburg) **43** (1), 88 (2001) [Phys. Solid State **43**, 90 (2001)].
3. A. Z. Pokrovskiĭ and B. I. Shumilo, Zh. Éksp. Teor. Fiz. **77** (4), 1417 (1979) [Sov. Phys. JETP **50**, 712 (1979)].
4. B. A. Strukov and A. P. Livanyuk, *Physical Principles of Ferroelectric Phenomena in Crystals* (Nauka, Moscow, 1995).
5. S. A. Kukushkin and A. V. Osipov, Prog. Surf. Sci. **56** (1), 1 (1996).
6. S. A. Kukushkin and A. V. Osipov, Usp. Fiz. Nauk **168** (10), 1083 (1998) [Phys. Usp. **41**, 983 (1998)].

Translated by G. Skrebtsov

Physics of the Solid State, Vol. 43, No. 2, 2001, pp. 329–336. Translated from Fizika Tverdogo Tela, Vol. 43, No. 2, 2001, pp. 316–322.

MAGNETISM AND FERROELECTRICITY

Influence of Domain Boundary Width on the Statics of 90° Domains in Epitaxial Ferroelectric Thin Films

A. Yu. Emel'yanov

Ioffe Physicotechnical Institute, Russian Academy of Sciences, Politekhnicheskaya ul. 26, St. Petersburg, 194021 Russia

Received May 16, 2000

Abstract—The influence of the domain boundary width on the statics of single 90° elastic domains (twins) in epitaxial ferroelectric tetragonal films grown on a cubic substrate is theoretically investigated. The inhomogeneous internal stresses arising in polydomain epitaxial systems are calculated by the effective dislocation method. The elastic energy stored in the heterostructure is determined. The equilibrium domain size is found and the stability diagram for single domains at different wall widths is constructed by minimizing the total internal energy of the system. It is demonstrated that, as the domain boundary width $2w$ increases, the stability region of 90° domains increases and qualitatively changes for ultrathin films when the parameter $2w$ exceeds the specific critical value $2w_{cr}$. The equilibrium width $2w^*$ of domain walls in thin films is predicted to be larger compared to the width $2w_0$ of domain boundaries in a macroscopic crystal. © *2001 MAIK "Nauka/Interperiodica".*

1. INTRODUCTION

In recent years, thin ferroelectric films have become the subject of numerous studies owing to their widespread use in the design of various devices, such as memory cells (DRAM and FeRAM), electrooptic switches, piezoelectric transducers, and pyroelectric detectors. The physical properties of thin films substantially depend on the character of their interaction with a substrate, which should be taken into account when these films are employed for technical purposes. Of particular interest are epitaxial thin films, because the specific features of the film–substrate interaction are most pronounced in these systems. One of these features is the generation of internal stresses due to the lattice misfit of the film and the substrate. These stresses can decrease through the formation of misfit dislocations in the high-temperature paraelectric phase. Another mechanism of the stress relaxation consists in forming a polydomain structure of the twin type upon transition from the paraelectric to the ferroelectric state. The polydomain structures were experimentally observed in $PbTiO_3$, $Pb(Zr_xTi_{1-x})O_3$, $(Pb_{1-x}La_x)TiO_3$, $KNbO_3$, and $YBa_2Cu_3O_7$ thin films grown on different substrates [1–8]. The formation of elastic domains can bring about a change in the macroscopic properties of films, specifically in their dielectric and piezoelectric responses [9, 10].

In all previous theoretical investigations of domain structures in ferroelectric films, the boundaries between 90° domains were treated as infinitely thin [9–17]. However, experimental observations in crystals, as a rule, revealed ferroelectric domain walls with a finite width. The order parameter within the domain wall varies in a continuous way, and its spatial variations can be characterized by the effective wall width $2w$, which, in different crystals, ranges from 1 to 5 nm in the direction normal to the domain walls [18, 19]. Moreover, the domain boundary width $2w$ can substantially increase at temperatures near the ferroelectric transition point T_c [20]. Since the distribution of internal stresses over a film and, hence, the stored elastic energy of an epitaxial system should depend on the $2w$ parameter, the influence of finite wall width should be taken into consideration in constructing the domain structure theory for ferroelectric films.

In the present work, this theory is developed as applied to single 90° domains in thin tetragonal films grown on a cubic substrate. The inhomogeneous stresses are calculated by the effective dislocation method [15, 16], which allows a correct inclusion of the influence of a free surface. First, we construct the dislocation–disclination models of mechanical stress sources in heterostructures with 90° domain walls of a finite width (Section 2). These models are used for calculating the elastic energy and the equilibrium size of a single 90° domain at different wall widths $2w$ (Section 3). Then, the stability diagram of single 90° domains in a tetragonal film at fixed parameters $2w$ is constructed using the energy approach (Section 4).

2. DISLOCATION–DISCLINATION MODELS OF THE *c*/*a*/*c* AND *a*/*c*/*a* STRUCTURES WITH A FINITE DOMAIN WALL WIDTH

Let us consider thin single crystals with a perovskite ($BaTiO_3$ and $PbTiO_3$) symmetry. The crystals are grown at the temperature $T_g > T_c$ on a cubic substrate whose boundary is parallel to the crystallographic plane (001). In the paraelectric cubic phase ($T > T_c$), the

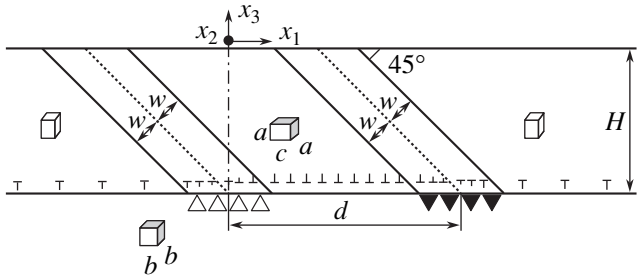

Fig. 1. Dislocation–disclination model of the *c*/*a*/*c* structure with a finite domain boundary width 2*w*. Positive and negative wedge disclinations are designated by closed and open triangles, respectively. Symbols ⊥ indicate the edge dislocation density ρ_{21}^{Σ}. The dislocation density component ρ_{12}^{Σ} is not shown.

crystallographic axes of the film are parallel to the corresponding axes of the substrate. In the ferroelectric phase ($T < T_c$), the tetragonal axis *c* is aligned along one of the edges of the initial cubic lattice. Therefore, three different types of elastic domains can be formed in the film: the *c* domains with the tetragonal axis perpendicular to the film surface and the a_1 and a_2 domains in which the *c* axes are aligned along the [100] and [010] directions, respectively.

Our prime interest here is in the *c*/*a*/*c* structure in a tetragonal film (Fig. 1). This structure is obtained by introducing a single *a* domain of size *d* into a single-domain film of the *c* type (the *c* monovariant). The *a*/*c*/*a* structure is formed in a similar way by introducing the *c* domain into the *a* monovariant. It is assumed that two 90° domain walls are tilted at an angle of 45° with respect to the "film–substrate" planar interface, are parallel to each other, and have the same width $2w > 0$. These domain structures play an important role at the initial stage of the formation of a polydomain structure in an epitaxial system at temperatures near T_c and have already been considered in [16] for the case of infinitely thin walls.

In the linear approximation, we ignore the deviations of order parameters in the ferroelectric film from their equilibrium values in a free bulk crystal. Hence, the spatial distributions of spontaneous strains $S_{ij}^0(\mathbf{r})$ ($i, j = 1, 2, 3$) in the epitaxial film can be calculated for the polydomain state of a free film. At a given distribution $S_{ij}^0(\mathbf{r})$, the elastic strains $S_{ij}(\mathbf{r})$ and the internal stresses in the film are calculated by the effective dislocation method as follows.

For the single-domain state of a film, the elastic stress field is homogeneous in the epitaxial layer and is absent in the substrate [11]. In the paraelectric phase of the film, the elastic strain components $S_{\alpha\beta}$ ($\alpha, \beta = 1, 2$) in the plane are equal to the corresponding misfit strains $S_{\alpha\beta}^m$ which arise from the mismatch between the lattice parameters of the film and the substrate. In the chosen crystallographic coordinate system (x_1, x_2, x_3) with the x_3 axis perpendicular to the film–substrate interface (Fig. 1), the misfit strains are written as

$$S_{11}^m = S_{22}^m = \frac{b^* - a_0}{a_0}, \quad S_{12}^m = S_{21}^m = 0, \qquad (1)$$

where a_0 is the lattice parameter for a free film at $T > T_c$ and b^* is the effective substrate lattice parameter [21], which accounts for the stress relaxation caused by the formation of misfit dislocations at the film–substrate interface. The spontaneous strains S_{ij}^0 ($i, j = 1, 2, 3$) arise below the transition temperature T_c. Therefore, the elastic strain components $S_{\alpha\beta}$ ($\alpha, \beta = 1, 2$) in the plane change and can be approximated by the difference $S_{\alpha\beta} \cong S_{\alpha\beta}^m - S_{\alpha\beta}^0$ at $S_{\alpha\beta}^0 \ll 1$.

For the polydomain state of a film, the total strains $S_{ij}^t(\mathbf{r})$ can be represented as $S_{ij}^t(\mathbf{r}) = S_{ij}(\mathbf{r}) + [S_{ij}^0(\mathbf{r}) - S_{ij}^m]\delta(V_f)$, where $\delta(V_f)$ is the Dirac delta function for the film volume V_f. In this formula, the components S_{i3}^m ($i = 1, 2, 3$) are formally taken equal to the elastic strains S_{i3} in the paraelectric phase of the film. On the other hand, the total strains $S_{ij}^t(\mathbf{r})$ in the epitaxial system should satisfy the compatibility condition $\varepsilon_{mki}\varepsilon_{nlj}S_{ij,kl}^t = 0$, where ε_{mki} is the antisymmetric Levi-Civitá tensor. Here, the subscripts after the comma indicate the differentiation with respect to the relevant coordinates, and the Einstein summation convention is applied. We introduce the densities $\rho_{ni}(\mathbf{r})$ of effective dislocations with the use of the relationships $\varepsilon_{mki}\rho_{ni,k} = \varepsilon_{mki}\varepsilon_{nlj}S_{ij,kl}$ [15]. After the calculations, we obtain the following expression for $\rho_{ni}(\mathbf{r})$:

$$\rho_{ni}(\mathbf{r}) = -\varepsilon_{nlj}[S_{ij}^0(\mathbf{r}) - S_{ij}^m]\delta_l(\Sigma) - \varepsilon_{nlj}S_{ij,l}^0(\mathbf{r})\delta(V_f), \quad (2)$$

where $\delta_l(\Sigma)$ ($l = 1, 2, 3$) is the Dirac delta function for the film–substrate interface Σ with the normal directed toward the substrate. The first term in formula (2) corresponds to the stress sources localized on the surface Σ. The last term in formula (2) describes the stress sources arising within the film, for example, in the presence of junctions between domain walls of different orientations [16].

By designating the lattice parameters of the tetragonal phase in a free crystal as *a* and $c > a$, nonzero spontaneous strains can be written in the form $S_{11}^0 = S_{22}^0 = (a - a_0)/a_0$ and $S_{33}^0 = (c - a_0)/a_0$ inside the *c* domain and in the form $S_{11}^0 = (c - a_0)/a_0$ and $S_{33}^0 = S_{22}^0 = (a - a_0)/a_0$ in the *a* domain. The S_{ij}^0 components of the spontaneous strain tensor can be transformed into the $S_{i'j'}^0$ com-

ponents in the Cartesian coordinate system (x_1', x_2, x_3') with the x_3' axis perpendicular to the domain walls. The $S^0_{1'1'}$, S^0_{22}, and $S^0_{3'3'}$ components are identical in the *c* and *a* domains, whereas the $S^0_{1'3'}$ components in the adjacent domains differ in sign. Note that the $S^0_{1'1'}$, S^0_{22}, and $S^0_{3'3'}$ components do not vary in going through the domain walls. Therefore, to a first approximation, they can be taken constant within the walls. It can also be assumed that the shear component $S^0_{1'3'}$ varies within the wall according to the theoretical calculations carried out for domain boundaries within the thermodynamic approach [18, 22, 23]. In the framework of these theories, the variation in the order parameter *Q* inside the wall for intrinsic ferroelastics is represented as $Q \sim \tanh(x_3'/w)$. A hyperbolic tangent profile is also a good approximation for the distribution of the shear strain inside the 90° domain wall in intrinsic ferroelectrics with a perovskite structure [23]: $S^0_{1'3'} \sim \tanh(x_3'/w)$. In order to simplify calculations, we assume that the strain $S^0_{1'3'}$ varies linearly inside the wall of a finite width 2*w*. Then, for the *c*/*a*/*c* structure, we have $S^0_{1'3'} = (c-a)x_3'/(2wa_0)$ inside the *c*/*a* wall, $S^0_{1'3'} = -(c-a)(x_3' - d/\sqrt{2})/(2wa_0)$ inside the *a*/*c* wall, $S^0_{1'3'} = -(c-a)/(2a_0)$ in the *c* domains, and $S^0_{1'3'} = (c-a)/(2a_0)$ in the *a* domain.

In the case under consideration, it can be assumed that the S^0_{11} and S^0_{33} strains do not depend on the x_2 coordinate and the S^0_{22} component is constant throughout the film. Then, for the *c*/*a*/*c* structure, from formulas (1) and (2), we derive the following nonzero dislocation densities at the film–substrate interface Σ:

$$\rho^{\Sigma}_{12} = -S_a\delta_3(\Sigma), \tag{3a}$$

$$\rho^{\Sigma}_{21} = \begin{cases} S_a\delta_3(\Sigma), & x_1 < -\sqrt{2}w; \\ \frac{1}{2}\left[S_a + S_c + (S_c - S_a)\frac{x_1}{\sqrt{2}w}\right]\delta_3(\Sigma), \\ -\sqrt{2}w \le x_1 \le \sqrt{2}w; \\ S_c\delta_3(\Sigma), & \sqrt{2}w < x_1 < d - \sqrt{2}w; \\ \frac{1}{2}\left[S_a + S_c + (S_c - S_a)\frac{d - x_1}{\sqrt{2}w}\right]\delta_3(\Sigma), \\ d - \sqrt{2}w \le x_1 \le d + \sqrt{2}w; \\ S_a\delta_3(\Sigma), & x_1 > d + \sqrt{2}w; \end{cases} \tag{3b}$$

where *d* is the size of the *a* domain along the x_1 axis (Fig. 1). Moreover, in these relationships, we introduced the misfit strains $S_a \equiv (a - b^*)/a_0$ and $S_c \equiv (c - b^*)/a_0$. The components ρ^{Σ}_{12} and ρ^{Σ}_{21} are two continuous distributions of edge dislocations for which the Burgers vectors are aligned along the x_2 and x_1 axes and the lines are directed along the x_1 and x_2 axes, respectively.

In addition to the two surface components ρ^{Σ}_{12} and ρ^{Σ}_{21}, there is a nonzero bulk dislocation density component $\rho^{V}_{2'3'}$, which for the *c*/*a*/*c* configuration, can be written as

$$\rho^{V}_{2'3'} = (S_a - S_c)[\delta(V^{c/a}_{DW}) - \delta(V^{a/c}_{DW})]/2\sqrt{2}w, \tag{4}$$

where $V^{c/a}_{DW}$ and $V^{a/c}_{DW}$ are the regions inside the *c*/*a* and *a*/*c* walls, respectively. The Burgers vectors of all the edge dislocations in relationship (4) are perpendicular to the domain walls. The $\rho^{V}_{2'3'}$ density corresponds to a set of bounded dislocation walls which are continuously distributed within the domain boundaries of width 2*w*. The dislocation distribution (4) induces the same stress field as two ensembles of rectilinear wedge disclinations [24] which continuously fill a part of the film–substrate interface inside the domain walls. The surface disclination density is $\xi = (S_c - S_a)/(2\sqrt{2}w)$, and the signs of disclinations located at the *c*/*a* and *a*/*c* boundaries are opposite.

The complete model of the *c*/*a*/*c* structure with a linear profile of the spontaneous strain $S^0_{1'3'}$ inside the domain walls of width 2*w* involves the homogeneous and inhomogeneous distributions ρ^{Σ}_{12} [formula (3a)] and ρ^{Σ}_{21} [formula (3b)] of effective edge dislocations and also two ensembles of disclinations with the density $\xi = (S_c - S_a)/(2\sqrt{2}w)$ within the *c*/*a* and *a*/*c* walls (Fig. 1). All the defects are located at the film–substrate interface, and the Burgers vector of the ρ^{Σ}_{21} dislocations inside the walls varies in a linear manner. The complete model for the *a*/*c*/*a* structure can be obtained from the model for the *c*/*a*/*c* structure by replacing S_a with S_c and S_c with S_a in formula (3b) for ρ^{Σ}_{21} and also by reversing the signs of disclinations; the component ρ^{Σ}_{12} remains the same.

3. ENERGY AND THE EQUILIBRIUM GEOMETRIC PARAMETERS OF THE *c*/*a*/*c* AND *a*/*c*/*a* DOMAIN CONFIGURATIONS WITH A FINITE WALL WIDTH

The constructed models of the *c*/*a*/*c* and *a*/*c*/*a* structures enable us to calculate the internal stresses T_{ij} in the epitaxial systems under consideration as the sum of the

T_{ij}^{ρ} and T_{ij}^{ξ} stresses produced by the effective dislocations and disclinations. In order to simplify the calculations, the film–substrate system will be treated as elastically isotropic and homogeneous and its elastic properties will be described by the effective shear modulus G and the Poisson ratio ν.

The T_{ij}^{ρ} stresses of the dislocation ensembles (3a) and (3b) are determined by the integration of the specific analytical functions f_{ij}^{ρ} obtained by Head [25] over the film–substrate interface. These functions provide a means of calculating the stresses of a single rectilinear edge dislocation aligned parallel to a free surface of the elastic half-space. In particular, the T_{11}^{ρ} component for the *c*/*a*/*c* configuration is calculated as follows:

$$\begin{aligned} T_{11}^{\rho} = \frac{G}{2\pi(1-\nu)}\Bigg\{&(1+\nu)S_a\int_{-L}^{L} f_{11}^{\rho}(x_1-x_1', x_3)dx_1' \\ &+ (S_c-S_a)\int_{\sqrt{2}w}^{d-\sqrt{2}w} f_{11}^{\rho}(x_1-x_1', x_3)dx_1' \\ &+ \frac{1}{2}(S_c-S_a)\int_{-\sqrt{2}w}^{\sqrt{2}w}\Bigg[\left(1+\frac{x_1'}{\sqrt{2}w}\right)f_{11}^{\rho}(x_1-x_1', x_3) \\ &+ \left(1-\frac{x_1'}{\sqrt{2}w}\right)f_{11}^{\rho}(x_1-x_1'-d, x_3)\Bigg]dx_1'\Bigg\}, \end{aligned} \tag{5}$$

where $f_{11}^{\rho}(x, y)$ is the function given in [25] and $2L$ is the film size along the x_1 axis. In turn, the T_{11}^{ξ} stress of the disclination ensemble in the *c*/*a*/*c* structure is calculated by integration of the $f_{11}^{\xi}(x, y)$ function (which is used for determining the relevant stress component of a single rectilinear wedge disclination [26]) within the domain walls:

$$\begin{aligned} T_{11}^{\xi} = \frac{G(S_a-S_c)}{4\pi\sqrt{2}w(1-\nu)}\int_{-\sqrt{2}w}^{\sqrt{2}w}&[f_{11}^{\xi}(x_1-x_1', x_3) \\ &- f_{11}^{\xi}(x_1-x_1'-d, x_3)]dx_1'. \end{aligned} \tag{6}$$

According to the general theory of defects [26], the elastic energy W^{el} is the sum of the energies W_b and W_{ξ} of the dislocation and disclination ensembles and also the energy $W_{b\xi}$ of the interaction between them. The W_b and W_{ξ} components are calculated as the works done by the inherent stresses when displacing the edges of a cut during the formation of defects of particular types. For example, the dislocation energy W_b for the *c*/*a*/*c* structure is written as

$$\begin{aligned} W_b = \frac{1}{2}\int_{-H}^{0} dx_3\Bigg\{&S_a\int_{-L}^{L}[T_{11}^{\rho}(x_1, x_3) - T_{22}^{\rho}(x_1, x_3)]dx_1 \\ &+ (S_c-S_a)\int_{\sqrt{2}w}^{d-\sqrt{2}w} T_{11}^{\rho}(x_1, x_3)dx_1 \\ &+ \frac{1}{2}(S_c-S_a)\int_{-\sqrt{2}w}^{\sqrt{2}w}\Bigg[\left(1+\frac{x_1}{\sqrt{2}w}\right)T_{11}^{\rho}(x_1, x_3) \\ &+ \left(1-\frac{x_1}{\sqrt{2}w}\right)T_{11}^{\rho}(x_1+d, x_3)\Bigg]dx_1\Bigg\}, \end{aligned} \tag{7}$$

where H is the film thickness (it is assumed that $2L \gg H$). The sum of the integrals dependent on L in relationship (7) is equal to the elastic energy W_c of the *c* monovariant. Hereafter, all the energies will be measured from this quantity W_c by determining the difference $\Delta W_b = W_b - W_c$. The integral expression for the disclination energy W_{ξ} is given by

$$\begin{aligned} W_{\xi} = \frac{G(S_a-S_c)}{4\sqrt{2}w}\int_{-H}^{0} dx_3(x_3+H) \\ \times\int_{-\sqrt{2}w}^{\sqrt{2}w}[T_{11}^{\xi}(x_1, x_3) - T_{11}^{\xi}(x_1+d, x_3)]dx_1. \end{aligned} \tag{8}$$

The energy $W_{b\xi}$ of interaction between the dislocation and disclination ensembles can be obtained from formula (7) by replacing the dislocation stresses T_{ii}^{ρ} by twice the stresses $2T_{ii}^{\xi}$ of the disclination system. With direct calculations, it is possible to demonstrate that $W_{b\xi} \equiv 0$ due to the symmetry of our problem.

After the substitution of formula (5) into relationship (7) and formula (6) into relationship (8), we first integrate with respect to the coordinate x_3 and transform the remaining double integrals over x_1 and x_1' into single integrals. This procedure leads to the analytical expressions for the energies ΔW_b and W_{ξ}. By summing the dislocation ΔW_b and disclination W_{ξ} components, we obtain the elastic energy ΔW^{el} (reckoned from the energy of the *c* monovariant) for the *c*/*a*/*c* configuration in the form

$$\Delta W^{el} = \frac{G(S_a-S_c)^2H^4}{16\pi(1-\nu)w^2}\Bigg\{2g\left(\frac{d}{2H}\right) + 2g\left(\frac{\sqrt{2}w}{H}\right)$$

$$-g\left(\frac{d+2\sqrt{2}w}{2H}\right)-g\left(\frac{d-2\sqrt{2}w}{2H}\right)\Bigg\} \qquad (9)$$

$$-\frac{2GH^2}{1-\nu}(1+\nu)S_a(S_a-S_c)\frac{d}{H}$$

with the dimensionless function $g(x)$ defined by the relationship

$$g(x)\equiv\left(8x^2-\frac{14}{3}\right)\ln(1+x^2)-\frac{2}{3}x^4\ln\left(1+\frac{1}{x^2}\right) \qquad (10)$$

$$+\frac{16}{3}x(4-x^2)\arctan(x).$$

At small strains S_a and $S_c \ll 1$, the ratio $2(1+\nu)S_a/(S_a - S_c)$ in formula (9) can be replaced by the parameter S_r/S_r^0, where $S_r \equiv (b^* - a)/(c - a) \approx S_a/(S_a - S_c)$ is the relative misfit strain [21] with threshold value $S_r^0 \equiv 1/(2 + 2\nu)$. Then, except for the common factor, the elastic energy ΔW^{el} becomes the function of three dimensionless parameters, d/H, $2w/H$, and S_r/S_r^0. For the $a/c/a$ structure, the ΔW^{el} energy measured from the energy of the a monovariant can be written in the form similar to formula (9) if the parameter S_r/S_r^0 is replaced by $2 - S_r/S_r^0$. Note that the ΔW^{el} energy [formula (9)] at $2w \longrightarrow 0$ asymptotically goes over into the expression for the elastic energy of the $c/a/c$ structure with infinitely thin walls, which was earlier obtained in [16].

The changes $\Delta U_{c/a}$ and $\Delta U_{a/c}$ in the $U_{c/a}$ and $U_{a/c}$ internal energies of heterostructures upon formation of the $c/a/c$ and $a/c/a$ configurations are represented by the sum of the elastic energy ΔW^{el} and the self-energy W^{self} of two 90° walls. Here, we neglect the change in the energy of film depolarization, because ferroelectrics of the perovskite family are characterized by a relatively high electrical conductivity. Therefore, bound polarization charges are almost completely compensated for by free charge carriers [27].

The self-energy of walls can be written as $W^{\text{self}} = 2\sqrt{2}\,\sigma H$ with the same specific surface energy σ for both walls. The change $\Delta U_{c/a} = U_{c/a} - U_c$ in the internal energy (reckoned from the energy U_c of the c monovariant) upon formation of the $c/a/c$ structure is represented using formula (9) in the form

$$\Delta U_{c/a} = \sigma\frac{H^2}{H_0}\left\{\frac{1}{4\pi}\left(\frac{H}{2w}\right)^2 F\left(\frac{d}{H},\frac{2w}{H}\right)-\frac{S_r}{S_r^0}\frac{d}{H}\right\} \qquad (11)$$

$$+2\sqrt{2}\sigma H,$$

where the function $F(d/H, 2w/H)$ is defined by the expression in the curly brackets in the right-hand side of formula (9) and the characteristic film thickness is $H_0 \equiv \sigma(1-\nu)/[G(S_a - S_c)^2]$ ($H_0 \sim 1$ nm in $BaTiO_3$ and $PbTiO_3$ films [9]). Relationship (11) for $\Delta U_{c/a}$ is valid only in the absence of overlap between domain walls ($d \geq 2\sqrt{2}w$). In the presence of overlap, it can be assumed, to a first approximation, that the $\Delta U_{c/a}$ energy at $d < 2\sqrt{2}w$ linearly varies from 0 at $d = 0$ to $\Delta U_{c/a}$ determined by formula (11) at $d = 2\sqrt{2}w$. A similar approximation is also applicable to the $\Delta U_{a/c}$ energy of the $a/c/a$ structure.

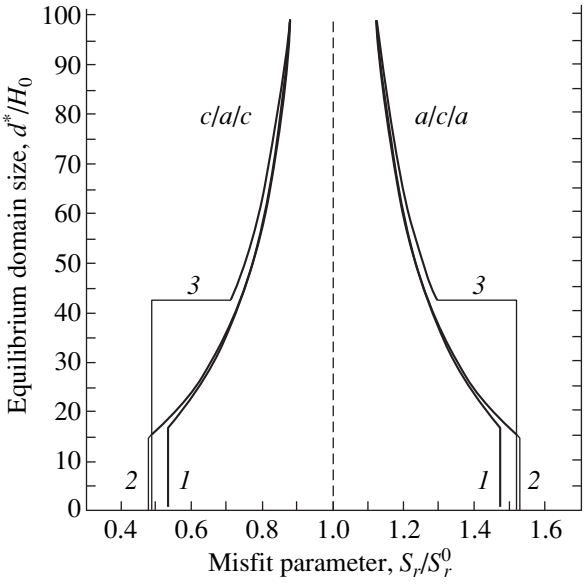

Fig. 2. Dependences of the equilibrium domain size d^* (in terms of H_0) on the misfit parameter $S_r/S_r^0 = 2(1+\nu)(b^* - a)/(c - a)$ at different normalized wall widths: (*1*) $2w/H_0 \leq 1$, (*2*) $2w/H_0 = 10$, and (*3*) $2w/H_0 = 30$. The film thickness is defined as $H = 10H_0$.

The numerical solution of the equation $\partial U/\partial d = 0$ with $U = \Delta U_{c/a}$ or $U = \Delta U_{a/c}$ provides a way of determining the equilibrium domain size d^* for the $c/a/c$ or $a/c/a$ configurations, respectively. From formula (9), it follows that the normalized domain size d^*/H_0 is a function of the normalized wall width $2w/H_0$, the misfit parameter S_r/S_r^0, and the film thickness H/H_0. The dependences of the parameter d^*/H_0 on the misfit parameter S_r/S_r^0 at a fixed thickness $H/H_0 = 10$ for three values of the wall width $2w/H_0$ are shown in Fig. 2. These dependences are symmetric with respect to the line $S_r/S_r^0 = 1$, and the size d^*/H_0 monotonically increases as the parameter S_r approaches S_r^0. The curves correspond to the $c/a/c$ configurations at $S_r/S_r^0 < 1$ and the $a/c/a$ configurations at $S_r/S_r^0 > 1$. In the case of $S_r/S_r^0 = 1$, these configurations have the same internal

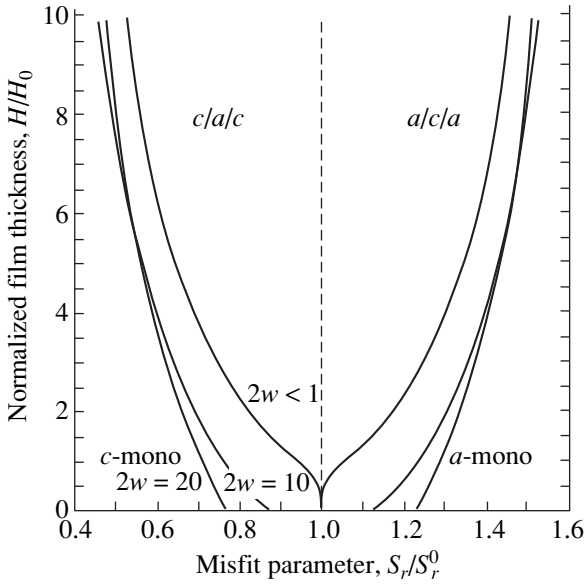

Fig. 3. Stability diagram of single domains in a tetragonal film grown on a cubic substrate. Domain wall width $2w$ is given in terms of H_0.

energies. The character of the dependence $d^*(S_r/S_r^0)$ at a fixed film thickness H/H_0 is determined by the parameter $2w/H_0$. Note that, at relatively small wall widths ($2w \le 10H_0$ at $H = 10H_0$), the domain size d^* jumpwise decreases from $d^* > 2\sqrt{2}w$ to zero (Fig. 2, curves *1*, *2*). At the same time, at large wall widths ($2w > 10H_0$ at $H = 10H_0$), these jumps occur from the values of $d^* = 2\sqrt{2}w$ in a horizontal plateau (Fig. 2, curve *3*) whose size increases with an increase in the wall width. In any case, domains with the size $d < 2\sqrt{2}w$ appear to be unstable, which is associated with the use of a linear approximation for the energy ΔU when the walls overlap.

4. STABILITY DIAGRAM FOR THE *c*/*a*/*c* AND *a*/*c*/*a* STRUCTURES AT A SPECIFIED WALL WIDTH

The changes ΔU^* in the internal energies upon formation of the *c*/*a*/*c* and *a*/*c*/*a* stable polydomain configurations can be determined by substituting the optimum domain width d^* (calculated in the preceding section) into relationship (11). The obtained quantity $\Delta U^*/\sigma H$ is a function of three parameters: the normalized wall width $2w/H_0$, the misfit parameter S_r/S_r^0, and the film thickness H/H_0. In order to construct the stability diagram for the *c*/*a*/*c* and *a*/*c*/*a* structures on the S_r/S_r^0–H/H_0 coordinates, let us compare the equilibrium energies of polydomain configurations with the energies of single-domain states at the fixed parameters $2w/H_0$. At $S_r/S_r^0 < 1$, the *c* monovariant is always more energetically favorable than the *a* monovariant [12]. Therefore, in this case, it is sufficient to analyze the energies of the *c*/*a*/*c* configurations. From relationships (11) and (10), it follows that the inequality $\Delta U^*_{c/a} < 0$, which is necessary for the stability of the *c*/*a*/*c* structure, is met only for films with thickness H larger than the specific critical thickness H^*. By solving the equation $\Delta U^*_{c/a} = 0$, it is possible to find the dependence of the normalized critical thickness H^*/H_0 on the misfit parameter S_r/S_r^0. In the stability diagram, this dependence is described by the line of the energy equivalence for the *c*/*a*/*c* structure and the *c* monovariant. Three of these lines at $S_r/S_r^0 \le 1$ for three values of the $2w/H_0$ parameter are depicted in Fig. 3.

The right-hand side of the diagram at $S_r/S_r^0 > 1$ can be constructed in a similar way by analyzing the energies of the *a*/*c*/*a* configurations at different parameters $2w/H_0$. The lines of the energy equivalence for the *a*/*c*/*a* structure and the *a* monovariant at $S_r/S_r^0 \ge 1$ are displayed in Fig. 3 for three values of the $2w/H_0$ width. The stability region of polydomain states lies between two vertical lines $S_r/S_r^0 = 0$ and 2 and is symmetric with respect to the straight line $S_r/S_r^0 = 1$. As the wall width $2w$ increases, the stability region of the *c*/*a*/*c* and *a*/*c*/*a* structures becomes wider, especially for films with small thickness $H \le H_0$. At $2w \ge 20H_0$, the equivalence lines overlap at different parameters $2w/H_0$. In this case, the structure with the larger wall width $2w$ turns out to be more stable at the thicknesses $H \le 2H_0$ and the configuration with the smaller width $2w$ is stable at $H \ge 5H_0$. Figure 3 shows the situation when the lines constructed at $2w/H_0 = 10$ and 20 in a certain region virtually merge together but do not intersect.

By using relationships (9)–(11), it is possible to demonstrate that the equilibrium domain size d^* in ultrathin films ($H \ll H_0$) is equal to $d^* \cong 2\sqrt{2}w$ in the stability region of polydomain states; i.e., the parameter d^* does not depend on the misfit parameter S_r/S_r^0. In turn, the value of d^* in very thick films ($H \gg 10H_0$) is independent of the wall width $2w$, because, in this case, $d^* \cong (3\pi/5)H(S_r/S_r^0)$ for the *c*/*a*/*c* structure and $d^* \cong (3\pi/5)H(2 - S_r/S_r^0)$ for the *a*/*c*/*a* structure. These results and relationship (11) make it possible to derive the asymptotic expressions for the equilibrium energy $\Delta U^*_{c/a}$ of the *c*/*a*/*c* structure for large and small film thicknesses H:

$$\Delta U^*_{c/a}/\sigma H = (2/3 - S_r/S_r^0)(2\sqrt{2}w/H_0) + 2\sqrt{2}, \quad H \longrightarrow 0, \tag{12a}$$

$$\Delta U^*_{c/a}/\sigma H = -(3\pi/5)(S_r/S_r^0)^2(H/H_0) + 2\sqrt{2}, \quad H \longrightarrow \infty. \tag{12b}$$

It follows from relationship (12a) that, for films with domain walls with a finite width $2w > 0$, the inequality $\Delta U^*_{c/a} < 0$ that determines the condition for stability of the *c*/*a*/*c* structure can be fulfilled even for ultrathin films with thickness $H \ll H_0$. This becomes possible when the misfit parameter S_r/S_r^0 exceeds the critical value S_c^{cr}, which is defined as $S_c^{cr} = 2/3 + H_0/w$ for the *c*/*a*/*c* structure. For the *a*/*c*/*a* configuration, the same is true at S_r/S_r^0 less than $S_a^{cr} = 4/3 - H_0/w$. Certainly, the *c*/*a*/*c* and *a*/*c*/*a* structures in ultrathin films can be stable configurations only when the conditions $S_c^{cr} \le 1$ and $S_a^{cr} \ge 1$ are met. The last inequalities are satisfied for films with a wall half-width *w* larger than the critical value $w_{cr} = 3H_0$. The larger the parameter $w \ge w_{cr}$, the wider the stability region of the polydomain state at $H < H_0$. In the case of $w < w_{cr}$ for ultrathin films, the monovariants are the stable configurations at any misfit parameters except for $S_r/S_r^0 = 1$.

From formula (12b) it follows that, at the large film thicknesses $H \gg 10H_0$, the $\Delta U^*_{a/c}$ and $\Delta U^*_{c/a}$ energies are independent of the wall width 2*w*. Therefore, at the sufficiently large parameters H/H_0, the curves constructed in Fig. 3 for different values of $2w/H_0$ merge together. Note that the domain size *d** jumpwise decreases down to zero in the lines of the energy equivalence for the polydomain states and monovariants (Fig. 3), as is observed in Fig. 2 for the dependences $d^*(S_r/S_r^0)$. For films with thickness *H* larger than the specific thickness H_{cr}, these jumps in the equivalence lines occur from the values of $d^* > 2\sqrt{2}w$, whereas, at $H \le H_{cr}$, the equilibrium size in these lines decreases from $d^* = 2\sqrt{2}w$ to zero. The H_{cr}/H_0 parameter monotonically increases with an increase in the domain boundary width $2w/H_0$. Note that H_{cr}/H_0 is relatively large for wide walls ($H_{cr}/H_0 \sim 100$ at $2w/H_0 = 20$).

As was assumed above, the wall width 2*w* in the epitaxial film coincides with the equilibrium width $2w_0$ of the domain boundaries in a macroscopic single crystal. However, in order to determine the equilibrium wall width 2*w** in the polydomain film, the total internal energy ΔU [see formula (11) in Section 3] should be minimized with respect to the parameter 2*w*. The energy ΔU involves two competing components: the elastic energy $W^{el} \equiv W^{el}(w)$ and the self-energy of the domain walls $\sigma \equiv \sigma(w)$. Analysis of relationship (9) demonstrates that the elastic component $W^{el}(w)$ monotonically decreases with an increase in the domain wall width 2*w* when the other parameters are fixed. This is associated with a weakening of long-range stresses in the epitaxial layer with an increase in the wall width. It is also evident that the self-energy $\sigma(w)$ of the domain boundaries becomes minimum at $w = w_0$. Examination of the dependence $\Delta U(w)$ leads to the conclusion that the equilibrium wall width 2*w** in a polydomain film is always larger than the wall width $2w_0$ in a free crystal. It is also possible to predict that the 2*w** parameter will considerably increase in the case of the stable polydomain states in thin films with thickness $H \le 5H_0 \sim 5$ nm. At the same time, for films with thickness $H \ge 30H_0 \sim 30$ nm, it is believed that the width 2*w** of walls in the film does not differ from the width $2w_0$ of domain boundaries in a free crystal for the observed parameters $2w_0 = 1$–5 nm.

5. CONCLUSION

The above analysis of the influence of the domain boundary width on the statics of 90° domains in the epitaxial ferroelectric thin films allowed us to draw the following conclusions.

(1) In thin films ($H < 100$ nm), the domain structures with 90° walls of finite width are universally more stable configurations as compared to similar structures with infinitely thin domain boundaries.

(2) The polydomain configurations with a finite wall width $2w > 0$ can exist in ultrathin films with thickness $H < 1$ nm. This inference corrects the conclusions concerning the instability of 90° domains with infinitely thin walls in these films [13, 15, 16].

(3) The equilibrium width of the 90° domain walls in films with thickness $H < 10$ nm can be substantially larger than the wall width in the bulk crystal.

ACKNOWLEDGMENTS

I am grateful to N.A. Pertsev for fruitful collaboration and helpful discussions of the results.

REFERENCES

1. B. S. Kwak, A. Erbil, B. J. Wilkens, *et al.*, Phys. Rev. Lett. **68** (25), 3733 (1992).
2. Y. Gao, G. Bai, K. L. Merkle, *et al.*, J. Mater. Res. **8** (1), 145 (1993).
3. R. Ramesh, T. Sands, and V. G. Keramidas, Appl. Phys. Lett. **63** (6), 731 (1993).
4. B. S. Kwak, A. Erbil, J. D. Budai, *et al.*, Phys. Rev. B **49** (21), 14865 (1994).
5. A. Seifert, F. F. Lange, and J. S. Speck, J. Mater. Res. **10** (3), 680 (1995).
6. Y. M. Kang, J. K. Ku, and S. Baik, J. Appl. Phys. **78** (4), 2601 (1995).
7. C. M. Foster, Z. Li, M. Buckett, *et al.*, J. Appl. Phys. **78** (4), 2607 (1995).
8. V. Gopalan and R. Raj, Appl. Phys. Lett. **68** (10), 1323 (1996).
9. N. A. Pertsev, G. Arlt, and A. G. Zembilgotov, Phys. Rev. Lett. **76** (8), 1364 (1996).

10. N. A. Pertsev and A. Yu. Emelyanov, Appl. Phys. Lett. **71** (25), 3646 (1997).
11. A. L. Roitburd, Phys. Status Solidi A **37** (1), 329 (1976).
12. W. Pompe, X. Gong, Z. Suo, and J. S. Speck, J. Appl. Phys. **74** (10), 6012 (1993).
13. J. S. Speck, A. C. Daykin, A. Seifert, *et al.*, J. Appl. Phys. **78** (3), 1696 (1995).
14. A. E. Romanov, W. Pompe, and J. S. Speck, J. Appl. Phys. **79** (8), 4037 (1996).
15. N. A. Pertsev and A. G. Zembilgotov, J. Appl. Phys. **78** (10), 6170 (1995).
16. N. A. Pertsev and A. Yu. Emel'yanov, Fiz. Tverd. Tela (St. Petersburg) **39** (1), 127 (1997) [Phys. Solid State **39**, 109 (1997)].
17. A. L. Roytburd, J. Appl. Phys. **83** (1), 228 (1998); **83** (1), 239 (1998).
18. E. K. H. Salje, *Phase Transitions in Ferroelastic and Coelastic Crystals* (Cambridge Univ. Press, Cambridge, 1993).
19. S. Stemmer, S. K. Streiffer, F. Ernst, and M. Rühle, Philos. Mag. A **71** (3), 713 (1995).
20. J. Chrosch and E. K. H. Salje, J. Appl. Phys. **85** (2), 722 (1999).
21. J. S. Speck and W. Pompe, J. Appl. Phys. **76** (1), 466 (1994).
22. G. R. Barsch and J. A. Krumhansl, Phys. Rev. Lett. **53** (11), 1069 (1984).
23. W. Cao and L. E. Cross, Phys. Rev. B **44** (1), 5 (1991).
24. R. de Wit, in *Fundamental Aspects of Dislocations*, Ed. by J. A. Simmons, R. de Wit, and R. Bullough (National Bureau of Standards, Washington, 1970; Mir, Moscow, 1977), Vol. 1, pp. 651–673; J. Res. Natl. Bur. Stand., Sect. A **77** (1), 49 (1973); **77** (3), 359 (1973); **77** (5), 607 (1973).
25. A. K. Head, Proc. R. Soc. London, Ser. A **66** (405), 793 (1953).
26. V. I. Vladimirov and A. E. Romanov, *Disclinations in Crystals* (Nauka, Leningrad, 1986).
27. G. Arlt and N. A. Pertsev, J. Appl. Phys. **70** (4), 2283 (1991).

Translated by O. Borovik-Romanova

Physics of the Solid State, Vol. 43, No. 2, 2001, pp. 337–344. Translated from Fizika Tverdogo Tela, Vol. 43, No. 2, 2001, pp. 323–330.

MAGNETISM AND FERROELECTRICITY

Permittivity of $BaTiO_3$ Epitaxial Films Grown on the $YBa_2Cu_3O_{7-\delta}$(001) Surface

Yu. A. Boĭkov* and T. Claeson**

** Ioffe Physicotechnical Institute, Russian Academy of Sciences, Politekhnicheskaya ul. 26, St. Petersburg, 194021 Russia*
e-mail: Yu.Boikov@shuvpop.ioffe.rssi.ru

*** Chalmers Technical University, Göteborg, S-41296 Sweden*

Received June 26, 2000

Abstract—The epitaxial heterostructures $YBa_2Cu_3O_{7-\delta}/BaTiO_3/YBa_2Cu_3O_{7-\delta}$ and $YBa_2Cu_3O_{7-\delta}$/(5 nm)$SrTiO_3/BaTiO_3$/(5 nm)$SrTiO_3/YBa_2Cu_3O_{7-\delta}$ are grown by the laser evaporation method on an $LaAlO_3$(100) substrate. The permittivity of a $BaTiO_3$ layer is approximately doubled (T = 300 K) when a $SrTiO_3$ thin layer is inserted between a ferroelectric layer and superconducting cuprate electrodes. A maximum in the temperature dependence of the permittivity for a barium titanate layer in the $YBa_2Cu_3O_{7-\delta}$/(5 nm)$SrTiO_3/BaTiO_3$/(5 nm)$SrTiO_3/YBa_2Cu_3O_{7-\delta}$ heterostructure is shifted by 70–80 K toward the low-temperature range with respect to its location in the corresponding dependence for the $BaTiO_3$ bulk single crystal. The bias voltage dependence of the permittivity for the $BaTiO_3$ grown layers exhibits a clearly pronounced hysteresis (T = 300 K). The superconducting transition temperature for the lower $YBa_2Cu_3O_{7-\delta}$ electrode in a superconductor/ferroelectric/superconductor heterostructure considerably depends on the rate of its cooling after the completion of the formation process. © *2001 MAIK "Nauka/Interperiodica".*

1. INTRODUCTION

The $BaTiO_3$ (BTO) compound is one of the best known representatives of a large family of perovskite-like ferroelectrics. The data obtained over the last 50 years on the dielectric properties of single-crystal and bulk ceramic BTO samples and also (Ba, Sr)TiO_3 (BSTO) solid solutions (close to the barium titanate region) allowed researchers to conclude that these ferroelectrics are promising materials for use in memory cells [1], electrooptic systems [2], and infrared detectors [3]. For various practical applications in microelectronics and microwave technology, BTO compounds should be prepared in the form of a film whose free surface (or both surfaces) contains conducting electrodes. The available data [4, 5] indicate that the absolute permittivities ε for polycrystalline films, their temperature dependences, and the response to the external electric field substantially differ from those for the bulk single crystals [6]. No systematic investigations into the dependence of the dielectric parameters of BTO epitaxial films on structure have hitherto been performed.

A close similarity between the crystal structures of cuprate superconductors and perovskite-like ferroelectrics offers strong possibilities of forming epitaxial superconductor/ferroelectric/superconductor heterostructures.

The purpose of this work was to investigate the structure and the parameters of BTO epitaxial films grown on $YBa_2Cu_3O_{7-\delta}$ (YBCO) surface. In order to reveal the dependence of the permittivity of a barium titanate layer sandwiched between thin-film superconducting cuprate electrodes on the microstructure of BTO/YBCO interfaces, we grew three-layer YBCO/BTO/YBCO systems and heterostructures in which strontium titanate thin (5 nm) layers were inserted between a ferroelectric layer and superconducting films. The mechanisms favorable for improving the microstructure of the YBCO/BSTO interface upon introduction of a $SrTiO_3$ (STO) buffer layer were discussed earlier in [7, 8].

2. EXPERIMENTAL TECHNIQUE

The heterostructures YBCO/BTO/YBCO and YBCO/STO(5 nm)/BTO/STO(5 nm)/YBCO were grown by the laser evaporation method (KrF, λ = 248 nm, τ = 30 ns) on a $LaAlO_3$(100) (LAO) substrate. Polycrystalline disks of YBCO, BTO, and STO, which were prepared according to the standard ceramic procedure, were used as targets. The laser radiation density at the target surface was 1.5 J/cm^2. The oxygen pressure P_O and the substrate temperature T_S in the course of the growth of the YBCO/BTO/YBCO and YBCO/STO(5 nm)/BTO/STO(5 nm)/YBCO heterostructures were equal to 0.5 mbar and 750°C, respectively. Upon completion of condensation, the hetero-

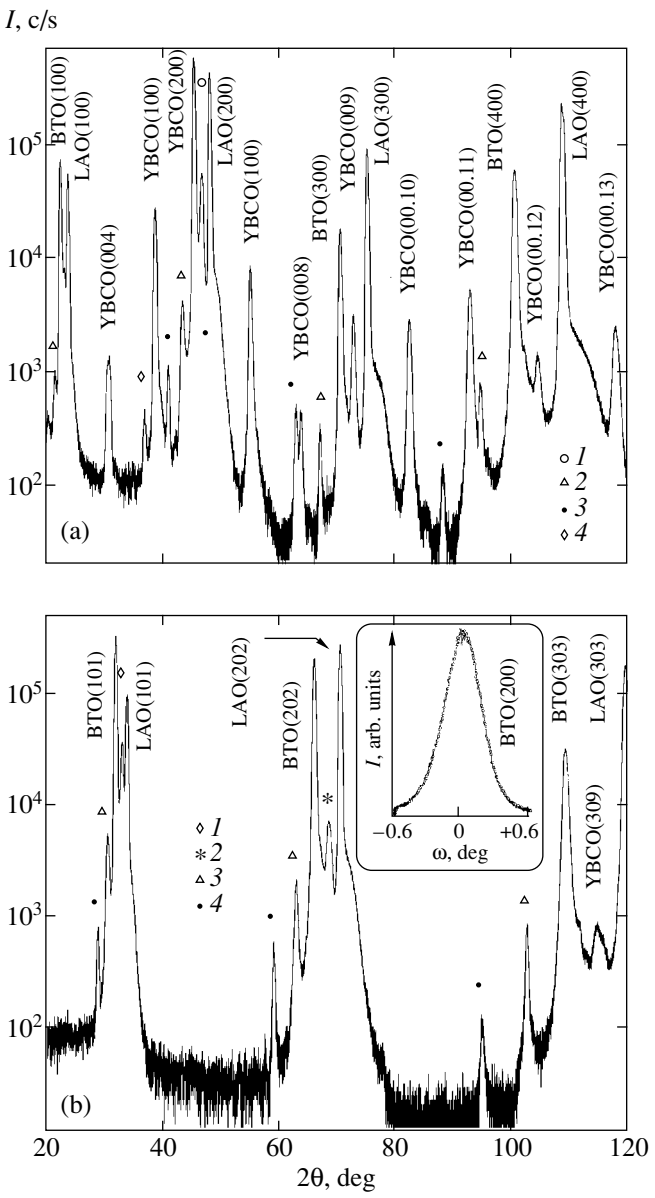

Fig. 1. (a) X-ray diffraction pattern (CuK_α, ω/2θ) for the YBCO(200 nm)/BTO(700 nm)/YBCO(200 nm) heterostructure grown on the LAO(100) substrate: (*1*) YBCO(006) peak, (*2*) CuK_β peak of LAO, (*3*) CuK_β peak of BTO, and (*4*) CuK_β peak of YBCO. Incident and reflected x-ray beams during the recording of the x-ray diffraction pattern lie in the plane perpendicular to the LAO(100) surface. v_T = 5 K/min. (b) X-ray diffraction pattern (CuK_α, ω/2θ) for the same heterostructure, but recorded with incident and reflected x-ray beams lying in the plane perpendicular to the LAO(101) surface: (*1*) YBCO(103) peak, (*2*) YBCO(206) peak, (*3*) CuK_β peak of LAO, and (*4*) CuK_β peak of BTO. The inset shows the rocking curve (CuK_α, ω – 2θ) measured for BTO(200) x-ray peak for the same heterostructure.

structures were cooled to room temperature in an oxygen atmosphere (P_O = 1 atm) at the rate v_T = 5–25 K/min.

The phase composition and the structure of the grown heterostructures were studied by x-ray diffraction (Philips X'pert MRD, ω/2θ- and φ-scans, rocking curves). In order to determine the unit cell parameters of the ferroelectric layer and superconducting films forming the superconductor/ferroelectric/superconductor heterostructure, the x-ray diffraction patterns were recorded with incident and reflected x-ray beams lying in the plane perpendicular to either the LAO(100) surface or the LAO(101) surface. The unit cell parameter $a_\perp$ of the ferroelectric layer in the direction perpendicular to the substrate plane was calculated using the 2θ value for the x-ray BTO(400) reflection. The unit cell parameter $a_\parallel$ in the substrate plane was determined from the relationship $1/d_{(303)} = [(3/a_\perp)^2 + (3/a_\parallel)^2]^{1/2}$, where $d_{(303)}$ is the interplanar distance calculated with the 2θ value for the x-ray BTO(303) reflection.

The data on the surface morphology of the grown films BTO and YBCO were obtain with an atomic-force microscope (NanoScope-IIIa).

Electrodes ($S = 0.2 \times 0.2$ mm^2) in the upper superconducting film and holes in the ferroelectric layer (for the formation of a contact with the lower YBCO electrode) were produced by photolithography and ion etching (Ar, 0.2 mA, 500 V).

The capacitance C and the loss tangent $\tan\delta$ for the prepared capacitor structures YBCO/BTO/YBCO and YBCO/STO(5 nm)/BTO/STO(5 nm)/YBCO were measured on an hp 4263A LCR meter (f = 100 kHz) with a bias voltage $V_b = \pm 2.5$ V applied to the superconducting electrodes and without it. The bias voltage was considered positive when "+" was applied to the upper electrode. The permittivity was determined from the expression $C = \varepsilon S/d$, where d = 700 nm is the ferroelectric layer thickness. The resistance R of the YBCO films grown on the LAO(100) and BTO/YBCO/LAO(100) substrates was measured with an LCR meter (f = 100 Hz) by the four-point probe method according to the van der Pau technique. The resistivity ρ of superconducting films was calculated by the formula $\rho = (\pi d_1/\ln 2)R$ [9], where d_1 = 200 nm is the superconducting film thickness. The superconducting transition temperature T_C for the YBCO films was determined from the temperature dependences of the resistance and the magnetic susceptibility χ. The critical current density j_C was determined from the current–voltage characteristics measured for bridges (50 μm long and 8 μm wide) prepared in the YBCO films by photolithography and ion etching methods.

3. RESULTS AND DISCUSSION

The BTO layers grown on the YBCO/LAO and STO(5 nm)/YBCO/LAO surfaces were investigated by x-ray diffraction and atomic-force microscopic methods. No systematic differences in their structure and surface morphology were revealed. However, the measured permittivity ε of the ferroelectric layer in the YBCO/BTO/YBCO heterostructure was consid-

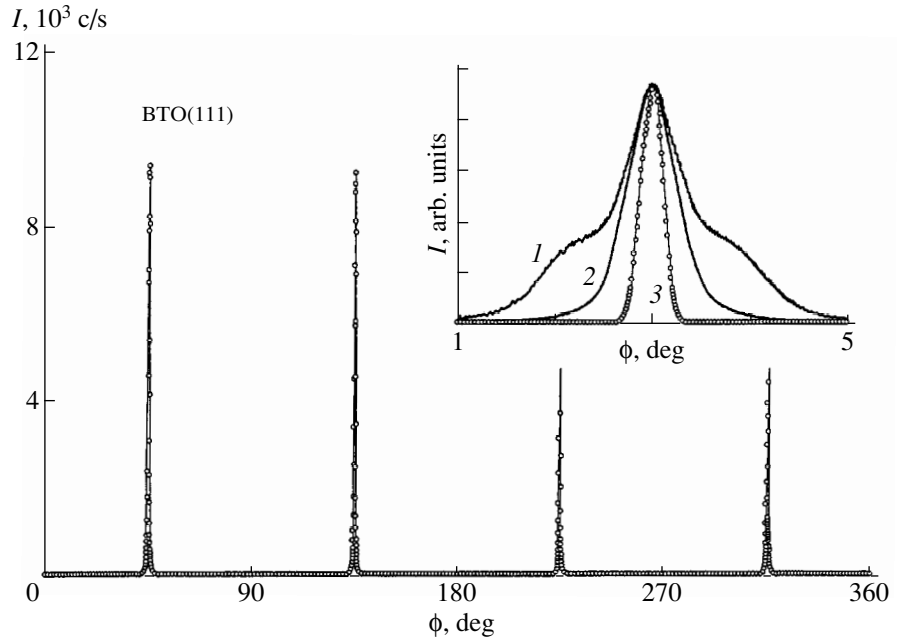

Fig. 2. X-ray (CuK_α) ϕ-scan for the BTO(111) reflection of the YBCO/BTO/YBCO/LAO heterostructure grown on the LAO(100) substrate at v_T = 5 K/min. The inset shows peaks in ϕ-scans (on an enlarged scale) for (*1*) YBCO(113), (*2*) BTO(111), and (*3*) LAO(111) reflections of the same heterostructure.

erably less than ε for the BTO layer in the YBCO/STO(5 nm)/BTO/STO(5 nm)/YBCO heterostructure. First, we will analyze the structural data for the grown layers and, then, discuss the specific features of the temperature and field dependences of the dielectric parameters of a BTO layer and also the origin of the degradation in the superconductivity parameters of YBCO films in multilayer epitaxial heterostructures.

3.1. Structure and morphology of the surface of layers forming the superconductor/ferroelectric/superconductor heterostructure. As follows from the x-ray diffraction data, the grown heterostructures were free from inclusions of minor phases (Figs. 1a, 1b). A small difference in the crystal lattice parameters upon lattice matching of LAO(100), YBCO(001), BTO(100), and STO(100) favors epitaxial growth of the YBCO/BTO/YBCO and YBCO/STO(5 nm)/BTO/STO(5 nm)/YBCO heterostructures on the lanthanum aluminate surface. The superconducting films and the intermediate barium titanate layer were well oriented in the azimuthal direction and with respect to the normal to the substrate plane (Figs. 1a, 1b, 2). The x-ray diffraction patterns of the YBCO/BTO/YBCO and YBCO/STO(5 nm)/BTO/STO(5 nm)/YBCO heterostructures, which were recorded with the incident and reflected x-ray beams lying in the plane perpendicular to the LAO(100) surface, contain only the YBCO(001), BTO(*n*00), and LAO(*n*00) peaks (Fig. 1a). The x-ray diffraction patterns which were obtained with incident and reflected x-ray beams lying in the plane perpendicular to the LAO(101) surface, in addition to the (*n*0*n*) peaks of the substrate and the ferroelectric layer, involve the (103), (206), and (309) peaks of the superconducting films (Fig. 1b). Four equidistant peaks are observed in the x-ray ϕ-scans for the BTO(111) and YBCO(113) reflections measured for the YBCO/BTO/YBCO/LAO and YBCO/STO(5 nm)/BTO/STO(5 nm)/YBCO/LAO heterostructures (Fig. 2). The full widths at half-maximum (FWHM) of the peaks in the ϕ-scan for the YBCO(113), BTO(111), and LAO(111) reflections of the YBCO/BTO/YBCO/LAO heterostructure are equal to 1.06°, 0.73°, and 0.26°, respectively (see inset in Fig. 2). The width of the peak in the ϕ-scan for the YBCO(113) reflection of the superconducting film grown on the LAO(100) substrate is equal to 0.45°. From the x-ray diffraction data obtained, we determined the following orientational relationships for films forming the superconductor/ferroelectric/superconductor heterostructure: YBCO(001)[010]// BTO(100)[010]// YBCO(001)[010]//LAO(100)[010].

According to the x-ray diffraction data, the unit cell parameter for a BTO layer (T = 300 K) in the direction perpendicular to the substrate plane $a_\perp = 3.997 \pm 0.001$ Å is less than the corresponding parameter in the substrate plane $a_\parallel = 4.020 \pm 0.001$ Å. This fact allows us to conclude that the *c* axis in the BTO layer grown on the YBCO(001)/LAO(100) surface is predominantly oriented along the substrate plane. The orientation of the polar axis in BTO epitaxial films is considerably affected by mechanical stresses arising from the difference between thermal expansion coefficients β of the ferroelectric material and the substrate [10]. In the tem-

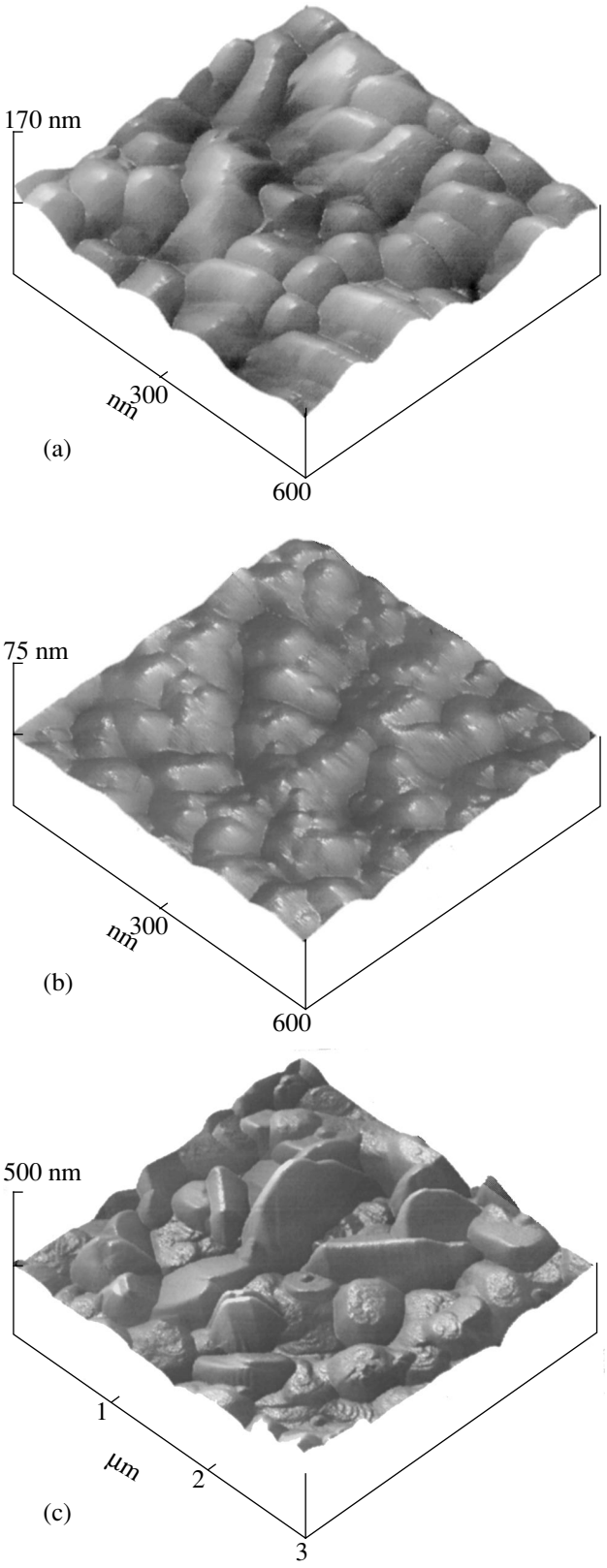

Fig. 3. Morphology of free surfaces of (a) the BTO(700 nm) layer grown on the YBCO(001)/LAO(100) surface, (b) the YBCO(200 nm) film on the LAO(100) surface, and (c) the YBCO(200 nm) film on the BTO(100)/YBCO(001)/LAO(100) surface. Images are obtained with an atomic-force microscope.

perature range 100–800°C, the thermal expansion coefficient for barium titanate ($\beta = 14.2 \times 10^{-6}$ K^{-1} [11]) is substantially larger than that for lanthanum aluminate ($\beta = 9.2 \times 10^{-6}$ K^{-1} [12]), which is responsible for the appearance of tensile mechanical stresses in the substrate plane in a BTO layer grown on the YBCO(001)/LAO(100) surface. The mechanical stresses arising in the BTO film due to the difference between the crystal lattice parameters for BTO(100), YBCO(001), and LAO(100) partially relax at temperatures close to T_S during the formation of misfit dislocations.

The full width at half-maximum of the rocking curve for the BTO(200) reflection of the YBCO/BTO/YBCO and YBCO/STO(5 nm)/BTO/STO(5 nm)/YBCO heterostructures falls in the range 0.4°–0.5° (see inset in Fig. 1a). The full width at half-maximum of the rocking curve for the (200) reflection of the substrate is equal to 0.22°. The considerable width of the rocking curves for BTO epitaxial films in the YBCO/BTO/YBCO and YBCO/STO(5 nm)/BTO/STO(5 nm)/YBCO heterostructures is explained by a high density of structural defects (grain boundaries, oxygen vacancies, misfit dislocations in interface regions, etc.). The degradation of the film structure is associated with a low mobility of adsorbed particles on the surface of a growing BTO film.

The peaks of the lower and upper YBCO films in the x-ray $\omega/2\theta$-scan for the YBCO/BTO/YBCO/LAO and YBCO/STO(5 nm)/BTO/STO(5 nm)/YBCO/LAO heterostructures (v_T = 5 K/min) were not resolved even at $2\theta > 100°$ (Figs. 1a, 1b). The unit cell parameters ($c = 11.682 \pm 0.001$ Å and $a = 3.862 \pm 0.001$ Å) for YBCO films in the YBCO/BTO/YBCO and YBCO/STO(5 nm)/ BTO/STO(5 nm)/YBCO heterostructures, which were determined from the x-ray diffraction patterns, are in good agreement with the data available in the literature for films and bulk samples of YBCO with a small deviation from the stoichiometry with respect to oxygen [13].

It can be seen from Fig. 3a that the BTO layer grown on the surface of a superconducting film has a granular structure. The sizes of crystal grains in the ferroelectric layer are equal to 100–150 nm (Fig. 3a). As follows from the widths of peaks in the x-ray ϕ-scans for the BTO(111) reflection, the azimuthal misorientation of crystallites in the ferroelectric layer, on the average, is equal to 0.7°. The main reason for the azimuthal misorientation of crystallites in the BTO layer is the difference between the crystal lattice parameters ($\Delta a \sim 4\%$) upon the lattice matching of BTO(100) and YBCO(001). The sizes of crystal grains in the YBCO film grown on the LAO(100) surface are two or three times less than those in the BTO layer grown on the YBCO(001)/LAO(100) surface (Fig. 3b). The surface of the YBCO film grown on the BTO(100)/YBCO(001)/LAO(100) surface was rough because of the large-sized crystallites rising above the

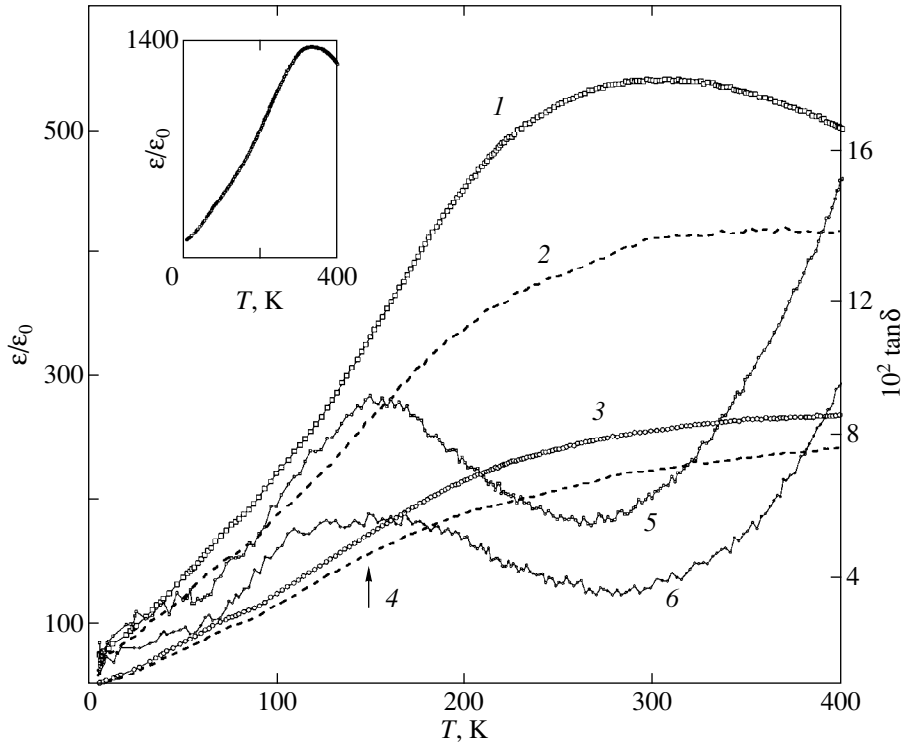

Fig. 4. Temperature dependences of (*1–4*) $\varepsilon/\varepsilon_0$ and (*5*, *6*) $\tan\delta$ for the BTO(700 nm) layer in (*1*, *2*, *5*) YBCO/STO(5 nm)/BTO/STO(5 nm)/YBCO and (*3*, *4*, *6*) YBCO/BTO/YBCO heterostructures. v_T = 5 K/min. Curves *2* and *4* are obtained at the bias voltage (V_b = +2.5 V) applied to superconducting electrodes. The inset shows the $\varepsilon/\varepsilon_0(T)$ curve for a BTO(700 nm) layer sandwiched between two $SrRuO_3$(100) epitaxial electrodes [14]. ε_0 is the permittivity of free space, f = 100 kHz.

other part of the superconducting film by 50–120 mm (Fig. 3c).

3.2. Dielectric parameters of a BTO layer. The measured permittivities ε for a BTO(100) layer in the YBCO/BTO/YBCO and YBCO/STO (5 nm)/BTO/STO(5 nm)/YBCO parallel-plate capacitor structures are substantially less than the permittivity measured along the *a* axis for BTO single crystals (T = 4.2–400 K) [6]. The reason for the low ε values, which were measured for a barium titanate layer inserted between two superconducting cuprate electrodes, is the deviation from the stoichiometry in the boundary regions of the BTO layer and the YBCO film and, as a consequence, the formation of a material layer with a low permittivity near the interface. At T = 300 K, the permittivity of a BTO layer in the YBCO/STO(5 nm)/BTO/STO(5 nm)/YBCO multilayer heterostructure is approximately twice as large as that of the ferroelectric layer in the YBCO/BTO/YBCO heterostructure (Fig. 4). The increase in the permittivity ε of the BTO layer upon introduction of STO(5 nm) buffer layers into the heterostructure is caused by improving the microstructure of ferroelectric–superconductor interfaces [7]. In the case when the superconducting cuprate electrodes in the YBCO/BTO/YBCO capacitor structure is replaced by electrodes made of $SrRuO_3$ (at T < 800°C, $SrRuO_3$ is chemically inert to barium titanate and provides a smaller difference in the crystal lattice parameters as compared to YBCO), the permittivity ε of a ferroelectric layer increases by a factor of three or six [14] (inset in Fig. 4).

The maximum in the dependence $\varepsilon(T)$ for a BTO layer in the YBCO/STO(5 nm)/BTO/STO(5 nm)/YBCO capacitor structure is shifted by 70–80 K toward the low-temperature range with respect to its location in the temperature dependence of the permittivity for a BTO single crystal [6]. The stabilization of the cubic phase at temperatures below 390 K was observed in BTO ceramic films with a crystallite size of the order of 20 nm [1]. A considerable shift in the maximum in the $\varepsilon(T)$ dependence toward the low-temperature range was observed for BTO epitaxial films with a decrease in the size of crystalline blocks from 200 to 50 nm [14].

When the bias voltage (±2.5 V) is applied to the superconducting electrodes, the maximum in the $\varepsilon(T)$ dependence for a BTO layer in the YBCO/BTO/YBCO and YBCO/STO(5 nm)/BTO/STO(5 nm)/YBCO capacitor structures shifts toward the high-temperature range (Fig. 4). An increase in the Curie temperature T_C for BTO single crystals in the electric field was clearly demonstrated in [15].

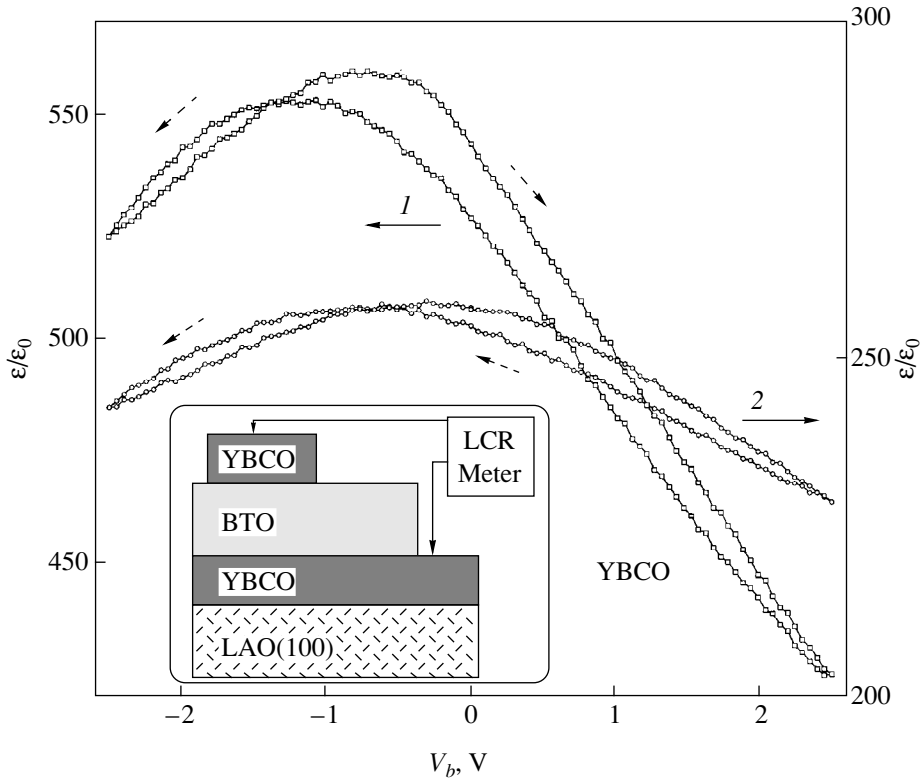

Fig. 5. Dependences of the permittivity on the bias voltage for the BTO(700 nm) layer in (*1*) YBCO/STO(5 nm)/BTO/STO(5 nm)/YBCO and (*2*) YBCO/BTO/YBCO heterostructures at $T = 300$ K. A hysteresis is observed in the $\varepsilon/\varepsilon_0(V_b)$ curves obtained for both heterostructures. A drawing of the parallel-plate capacitor structure is shown in the inset. $f = 100$ kHz, $v_T = 5$ K/min.

A clearly pronounced hysteresis is observed in the dependences of the permittivity for a BTO layer at $T = 300$ K on the bias voltage applied to YBCO electrodes (Fig. 5). The measured dependences $\varepsilon(V_b)$ indicate that, at $T = 300$ K, the BTO layer in the grown heterostructures is in the ferroelectric phase. When the voltage V_b changes from –2.5 to +2.5 V, the $\varepsilon(V_b)$ curves for a BTO layer in the YBCO/BTO/YBCO and YBCO/STO(5 nm)/BTO/STO(5 nm)/YBCO heterostructures exhibit a clear maximum, which is shifted toward negative V_b values with respect to the point $V_b = 0$. This shift of the maximum in the $\varepsilon(V_b)$ curves for the BTO layer is partly determined by the differences in electronic parameters of the lower and upper interfaces between the ferroelectric and the superconductor. A drawing of the YBCO/BTO/YBCO parallel-plate capacitor structure is shown in the inset in Fig. 5.

The appearance of a maximum in the $\tan\delta(T)$ curves for a BTO layer in the YBCO/BTO/YBCO and YBCO/STO(5 nm)/BTO/STO(5 nm)/YBCO heterostructures at $T \approx 160$ K is explained by the interaction of electromagnetic radiation with ferroelectric domain walls. When a bias voltage of ±2.5 V is applied to the superconducting electrodes, the value of $\tan\delta$ for the BTO layer decreases ($T < 200$ K), which is caused by an increase in the mean domain size in an external electric field. The drastic increase in $\tan\delta$ with an increase in temperature at $T > 300$ K (Fig. 4) is associated with an increase in the electrical conductivity of a ferroelectric layer due to the ionization of donor centers (oxygen vacancies [8]). In the temperature range 300–400 K, the $\tan\delta$ value for a BTO layer in the YBCO/BTO/YBCO and YBCO/STO(5 nm)/BTO/STO(5 nm)/YBCO heterostructures increases when measurements are carried out in an external electric field.

3.3. Parameters of YBCO films in the YBCO/BTO/YBCO heterostructure. The values of T_C and j_C for YBCO films grown on the LAO(100) surface fall in the ranges 88–91 K and $(1–3) \times 10^6$ A/cm^2, respectively. The Curie temperature T_C for an YBCO film in the BTO(700 nm)/YBCO(200 nm)/LAO(100) heterostructure essentially depends on the cooling rate of the sample after the completion of the condensation process. At $v_T = 25$ K/min, the T_C temperature, which was determined from the temperature dependence of χ for the YBCO film coated with a BTO layer 700 nm thick, is equal to 50–55 K (see inset in Fig. 6) and the unit cell parameter c of the superconductor lies in the range 11.71–11.70 Å. As the cooling rate v_T decreases to 5 K/min, the T_C temperature for an YBCO layer in the BTO(700 nm)/YBCO(200 nm)/LAO(100) hetero-

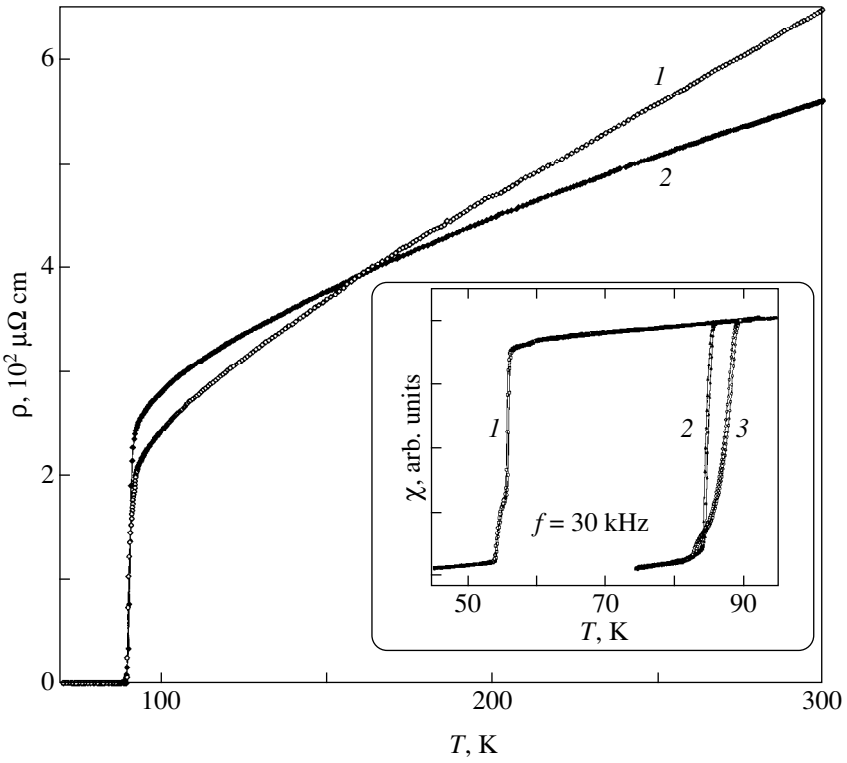

Fig. 6. Temperature dependences of (*1*) ρ for the YBCO(200 nm) film grown on the LAO(100) substrate and (*2*) ρ/2.5 for a superconducting film 200 nm thick grown on the BTO(700 nm)/YBCO(200 nm)/LAO(100) substrate. v_T = 5 K/min. The inset shows temperature dependences of the magnetic susceptibility for the (*1*, *2*) BTO(700 nm)/YBCO(200 nm)/LAO(100) and (*3*) YBCO(200 nm)/BTO(700 nm)/YBCO(200 nm)/LAO(100) heterostructures formed at different rates v_T, K/min: (*1*) 25 and (*2*, *3*) 5.

structure increases to 85 K (inset in Fig. 6) and the unit cell parameter *c* decreases approximately by 0.02 Å. The BTO(700 nm) layer grown on the surface of the YBCO film is the antidiffusion buffer which substantially decreases the rate of oxygen saturation of the YBCO film. The capacitance *C* of the YBCO/BTO/YBCO capacitor structure, which was cooled at the rate v_T = 25 K/min, is 50–80% less than that of the structure cooled at the rate v_T = 5 K/min. At high cooling rates v_T, the thickness of a layer with violated stoichiometry increases. This layer has a low permittivity ε and is located at the YBCO/BTO interface. The thickness of the layer with a low permittivity ε increases at the expense of both the ferroelectric layer and the superconducting film. According to [16], the YBCO oxygen-depleted ceramic samples are characterized not only by high resistivity ρ, but also by low permittivity $\varepsilon/\varepsilon_0 < 10$.

As follows from the data shown in Fig. 2, the azimuthal misorientations of crystallites in the upper and lower YBCO films in the YBCO/BTO/YBCO heterostructure differ by a factor of two or four. An increase in the misorientation of crystal grains in the YBCO film brings about an increase in the stoichiometry violation in the intercrystalline boundary region. The large azimuthal misorientation of the crystallites is one of the reasons for an increase in the resistivity ρ and a decrease in the critical current density j_C for the YBCO film formed on the BTO(700 nm)/YBCO(200 nm)/LAO substrate, as compared to these parameters for a superconducting film grown on the LAO(100) substrate.

4. CONCLUSION

The fundamental similarity between the structures of perovskite-like ferroelectrics and cuprate superconductors is favorable to the growth of oriented BTO layers on the surface of YBCO epitaxial films. The BTO(700 nm) layer grown on the YBCO(001) surface consists of crystal grains separated by low-angle boundaries. The stoichiometry violation in the YBCO/BTO interface region encourages the formation of a layer with a low permittivity ε. At *T* = 300 K, the ε value for the BTO layer, which was calculated from the capacitance of the YBCO/BTO(700 nm)/YBCO and YBCO/STO(5 nm)/BTO(700 nm)/STO(5 nm)/ YBCO capacitor structures, is considerably less than the permittivity of barium titanate single crystals. An increase in the loss tangent $\tan\delta$ with an increase in the temperature at *T* > 300 K is caused by an increase in the electrical conductivity of the ferroelectric layer. The BTO(700 nm) layer grown on the YBCO film surface is

the antidiffusion barrier which sharply decreases the rate of oxygen saturation of the superconductor. The azimuthal misorientation of crystal grains in the YBCO(001) film grown on the BTO(100)/YBCO(001)/LAO(100) surface and also the defects arising in the bulk of crystallites due to roughening of the free surface of a ferroelectric layer are responsible for the degradation of the superconductivity parameters of the upper YBCO layer in the YBCO/BTO/YBCO heterostructure.

ACKNOWLEDGMENTS

This work was supported by the Program of the scientific cooperation between the Russian Academy of Sciences and the Royal Swedish Academy of Sciences (project TFR no. 240-97-382), the Russian Foundation for Basic Research (project no. 98-02-18222), and the Research Program "Combination," the Direction "Superconductivity" (project no. 98041).

REFERENCES

1. M. H. Frey and D. A. Payne, Appl. Phys. Lett. **63**, 2753 (1993).
2. D. M. Gill, B. A. Block, C. W. Conrad, *et al.*, Appl. Phys. Lett. **69**, 2968 (1996).
3. J.-G. Cheng, X.-J. Meng, J. Tang, *et al.*, Appl. Phys. Lett. **75**, 3402 (1999).
4. H. B. Sharma, H. N. K. Sarma, and A. Mansingh, J. Appl. Phys. **85**, 341 (1999).
5. I. Lubomirsky, D. T. Chang, and O. M. Stafsudd, J. Appl. Phys. **85**, 6690 (1999).
6. W. J. Merz, Phys. Rev. **76**, 1221 (1949).
7. Yu. A. Boikov, Z. G. Ivanov, A. N. Kiselev, *et al.*, J. Appl. Phys. **78**, 4591 (1995).
8. Yu. A. Boikov and T. Claeson, Supercond. Sci. Technol. **12**, 654 (1999).
9. T. I. Kamins, J. Appl. Phys. **42**, 4357 (1971).
10. V. Srikant, E. J. Tarsa, D. R. Clarke, and J. S. Speck, J. Appl. Phys. **77**, 1517 (1995).
11. R. W. G. Wyckoff, *Crystal Structures* (Wiley, New York, 1964), Vol. 2, p. 391.
12. C. Zuccaro, M. Winter, N. Klein, and K. Urban, J. Appl. Phys. **82**, 5695 (1997).
13. C. B. Eom, J. Z. Sun, K. Yamamoto, *et al.*, Appl. Phys. Lett. **55**, 595 (1989).
14. Yu. A. Boikov and T. Claeson, J. Appl. Phys. (2001) (in press).
15. W. J. Merz, Phys. Rev. **91**, 513 (1953).
16. D. Winkler, Y. M. Zhang, P. A. Nilsson, and T. Claeson, Phys. Rev. Lett. **72**, 1260 (1994).

Translated by O. Borovik-Romanova

Physics of the Solid State, Vol. 43, No. 2, 2001, pp. 345–349. Translated from Fizika Tverdogo Tela, Vol. 43, No. 2, 2001, pp. 331–335.

LATTICE DYNAMICS AND PHASE TRANSITIONS

Heat Capacity and the *p–T* Phase Diagram of Pb_2MgTeO_6 Elpasolite

M. V. Gorev*, I. N. Flerov*, and Ph. Sciau**

** Kirenskiĭ Institute of Physics, Siberian Division, Russian Academy of Sciences, Akademgorodok, Krasnoyarsk, 660036 Russia*
e-mail: gorev@iph.krasn.ru

*** CNRS Center for Materials Improvement and Structural Investigations, Tuluza, 31055 France*

Received June 26, 2000

Abstract—The heat capacity of Pb_2MgTeO_6 is measured in the temperature range 80–300 K. It is found that the heat capacity exhibits an anomaly associated with the phase transition at $T_0 = 186.9$ K. The thermodynamic parameters of the structural transformation are determined. The effect of hydrostatic pressure up to 0.5 GPa on the phase transition temperature is examined. © *2001 MAIK "Nauka/Interperiodica".*

1. INTRODUCTION

Oxygen-containing compounds with a perovskite structure ABO_3 ($Pm\bar{3}m$, $Z = 1$) are usually considered model objects owing to the great diversity of their physical properties and the relatively simple structure of their crystal lattice. The specific feature of perovskites is the striking flexibility of their structure, which makes it possible to change their atomic composition over a wide range and, thus, to achieve the desirable properties of materials. One possible way of affecting their properties is to replace the B cation by two different cations B' and B''. At certain ratios between ionic radii and charges, the cations can undergo an ordering with the formation of an elpasolite structure (ordered perovskite) $A_2B'B''O_6$ ($Fm\bar{3}m$, $Z = 4$). A change in the degree of ordering of the B' and B'' cations can substantially affect the physical properties of compounds and the nature of their structural transformations. The compositionally disordered (partly or completely) compounds are relaxors; i.e., they undergo diffuse (smeared) phase transitions and exhibit a dispersion of permittivity. Conversely, the ordered compounds undergo sharp phase transitions with a decrease in the temperature.

Despite extensive investigations of these compounds by different methods, many fundamental problems still remain unsolved. For all these compounds, the symmetry of distorted phases and even their number, as well as the mechanism of phase transitions, have been debated in the literature up to now. Particular attention has been concentrated on a large family of lead-containing compounds $Pb_2B'B''O_6$, among which are different-type relaxors and compositionally ordered perovskites.

The Pb_2MgTeO_6 compound was first studied in [1, 2]. The dielectric measurements performed by Politova and Venevtsev [2] revealed a small anomaly in $\varepsilon(T)$ near 190 K. The first-order phase transition at this temperature was confirmed by the structural investigations carried out by Baldinozzi *et al.* [3]. Apart from the anomaly observed at ~190 K, a small change in the permittivity was found at 145 K in [4]. Some parameters of the Raman spectra also exhibited an anomalous behavior in the temperature range 150–142 K. It should be noted that this feature was observed only in measurements upon cooling.

Baldinozzi *et al.* [4, 5] proved that the low-temperature phases are the incommensurate phases with the modulation vector $(\delta\delta\delta)$, where δ is close to 0.107 at 8 K. Analysis of the experimental data allowed these authors to make the conclusion that the phase transformation at 190 K is an improper ferroelastic transition. A trigonal ferroelastic distortion arises as a secondary order parameter upon mode condensation at an incommensurate point of the Brillouin zone. The intermediate and low-temperature phases have the $R\bar{3}m(\delta\delta\delta)$ and $R\bar{3}(\delta\delta\delta)$ symmetries, respectively.

The phase transition to the incommensurate phase is a fairly rare phenomenon in mixed oxygen-containing perovskites. Only three representatives of this family with the aforementioned transitions, namely, Pb_2CoWO_6 [6, 7], Pb_2CdWO_6 [8], and $PbSc_{1/2}Ta_{1/2}O_3$ [9], are known to date. The characteristic feature of the Pb_2MgTeO_6 compound is an extremely wide stability range of the incommensurate phase. No transitions to the commensurate phase was found down to 6 K [3, 4].

Another feature of the Pb_2MgTeO_6 compound is a rather unusual temperature behavior of the thermal ellipsoid parameters for lead ions. According to structural investigations, the $Pb_2B'B''O_6$ compounds are characterized by a high degree of positional disordering of lead ions in the initial cubic phase. For a number of

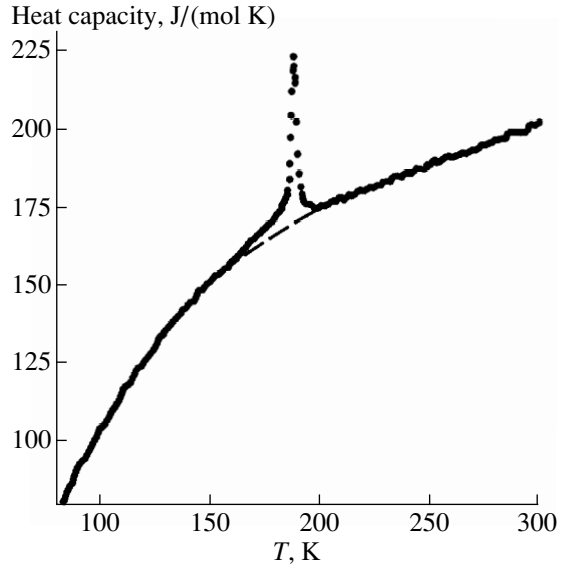

Fig. 1. Temperature dependence of the heat capacity of Pb_2MgTeO_6. The dashed line represents the lattice heat capacity.

compounds (Pb_2CoWO_6 [10], Pb_2MgWO_6 [11], and Pb_2CdWO_6 [8]), the thermal ellipsoid parameters of lead ions become normal in the distorted phases, which suggests the ordering of lead ions. For other elpasolites, specifically for Pb_2MgTeO_6 [5], these parameters remain anomalously large. Moreover, soft modes were revealed in all these compounds. At present, the ordering processes, soft modes, and their interaction upon successive structural transformations in ordered perovskites have been studied intensively.

In the present work, we thoroughly investigated the *p–T* phase diagram and the heat capacity of the Pb_2MgTeO_6 compound over a wide range of temperatures. The purpose of this work was to determine the thermodynamic parameters of the phase transitions and to elucidate the role of the ordering processes in two groups of oxygen- and lead-containing elpasolites, which differ in the behavior of the thermal ellipsoid parameters of lead ions. It is this heat capacity that can provide reliable information on phase transitions, irrespective of their nature and mechanisms. At the same time, the data on the thermodynamic characteristics of the phase transitions (enthalpies and entropies) are required in the refinement of different models for structural transformations. In turn, analysis of the *p–T* phase diagrams enables one to gain a better insight into the interrelation between successive structural distortions in different representatives of the family under consideration.

2. EXPERIMENTAL TECHNIQUE

The powder samples to be studied were prepared by solid-phase synthesis from a stoichiometric mixture of initial oxides [3] and were used earlier in structural and Raman studies [4, 5]. Analysis of x-ray diffraction patterns showed that the sample contains a minor amount of Pb_3TeO_6 and $PbTeO_3$ impurities. No indications of the composition disordering of Mg and Te ions was found.

The heat capacity was measured using an adiabatic calorimeter in the temperature range 80–300 K. A powder sample (4.25 g) was placed in an indium cell and was sealed in a helium atmosphere. The heat capacity of the cell was measured in a separate experiment. The measurements were carried out upon continuous and discrete heating. In their immediate vicinity, the phase transitions were investigated by the quasi-static thermogram method at the mean rates of temperature change $|dT/dt| \approx (1–1.5) \times 10^{-2}$ K/min.

The effect of hydrostatic pressure on the phase transition temperature was studied with the same sample as was used in the calorimetric measurements. The change in the phase transition temperature was determined by differential thermal analysis with the use of a copper–germanium thermocouple. A quartz reference sample was placed on one junction of the thermocouple, and a small copper vessel (~0.05 cm^3) with the studied compound in it was placed on another junction of the thermocouple. The high sensitivity of the thermocouple made it possible to measure the phase transitions with a small change in the enthalpy. A pressure as high as 0.5 GPa was produced in a chamber of the cylinder–piston type, which was connected to a booster. A mixture of a silicone oil and pentane was used as a pressure transmitting medium. The pressure was measured by a manganin resistance pressure gauge, and the temperature was measured using a copper–constantan thermocouple. The errors of measurements were equal to $\pm 10^{-3}$ GPa and ±0.3 K, respectively.

3. RESULTS

The results of our measurements of the heat capacity $C_p(T)$ are displayed in Fig. 1. It is seen that $C_p(T)$ exhibits only one anomaly with a maximum at $T_0 = 187.1 \pm 0.5$K. Figure 2 shows the experimental data on the heat capacity in the temperature range in which, according to Baldinozzi *et al.* [4], specific features in the behavior of the permittivity and the Raman spectrum parameters are observed as a result of the second phase transition. The measurements were performed upon heating and cooling. In experiments upon cooling, the sample was preliminarily heated above 190 K, i.e., above the temperature of the transition from the cubic phase. A relatively small, regular scatter of the experimental points with respect to the smoothed curve $C_p(T)$ upon both heating and cooling indicates that any anomaly in the heat capacity of the studied sample in the temperature range 133–147 K is absent, to within about 0.5% of the total heat capacity of the sample.

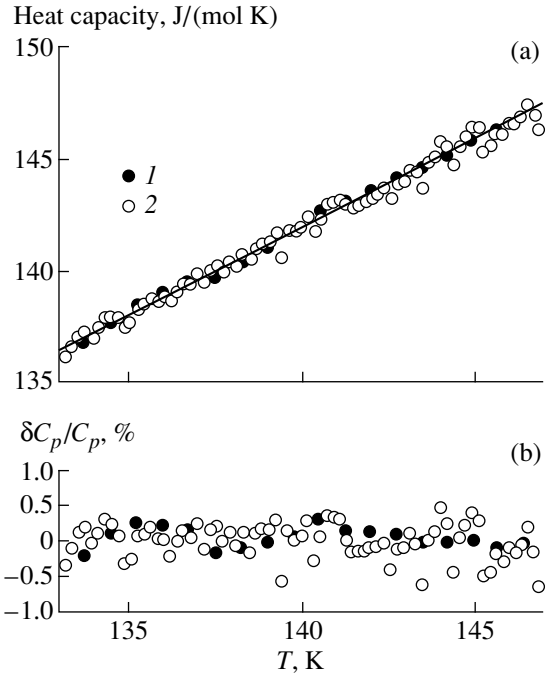

Fig. 2. (a) Temperature dependences of the heat capacity measured upon continuous and discrete heating of Pb_2MgTeO_6 in the range of the second phase transition assumed in [9] and (b) deviations of the experimental points from the smoothed dependences: (*1*) heating and (*2*) cooling.

Thermographic investigations in the vicinity of the phase transition allowed us to refine the transition temperature $T_0 = 186.9 \pm 0.1$ K and to determine its hysteresis $\delta T_0 = 0.63 \pm 0.05$ K. The experimental heat capacities measured using a continuous heating technique upon heating and cooling in the phase transition range are displayed in Fig. 3. The anomaly observed in the heat capacity is strongly asymmetric. Note that the heat capacity decreases considerably more slowly in the temperature range above the phase transition. As follows from the thermographic data, the latent heat of the phase transition has a small value ($\delta H_0 = 200 \pm 10$ J/mol). The corresponding change in the entropy is $\delta S_0 = \delta H_0/T_0 \cong 1.1$ J/(mol K). A slight difference between the phase transition temperature and the temperature reported in the literature can be associated with difficulties in its accurate determination from the data of dielectric measurements and a high rate of change in temperature dT/dt in these experiments [4].

The integrated thermodynamic characteristics of the phase transition were obtained in processing the anomalous contribution of the heat capacity $\Delta C_p(T) = C_p(T) - C_l(T)$. The lattice heat capacity $C_l(T)$ was determined by the approximation of the experimental data far from the phase transition temperature with the use of the Debye and Einstein functions. The temperature dependence of the lattice heat capacity is shown by the dashed line in Fig. 1. The heat capacity anomaly is observed in a rather wide range of temperatures (from 130 to 230 K). The entropy of the phase transition was calculated by integration of the $\Delta C_p(T)/T$ function. The temperature dependence of the entropy of phase transition is displayed in Fig. 4. The total entropy change ΔS_0 is equal to 2.59 ± 0.25 J/(mol K). The ratio $\delta S_0/\Delta S_0 \approx 0.42$ indicates that the phase transition is the first-order transformation close enough to a tricritical point.

Figure 5 shows the *p–T* phase diagram of Pb_2MgTeO_6. No anomalies that could be assigned to the pressure-induced transitions (except for the transition from the cubic phase) were found in the pressure range covered. The phase boundary is described by the linear dependence $T(p) = a + bp$ with the coefficients $a = 186.9 \pm 0.1$ K and $b = -6.07 \pm 0.10$ K/GPa.

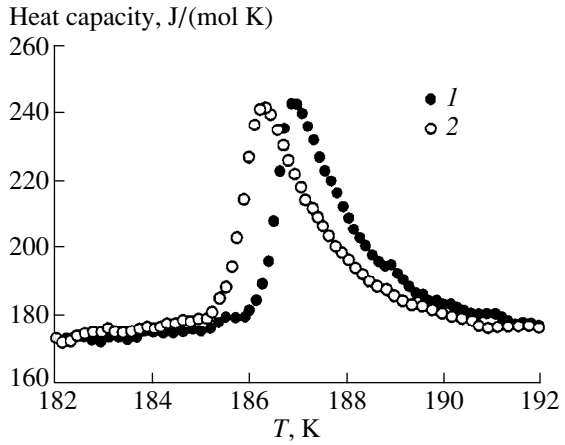

Fig. 3. Temperature dependences of the heat capacity measured upon (*1*) heating and (*2*) cooling in the vicinity of the phase transition in Pb_2MgTeO_6.

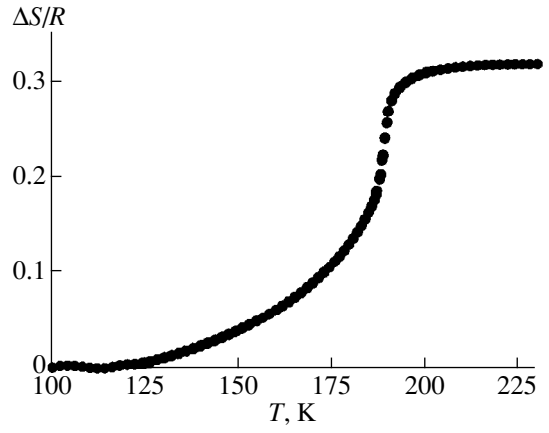

Fig. 4. Temperature dependence of the entropy of phase transition in Pb_2MgTeO_6.

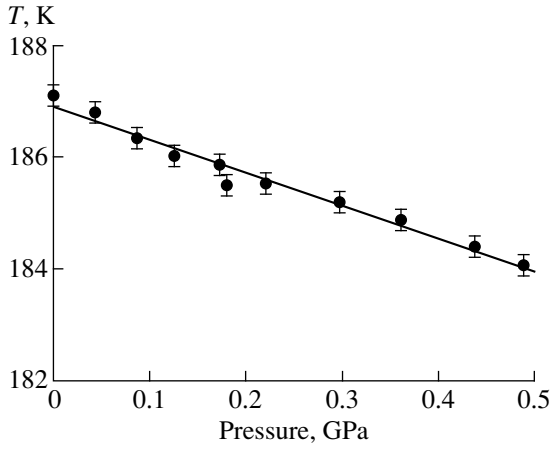

Fig. 5. The p–T phase diagram for Pb_2MgTeO_6.

4. DISCUSSION AND CONCLUSIONS

The main thermodynamic characteristics of the phase transitions in Pb_2MgTeO_6 and two oxygen-containing ordered perovskites studied in our earlier works [12, 13] are listed in the table. It is seen that the entropy change upon the phase transition in Pb_2MgTeO_6 is substantially less than the quantity ΔS for the other studied compounds. In order to elucidate the reasons for this difference, we will consider the structural characteristics of the cubic and distorted phases in these compounds.

The cubic phase in Pb_2MgTeO_6, as well as in the other representatives of this family, is characterized by a high degree of positional disordering of lead ions [10, 11]. The refinement of the structure of the $Fm\bar{3}m$ phase in Pb_2MgWO_6 and Pb_2CoWO_6, in the case when the lead ions have only one position and occupy only the 8*c* sites, leads to large values of the thermal vibration parameters and the R factors. The best R factors are obtained for the case when the lead ions move in a multiple-well potential and occupy 12 equivalent positions [10, 11]. Unfortunately, the available experimental data were insufficient to perform a similar analysis for Pb_2MgTeO_6 [5]. Nonetheless, the large thermal parameter suggests that lead ions in this compound are also displaced from the 8*c* positions and disordered.

Structural and thermodynamic characteristics of phase transitions in $Pb_2B'B''O_6$ ordered perovskites

Characteristic	Pb_2MgWO_6	Pb_2CoWO_6	Pb_2MgTeO_6
T_1, K	312.8 ± 0.2	302.7 ± 0.5	186.9 ± 0.1
G_1	*Pmcn*	Incommensurate	$R\bar{3}(\delta\delta\delta)$
δT_1, K	2.45 ± 0.2	~1	0.63 ± 0.05
dT_1/dp, K GPa^{-1}	–32.8 ± 1.5	37.4 ± 5.0	–6.07 ± 0.10
$\Delta S_1/R$	1.69 ± 0.14	1.15 ± 0.18	0.31 ± 0.03
T_2, K		256.2 ± 0.5	
G_2		*Pmcn*	
δT_2, K		11.4	
dT_2/dp, K GPa^{-1}		–220 ± 38	
$\Delta S_2/R$		0.18 ± 0.02	
Reference	[11, 12, 13]	[7, 13]	[4, 5], this work

In Pb_2MgWO_6 and Pb_2CoWO_6, the phase transitions bring about the ordering of the lead atoms. In Pb_2MgTeO_6, the thermal parameters of lead ions remain anomalously large with a decrease in the temperature, which indicates that the lead ions remain disordered in the low-temperature distorted phase [5]. A similar situation is also observed in $PbFe_{0.5}Nb_{0.5}O_3$ [14], $PbSc_{0.5}Nb_{0.5}O_3$ [15], and $PbFe_{0.5}Ta_{0.5}O_3$ [16].

In the cubic phases of all the aforementioned compounds, the thermal parameters of oxygen ions are also rather large. As the phase transition temperature is approached upon cooling, the thermal ellipsoid for the oxygen ions becomes increasingly flattened, which was attributed [5] to the softening of the modes responsible for the phase transition.

As regards the structural features associated with the lead ions, it seems likely that there exists a difference between the compounds in which the main distortion is rhombohedral and those in which it is pseudotetragonal. In the latter compounds, no positional disordering of the lead ions is observed in the low-temperature phase. Actually, in Pb_2MgWO_6 and Pb_2CoWO_6, the large thermal ellipsoid parameters for the lead ions in the cubic phase become normal below the phase transition temperatures [11]. The significant role of the lead ordering in the mechanism of phase transitions is also confirmed by the results of calorimetric investigations of these compounds [12, 13]: the entropy change is $\Delta S/R \approx \ln 4 - \ln 6$.

One reason for this behavior of the lead ions can be their tendency toward the formation of tetrahedral coordination polyhedra PbO_4 [17]. These polyhedra were found in the pseudotetragonal low-temperature phase of Pb_2MgWO_6 [11]. In the case of rhombohedral symmetry, the ordering of the lead ions on a threefold axis can result only in the PbO_3 configuration. The PbO_4 configuration can be realized in this symmetry when the lead ions are displaced from the threefold axis and are disordered over several positions. The absence of a substantial change in the positional disordering of lead ions upon phase transition in Pb_2MgTeO_6 is supported by the entropy change $\Delta S/R = 0.31$, which was obtained in the present work.

The parameters of the p–T phase diagrams for the compounds under considerations (see table) are also noteworthy. The substantial difference in the values of dT_1/dp stands out. In this respect, it is necessary to return to the question about the existence of the second

phase transition in Pb_2MgWO_6. As was noted in our earlier work [13], the p–T diagrams for the Pb_2MgWO_6 and Pb_2CoWO_6 compounds can be treated as related. To put it differently, the line of the phase transition $Fm\bar{3}m \longrightarrow Pmcn$ in the magnesium compound is split when the unit cell volume changes and the intermediate incommensurate phase is formed in cobalt elpasolite. In our opinion, this is the main reason why both the magnitudes of dT_1/dp and their signs differ for these elpasolites. A small shift in T_1 under a pressure in Pb_2MgTeO_6 counts in favor of the difference in the mechanism of phase transition in this compound, which is in agreement with the data of structural and calorimetric investigations. As regards the second phase transition in this compound, the question remains open.

ACKNOWLEDGMENTS

This work was supported by the Russian Foundation for Basic Research (project no. 00-15-96790) and the Krasnoyarsk Regional Scientific Foundation (project no. 9F0213).

REFERENCES

1. G. Bayer, J. Am. Ceram. Soc. **46**, 604 (1963).
2. E. D. Politova and Yu. N. Venevtsev, Dokl. Akad. Nauk SSSR **209** (4), 838 (1973) [Sov. Phys. Dokl. **18**, 264 (1973)].
3. G. Baldinozzi, Ph. Sciau, J. Moret, and P. A. Buffat, Solid State Commun. **89** (5), 441 (1994).
4. G. Baldinozzi, Ph. Sciau, and A. Bulou, J. Phys.: Condens. Matter **9**, 10531 (1997).
5. G. Baldinozzi, D. Grebille, Ph. Sciau, *et al.*, J. Phys.: Condens. Matter **10**, 6461 (1998).
6. H. Tamura, Ferroelectrics **21**, 449 (1978).
7. Ph. Sciau, K. Krusche, P. A. Buffat, and H. Schmid, Ferroelectrics **107**, 235 (1990).
8. Ph. Sciau and D. Grebille, in *Proceedings of the International Conference on Aperiodic Crystals, Aperiodic'94* (World Scientific, Singapore, 1994), p. 460.
9. C. A. Randell, S. A. Markgraf, A. S. Bhalla, and K. Baba-Kishi, Phys. Rev. B **40**, 413 (1989).
10. G. Baldinozzi, Ph. Sciau, and J. Lapasser, Phys. Status Solidi A **133**, 17 (1992).
11. G. Baldinozzi, Ph. Sciau, M. Pinot, and D. Grebille, Acta Crystallogr., Sect. B: Struct. Sci. **B51**, 668 (1995).
12. I. N. Flerov, M. V. Gorev, and Ph. Sciau, Fiz. Tverd. Tela (St. Petersburg) **41** (9), 1686 (1999) [Phys. Solid State **41**, 1544 (1999)].
13. I. N. Flerov, M. V. Gorev, and Ph. Sciau, J. Phys.: Condens. Matter **12**, 559 (2000).
14. N. Lampis, Ph. Sciau, and A. G. Lehmann, J. Phys.: Condens. Matter **11**, 3489 (1999).
15. C. Malibert, B. Dkhil, J. M. Kiat, *et al.*, J. Phys.: Condens. Matter **9**, 7485 (1997).
16. A. G. Lehmann and Ph. Sciau, J. Phys.: Condens. Matter **11**, 1235 (1999).
17. N. Revezzi and Ph. Sciau, J. Solid State Chem. **139**, 332 (1998).

Translated by O. Borovik-Romanova

Physics of the Solid State, Vol. 43, No. 2, 2001, pp. 350–354. Translated from Fizika Tverdogo Tela, Vol. 43, No. 2, 2001, pp. 336–340.

LATTICE DYNAMICS AND PHASE TRANSITIONS

X-ray Diffraction Study of a Sequence of Phase Transitions in Cs_2HgCl_4 Crystals

B. Sh. Bagautdinov[1, 2], I. D. Brown[2], Yu. I. Yuzyuk[3], and V. P. Dmitriev[3]

[1] *Institute of Solid-State Physics, Russian Academy of Sciences, Chernogolovka, Moscow oblast, 142432 Russia*

[2] *Brockhouse Institute of Materials Research, McMaster University, Hamilton, Ontario, L8S 4M1 Canada*
e-mail: bagautdi@issp.ac.ru

[3] *Research Institute of Physics, Rostov State University, pr. Stachki 194, Rostov-on-Don, 344014 Russia*

Received April 5, 2000; in final form, June 29, 2000

Abstract—The temperature behavior of lattice parameters and diffraction patterns of the reciprocal lattice in Cs_2HgCl_4 crystals is studied by x-ray diffraction in the temperature range from 4.2 to 300 K. A sequence of phase transitions is observed and attributed to the evolution of incommensurate and commensurate modulations along the crystallographic **a** and **c** axes of a unit cell in the initial *Pnma* structure. © *2001 MAIK "Nauka/Interperiodica".*

1. INTRODUCTION

Cesium tetrachloromercurate Cs_2HgCl_4 belongs to the family of A_2BX_4 crystals and has a β-K_2SO_4 structure (*Pnma*, $Z = 4$, $c > a > b$) at room temperature [1]. Most of the known compounds with incommensurate phases belong to the A_2BX_4 family. Investigations into the physical properties of Cs_2HgCl_4 crystals revealed a series of phase transitions occurring upon cooling [2–7]. The behavior of the ^{35}Cl NQR lines and permittivity suggests [3, 6] the existence of a transition in the incommensurate phase below 219 K. Dielectric measurements also revealed the polar properties in the temperature ranges 196.4–184.5 and 172.1–164.7 K. The combination of incommensurate and ferroelectric phases stimulates interest in the Cs_2HgCl_4 compound. However, the available data on the temperatures of phase transitions in Cs_2HgCl_4 and their sequence are contradictory. In order to clarify the structural aspects of the sequence of phase transitions in Cs_2HgCl_4 crystals, we carried out a systematic x-ray diffraction investigation of the configuration of the reciprocal lattice and measured the interplanar spacings in a wide temperature range from 4.2 to 300 K.

2. EXPERIMENTAL TECHNIQUE

Crystals of Cs_2HgCl_4 were grown by evaporation from an aqueous solution at room temperature [1]. We studied optically transparent single-crystals (100), (010), and (001) sections $1.8 \times 1.5 \times 0.3$ mm in size, which were cut from the same crystal. The samples intended for measurements were placed in a helium cryostat, ensuring constancy of temperature to within 0.05 K. The temperature evolution of satellite reflections was studied on a Huber high-resolution four-circle diffractometer with a rotating anode (CuK_α radiation, graphite monochromator). The intensities of x-rays reflected from the sample surface were recorded in the $\theta/2\theta$ and θ scan modes and from the undistorted network of the reciprocal lattice (**q** scan mode). The scanning along the chosen directions of the reciprocal lattice was carried out with a step $\Delta q = 0.005$. An analysis of the systematic absences in diffraction reflections and the search for satellite reflections were carried out by scanning in the basal planes (*hk*0), (0*kl*), and (*h*0*l*). The lattice parameters were measured on a Siemens D500 two-circle diffractometer (CuK_α radiation) adapted for single-crystal goniometry. The interplanar spacings along the crystallographic axes of the initial high-temperature *Pnma* phase were determined from the centers of gravity of the Bragg reflections (12, 0, 0) (diffraction angle $2\theta \sim 140°$), (0, 8, 0) ($2\theta \sim 108°$), and (0, 0, 16) ($2\theta \sim 133°$) recorded in the $\theta/2\theta$ scan mode. The accuracy of measurements was no worse than 2×10^{-4} Å.

3. RESULTS AND DISCUSSION

3.1. Modulation along the a axis. The configuration of the Cs_2HgCl_4 reciprocal lattice of the initial *Pnma* phase with systematic absences (*hk*0: $h = 2n + 1$, 0*kl*: $k + l = 2n + 1$) remained unchanged upon cooling to 221 K. Below $T_i = 221$ K, satellite reflections appeared in the diffraction experiment on the (*hk*0) reflecting plane in the direction of the **a*** axis, indicating the evolution of structural modulations (Fig. 1). The positions of the first-order satellite reflections are described by the vector $\mathbf{q} = (4/5 - \delta)\mathbf{a}^*$ from the allowed reflections (*hk*0: $h = 2n$) or by the vector $\mathbf{q} = (1/5 + \delta)\mathbf{a}^*$ from the forbidden reflections (*hk*0: $h = 2n + 1$), where **a*** is the reciprocal lattice vector for the ini-

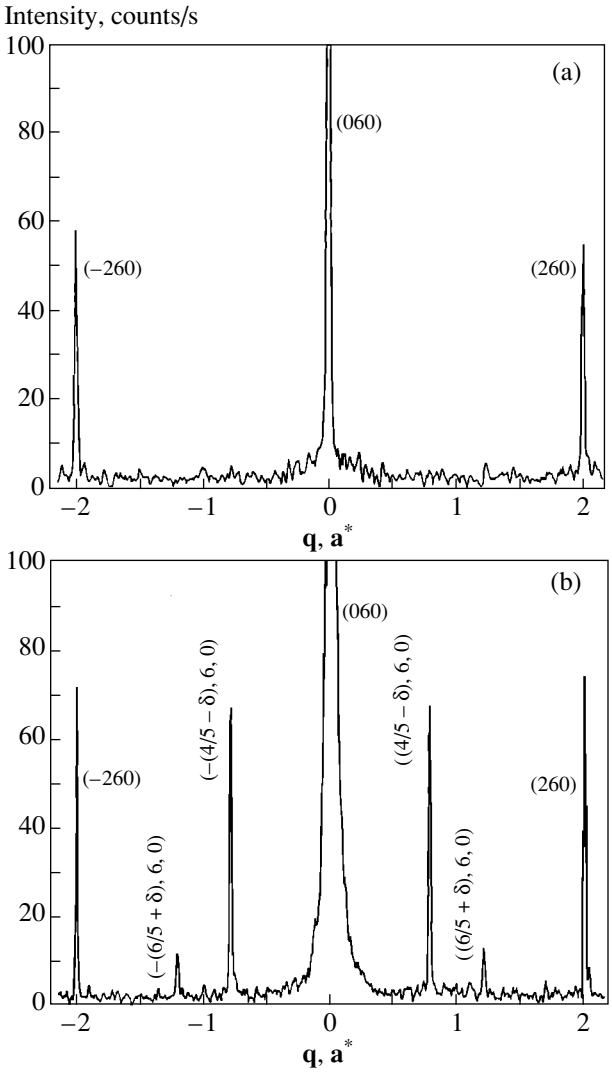

Fig. 1. Diffraction patterns for the series (*h*60) in the (a) initial *Pnma* phase (T = 293 K) and (b) temperature range of the incommensurate phase (T = 197 K). In addition to Bragg reflections, satellite reflections are detected in the incommensurate phase.

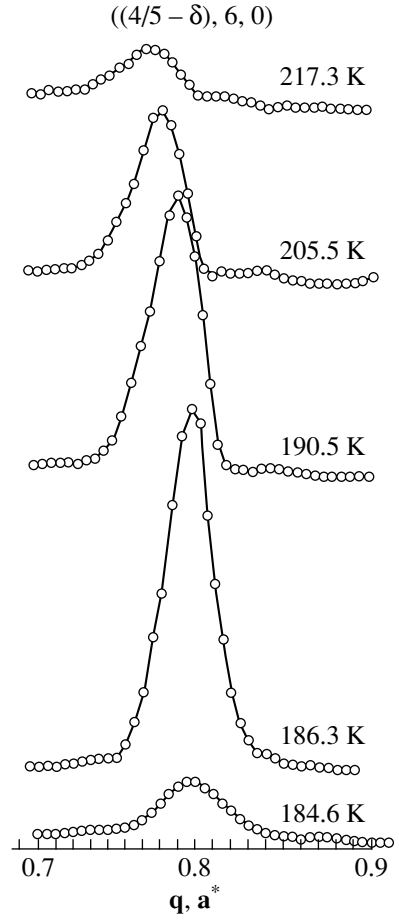

Fig. 2. Temperature behavior of the satellite reflection (4/5 – δ, 6, 0). The change in the position and intensity can be clearly seen.

tial *Pnma* phase and δ is the incommensurability parameter. The temperature behavior of the first-order satellite (4/5 – δ, 6, 0) is illustrated in Fig. 2. The changes in the position and intensity of satellite reflections upon a change in temperature indicate a incommensurate nature of modulation. The behavior of the modulation wave vector **q** = (1/5 + δ)**a*** as a function of temperature is shown in Fig. 3. Satellites appear at T_i = 221 K with δ = 0.045 and upon cooling, approach the rational positions that correspond to the wave vector **q** = 1/5**a*** at 185 K with δ = 0. In this case, the satellite intensity abruptly decreases and vanishes upon further cooling below 184 K. Heating of the samples reveals a hysteresis behavior: commensurate modulations with **q** = 1/5**a*** cover the temperature range from 184 to 195 K, after which the modulation vector tends

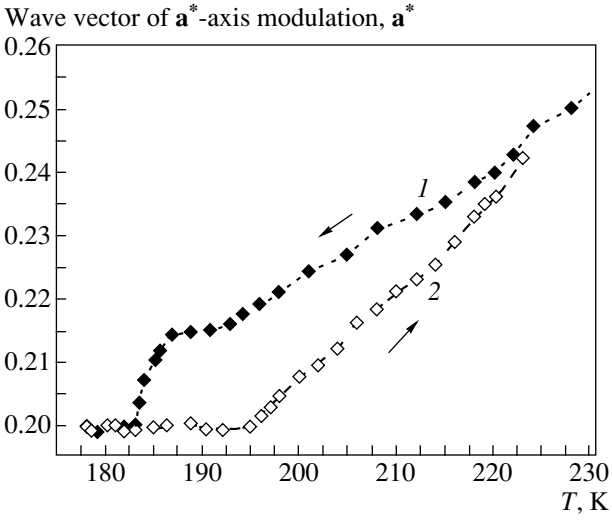

Fig. 3. Temperature dependences of the wave vector of modulations along the **a*** axis upon (*1*) cooling and (*2*) heating of the sample.

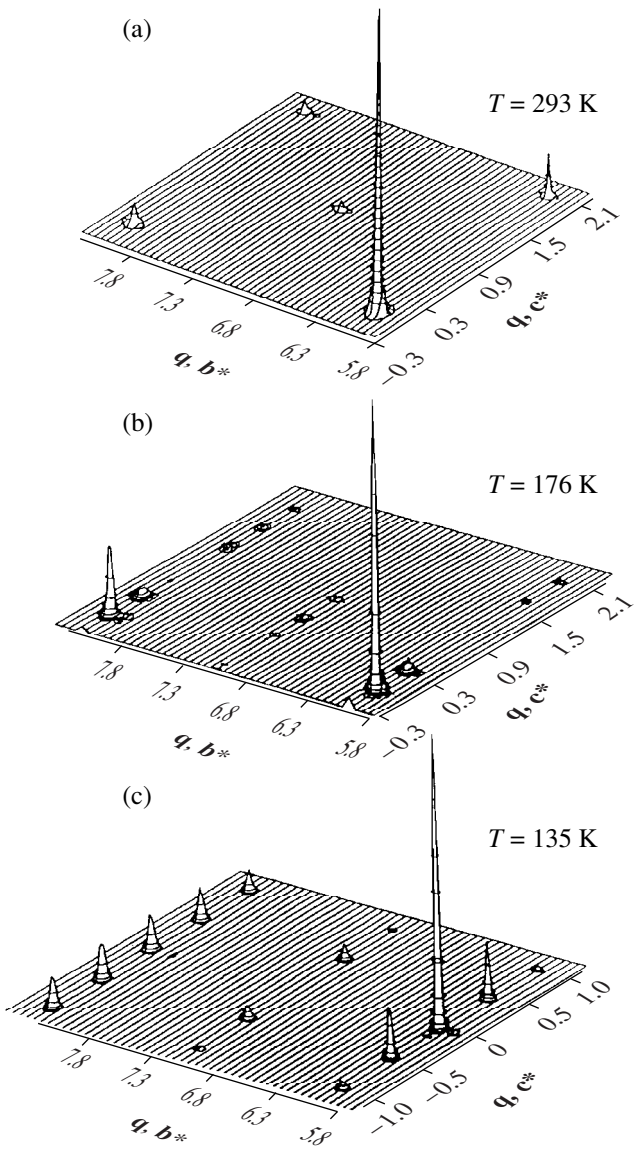

Fig. 4. Maps of the distribution of the scattered intensity in a region on the (0*kl*) plane at (a) 293, (b) 177, and (c) 135 K. Satellite reflections are detected along the axis **c*** (panels b and c).

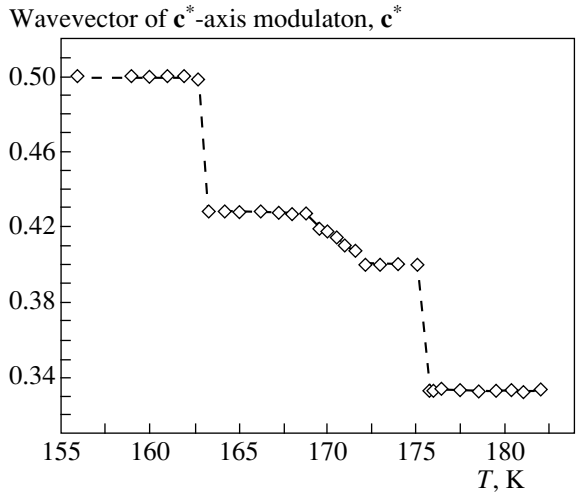

Fig. 5. Temperature dependence of the wave vector of modulations along the **c*** axis. The data are obtained during sample cooling.

to the value $\mathbf{q}(T_i)$. The global nature of the hysteresis loop embracing the temperature ranges of the existence of the incommensurate and commensurate phases is probably associated with the interaction of modulations with structural defects. No satellites of higher harmonics were detected, which points to the predominantly sinusoidal shape of the modulation wave. In the entire temperature range above 184 K, Bragg reflections obeyed the conditions corresponding to the glide planes *a* (*hk*0: $h = 2n$) and *n* (0*kl*: $k + l = 2n$). These conditions are in accord with the space groups of the initial paraelectric *Pnma* phase, the averaged *Pnma* structure in the incommensurate phase, and the polar $Pn2_1a$ phase. In the temperature range of the incommensurate phase (195–221 K), the satellites correspond to the condition *hk*0*m*: $k + m = 2n$, which indicates the $Pnma(\alpha, 0, 0)0ss$ group typical of A_2BX_4 compounds in the four-dimensional superspace representation [8]. Since dielectric measurements [5, 6] revealed the polar properties in the temperature range of the commensurate phase (184–195 K), the corresponding space group is noncentrosymmetric, i.e., $Pn2_1a$.

3.2. Modulation along the c axis. Below 184 K, satellites are detected in the (0*kl*) and (*h*0*l*) planes of the reciprocal lattice in the direction of the **c*** axis. Figure 4 shows a map of the two-dimensional distribution of the scattered intensity on the (0*kl*) plane. It can be seen that at low temperatures, satellites are observed in the positions corresponding to $\mathbf{q} = \gamma\mathbf{c}^*$. Consequently, the direction of modulations of the structure changes at 184 K: the wave vector $\mathbf{q} = \alpha\mathbf{a}^*$ is transformed into $\mathbf{q} = \gamma\mathbf{c}^*$. A detailed temperature analysis of satellites along the **c*** axis revealed the following transformations of the modulation wave vector: T_1 = 184 K, $\mathbf{q} = \mathbf{c}^*/3$; T_2 = 175 K, $\mathbf{q} = 2\mathbf{c}^*/5$; T_3 = 172 K, $\mathbf{q} = (3/7 - \delta)\mathbf{c}^*$; T_4 = 169 K, $\mathbf{q} = 3\mathbf{c}^*/7$; T_5 = 163 K, $\mathbf{q} = \mathbf{c}^*/2$; and T_6 = 112 K, $\mathbf{q} = \mathbf{c}^*/2$ (Fig. 5). The structure with a unit cell doubled along the **c** axis ($\mathbf{q} = \mathbf{c}^*/2$) remains unchanged down to 4.2 K. Thus, all phase transitions in Cs_2HgCl_4 crystals in the temperature range from 221 to 163 K are associated with rearrangements of modulations. At 112 K, Bragg reflections were detected in the positions 0*k*0: $k = 2n$, indicating a phase transition with a change in the symmetry of the structure from $P2_1/c$ (163–112 K) to *Pc*. It should be noted that in incommensurate phases of most of the A_2BX_4 compounds, modulations propagate along the pseudohexagonal axis **a**, while modulations along the **c** axis were detected only in a few

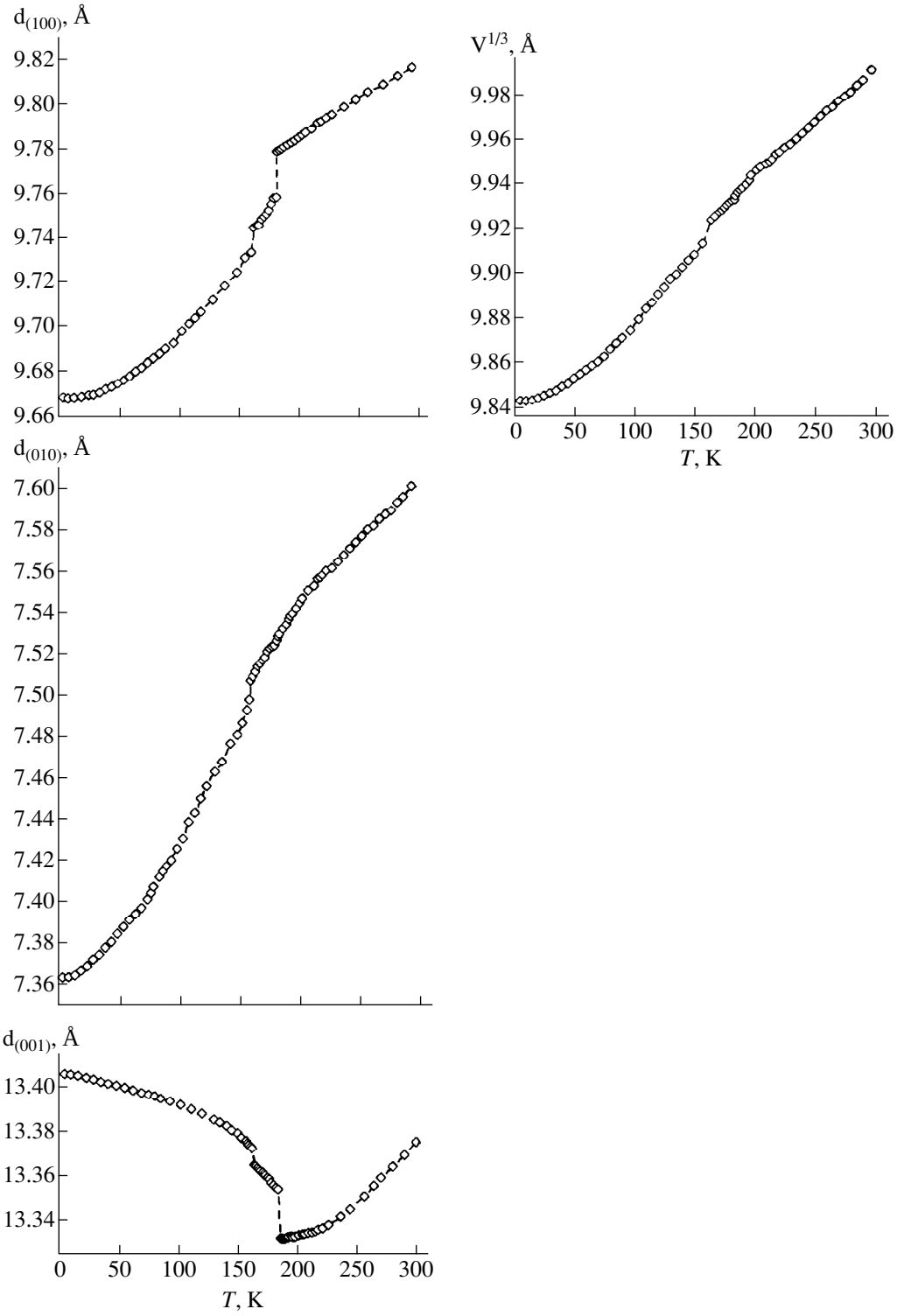

Fig. 6. Temperature dependences of the interplanar spacings $d_{(100)}$, $d_{(010)}$, and $d_{(001)}$ and the lattice volume of the Cs_2HgCl_4 crystal. Measurements are made in the heating mode. For convenience of comparison with the lattice parameters, the volume data are presented in the power form. The phase transition at T_5 = 163 K is accompanied by a change in volume by 0.3%.

A_2BX_4 compounds [9]. Cs_2HgCl_4 is the first crystal of the A_2BX_4 family in which the structure is modulated first along the axis **a*** and then along the **c*** axis of the initial *Pnma* structure.

3.3. Temperature behavior of interplanar spacings. The structure of the Cs_2HgCl_4 crystal at room temperature was characterized by the following lattice parameters: a = 9.8136(9) Å, b = 7.6018(6) Å, and

Thermal expansion coefficients in the temperature ranges of Cs_2HgCl_4 phases ($\times 10^{-5}$ K^{-1})

Temperature range, K	Wave vector	α_{100}	α_{010}	α_{001}
300–221	–	3.98	7.64	3.66
221–195	$(1/5 - \delta)\mathbf{a}^*$	4.11	9.53	1.13
195–184	$1/5\mathbf{a}^*$	3.39	11.03	0.59
184–175	$1/3\mathbf{c}^*$	9.42	6.31	–4.69
175–172	$2/5\mathbf{c}^*$	5.69	8.99	–4.55
172–169	$(3/7 - \delta)\mathbf{c}^*$	2.79	10.18	–4.11
169–163	$3/7\mathbf{c}^*$	3.48	13.41	–3.89
163–112	$1/2\mathbf{c}^*$	7.67	13.35	–3.24
112–4.2	$1/2\mathbf{c}^*$	3.09	7.11	–1.64

c = 13.4201(9) Å [10]. The relationship $c \sim \sqrt{3}b$ indicates a pseudohexagonal structure of the β-K_2SO_4 type. The results of measurements of the interplanar spacings $d_{(100)}$, $d_{(010)}$, and $d_{(001)}$ and the lattice volume as functions of temperature in the range from 4.2 to 300 K are displayed in Fig. 6. The thermal expansion coefficients that correspond to the regions of the existence of the observed phases are presented in the table. The temperature dependences of the parameters exhibit clearly manifested anomalies in the phase transition range at T_1 = 184 K and T_5 = 163 K. The jumps in the parameters and the temperature hysteresis loops (ΔT = 1.5 K) in the vicinity of these temperatures indicate a first-order phase transition. A distinguishing feature of the thermal expansion of Cs_2HgCl_4 is the slowing down of variation in the parameter c upon a transition to the incommensurate phase and the sign reversal of the thermal expansion coefficient below 184 K. It should be noted that, upon a transition to the incommensurate state, many crystals display a similar slowing down of variations in the thermal expansion coefficient and even its vanishing along a direction perpendicular to the wave vector [11].

Thus, the above analysis led to the conclusion that starting from T_i = 221 K, processes associated with a rearrangement in the modulated structure occur in Cs_2HgCl_4 crystals upon cooling. This manifests itself in the behavior of satellite reflections. As a result of cooling, the incommensurate and commensurate modulated states are formed in the structure. Eight phase transitions were found at the temperatures T_i = 221 K ($\mathbf{q} = (1/5 + \delta)\mathbf{a}^*$), T_c = 195 K ($\mathbf{q} = \mathbf{a}^*/5$), T_1 = 184 K ($\mathbf{q} = \mathbf{c}^*/3$), T_2 = 175 K ($\mathbf{q} = 2\mathbf{c}^*/5$), T_3 = 172 K ($\mathbf{q} = (3/7 - \delta)\mathbf{c}^*$), T_4 = 169 K ($\mathbf{q} = 3\mathbf{c}^*/7$), T_5 = 163 K ($\mathbf{q} = \mathbf{c}^*/2$), and T_6 = 112 K ($\mathbf{q} = \mathbf{c}^*/2$). A distinguishing feature of modulations in Cs_2HgCl_4 is their switching over from the pseudohexagonal direction **a** to the perpendicular direction **c**. The variations in the interplanar spacings occur with jumps in the first-order phase transition range at 184 and 163 K.

ACKNOWLEDGMENTS

The authors are grateful to V.I. Pakhomov (Institute of General and Inorganic Chemistry, Russian Academy of Sciences) for supplying the crystals, B.D. Gaulin (McMaster University, Canada), and I.M. Shmyt'ko (Institute of Solid-State Physics, Russian Academy of Sciences) for providing x-ray instruments with helium cryostats.

REFERENCES

1. S. A. Linde, A. Ya. Mikhaĭlova, V. I. Pakhomov, *et al.*, Koord. Khim. **9** (7), 998 (1983).
2. V. V. Petrov, V. G. Pitsyuga, V. A. Gordeev, *et al.*, Fiz. Tverd. Tela (Leningrad) **25** (11), 3465 (1983) [Sov. Phys. Solid State **25**, 1995 (1983)].
3. A. A. Boguslavskiĭ, R. Sh. Lotfullin, M. V. Simonov, *et al.*, Fiz. Tverd. Tela (Leningrad) **27** (2), 523 (1985) [Sov. Phys. Solid State **27**, 321 (1985)].
4. V. V. Petrov, A. Yu. Khalakhnin, V. G. Pitsyuga, and V. E. Yachmenov, Fiz. Tverd. Tela (Leningrad) **30** (5), 1563 (1988) [Sov. Phys. Solid State **30**, 906 (1988)].
5. V. P. Dmitriev, Yu. I. Yuzyuk, A. V. Tregubchenko, *et al.*, Fiz. Tverd. Tela (Leningrad) **30** (4), 1214 (1988) [Sov. Phys. Solid State **30**, 704 (1988)].
6. S. N. Kallaev, V. V. Gladkiĭ, V. A. Kirikov, *et al.*, Fiz. Tverd. Tela (Leningrad) **31** (7), 291 (1989) [Sov. Phys. Solid State **31**, 1267 (1989)].
7. O. G. Vlokh, V. G. Gribik, A. V. Kityk, *et al.*, Kristallografiya **35** (6), 1483 (1990) [Sov. Phys. Crystallogr. **35**, 873 (1990)].
8. P. M. de Wolff, T. Janssen, and A. Janner, Acta Crystallogr., Sect. A: Cryst. Phys., Diffr., Theor. Gen. Crystallogr. **A37**, 625 (1981).
9. G. Madariaga, M. Alberdi, and F. J. Zuniga, Acta Crystallogr., Sect. C: Cryst. Struct. Commun. **C46**, 299 (1990).
10. B. Bagautdinov, J. Luedecke, M. Schneider, and S. van Smaalen, Acta Crystallogr., Sect. B: Struct. Sci. **B54**, 626 (1998).
11. B. Sh. Bagautdinov and V. Sh. Shekhtman, Fiz. Tverd. Tela (St. Petersburg) **41** (1), 137 (1999) [Phys. Solid State **41**, 123 (1999)].

Translated by N. Wadhwa

Physics of the Solid State, Vol. 43, No. 2, 2001, pp. 355–364. Translated from Fizika Tverdogo Tela, Vol. 43, No. 2, 2001, pp. 341–349.

LOW-DIMENSIONAL SYSTEMS AND SURFACE PHYSICS

On the Finite Thermal Conductivity of a One-Dimensional Rotator Lattice

A. V. Savin* and O. V. Gendel'man**

** State Institute of Physicotechnical Problems, Moscow, 119034 Russia*

*** Semenov Institute of Chemical Physics, Russian Academy of Sciences, ul. Kosygina 4, Moscow, 117977 Russia*

e-mail: asavin@center.chph.ras.ru

e-mail: ovgend@center.chph.ras.ru

Received March 28, 2000; in final form, May 11, 2000

Abstract—A heat transfer process is studied in a one-dimensional lattice of coupled rotators in which the orientation interaction between neighboring units is described by the periodic potential. Using this system as an example, it is demonstrated for the first time that one-dimensional lattices with a finite thermal conductivity in the thermodynamic limit can exist without substrate potential. As the temperature increases, the given system transforms from the state with an infinite thermal conductivity to the state with a finite thermal conductivity. The finiteness of the thermal conductivity stems from the existence of localized stationary excitations that interfere with heat transfer in the lattice. The lifetime and the concentration of these excitations increase with an increase in the temperature, which leads to a monotonic decrease in the thermal conductivity coefficient.

1. INTRODUCTION

Heat conduction in a one-dimensional lattice is a classical problem concerned with the justification of the macroscopic Fourier thermal conductivity law (the proportionality of the heat flux to the temperature gradient) at the microscopic level. Anomalies of the thermal conductivity in nonlinear systems are well known, beginning with the famous work of Fermi, Pasta, and Ulam [1]. In integrable systems (harmonic lattices and Toda chains) and systems close to them, temperature gradients are not formed and the Fourier law is not valid (the systems possess an infinite thermal conductivity). According to [2], the nonintegrability of a system is the necessary condition for finiteness of the thermal conductivity. However, recent works dealing with the Fermi–Pasta–Ulam lattice [3–5] and the diatomic Toda chain [6] demonstrated that the nonintegrability alone does not ensure fulfillment of the Fourier law. The nonintegrability of these systems leads to the formation of a linear temperature gradient, but the heat flux is proportional to $1/N^{\alpha}$ (rather than to $1/N$), where $0 < \alpha < 1$ and N is the dimensionless length of the chain. Therefore, these systems also possess an infinite thermal conductivity in the thermodynamic limit $N \longrightarrow \infty$. The analytical estimates made by Lepri *et al.* [5] in the low amplitude strain approximation indicate that any one-dimensional chain with an acoustic phonon branch should have an infinite thermal conductivity.

On the other hand, there exist a number of specially constructed one-dimensional nonintegrable systems that are characterized by a finite thermal conductivity [7, 8]. A finite thermal conductivity was found within the Frenkel–Kontorova model [9, 10] and also for a chain with other anharmonic potentials of a substrate [11]. In this case, the linear temperature gradient is formed and the heat flux is proportional to $1/N$. An essential feature of all these models is the presence of an external potential that simulates the interaction between the chain and substrate. These systems have no translational invariance, and the total momentum is not preserved in them. Hatano [6] assumed that the external potential plays the key role in providing a finite thermal conductivity. It was hypothesized that an infinite thermal conductivity is inherent in all the isolated one-dimensional lattices in which the lack of external forces leads to preserving the total momentum of the system.

This paper is concerned with the numerical simulation of a heat transfer process in a one-dimensional lattice with a preserved momentum (more precisely, an angular momentum), namely, the chain consisting of identical rotators with a periodic potential of the interaction between the nearest neighbors. In this system, an increase in the temperature leads to a crossover from an infinite to a finite thermal conductivity, which does not contradict the main inference made in [5] but disproves the above hypothesis. It was shown that this behavior of the system is associated with the excitation of localized rotational modes which concentrate the thermal energy and are efficient phonon scatterers.

2. MODEL

An example of the one-dimensional lattice consisting of identical rotators is provided by a linear macromolecule which can undergo torsional strains (internal

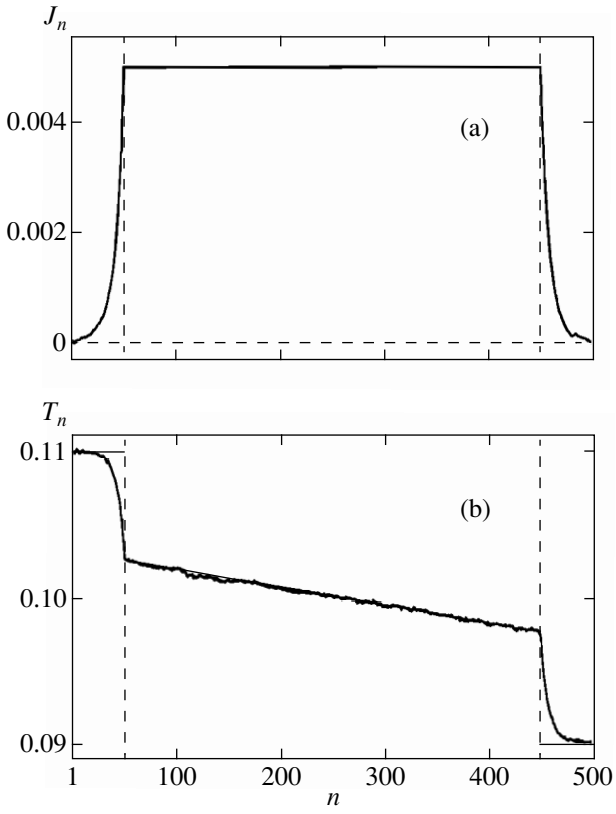

Fig. 1. Distributions of (a) the local heat flux J_n and (b) the local temperature T_n over a chain with periodic interaction potential ($N = 500$, $N_0 = 50$, $T_+ = 0.11$, $T_- = 0.09$, and the averaging time $t = 5 \times 10^6$).

rotations around rigid valence bonds) in addition to longitudinal strains. In this case, the interstitial interaction potential is a periodic function (upon rotation through 360°, a unit transforms into the initial state).

As a model, we chose a chain of molecules separated by a fixed distance l. We assume that the molecules can execute only rotations around the chain axis. Let $\phi_n(t)$ be a variable that specifies the rotation of the nth monomer in the chain in a fixed coordinate system. Then, a dimensionless Hamiltonian of the system has the form

$$H = \sum_n \left\{ \frac{1}{2}\dot{\phi}_n^2 + U(\phi_{n+1} - \phi_n) \right\}, \quad (1)$$

where the dot designates the differentiation with respect to time t and the interstitial interaction potential (rotation potential) $U(\phi)$ is the nonnegative periodic function with a period of 2π, which satisfies the following conditions: $U(0) = 0$, $U'(0) = 0$, and $U''(0) = 1$.

For definiteness, we will use the interaction potential in the simplest form

$$U(\phi) = 1 - \cos\phi. \quad (2)$$

3. CHAIN THERMALIZATION

The Nosé–Hoover thermostat is usually used in numerical simulations of thermal conductivity [3, 4, 6]. However, Fillipov *et al.* [12] showed that this thermostat does not provide an adequate chain thermalization. Hence, we employed the classical Langevin thermostat.

Let us consider a finite chain consisting of N units. The chain ends are immersed in the Langevin thermostat at temperatures T_+ and T_-. The appropriate set of equations of chain motion has the form

$$\begin{aligned} \ddot{\phi}_n &= F(\phi_{n+1} - \phi_n) - F(\phi_n - \phi_{n-1}) - \gamma\dot{\phi}_n + \xi_n, \\ n &= 1, \ldots, N_0; \\ \ddot{\phi}_n &= F(\phi_{n+1} - \phi_n) - F(\phi_n - \phi_{n-1}), \\ n &= N_0 + 1, \ldots, N - N_0; \\ \ddot{\phi}_n &= F(\phi_{n+1} - \phi_n) - F(\phi_n - \phi_{n-1}) - \gamma\dot{\phi}_n + \eta_n, \\ n &= N - N_0 + 1, \ldots, N, \end{aligned} \quad (3)$$

where $F(\phi) = dU(\phi)/d\phi$, N_0 is the length of the terminal chain fragments immersed in the thermostat, γ is the relaxation coefficient, and ξ_n and η_n denote the Gaussian white noise that simulates the interaction with the thermostat $\langle\xi_n(t)\rangle = 0$, $\langle\eta_k(t)\rangle = 0$, $\langle\xi_n(t_1)\eta_n(t_2)\rangle = 0$, $\langle\xi_n(t_1)\xi_k(t_2)\rangle = 2\gamma T_+\delta_{nk}\delta(t_2 - t_1)$, and $\langle\eta_n(t_1)\eta_k(t_2)\rangle = 2\gamma T_-\delta_{nk}\delta(t_2 - t_1)$.

The set of equations of motion (3) was integrated numerically. After the attainment of a thermal equilibrium, the chain is characterized by the temperature gradient

$$T_n = \langle\dot{\phi}_n^2(t)\rangle_t = \lim_{t\to\infty}\frac{1}{t}\int_0^t \dot{\phi}_n^2(\tau)d\tau \quad (4)$$

and the local heat flux

$$J_n = \langle j_n(t)\rangle_t = \lim_{t\to\infty}\frac{1}{t}\int_0^t j_n(\tau)d\tau, \quad (5)$$

where $j_n = -[F(\phi_{n+1} - \phi_n) + F(\phi_n - \phi_{n-1})]\dot{\phi}_n/2$. The calculations were carried out with the parameters $\gamma = 0.1$; $N_0 = 50$; $N = 150$, 200, 300, 500, 700, 900, 1300, 1700, 2100, and 2400; and the initial conditions for the ground state of the chain $\{\phi_n = 0, \dot{\phi}_n = 0\}_{n=1}^N$. The lattice came into thermal equilibrium with the thermostat for time $t = 10^5$. The mean values of the temperature gradient (4) and the local heat flux (5) were determined from the subsequent dynamics of the system for time $t = 10^6$–10^7.

This method of thermalizing the chain allows us to solve the problem of the boundary conditions. The distributions of the heat flux J_n and the temperature profile T_n over the chain (Fig. 1) demonstrate that a free heat flux is observed in an internal chain fragment $N_0 < n \le N - N_0$. The temperature gradient is linear, and the local

heat flux does not depend on the number of the chain unit: $J_n = J$. Consequently, the thermal conductivity coefficient can be determined using only an internal chain fragment; that is,

$$\kappa(N_1) = JN_1/(T_{N_0+1} - T_{N-N_0}), \quad (6)$$

where $N_1 = N - 2N_0$ is the length of this fragment. The limiting value

$$\kappa = \lim_{N_1 \to \infty} \kappa(N_1) \quad (7)$$

corresponds to the thermal conductivity coefficient of the chain at the temperature $T = (T_+ + T_-)/2$.

The thermal conductivity coefficient can also be found from the Green–Kubo formula [13]:

$$\kappa_c = \lim_{t \to \infty} \lim_{N \to \infty} \frac{1}{NT^2} \int_0^t c(\tau) d\tau, \quad (8)$$

where $c(t) = \langle J_s(\tau) J_s(\tau - t) \rangle_\tau$ is the correlation function and $J_s(t) = \sum_n j_n(t)$ is the total heat flux in the chain.

The correlation function $c(t)$ was determined with the use of a finite cyclic chain with $N = 4000$, which was completely immersed in the Langevin thermostat. The dynamics of the isolated chain was considered after the attainment of thermal equilibrium between the chain and the thermostat. In order to improve the accuracy in the determination of the correlation function, we used its value averaged over 500 different realizations of the initial chain thermalization.

4. THERMAL CONDUCTIVITY OF A CHAIN WITH THE PERIODIC POTENTIAL OF INTERSTITIAL INTERACTION

The numerical simulation of the chain dynamics revealed a critical temperature in the range $0.2 < T_0 < 0.3$. At $T < T_0$, the chain shows an infinite thermal conductivity, and at $T > T_0$, its thermal conductivity has a finite value. The dependence of κ on N_1 at temperatures $T = 0.2$ and 0.3 is displayed in Fig. 2. It is seen from Fig. 2 that, at $T = 0.2$, the thermal conductivity coefficient κ increases as $N_1^{0.26}$ with an increase in the chain length N_1. Therefore, limit (7) is equal to infinity. At $T = 0.3$, as the chain length N_1 increases, the thermal conductivity $\kappa(N_1)$ tends to the finite value $\kappa = 31.8$; i.e., the thermal conductivity of the chain is finite at this temperature. The dependence $\kappa(N_1)$ at temperature $T = 1$ is given in the table.

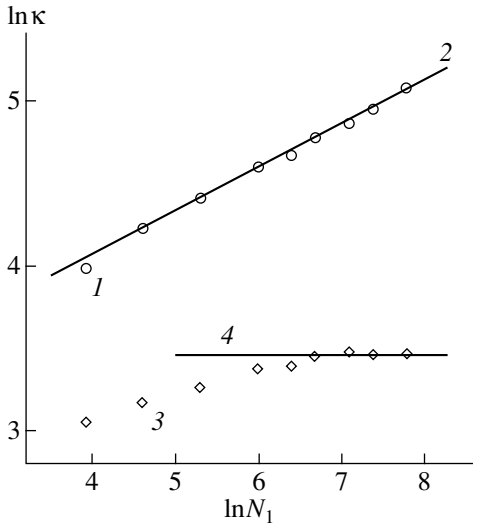

Fig. 2. Dependences of the natural logarithm of the thermal conductivity coefficient κ on the natural logarithm of the internal chain fragment length N_1. Circles *1* correspond to the numerically calculated values at temperature $T = 0.2$ ($T_+ = 0.21$ and $T_- = 0.19$). Straight line *2* approximating this dependence has the slope $\delta = 0.26$. Squares *3* indicate the numerically calculated values at temperature $T = 0.3$ ($T_+ = 0.33$ and $T_- = 0.27$). Straight line *4* approximating this dependence has zero slope ($\kappa = 31.8$).

Investigation into the behavior of the correlation function $c(t)$ at $t \longrightarrow \infty$ confirmed the statement that the thermal conductivity of the chain is a finite quantity. At temperature $T > T_0$, the correlation function exponentially tends to zero; hence, it follows that the integral in formula (8) converges, and, therefore, the thermal conductivity coefficient κ_c has a finite value. The character of the decrease in the correlation function with an increase in the time is clearly seen from Fig. 3. At $T_0 < T < 2$, the function monotonically tends to zero (Fig. 3a). At $T > 2$ (Fig. 3b), $c(t)$ is an oscillating decreasing function [oscillations encourage a more rapid convergence of the integral in formula (8)]. As follows from the table, two methods used to determine the thermal conductivity coefficient lead to very close results.

Let us now consider the dependence of the thermal conductivity coefficient κ on the chain temperature T. According to the calculations of the thermal conductiv-

Dependences of the thermal conductivity coefficient κ on the length N_1 of an internal chain fragment and the thermal conductivity coefficient κ_c calculated by the Green–Kubo formula at temperature $T = (T_+ + T_-)/2$

T_+	T_-	$\kappa(50)$	$\kappa(100)$	$\kappa(200)$	$\kappa(400)$	$\kappa(600)$	$\kappa(800)$	κ_c
0.33	0.27	21.14	23.67	25.96	29.04	29.59	29.54	28.47
1.1	0.9	0.506	0.574	0.634	0.572	0.613	0.612	0.55

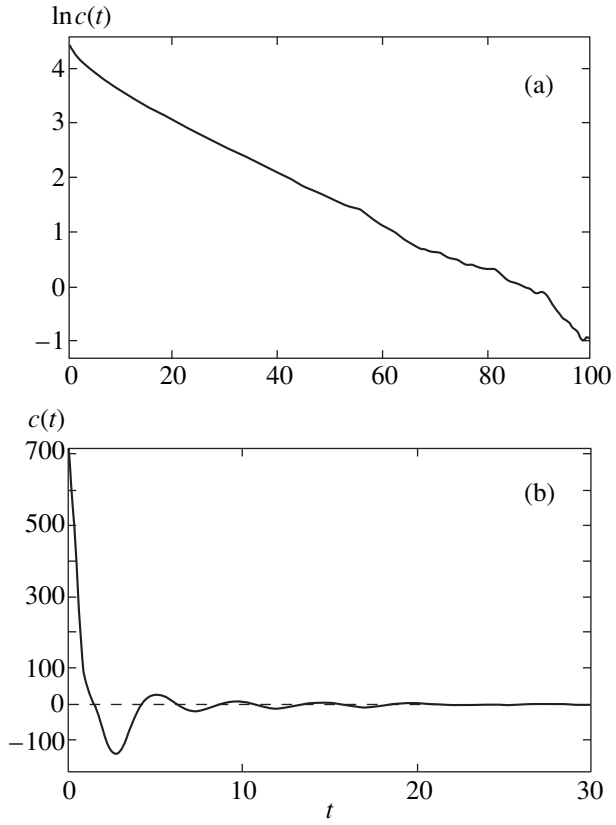

Fig. 3. (a) Exponential decay of the correlation function $c(t)$ at temperature $T < 2$ ($T = 0.5$ and thermal conductivity coefficient $\kappa_c = 5.044$) and (b) oscillations of the function at $T > 2$ ($T = 2.5$ and thermal conductivity coefficient $\kappa_c = 0.014$).

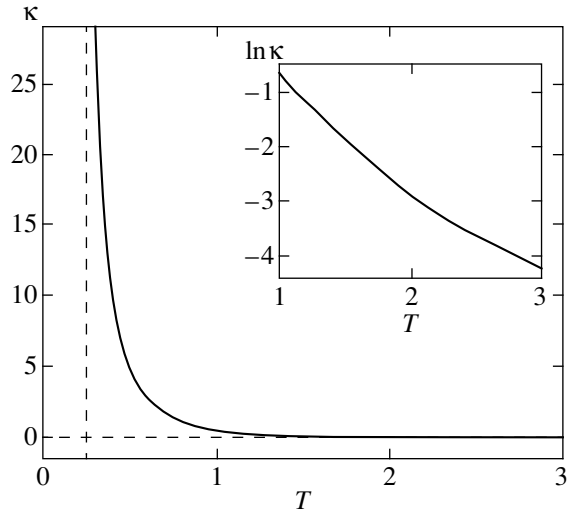

Fig. 4. Dependence of the thermal conductivity coefficient κ on the chain temperature T.

ity from the Green–Kubo formula (8), the κ coefficient decreases monotonically with an increase in the temperature. This dependence is depicted in Fig. 4. The thermal conductivity tends to infinity at $T \longrightarrow T_0$ and exponentially decreases at $T \longrightarrow \infty$.

5. DEPENDENCE OF THE HEAT FLUX ON TEMPERATURE GRADIENT

Now, we dwell on the dependence of the heat flux J on the temperature difference ΔT. For this purpose, we consider a finite chain containing $N = 300$ units with zero temperature at the right end ($T_- = 0$). Then, the temperature difference is defined as $\Delta T = T_+$. In this case, the heat flux can be defined as the friction work at the right end of the chain:

$$J_0 = \gamma \sum_{n = N - N_1 + 1}^{N} T_n. \qquad (9)$$

The numerical integration of the set of equations of motion (3) demonstrates that this value coincides with the local heat flux in an internal chain fragment: $J_n = J_0$ at $n = N_1 + 1, \ldots, N - N_1$. This coincidence confirms that the local heat flux (5) is correctly determined.

Figure 5 shows the dependence of the heat flux J_0 on the temperature difference ΔT. As can be seen from Fig. 5, the heat flux first increases monotonically with an increase in the temperature difference. At the temperature $T = T_r = 1.3$, the flux reaches a maximum (saturation). A further increase in the temperature difference brings about a gradual decrease in the flux. Such an unusual behavior of the system is associated with the specific properties of phonons and the presence of localized rotational modes in the chain at high temperatures, which prevents phonon motion. Let us analyze in detail the properties of these excitations.

6. PERIODIC WAVES OF CONSTANT PROFILE

We consider the dispersion law of nonlinear periodic waves

$$\phi_n(t) = \phi(n - st) \equiv \phi(z), \qquad (10)$$

where z is the wave variable ($z = n - st$) and $\phi(z)$ is the periodic function with the period L ($\phi(z + L) \equiv \phi(z)$). Within the low amplitude approximation ($|\phi(z)| \ll \pi$), the dispersion equation takes the form

$$\omega^2(q) = 2(1 - \cos q), \qquad (11)$$

where $q = 2\pi/L$ is the wave number and L is the wavelength ($L \geq 2$). The phase wave velocity is defined as $s = \omega(q)/q$ [the velocity of low-amplitude long-wavelength phonons $s_0 = \lim_{q \to 0} \omega(q)/q = 1$]. The nonlinearity of the interstitial interaction potential leads to the fact that the velocity (frequency) of the periodic wave (10) depends not only on the wavelength L, but also on its amplitude A.

The form and the velocity of the wave can be determined by the pseudospectral method [14]. The numerical calculations revealed that, for each wavelength $L \geq 2$, there exists a maximum amplitude $A(L)$. The amplitude of the periodic wave cannot exceed this value [$A \leq A(L)$], and the amplitude of relative rotations of chain mole-

cules $A_\varphi = \max|\phi(z+1) - \phi(z)|$ is not larger than its natural maximum equal to 2. The periodic waves have the property of energy saturation; the maximum energy $E(L)$ therein corresponds to the temperature $T(L) \simeq 1.8$.

Analysis of the periodic waves allows us to conclude that the chain of coupled rotators is characterized by the critical temperature $T_0 \approx 1.8$, above which the vibrational modes of the chain cannot be thermalized. At $T = T_0$, the vibrational modes are saturated, become unstable, and begin to lose excess energy. A further increase in the temperature does not lead to an increase in the total energy of the vibrational modes in the chain. The nonlinearity of vibrational modes stems from the negative anharmonicity of the interstitial interaction potential and, hence, results in a monotonic increase in their heat capacity with an increase in the temperature.

7. LOCALIZED ROTATIONAL MODES

Since the interstitial interaction energy is limited, localized rotational modes can exist in the chain. In a more general case, these modes were thoroughly studied by Takeno and Peyrard [15]. The rotational mode corresponds to the rotation of one molecule when its neighbors remain virtually immobile. To a first approximation, the mode dynamics is approximated by the rotation of one molecule at the fixed neighbors. Within this approximation, the motion of a molecule is described by the pendulum equation. At the energy $E \geq \max U(\phi) = 2$, the motion of a molecule corresponds to a uniform rotation. As the energy E increases, the rotation frequency ω monotonically increases from 0 to $+\infty$. The motion of neighboring molecules affects the rotation. The numerical simulation of the rotation demonstrated that the localized excitation is stable only at frequencies $\omega \geq \omega_0 = 2.173$. The frequency dependence of the rotational energy is well approximated by the parabola $\omega^2/2$, which corresponds to the energy of free rotation of one molecule in the chain. As the energy increases, the heat capacity of the mode monotonically decreases and tends to 1/2 (the heat capacity of an isolated rotator) at $E \longrightarrow \infty$.

Thus, the system under investigation exhibits phonons (nonlinear vibrational modes) with the frequency spectrum $0 \leq \omega \leq 2$ and localized rotational modes with the frequency spectrum $\omega \geq \omega_0 > 2$. The appearance of the rotational modes in the chain should lead to a decrease in the heat capacity of the system.

8. DISTRIBUTION OF THERMAL VIBRATION ENERGY OVER NONLINEAR MODES

Now, let us analyze the frequency distribution of thermal vibration energy in a chain. To accomplish this, we numerically determine the density of distribution of the frequency spectrum of the $\dot{\phi}_n(t)\exp[i\phi_n(t)]$ function.

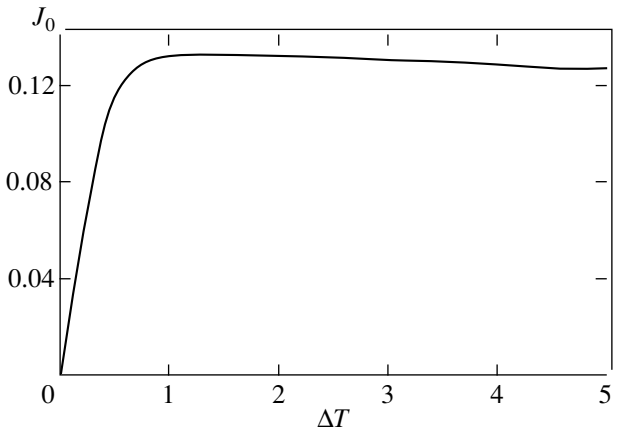

Fig. 5. Dependence of the heat flux J_0 on the temperature difference ΔT ($N = 300$, $N_0 = 50$, $T_+ = \Delta T$, and $T_- = 0$).

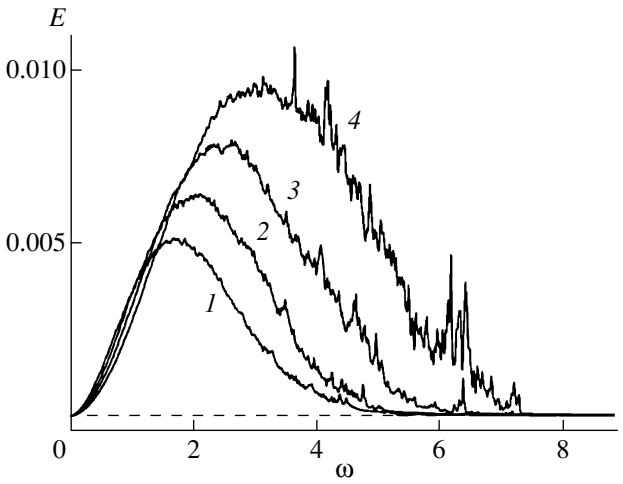

Fig. 6. Distributions of the thermal vibration energy E over frequencies ω for a particle in the chain at temperature T = (*1*) 1.4, (*2*) 2, (*3*) 3, and (*4*) 5.

For a chain with the harmonic interaction potential $U(\phi) = \phi^2/2$, the density of energy distribution is given by

$$E(\omega) = 2T/\pi\sqrt{\omega_a^2 - \omega^2}, \quad 0 \leq \omega \leq \omega_n, \qquad (12)$$

where $\omega_a = 2$ is the maximum frequency of phonons.

At a low temperature ($T = 0.1$), the energy distribution virtually coincides with distribution (12). In this case, the total energy is distributed among the vibrational modes with frequencies $\omega < \omega_0$. An increase in the temperature leads to a shift in the spectrum toward the frequency range of localized rotations $\omega > \omega_0$ (Fig. 6).

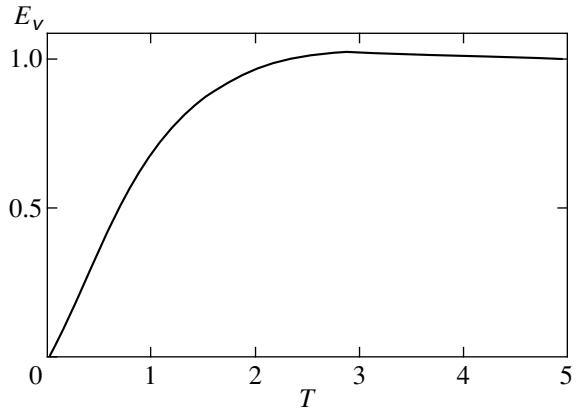

Fig. 7. Dependence of the phonon thermalization energy E_v (per unit of the chain) on the chain temperature T.

The thermalization energy of vibrational modes is defined as

$$E_v = \int_0^{\omega_0} E(\omega)d\omega.$$

The dependence of the energy E_v on temperature T is depicted in Fig. 7. At $T \ll 2$, the E_v energy increases in direct proportion to the temperature. A considerably slower increase in the energy is observed at $T \approx 1$, and the energy reaches a maximum at $T = 2.5$. A further increase in the temperature results only in an insignificant decrease in the energy. As was predicted above, the energy saturation of low-frequency vibrational modes takes place. As the temperature increases still further, an increase in the energy is observed only for stationary localized rotational modes.

Since the energy transfer in the chain can occur only through phonons (vibrational modes), their energy saturation explains the unusual dependence of the heat flux J_0 on the temperature gradient ΔT (Fig. 5). However, the saturation effect cannot be responsible for the finite thermal conductivity of the chain. Its explanation requires consideration of the interaction between phonons and localized rotational modes.

9. EFFECT OF LOCALIZED EXCITATIONS ON THE ENERGY TRANSFER

The rotational modes (localized rotations) are the stationary excitations of the chain. These modes cannot contribute to the thermal energy transfer and should lead to a decrease in the thermal conductivity of the chain. Now, we examine their interaction with thermal phonons. For this purpose, we consider the chain containing $N = 300$ molecules with temperatures $T_+ = 0.02 > 0$ at the left end and $T_- = 0$ at the right end. At the initial instant, the chain is in the ground state ($\phi_n \equiv 0$ and $\dot{\phi}_n \equiv 0$). The rotational mode with the energy $E = 16$ is placed at site $n = N/2$ in the center of the chain. Let us analyze the heat transfer in the chain. The distribution of the energy E_n over the chain is shown in Fig. 8a, and the dependence of the mode (localized rotation) energy E on time t is displayed in Fig. 8b. It can be seen from Fig. 8 that the localized mode at the chain center impedes the motion of all thermal phonons. As a result, only the left half of the chain undergoes thermalization and the right half remains nonthermalized (Fig. 8a). The pressure exerted by phonons on the localized mode in the chain center results in its progressive destruction. The energy of the mode decreases monotonically (Fig. 8b). At the instant $t = 28000$, the localized excitation is destroyed and the heat flux arises in the chain. The simulation performed allows us to conclude that the localized excitations interfere with the heat transfer in the chain and have a finite lifetime in the thermalized chain.

In order to elucidate how the localized modes affect the energy transfer, we investigate the thermal energy relaxation in the chain. It is assumed that a finite chain with $N = 300$ is immersed in the Langevin thermostat. After the thermalization of the chain, the thermostat is removed. Friction is introduced at the chain ends to ensure energy absorption. To accomplish this, it is sufficient to put $T_+ = T_- = 0$ in the set of equations of motion (3). The numerical simulation of the dynamics revealed the presence of localized rotational modes in the chain. At temperature $T = 1$, their lifetime is short. These modes are rapidly destroyed as a result of interaction with phonons and do not preclude energy withdrawal from the chain (Fig. 9a). At temperature $T = 2$, the localized rotations have long lifetimes and exert an appreciable effect on the mechanism of the energy withdrawal. The withdrawal takes place only after the destruction of the terminal localized modes. As a result of this process, only one localized state remains in the chain (Fig. 9b). A stepwise character of the energy withdrawal is especially pronounced at temperature $T = 3$ (Fig. 9c).

Therefore, the heat transfer in the chain can be qualitatively described as a sequence of random local energy crossovers which occur upon each destruction of a stationary localized mode. An increase in the temperature brings about an increase in the energy of these modes, their lifetime, and, hence, the time intervals between random energy crossovers. This mechanism, together with the phonon saturation effect, explains a decrease in the heat flux J_0 with an increase in the temperature at $T > T_0$ (Fig. 5).

10. A CHAIN WITH THE HYPERBOLIC POTENTIAL OF INTERSTITIAL INTERACTION

The above results should evidently be legitimate for a chain with any periodic potential of interstitial interaction. The finiteness of the thermal conductivity is due to the presence of stationary, strongly localized rotational modes in the chain. These modes arise only

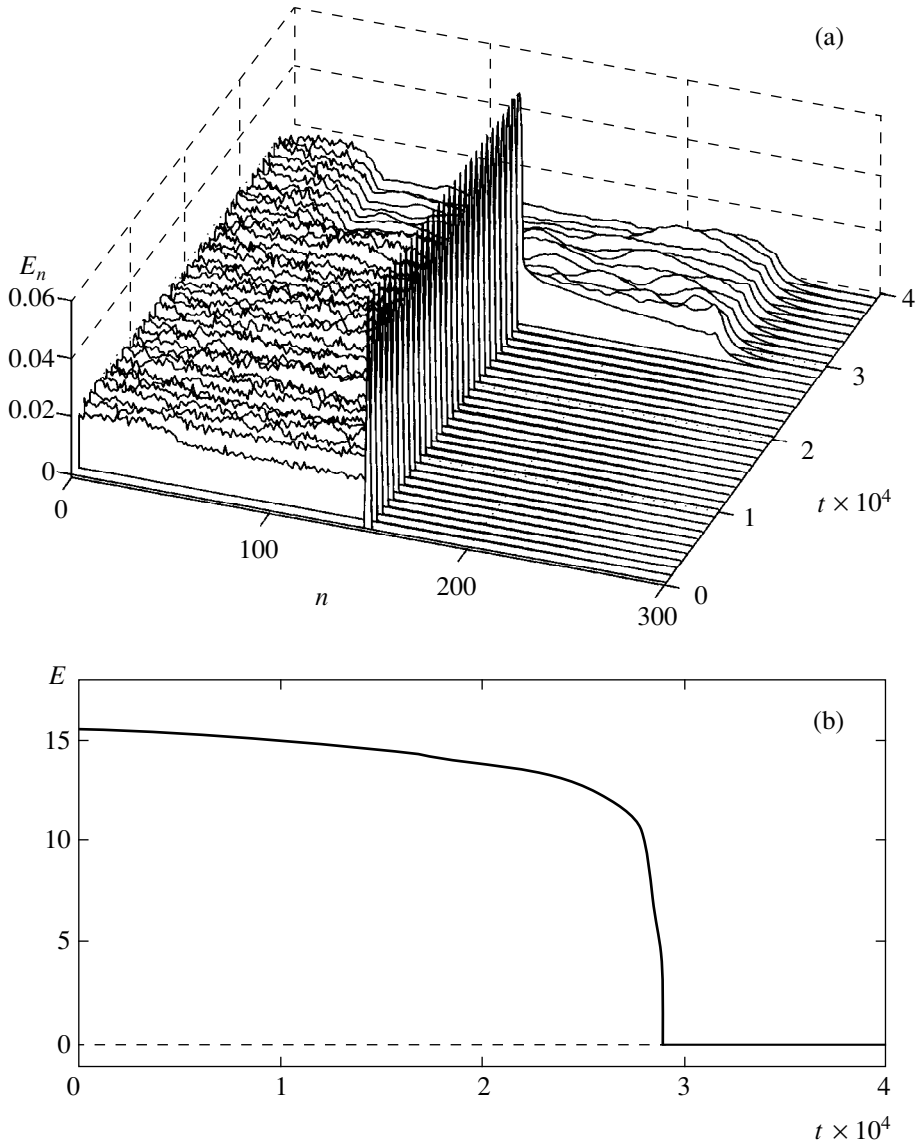

Fig. 8. Interaction of the rotational mode with thermal phonons: (a) distribution of the energy E_n over the chain and (b) dependence of the mode energy E on time t.

owing to the boundedness of the interaction potential. For comparison, we consider a chain with the unbounded hyperbolic interaction potential

$$U(\phi) = \sqrt{1 + \phi^2} - 1. \quad (13)$$

Similar to the periodic potential (2), potential (13) has a negative quartet anharmonicity but is the unbounded function. At $\phi \longrightarrow \pm\infty$, the potential increases as the linear function $\pm\phi - 1$.

The numerical simulation showed that a chain with potential (13) has an infinite thermal conductivity over the entire temperature range covered. As the length N_1 of an internal chain fragment increases, the thermal conductivity coefficient κ of the chain increases as N_1^δ, where the exponent δ is less than unity. For example, at $T = 2$, the exponent δ is equal to 0.29. At all temperatures, the correlation function $c(t)$ tends to zero as t^α ($-1 < \alpha < 0$). In particular, at $T = 2$, the exponent α is equal to –0.82. Hence, it follows that the integral in the Green–Kubo formula (8) diverges and the thermal conductivity coefficient κ_c is equal to infinity. Consequently, taken alone, the negativeness of the quartet anharmonicity (in complete agreement with the conclusions made in [3–6]) does not ensure finite thermal conductivity. This allows us to conclude that the boundedness of the interaction potential plays the key role in providing finite thermal conductivity of an isolated chain.

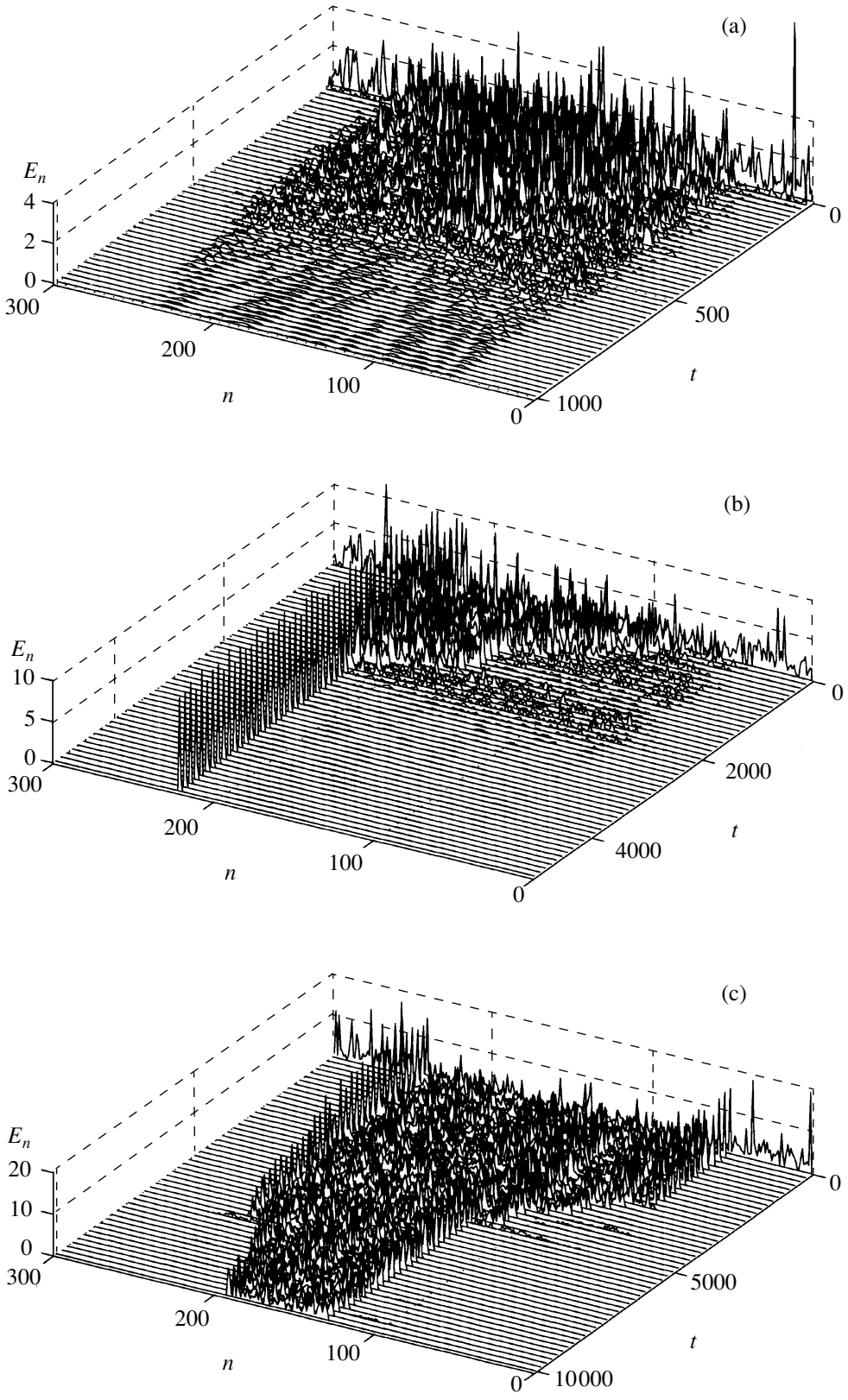

Fig. 9. Energy relaxation of the thermalized chain at temperature T = (a) 1, (b) 2, and (c) 3. Dependences of the local energy E_n on the number n of the chain unit and on the time t. At the initial instant, the system has the temperature T; then, the dynamics of the chain with the absorbing ends is considered (N = 300, N_0 = 50, and $T_+ = T_- = 0$).

11. TEMPERATURE DEPENDENCE OF THE HEAT CAPACITY FOR A CHAIN

For a system with the unbounded interaction potential (13), the heat capacity of a chain $C = d\langle E\rangle/dT$ increases monotonically with an increase in temperature T (Fig. 10). In a chain with the periodic interaction potential (2), the heat capacity associated with the excitation of periodic waves also increases monotonically, but the heat capacity governed by the rotational modes decreases with an increase in the temperature. Therefore, the heat capacity increases at $T \le 0.4$ and monotonically decreases at $T > 0.4$ (Fig. 10). Consequently, it can be concluded that the vibrational modes predominantly contribute to the heat capacity of the system in the former temperature range, and the rotational modes, in the latter range. Thus, the main contribution to the nonlinear dynamics is made by the negative anharmonicity at $T \le 0.4$ and the boundedness of the interaction potential at $T > 0.4$. The temperature that corresponds to the heat capacity at a maximum is close to the temperature of the crossover from an infinite to finite thermal conductivity.

In a chain with the bounded interaction potential, the heat capacity C tends to 1/2 at $T \longrightarrow \infty$. The heat capacity $C = 1/2$ corresponds to a system of uncoupled particles. Qualitatively, we can assert that an increase in the temperature is accompanied by a phase transition from a system of coupled particles to a system of free particles.

Thus, the investigation of the chain consisting of identical rotators with a periodic potential of interaction between the nearest neighbors demonstrated that an increase in the temperature is attended by a crossover from an infinite to a finite thermal conductivity. This is in agreement with the main result obtained by Lepri *et al.* [5], who showed that any isolated one-dimensional chain should possess an infinite thermal conductivity due to the absence of long-wavelength phonon scattering. The arguments of these authors are valid only for low-amplitude strains, i.e., for low temperatures.

An increase in the temperature of the chain under investigation gives rise to localized rotational excitations which prevent free motion of phonons. Note that the localized excitations—discrete breathers—also exist in the Fermi–Pasta–Ulam chain [3–5]. The fundamental difference resides in the fact that they do not preclude motion of long-wavelength phonons. The breathers can only filter off phonons with a particular wavelength [16], whereas the rotational excitations prevent the motion of all phonons, irrespective of their wavelength and frequency.

In the chain under consideration, phonons possess a finite energy capacity. As the temperature increases, their energy increases until a maximum is reached. A further increase in the temperature does not lead to an increase in the energy. The periodic waves become unstable, and their excess energy upon decay goes into the formation of stationary rotational excitations which interfere with the heat transfer. In this case, the mechanism of the heat transfer can be described as a sequence of random local energy crossovers that occur upon each destruction of stationary excitation. This mechanism accounts for a decrease in the thermal conductivity of the chain with an increase in the temperature. Actually, as the temperature increases, an increase in the energy is observed only for localized excitations. Their lifetime increases, and, hence, the frequency of local energy crossovers decreases. The heat capacity of the chain decreases monotonically with an increase in the temperature and tends to 1/2, which corresponds to the heat capacity of a system consisting of uncoupled particles. In the high-temperature limit, the system under consideration transforms into a chain of uncoupled rotators with zero thermal conductivity.

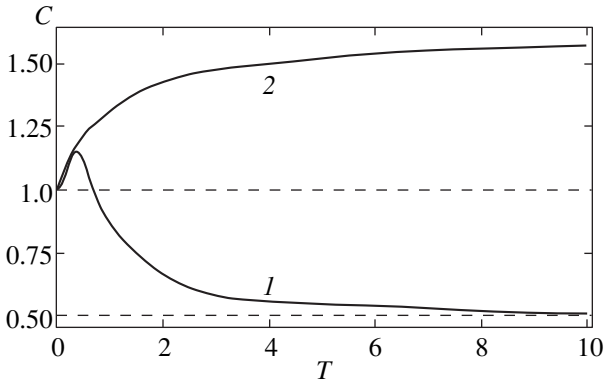

Fig. 10. Dependences of the heat capacity C on the temperature T for chains with (*1*) periodic and (*2*) hyperbolic interaction potentials.

ACKNOWLEDGMENTS

This work was supported by the Russian Foundation for Basic Research, project no. 98-03-333-66a.

A.V. Savin acknowledges the support of the International Association of Assistance for the promotion of co-operation with scientists from the New Independent States of the former Soviet Union, project INTAS no. 96-158.

REFERENCES

1. E. Fermi, J. Pasta, and S. Ulam, Los Alamos Sci. Lab. Rep. **LA-1940** (1955).
2. O. V. Gendel'man and L. I. Manevich, Zh. Éksp. Teor. Fiz. **102**, 511 (1992) [Sov. Phys. JETP **75**, 271 (1992)].
3. S. Lepri, L. Roberto, and A. Politi, Phys. Rev. Lett. **78**, 1896 (1997).
4. S. Lepri, R. Livi, and A. Politi, Physica D (Amsterdam) **119**, 140 (1998).
5. S. Lepri, R. Livi, and A. Politi, Europhys. Lett. **43**, 271 (1998).

6. T. Hatano, Phys. Rev. E **59**, R1 (1999).
7. G. Casati, J. Ford, F. Vivaldi, and V. M. Visscher, Phys. Rev. Lett. **52**, 1861 (1984).
8. T. Prosen and M. Robnik, J. Phys. A **25**, 3449 (1992).
9. M. J. Gillan and R. W. Holloway, J. Phys. C **18**, 5705 (1985).
10. B. Hu, B. Li, and H. Zhao, Phys. Rev. E **57**, 2992 (1998).
11. G. P. Tsironis, A. R. Bishop, A. V. Savin, and A. V. Zolotaryuk, Phys. Rev. E **60**, 6610 (1999).
12. A. Fillipov, B. Hu, B. Li, and A. Zeltser, J. Phys. A **31**, 7719 (1998).
13. R. Kubo, M. Toda, and N. Hashitsume, in *Statistical Physics*, Vol. 2: *Nonequilibrium Statistical Mechanics* (Springer-Verlag, Berlin, 1991), Springer Ser. Solid-State Sci. **31** (1991).
14. J. C. Eilbeck and R. Flesch, Phys. Lett. A **194**, 200 (1990).
15. S. Takeno and M. Peyrard, Physica D (Amsterdam) **92**, 140 (1996).
16. S. Flach and C. H. Willis, Phys. Rep. **295**, 181 (1998).

Translated by O. Borovik-Romanova

Physics of the Solid State, Vol. 43, No. 2, 2001, pp. 365–372. Translated from Fizika Tverdogo Tela, Vol. 43, No. 2, 2001, pp. 350–356.

LOW-DIMENSIONAL SYSTEMS AND SURFACE PHYSICS

Quasi-stationary States of Electrons and Holes in an Open Composite Cylindrical Quantum Wire

N. V. Tkach and V. A. Golovatskiĭ

Chernovtsy State University, ul. Kotsyubinskogo 2, Chernovtsy, 58012 Ukraine

Received March 27, 2000; in final form, June 13, 2000

Abstract—The energies of the quasi-stationary states of electrons and holes in an open composite cylindrical quantum wire are calculated within the effective-mass approximation by means of the *S*-matrix theory. Specific calculation is carried out for the HgS/CdS/HgS system. The poles of the *S* matrix in the complex energy plane are studied. The dependences of the lifetimes of quasiparticles in quasi-stationary resonance states on the longitudinal quasi-momentum and geometric parameters of the nanosystem are obtained. It is shown that the quasiparticle lifetimes in the resonance states exponentially diminish as the longitudinal quasi-momentum increases.

INTRODUCTION

The attention of many scientists has been drawn to the physical processes that occur in one-dimensional and zero-dimensional nanosystems after the first successes in the creation of semiconductor quantum-dot and quantum-wire lasers were achieved in the 1990s [1, 2]. A vast amount of both theoretical and experimental works now exists in this field of research. Ordered arrays of quantum dots and wires, as well as multilayer spherical nanoheterostructures, can be created by modern technological methods [3, 4]. This stimulated interest in the theoretical study of quasiparticle spectra and the interaction between quasiparticles (electrons, holes, excitons, and phonons) in these systems. The theory describing the spectra of electrons, holes, and excitons and the interaction between these quasiparticles and phonons was developed for spherical multilayer nanosystems in [3, 5, 6] and for cylindrical multilayer nanosystems in [7]. It is assumed in the theory that the external medium in which a multilayer spherical nanostructure is situated is a maximal potential barrier in comparison with the internal layers and, thus, that the system is closed.

Modern technological methods (for example, the ion-substitution method [3, 4]) make it possible to create so-called open nanoheterostructures, in which the potential energy of a quasiparticle is minimal in the external medium and, therefore, the quasiparticle can move to infinity. The energy spectrum is quasi-stationary in these systems, and, therefore, the corresponding states are characterized by finite lifetimes due to the fact that the quasiparticles can penetrate through the potential barriers of the nanosystem.

Open systems are interesting, because they can be used as an elementary base for computers [8].

The quasi-stationary spectrum of electrons and holes in an open spherical HgS/CdS/HgS nanoheterostructure was theoretically studied in [9]. The spherical symmetry of the system made it possible to extend the *S*-matrix method known from nuclear theory [10] to the case where the mass of a quasiparticle in the different layers of the system is different and, therefore, to investigate the energy spectrum and lifetimes of electrons and holes in the quasi-stationary states.

The aim of this paper is to theoretically investigate the resonance energies and lifetimes of electrons and holes in the quasi-stationary states of an open composite cylindrical quantum wire (CCQW), in particular, in the HgS/CdS/HgS nanosystem. The solution of this problem is more complicated than that in the case of an open composite spherical quantum dot (CSQD) [9], since the cylinder nanosystem has lower symmetry and the electrons and holes have a quasi-momentum (parallel to the axial axis). This results in a complicated analytical expression for the *S*-matrix; the resonance energies and lifetimes can be calculated from this expression only numerically.

1. THE HAMILTONIAN AND WAVEFUNCTIONS OF AN ELECTRON AND A HOLE IN AN OPEN CCQW

We investigate the electron and hole spectra of an open cylinder nanostructure (composite cylindrical quantum wire) which consists of an HgS core (well *0*) and a CdS layer (barrier *1*) placed in an infinite HgS medium (well *2*). The scheme of the open CCQW and the schematic diagram of the potential energies of an electron and a hole in it are shown in Fig. 1. Since we are not going to investigate the behavior of electrons and holes in a magnetic field here, their spins are not taken into account. Assuming the energy bands of the

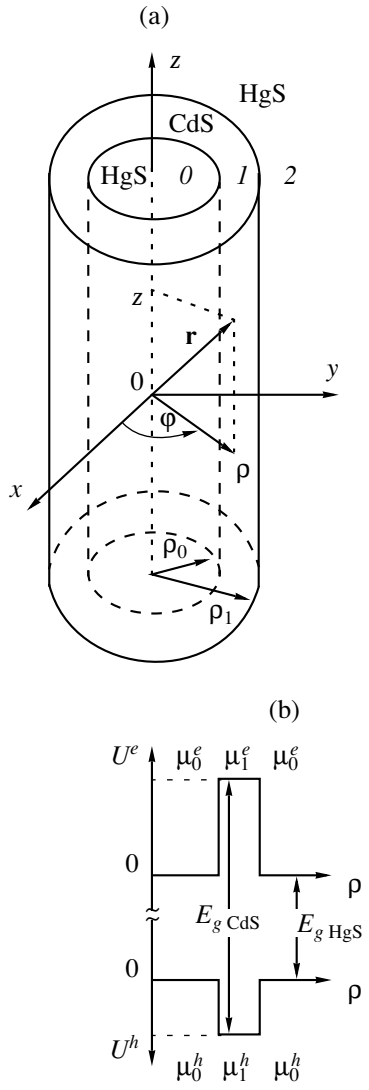

Fig. 1. (a) Geometric scheme and (b) schematic potential-energy diagram for an electron and a hole in the CCQW.

light and heavy holes to be independent in the particular HgS/CdS/HgS composite cylindrical quantum wire under investigation, the theories for electrons and holes are the same in the effective-mass approximation; for this reason, further calculations are performed only for the electron without loss of generality. The difference between the spectral properties of the electrons and holes appears only in the stage of numerical calculations because of the difference in the effective masses of the quasiparticles and in the potential fields acting on them. Relevant analysis is given in the next section.

In the cylindrical coordinate system with the origin at the center of the heterostructure, the electron is characterized by effective mass $\mu(\rho)$ and potential energy $U(\rho)$, which are functions of the distance from the axial axis of the CCQW, because their magnitudes are different in the different media:

$$\mu(\rho) = \begin{cases} \mu_0, & \rho < \rho_0 \\ \mu_1, & \rho_0 \le \rho \le \rho_1 \\ \mu_0, & \rho > \rho_1, \end{cases}$$
$$U(\rho) = \begin{cases} 0, & \rho < \rho_0 \\ U, & \rho_0 \le \rho \le \rho_1 \\ 0, & \rho > \rho_1. \end{cases} \quad (1)$$

Since the effective mass depends on ρ, the Shrödinger equation has the following form [11, 12]:

$$\left(-\frac{\hbar^2}{2}\nabla\frac{1}{\mu(\rho)}\nabla + U(\rho)\right)\Psi(\mathbf{r}) = E\Psi(\mathbf{r}). \quad (2)$$

Taking into account the axial symmetry, a solution of this equation is sought in the form

$$\Psi(\rho, \varphi, z) = \frac{1}{\sqrt{L}}R(\rho)e^{im\varphi}e^{ikz}, \quad m = 0, \pm1, \pm2, \ldots, \quad (3)$$

where $R(\rho)$ is a radial wave function.

Substituting Eq. (3) into Eq. (2) yields the following equation for the radial wave function:

$$\left\{-\frac{\hbar^2}{2}\left[\frac{1}{\rho}\frac{\partial}{\partial\rho}\left(\frac{\rho}{\mu(\rho)}\frac{\partial}{\partial\rho}\right) - \frac{m^2}{\rho^2\mu(\rho)} - \frac{k^2}{\mu(\rho)}\right] + U(\rho) - E\right\}R_{mk}(\rho) = 0. \quad (4)$$

It is seen from Eq. (4) that the magnetic quantum number m and quasi-momentum k are parameters of the equation and, therefore, of the function $R_{mk}(\rho)$. It makes sense to seek this function in the form

$$R_{mk}(\rho) = \begin{cases} R^0_{mk}(\rho), & \rho < \rho_0 \\ R^1_{mk}(\rho), & \rho_0 \le \rho \le \rho_1 \\ R^0_{mk}(\rho), & \rho > \rho_1. \end{cases} \quad (5)$$

Substituting Eq. (5) into Eq. (4) results in three equations of the same type,

$$\left[\frac{\partial^2}{\partial\rho^2} + \frac{1}{\rho}\frac{\partial}{\partial\rho} - \frac{m^2}{\rho^2} + \frac{2\mu_i}{\hbar^2}\left(E - U_i - \frac{\hbar^2k^2}{2\mu_i}\right)\right]R^i_{mk}(\rho) = 0, \quad (i = 0, 1, 2), \quad (6)$$

whose solutions are linear combinations of Hankel functions of different arguments:

$$R_{mk}(\rho) = \begin{cases} R^0_{mk}(\rho) = A^{(0)}_m[H^-_m(\chi_0\rho) \\ + H^+_m(\chi_0\rho)], \quad \rho < \rho_0 \\ R^1_{mk}(\rho) = A^{(1)}_m[H^-_m(i\chi_1\rho) \\ + S^1_{mk}(E)H^+_m(i\chi_i\rho)], \quad \rho_0 \le \rho_0 \le \rho_1 \\ R^2_{mk}(\rho) = A^{(2)}_m[H^-_m(\chi_0\rho) \\ + S_{mk}(E)H^+_m(\chi_0\rho)], \quad \rho > \rho_1, \end{cases} \tag{7}$$

where

$$\chi_0 = \sqrt{\frac{2\mu_0}{\hbar^2}E - k^2}, \quad i\chi_1 = \sqrt{\frac{2\mu_1}{\hbar^2}(U-E) - k^2}. \tag{8}$$

All coefficients A and both S matrices are uniquely determined by the conditions of continuity of the wave function and of the probability flux density at both boundaries between the media and by the normalization condition.

Analytical calculations result in the following expression for $S_{mk}(E)$:

$$S_{mk}(E) = \frac{\mu_0 F_m(E)H^-_m(\chi_0\rho_1) - \mu_1\chi_0[H^-_{m-1}(\chi_0\rho_1) - H^-_{m+1}(\chi_0\rho_1)]}{\mu_0 F_m(E)H^+_m(\chi_0\rho_1) - \mu_1\chi_0[H^+_{m-1}(\chi_0\rho_1) - H^+_{m+1}(\chi_0\rho_1)]}, \tag{9}$$

where

$$F_m(E) = \frac{i^{2m-1}\pi\chi_1[I_{m-1}(\chi_1\rho_1) + I_{m+1}(\chi_1\rho_1)] + \chi_1[K_{m-1}(\chi_1\rho_1) + K_{m+1}(\chi_1\rho_1)][S^1_{mk}(E) - 1]}{i^{2m-1}\pi I_m(\chi_1\rho_1) - K_m(\chi_1\rho_1)[S^1_{mk}(E) - 1]}, \tag{10}$$

$$S^1_{mk}(E) = \frac{\mu_1\chi_0 H^-_m(i\chi_1\rho_0)[J_{m-1}(\chi_0\rho_0) - J_{m+1}(\chi_0\rho_0)] - \mu_0\chi_1 J_m(\chi_0\rho_0)[H^-_{m-1}(i\chi_1\rho_0) - H^-_{m+1}(i\chi_1\rho_0)]}{\mu_1\chi_0 H^+_m(i\chi_1\rho_0)[J_{m-1}(\chi_0\rho_0) - J_{m+1}(\chi_0\rho_0)] + \mu_0 i\chi_1 J_m(\chi_0\rho_0)[H^+_{m-1}(i\chi_1\rho_0) - H^+_{m+1}(i\chi_1\rho_0)]}, \tag{11}$$

and $I_m(z)$ and $K_m(z)$ are the modified Bessel functions (Bessel functions of an imaginary argument). The scattering matrix $S_{mk}(E)$ is a complicated complex function. According to the general theory [10], quasi-stationary states are determined by the S-matrix poles in the complex energy plane:

$$\tilde{E} = E_1 - iE_2. \tag{12}$$

The real part E_1 is equal to the energy of the quasi-stationary state, while the imaginary part $E_2 = \Gamma/2$ determines the broadening associated with quasiparticle tunneling through the barrier.

For the S matrix of an open spherical nanoheterostructure [9], analytical solutions of the dispersion equation for $l = 0, 1$ have been found. In contrast to this case, the similar problem for the cylindrical nanosystem under investigation can be solved only numerically. It should also be noticed that a new fundamental feature appears in this problem: contrary to the zero-dimensional problem, the S matrix depends on two variables, E and k, in the one-dimensional problem. Due to this fact, both the energy (E) and lifetime (τ) of the quasiparticle in quasi-stationary states are functions of the quasi-momentum.

An example of the numerical calculation of the real and imaginary parts of the S matrix and the position of its pole in the complex plane of energy $\tilde{E}$ is shown in Fig. 2. The calculation was carried out for the electron at $k = 0$ in the HgS/CdS/HgS composite cylindrical quantum wire with the material parameters listed in Table 1 and the geometric parameters $\rho_0 = 15a_{\mathrm{HgS}}$ and $\rho_1 - \rho_0 = 5a_{\mathrm{CdS}}$. The results correspond to the vicinity of the energy of the lowest quasi-stationary state E_{10} ($n = 1$, $m = 0$).

It is seen from Fig. 2 that the behavior of the S matrix as a function of the complex variable $\tilde{E}$ is distinctive: both the real and imaginary parts of the S matrix are smooth functions everywhere in the complex plane, except in the close vicinity of the pole (~10^{-5} meV), where they undergo an unremovable discontinuity at the same point (E_{10}, $-i\Gamma_{10}/2$).

2. RESULTS AND DISCUSSION

Analytical calculation of the S matrix and the positions of its poles in the complex energy plane makes it possible to study the resonance energies E and lifetimes τ of the quasi-stationary states of electrons and holes as functions of their quasi-momentum and geometric parameters of the CCQW.

Table 1. The crystal parameters

Crystal	μ_e/m_0	μ_h/m_0	a, Å	E_g, eV	V_e, eV	V_h, eV
CdS	0.2	0.7	5.818	2.5	1.35	0.65
HgS	0.036	0.044	5.851	0.5	0	0

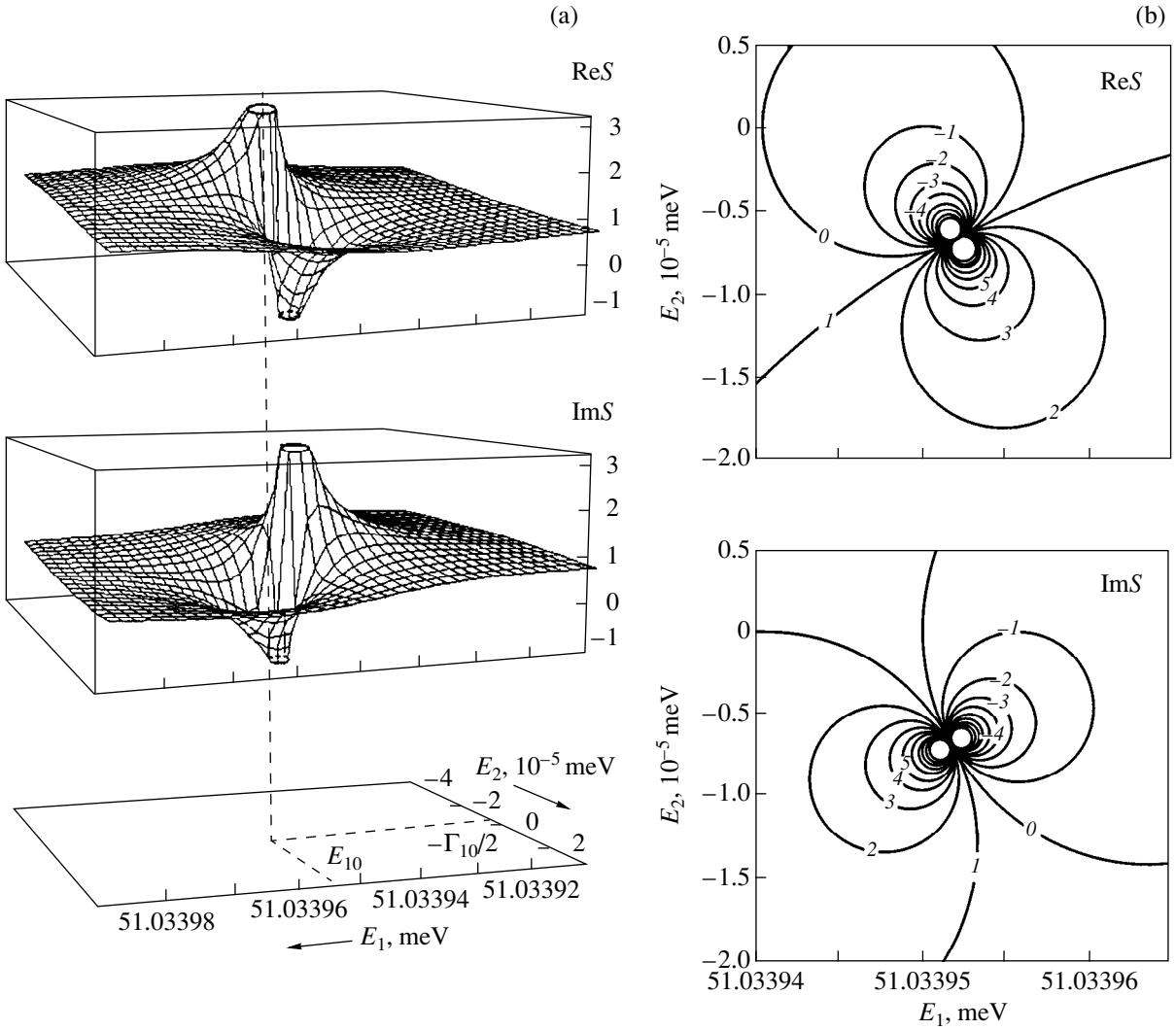

Fig. 2. (a) Dependences of the real and imaginary parts of the S matrix on $\tilde{E} = E_1 - iE_2$ and the position of its pole in the complex plane at $n_{HgS} = 15$ and $n_{CdS} = 5$ and (b) the lines of constant values of ReS and ImS in the complex $\tilde{E}$ plane ("topogram").

Figure 3 shows the calculated resonance energies $E_{nm}^{e,h}(k)$ and lifetimes $\tau_{nm}^{e,h}(k)$ of electrons and holes in several quasi-stationary states of the HgS/CdS/HgS composite cylindrical quantum wire as functions of the longitudinal quasi-momentum k at $\rho_0 = 15a_{HgS}$ and $\rho_1 - \rho_0 = 5a_{CdS}$. This figure also shows the dispersion laws of the quasiparticles in the components of the CCQW ($E_{HgS}^{e,h} = \frac{\hbar^2 k^2}{2\mu_{HgS}^{e,h}}$, $E_{CdS}^{e,h} = U^{e,h} + \frac{\hbar^2 k^2}{2\mu_{CdS}^{e,h}}$). The electron energy is measured from the bottom of the HgS conduction band (the top of the corresponding panel), and the hole energy is measured from the top of the HgS valence band (the bottom of the panel).

As is seen form Fig. 3, the $E_{HgS}(k)$ and $E_{CdS}(k)$ curves divide the (E, k) plane into three domains. In domain I, there are no poles of the S matrix and, therefore, no quasiparticle states. In domain II, the S matrix has poles in the plane of complex energy $\tilde{E} = E - i\Gamma/2$ at specific values of quasi-momentum k. The real and imaginary parts of the corresponding complex energy, E and $\Gamma/2$, are nonzero and determine the resonance energy and lifetime $\tau \sim \Gamma^{-1}$ of the quasiparticle in the quasi-stationary state. The quasiparticles are in stationary states of the continuous energy spectrum ($|S| = 1$) in domain III.

Let us consider the quasi-stationary states of electrons and holes corresponding to the most interesting domain, domain II, in detail. As is seen, there is a number of quasi-stationary states in which the electrons and holes can move along the inner cylinder of the CCQW with quasi-momentum k.

The number of energy bands is determined by the geometric parameters of the CCQW, the effective mass,

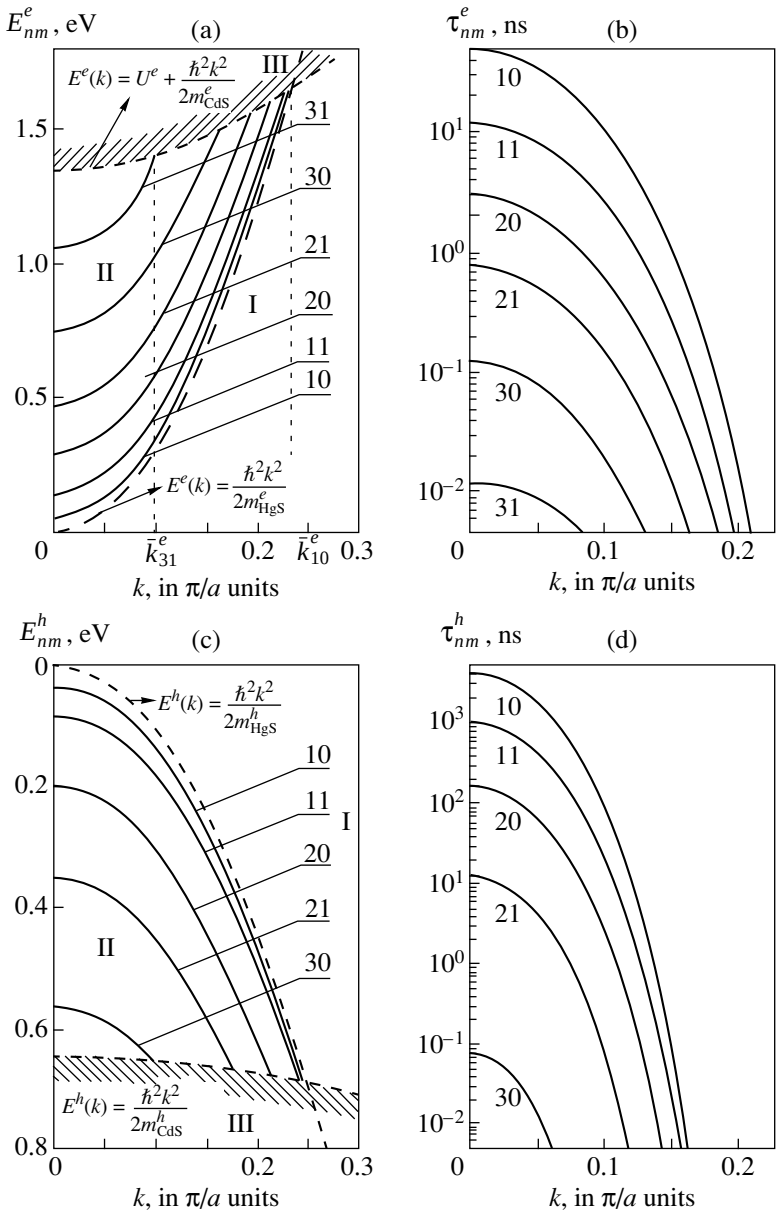

Fig. 3. Dependences of the resonance energies of (a) an electron and (c) a hole and the lifetimes of (b) the electron and (d) the hole on the longitudinal quasi-momentum for different quasi-stationary states.

and the potential energy of the quasiparticle. The main features of $E^{e,h}_{nm}(k)$ are the following. The dependence of the quasiparticle energy on the quasi-momentum is closely approximated by the quadratic law $E^{e,h}_{nm}(k) = E^{e,h}_{nm} + \frac{\hbar^2k^2}{2\mu^{e,h}_{nm}}$ in all resonance states. Here, $E^{e,h}_{nm}$ is determined by the corresponding pole of the S matrix at $k = 0$ and the values of the quasiparticle effective masses $\mu^{e,h}_{nm}$, correlated by the presence of the different media in the CCQW, are close to the corresponding effective masses in HgS (Table 2). The correlated effective mass of the quasiparticle increases only slightly with the band index N, because the "effective height" of the potential barrier decreases and the quasiparticle moving along the inner HgS cylinder penetrates more and more deeply into the CdS, where its effective mass

Table 2. Correlated effective masses in the resonance states

nm	10	11	20	21	30	31
μ^e_{nm}	0.0363	0.0371	0.0372	0.0376	0.0385	0.0391
μ^h_{nm}	0.0453	0.0461	0.0463	0.0477	0.0499	–

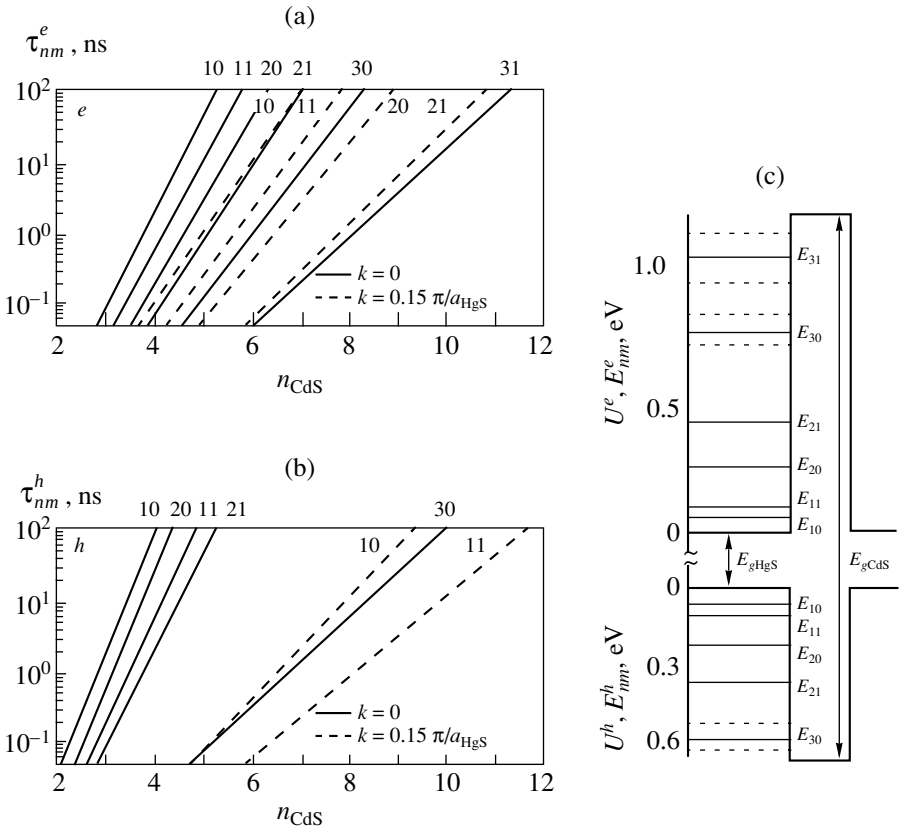

Fig. 4. Dependences of the lifetimes of (a) the electron and (b) the hole on the barrier width at $n_{HgS} = 15$ and (c) a schematic potential-energy diagram and the positions of the resonance levels of the electron and the hole at $n_{HgS} = 15$ and $n_{CdS} = 5$.

is larger than that in HgS. All the bands of quasiparticle resonance energies E_N are characterized by maximal longitudinal quasi-momentum $\bar{k}^{e,h}_{nm}$, which is significantly less than π/a. The value of $\bar{k}^{e,h}_{nm}$ is derived from the equation

$$E^{e,h}_N(k) = U^{e,h} + \frac{\hbar^2 k^2}{2\mu^{e,h}_{CdS}}. \qquad (13)$$

Obviously, the larger the N, the less the value of $\bar{k}^{e,h}_{nm}$.

The important feature of the resonance spectrum of quasiparticles in the open CCQW is that the quasiparticle lifetime ($\tau^{e,h}_{nm}$) in the specific (nm) state decreases sharply (exponentially) as the longitudinal quasi-momentum increases (Figs. 3b, 3d). For example, as is seen from Fig. 3b, the electron lifetime in the (10) state at $k = 0.2$ is three orders of magnitude less than that at $k = 0$. Physically, this is because the effective height of the potential barrier decreases with an increase in k and the quasiparticle has a larger probability of penetrating into the outside of the CCQW. For the same reason, the lifetimes of the quasiparticles decrease sharply with a growth in N.

In connection with the revealed peculiarity of the open CCQW, it can be concluded that a quantum wire of this type can be used as a separator of quasiparticles through their quasi-momenta in nanotechnology: it can eliminate (through the barrier) fast quasiparticles and transmit slow quasiparticles moving in the inner cylinder (potential well).

Figure 4 shows the calculated dependences of the energies E_{nm} and lifetimes $\tau_{nm} = \hbar/\Gamma_{nm}$ of an electron and a hole in the state with magnetic quantum numbers $m = 0$ and 1 on the geometric parameters of the cylinder nanosystem. The solid lines correspond to $k = 0$, and the dashed lines, to $k = 0.15$. Since the positions of the resonance energy levels E_{nm} of the electron and the hole are virtually unchanged, their values are schematically shown in Fig. 4c. The dependences of the lifetimes of the electron and the hole τ_{nm} on the number of CdS monolayers n_{CdS} are shown in Figs. 4a and 4b, respectively.

Regardless of the value of the quasi-momentum, the lifetime of both quasiparticles in all states exponentially increases with the barrier thickness. At a fixed barrier thickness, the smaller the energy of the corresponding state, the larger the lifetime. Physically, this is because a decrease in the quasiparticle energy in a fixed state is equivalent to an increase in the effective power

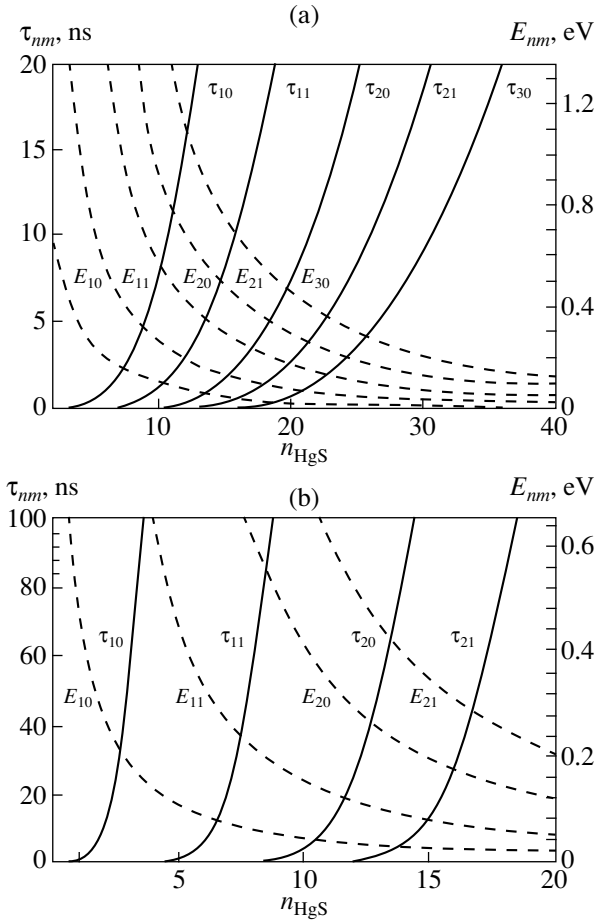

Fig. 5. Dependences of the resonance energies E_{nm} (dashed lines) and lifetimes τ_{nm} (solid lines) on the width of the potential well n_{HgS} at $n_{CdS} = 5$ for (a) the electron and (b) the hole.

of the barrier, which prevents the particles from penetrating through the barrier and, therefore, increases the lifetime in the quantum well. Since the inequality $m_h > m_e$ occurs, the lifetime of the hole is always larger than the electron lifetime, all other things being equal, because it is more difficult for the hole to penetrate through the barrier.

Figure 5 shows the calculated dependences of the energies E_{nm} and lifetimes τ_{nm} of an electron (Fig. 5a) and hole (Fig. 5b) on the width of the material of the well (n_{HgS}) at a fixed width ($n_{CdS} = 5$) of the barrier material. It is seen from this figure that an increase in the width of the quantum well results in a quadratic-law decrease in the absolute value of the ground-state energy. In this case, as was already mentioned, the lifetimes of the electron and the hole in the corresponding states increase.

It is interesting to compare the energies and lifetimes of the quasiparticles in the CCQW and corresponding CSQD having identical radii of their wells and equal widths of their barriers. In this case, since the systems possess different symmetry, it makes sense to compare only those energy levels (and corresponding lifetimes) that have the same index counted from the lowest level.

In this case, as is seen from Fig. 6, if $k = 0$ and the geometric parameters of the wells and barriers of the CCQW and CSQD are the same, the corresponding energy levels in the quantum wire are always lower (and the lifetimes in these states are larger) than those in the quantum dot. The result obtained is clear from the physical point of view; since the volume of the cylinder well is infinitely large in contrast to that of the spherical well under the same conditions, the corresponding levels in the quantum wire are lower than those in the quantum dot and, therefore, the power of the barrier in the quantum wire is larger than that in the quantum dot. The ratio between the lifetimes reflects this fact.

Thus, the *S*-matrix method makes it possible to calculate the spectral characteristics of both composite spherical [9] and open cylindrical quantum nanostructures with resonance quasi-stationary states. The general conclusion is that the positions of the energy levels

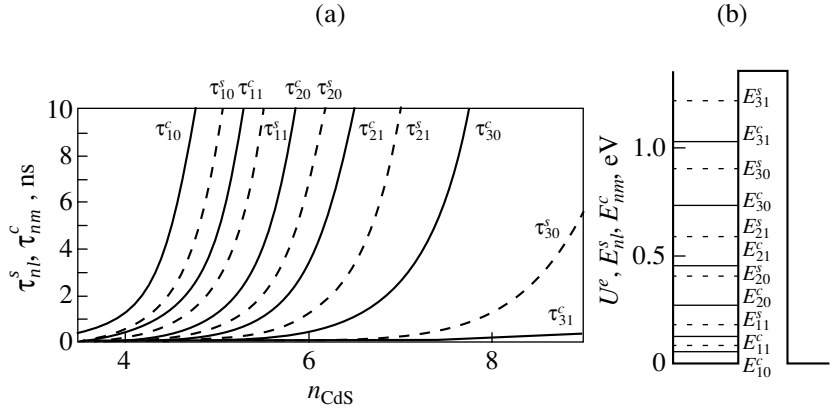

Fig. 6. (a) Dependence of the electron lifetime on the barrier width and (b) the positions of the energy levels in the CCQW (solid lines) and CSQD [9] (dashed lines).

of the electron and the hole are almost insensitive to the thickness of the barriers, but very sensitive to the width of the quantum wells. Changes in the width of the well and of the barriers are accompanied by essential changes in the quasiparticle lifetimes in the quasi-stationary states. The fact that the lifetimes of the quasiparticles in the resonance states exponentially decrease with an increase in their quasi-momenta makes it possible to use open CCQWs as spatial separators of quasiparticles through their velocities in elements of nanotechnological devices.

REFERENCES

1. S. Simhony, E. Kapon, T. Colas, *et al.*, Appl. Phys. Lett. **59**, 2225 (1991).
2. N. Kirstaedter *et al.*, Electron. Lett. **30**, 1416 (1994).
3. D. Schooss, A. Mews, A. Eychmuller, and H. Weller, Phys. Rev. B **49**, 17072 (1994).
4. A. Mews, A. V. Kadavanich, U. Banin, and A. P. Alivasatos, Phys. Rev. B **53**, R13242 (1996).
5. N. V. Tkach, V. A. Golovatskiĭ, O. N. Voĭtsekhovskaya, and M. Ya. Min'kova, Ukr. Fiz. Zh. **43**, 745 (1998).
6. N. V. Tkach, Fiz. Tverd. Tela (St. Petersburg) **39**, 1109 (1997) [Phys. Solid State **39**, 995 (1997)].
7. M. Tkach, J. Phys. Stud. **3**, 377 (1999).
8. Das Sarma and V. B. Campos, Phys. Rev. B **49**, 1867 (1994).
9. N. V. Tkach and V. A. Golovatskiĭ, Fiz. Tverd. Tela (St. Petersburg) **41**, 2081 (1999) [Phys. Solid State **41**, 1911 (1999)].
10. A. I. Baz', Ya. B. Zel'dovich, and A. M. Perelomov, *Scattering, Reactions, and Decays in Nonrelativistic Quantum Mechanics* (Nauka, Moscow, 1971, 2nd ed.; Israel Program for Scientific Translations, Jerusalem, 1966).
11. K. C. Yung and J. H. Yee, Phys. Rev. A **50**, 104 (1994).
12. G. O. Hai, F. M. Peeters, and J. T. Devreese, Phys. Rev. B **48**, 4666 (1993).

Translated by A. Poushnov

Physics of the Solid State, Vol. 43, No. 2, 2001, pp. 373–376. Translated from Fizika Tverdogo Tela, Vol. 43, No. 2, 2001, pp. 357–359.

LOW-DIMENSIONAL SYSTEMS AND SURFACE PHYSICS

Silicon Nanocluster Formation under Electron-Beam-Induced Modification of a Silicate Matrix

V. N. Bogomolov, S. A. Gurevich, M. V. Zamoryanskaya, A. A. Sitnikova, I. P. Smirnova, and V. I. Sokolov

Ioffe Physicotechnical Institute, Russian Academy of Sciences, Politekhnicheskaya ul. 26, St. Petersburg, 194021 Russia

Received May 23, 2000

Abstract—A cathodoluminescence band in the green spectral region is observed in silicate matrices when the excitation density exceeds a certain threshold value. This band is due to the formation of silicon nanoclusters 4–5 nm in size and becomes manifest at SiO_2/Si interfaces when impurities are introduced into the silicate matrix, as well as under electron-beam irradiation. © *2001 MAIK "Nauka/Interperiodica".*

The cathodoluminescence (CL) spectra of thermally grown oxide films on silicon are determined by the type of substrate used and the actual film preparation conditions [1, 2]. The main objective of this work was to investigate the dependence of CL spectra on the structure of silicate matrices and to determine the conditions for the modification of this structure under electron-beam irradiation, which gives rise to the appearance of emission bands in the 2.0- to 2.5-eV interval.

1. EXPERIMENTAL TECHNIQUES

The main methods used in the study were local cathodoluminescence, transmission electron microscopy (TEM), and measurement of the current–voltage (*I–V*) characteristics.

The subjects of the study were primarily SiO_2 films grown on *n*- and *p*-type silicon by high-temperature oxidation in dry or humid oxygen, as well as model systems, more specifically, silicon dioxide/silicon films doped during their formation by boron and copper, various quartz glasses, opals, α quartz, and uranium-doped silicon dioxide.

2. EXPERIMENTAL RESULTS

Cathodoluminescence spectra of silicate systems, including thermally grown films, have two well-known bands associated with native SiO_2 defects, namely, a red one peaking at 1.9 eV (due to non-bridging oxygen) and a blue one peaking at 2.65 eV (twofold-coordinated silicon) [3, 4]. We developed a technique of layer-by-layer analysis of oxide films by cathodoluminescence with a spatial resolution no worse than 10 nm [1, 2]. Depth-resolved studies of thermal films showed that cathodoluminescence spectra obtained from a film–substrate interface feature additional bands in the green spectral region (2.0–2.5 eV). The position and intensity of these bands vary depending on the silicon type and the technology of the film preparation. The bands are the strongest for films grown on *p* silicon. A layer-by-layer analysis of thermal oxide films on *p* silicon showed that the band in the green spectral region appears on the interface and on the adjoining oxide layers 0.1–0.2 μm thick. This band peaks at 2.2–2.3 eV. The bands measured on *n* silicon are much weaker and are seen as a shoulder on the strong blue band (2.65 eV). This shoulder shifts in position from 2.1 eV at the interface to 2.4 eV near the surface for a 0.4 μm thick film [4]. It should be noted that the position and intensity of these bands correlate with the density of the oxide film and the position of the green band maximum correlates with the micropore size. TEM images of oxide films grown on *p* silicon reveal that the film density near the interface (up to 0.1–0.2 μm thick) is substantially smaller than that in the outer layers [2], with the oxide density changing in a jump. This may be due to boron redistribution in the Si–SiO_2 system. The interface reveals microrecesses up to 6 μm in diameter. The diameter of the microrecesses and their number decrease as one moves away from the Si–SiO_2 interface [5]. There is a certain correlation between the CL intensity distribution in the 2.0- to 2.5-eV region and the silicate matrix density.

To establish the nature of the centers responsible for the green bands, we studied cathodoluminescence spectra of various silicate systems, as well as of silicon dioxide with impurities differing strongly in their properties, namely, boron, copper, and uranium. In order to compare the experimental spectra and determine the position of the maxima of the broad bands with a higher accuracy, the spectra obtained were deconvolved into their constituents. This deconvolution was made using the ORIGIN 6.0 code. This was done under the assumption that the band shape can be fit-

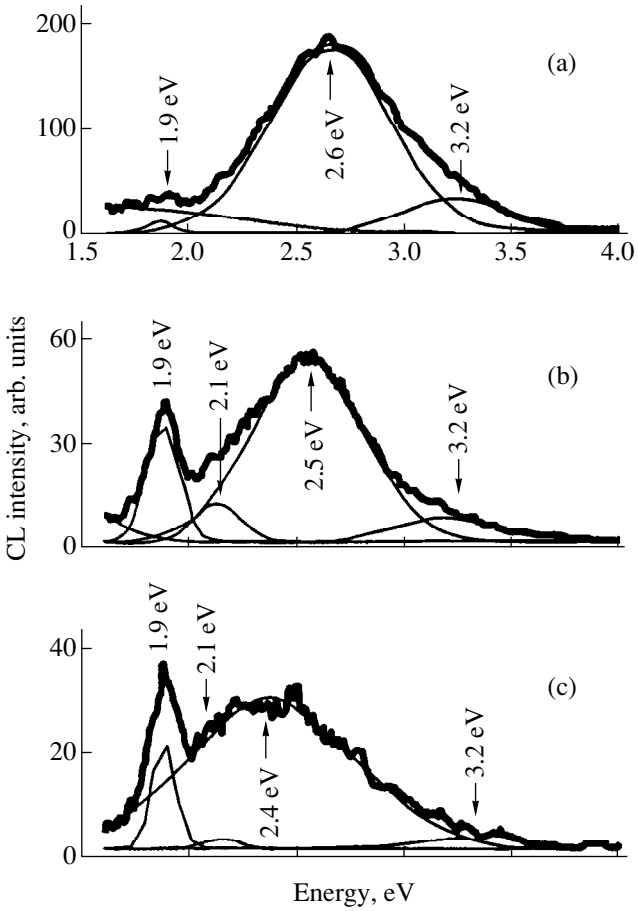

Fig. 1. Cathodoluminescence spectra of uranium-doped SiO_2. Uranium content (wt %): (a) 1, (b) 3, and (c) 8.

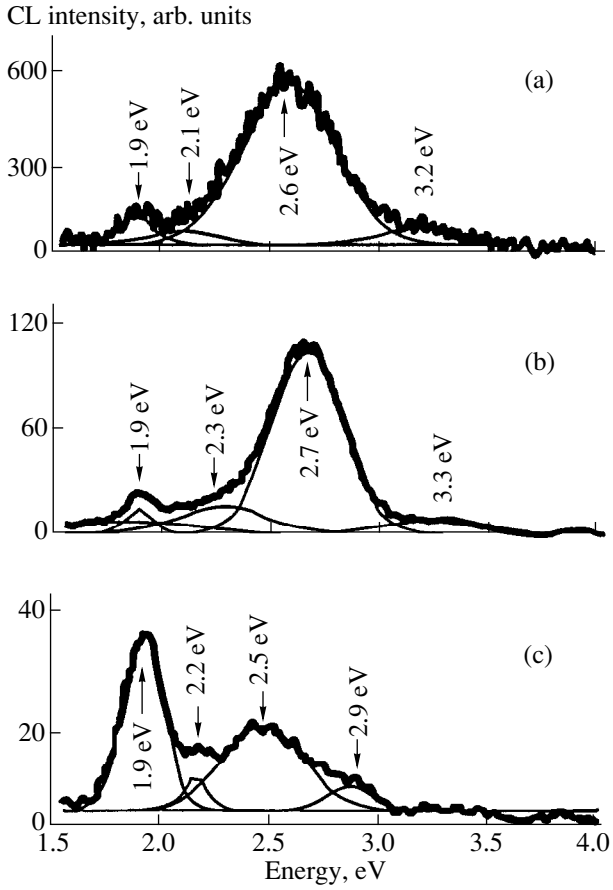

Fig. 2. Cathodoluminescence spectra of a SiO_2 film activated by various impurities: (a) boron and (b, c) copper (10 and 20 wt %, respectively).

ted by Gaussians. The thin lines in the figures presented in this paper show the results of the deconvolution.

Figure 1 presents cathodoluminescence spectra of silicon oxide with a uranium impurity. One readily sees that the higher the uranium content, the lower the integrated emission intensity and the more pronounced the green shift of the emission spectrum.

Figure 2 displays the cathodoluminescence spectra of an oxide film doped by boron and copper. The spectra of samples containing small amounts of impurities (boron and copper) exhibit the bands as a weak shoulder, but one can also see an additional UV band (3.1–3.2 eV). The emission spectrum of the sample with a higher copper content is similar to the CL spectrum of uranium-doped (8 wt %) silicon oxide. These results allow one to conclude that the composition of the silicon dioxide emission depends on the impurity content rather than on the nature of the impurity element. This implies that the variation of the emission spectra is associated with the formation of some structural defects in the silicate matrix itself.

Similar cathodoluminescence spectra in the green region (2.1–2.2 eV) appear in various silicate matrices as the excitation density increases. The spectral variation with excitation density has the same pattern for all the samples studied (Fig. 3). Note that each of the silicate matrices studied here can be associated with a certain threshold excitation density, above which the emission band peaking at 2.1–2.2 eV appears in the spectrum. For porous materials (opals, silica gels), this threshold is 20–40 times lower than that for denser ones. As the excitation density is increased further, the 2.1- to 2.2-eV band becomes dominant. In [6], this band is assigned to silicon nanoclusters.

High excitation densities not only stimulate radiation-induced defect formation in silicate systems but also result in a strong local heating of the sample. This may entail evaporation and partial decomposition of the material. The decomposition brings about removal of oxygen, producing free silicon atoms in the bulk of the silicate matrix, which may form nanoclusters in the pores which are created in the course of decomposition or are already available in the structure of this matrix.

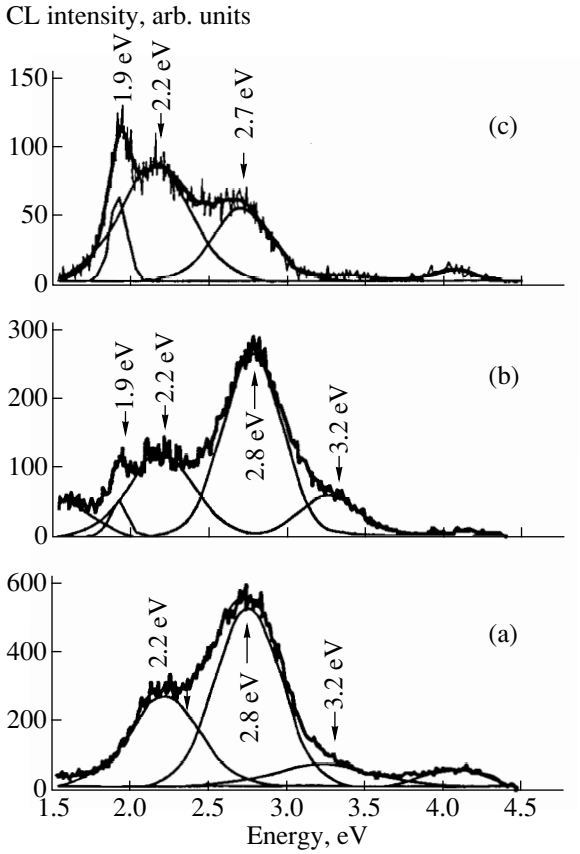

Fig. 3. CL spectra obtained at high excitation densities (20 kV, 50 nA, beam diameter 3 μm) for (a) opal, (b) SiO_2 : Cu/SiO_2/Si films (C_{Cu} = 10 wt %), and (c) a thermally grown film.

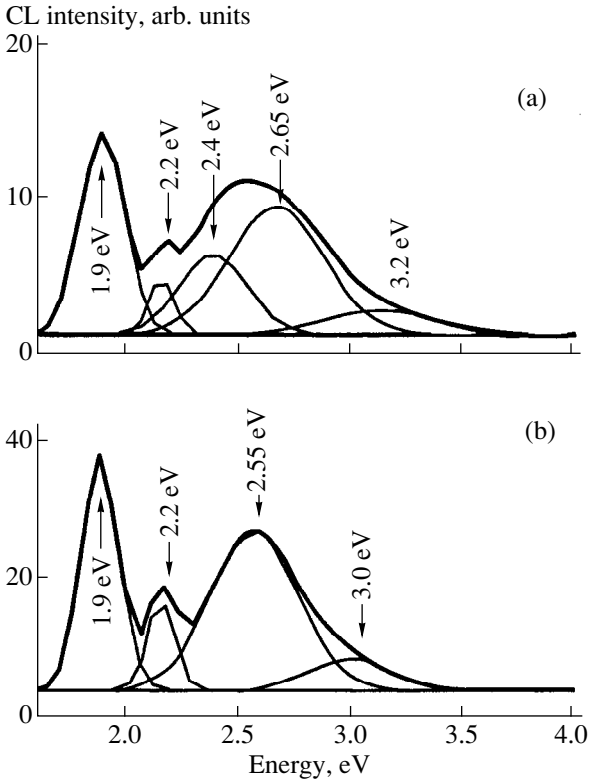

Fig. 4. CL spectra of the opal obtained under various excitation conditions. Voltage (kV), current (nA), and exposure time (ms): (a) 10, 1.5, and 100; and (b) 10, 1.5, and 300, respectively.

The size of the nanoclusters is determined by that of the voids in the sample.

These considerations underlie the choice for further study of a sample with known dimensions of its voids, namely, opal. Opals are regularly arranged arrays of silicon oxide spheres 200–250 nm in diameter. Opals have voids measuring 5, 10, and 15 nm. As the excitation density is increased, small nanoclusters form, which subsequently fill the smallest (5 nm) pores. The scatter in the size of such pores is small, and they should produce a relatively narrow band in the CL spectrum. Figure 4 presents opal spectra obtained under the same excitation conditions but for different exposure times to electrons. One readily sees that the blue and UV bands shift to longer wavelengths after prolonged irradiation of opals by electrons, while the 2.2-eV band becomes more distinct and intense. Optical and scanning electron microscope images reveal clearly pronounced changes in the structure of the excited microvolume; i.e., the silicate matrices undergo modification. In addition to spectral studies, we also measured the absorbed electron current in modified and unmodified opals. In the modified regions of the opal, the absorbed current was found to exceed that in the unmodified ones by 10–20 times, which implies the formation of conduction channels in these regions. The formation of silicon nanoclusters in opals following the modification was confirmed by TEM images. The TEM studies reveal that, on the surface of SiO_2 spheres 250 nm in diameter, there are silicon nanoclusters 4 to 5 nm in size.

The results of this study can be summed up as follows:

(i) Local heating of silicate matrices by a high-power electron beam results in modification of the samples, entailing the formation of silicon nanoclusters. This modification is the most pronounced in porous materials, namely, opals and silica gels.

(ii) Introduction of impurities in silicate matrices gives rise to the formation of interfaces at which silicon nanoclusters are deposited.

(iii) Electron irradiation of silicate materials can be used to produce silicon nanoclusters in a silicate matrix, with the matrix itself serving as the source of silicon and the geometry of the nanocluster arrangement being determined by the diameter and trajectory of the electron beam [7].

(iv) The green band, perhaps, is associated with the Si–SiO_2 interface [8].

REFERENCES

1. M. V. Zamoryanskaya and V. I. Sokolov, Fiz. Tverd. Tela (St. Petersburg) **40**, 1984 (1998) [Phys. Solid State **40**, 1797 (1998)].
2. M. V. Zamoryanskaya, V. I. Sokolov, A. A. Sitnikova, and C. G. Konnikov, Solid State Phenom. **63–64**, 237 (1998).
3. L. N. Skuja and A. R. Silin, Phys. Status Solidi A **70**, 43 (1982).
4. J. P. Mitchell and D. G. Denure, Solid-State Electron. **16**, 825 (1973).
5. S. A. Litvinenko and V. I. Sokolov, Phys. Status Solidi A **116**, 615 (1989).
6. V. G. Baru, M. I. Elinson, V. A. Zhitov, *et al.*, Mikroélektronika **27**, 45 (1998).
7. V. N. Bogomolov, M. V. Zamoryanskaya, and V. I. Sokolov, RF Patent No. 215308.
8. V. N. Bogomolov, Phys. Rev. B **51**, 17040 (1995).

Translated by G. Skrebtsov

Physics of the Solid State, Vol. 43, No. 2, 2001, pp. 377–379. Translated from Fizika Tverdogo Tela, Vol. 43, No. 2, 2001, pp. 360–362.

LOW-DIMENSIONAL SYSTEMS AND SURFACE PHYSICS

Energy Distribution of Alkali-Metal Atoms under Electron-Stimulated Desorption from the Surface of Oxidized Refractory Substrates

S. Yu. Davydov

Ioffe Physicotechnical Institute, Russian Academy of Sciences, Politekhnicheskaya ul. 26, St. Petersburg, 194021 Russia

Received June 16, 2000

Abstract—An analysis is made of experimental data on the dependence of the energy distributions of Li, Na, and Cs atoms emitted in electron-stimulated desorption on their concentration on the surface of oxidized tungsten and molybdenum substrates.

Systematic investigation into the electron-stimulated desorption (ESD) of neutral particles began, in contrast to that of ions, comparatively recently [1]. The ESD of lithium and cesium atoms from the oxidized surface of tungsten (Li, Cs/O–W) and of sodium atoms from that of molybdenum (Na/O–Mo) have been studied [2, 3]. It was found that the energy distribution of desorbed atoms is a standard Gaussian, which shifts toward lower energies with increasing coverage Θ (i.e., the relative concentration of alkali adatoms) while practically not changing in shape and width. It is well known that the ground state of an adsorption system varies substantially with coverage [4, 5], which is particularly true for the adsorption of alkali metals. Therefore, the absence of any distinct changes, however small, in the shape of the ESD atom energy-distribution profile appears strange at first glance. We analyze here the experimental data of [2, 3] in order, first, to find the conditions favoring a constant width of the energy distribution and, second, to discuss the physical reasons for this phenomenon.

Consider the energy diagram of desorption (for more details, see [2]) shown in Fig. 1. The potentials of the "ground" and "excited"[1] states can be presented by the Morse, V_1, and Born, V_2, potentials, respectively:

$$V_1 = D\{\exp[-\gamma(x-x_0)]\} - 2\{\exp[-(\gamma/2)(x-x_0)]\},$$
$$V_2 = B\exp(-\beta x). \quad (1)$$

Here, D and B are energy constants; γ and β are the characteristic reciprocal lengths of the V_1 and V_2 potentials, respectively; and x_0 is the equilibrium distance of the adatom from the substrate surface. When formulated in this way, the problem becomes equivalent to that of ion desorption [6]. As follows from Fig. 1, the width of the energy distribution of desorbed atoms ΔE can be written as

$$\Delta E = V_2(x_0-\Delta x) - V_2(x_0+\Delta x) = 2B(x_0)\sinh(\beta\Delta x), \quad (2)$$

where Δx is the potential-well half-width in the ground state (Fig. 1) and

$$B(x_0) = B\exp(-\beta x_{x_0}). \quad (3)$$

We now require $d(\Delta E)/d\Theta = 0$ and take into account that $B(x_0(\Theta)) = E_{\max}(\Theta)$, where $E_{\max}$ is the kinetic energy at which the energy distribution of ESD atoms $N(E)$ has a maximum (Fig. 1). We thus obtain

$$\frac{dy}{d\Theta} = -\tanh y\frac{d\ln E_{\max}(\Theta)}{d\Theta}, \quad y \equiv \beta\Delta x, \quad (4)$$

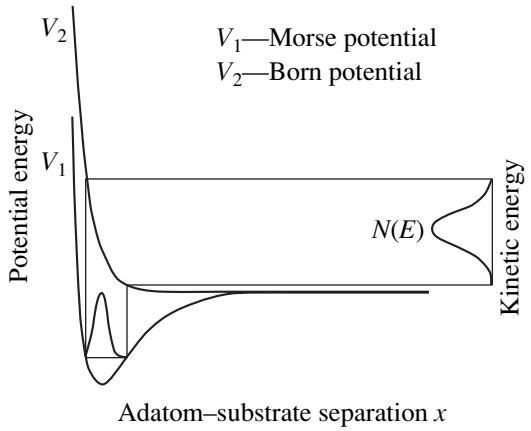

Fig. 1. Schematic of desorption process for zero coverage Θ. The potential energies of an atom in the "ground" adsorbed state, V_1, and in the "excited" state, V_2, are shown on the left by thick solid lines. The thin line specifies the probability for an adatom to reside in the vicinity of the equilibrium point x_0 in the "ground" state. The ESD atom distribution $N(E)$ in kinetic energy E is shown on the right.

[1] The quotation marks are to stress that, strictly speaking, the desorption process considered here can actually be the last step in a multistage process (see discussion in [2, 3]).

1063-7834/01/4302-0377$21.00

ESD energy E_{max} corresponding to the maximum in the $N(E)$ distribution of the ESD atoms and the relative potential-well half-width $\delta(\Delta x)/\Delta x/\Delta x$ vs. coverage Θ

Θ	0.05	0.125	0.25	0.375	0.5	0.75
Li/O–W [2]						
B_{max}, eV	–	0.225	0.21	–	0.195	0.17
$\delta(\Delta x)/\Delta x$	–	–	0.069		0.074	0.137
Cs/O–W [2]						
E_{max}, eV	0.39	0.38	0.375	0.36		
$\delta(\Delta x)/\Delta x$	–	0.032	0.02	0.041		
Na/O–Mo [3]						
E_{max}, eV		0.22	0.2		0.19	0.17
$\delta(\Delta x)/\Delta x$		–	0.118		0.065	0.097

where y is the reduced dimensionless half-width of the potential well. If we assume, by way of simplification, that the shift of E_{max} is directly proportional to the coverage, i.e., that $dE_{max}(\Theta)/d\Theta = -k$, where k is a constant, then

$$\frac{dy}{d\Theta} = \frac{k}{E_{max}(\Theta)}\tanh y. \quad (5)$$

If the maximum in the energy distribution shifts with increasing coverage toward lower energies ($k > 0$), as was observed in [2, 3], then the potential well becomes broader.

Let us make some estimates. Using the data of [6], we set $\beta = 3.5$–7 Å^{-1} and $\Delta x \sim \alpha^{-1}$, where α is the characteristic reciprocal length of the wave-function decay in the ground state ($\alpha = 17$–32 Å^{-1}). Then $y \approx 0.1$–0.5, $\tanh y \approx y$, and the variation of the well half-width $\delta(\Delta x)$ can be calculated from the expression

$$\frac{\delta(\Delta x)}{\Delta x} = -\frac{\Delta E_{max}(\Theta)}{E_{max}(\Theta)}, \quad (6)$$

where $\Delta E_{max}(\Theta)$ is the shift of the peak position in the energy distribution due to a coverage transition from Θ_1 to $\Theta_2 = \Theta_1 + \Delta\Theta$. One may conveniently accept $E_{max}(\Theta)$ to be equal to $[E_{max}(\Theta_1) + E_{max}(\Theta_2)]/2$. Having determined $\Delta E_{max}(\Theta)$ from the experiment for certain values of $\Delta\Theta$, one can find the change in the relative potential-well width $\delta(\Delta x)/\Delta x$.

The results of treatment of the experimental data presented in [2, 3] are listed in the table. The values of the kinetic energy of the ESD atoms and of the relative broadening of the potential well are very small. Therefore, it is clear that determination of $\delta(\Delta x)/\Delta x$ will unavoidably be done with errors (possibly, quite large). However, the fact that the well width increases with increasing coverage may be considered proven.

Using the definition in Eq. (3) of the quantity $B(x_0)$, we obtain

$$\frac{dB(x_0)}{dx_0} = -\beta B(x_0) < 0. \quad (7)$$

On the other hand, because $B(x_0(\Theta)) = E_{max}(\Theta)$ (see Fig. 1), we have

$$\frac{dB(x_0)}{dx_0} = \left(\frac{dx_0}{d\Theta}\right)^{-1}\left(\frac{dE_{max}(\Theta)}{d\Theta}\right). \quad (8)$$

The first factor in Eq. (8) is positive, because an alkali adatom is depolarized with increasing coverage; indeed, as Θ changes from 0 to 1, the adatom transfers from a nearly ionic state with a radius r_i to a nearly atomic state with a radius $r_a > r_i$ [4, 5], so that, for an estimate, one can set

$$x_0 = nr_a + (1-n)r_i, \quad (9)$$

where $n \le 1$ is the number of electrons on an alkali adatom. The second term in Eq. (8) is negative, which follows from experiments [2, 3]. Hence, $B(x_0)$ is a decreasing function, which is in agreement with Eq. (7).

As follows from Eq. (9),

$$dx_0/d\Theta = (r_c - r_i)(dn/d\Theta). \quad (10)$$

It can be shown (see, e.g., [7] and the references therein) that, if one takes into account the dipole–dipole repulsion of equally charged adatoms,[2] the dependence of the occupation number of electrons n on coverage, i.e., $dn/d\Theta$, can be written in the form

$$dn/d\Theta = (3/2)\sqrt{\Theta}(1-n)\rho\xi,$$
$$\rho = \pi^{-1}\frac{\Gamma}{[\phi - I - \Theta^{3/2}\xi(1-n)]^2 + \Gamma^2}, \quad (11)$$
$$\xi = 2e^2l^2N_{ML}^{3/2}A.$$

Here, ρ is the density of states on the adatom at the energy coinciding with the Fermi level in the substrate; ϕ is the work function of the oxidized metal substrate; I is the ionization potential of the alkali atom; Γ is the adatom quasi-level half-width; ξ is an energy parameter describing the dipole–dipole repulsion of adatoms; l is one-half of the surface-dipole arm, which, for our problem, may be set equal to the sum of x_0 and the oxygen atom radius; N_{ML} is the number of alkali metal atoms in a monolayer that are adsorbed per unit area of the substrate surface; e is the electronic charge; and A is a numerical coefficient (~10), which is only weakly dependent on the adsorbed layer geometry.

Having calculated n in a self-consistent way, one can find $B(x_0)$ and, hence, the parameters of the Born potential. When calculating the "ground" state described

[2] The dipole is formed by the charged adatom and its image in the metal.

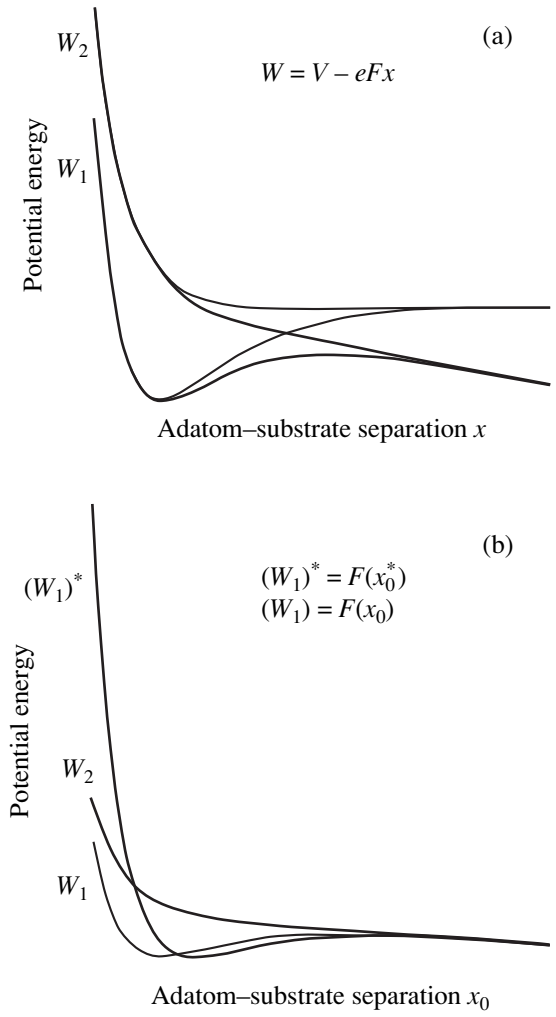

Fig. 2. Schematic of the desorption process for finite coverages Θ. (a) Variation of the Morse ($V_1 \longrightarrow W_1 = V_1 - eFx$) and Born ($V_2 \longrightarrow W_2 = V_2 - eFx$) potentials in the electric field F created by the surface dipoles. The thin lines identify the terms corresponding to zero coverage. (b) Variation of the W_1 potential corresponding to the equilibrium position x_0 under adatom depolarization; $W_1(x_0) \longrightarrow W_1^*(x_0^*)$, where $x_0^* > x_0$ is the new equilibrium position corresponding to a finite adatom concentration Θ. The thin line identifies the term corresponding to zero coverage.

by the Morse potential, one has simply to take into account the dependence of x_0 and D on the coverage by equating D to the adsorption energy E_{ads}. Thus, by deriving the values of $E_{max}(\Theta)$ and $E_{ads}(\Theta)$ from the experiment, one can extract additional information on the microscopic characteristics of the adsorption system.

Thus, we have formally established that, in order to explain the observed energy distributions, the potential well should broaden and the Born repulsion should decrease with increasing coverage. Consider the physical mechanism of these variations.

Figure 2a schematically presents the effect exerted on a single adatom by the electric field (to make the presentation more revealing, the field strength F is assumed constant) produced by all other adatoms. We readily see that, first, the width of the potential well increases (the thick lines) compared to the case of a single adatom (the thin lines), and, second, the amplitude of the Born potential decreases. However, the changes in the potentials $W_{1,2} = V_{1,2} - eFx$ become noticeable only for $x > x_0$. As a result of the latter fact, the lower edge of the energy distribution $N(E)$ shifts toward lower kinetic energies, while its upper edge shifts only insignificantly. Note that the energy distribution $N(E)$ grows in width.

Figure 2b shows the dependence of the Morse potential on the equilibrium distance x_0, which increases ($x_0 \longrightarrow x_0^* > x_0$) with increasing coverage Θ because of the adatom depolarization. As follows from Fig. 2b, this results in a considerable shift of the upper edge of $N(E)$ toward lower kinetic energies, which exceeds the shift of the lower edge. In this way, the increase of the potential-well width compensates the broadening of $N(E)$. Thus, the shift of the adatom equilibrium position caused by depolarization and the field-induced potential-well broadening can, generally speaking, result in both broadening and contraction of the $N(E)$ distribution of ESD atoms, depending on the actual shape and mutual position of the Morse and Born potentials. In the desorption of alkali metals from oxidized tungsten and molybdenum surfaces, these effects cancel.

ACKNOWLEDGMENTS

The author is indebted to V.N. Ageev, who called the author's attention to this problem, for a fruitful discussion.

This work was supported by the Russian State Program "Surface Atomic Structures," project no. 4.5.99.

REFERENCES

1. V. N. Ageev, O. P. Burmistrova, and Yu. A. Kuznetsov, Usp. Fiz. Nauk **158** (3), 389 (1989) [Sov. Phys. Usp. **32**, 588 (1989)].
2. V. N. Ageev, Yu. A. Kuznetsov, and N. D. Potekhina, Surf. Sci. **367** (1), 113 (1996).
3. V. N. Ageev and Yu. A. Kuznetsov, Fiz. Tverd. Tela (St. Petersburg) **40** (4), 768 (1998) [Phys. Solid State **40**, 707 (1998)].
4. O. M. Braun and V. K. Medvedev, Usp. Fiz. Nauk **157** (4), 631 (1989) [Sov. Phys. Usp. **32**, 328 (1989)].
5. S. Yu. Davydov, Poverkhnost' **8**, 17 (1991).
6. M. Nishijima and F. M. Propst, Phys. Rev. B **2** (7), 2368 (1970).
7. S. Yu. Davydov, Fiz. Tverd. Tela (St. Petersburg) **41** (9), 1543 (1999) [Phys. Solid State **41**, 1413 (1999)].

Translated by G. Skrebtsov

Physics of the Solid State, Vol. 43, No. 2, 2001, pp. 380–385. Translated from Fizika Tverdogo Tela, Vol. 43, No. 2, 2001, pp. 363–368.

LOW-DIMENSIONAL SYSTEMS AND SURFACE PHYSICS

Silicon Interaction with the (0001) Surface of La and Gd Layers

A. Yu. Grigor'ev, O. V. Krupin, D. V. Vyalykh, Yu. S. Dedkov, A. M. Shikin, G. V. Prudnikova, and V. K. Adamchuk

Research Institute of Physics (Petrodvorets Branch), St. Petersburg State University, Ul'yanovskaya ul. 1, Petrodvorets, 198904 Russia

e-mails: shikin@paloma.spbu.ru, adamchuk@paloma.spbu.ru, prudnikg@paloma.spbu.ru

Received June 22, 2000

Abstract—A study is reported on a system consisting of a Si layer on the surface of rare-earth metals (REMs), which is the reverse of a rare-earth metal on silicon, the system of current widespread interest. Interaction of silicon with the (0001) surface of trivalent La and Gd single-crystal layers grown on a W(110) surface is studied by Auger spectroscopy combined with layer-by-layer argon-ion etching of the system and photoelectron spectroscopy. It is found that silicon interacts with the La(0001) and Gd(0001) surfaces even at room temperature with the formation of silicide, but no mutual mixing of the silicon and substrate atoms occurs. When the Si/La(0001) and Si/Gd(0001) systems are heated at 400°C, silicon does not diffuse into the bulk of the metal substrate or to the REM/W(110) interface. © *2001 MAIK "Nauka/Interperiodica"*.

1. INTRODUCTION

In recent years, investigations into physicochemical processes in rare-earth-metal–silicon systems have been attracting considerable attention [1]. Interest in these systems is stimulated by their technological potential and the fundamental problems concerning the formation and properties of a metal–semiconductor interface. Most studies of rare-earth-metal–Si systems deal with adsorption of the metal and epitaxial growth of rare-earth metal (REM) silicides on the surface of a single-crystal silicon substrate [1–5]. The increasing interest in layered systems has recently initiated studies dealing with the formation of thin layers of semiconductors, specifically of silicon, on the surface of metals [6, 7]. Earlier [8], we investigated the specific features of the electronic and crystal structures of the systems formed upon deposition of thin silicon layers onto the surface of single-crystal Gd(0001) and Dy(0001) layers, followed by their heating. It was shown that these systems represent essentially single-crystal Gd and Dy layers with Gd and Dy silicide islands lying on the surface of the corresponding metal layers and occupying a small area of the surface of the system.

This paper reports on a study of the systems formed by room-temperature deposition of Si layers, 3 to 50 Å thick, onto the (0001) face of Gd and La single-crystal layers with subsequent heating. The systems were investigated by Auger electron spectroscopy combined with layer-by-layer ion etching and photoelectron spectroscopy. The objects chosen for the study were the Si/Gd(0001) and Si/La(0001) systems, because the first of them has already been investigated and could serve as a reference for the present experiment and the second system could be used for comparing the results obtained on the Si/Gd and Si/Dy structures with systems in which a light trivalent REM is used as a substrate for silicon adsorption. This work was aimed at investigating the processes involved in the interaction of silicon with the (0001) surface of single-crystal La and Gd layers in the course of silicon deposition onto their surfaces and subsequent heating of the systems. We found that the deposited silicon chemically reacts at room temperature with the Gd(0001) and La(0001) surfaces to form the corresponding silicide, with no mutual diffusion of the silicon and metal atoms. As the thickness increases, silicon forms a surface solid layer coating the metal surface and the silicide produced on the interface. When the Si/Gd(0001) and Si/La(0001) systems thus formed are heated at 400°C, silicon does not diffuse into the bulk of La and Gd or to the REM/W(110) interface.

2. EXPERIMENTAL TECHNIQUE

The interaction of silicon with the (0001) surface of La and Gd single-crystal layers grown on the W(110) surface was studied by photoelectron and Auger electron spectroscopy during Si thin-film deposition onto the surface of the metal layers, followed by heating, and in the course of layer-by-layer argon-ion etching of the system thus formed. The photoelectron spectroscopy experiments were carried out on a TGM-3 channel of the BESSY-I synchrotron storage ring (Berlin) with the use of a WSW–ARIES electron analyzer with angular and energy resolution. The total energy resolution of the system was about 150 meV. The photoelectron spectra presented in this work were measured in the

1063-7834/01/4302-0380$21.00

photoelectron takeoff direction normal to the sample surface at an excitation energy of 35 eV, which corresponds approximately to electron emission from the center of the Brillouin zone of La and Gd crystals. Auger electron spectroscopy and layer-by-layer argon-ion etching were performed under laboratory conditions similar to those of the experiments conducted on the BESSY-I. The Auger spectra were recorded with a four-grid retarding-field secondary-electron analyzer at a primary electron energy of 1 keV. The layer-by-layer etching of the samples was carried out by argon ions with a kinetic energy of 1 keV (the angle of incidence on the sample was 60°). The vacuum in both experimental setups was better than 1×10^{-10} torr and deteriorated to 5×10^{-10} torr during the deposition of the metal and silicon films. During the layer-by-layer etching, the argon pressure was 1×10^{-6} torr.

The La and Gd single-crystal layers, about 100 Å thick and with the (0001)-oriented surface, were prepared by the standard technique on the W(110) surface, which provides high crystal perfection and surface cleanness [9]. The metal layers were deposited from a tantalum crucible heated by electron bombardment, and silicon was evaporated from a silicon plate (*n*-Si) heated by direct dc passage.

3. RESULTS

Figure 1 shows the Auger electron spectra of a clean La(0001) surface with 3-, 15-, and 50-Å-thick silicon layers deposited onto it at room temperature and the spectra of a 15-Å-thick Si/La(0001) system formed upon heating at 400°C for 5 min. The lanthanum La(*NOO*), La(*NOV*), and silicon Si(*LVV*) Auger peaks at 59, 78, and 90.5 eV, respectively, are characteristic features of these spectra. Adsorption of a 3-Å-thick Si layer on the La(0001) surface gives rise to the silicon Si(*LVV*) feature in the Auger spectrum of the system. A further increase in silicon concentration on the surface of the system to 15 Å and, subsequently, to 50 Å results in an increase in the intensity of the silicon Auger signal; in the process, the intensity of the signals associated with Auger transitions in the metal decreases gradually, and for a silicon layer 50 Å thick, these signals are not observed in the spectrum. It is readily seen from Fig. 1 that the Auger peaks of both lanthanum and silicon in the Si/La(0001) system vary only weakly in energy in all stages of film formation and lie approximately at the positions that correspond to the pure bulk crystals of the metal and silicon. At the same time, the shape of the Si(*LVV*) Auger peak undergoes changes. This shape is qualitatively characterized by the *A*/*B* ratio of the height of the maximum to the depth of the minimum with respect to the background level, as is shown in Fig. 1. The shape of the peak obtained for the Si layer 50 Å thick coincides with that characteristic of pure crystalline silicon [10]. The shape of the Si(*LVV*) Auger peak for a 3-Å-thick silicon layer differs from that for pure crystalline silicon, which manifests itself

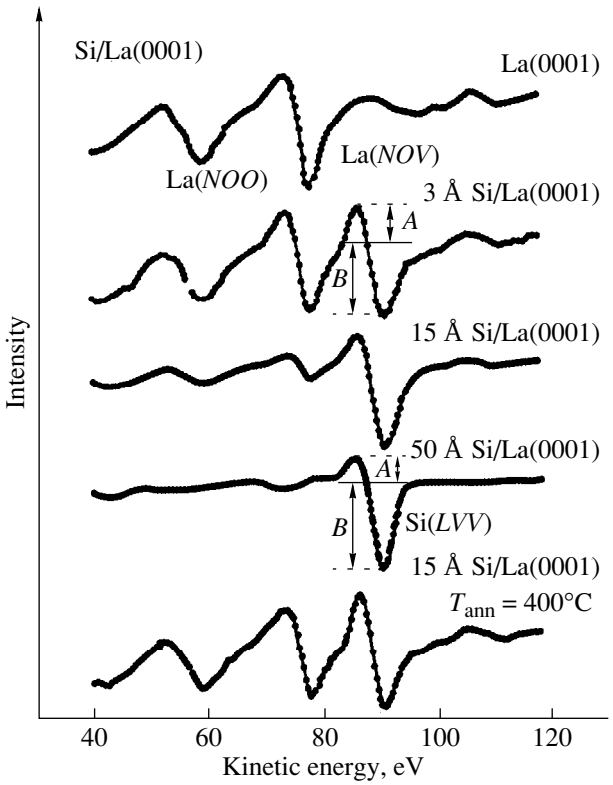

Fig. 1. Evolution of the Auger electron spectra in the course of room-temperature deposition of silicon layers of different thicknesses (3, 15, and 50 Å) onto the surface of an La(0001)/W(110) single-crystal layer and after heating of the system at 400°C.

in an increase in the *A*/*B* ratio. Upon heating the 15-Å-thick Si/La(0001) system at 400°C, the intensity of the lanthanum Auger signals in the spectrum increases to a value close to their initial intensity measured before silicon deposition on the metal surface. The shape of the silicon Auger peak varies substantially, and the *A*/*B* ratio for the system formed as a result of the heating is increased compared to that for pure silicon.

The Auger spectra of the Si/Gd(0001) system (Fig. 2) change in the same way as those of Si/La(0001). Figure 2 shows the Auger spectra for a clean Gd(0001) surface, silicon layers (3, 12, and 50 Å thick) deposited onto the Gd(0001) surface at room temperature, and a 12-Å-thick Si/Gd(0001) system heated at 400°C. The Si/Gd(0001) system is characterized by gadolinium Auger peaks at kinetic energies of 111 eV [Gd(*NOV*)] and 141 eV [Gd(*NVV*)] and by a silicon Si(*LVV*) Auger peak at 92 eV. Similar to the Si/La(0001) system, deposition of silicon onto the Si/Gd(0001) surface results in an increase in the intensity of the silicon Auger signal and a gradual decrease in the intensity of the metal Auger signals. Adsorption of a thick Si layer leads to the formation of a system whose Auger spectrum is similar to that of pure silicon. Heating the 12-Å-thick Si/Gd(0001) system at 400°C brings about an increase

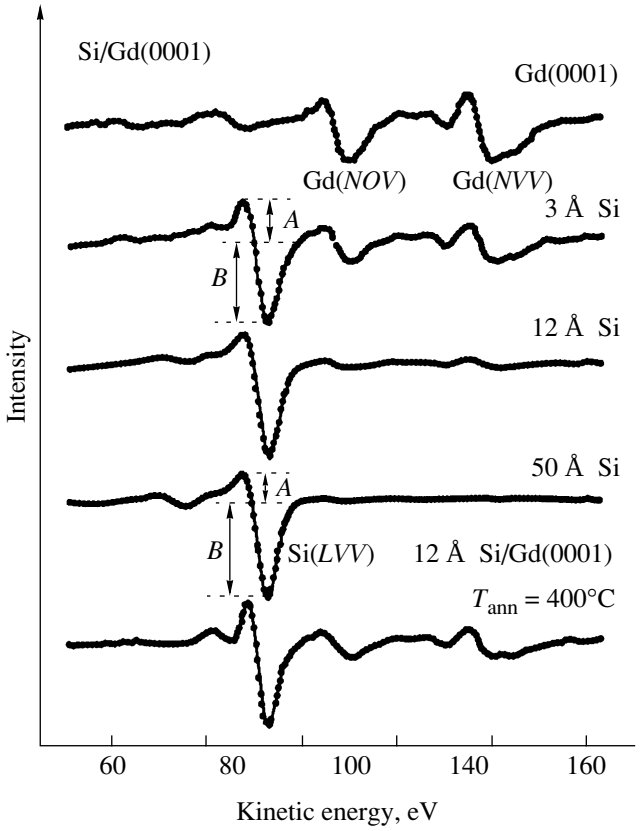

Fig. 2. Evolution of the Auger electron spectra in the course of room-temperature deposition of silicon layers of different thicknesses (3, 12, and 50 Å) onto the surface of a Gd(0001)/W(110) single-crystal layer and after heating of the system at 400°C.

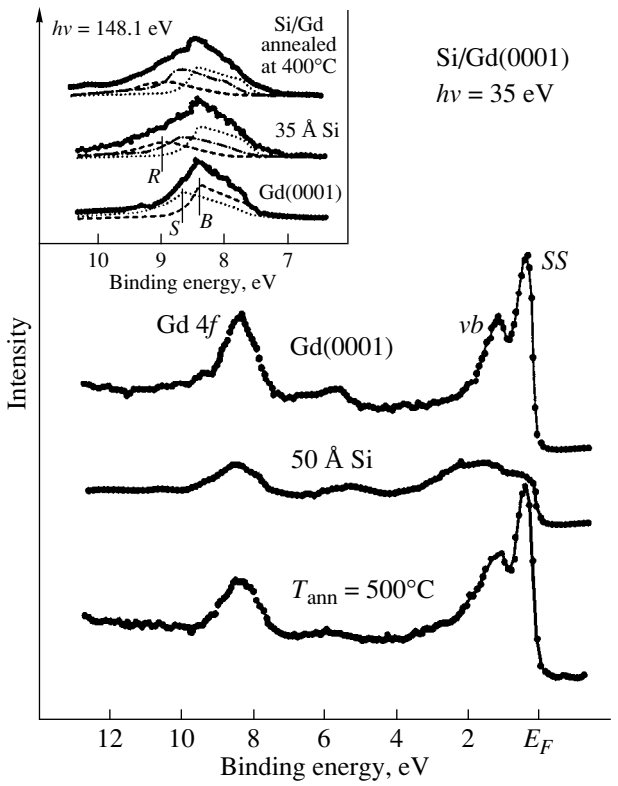

Fig. 3. Photoelectron spectra of the Gd valence band and Gd 4*f* electrons for a clean Gd(0001)/W(110) layer and a 50-Å-thick Si/Gd(0001)/W(110) system formed at room temperature and after heating at 500°C. The inset shows photoemission spectra of the Gd 4*f* electrons at the photoexcitation energy $h\nu$ = 148.1 eV, which corresponds to the resonant excitation energy of the 4*d*–4*f* transition in the metal, for a clean Gd(0001) surface, and a 35-Å-thick Si/Gd(0001) system produced at room temperature and after heating at 400°C.

in the intensity of the Gd Auger signals and a change in the shape of the silicon Auger peak. As in the case of Si/La(0001), the shape of the Si(*LVV*) Auger peak, which differs from that of bulk silicon, is also observed for the system formed upon the adsorption of a thin Si layer 3 Å thick on the Gd(0001) surface at room temperature.

Figure 3 displays the photoemission spectra recorded at a normal photoelectron takeoff from the sample surface for a clean Gd(0001) surface, after deposition of a 50-Å-thick Si layer onto the surface of the metal, and for a 50-Å-thick Si/Gd(0001) system heated at 500°C for 5 min. The spectrum of the clean Gd(0001) surface is characterized by peaks corresponding to photoemission from surface states near the Fermi level, *d* states of the valence band at a binding energy of approximately 1.2 eV, and 4*f* states of the metal at 8.3 eV. The emission near 6 eV is due to a slight oxygen impurity present on the metal surface. As is seen from Fig. 3, after the deposition of the Si layer 50 Å thick onto the Gd(0001) surface, the features corresponding to the surface states and the Gd valence band practically disappear in the spectrum of the system and the 4*f* signal of the metal decreases substantially in intensity (by approximately a factor of four). At the same time, a new broad feature is observed at a binding energy of approximately 2 eV. Heating of the system thus formed at 500°C restores the spectral features characteristic of a clean Gd(0001) surface. In this case, the 4*f* electron photoemission intensity increases to a value close to that of the Gd 4*f* electrons from a clean Gd(0001) surface. As a result, after the heating, the photoemission spectrum of the 50-Å-thick Si/Gd(0001) system becomes similar to that of the clean Gd(0001) surface before silicon deposition.

The inset to Fig. 3 shows the photoemission spectra of the region of the Gd 4*f* electronic states which were recorded at a resonant excitation energy of 148.1 eV. The spectra are shown for a clean Gd(0001) surface, a 35-Å-thick Si layer deposited onto the Gd(0001) surface at room temperature, and a 35-Å-thick Si/Gd(0001) system subjected to heating at 400°C. Analysis of the results obtained revealed that the spectra contain several components corresponding to the emission of 4*f*

electrons of different groups of atoms. The spectrum of a clean Gd(0001) surface consists of the component *B* due to photoemission from atoms in the bulk and the photoemission component *S* originating from atoms localized on the Gd surface. As is seen from the figure, adsorption of a 35-Å-thick Si layer reduces the intensity of the surface component *S* as compared to the total intensity of emission from the 4*f* states and results in the appearance of a new 4*f* emission component *R*. Heating the system brings about an increase in the intensity of the surface component and a decrease in that of the new component.

4. DISCUSSION

As follows from an analysis of Figs. 1 and 2, deposition of a thin Si layer 3 Å thick onto the La(0001) and Gd(0001) surfaces at room temperature results in the appearance of a Si(*LVV*) Auger peak in the spectra of the systems and its shape differs from that in the Auger spectrum of pure single-crystal silicon [10]. Because the Si(*LVV*) Auger peak is an indication of the chemical state of the Si atoms, the difference between its shape and the shape of the peaks characteristic of pure bulk silicon suggests a change in the chemical state of the silicon atoms in these systems compared to that in bulk silicon. This implies that, at room temperature, silicon chemically interacts with REM atoms on the La(0001) and Gd(0001) surfaces. This is supported by the appearance of a new reactive component *R* in the Gd 4*f* photoemission spectrum of the system formed by room-temperature deposition of a silicon layer 35 Å thick on the Gd(0001) surface (see inset in Fig. 3).

Further deposition of silicon results in a weakening of the metal substrate signals in the Auger spectra of the Si/La and Si/Gd systems, and they disappear completely at a silicon layer thickness of 50 Å. The features associated with the valence band and the surface state of the metal overlap with a new broad feature in the photoemission spectrum of the system (Fig. 3). According to studies on the electronic states of the Si valence band, this feature observed in the photoemission spectrum of the 50-Å-thick Si/Gd(0001) system can be assigned to the formation of sp^3 hybridized bonds between silicon atoms [11]. Therefore, it can be concluded that deposition of a sufficiently thick silicon layer (50 Å) onto an REM surface at room temperature brings about the formation of a continuous layer of silicon with the properties of bulk Si, which covers the metal surface and the silicide layer formed at the interface.

The formation of a continuous silicon layer on the surface of the system produced by room-temperature deposition of a 50-Å-thick silicon layer onto the La(0001) and Gd(0001) surfaces allows us to conclude that, at room temperature, atoms from the deposited silicon layer and from the metal substrate do not undergo mutual diffusion to the extent which would involve a considerable part of the deposited silicon. It can be assumed that the high stability of the La(0001) and Gd(0001) single-crystal surfaces or of the silicide layer formed on these surfaces at room temperature creates a barrier to mutual diffusion of the silicon and metal atoms. The question naturally arises as to whether such a barrier can be overcome, for instance, by heating the system to a high temperature at which mutual diffusion of the silicon and metal atoms would take place.

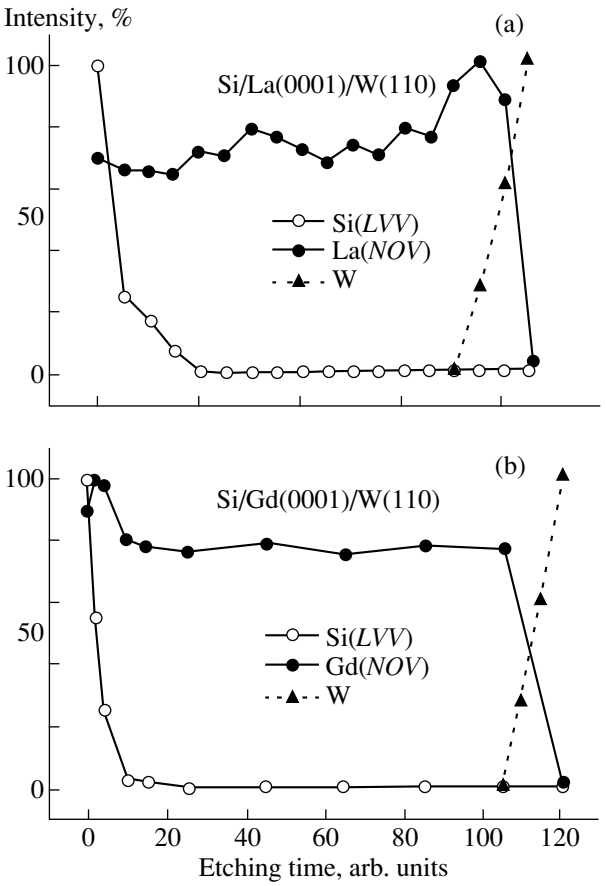

Fig. 4. Relative variation of the Si($L_{23}VV$), La($N_{45}O_{23}V_{67}$), and Gd($N_{45}O_{23}V_{67}$) Auger peak amplitudes in the course of layer-by-layer etching of (a) 15-Å Si/La(0001)/W(110) and (b) 12-Å Si/Gd(0001)/W(110) systems preliminarily heated at 400°C.

As can be seen from the Auger spectra of the 15-Å Si/La(0001) and 12-Å Si/Gd(0001) systems heated at 400°C, the heating results in an increase in the intensity of the Auger signals of the metals as compared to silicon (Figs. 1, 2). The shape of the Si(*LVV*) Auger peak also changes and becomes similar to that observed in the case of the epitaxial REM silicides on the surface of single-crystal silicon [10]. The fact that the energy location of the Auger peaks virtually does not change for the system after the heating, as compared to a clean metal surface and a bulk silicon layer, suggests a covalent nature of the chemical interaction with a weak

charge transfer between the atoms, which is characteristic of chemical bonding in REM silicides. The heating of even a thick (50 Å) Si layer deposited onto the Gd(0001) surface at room temperature produces a system whose valence-band photoemission spectrum is similar to that of a clean Gd(0001) surface, even though the presence of silicon on the surface becomes manifest in the observation of a reactive component in the 4*f* electron photoemission of the metal (see inset in Fig. 3). This means that the system consists of considerable areas of clean metal surface and regions coated by metal silicide occupying a smaller part of the surface area of the system. This is supported by the fact that the silicide does not provide a noticeable contribution to the valence-band photoemission spectra of the heated system. If we assume that upon heating, silicon atoms form silicide which builds up on the surface in the form of islands, it becomes difficult to understand why the silicide formed from a silicon layer 50 Å thick weakly manifests itself in the valence-band photoemission spectra of the system. It can be assumed that the major part of silicon leaves the surface in the course of heating. One possible explanation for this effect could be the diffusion of silicon into the bulk of the metal substrate or to the REM/W(110) interface.

In order to establish whether Si atoms diffuse under heating of the system into the bulk of the metal or to the REM/W(110) interface, the heated 12-Å Si/Gd(0001) and 15-Å Si/La(0001) systems were subjected to layer-by-layer etching with Ar^+ ions. The etching of each layer was followed by the recording of Auger electron spectra. Analysis of the results obtained revealed dependences of the intensities of the Si(*LVV*), La(*NOV*), and Gd(*NOV*) Auger signals on the depth of the removed layer, which are displayed in Figs. 4a and 4b for the Si/La(0001) and Si/Gd(0001) systems, respectively. These dependences reproduce the depth profiles of the silicon and metal concentrations in the system. We readily see that the intensity of the silicon Auger signal and, hence, the silicon atom concentration on the surface of the system decrease with an increase in the thickness of the removed layer. As the depth of etching increases, the silicon concentration in both the Si/La and Si/Gd systems decreases almost to zero and the silicon Auger signal does not appear until the etching is terminated; in this case, the Auger spectra contain only the signal due to the tungsten substrate. The intensities of the La and Gd Auger signals undergo changes at the beginning and the end of the etching, i.e., at the Si/REM and REM/W(110) interfaces, which is accounted for by the effect of the interface structure. On the whole, the Auger signal intensity of the metal in the system varies only weakly with the depth of the removed layer and decreases to zero at the end of the etching, when the Auger signal due to the tungsten substrate appears.

The depth profiles of the Si and metal atoms in the Si/La(0001) and Si/Gd(0001) systems indicate that Si is present only on the surface of the systems and not in the bulk of the metal or at the REM/W(110) interface. Therefore, we can conclude that heating of the Si/La(0001) and Si/Gd(0001) systems does not give rise to diffusion of silicon atoms into the bulk of the metal substrate or to the tungsten substrate interface. This suggests that, upon heating of the Si/La(0001) and Si/Gd(0001) systems, silicon and silicide formed at the interface between the deposited silicon layer and the metal substrate diffuse over the surface of the single-crystal metal layer and build up on surface defects, such as breaks in the metal layer, or at the sample boundary, which may become a subject of further study of the Si/REM system.

5. CONCLUSION

The present study of the Si/La(0001) and Si/Gd(0001) systems by photoemission and Auger electron spectroscopy combined with layer-by-layer Ar^+ ion etching allowed us to conclude that deposition of a silicon layer onto Gd(0001) and La(0001) surfaces at room temperature activates the formation of silicide at the Si/REM interface; however, no mutual diffusion of silicon and metal atoms occurs. Further deposition of silicon brings about the formation of a continuous silicon layer on the surface of the system. When the Si/La(0001) and Si/Gd(0001) systems are heated at 400°C, silicon atoms do not diffuse into the bulk of the substrate or to the REM/W(110) interface. It was conjectured that silicon and silicide formed at the Si/REM interface at room temperature diffuse under heating over the (0001) surface of the single-crystal metal and build up on surface defects and at the sample boundary.

ACKNOWLEDGMENTS

The authors are grateful to the administration and personnel of the BESSY I Synchrotron Radiation Center (Berlin, Germany) for the opportunity to perform photoemission experiments on a synchrotron beam. The authors thank Prof. G. Kaindl and O. Weschke of the Free University (Berlin) for providing the research equipment on which to carry out the photoemission experiments and for their useful discussions of the results.

This work was supported by the "Surface Atomic Structures" Program (project no. 2.1.99) and the Russian Foundation for Basic Research (project no. 96-02-00045G).

REFERENCES

1. Falko P. Netzer, J. Phys.: Condens. Matter **7**, 1023 (1995).
2. L. Braicovich, *The Chemical Physics of Solid Surfaces and Heterogeneous Catalysis*, Ed. by D. A. King and D. P. Woodruff (Elsevier, Amsterdam, 1988), Vol. 5.

3. R. Anderson, J. E. Baglin, J. J. Dempsey, *et al.*, Appl. Phys. Lett. **35**, 285 (1979).
4. K. N. Tu, R. D. Thompson, and B. Y. Tsaur, Appl. Phys. Lett. **38**, 626 (1981).
5. H. Norde, Pires J. de Sousa, F. M. Heurle, *et al.*, Appl. Phys. Lett. **38**, 626 (1981).
6. J. A. Martín-Gago, C. Rojas, C. Polop, *et al.*, Phys. Rev. B **59**, 3070 (1999).
7. T. Suzuki and Y. Gotoh, Thin Solid Films **330**, 125 (1998).
8. A. M. Shikin, A. Yu. Grigor'ev, G. V. Prudnikova, *et al.*, Fiz. Tverd. Tela (St. Petersburg) **42**, 942 (2000) [Phys. Solid State **42**, 973 (2000)].
9. C. Schüßler-Langeheine, R. Meier, H. Ott, *et al.*, Phys. Rev. B **60**, 3449 (1999).
10. M. Sancrotti, A. Iandelli, G. L. Olcese, and A. Palenzona, Phys. Rev. B **44**, 3328 (1991).
11. G. Le Lay, M. Göthelid, T. M. Grehk, *et al.*, Phys. Rev. B **50**, 14277 (1994).

Translated by G. Skrebtsov

Physics of the Solid State, Vol. 43, No. 2, 2001, pp. 386–396. Translated from Fizika Tverdogo Tela, Vol. 43, No. 2, 2001, pp. 369–378.

POLYMERS AND LIQUID CRYSTALS

The Supersymmetric Theory of Disordered Heteropolymers

A. I. Olemskoĭ and V. A. Brazhnyĭ

Sumy State University, Sumy, 244007 Ukraine
e-mail: alexander@olem.sumy.ua
valera@ssu.sumy.ua

Received July 27, 1999

Abstract—The effective equation of motion for describing the alternation of monomers of different sorts along a heteropolymer chain is proposed. This equation is used for constructing a self-consistent supersymmetric scheme that makes it possible to derive equations for the structure factor and the Green function. The effects of memory and ergodicity loss are studied as functions of the temperature and the intensity of the frozen disorder in the alternation of monomers. The phase diagram that determines the existence domains of nonergodic and frozen states is constructed. © *2001 MAIK "Nauka/Interperiodica".*

1. INTRODUCTION

In recent years, considerable interest has been expressed by researchers in disordered heteropolymers which represent random sequences of monomers of different sorts (see [1–3] and references therein). As the temperature decreases, these systems can undergo phase transformations of two types: glass transition and microphase separation. In the course of the glass transition, among the possible states of an infinite set, a disordered heteropolymer chooses the sole nonequilibrium but stationary state at which a certain conformation and a sequence of alternating monomers (of the DNA-type molecule) are fixed. The problem of describing these transitions reduces to the development of the simplest and most adequate procedure for averaging thermodynamic quantities over a frozen disorder. A similar problem first arose in the study of spin glasses [4].

The microphase separation phenomenon inherent in block copolymers resides in the formation of a spatial periodic distribution of monomers in the form of one-dimensional lamellar structures, hexagonal lattices of cylinders, body-centered lattices of spheres, etc. [2, 3]. The characteristic feature of these structures lies in the fact that the chemical bond between blocks prevent the macroscopic separation observed in homopolymer solutions. The microphase separation was initially studied in terms of the mean-field theory for an *A–B* block copolymer with an arbitrary fraction f of monomers of the *A* sort [5]. It was found that, at $f \neq 0.5$, a decrease in the temperature leads to a first-order phase transition with the formation of a spatial periodic structure whose wavelength $2\pi/k_0$ is of an order of the block size and does not depend on the temperature. Since the phase transition results in the divergence of the structure factor on the surface of a sphere $k_0 \neq 0$ rather than at the only point $k_0 = 0$ (as is the case in the macrophase separation), the order parameter fluctuations make a divergent contribution to the thermodynamic quantities [6]. As a result, at $f = 0.5$, a continuous second-order phase transition transforms into a weak first-order phase transition and the phase diagram changes substantially [7]. When changing over from the block copolymer to the disordered heteropolymer, both transformations (glass transition and microphase separation) take place; however, there appears a strong temperature dependence of the spatial period [1, 8]. Moreover, the field approach demonstrated that fluctuations suppress both the microphase separation and the glass transition in a disordered polymer [9, 10].

As in the case of spin glasses [4], the theory of disordered heteropolymers is based on the replica method (see [1]). In addition, the transfer-matrix method [11], the kinetic approach [12], and other methods [13] were used; however, the range of their applicability appeared to be appreciably narrower than that of the replica approach. At the same time, it is known from the spin glass theory that the replica method in the framework of the Sherrington–Kirkpatrick model [14] turns out to be equivalent to the supersymmetric approach [15]. Except for the known disadvantages of the replica method, the advantage of the supersymmetric approach stems from the fact that only two superfield components with a clear physical meaning play a significant part within the simplest scheme [16].

The supersymmetric scheme, as applied to polymers, was proposed by Vilgis [17]; however, this approach had no further development. The present work was undertaken with the aim of filling this gap. As will be shown below, the introduction of the supersymmetric approach for describing the system with a frozen disorder is as natural as the application of complex calculus to the phase transition theory (see also [18]).

This paper is organized as follows. In Section 2, we obtain the effective equation of motion for describing the alternation of monomers of different sorts along a polymer chain [19]. The form of this equation is speci-

fied by the effective Hamiltonian of an disordered heteropolymer, which is defined in Section 3. In Section 4, on the basis of the standard generating functional method [20], which accounts for the effective equation of motion, we construct the supersymmetric field theory for describing the behavior of the system. In Section 5, we expand the supersymmetric correlator in the optimum basis set and deduce the structure factor and the retarded Green function for which the self-consistent equations are found [21]. These quantities allow us to describe (Section 6) the memory and nonergodicity parameters as functions of the Flory parameter and the frozen disorder in the alternation of monomers of different sorts. The discussion of the results obtained is given in Section 7.

2. EFFECTIVE EQUATION OF MOTION

As is known, the field scheme for stochastic systems is based on the Langevin dynamic equation [20]. However, the presence of covalent bonds forming the polymer chain renders this scheme inefficient, because the dynamic theory of polymers is much more complex compared to statistical mechanics of usual many-particle systems [22]. Therefore, in order to describe the disordered heteropolymer, it is necessary to obtain the effective equation of motion instead of the dynamic equation.

Let us consider the simplest case of a homopolymer that can be considered a Gaussian chain for which the probability density of determining the vector $\mathbf{R}$ connecting the chain origin with the Nth node is specified by the function $\Psi(\mathbf{R}, N)$. This function satisfies the Schrödinger equation with the imaginary time $-iN$ [22]:

$$\partial\Psi/\partial N = (D\partial^2/\partial\mathbf{R}^2 - U(\mathbf{R}, N))\Psi, \quad (1)$$

where $N \gg 1$ is the number of monomers, $D = b^2/6$ is the effective diffusion coefficient determined by the Kuhn segment length b, and $U(\mathbf{R}, N)$ is the external field. In the limit $N \longrightarrow \infty$, the solution to Eq. (1) can be written as

$$\Psi(\mathbf{R}, N) = \int \exp(-S_{\mathbf{R},N}\{\mathbf{r}(n)\}/2D)D\mathbf{r}(n), \quad (2)$$

where the functional integration is performed over the dependence of the coordinate $\mathbf{r}(n)$ of a monomer on its number n in the chain; and the action $S(\mathbf{R}, N) \equiv S_{\mathbf{R}N}\{\mathbf{r}(n)\} = \int_0^N L_0(\mathbf{r}(n))dn$, which corresponds to the chain ends at the fixed points $\mathbf{r}(0) = \mathbf{O}$ and $\mathbf{r}(N) = \mathbf{R}$, is determined by the Lagrangian of the Euclidean field theory [20, 22]:

$$L_0 = \frac{1}{2}\left(\frac{d\mathbf{r}(n)}{dn}\right)^2 + 2DU(\mathbf{r}, n). \quad (3)$$

Here, the first term obtained in the continuum approximation $\mathbf{r}(n+1) - \mathbf{r}(n) \longrightarrow d\mathbf{r}(n)/dn$ plays the role of kinetic energy and accounts for the presence of a covalent bond between chain monomers [22]. Substitution of distribution (2) into Eq. (1) gives the Jacobi-type equation

$$\frac{\partial S}{\partial N} = D\frac{\partial^2 S}{\partial\mathbf{R}^2} - \frac{1}{2}\left(\frac{\partial S}{\partial\mathbf{R}}\right)^2 + 2DU. \quad (4)$$

By introducing the generalized momentum $\mathbf{p} \equiv \partial S/\partial\mathbf{R}$ and the total derivative $d\mathbf{p}/dN \equiv \partial\mathbf{p}/\partial N + (\mathbf{p}\partial/\partial\mathbf{R})\mathbf{p}$, we reduce the nonlinear equation (4) to the Burgers linear equation

$$d\mathbf{p}/dN = D(\partial^2\mathbf{p}/\partial\mathbf{R}^2 + 2\partial U/\partial\mathbf{R}). \quad (5)$$

Relationships (1)–(5) provide the basis for the theory of direct polymers, the kinetic theory of surface roughening, etc. (see [23]).

In our case, an important point is that the Schrödinger equation (1) transforms into the Fokker–Planck equation [24]

$$\frac{\partial P}{\partial N} = \left(D\frac{\partial^2}{\partial\mathbf{R}^2} - \frac{\partial}{\partial\mathbf{R}}\mathbf{F}\right)P, \quad (6)$$

if we introduce the probability

$$P(\mathbf{R}, N) = \Psi(\mathbf{R}, N)\exp\{-V(\mathbf{R})/2D\}. \quad (7)$$

The dependence of this probability on $\mathbf{R}$ is governed by the effective potential

$$V \equiv -\int \mathbf{F}\,d\mathbf{R}, \quad (8)$$

where the force $\mathbf{F}$ is related to the initial potential U as follows:

$$U = \frac{1}{4D}\mathbf{F}^2 + \frac{1}{2}\frac{\partial\mathbf{F}}{\partial\mathbf{R}}. \quad (9)$$

According to the theory of stochastic systems [25], the Fokker–Planck equation (6) corresponds to the Langevin equation

$$\partial\mathbf{R}/\partial N = \mathbf{F}(\mathbf{R}, N) + \zeta(N), \quad (10)$$

which determines the stochastic dependence $\mathbf{R} = \mathbf{R}(N)$. Here, the Langevin source ζ is fixed by the white noise conditions

$$\langle\zeta(N)\rangle = 0, \quad \langle\zeta(N)\zeta(N')\rangle = 2D\delta(N - N'), \quad (11)$$

where the angle brackets designate the averaging over distribution (7).

In order to change over from the above case of a homopolymer to the main subject of our investigation, namely, the disordered heteropolymer *A–B*, it is necessary to take into account that the stochasticity manifests itself not only in the spatial arrangement of monomers, but also in the alternation of their sorts *A* and *B* along the chain. Formally, this is reflected by assigning the Ising variable $\theta(n)$ to each nth node [$\theta(n) = 1$ if the nth monomer is of the *A* sort and $\theta(n) = -1$ in another case]. With an increase in the node number n, the variable $\theta(n)$ changes in much the same manner as the spin

reorientation in the Glauber dynamics [26]. For the effective spin $\sigma(n) \equiv \theta(n) - \overline{\theta(n)}$, which is reckoned from the mean value $\overline{\theta(n)}$, the transfer matrix method leads to the correlator [11]

$$\overline{\sigma(n)\sigma(n')} = C_2 \exp(-|n-n'|/l),$$
$$C_2 \equiv 4f(1-f), \quad f \equiv (1/2)(1+\overline{\theta(n)}), \tag{12}$$

where the bar means the averaging over the composition (frozen) disorder, l is the correlation length, and f is the fraction of monomers of the A sort.

It can easily be shown that the pseudospin variable $\sigma(n)$ defined by the exponential correlator (12) obeys the effective equation of motion

$$d\sigma/dn = -\sigma/l + s(n), \tag{13}$$

where the stochastic source $s(n)$ is represented by the white noise

$$\overline{s(n)} = 0, \quad \overline{s(n)s(n')} = 2C_2 l^{-1}\delta(n-n'). \tag{14}$$

According to Eq. (13), the relationship between the microscopic quantity $\sigma(n)$ and the stochastic variable $s(n)$ has the form

$$\sigma(n) = \int_0^n e^{-(n-m)/l} s(m)\,dm. \tag{15}$$

Conditions (14) are met when the white noise $s(n)$ is described by the Gaussian distribution

$$P\{s(n)\} = (4C_2\pi/l)^{-1/2} \exp\left\{-\frac{l}{4C_2}\int_0^N s^2(n)\,dn\right\} \tag{16}$$

with the frozen disorder intensity $4C_2 l^{-1}$. Correspondingly, the order parameter is determined by the local mean

$$\eta(\mathbf{r}, n) \equiv (4C_2)^{-1/2}\overline{\sigma(n)\delta(\mathbf{r}-\mathbf{r}(n))}. \tag{17}$$

Hereafter, the monomer volume will be taken equal to unity.

Compared to equality (10), the effective equation of motion for field (17) should contain the term $D\partial^2\eta/\partial\mathbf{r}^2$, which accounts for the presence of an inhomogeneity. By changing over to the Fourier transform,

$$\eta_{\mathbf{k}}(n) = N^{-1/2}\int \eta(\mathbf{r}, n) e^{-i\mathbf{kr}}\,d\mathbf{r}, \tag{18}$$

for which this inhomogeneity takes the form $-Dk^2\eta_k$, we obtain

$$\partial\eta_{\mathbf{k}}/\partial n = -(ak)^2\eta_{\mathbf{k}} - \partial\mathcal{H}/\partial\eta_{\mathbf{k}}^* + \zeta_{\mathbf{k}}. \tag{19}$$

Here, as before, the continuum limit $n \gg 1$ is used for the effective time n, the characteristic monomer scale is specified by the renormalized segment length $a \equiv D^{1/2} = 6^{-1/2}b$, the force $f_{\mathbf{k}} = -\partial\mathcal{H}/\partial\eta_{\mathbf{k}}^*$ [cf. relationship (8)] is determined by the effective Hamiltonian $\mathcal{H}$, and the white noise is fixed by the conditions

$$\langle\zeta_{\mathbf{k}}\rangle = 0, \quad \langle\zeta_{\mathbf{k}}^*(n)\zeta_{\mathbf{k}'}(n')\rangle = \delta_{\mathbf{k}\mathbf{k}'}\delta(n-n'), \tag{20}$$

where the angle brackets mean the averaging over the thermal disorder, which, unlike the white noise conditions (11), is normalized to unity.

3. EFFECTIVE HAMILTONIAN

In order to derive the effective Hamiltonian $\mathcal{H}\{\eta\} \equiv \Omega'\{m\}$ [27] which determines the form of Eq. (19), we consider the thermodynamic potential $\Omega'\{m\}$ obtained by averaging over the conformation and composition disorders. The corresponding mean of the order parameter (17) has the form

$$m(\mathbf{r}) \equiv \sum_n \langle\eta(\mathbf{r}, n)\rangle = (4C_2)^{-1/2} \times \sum_n \overline{\langle\sigma(n)\delta(\mathbf{r}-\mathbf{r}(n))\rangle}. \tag{21}$$

According to the standard procedure [20], the statistical sum of the system can be written in the form of a functional integral

$$Z = \int Dm(\mathbf{r}) \exp\left\{C_2\chi\int m^2(\mathbf{r})\,d\mathbf{r}\right\} \times \overline{\left\langle \delta\left\{\sum_n \delta(\mathbf{r}-\mathbf{r}(n)) - 1\right\}\right.} \times \left.\overline{\delta\left\{\sum_n (4C_2)^{-1/2}\sigma(n)\delta(\mathbf{r}-\mathbf{r}(n)) - m(\mathbf{r})\right\}}\right\rangle. \tag{22}$$

Here, $\chi > 0$ is the Flory composition parameter, the first δ-function takes into account the incompressibility condition, and the second δ-function accounts for the definition of the order parameter (21). Then, it is necessary to represent the δ-functions in the form of a Laplace functional expansion in terms of the auxiliary fields J_ρ and J_m. As a result, relationship (22) takes the exponential form with the index $\int(J_\rho + J_m m)\,d\mathbf{r} - \Omega\{J_\rho, J_m\}$, where the last term is the free energy averaged over conformational and configurational sets at the specified fields J_ρ and J_m. The stationary values $\bar{J}_\rho$ and $\bar{J}_m$ of these fields are determined by the conditions $\delta\Omega/\delta J_\rho = 0$ and $\delta\Omega/\delta J_m = -m$. Substitution of these values into the

functional $\Omega\{J_\rho, J_m\}$ gives the thermodynamic potential defined by the expression $Z = \int Dm_{\mathbf{k}} \exp(-\Omega'\{m_{\mathbf{k}}\})$, where (for more details, see [1, 11, 28])

$$\Omega' = \sum_{\mathbf{k}} \tau_{\mathbf{k}} |m_{\mathbf{k}}|^2 + \frac{1}{2}\sum_{\mathbf{k}\mathbf{k}'} w_{\mathbf{k}\mathbf{k}'} |m_{\mathbf{k}}|^2 |m_{\mathbf{k}'}|^2 + \int v(\mathbf{r}) d\mathbf{r}, \quad \tau_{\mathbf{k}} \equiv \tau + (ak)^2, \quad \tau \equiv l^{-1} - C_2\chi. \tag{23}$$

Here, the contribution from the inhomogeneity is included in the quadratic term, the appearance of the terms proportional to l^{-1} is associated with the procedure of averaging over the frozen disorder in distribution (15), and the term containing the kernel $w_{\mathbf{k}\mathbf{k}'} = 4N^{-1}(la)^{-2}(\mathbf{k}^2 + \mathbf{k}'^2)^{-1}$ arises from the averaging over distribution (7) (the given relationship is consistent with the results obtained in [1, 11], whereas the replica method leads to the opposite sign [9, 29]). The last term accounting for the self-action effects can be represented by the expansion [1, 11]

$$v = -(\mu/3!)m^3 + (\lambda/4!)m^4, \quad \mu \equiv 12C_3C_2^{-1/2}l^{-1}, \quad \lambda \equiv 24(1 + 5C_3^2/C_2)l^{-1}, \quad C_2 \equiv 4f(1-f), \quad C_3 \equiv |1-2f|. \tag{24}$$

As mentioned above, the applied method is based on formulas (12), which enable one to express the correlators of the frozen disorder with the use of transfer matrices. The replica method is more popular. In the framework of this method, the field J_m and the order parameter m acquire the replica index α over which the summation from 1 to $n \longrightarrow 0$ should be carried out in Hamiltonian (23) [4]. Then, the quadratic contribution is given by

$$\frac{1}{2}\sum_{\mathbf{k}\alpha} A_{\alpha\alpha}(\mathbf{k})|m_\alpha(\mathbf{k})|^2 + \frac{1}{2}\sum_{\substack{\mathbf{k}\\ \alpha\neq\beta}} A_{\alpha\beta}(\mathbf{k})m_\alpha(\mathbf{k})m_\beta(-\mathbf{k}), \tag{25}$$

where $A_{\alpha\alpha}(\mathbf{k}) \longrightarrow 2\tau_{\mathbf{k}}$ in the limit $n \longrightarrow 0$ for the coincident replicas. As was shown by the example of spin glasses, the characteristic feature of the systems with a frozen disorder resides in a hierarchic structure of the state space, which is characterized by a random overlap of different replicas [4]. Consequently, the overlap parameter $A_{\alpha\beta}(\mathbf{k})$ in the second term in formula (25) is a stochastic quantity over which the averaging should be performed. We assume that the corresponding distribution has the simplest Gaussian form

$$\mathcal{P}\{A_{\alpha\beta}(\mathbf{k})\} \propto \exp\left\{-\frac{1}{8}\sum_{\substack{\mathbf{k}_1\mathbf{k}_2\\ \alpha\neq\beta}} u^{-1}_{\mathbf{k}_1\mathbf{k}_2} A_{\alpha\beta}(\mathbf{k}_1)A_{\alpha\beta}(-\mathbf{k}_2)\right\} \tag{26}$$

with the variance $u_{\mathbf{k}_1\mathbf{k}_2} \equiv \sigma^2(la)^{-2}N^{-1}(\mathbf{k}_1^2 + \mathbf{k}_2^2)^{-1}$, which is specified by the parameter σ (see [9]). Then, after the averaging of the statistical sum $Z = \int Dm_{\mathbf{k}} \exp(-\Omega'\{m_{\mathbf{k}}\})$, the second term in formula (25) takes the form

$$-\frac{1}{2}\sum_{\substack{\mathbf{k}_1\mathbf{k}_2\\ \alpha\neq\beta}} u_{\mathbf{k}_1\mathbf{k}_2} m_\alpha(\mathbf{k}_1)m_\beta(-\mathbf{k}_1)m_\alpha(-\mathbf{k}_2)m_\beta(\mathbf{k}_2). \tag{27}$$

As a result, the thermodynamic potential (23) has the replica form

$$\Omega' = \sum_{\mathbf{k}\alpha} \tau_{\mathbf{k}} |m_\alpha(\mathbf{k})|^2 + \frac{1}{2}\sum_{\substack{\mathbf{k}_1\mathbf{k}_2\\ \alpha}} w_{\mathbf{k}_1\mathbf{k}_2} |m_\alpha(\mathbf{k}_1)|^2 |m_\alpha(\mathbf{k}_2)|^2 + \sum_\alpha \int v(m_\alpha) d\mathbf{r} - \frac{1}{2}\sum_{\substack{\mathbf{k}_1\mathbf{k}_2\\ \alpha\neq\beta}} u_{\mathbf{k}_1\mathbf{k}_2} m_\alpha(\mathbf{k}_1)m_\beta(-\mathbf{k}_1) \times m_\alpha(-\mathbf{k}_2)m_\beta(\mathbf{k}_2). \tag{28}$$

Relationship (28) eliminates the above contradiction in the choice of the effective Hamiltonian form: the positive contribution determined by the second term is associated with the interreplica interaction (see [1, 11]), whereas the negative contribution found in [9, 29] stems from the overlap of replicas. The different origin of these terms manifests itself in the fact that the former term leads to the renormalization of the quantity $\tau_{\mathbf{k}}$ and the latter term is responsible for the memory and nonergodicity effects.

In order to perform this renormalization (see [27]), one of the multipliers $|m_\alpha(\mathbf{k})|^2$ in the second term in relationship (28) should be replaced using the mean-field approximation by the bare Green function $G_{\mathbf{k}_0}$, which corresponds to $v = 0$ and $u_{\mathbf{k}_1\mathbf{k}_2} = 0$ and is determined by the equality independent of the number of the replica α; that is,

$$G^{-1}_{\mathbf{k}_0} = r + 2a^2(k - k_0)^2. \tag{29}$$

The parameters r and k_0 can be found by substituting relationship (29) into the corresponding Dyson equation:

$$G^{-1}_{\mathbf{k}_0} = \tau_{\mathbf{k}} + \sum_{\mathbf{k}'} w_{\mathbf{k}\mathbf{k}'} G_{\mathbf{k}'_0}. \tag{30}$$

Then, after the integration over the wave vector $\mathbf{k}'$, we obtain

$$r = \tau + (3/4\pi)l^{-2}(2r)^{-1/2}, \quad k_0^{-1} = 2\pi^{1/2}l(2r)^{1/4}a. \tag{31}$$

According to the first of these equalities, as the initial temperature difference τ increases, the positive parameter r smoothly increases with the asymptotics $r \sim \tau^{-2}$ at $\tau < 0$ and $r \sim \tau$ at $\tau \gg 1$ (Fig. 1a). This means that the

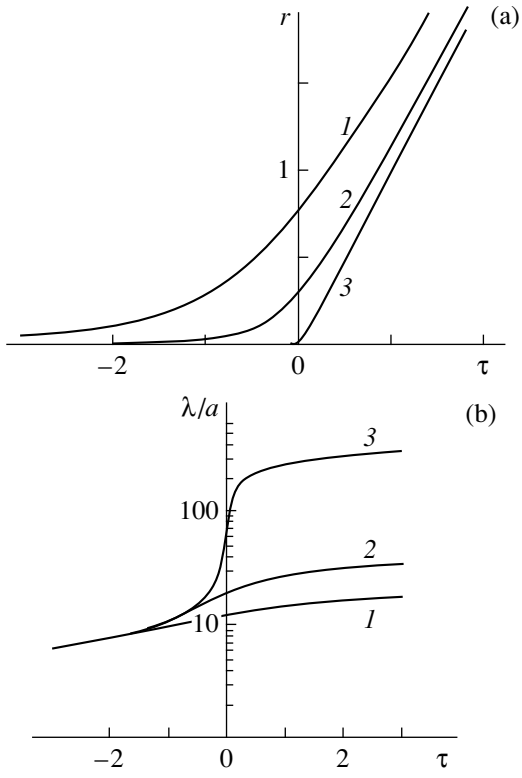

Fig. 1. Dependences of (a) the parameter r and (b) the period λ on τ at different correlation lengths l = (*1*) 0.5, (*2*) 1, and (*3*) 10.

fluctuations in the absence of self-action stabilize the disordered heteropolymer with respect to the microphase separation [9]. Specifically, according to the condition $r > 0$, only the first-order phase transition is possible. The second equality (31) determines the dependence of the spatial period $\lambda = 2\pi/k_0$ on the parameter r, which is inherent in disordered heteropolymers [1]. As can be seen from Fig. 1b, an increase in the temperature difference τ leads to a monotonic increase in the value of λ from 0 to ∞. Note that the larger the correlation length l, the faster the change in the period λ near the point $\tau = 0$.

The final expression for the Hamiltonian of the disordered heteropolymer follows from the thermodynamic potential (28) renormalized by fluctuations:

$$\mathcal{H} = \sum_{\mathbf{k}\alpha} \tau_{\mathbf{k}} |\eta_\alpha(\mathbf{k})|^2 + \sum_\alpha \int v(\eta_\alpha) d\mathbf{r}$$

$$- \frac{1}{2} \sum_{\substack{\mathbf{k}_1\mathbf{k}_2 \\ \alpha \neq \beta}} u_{\mathbf{k}_1\mathbf{k}_2} \eta_\alpha(\mathbf{k}_1)\eta_\beta(-\mathbf{k}_1)\eta_\alpha(-\mathbf{k}_2)\eta_\beta(\mathbf{k}_2), \quad (32)$$

$$r_{\mathbf{k}} \equiv r + 2a^2(k-k_0)^2, \quad u_{\mathbf{k}_1\mathbf{k}_2} \equiv \sigma^2 (la)^{-2} N^{-1} (\mathbf{k}_1^2 + \mathbf{k}_2^2)^{-1}.$$

Here, the kernel $v(\eta_\alpha)$ is defined by relationships (24), in which m is replaced by η_α.

4. INTRODUCTION OF SUPERFIELD

With the aim of constructing the supersymmetric scheme, let us consider the generating potential [20]

$$Z\{\eta_{\mathbf{k}}\} = \left\langle \delta\left(\frac{\partial \eta_{\mathbf{k}}}{\partial n} + \frac{\delta \mathcal{H}}{\delta \eta_{\mathbf{k}}^*} - \zeta_{\mathbf{k}}\right) \det \left| \frac{\delta \zeta_{\mathbf{k}}}{\delta \eta_{\mathbf{k}}} \right| \right\rangle, \quad (33)$$
$$\delta\mathcal{H}/\delta\eta_{\mathbf{k}}^* \equiv \partial\mathcal{H}/\partial\eta_{\mathbf{k}}^* + 2a^2(k-k_0)^2\eta_{\mathbf{k}},$$

where the angle brackets mean the averaging over the noise $\zeta_{\mathbf{k}}(n)$, the δ-function accounts for the form of the effective equation of motion (19), and the determinant is the Jacobian of transformation from the variable $\zeta_{\mathbf{k}}$ to $\eta_{\mathbf{k}}$. Now, we write the δ-function as a Laplace functional integral over the field $\varphi_{\mathbf{k}}(n)$. To derive relationship (33) in a canonical exponential form, we represent the determinant with the use of the Grassmann conjugate fields $\psi_{\mathbf{k}}(n)$ and $\bar{\psi}_{\mathbf{k}}(n)$, which satisfy the conditions [20]; that is,

$$\{\psi, \psi\} = \{\psi, \bar{\psi}\} = \{\bar{\psi}\bar{\psi}\} = 0,$$
$$\int D\psi = \int D\bar{\psi} = 0, \quad \int \bar{\psi}\psi D^2\psi = 1, \quad (34)$$
$$D^2\psi \equiv D\psi D\bar{\psi},$$

where the curly brackets designate the anticommutator. The averaging in relationship (33) over $\zeta_{\mathbf{k}}(n)$ with a Gaussiann distribution defined by formulas (20) gives the standard representation of the partition function

$$Z\{\eta\} = \int P\{\eta, \varphi; \psi, \bar{\psi}\} D\varphi D^2\varphi,$$
$$P\{\eta, \varphi; \psi, \bar{\psi}\} = \exp(-S\{\eta, \varphi; \psi, \bar{\psi}\}),$$
$$S = \int_0^N L dn, \quad L = \int [(\varphi\dot{\eta} - \bar{\psi}\dot{\psi} - \varphi^2/2) \quad (35)$$
$$+ (\mathcal{H}'\{\eta\}\varphi - \bar{\psi}\mathcal{H}''\{\eta\}\psi)] d\mathbf{r}.$$

Here, the dot designates the derivative with respect to the effective time and the prime denotes the functional derivative with respect to field (17).

With the use of direct substitution, it is easy to show that the Lagrangian which corresponds to the last equality in relationships (35) takes the canonical form [21]

$$L = \int \Lambda(\Phi) d^2\theta, \quad \Lambda \equiv \sum_{\mathbf{k}} (\bar{\mathcal{D}}\Phi_{\mathbf{k}}^*)(\mathcal{D}\Phi_{\mathbf{k}}) + \mathcal{H}\{\Phi_{\mathbf{k}}\}, \quad (36)$$
$$d^2\theta \equiv d\theta d\bar{\theta}$$

by introducing the supersymmetric operators

$$\mathcal{D} \equiv \frac{\partial}{\partial\bar{\theta}} - 2\theta\frac{\partial}{\partial n}, \quad \bar{\mathcal{D}} \equiv \frac{\partial}{\partial\theta} \quad (37)$$

and the four-component superfield

$$\Phi = \eta + \bar{\psi}\theta + \bar{\theta}\psi + \bar{\theta}\theta\varphi, \quad (38)$$

where the Grassmanian coordinates θ and $\bar{\theta}$ meet the same conditions (34) as the fields ψ and $\bar{\psi}$. The functional $\mathcal{H}\{\Phi\}$ has the form defined by relationship (32), in which the order parameter $\eta_{\mathbf{k}\alpha}$ is replaced by the superfield $\Phi_{\mathbf{k}}(\theta)$. In this case, the replica index α goes over into the Grassmanian variable θ, which is the formal reason for the identity between the replica method and the supersymmetric approach. The advantage of the latter approach is provided by the Grassmanian properties (34) whose fulfillment corresponds to the replica limit $n \longrightarrow 0$.

According to [16, 21], the combination $\bar{\psi}\psi$ determines the density of antiphase boundaries and the use of the four-component superfield corresponds to the strong segregation limit [2, 3]. We restrict our consideration to the simpler case of a weak segregation for which the interfaces are absent. Then, superfield (38) reduces to the two-component form

$$\phi = \eta + \vartheta\varphi. \quad (39)$$

Here, we introduced the self-consistent nilpotent quantity $\vartheta \equiv \bar{\theta}\theta$. Correspondingly, Lagrangian (36) takes the simple form

$$L = \int \lambda(\phi)d\vartheta, \quad \lambda \equiv \sum_{\mathbf{k}} \phi_{\mathbf{k}}^* D\phi_{\mathbf{k}} + \mathcal{H}\{\phi_{\mathbf{k}}\},$$
$$D = -\frac{\partial}{\partial\vartheta} + \left(1 - 2\vartheta\frac{\partial}{\partial\vartheta}\right)\frac{\partial}{\partial n}. \quad (40)$$

When written in terms of components of field (39), the equation of motion

$$D\phi_{\mathbf{k}} = -\delta\mathcal{H}/\delta\varphi_{\mathbf{k}}^* \quad (41)$$

leads to equations for the order parameter $\eta(n)$ and the amplitude of the most probable fluctuation $\varphi(n)$ of the conjugate field (see [21]).

5. CORRELATORS

In order to determine the supercorrelator

$$C_{\mathbf{k}}(n, \vartheta; n', \vartheta') \equiv \langle \phi_{\mathbf{k}}^*(n, \vartheta)\phi_{\mathbf{k}}(n', \vartheta')\rangle, \quad (42)$$

we multiply the equation of motion (41) by $\phi_{\mathbf{k}}^*$ and carry out the averaging. As a result, for the bare correlator that corresponds to the parameters $v = u = 0$ in Hamiltonian (32), we obtain [21]

$$C_{\nu\mathbf{k}}^{(0)}(\vartheta, \vartheta') = \frac{1 + (r_{\mathbf{k}} - i\nu)\vartheta + (r_{\mathbf{k}} + i\nu)\vartheta'}{r_{\mathbf{k}}^2 + \nu^2}. \quad (43)$$

Here, we used the "frequency" Fourier transform

$$C_\nu = \int_0^N C(n)e^{i\nu n}dn. \quad (44)$$

The Grassmanian structure of relationship (43) suggests that an arbitrary supercorrelator can be expanded in terms of the supersymmetric unit vectors

$$A(\vartheta, \vartheta') = \vartheta, \quad B(\vartheta, \vartheta') = \vartheta', \quad T(\vartheta, \vartheta') = 1. \quad (45)$$

Any **X**, **Y**, and **Z** of these unit vectors satisfy the functional product

$$X(\vartheta, \vartheta') = \int Y(\vartheta, \vartheta'')Z(\vartheta'', \vartheta)d\vartheta''. \quad (46)$$

Specifically, the supersymmetric unit vectors (45) conform to the following multiplication rules: $\mathbf{A}^2 = \mathbf{A}$, $\mathbf{B}^2 = \mathbf{B}$, $\mathbf{BT} = \mathbf{T}$, and $\mathbf{TA} = \mathbf{T}$; all the other products are equal to zero. Therefore, the set **A**, **B**, and **T** is complete and it is convenient to expand supercorrelator (42) in this set:

$$\mathbf{C} = G_+\mathbf{A} + G_-\mathbf{B} + S\mathbf{T}. \quad (47)$$

Hereinafter, the subscripts **k** and ν will be omitted for brevity. By using definitions (39) and (42) for the coefficients of expansion (47), we have

$$G_+ = \langle \eta\varphi^*\rangle, \quad G_- = \langle \eta^*\varphi\rangle, \quad S = \langle |\eta|^2\rangle. \quad (48)$$

Thus, the quantities $G_\pm$ are the advanced and retarded Green functions and S is the structure factor. According to relationships (43), (45), and (47), the components of the primeval correlator $\mathbf{C}^{(0)}$ have the standard form

$$G_\pm^{(0)} = (r \pm i\nu)^{-1}, \quad S^{(0)} = G_+^{(0)}G_-^{(0)} = (r^2 + \nu^2)^{-1}. \quad (49)$$

The self-consistent behavior of the system is determined by the Dyson equation, which, as applied to the heteropolymer, takes the form [18, 21]

$$\mathbf{C}^{-1} = (\mathbf{C}^{(0)})^{-1} - u\mathbf{C} - \mathbf{\Sigma}, \quad (50)$$

where $u = \sigma^2(2N)^{-1}(lak_0)^{-2}$ is the characteristic value of the interreplica overlap potential $u_{\mathbf{kk}'}$ at $\mathbf{k} = \mathbf{k}' \equiv \mathbf{k}_0$. By analogy with relationship (47), the self-energy superfunction $\mathbf{\Sigma}$, which describes the self-action effects can be expanded in terms of supersymmetric unit vectors:

$$\mathbf{\Sigma} = \Sigma_+\mathbf{A} + \Sigma_-\mathbf{B} + \Sigma\mathbf{T}. \quad (51)$$

Then, with due regard for relationship (49), the components of the Dyson equation (50) have the form [21]

$$G_\pm^{-1} + uG_\pm = (r \pm i\nu) - \Sigma_\pm, \quad (52a)$$

$$S = (1 + 2\pi C_2 l^{-1}\delta(\nu) + \Sigma)G_+G_-(1 - uG_+G_-)^{-1}. \quad (52b)$$

Here, the term containing the δ function is associated with the presence of the frozen disorder.

For the purpose of closing system (52), the components of the self-energy superfunction should be expressed in terms of supercorrelators. The use of the supersymmet-

ric perturbation theory [21] demonstrates that the matrix element of the self-energy superfunction with allowance made for the cubic and biquadratic anharmonicities [see expression (24)] can be written as

$$\Sigma(z, z') = \frac{\mu^2}{2}(C(z, z'))^2 + \frac{\lambda^2}{6}(C(z, z'))^3, \quad (53)$$

where $z \equiv \{\mathbf{r}, n, \vartheta\}$. An essential feature of this relationship is that the multiplication of matrix elements of the $C(z, z')$ supercorrelators should be considered in the usual rather than in the functional sense [15, 21]. As a result, the components of the self-energy superfunction (53) take the form

$$\Sigma_{\pm}(n) = \left(\mu^2 + \frac{\lambda^2}{2}S(n)\right)S(n)G_{\pm}(n), \quad (54a)$$

$$\Sigma(n) = \frac{1}{2}\left(\mu^2 + \frac{\lambda^2}{3}S(n)\right)S^2(n). \quad (54b)$$

It should be noted that, here, we used the space–time representation.

6. INCLUSION OF THE MEMORY AND NONERGODICITY EFFECTS

According to Edwards and Anderson [30], we introduce the composition memory parameter $q \equiv \langle\eta(n = N)\eta(n = 0)\rangle$ whose magnitude determines the correlation in the alternation of monomers along the entire polymer chain. Moreover, we use the nonergodicity parameter $\Delta \equiv g_0 - g$, which is defined by the difference between the isothermal $g_0 \equiv G_-(\nu = 0)$ and thermodynamic $g \equiv G_-(\nu \longrightarrow 0)$ susceptibilities. Then, the main correlators can be written in the extended form

$$G_{\pm}(\nu) = \Delta + G_{\pm 0}(\nu), \quad S(n) = q + S_0(n), \quad (55)$$

where the subscript 0 indicates the terms corresponding to the ergodic system without memory. Substitution of components (55) into relationships (54) gives

$$\Sigma_{\pm}(n) = \left(\mu^2 + \frac{\lambda^2}{2}q\right)q(\Delta + G_{\pm 0}(n)) + \Sigma_{\pm 0}(n), \quad (56a)$$

$$\Sigma_{\pm 0}(n) \equiv (\mu^2 + \lambda^2 q)S_0(n)G_{\pm 0}(n) + \frac{\lambda^2}{2}S_0^2(n)G_{\pm 0}(n),$$

$$\Sigma(n) = \frac{1}{2}\left(\mu^2 + \frac{\lambda^2}{3}q\right)q^2 + \left(\mu^2 + \frac{\lambda^2}{2}q\right)qS_0(n) + \Sigma_0(n), \quad (56b)$$

$$\Sigma_0(n) \equiv \frac{1}{2}(\mu^2 + \lambda^2 q)S_0^2(n) + \frac{\lambda^2}{6}S_0^3(n).$$

Here, the terms vanishing in the absence of memory are separated, the terms nonlinear with respect to the $G_{\pm 0}$ and S_0 correlators are combined in the $\Sigma_{\pm 0}$ and Σ_0 components, and the product $S_0\Delta \approx 0$ is omitted. It is characteristic that the "time" representation has been applied to determine components (56) of the self-energy superfunction, whereas the Dyson equation involves them in the "frequency" representation. This problem can be overcome by using the fluctuation-dissipative theorem [21]:

$$S_0(n \longrightarrow 0) = G_{\pm 0}(\nu \longrightarrow 0) \equiv g, \quad (57a)$$

$$\Sigma_{\pm 0}(\nu \longrightarrow 0) = \Sigma_0(n \longrightarrow 0) \equiv \frac{1}{2}(\mu^2 + \lambda^2 q)q^2 + \frac{\lambda^2}{6}g^3, \quad (57b)$$

where expression (56b) is included in the last relationship.

Substitution of the Fourier transforms of components (55) and (56) into the Dyson equation (52b) with due regard for relationships (57) leads to the following expressions:

$$q_0\left[1 - ug_0^2 - \frac{1}{2}\left(\mu^2 + \frac{\lambda^2}{3}q_0\right)q_0g_0^2\right] = C_2 l^{-1}g_0^2, \quad (58)$$

$$S_0 = \frac{(1 + \Sigma_0)G_+G_-}{1 - [u + (\mu^2 + \lambda^2 q/2)q]G_+G_-}. \quad (58a)$$

The first of these equations corresponds to δ-like contributions at $\nu = 0$ (this is indicated by the subscript 0) and reflects the memory effects, and the second equation is defined at the frequency $\nu \longrightarrow 0$. In this case, the characteristic product $G_+G_- \longrightarrow g^2$, and the pole of the structure factor (58a), that is,

$$u + \left(\mu^2 + \frac{\lambda^2}{2}q\right)q = g^{(-2)}, \quad g \equiv G_-(\nu \longrightarrow 0), \quad (59)$$

determines the point of ergodicity loss. By inserting the corresponding components (56a) and (57b) of the energy eigenfunction into the Dyson equation (52a) and taking into account the definition $g \equiv G_-(\nu \longrightarrow 0)$, we obtain the equation that relates the microscopic susceptibility to the memory parameter; that is,

$$1 - rg + ug^2 + \frac{\mu^2}{2}g[(g + q)^2 - q^2] + \frac{\lambda^2}{6}g[(g + q)^3 - q^3] = 0. \quad (60)$$

The set of Eqs. (58)–(60) describes the thermodynamic behavior of the disordered heteropolymer near the point of the ergodicity loss. By analogy with the spin glass theory [4], relationships (58) and (60) play the role of Sherrington–Kirkpatrick equations, and Eq. (59) determines the point of the de Almeida–Thouless instability. In this case, it should be remembered that, for a nonergodic system, it is necessary to differentiate the macroscopic and microscopic memory parameters q_0 and q and the corresponding susceptibilities g_0 and g (see [18, 21]). This hierarchy is explained by the fact that the microscopic characteristics that correspond to the limit $\nu \longrightarrow 0$ are the usual thermodynamic parameters and depend on the temperature (the Flory parameter χ). At

the same time, the macroscopic quantities q_0 and g_0 correspond to the point $\nu = 0$, depend on the frozen disorder parameter l, and, in the nonergodic region, acquire the values characteristic of the ergodicity loss point.

Since the system consisting of three Eqs. (58)–(60) is insufficient for determining the four parameters q_0, g_0, q, and g, it should be completed by the equality

$$q\left[1 - ug^2 - \frac{1}{2}\left(\mu^2 + \frac{\lambda^2}{3}q\right)qg^2\right] = C_2 l^{-1} g^2, \qquad (61)$$

which is a microscopic analog of Eq. (58) obtained after the separation of singular components. As is known from the spin glass theory [4], nonergodic systems exhibit a hierarchy of such singularities which corresponds to a set of infinitely decreasing "frequencies" $\nu \longrightarrow 0$. It is clear that Eqs. (58) and (61) correspond to $\nu = 0$ and the minimum ν among these frequencies. In turn, equality (59) at $\nu = 0$ gives

$$u + \left(\mu^2 + \frac{\lambda^2}{2}q_0\right)q_0 = g_0^{-2}, \quad g_0 \equiv G_-(\nu = 0). \qquad (62)$$

Equations (58) and (60)–(62) form the complete system for the determination of the q_0, g_0, q, and g quantities.

7. DISCUSSION

According to equalities (58) and (62), the macroscopic memory parameter q_0 is determined by the cubic equation

$$(\mu^2/2 + \lambda^2 q_0/3)q_0^2 = C_2 l^{-1}. \qquad (63)$$

The characteristic dependences $q_0(l)$ on the frozen disorder intensity are displayed in Fig. 2. At $f = 0.5$, when the contents of the A and B monomers are identical, the first term in Eq. (63) disappears and $q_0 \propto l^{1/3}$. In the case of diluted copolymer, for which the condition $f \ll 1$ ($C_2 \ll C_3$) is met, we obtain the dependence $q_0 \propto fl^{1/2}$.

The simultaneous solution of Eqs. (58), (60), and (62) gives the ergodicity loss point χ_0 whose location as a function of the correlation length l is shown in Fig. 3 (heavy line). It is characteristic that a nonzero value of the χ_0 parameter appears at the l value that exceeds the critical point. With a further increase in l, the χ_0 parameter reaches a maximum and, then, decreases monotonically. In this case, as could be expected, the ergodic region lying below the $\chi_0(l)$ dependence decreases with an increase in the correlation length. The condition $dg/d\chi = -\infty$, together with Eqs. (60) and (61), leads to the equality

$$u + \mu^2(g_f + q) + \frac{\lambda^2}{2}(g_f + q)^2 = g_f^{-2}. \qquad (64)$$

This equality determines the Flory parameter χ_f at the freezing point, below which the microscopic susceptibility g is equal to zero (Fig. 4). The corresponding

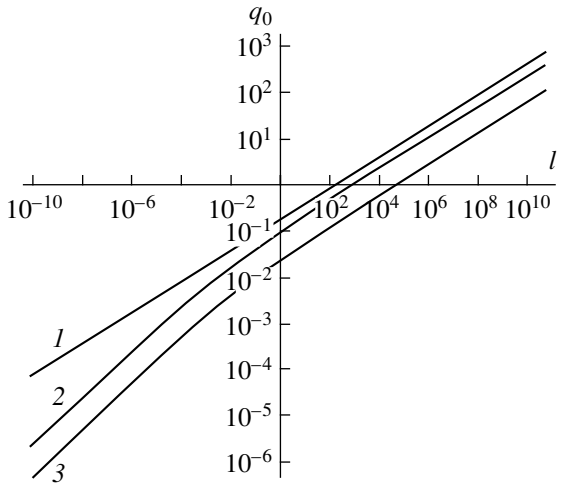

Fig. 2. Dependences of the macroscopic memory parameter q_0 on the correlation length l at different monomer fractions f = (*1*) 0.5, (*2*) 0.3, and (*3*) 0.1.

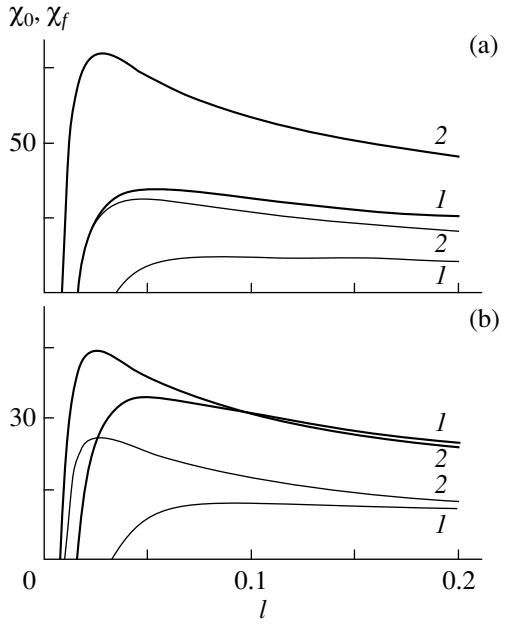

Fig. 3. Dependences of the characteristic Flory parameters at the ergodicity loss point χ_0 (heavy lines) and the freezing point χ_f (thin lines) on the correlation length l for (a) $\sigma = 0$ and different compositions f = (*1*) 0.5 and (*2*) 0.3 and (b) f = 0.5 and different interreplica overlap parameters σ = (*1*) 0 and (*2*) 2.

dependence $\chi_f(l)$ on the correlation length is depicted by the thin line in Fig. 3. It is significant that the $\chi_f(l)$ curve lies below the ergodicity loss curve $\chi_0(l)$ and has the same shape. The influence of the fraction of monomers of the A sort on the χ_0 and χ_f parameters is illustrated in Fig. 3a. These parameters increase as the heteropolymer composition deviates from the equiatomic composition. A more complex behavior is observed

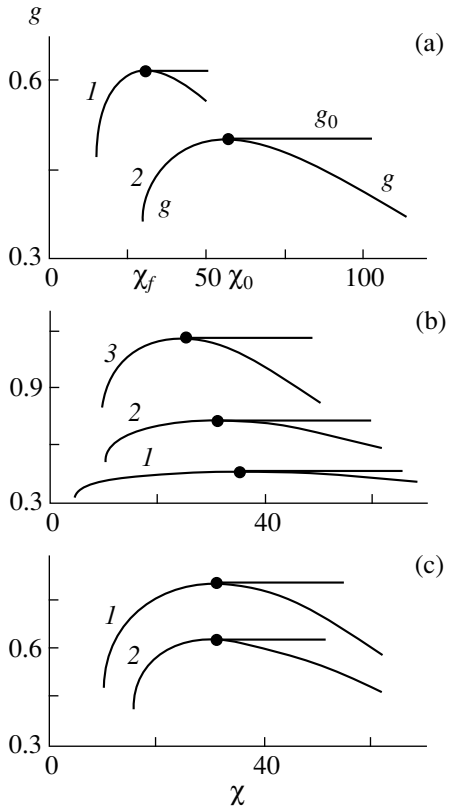

Fig. 4. Dependences of the microscopic g and macroscopic g_0 susceptibilities on the χ parameter for (a) $\sigma = 0$, $l = 0.1$, and different compositions $f = (1)$ 0.5 and (2) 0.3; (b) $f = 0.5$, $\sigma = 0$, and different correlation lengths $l = (1)$ 0.05, (2) 0.1, and (3) 0.2; and (c) $f = 0.5$, $l = 0.1$, and different interreplica overlap parameters $\sigma = (1)$ 0 and (2) 2.

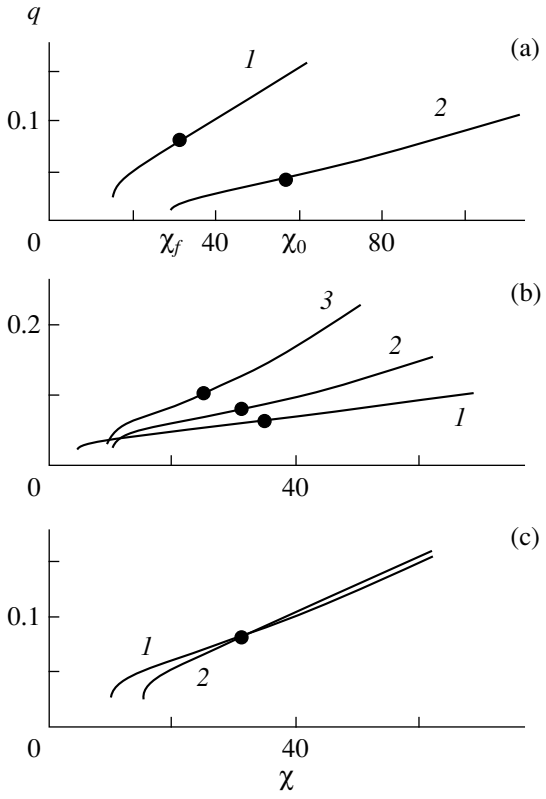

Fig. 5. Dependences of the microscopic memory parameter q on the Flory parameter χ for (a) $\sigma = 0$, $l = 0.1$, and different compositions $f = (1)$ 0.5 and (2) 0.3; (b) $f = 0.5$, $\sigma = 0$, and different correlation lengths $l = (1)$ 0.05, (2) 0.1, and (3) 0.2; and (c) $f = 0.5$, $l = 0.1$, and different interreplica overlap parameters $\sigma = (1)$ 0 and (2) 2.

with an increase in the interreplica overlap parameter σ (Fig. 3b). As the σ parameter increases, both parameters χ_0 and χ_f increase at small l, whereas the χ_0 parameter decreases at large l.

Figure 4 displays the dependences of the macroscopic g_0 and microscopic g susceptibilities on the parameter χ (below the ergodicity loss point χ_0, these susceptibilities, as well as the corresponding memory parameters q_0 and q, coincide). The dependence $g(\chi)$ terminates at the point $\chi = \chi_f$, below which the susceptibility g takes a zero value corresponding to the frozen state. Above the ergodicity loss point χ_0, the macroscopic susceptibility g_0 is constant and microscopic susceptibility g [determined by the simultaneous solution of Eqs. (60) and (61)] decreases monotonically. As can be seen from Fig. 4a, as the composition deviates from $f = 0.5$, the susceptibilities at the ergodicity loss and freezing points decrease and the corresponding values of χ_0 and χ_f increase. Figure 4b depicts the dependences $g(\chi)$ and $g_0(\chi)$ at different correlation lengths l. As expected, an increase in l results in a narrowing of the ergodic region. The influence of the interreplica overlap is shown in Fig. 4c. An increase in the corresponding parameter σ brings about a decrease in the susceptibilities $g(\chi)$ and $g_0(\chi)$, and, hence, the interreplica overlap hinders the glass transition in the heteropolymer.

The dependences of the microscopic memory parameter q on the thermodynamic parameter χ are displayed in Fig. 5. The distinctive feature is the absence of memory in the frozen region (below χ_f). The nonzero value of q appears at the freezing point χ_f, and a further increase in χ leads to an increase in the memory parameter. The jumpwise behavior of the q parameter suggests that this transition is a first-order transformation. It is evident that the contribution from fluctuations to the thermodynamic potential of the heteropolymer is the physical reason for the above jump. It can be seen from Fig. 5a that the dependence $q(\chi)$ becomes more flattened as the composition deviates from $f = 0.5$. By contrast, an increase in the correlation length l results in a steeper increase in the memory parameter (Fig. 5b). Finally, as is seen from Fig. 5c, the effect of the interreplica overlap parameter σ above and below the ergodicity loss point turns out to be opposite.

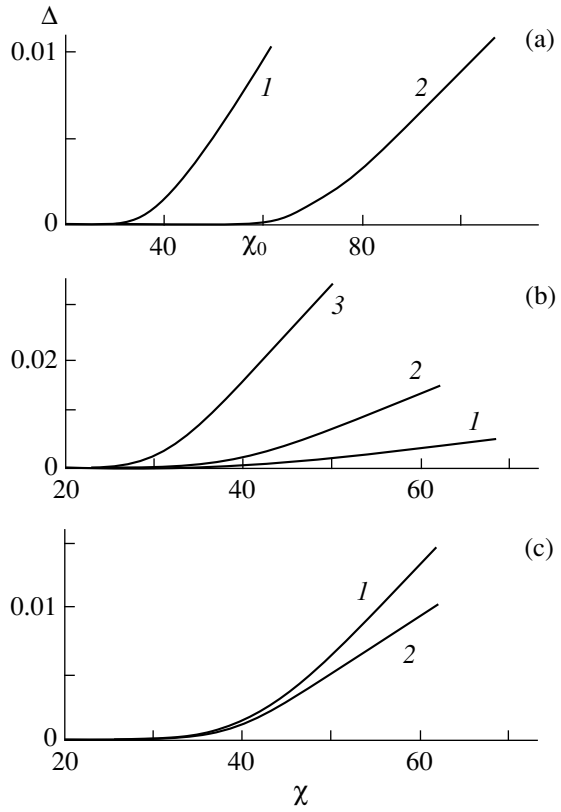

Fig. 6. Dependences of the nonergodicity parameter Δ on the χ parameter for (a) σ = 0, *l* = 0.1, and different compositions *f* = (*1*) 0.5 and (*2*) 0.3; (b) *f* = 0.5, σ = 0, and different correlation lengths *l* = (*1*) 0.05, (*2*) 0.1, and (*3*) 0.2; and (c) *f* = 0.5, *l* = 0.1, and different parameters σ = (*1*) 0 and (*2*) 2.

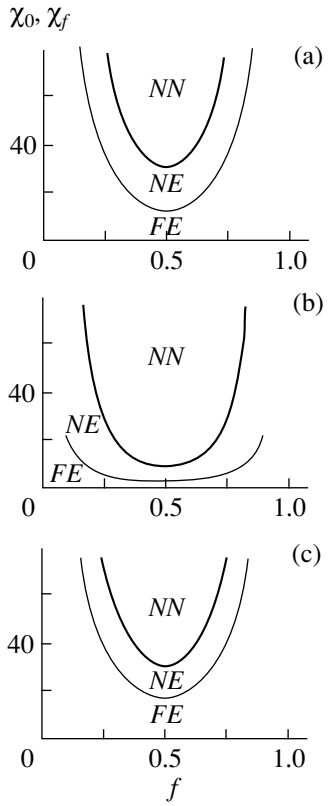

Fig. 7. Phase diagrams of a disordered heteropolymer for (a) σ = 0, *a* = 1, and *l* = 0.1; (b) σ = 0, *a* = 1, and *l* = 5; and (c) σ = 2, *a* = 1, and *l* = 0.1. Heavy lines show the ergodicity losses, and thin lines indicate the freezing. *FE*, *NE*, and *NN* correspond to the frozen ergodic, nonfrozen ergodic, and nonfrozen nonergodic phases, respectively.

As follows from the data shown in Fig. 6, the nonergodicity parameter $\Delta(\chi)$ monotonically increases with an increase in χ beginning with the ergodicity loss point χ_0. The deviation of composition from $f = 0.5$, a decrease in the correlation length *l*, and an increase in the interreplica overlap σ lead to a weakening of the nonergodicity effects.

The form of the phase diagram, which determines the possible thermodynamic states at different Flory parameters χ and compositions *f*, plays an important role in the search for new polymers with controlled properties. According to Fig. 7, this diagram for both the freezing point $\chi_f(f)$ and the ergodicity loss point $\chi_0(f)$ has the form of a concave curve. Note that the region of large χ values and compositions close to $f = 0.5$ corresponds to the nonergodic nonfrozen state. As the values of χ and $|f - 1/2|$ decrease, the system undergoes a transition, first, to the ergodic state and, then, to the frozen state. A comparison of Figs. 7a and 7b shows that the regions of the nonfrozen and nonergodic phases become wider with an increase in the correlation length *l*. By contrast, it is seen from Figs. 7a and 7c that the overlap between replicas results in their narrowing.

ACKNOWLEDGMENTS

We are grateful to S.I. Kuchanov for the formulation of the problem and participation in discussions of the results.

This work was supported in part by the Ukrainian State Committee of Science and Engineering, project no. 2.4/4.

REFERENCES

1. C. D. Sfatos and E. I. Shakhnovich, Phys. Rep. **288**, 77 (1997).
2. F. S. Bates and G. H. Fredrickson, Annu. Rev. Phys. Chem. **41**, 525 (1990).
3. R. Holyst and T. A. Vilgis, cond-mat/9603063 (1996).
4. M. Mezard, G. Parisi, and M. A. Virasoro, *Spin Glass Theory and Beyond* (World Scientific, Singapore, 1987).
5. L. Leibler, Macromolecules **13** (6), 1602 (1980).
6. S. A. Brazovskiĭ, Zh. Éksp. Teor. Fiz. **68** (1), 175 (1975) [Sov. Phys. JETP **41**, 85 (1975)].
7. G. H. Fredrickson and E. Helfand, J. Chem. Phys. **87** (1), 697 (1987).
8. V. S. Pande, A. Yu. Grosberg, and T. Tanaka, Phys. Rev. E **51** (4), 3381 (1995).

9. A. V. Dobrynin and I. Ya. Erukhimovich, J. Phys. I **5** (3), 365 (1995).
10. S. Stepanov, A. V. Dobrynin, T. A. Vilgis, and K. Binder, J. Phys. I **6**, 837 (1996).
11. G. H. Fredrickson, S. T. Milner, and L. Leibler, Macromolecules **25** (23), 6341 (1992).
12. E. G. Timoshenko, Yu. A. Kuznetsov, and K. A. Dawson, Phys. Rev. E **54** (4), 4071 (1996).
13. A. Yu. Grosberg, Usp. Fiz. Nauk **167** (2), 130 (1997) [Phys. Usp. **40**, 125 (1997)].
14. D. Sherrington and S. Kirkpatrick, Phys. Rev. Lett. **35** (26), 1792 (1975).
15. J. Kurchan, J. Phys. I **2**, 1333 (1992).
16. A. I. Olemskoi, I. V. Koplyk, and V. A. Brazhnyi, J. Phys. Stud. **1** (3), 324 (1997).
17. T. A. Vilgis, J. Phys. A **24**, 5321 (1991).
18. S. L. Ginzburg, Zh. Éksp. Teor. Fiz. **85** (6), 2171 (1983) [Sov. Phys. JETP **58**, 1260 (1983)].
19. A. I. Olemskoi, Physica A (Amsterdam) **265** (2–4), 545 (1999).
20. J. Zinn-Justin, *Quantum Field Theory and Critical Phenomena* (Clarendon Press, Oxford, 1993), p. 914.
21. A. I. Olemskoi and V. A. Brazhnyi, Physica A (Amsterdam) **271**, 368 (1999); cond-mat/9812286 (1998).
22. M. Doi and S. F. Edwards, *The Theory of Polymer Dynamics* (Clarendon Press, Oxford, 1986), p. 391.
23. T. Halpin-Healy and Y.-C. Zhang, Phys. Rep. **254** (4–6), 215 (1995).
24. A. I. Olemskoĭ, Usp. Fiz. Nauk **168** (3), 287 (1998) [Phys. Usp. **41**, 269 (1998)].
25. H. Risken, *The Fokker–Planck Equation* (Springer-Verlag, Berlin, 1989), p. 472.
26. R. J. Glauber, J. Math. Phys. **4** (2), 294 (1963).
27. E. I. Kats, V. V. Lebedev, and A. R. Muratov, Phys. Rep. **228** (1–2), 1 (1993).
28. A. I. Olemskoĭ and V. A. Brazhnyĭ, Ukr. Fiz. Zh. **44** (7), 292 (1999).
29. E. I. Shakhnovich and A. M. Gutin, J. Phys. (Paris) **50** (14), 1843 (1989).
30. S. F. Edwards and P. W. Anderson, J. Phys. F **5**, 965 (1975).

Translated by O. Borovik-Romanova

Physics of the Solid State, Vol. 43, No. 2, 2001, pp. 397–400. Translated from Fizika Tverdogo Tela, Vol. 43, No. 2, 2001, pp. 379–382.

POLYMERS AND LIQUID CRYSTALS

The Photovoltaic Effect in Poly(alkylthiophene) Films on a Silicon Substrate

A. S. Komolov

Research Institute for Physics, St. Petersburg State University, Ulyanovskaya ul. 1, St. Petersburg, 198504 Russia

e-mail: komolov@mph.phys.spbu.ru

Received May 12, 2000

Abstract—A study of photovoltage was made for a series of sandwich structures on the basis of poly(3-dodecylthiophene) films having characteristic thicknesses 100 and 500 nm and being deposited on *n*-Si and *p*-Si substrates from a solution. Semitransparent Al and Au electrodes were obtained on the surfaces of these films by thermal evaporation. A clear photoresponse was obtained in films on an *n*-Si substrate. Two distinct spectral components of the photovoltage were observed in the 1.3- to 3.6-eV (900–300 nm) energy range for incident quanta. The first component corresponds to the absorption edge of the Si substrate (1.4–1.6 eV). The other corresponds to the π–π* absorption of the polythiophene films (1.7–2.1 eV). The dependences of the photovoltage upon radiation intensity are different for these two spectral components. The relaxation time of the photoresponse for the second component, corresponding to the absorption in the film, is 10–20 min. This is 3–4 orders of magnitude higher than the relaxation time for the first component. A model of the potential barrier at the polythiophene/*n*-Si interface, allowing one to explain the main experimental results, is proposed. This barrier is formed as a result of the chemical interaction of the polythiophene molecules with the substrate. © *2001 MAIK "Nauka/Interperiodica".*

INTRODUCTION

Recently, the electronic properties of thin films of semiconductor polymers such as polypyrrole, polyphenylene venylene, and polythiophene have attracted the great interest of researchers [1–3]. This is due to the possibility of using these films in light-emitting and photoelectric microelectronic devices [3–5]. The charge transport in such structures is discussed under the assumption that the potential varies linearly through the thickness of the film [6]. The study of the interaction of such organic films with metals and semiconductors is of importance for understanding the physicochemical mechanisms of photovoltaic processes. The interaction processes that accompany the thermal deposition of organic films are intensively studied by electronic spectroscopy [7, 8]. It is shown that the interaction of aromatic macromolecules, such as polythiophene, with metallic or semiconductor substrates is typically accompanied by the formation of donor–acceptor bonds with a negative-charge transfer from the interface into the substrate [7, 9–11]. To take these processes into account, one needs to go beyond the linear approximation to the potential variation in the film and take into consideration the potential barrier at the interface.

The results of investigations of the photovoltage spectrum and of the dependences of the photovoltage upon radiation intensity and its transient characteristics are analyzed in this work for a series of structures containing poly(alkylthiophene) films. The phenomena observed are discussed taking into account both the energy band characteristics of these films and the properties of the potential barrier at the boundary between the film and the *n*-Si substrate.

1. EXPERIMENT

The layered structures under investigation were based on films of regular poly(3-dodecylthiophene) (PDDT) (Fig. 1) deposited from its solution in xylene. The film thicknesses were 500 and 100 nm, as determined by both the capacity voltage characteristics method [12] and optical interference microscopy. The length of the polymer PDDT chains was as large as 50 thiophene monomers, as follows from comparison of the optical absorption spectra for the films studied with literature data [13, 14].

The films were deposited on *n*-Si and *p*-Si substrates (10 Ω cm) which were subjected to etching in HF and boiling in an H_2O_2/H_2SO_4 mixture before film deposition. After this standard procedure, a 3–4 nm thick silicon oxide layer remained on the surface [12]. The upper electrodes were deposited on the film surface by thermal evaporation of semitransparent layers of Au or Al in vacuum (10^{-5} torr) and had a cross-section area of 0.1 cm^2. The decrease in the intensity of incident radiation inside the semitransparent electrode was measured and taken into account in the course of analysis of the photovoltaic characteristics.

1063-7834/01/4302-0397$21.00

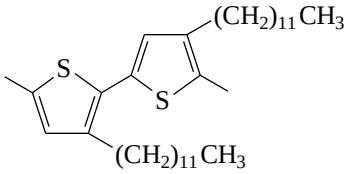

Fig. 1. Chemical structure of a fragment of the poly(3-dodecylthiophene) molecule.

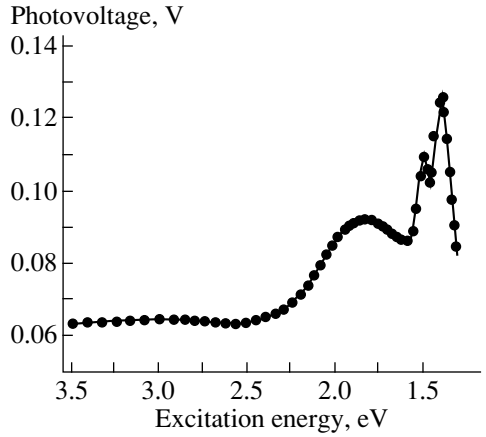

Fig. 2. The photovoltage spectrum for the *n*-Si/PDDT/Au structure. The radiation intensity is 10^{14} photon/(cm^2 s).

The investigation of photovoltage was carried out under atmospheric conditions at room temperature on an automatic setup, which was described in detail in our previous work [15]. To measure the spectral characteristics, radiation of an intensity of 10^{14} photon/(cm^2 s) was used. This corresponds to $(2–7) \times 10^{-5}$ W cm^{-2} in the range of incident quantum energies, 1.3–3.6 eV, used (900–300-nm wavelength range).

2. RESULTS AND DISCUSSION

A distinct photovoltaic effect is detected in structures prepared on an *n*-Si substrate. The external electrode possessed a positive potential relative to the substrate. Its values were as large as 0.15 V under the action of 10^{14} photon/(cm^2 s) radiation in the visible wavelength range. The observed photovoltage values are considerably higher than those presented in the literature for analogous structures [5]. The photovoltage in the *n*-Si/film/Au structure exhibits a distinct spectral dependence in the 1.3–3.6 eV quantum energy range (Fig. 2). The photovoltage spectrum has two distinct components. One of them (the sharpest peaks) is situated within the 1.4–1.6 eV energy range. This component is due to radiation absorption in the boundary layer of the *n*-Si substrate [13, 16]. The other spectral component of the photovoltage is represented by a broader peak in the 1.7–2.2 eV range. Its energetic position corresponds to the absorption energy of the interband π–π^* transitions in the polythiophene film. This energy lies in the 2.1–2.2 eV range according to the spectrum of the optical absorption of the PDDT films [13] and to the literature data [2, 17]. It should be noted that we also detected two spectral components when studying the photovoltage in structures based on semiconductor organic films of a different type on *n*-Si substrates [15].

The dependences of the photovoltage upon radiation intensity and the transient characteristics are found to be different for these two voltage components. The dependences of the photovoltage in the *n*-Si/PDDT/Au structures upon radiation intensity are shown in Fig. 3. In the case of the spectral component resulting from radiation absorption in the film (a quantum energy of 1.9 eV), the intensity dependence of the photovoltage (Fig. 3a) has a power-law character with an exponent of about 0.5. When the incident quantum energy is 1.4 eV (Fig. 3b), the photovoltage increases in proportion to the logarithm of the intensity. This is typical of the photovoltage resulting from the photoexcitation of charge carriers in the depletion Schottky layer [18].

Relaxation times as long as tens of seconds (Fig. 4a) are typical of transient photovoltage characteristics in the absorption band of PDDT films. This can be due to localized states and the low mobility of charge carriers in these films, as was indicated in the literature [3, 19]. The relaxation time of the transient characteristics is several orders of magnitude lower near the absorption edge for silicon, 1.4 eV (Fig. 4b).

For the structures with an *n*-Si substrate, the discovered photovoltaic effect does not depend upon the external electrode material (Au or Al). Moreover, analogous results were obtained by us in the case when a slow electron beam in vacuum was used instead of an external electrode [20].

One can conclude that the external electrode/film interface does not influence the observed effect. An interesting experimental result is that the photovoltage characteristics are the same for the 100- and 500-nm thick PDDT films. This suggests that even the photovoltage observed in the spectral PDDT absorption band is due to processes proceeding in the film region near the *n*-Si/film interface rather than in the bulk of the film. In the studied structures with the *p*-Si substrate, the photovoltaic effect was not observed. The photovoltage was also not detected in the structures of the metal/film/metal type for different combinations of substrates and upper electrodes made of Au and Al.

The occurrence of photovoltage with two components in the studied structures with an *n*-Si substrate can be explained using a band energetic diagram (Fig. 5). A simplified version of this diagram was previously used by us to explain the conduction properties of a series of structures based on PDDT films [13]. Different values of the band energetic parameters of *n*-Si,

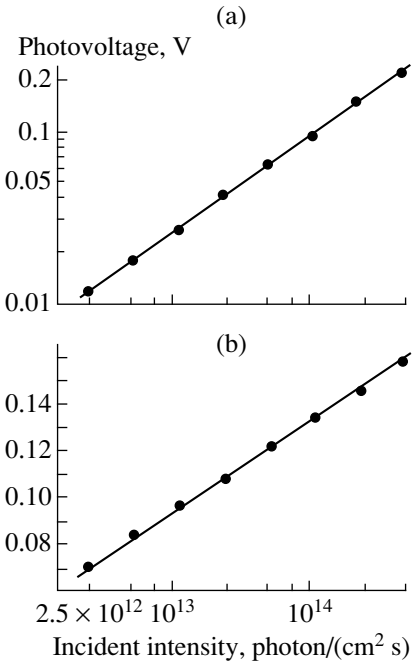

Fig. 3. Dependences of the photovoltage radiation intensity for the energies of incident quanta of (a) 1.9 and (b) 1.4 eV.

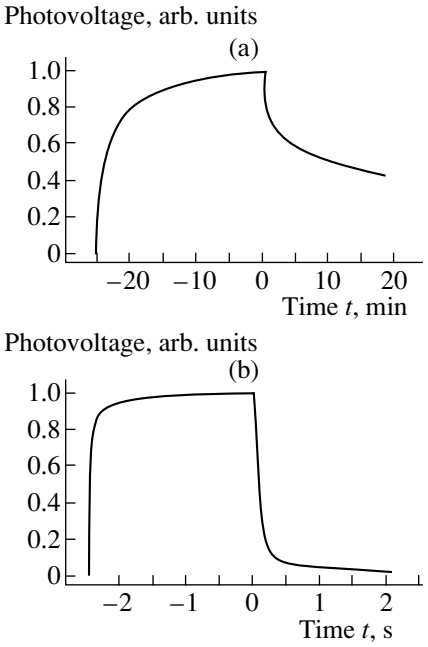

Fig. 4. Transient photovoltage characteristics for the *n*-Si/PDDT/Au structure for the energies of incident quanta of (a) 1.9 and (b) 1.4 eV.

PDDT films, and metal electrodes are used in the diagram. These values correspond to the data of [4, 6, 16], as well as to our data on the optical absorption of the PDDT films [17]. The band edges E_c and E_v in PDDT are understood in the same sense as in the case of noncrystalline semiconductors [2]. Of great importance in the formation of photovoltage is the band bending occurring in the vicinity of the *n*-Si/PDDT interface (Fig. 5). The amount of band bending in *n*-Si and in the film have been evaluated using the fact that the photovoltage growth reaches its saturation for intensities exceeding 5×10^{14} photon/(cm^2 s). It is assumed that there is a thin SiO_2 layer at the interface. The role of this layer in the observed photovoltaic processes has not yet been completely elucidated.

The main reason for the band bending (Fig. 5) is a PDDT π-electron orbital pulling towards the substrate. The existence of such a charge transfer was proven experimentally by studying the interaction of various aromatic molecules with a silicon surface [7, 9–11]. Additional negative charge at the interface causes the formation of a depletion layer in *n*-Si. Pulling of the π-electron orbitals of PDDT molecules as a result of the donor–acceptor interaction with the substrate leads to the formation of a positive charge layer in the PDDT film near the interface. The characteristic thickness of such a layer is 10 nm [7, 9]. The photo holes, excited in this layer, drift towards the interface and compensate its negative charge. This is accompanied by lowering of the potential barrier at the interface, which leads to creation of the photovoltage component in the 1.7–2.2 eV quantum energy range. The value of the barrier lowering is proportional to the concentration of the photoexcited holes, which leads to the power-law dependence of the photoresponse on intensity (Fig. 3a). Slow relaxation of the photovoltage is caused by photohole drift in the vicinity of the polarization barrier in the film. The other photovoltage component, situated in the 1.4–1.6 eV quantum energy range, is associated with photoelectric processes in the depletion *n*-Si layer taking place according to the Schottky mechanism, which explains the linear dependence of the photovoltage on the logarithm of the intensity and the relatively rapid photovoltage relaxation. The absence of the photovoltage in the studied structures with the *p*-Si substrate is due to the fact that even if the formation of the donor–acceptor bonds at the interface is possible, the negative charge will be screened by the majority charge carriers in the *p*-Si. Since the concentration of these carriers is fairly large, band bending in the vicinity of the interface will virtually not take place.

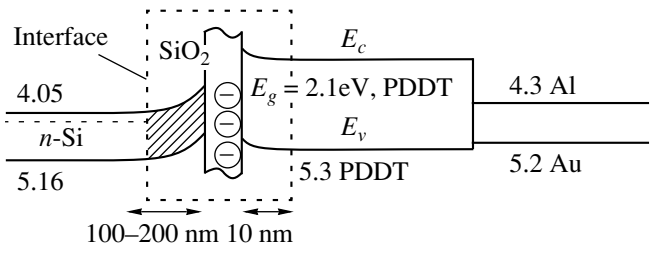

Fig. 5. Band energetic diagram for the *n*-Si/SiO_2/PDDT/Au (or Al) structure. The Fermi energy of the metal electrodes, the electron affinity, the ionization potential of Si, and the ionization potential of the PDDT film are measured in eV.

ACKNOWLEDGMENTS

This work was supported by the Russian Foundation for Basic Research, grant no. 99-03-33427, and the Russian State program "Surface Atomic Structures," grant no. 4.3.99.

REFERENCES

1. M. Nechtstein, in *Organic Conductors*, Ed. by J. P. Farges (Marcel Dekker, New York, 1994), p. 647.
2. C. Ziegler, in *Handbook of Organic Conductive Molecules and Polymers*, Ed. by H. S. Nalwa (Wiley, New York, 1997), p. 677.
3. R. H. Friend and N. C. Greenham, in *Handbook of Conducting Polymers*, Ed. by T. A. Skotheim, R. L. Elsenbaumer, and J. R. Reynolds (Marcel Dekker, New York, 1998, 2nd ed.), p. 823.
4. Y. Yang, MRS Bull., No. 6, 31 (1997).
5. C. Kvarnstrom and A. Ivaska, in *Handbook of Organic Conductive Molecules and Polymers*, Ed. by H. S. Nalwa (Wiley, New York, 1997), p. 487.
6. I. D. Parker, J. Appl. Phys. **75** (3), 1656 (1994).
7. H. Iskii, K. Sugiyama, E. Ito, and K. Seki, Adv. Mater. **11** (8), 605 (1999).
8. W. R. Salaneck, S. Statsfrom, and J. L. Bredas, in *Conjugated Polymer Surfaces and Interfaces* (Cambridge Univ. Press, Cambridge, 1996), p. 1.
9. Th. Kugler, U. Thibaut, M. Abraham, *et al.*, Surf. Sci. **260**, 64 (1992).
10. T. Chasse, C. I. Wu, I. G. Hill, and A. Kahn, J. Appl. Phys. **85** (9), 6589 (1999).
11. I. G. Hill and A. Kahn, J. Appl. Phys. **84** (10), 5583 (1998).
12. A. S. Komolov, V. Monakhov, K. Schaumburg, *et al.*, Phys. Low-Dimens. Struct. **10**, 41 (1997).
13. A. S. Komolov, K. Schaumburg, and V. Monakhov, Synth. Met. **105** (1), 29 (1999).
14. T. Bjornholm, D. Greve, T. Geisler, *et al.*, Adv. Mater. **8** (11), 920 (1996).
15. A. S. Komolov, K. Schaumburg, and V. Monakhov, Thin Solid Films **311** (1–2), 259 (1997).
16. S. M. Sze, *Physics of Semiconductor Devices* (Wiley, New York, 1981; Mir, Moscow, 1984), Sect. 1.6, Append. H.
17. J. L. Bredas, G. B. Street, B. Themans, *et al.*, J. Chem. Phys. **83** (3), 1323 (1985).
18. R. H. Bube, *Photoelectronic Properties of Semiconductors* (Cambridge Univ. Press, Cambridge, 1992), p. 318.
19. H. G. Keiss, *Conjugated Conducting Polymers* (Springer-Verlag, Berlin, 1992).
20. E. F. Lazneva, N. Andreeva, A. S. Komolov, *et al.*, Phys. Low-Dimens. Struct. **10**, 71 (1997).

Translated by A. Sonin